University of Oxford

Department of Chemistry



Layered Double Hydroxide-based Core-shells for CO_2 Adsorption and Conversion

Meng Lyu

Keble College

Trinity 2021

This thesis is submitted in partial fulfilment of the requirement for the degree of

Doctor of Philosophy at the University of Oxford

Preface

The work described in this thesis was carried out in the Chemistry Research Laboratory at the University of Oxford between November 2017 and June 2021 under the supervision of Professor Dermot O'Hare. All the work was performed by the author unless otherwise stated and no part has been previously submitted for any other degree.

Part of the work contained in this thesis has been published in the following article.

M. Lyu, C. Chen, J.-C. Buffet, and D. O'Hare, *New J. Chem.*, 2020, **44**, 10095-10101.

Abstract

Layered Double Hydroxide-based Core-shells for CO_2 Adsorption and Conversion

Meng Lyu **D.Phil Thesis**

Keble College **Trinity Term 2021**

This thesis discusses the development of novel layered double hydroxide-based (LDH-based) core-shells as CO_2 adsorbents and as catalysts for the both the selective hydrogenation of CO_2 to methanol and conversion to olefins.

Chapter 1 offers a brief introduction of LDHs as 2D anionic layered materials with versatile composition and wide application, and LDH based core-shell materials which can combine both advantages of inorganic cores and LDHs to display synergy effects. The background literature relating to CO_2 adsorption, CO_2 hydrogenation to methanol and CO_2 conversion to olefins are introduced. The application of LDH and LDH-based core-shell materials in these fields is also presented and discussed.

Chapter 2 describes the synthesis and characterisation a series of zeolite@Mg_2Al-LDH core-shell materials and the application of these materials as CO_2 adsorbents. It was found that core-shells containing 5 wt% LDH exhibit the highest CO_2 sorption capacity (5.75 mmol/g at 1 bar and 35 °C), better than most of the core-shell adsorbents and competing with some MOFs.

Chapter 3 systematically investigates the synthesis of mesoporous SiO_2@Cu_xZnAl-LDH core-shells (mSiO_2@Cu_xZnAl-LDH). The effect of metal solution addition rate, reaction pH, LDH content in the core-shell, copper loading of the LDH, concentration of reaction mixture, pre-treatment (aluminium nitrate wet impregnation) and the roles of the silica on the crystallinity, composition and morphology of core-shells are explored.

Chapter 4 focuses on the application of mSiO_2@Cu_xZnAl-LDH for the selective hydrogenation of CO_2 to methanol. The effect of copper loading and the effect of silica core on the catalytic activity was investigated using ES757@Cu_xZnAl LDH and mSiO_2@Cu_2ZnAl-LDH, respectively. ES757@$Cu_{1.3}$ZnAl exhibits the best space time yield of methanol due to the highest copper metal nanoparticle surface. It was found that catalysts derived from ES757@$Cu_{1.3}$ZnAl LDH and mSiO_2@Cu_2ZnAl LDH can outperform current industry standards for methanol production at a lower copper loadings.

Chapter 5 presents the design of zeolite@$Cu_{1.3}$ZnAl-LDHs and their catalytic evaluation for the conversion of CO_2 to olefins. Preliminary catalytic results were obtained, it was noted that the sodium in the reaction mixture modified the acidity of zeolite and changed the product selectivity. Alternatives to modify the acidity of catalyst were conducted which includes post-treatment with ammonium salt and sodium-free synthesis.

Chapter 6 summarised the findings of the work of this thesis. Chapter 7 describes the experimental details of the work presented in this thesis. Supplementary information and data referred to in the main content are found in the Appendices.

Acknowledgements

The last four years have been a long journey with fun and challenge. There are so many people to whom I am immensely grateful. Without you, this journey would likely not have been possible and certainly not interesting.

Firstly, I would like to thank my supervisor, Professor Dermot O'Hare, for welcoming me into your group, and for all the guidance and advice throughout my studies. Secondly, I would like to thank China Scholarship Council and University of Oxford for the financial support, receiving the China Scholarship Council-University of Oxford scholarship has been a privilege and I am incredibly thankful for it.

I'm sincerely grateful to Chunping. Thank you for being incredibly supportive and inspiring during the past four years. Your help (both inside lab and outside), encouragement and supervision has been vital and enormously appreciated. I would like to acknowledge JC for all the support, help and patience. Thank you to Zoe for all those speedy corrections, they were life-savers.

Many thanks to Justin and Maureen: we've made it! It has been great to explore the LDH with you Justin. Thank you to Maureen for sharing the cute cats and memes. Thank you for being awesome lab colleagues, for having supported me and had to put up with my stresses for the past four years of study!

To Clara, an immense thank you for your guidance and mentorship in my first year. Thank you to Jingfang and Dana for all the chats, discussion and help troubleshoot the 'wares (hard-, soft-, etc.) Many thanks to Phil for all the inspiring and useful chats, the knowledge you've shared and the fun we had.

The rest of the O'Hare group members, past and present, thank you for making the last four years enjoyable and entertaining.

Thanks also goes the people who have helped with some of the chemistry; Nick for ssNMR, Simon for answering all my TOPAS questions, Jianwei for all the catalytic ability testing, Neil, Jennifer and other technicians of DCCEM for the TEM, SEM and HR-SEM training and troubleshooting.

I am also grateful to everyone who found the time to proofread this thesis; your suggestions have been invaluable.

Outside of the lab, I would like to thank my friends and flatmates. Thank you to Hong for being a nice flatmate who has contributed to some amazing memories. Thank you to Yinuo for introducing me fantastic fictions and all the chats about the literature. Thank you to Danlei for sharing the cooking knowledge.

Lastly, my biggest thanks to my incredible family (especially my parents, my cousin Yang and her husband) for their love and endless support through my studies. You mean the world to me, and I couldn't have done any of this without you.

Nomenclature

Below is a summary of some of the commonly used terms throughout the thesis.

Term	Definition
°C	Degrees Celsius
Å	Angstrom (10^{-10} m)
a.u.	Arbitrary units
AMOST	Aqueous miscible organic solvent treated
BET	Brunauer-Emmett-Teller
BJH	Barrett-Joyner-Halenda
CDL	Crystal domain length
CHN	Carbon, hydrogen and nitrogen
CPMAS	Cross-polarization magic angle spinning
CO_2	Carbon dioxide
DCCEM	David Cockayne Centre for Electron Microscopy
DFT	Density functional theory
DI	Deionized
DPMAS	Direct-polarisation magic angle spinning
dTG	First derivative of thermal gravimetric analysis curve
EA	Elemental analysis
FID	Flame ionization detector
FTIR	Fourier transform infrared
g	Gram
GHSV	Gas hourly space velocity
h	Hour(s)
HR-SEM	High resolution scanning electron microscopy

ICP-MS	Inductively coupled plasma mass spectrometry
ICP-OES	Inductively coupled plasma atomic emission spectroscopy
kJ	Kilojoule
LDH	Layered double hydroxide
LDO	Layered double oxide
M^{II}	Divalent metal ion
MeOH	Methanol
MHz	Megahertz
mmol	Millimol (×10–3 mol)
mM	Millimolar ($\times 10^{-3}$ mol/L)
μm	Micrometre ($\times 10^{-6}$ m)
MMT	Montmorillonite
NaOH	Sodium hydroxide
Na_2CO_3	Sodium carbonate
nm	Nanometre ($\times 10^{-9}$ m)
O_h	Octahedral
PCC	Post-combustion carbon capture
PSD	Pore size distribution
RH	Relative humidity
rpm	Rotations per minute
SEM	Scanning electron microscopy
SEM-EDS	Scanning electron microscopy energy dispersive X-ray spectroscopy
ssNMR	Solid-state NMR
stp	standard temperature and pressure
STEM	Scanning transmission electron microscopy
TCD	Thermal conductivity detector
T_d	Tetrahedral

TEM	Transmission electron microscopy
TEM-EDS	Transmission electron microscopy energy dispersive X-ray spectroscopy
TGA	Thermogravimetric analysis
TPD	Temperature programmed desorption
TPR	Temperature programmed reduction
wt%	Weight percentage
XRD	X-ray diffraction
zgbs	Predefined pulse programme set by Bruker

Table of content

Chapter 1 Introduction **1**

1.1 Layered double hydroxides (LDHs) **1**

1.1.1 Structure and composition 1
1.1.2 Synthesis methods 3
1.1.3 Layered double oxides (LDOs) 6
1.1.4 Applications 7

1.2 Layered double hydroxide-based core-shell composites **7**

1.2.1. Synthesis methods 9
1.2.2. Varation of cores and applications 11
1.2.3. Characterisation of core-shells 11

1.3 CO_2 capture and utilisation **15**

1.3.1. CO_2 capture 16
1.3.1.1. Solid adsorbents for carbon capture 18
1.3.1.1.1 LDH-based adsorbents for post-combustion CO_2 capture 20
1.3.1.1.2 Core-shell adsorbents for carbon capture 22
1.3.2. CO_2 utilisation 23
1.3.2.1. Catalytic CO_2 hydrogenation to methanol 24
1.3.2.1.1. LDH-based catalysts for CO_2 to methanol 27
1.3.2.1.2. Core-shell catalysts for CO_2 to methanol 28
1.3.2.2. Catalytic CO_2 conversion to olefins 30
1.3.2.2.1. LDH-based catalysts for CO_2 to olefins 32
1.3.2.2.2. Core-shell catalysts for CO_2 to olefins 33
1.3.2.2.3. LDH-based core-shell catalysts for CO_2 to olefins 34

1.4 Scope of thesis **35**

1.5 References **36**

Chapter 2. Synthesis and CO_2 capture of Zeolite@Mg_2Al-CO_3-LDH core-shell materials **45**

2.1. Introduction **45**

2.2. Synthesis and characterisation of Z13X@Mg_2Al-CO_3-LDH **46**

2.2.1. Synthesis and characterisation of Z13X@Mg_2Al-CO_3-LDH 46
2.2.2. Effect of metal nitrate addition rate 54
2.2.3. Effect of ageing time 59
2.2.4. Effect of LDH fraction 62

2.3. CO2 capture performance of Z13X@Mg_2Al-CO_3-LDH **68**

2.3.1. Effect of addition time and ageing time 76
2.3.2. Effect of LDH fraction in Z13X@Mg_2Al-CO_3-LDH 76

2.4. Conclusions 78

2.5. Reference 80

Chapter 3 Synthesis and characterisation of porous SiO_2@Cu_xZnAl-CO_3-LDH core-shell materials 83

3.1 Introduction 83

3.2 Synthesis and characterisation of MCM-48@Cu_xZnAl-CO_3-LDH 85

3.2.1. Synthesis and characterisation of MCM-48@$Cu_{1.3}ZnAl$-CO_3-LDH 85
3.2.2. The effect of varying the reaction conditions 96
3.2.3. Variation of copper content 104
3.2.3.1. Variation of LDH content 105
3.2.3.2. Variation of Cu density in LDH 109

3.3 Synthesis and characterisation of ES757@Cu_xZnAl-CO_3-LDH 121

3.3.1. The effect of synthetic conditions on ES757@Cu_4ZnAl-CO_3-LDH 121
3.3.2. The effect of Cu content on ES757@Cu_xZnAl-CO_3-LDH 128

3.4 Synthesis of mesoporous SiO_2@Cu_2ZnAl-CO_3-LDH 134

3.5 Conclusions 145

3.6 References 147

Chapter 4 Evaluation of porous SiO_2@Cu_xZnAl-CO_3-LDH for catalytic hydrogenation of CO_2 to methanol 151

4.1 Introduction 151

4.2 The effect of Cu loading on ES757@Cu_xZnAl-CO_3-LDH derived catalysts 152

4.2.1. Activation of ES757@Cu_xZnAl-LDH 152
4.2.2. Catalytic performance and copper dispersion of ES757@Cu_xZnAl 158

4.3 The effect of silica core on catalytic performance 165

4.4 Benchmarking studies of catalytic performance 169

4.5 Conclusions and outlook 171

4.6 References 173

Chapter 5. Studies of CO_2 to olefins conversion using a ZSM-5@$Cu_{1.3}ZnAl$-CO_3-LDH core-shell catalyst precursor 175

5.1. Introduction 175

5.2. Synthesis and characterisation of ZSM-5@$Cu_{1.3}ZnAl$-CO_3-LDH 176

5.3. Preliminary studies of CO_2 to olefins conversion using ZSM@$Cu_{1.3}$ZnAl-LDH 187

5.3.1. Reaction conditions and setup 187
5.3.2. Catalytic results for ZSM@$Cu_{1.3}$ZnAl....188

5.4. Variations of acidity of ZSM@$Cu_{1.3}$ZnAl-LDH via post-treatment methods....191

5.4.1. Post-treatment with ammonium salts....191
5.4.2. Studies of catalyst acidity 194

5.5. Sodium-free synthesis of ZSM@$Cu_{1.3}$ZnAl-LDH....198

5.5.1. Homogeneous precipitation 198
5.5.2. Co-precipitation with organic base 202

5.6. Conclusions and Outlook....208

5.7. References....209

Chapter 6 Conclusions and Outlook....213

Chapter 7. Experimental Details....219

7.1. Analytical techniques for characterisation....219

7.2. Experimental details for Chapter 2....223

7.2.1. Materials 223
7.2.2. Synthesis procedure of Z13X@Mg_2Al-LDH 223
7.2.3. Synthesis procedure of Z13X@Mg_2Al-CO_3-LDH with different dropping time or ageing time....224
7.2.4. Synthesis procedure of Z13X@Mg_2Al-CO_3-LDH with different LDH content 224
7.2.5. Synthesis of Z13X@Mg_2Al layered double oxide (LDO) core-shells 225
7.2.6. CO_2 adsorption ability test....225
7.2.7. CO_2 temperature programmed desorption (TPD)....225

7.3. Experimental details for Chapter 3....226

7.3.1. Materials 226
7.3.2. General synthesis procedure of MCM-48@$Cu_{1.3}$ZnAl-CO_3-LDH....226
7.3.3. Synthesis of MCM-48@$Cu_{1.3}$ZnAl-CO_3-LDH with varied synthetic condition 227
7.3.4. Synthesis of MCM-48@CuZnAl-CO_3-LDH with varied Cu content....228
7.3.5. General synthesis procedure of ES757@Cu_4ZnAl-CO_3-LDH 229
7.3.6. Synthesis of ES757@Cu_4ZnAl-CO_3-LDH with varied synthetic condition....229
7.3.7. Synthesis of ES757@Cu_xZnAl-CO_3-LDH with varied Cu content....230
7.3.8. Synthesis of mesoporous mSiO_2@Cu_2ZnAl-LDH 231

7.4. Experimental details for Chapter 4....232

7.4.1. Activation of catalyst precursors (mSiO_2@Cu_xZnAl-CO_3-LDH) 232
7.4.2. Hydrogen temperature programmed reduction (H_2-TPR) 232
7.4.3. Catalytic tests for CO_2 hydrogenation reaction 233

7.4.4. Nitrous oxide (N_2O) reduction of ES757@Cu_xZnAl catalysts 233

7.5. Experimental details for Chapter 5 234

7.5.1. Materials 234
7.5.2. Synthesis procedure of ZSM-5@$Cu_{1.3}$ZnAl-CO_3-LDH 234
7.5.3. Ammonium bicarbonate treated ZSM-5@$Cu_{1.3}$ZnAl-CO_3-LDH 235
7.5.4. Homogeneous precipitation synthesis of $Cu_{1.3}$ZnAl-CO_3-LDH 236
7.5.5. Sodium-free co-precipitation of H-ZSM-5@$Cu_{1.3}$ZnAl-CO_3-LDH 236
7.5.6. Activation of catalyst precursors 237
7.5.7. NH3 temperature programmed desorption (TPD) traces 237
7.5.8. Catalytic test for CO_2 hydrogenation reaction 238
7.5.9. Catalytic test for methanol to olefins (MTO) reaction on H-ZSM-5 239

7.6. Reference 239

Appendix A. Appendices to Chapter 2 ..... A-1
A.1 Characterisation for Z13X@Mg_2Al LDH A-1
A.2 Z13X@Mg_2Al LDHs with varied metal addition time A-5
A.3 Z13X@Mg_2Al LDHs with varied ageing time A-7
A.4 Z13X@Mg_2Al LDHs with varied LDH content A-10
A.5 Z13X@Mg_2Al LDOs A-13
A.6 Reference A-14

Appendix B: Appendix for Chapter 3 1
B.1 Synthesis and characterisation of MCM-48@Cu_xZnAl-CO_3-LDH B-1
B.2 Synthesis and characterisation of ES757@Cu_xZnAl-CO_3-LDH B-15
B.3 Synthesis and characterisation of mesoporous mSiO_2@Cu_2ZnAl-CO_3-LDH B-22
B.4 Reference B-27

Appendix C.Appendix for Chapter 4 ..... C-1
C.1 Characterisation of ES757@Cu_xZnAl-LDO C-1
C.2 Characterisation of ES757@Cu_xZnAl catalysts C-1
C.3 Reference C-6

Appendix D. Appendix for Chapter 5 ..... D-1
D.1 Synthesis and characterisation of ZSM-5@$Cu_{1.3}$ZnAl LDH D-1
D.2 Post-treatment with ammonium salts D-3
D.3 Homogeneous precipitation D-4
D.4 Co-precipitation with organic base D-5
D.5 Reference D-6

Chapter 1 Introduction

1.1 Layered double hydroxides (LDHs)

Layered double hydroxides (LDHs), also known as hydrotalcite-like compounds, are a family of anionic 2D layered materials, which can be both natural or synthetic.[1–3] Naturally existing hydrotalcite was discovered in Sweden in 1842 as a hydroxycarbonate of magnesium and aluminium.[2] The first exact formula of hydrotalcite [$Mg_6Al_2(CO_3)(OH)_{16}\cdot 4H_2O$] was determined by E. Manasse in 1915.[2,4] In 1942, Feitknecht prepared the first synthetic LDH.[1,5] Since 1970, when the hydrotalcite-like compounds were reported to be an excellent precursor of hydrogenation catalysts, extensive research has been conducted on LDH.[2,6]

1.1.1 Structure and composition

The general formula of LDHs is $(M^{a+}_{1-x}M^{b+}_{x}(OH)_2)^{y+}(A^{n-})_{y/n}\cdot mH_2O$, where M^{a+} and M^{b+} represent monovalent/divalent and trivalent/tetravalent metal cations respectively, and A^{n-} represents the interlayer anion.[1–3] LDH has versatile composition as shown in Figure 1.1.[1,2,7–15] Common M^{a+} includes Mg^{2+}, Co^{2+}, Ni^{2+}, Cu^{2+}, Zn^{2+}, and Cd^{2+}.[1,2] Research has found that monovalent Li^+ and large Ca^{2+} and Ba^{2+} cations can also be incorporated in the LDH structure.[8–10] Common M^{b+} contains Al^{3+}, Ga^{3+}, In^{3+}, Fe^{3+}, Mn^{3+}, Ti^{4+} and Zr^{4+}.[1,2] Multiple M^{a+} and M^{b+} cations can be incorporated in an LDH at the same time and give ternary, quaternary and quinary LDHs (e.g. MgCoAl-LDH,[16] CuNiZnAl-LDH[17] and CuZnMnFeAl-LDH[18]). Moreover, noble metals such as Au and Ag can be doped onto LDHs and present as a minor component (0.04-5 mol%).[7,15] The reported A^{n-} range from halide ions, common inorganic anions (e.g. CO_3^{2-}, NO_3^-, OH^-, SO_4^{2-} and ClO_3^-),[1,2] $SiO(OH)_3^-$,[11] transition metal complexes (e.g.

$Fe(CN)_6^{3/4-}$),[12,13] and organic ions (e.g. aliphatic and aromatic carboxylates).[12,14]

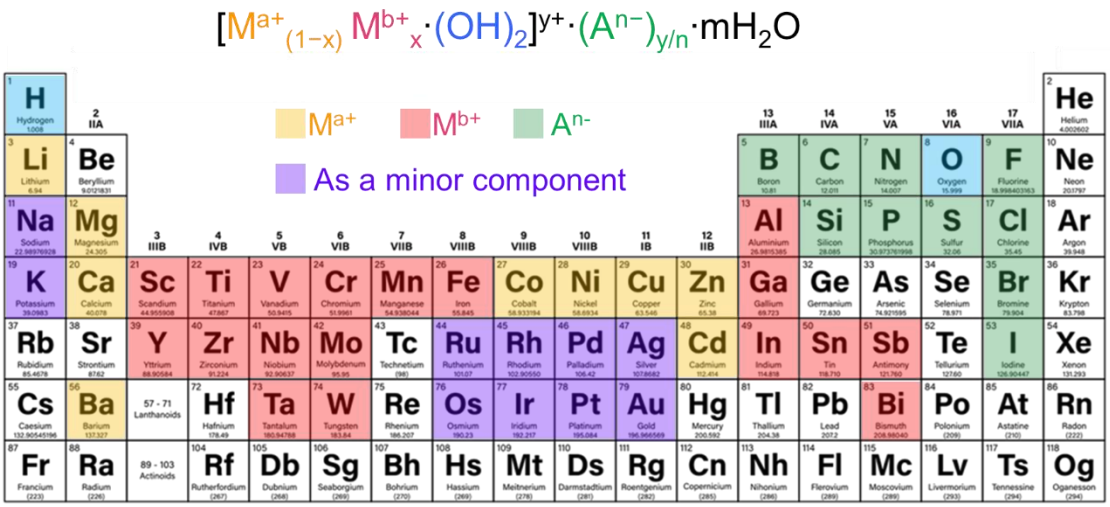


Figure 1.1 Elements in the periodic table that have been reported to be present in LDH. M^{a+}, M^{b+}, A^{n-} and minor components are coloured with yellow, red, green, and purple respectively. O and H are highlighted in blue.

The structure of LDH is similar to that of brucite, $Mg(OH)_2$, of which the metal hydroxide octahedra form infinite layers by edge-sharing; layers are stacked on the top of each other by hydrogen bonding.[2,6] When M^{a+} is partial substituted by M^{b+} with higher valency, it generates a net positive charge in metal hydroxide layer which is compensated by A^{n-} interlayer anions, forming an LDH with host-guest layer structure (Figure 1.2a).[1–3] To form a pure LDH phase, the amount of M^{b+} (x) should be controlled within a range; for example, pure MgAl-LDH can only be formed for $0.17 \leq x \leq 0.33$.[2]

The metal hydroxide layers may be stacked in different polytypes (one-layer, two-layers, three-layers, six-layers) and give different symmetries (mainly hexagonal and rhombohedral, denoted as H and R respectively).[6,19] Three examples are shown in Figure 1.2b, where '1H' means LDH stacked in a one-layer polytype and the unit cell has a hexagonal symmetry.[6,20,21] Most of the reported LDH possess a 2H or 3R polytypes or a combination of both.[6,22]

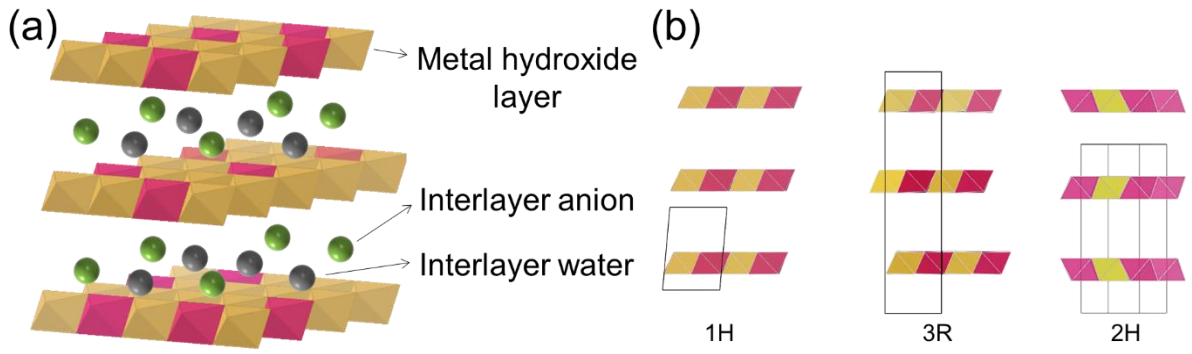


Figure 1.2 Graphical representation of (a) LDH and (b) examples of the polytype of LDH crystals.[20,21] M^{a+}, M^{b+} cations, interlayer anions and water molecules are represented by yellow, red, green balls and black balls, respectively.

Powder X-ray diffraction (XRD) is an essential technique to characterise LDH. The layered structure gives a set of (00*l*) Bragg reflections that can be used to study the environment of the interlayer gallery. The larger interlayer anions lead to a larger d_{00l}, i.e. (00*l*) reflections shift to a lower 2θ position. The position of (110) Bragg reflection allows the determination of metal-metal distance (d_{110}) and thus estimating metal composition. For example, the d_{110} of MgAl-LDH should increase with increasing Mg/Al ratio as the 6-coordinate Mg^{2+} (0.072 nm) is larger than Al^{3+} (0.054 nm).[23,24] The position of (01*l*) and (10*l*) Bragg reflections can be used to determine the stacking sequence.[6]

1.1.2 Synthesis methods

LDH can be synthesised using many synthetic methods. Co-precipitation is arguably the most widely used.[19,25] In this method, the metal salt solution was mixed with a base solution and a solution containing target anions to initiate the nucleation and crystal growth of LDH. To ensure two or more metals precipitate simultaneously, it is vital to control the pH of the reaction mixture. Figure 1.3a shows an example of the co-precipitation setup: the metal cation solution is added to an aqueous solution with desired interlayer anions at a constant pH (controlled by

adding a base solution).[25] It should be noted that the interlayer anions should have a high affinity to the metal hydroxide layer. Otherwise, the anions from the metal salts will be intercalated and contaminate the LDH.[25] Carbonate- and sulfate-intercalated LDH can be easily made under air due to the high affinity of metal hydroxide for CO_3^{2-} and SO_4^{2-}. However, for anions with low affinity (such as Cl^- and NO_3^-), co-precipitation needs to be conducted under an N_2 atmosphere to avoid carbonate contamination from dissolved atmospheric CO_2.[25] A variety of LDHs (including most of the transition metal-LDH and LDH intercalated with large biomolecules) have been prepared with this facile and scalable co-precipitation method. Moreover, hydrothermal treatment can be employed afterwards to improve the crystallinity of LDH.[14,25]

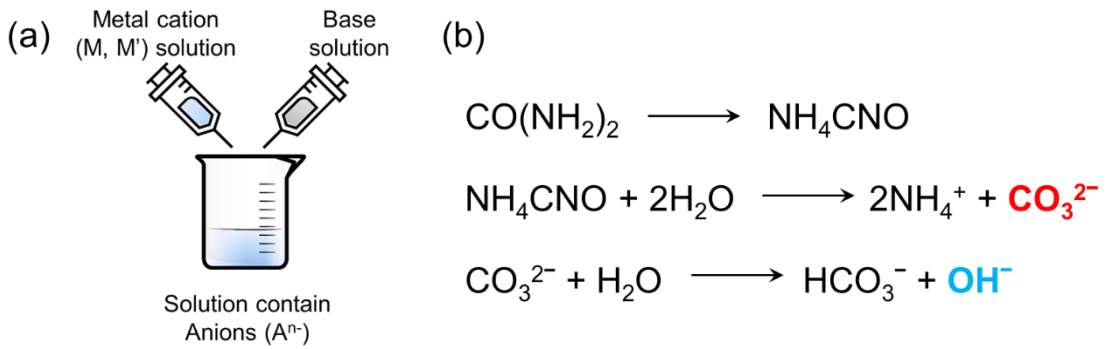


Figure 1.3 (a) Illustration for co-precipitation at low supersaturation. (b) Hydrolysis of urea and carbonate.

Homogeneous precipitation is well-known for preparing LDH with high crystallinity, narrow particle size distribution and large particle size. In homogeneous precipitation, an aqueous solution of metal salt and urea was thermally treated at a certain temperature and time to generate LDH. The hydrolysis of urea releases ammonia and carbonate, which further hydrolyses to provide hydroxyl ions (to form metal hydroxide) and a basic environment (Figure

1.3b). The pH of the reaction is between 7–9 depending on the reaction temperature, suitable for precipitating a large number of metal hydroxides.[25,26] The slow decomposition of urea leads to a slow nucleation of LDH.[27] Therefore, the obtained LDH particles are usually highly crystalline and uniform.[25–27] However, the homogeneous method can only form carbonate-intercalated LDH. To obtain LDH with other anions, an additional anion exchange process is required. Moreover, some of transition metals form water-soluble complexes with ammonia.[28–30] Precise control of the LDH composition becomes troublesome when transition metals are present.

Reverse micelle microemulsion has been reported to produce LDH with small and uniform particles.[31,32] It can be regarded as a modified precipitation (co-precipitation or homogeneous precipitation) method. Surfactant and organic solvent are added to the metal salt solution and form 'water pool' (micelle).[31,32] The nucleation and crystal growth of LDH occurs in those small water pools rather than in a bulk environment.[31,32] Wang *et al.* reported adding sodium dodecyl sulfate, isooctane and 1-butanol to the solution of Co^{2+}, Al^{3+} and urea (Figure 1.4a).[32] Once the mixture was heated, the hydrolysis of urea started (Figure 1.4b) and initiated the formation of LDH (Figure 1.4c and d).[32] The drawback of the reverse micelle microemulsion method is that the use of surfactant and the small size of platelet requires a costly and time-consuming washing process.

Ion-exchange,[25,32,33] reconstruction (rehydration),[25] and the sol-gel[34] are among other reported methods.

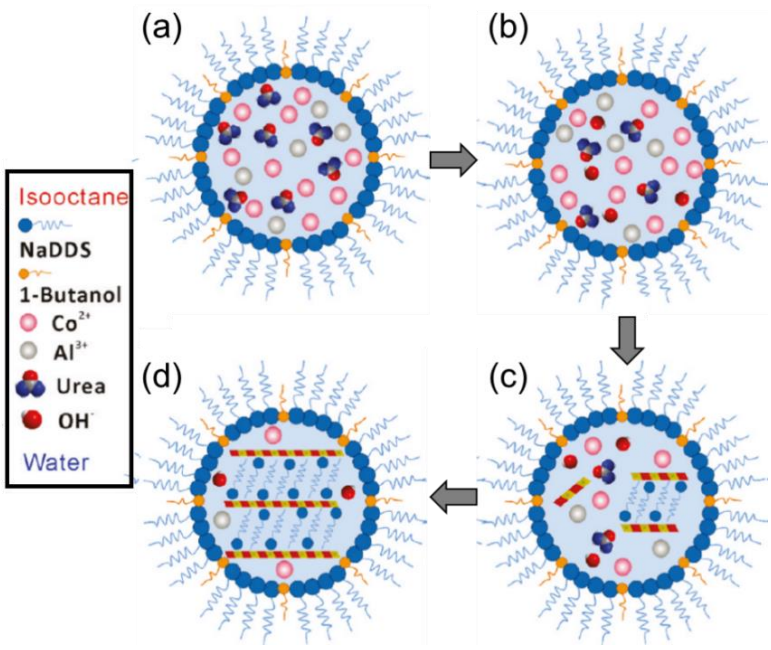


Figure 1.4 Schematic representation of preparing LDH via reverse micelle microemulsion. (a) the mixture of metal salts and urea inside a micelle; (b) the urea starts to hydrolysis; (c) the nucleation of LDH and crystal growth and (d) the LDH product in the water pool. Reproduced with permission from literature.[32]

1.1.3 Layered double oxides (LDOs)

Calcining LDH between a certain temperature range (300–600 °C) removes the water, hydroxyl group and interlayer anions, produces a mixed metal oxide, commonly named as layered double oxide (LDO). The resulting LDO exhibits a similar morphology to the LDH precursor and similar metal dispersion (homogeneously mixed at the atomic level and gives uniform microstructures),[35–37] making them excellent candidates for mixed metal oxides or nanoalloy catalyst precursors[36–39] and gas adsorbents.[40–42]

Moreover, LDO demonstrates a 'memory effect'. When exposed to water and anions, the LDO will uptake them to regenerate the layered structure and form LDH (Figure 1.5). As the reconstruction occurs regardless of the type of anions, LDO is normally used to prepare LDH intercalated with large organic ions[12] or with anions having a low affinity to metal hydroxide

(e.g. nitrate and chloride).[25] It should be noted that calcining LDH at high temperature (e.g. above 600 °C) produces metal oxide with a spinel structure which cannot be reconstructed back to LDH.[43]

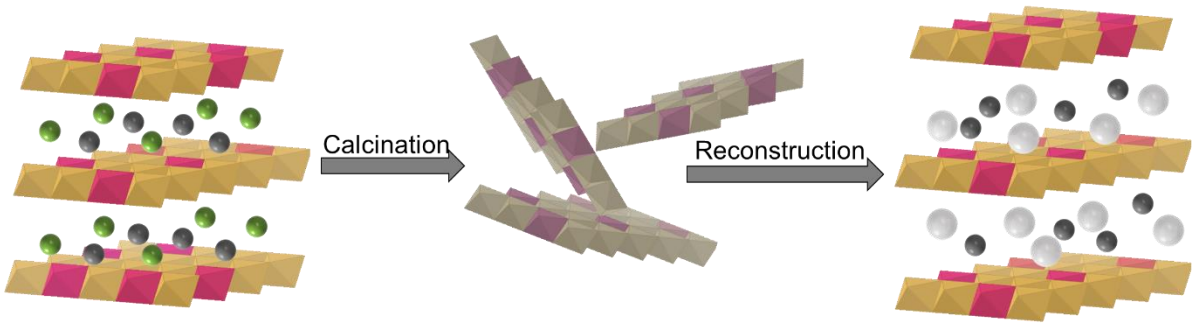


Figure 1.5 Schematic representation of LDH converts to LDO via calcination and LDO reconstructs to LDH. Two types of interlayer anions and water molecules are represented by green, white and black balls, respectively

1.1.4 Applications

The versatile composition, homogeneous dispersion of metals and host-guest structure make LDHs great potential in applications such as catalysts,[44,45] supercapacitors,[46,47] gas separation,[48] water treatment[49] and drug delivery.[50,51]

1.2 Layered double hydroxide-based core-shell composites

The high surface charge and high hydrophilicity of LDH lead to heavy aggregation between LDH nanosheets.[52–55] LDHs intercalated by common inorganic anions (such as CO_3^{2-}, SO_4^{2-}, Cl^- and NO_3^-) and prepared from conventional co-precipitation or homogeneous precipitation method show very low surface area of 1–50 m^2/g and have a stone-like morphology (Figure 1.6a).[52,54]

A number of methods have been used to avoid the aggregation of LDH and produce delaminated

nanosheets with high surface area, well-exposed active sites and efficient mass transfer.[52–55] This includes using inhibitors (e.g. formamide) to weaken the interaction between layer and interlayers (Figure 1.6b),[56,57] intercalating LDH with large interlayer anions (e.g. dodecyl sulfate) to separate metal hydroxide layers (Figure 1.6c),[58–60] replacing interlayer water with organic solvents having a low boiling point to disturb the interlayer environment, as in the aqueous miscible organic solvent treatment (AMOST) method (Figure 1.6d),[52–55] and mobilising LDH on a support to afford core-shell composites, core@LDH (Figure 1.6e).[61–69]

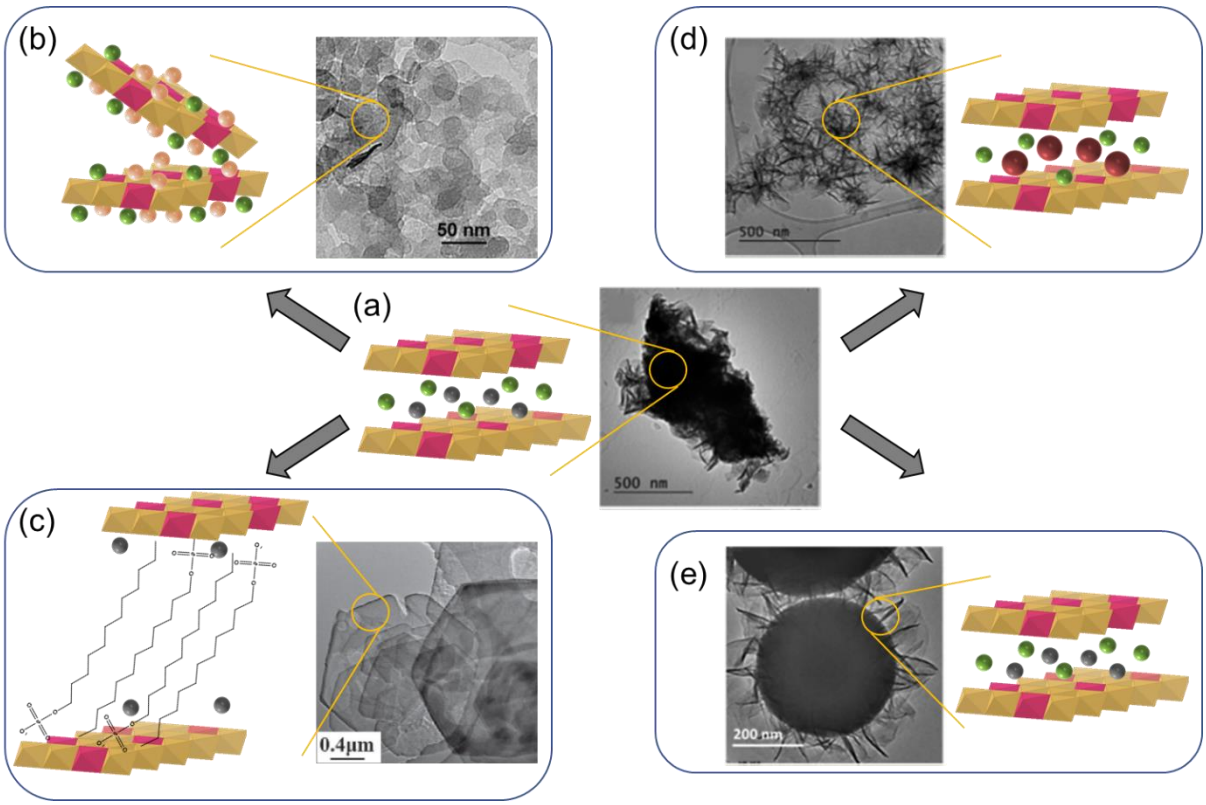


Figure 1.6 TEM images and graphical representation of LDH structure for (a) LDH prepared from co-precipitation,[54] (b) exfoliated LDH using formamide,[56] (c) exfoliated LDH using large interlayer anions,[70] (d) exfoliated LDH by replacing interlayer water molecules[54] and (e) mobilising LDH on a support.[65] Interlayer anions, water molecules, formamide, organic solvent molecules are represented by green, grey, orange, and red balls respectively.

A combination of these methods can be used to get an even better exfoliation. The O'Hare group has reported that once the LDH is supported on non-porous silica, the surface area increases

from 11 to 107 m^2/g, which is further increased once the core-shell is treated with the AMO solvent.[62,65]

Currently, there is increasing interest in core@LDHs because the core-shell structure allows the combination of both advantages from LDHs and core materials. which can be designed to afford nano-composites with high surface area,[64,67,69,71] specific magnetic properties,[72,73] multiple functionalities such as catalytic ability towards tandem reactions,[74,75] gas adsorption capacity[76,77] and biocompatibility.[51,78]

1.2.1. Synthesis methods

Core@LDH can be prepared via several methods. Recently, the O'Hare group has generated a series of SiO_2@MgAl-LDH and zeolite@MgAl-LDH core-shell using the co-precipitation method.[63–69] The metal salt solution was added to the dispersion of core material and target anions at a constant pH. As the surface of silica and zeolite in the aqueous dispersion carries a negative charge, it attracts the LDH nuclei via electrostatic interaction.[62] No pretreatment was required (Figure 1.7a). It has been found that the stirring conditions of the reaction, the amount and the addition rate of the metal salt solution will affect the LDH coverage and shell thickness of the final product.[63,79] Chen *et al*. demonstrated that using a metal nitrate to silica ratio of 14.4 mmol/g obtains almost full coverage of SiO_2 by MgAl LDH.[79] Adding a lower or higher amount of metal nitrate leads to low coverage or the formation of unbound free LDH clusters, respectively.[79] Kwok *et al*. reported that adding metal salt at 0.86 mmol/h speed and stirring the reaction mixture at 500 rpm speed obtained SiO_2@Mg_2Al LDH with thin LDH shell thickness and high surface area (100 m^2/g); increasing the addition rate to 0.43 mmol/g reduces the

surface area to 54 m^2/g.[63]

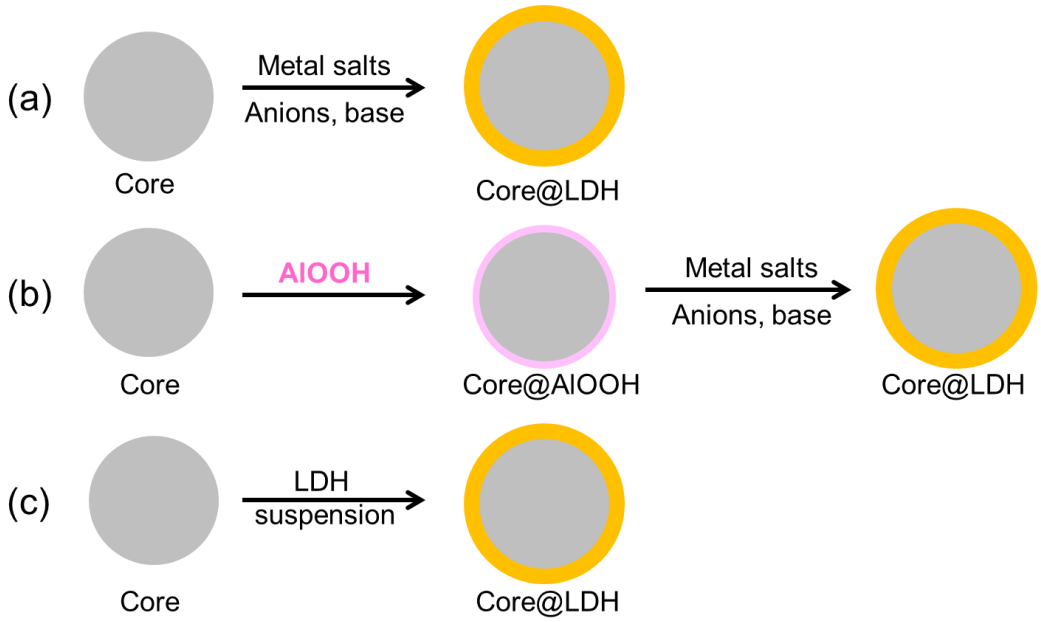


Figure 1.7 Graphical illustration of preparing core@LDH via (a) co-precipitation, (b) sol-gel and (c) disposition method.

Sol-gel is another method to *in-situ* fabricate LDH shell on a core, which involves pre-coating the core with aluminium hydroxide oxide (AlOOH) shell and then converting this shell to LDH (Figure 1.7b).[80–82] Duan and co-workers have applied this method to immobilise LDH on silica and man-made supports (paper, cloth and sponge).[80–82] A drawback of this method is that the AlOOH coating process has to be repeated several times to get enough AlOOH for the growth of LDH, which is time-consuming.[80–82]

A third method is the direct deposition which involves mixing a core suspension and a LDH suspension to produce core@LDH (Figure 1.7c).[51,83] The surface of the core commonly has a negative charge (e.g. SiO_2 in aqueous solution) so that the positively charged metal hydroxide layer will be attracted. Li *et al.* reported using a delaminated LDH suspension to deposit a single layer LDH onto polystyrene spheres (PSS). They then repeated this step 19 times and produce

a LDH shell with 16 nm thickness.[83]

1.2.2. Varation of cores and applications

To date, core@LDH materials has been prepared using silica,[62,63,65,67,71] zeolite,[84] carbon,[85,86] metal oxide,[72,87] polymer,[83] and DNA[88] cores and have shown great potential in catalysis,[89–92] supercapacitor,[93–95] drug delivery,[51,88,96] gas adsorption[76,77] water treatment,[72,82,97] and flame retardant materials.[55]

Moreover, core@LDH hybrids have shown synergistic effects. O'Hare and co-workers have reported using silica@LDH and zeolite@LDH as catalyst supports for slurry-phase ethylene polymerisation, which show up to three times higher catalytic activity compared to the core or shell alone. This superior performance was attributed to the synergistic effect of core-shell structure.[98] Wang *et al.* reported Cu_2O@ZnCr-LDH core-shell photocatalyst exploiting the band gap matching between Cu_2O and ZnCr-LDH to enhance catalytic activity and photostability towards water-splitting reaction.[99] Li *et al.* reported Co_3O_4@NiCoAl-LDH core-shell nanowire with improved electrochemical performance and cycling stability attributing to the synergistic effect.[100] Ni *et al.* published porous graphitised carbon@NiFe LDH with outstanding catalytic activity and stability towards an oxygen evolution reaction because of the increased exposure of active sites afforded by the core-shell structure compared with NiFe LDH alone system.[101]

1.2.3. Characterisation of core-shells

The techniques used to study the core-shells include powder XRD, thermogravimetric analysis (TGA), Fourier transform infrared spectroscopy (FTIR), elemental analysis, electron

microscopy, and gas physisorption isotherm especially the N_2 physisorption isotherm. Among them, the gas physisorption isotherm provides information on the porosity and surface area.

In 2015, the International Union of Pure and Applied Chemistry (IUPAC) has updated its manual on reporting the data of physisorption on solid materials/adsorbents.[102]In 2015, the International Union of Pure and Applied Chemistry (IUPAC) updated its manual on reporting the physisorption data for solid materials/adsorbents.[102] In this report, IUPAC suggested that the physisorption isotherms can be divided into eight types (Figure 1.8).[102]

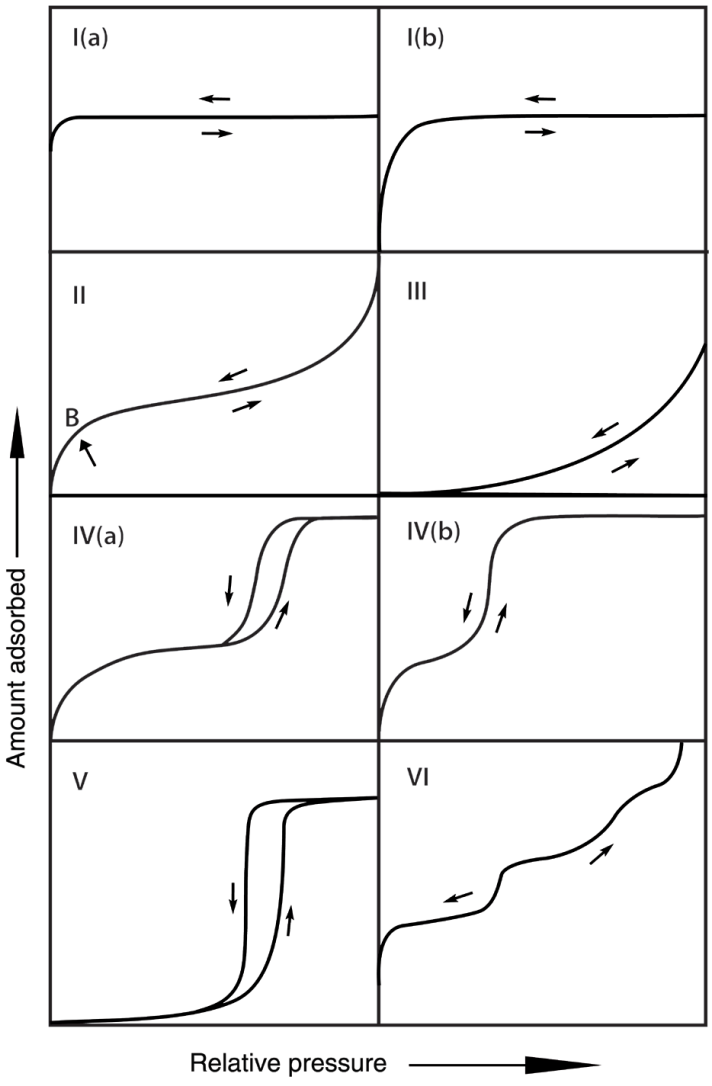


Figure 1.8 Classification of physisorption isotherm according to the IUPAC 2015 report. Reproduced with permission from the literature.[102]

Type I(a) isotherms are given by microporous materials with micropore size ≤ 1 nm; type I(b) isotherms are given by porous materials with pore size between 1 nm and 2.5 nm; type II isotherms are given by nonporous or macroporous (pore size > 50 nm) materials; nonporous or macroporous materials with weak adsorbent-adsorbate interaction will give type III isotherm.[102] Mesoporous adsorbents with pore size between 4–20 nm will produce type IVa isotherm, while mesoporous adsorbents with pore size between 2–4 nm will give type IVb isotherm.[102] Type V isotherms represent water adsorption on hydrophobic microporous or mesoporous adsorbents.[102] Type VI isotherms are observed for layer-by-layer adsorption on a highly uniform nonporous surface.[102]

The pore structure of the adsorbent affects the desorption of the adsorbate and therefore sometimes the hysteresis loops occur.[102] IUPAC also classifies the shape of the hysteresis loops (Figure 1.9).[102]

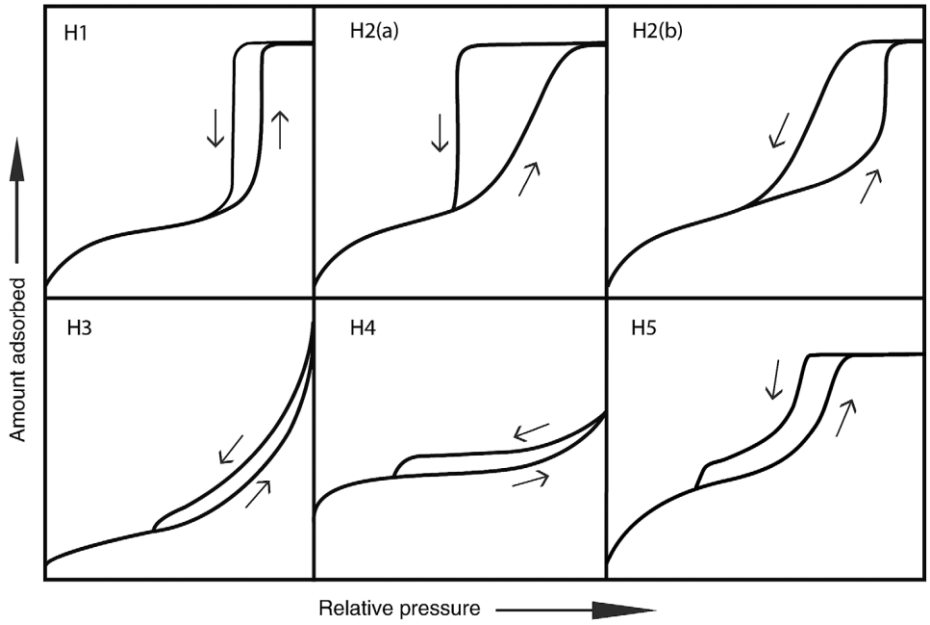


Figure 1.9 Classification of the hysteresis loops given by IUPAC. Reproduced with permission from the literature.[102]

Uniform mesopores will lead to H1 hysteresis loops.[102] The observation of H2 hysteresis loops indicates a complex pore structure, for example, an ink-bottle shaped pore network.[102,103] H2a loops are found when the pore neck size distribution is narrower than the pore cavity size distribution (e.g. the size of the pore neck is the same while the size of the pore cavity varies).[102,103] When the opposite occurs, H2b loops are observed, e.g. the size of the pore neck varies while the size of the pore cavity is the same.[102,103] Non-rigid aggregates of plate-like particles will result in H3 loops.[102] H4 loops can be given by aggregated crystals of zeolites and some mesoporous zeolites.[102] H5 loops are found when both open and partially blocked mesopores present in the adsorbents.[102]

The Brunauer–Emmett–Teller (BET) method is widely used to evaluate the surface area of adsorbents.[102,104] The BET method involves two stages. The first one is to work out the molar amount of gas molecules required to form a monolayer on the absorbents (so called specific monolayer capacity).[102,104] In this stage, equation 1.1 is used, where p/p^0 is the relative pressure, $\mathbf{n}$ is the molar amount of gas adsorbed at the relative pressure p/p^0, $\mathbf{n_m}$ is the specific monolayer capacity and C is a constant related to the adsorption energy of monolayer.[102,104]

$$\frac{p/p^0}{\mathbf{n}(1-\frac{p}{p^0})} = \frac{1}{\mathbf{n_m}C} + \frac{C-1}{\mathbf{n_m}C}\left(\frac{p}{p^0}\right) \qquad \text{Equation 1.1}$$

Subsequently, the BET specific surface area of the adsorbents can be calculated from equation 1.2, where a_s(BET) is the BET specific area of the adsorbents (of mass m), σ_m is the molecular cross-sectional area of the adsorbate and N is the Avogadro's number. The σ_m for nitrogen is assumed to be 0.162 nm^2.[102,104]

$a_s(BET) = \mathbf{n_m} N \sigma_m / m$ Equation 1.2

The pore size distribution (PSD) of the adsorbents can be computed by applying various methods. Developed in 1951, the Barrett, Joyner and Halenda (BJH) method has been extensively used to predict the PSD of materials with wide mesopores or macropores, i.e. pore size greater than 10 nm.[102,104,105] In analysing the PSD of narrow mesopores and micropores (pore size ≤ 10 m), the BJH method is problematic because it does not consider the interactions between the adsorbents and adsorbates (e.g. adsorption potential).[102,104–106] Therefore, the BJH method may underestimate the pore size by ca. 20–30%.[102,104,105,107]

On the contrary, the density functional theory (DFT) considers the physical effects of adsorbent-adsorbate interaction and pore geometry, which can provide a more reliable PSD for porous material with pore size ≤ 10 m (comparing to BJH method).[102,104,106,107] It should be emphasized that the DFT method can only provide a reliable assessment of PSD when an appropriate DFT kernel has been selected (i.e. the adsorptive/adsorbent pair, the assumed pore geometry and the adsorption/desorption branch of the experimental system are compatible with that of the DFT kernel); failure to apply the appropriate DFT kernel will only lead to a meaningless PSD result.[102,104,106,107]

1.3 CO_2 capture and utilisation

Greenhouse gases effectively absorb and emit the radiation emitted by Earth in the thermal infrared (IR) region (wavelength between 4 and 30 μm) and keep Earth warm.[108,109] Primary greenhouse gases include carbon dioxide (CO_2), water (H_2O), methane (CH_4), ozone (O_3) and

nitrous oxide (N_2O).[108] Nitrogen (N_2) and oxygen (O_2) gases are not greenhouse gases because they have no dipole moment and do not interact strongly with the thermal IR radiaion.[109,110] Recently, global warming and the climate crisis have become a global issue which is credited to the emission of greenhouse gases, especially CO_2.[111]The sharp growth in global population and the rapid industrial expansion has led to a dramatic increase in global energy demand, which is mainly satisfied by fossil fuels (coal, natural gas and oil) and causes an enormous release of carbon dioxide.[112–115] The 5th Intergovernmental Panel on Climate Change (IPCC) report has set a goal for limiting global warming to 2 °C (compared to pre-industrial times) and pursuing a goal of 1.5 °C.[116] If the current CO_2 emission rate continues, the world will reach a global warming of 1.5 °C around 2040.[116] Therefore, it is urgent to slow this increase by reducing the anthropogenic CO_2 emissions. Replacing fossil-fuel resources with cleaner energy source such as solar and wind would be ideal; however, it is a long-term effort to obtain the large-scale industrial implementation of clean energy which has not made a considerable contribution in reducing the CO_2 emission by far.[111,113] A more feasible way is to develop carbon capture and CO_2 utilisation technology. This technology seeks not only to eliminate the anthropogenic CO_2 emissions by capturing it from various emission points or directly from the air, but also to obtain benefits through recycling CO_2 into value-added chemicals such as alcohols and olefins.[111,117,118]

1.3.1. CO_2 capture

Fossil fuel based power plants are the single-largest CO_2 emission source which accounts for around one-third of total CO_2 emission.[119,120] Therefore, developing carbon capture

technologies that are suitable for fossil-fuel power plants are of typical interest. Among them, post-combustion capture (PCC) technology is a particularly promising option which is also economically friendly because other technologies such as pre-combustion or oxy-fuel require additional modification to existing power plants, e.g., pre-combustion requires installation of fuel reforming domain (transform fossil fuel to syngas, H_2 and CO) and oxy-fuel requires an expensive air separation plant.[119,121]

Flue gas is a mixture of N_2 (67–77 vol%), CO_2 (8–14 vol%) and H_2O (8–20 vol%), which is emitted at ambient pressure and elevated temperature (150–1200 °C depending on heat transfer during emission).[122,123] A schematic diagram of PCC is presented in Figure 1.10. The flue gas will go through a carbon capture sector to remove CO_2 before being vented to the atmosphere.[124,125] Subsequently, the collected CO_2 will be regenerated and stored in secure mediums such as depleted oil, gas wells and deep ocean, or converted into useful chemicals.[118,124,125]

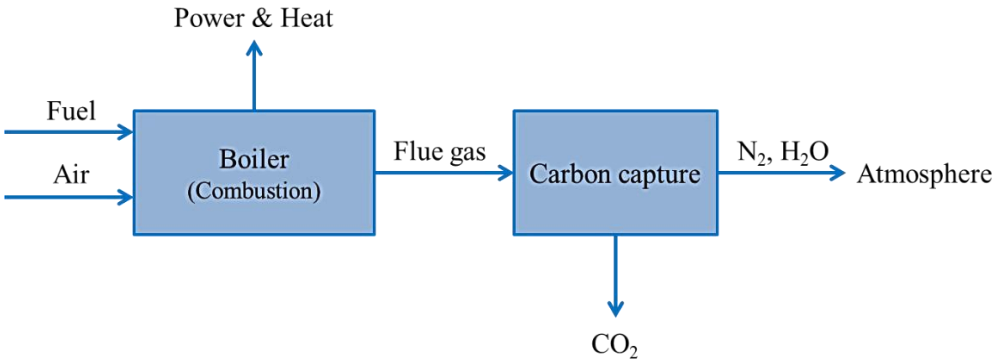


Figure 1.10 A brief scheme of post-combustion carbon captures process.[124]

Developed in the 1930s, amine scrubbing remains the dominant commercialised PCC technology.[126] Amine scrubbing is designed to use an aqueous solution of amine, e.g.

monoethanolamine and diethanolamine, to strip CO_2 from flue gas.[126] Although 85–90% CO_2 can be removed by this technology,[127] the high energy penalty (20–30% of the energy generated by the power plants) required by the subsequent regeneration of CO_2 (or the sorbent) sets an economic barrier for the application of amine scrubbing.[128] Besides, this technology possess several drawbacks, such as the corrosiveness and unavoidable degradation of active amine sorbents and the large system size for liquid amine scrubbing.[128]

As an alternative, porous solid materials including zeolites,[129–131] activated carbons,[121] metal-organic-frameworks,[132,133] metal oxides (such as CaO and MgO),[134,135] and LDHs (and its derivative LDOs) have been demonstrated as potential sorbents for PCC (Figure 1.11).[111,119]

1.3.1.1. Solid adsorbents for carbon capture

Zeolites are a family of porous crystalline aluminosilicates that are well-known for their low cost and high chemical stability. They are extensively used as adsorbents for gas separation and as catalysts in petroleum and chemical industries.[114,136,137] Zeolite 13X is a benchmark solid sorbent for PCC, which exhibits 4.5 mmol/g CO_2 capacity at 25 °C under 1 bar CO_2.[129,130] Zeolite 13X uptakes CO_2 via physisorption and requires much less regeneration energy (0.09–1.1 MJ/kg_{CO2}) in comparison with amine scrubbing (4.2–4.8 MJ/kg_{CO2}).[129,130] However, a drawback for Zeolite 13X and other zeolites is that under a humid environment, water molecules will take competitive adsorption with CO_2 and leads to a diminished CO_2 capacity.[130,131]

Activated carbon is well-known for its low cost, wide availability and tunable adsorptive

properties.[119] Dreisbach *et al.* reported that a commercial active carbon (Norit R1) shows 12 mmol/g CO_2 capacity at 25 °C and 56.3 bar.[138] Moreover, activated carbon adsorbs CO_2 via a mild adsorption strength requiring low regeneration energy (less than zeolite 13X),[139] exhibits excellent reversibility and less affected by the moisture in the flue gas.[119,140] However, the weak interaction between activated carbon and CO_2 leads to a low CO_2 capacity at ambient pressure, i.e. 2.1 mmol/g CO_2 capacity at 15 °C under 1 bar.[119,141]

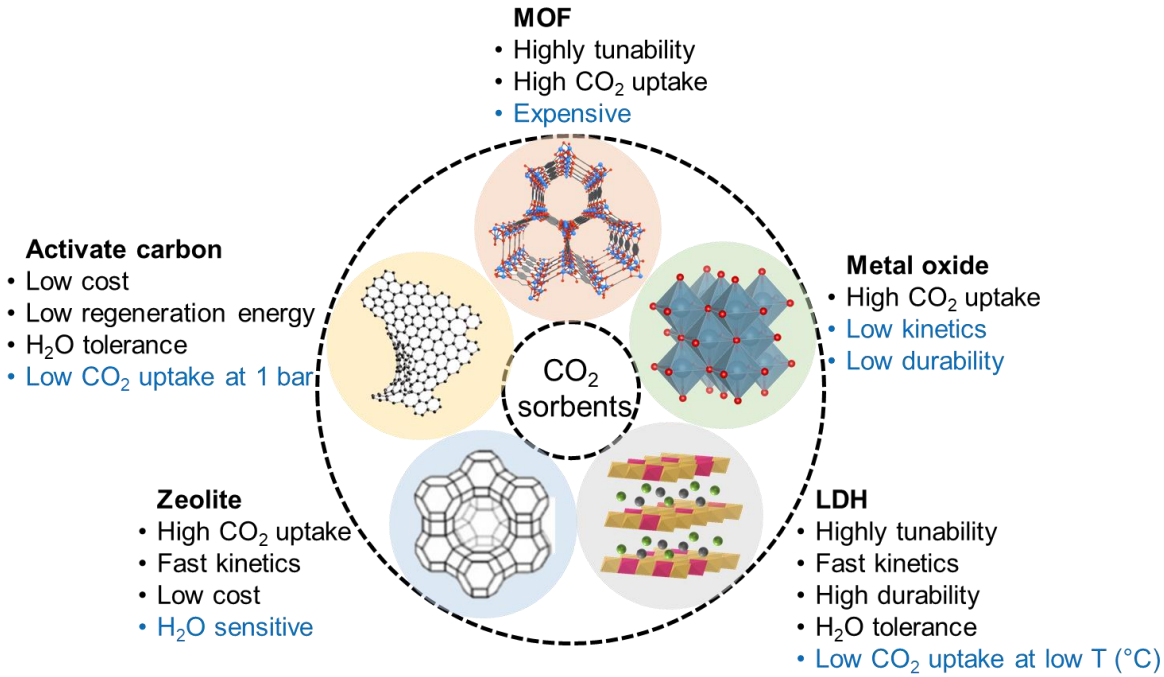


Figure 1.11 Illustration of solid sorbents for CO_2 capture and their advantages and disadvantages.

Metal-organic frameworks (MOFs) are crystalline materials built by metal-based nodes and organic linkers.[142,143] The precise chemical and structural tunability of MOFs (e.g. the surface property and pore size can be modified by altering the linkers used in synthesis) equips this novel material with great potential in fields such as gas separation, catalysis and drug delivery.[132,143] Mg-MOF-74 is the record holder for room temperature (25 °C) and ambient temperature CO_2 adsorbents, exhibiting 8.61 mmol/g CO_2 capacity.[133,144,145] In Mg-MOF-74,

the coordinatively unsaturated Mg^{2+} acts as Lewis acid site to polarise CO_2 molecules, leading to a high CO_2 uptake and a high CO_2/N_2 selectivity.[132,133] However, open Mg^{2+} site prefers to coordinate with water molecules rather than carbon dioxide. The carbon capture ability of Mg-MOF-74 is strongly undermined in the presence of water, e.g. only 16% CO_2 capacity remains under 70% relative humidity (RH).[130,146] Other drawbacks of MOFs including complicated synthesis and high cost.[133,147]

Basic metal oxides such as CaO and MgO can adsorb CO_2 by forming carbonate and achieve a fairly high theoretical CO_2 capacity, e.g.17.8 mmol/g for CaO. Although the reported CO_2 uptake value (11.6–13.4 mmol/g) is lower than the theoretical value, they are still higher than most solid sorbents.[119,148,149] However, the kinetics of the CaO carbonation with CO_2 at 1 bar is very slow, which requires reacting at high temperature (over 600 °C) for about 10 hours to accomplish a complete transformation.[150] In comparison, zeolite meets over 90% CO_2 capacity at 1 bar within several minutes.[151] Moreover, unlike the physisorbents (such as zeolite and activated carbons), the metal oxide has low durability due to the sintering during the regeneration of the sorbent, e.g. it can lose 50–80% CO_2 capacity within 20 cycles.[119]

1.3.1.1.1 LDH-based adsorbents for post-combustion CO_2 capture

Both LDHs and their calcined product LDOs can be used as the CO_2 adsorbents, and they have been investigated for several reasons. Firstly, is the high tunability; a number of studies have shown that the CO_2 capacity of LDH or LDO can be modified by changing the metal composition, interlayer anion, morphology and calcination condition.[40,42,48,152,153] The Attwood group reported that by changing the interlayer anion from Cl^- to ClO_4^-, the carbon capture

ability of Mg_3Al-LDO at 330 °C under 1 bar increases by 8 times (from 0.44 mmol/g to 3.55 mmol/g).[154] The Xu group noted that by partially substituting Ca with Co, the CO_2 uptake increases, i.e. $Ca_{1.5}Co_{1.5}Al$-LDO and Ca_3Al-LDO exhibit CO_2 uptake of 1.39 mmol/g and 0.87 mmol/g respectively at 350 °C under 1 bar.[155]

Hutson *et al.* observed that the physisorption and chemisorption proportion and the CO_2 capacity can be tuned by modifying the calcination temperature of LDH;[156] when heated at 200 °C, the adsorbent is a dehydrated MgAl-CO_3-LDH and CO_2 uptake is dominant by chemisorption, which occupies 54.6% of total uptake (0.60 mmol/g at 200 °C and 1 bar). Calcining the LDH at 400 °C produces more porous LDO and leads to a physisorption dominant (81.6%) CO_2 uptake (0.90 mmol/g at 200 °C and 1 bar).[156] The combination of physisorption and chemisorption for LDH and LDO make them exhibit faster kinetics (saturated within several tens of minutes) and better durability than the pure chemisorbents (e.g. metal oxides).[119,156]

An interesting property for LDH and LDO adsorbents is that water content in the feed gas has a positive effect on their CO_2 capacity. Reddy *et al.* reported that MgAl-LDO exhibits higher CO_2 capacity with a wet gas feed (0.71 mmol/g at 200 °C, 1 bar and 12% relative humidity) than a dry gas feed (0.61 mmol/g at 200 °C and 1 bar).[157] Torres-Rodríguez *et al.* observed that the CO_2 uptake of Mg_3Al-LDO increases when the relative humidity (RH) of the gas feed increases from 40% to 70% and reaches an optimal value at 2.13 mmol/g (at 50°C and 1 bar with 70% RH).[158] Coenen *et al.* proposed that more active sites for CO_2 adsorption were obtained for a mixture of MgAl-LDO and Al_2O_3 when water presents in the gas feed.[159]

However, a clear determination of the benefits of LDO is yet to be made.[119]

The CO_2 capacity of LDH at high pressure and high temperature is in the same order of magnitude as that of zeolite-13X. For example, Mg_3Al-LDH exhibits 3.8 mmol/g CO_2 uptake at 30 °C and 32.8 bar[160] and zeolite 13X possesses 6.9 mmol/g CO_2 uptake at 35 °C and 33.6 bar.[161] However, at moderate temperature and low pressure, the CO_2 capacities of LDH and LDO are not high. Ding *et al.* reported that hydrotalcite exhibits 0.9 mmol/g CO_2 capacity at 208 °C under 1 bar and 30% RH.[162] Wang *et al.* reported that MgFe-LDO shows 0.46 mmol/g CO_2 uptake at 200 °C and 1 bar.[153] Several methods have been developed to improve the CO_2 capacity of LDH and LDO sorbents, which includes exfoliating LDH,[41] doping with alkali metals (e.g. potassium)[119,163] or amines[164,165] and immobilising LDH on a support.[77]

1.3.1.1.2 Core-shell adsorbents for carbon capture

Recently, core-shell sorbents have been developed for carbon capture because of their potential in having high surface area, high stability and combine both the advantages of core and shell.[78,166–168] Al-Naddaf *et al.* coated zeolite 5A with MOF-74 to produce a 5A@MOF-74 core-shell.[166] They noted that the core-shell (with the zeolite 5A to MOF-74 weight ratio of 5: 95) exhibits a similar morphology to MOF-74 and shows higher surface area and higher pore volume than the parent materials.[166] The authors attributed the increase in core-shell surface area to the formation of mesopores at the MOF-zeolite interface.[166,169] The CO_2 capacity of zeolite 5A and MOF-74 is mainly determined by the amount of CO_2 physically adsorbed; the larger the surface area, the higher the CO_2 capacity.[166] Consequently, the core-shell (with higher surface area) exhibits better CO_2 capacity (13.8 mmol/g at 25 °C and 20 bar) than the parent

zeolite 5A and MOF-74 (6.1 mmol/g and 10.6 mmol/g under the same conditions).[166] Yang *et al.* reported coating a Li-decorated zeolite-13X (LiX) with the ZIF-8 to produce a core-shell LiX@ZIF-8. The CO_2 capacity of the core-shell (3.2 mmol/g at 25 °C and 1bar) is lower than that of LiX, but higher than that of ZIF-8 under the dry condition (4.9 mmol/g and 0.7 mmol/g, respectively). In the humid environment, the hydrophobic ZIF-8 protects the hydrophilic LiX core from moisture, and to a certain extent avoids the competitive adsorption between CO_2 and water.[168] As a result, LiX@ZIF-8 exhibits higher CO_2 capacity (1.73 mmol/g at 35 °C and 1 bar with 50% RH) than both LiX and ZIF-8 (0.6 mmol/g and 0.22 mmol/g respectively).[168] Moreover, the prepared core-shell shows good stability over 50 adsorption-desorption cycles (retaining >70% CO_2 capacity).[168]

1.3.2. CO_2 utilisation

After CO_2 is captured, it will normally need to be desorbed, concentrated, compressed and sequestered underground.[170] Considering that the long-term storage suffers from the high costs and the risk of CO_2 leakage,[171,172] CO_2 utilisation technology which involves recycling CO_2 to valuable chemicals, e.g. urea, formic acid and fuels, is an environmentally and economically friendly alternative.[173–175]

However, CO_2 is chemically and thermodynamically inert (bond-dissociation energy for C=O bond is 750 kJ/mol, closing to 941 kJ/mol for N≡N),[176–178] which means converting CO_2 will be energy-consuming and costly; introducing another reactant with high Gibbs free energy (such as hydrogen) would make the reaction more thermodynamically favourable.[179] Therefore, CO_2 hydrogenation has drawn significant attention, and the target chemicals include alcohols,

dimethyl ether and hydrocarbons.[180]

1.3.2.1. Catalytic CO_2 hydrogenation to methanol

Methanol is the building block for plastics and biofuels and is regarded as an essential chemical.[180] The global market of methanol has doubled from 2006 to 2016 and is anticipated to further increase at an annual rate of 4% during 2017–2026.[181–183] Methanol can also be used as the storage medium for clean energy (such as solar and wind) which is more stable and easy to transport than hydrogen.[184,185] Moreover, traditional methanol production is fossil-fuel based and emits CO_2 at a ratio of *ca* 0.5–0.7 ton_{CO_2}/ton_{MeOH}.[186] Developing CO_2 hydrogenation to methanol is also conducive to the reduction of CO_2 emissions.[186]Heterogeneous catalysts for CO_2 hydrogenation to methanol have been widely studied over the last several decades.[180] Some examples are listed in Table 1.1. In addition to the CO_2 conversion rate and methanol selectivity, the space-time yield (STY) of methanol is also listed to indicate the catalytic ability of the catalysts. STY is the quantity of product produced per unit weight of the catalyst per unit time and is a factor that is widely used in the study of gaseous reaction with continuous gas feeding.[180,187]

Depending on the main active sites in the catalysts, they can be divided into several types: 1) Cu-based (Entry 1–4), 2) precious-metal-based, e.g. Pt and Pd, (Entry 5–7), 3) metal oxide solutions, e.g. ZnO-ZrO_2, (Entry 8–9), 3) In_2O_3-based (Entry 10–11) and 4) nanoalloys, e.g. PdCu, PdGa, Co_5Ga_3, (Entry 6–7 and 12–13). Introducing promoters, e.g. alkali metals, transition metals and rare-earth metals (Entry 4, 6, 9, and 17) and supports, which include various metal oxide, e.g. Al_2O_3, ZrO_2 and ZnO, silica and carbon (Entry 1–7 and 11–13) are

two common ways to improve catalytic performance.[75,180,188,189] MOFs can play a multifunctional role in the catalysts, including acting as support (Entry 14–16), providing active sites (Entry 14–16), isolating and protecting the active species (Entry 15) or as the precursors for metallic species, metal oxides and carbon support (Entry 16).[180]

Table 1.1 Summary of catalysts, reaction conditions and catalytic performance for CO_2 to methanol (CO_2 conversion, methanol selectivity and space-time-yield (STY)). A H_2:CO_2 = 3:1 gas feed was used.

Entry	Catalyst	Press/bar	Temp/°C	CO_2 conv/%	MeOH selec/%	MeOH STY/g_{MeOH} g_{cat}/h
1	$Cu/ZnO/Al_2O_3$[a190]	360	260	65.8	77.3	7.7
2	$Cu/ZnO/Al_2O_3$[191]	50	210	< 3	85	–
3	$Cu/ZnO/ZrO_2$[192]	30	240	18.2	41.6	0.06
4	$Cu\text{-}K/Al_2O_3$[b193]	100	200	2.8	62.2	0.03
5	Pd/Ga_2O_3[194]	50	250	19.6	51.5	0.68
6	PdZn/ZnO	30	250	5.8	69.7	0.08
7	Pt_4Co/C[195]	32	150	–	–	7.66
8	$ZnO\text{-}ZrO_2$[196]	50	320	10	86	0.74
9	$CdZrO_x$[197]	20	300	5.4	80	–
10	In_2O_3[c198]	50	300	–	100	0.2
11	$Y\text{-}In_2O_3/ZrO_2$[c199]	40	300	7.6	69.0	0.42
12	$PdCu/ZrO_2$[200]	41	250	15.8	26.8	0.06
13	Ni_5Ga_3/SiO_2[201]	1	210	–	–	0.24
14	Pd-Zn@ZIF-8-1[202]	45	290	13	66	0.58
15	Cu⊂UiO-66	10	175	3	100	–
16	Cu_2@ZIF-8[203]	45	260	22	54	0.93
17	CuZnAlZr[204]	30	250	18.7	33.7	0.25
18	CuZnAlZr[205]	50	190	10.7	81.8	0.087
19	PdZnAl[206]	30	250	0.6	60	0.02
20	$Cu/mSiO_2$[207]	270	50	4.0	15.6	0.01
21	$Cu@mSiO_2$[207]	270	50	12.6	17.8	0.05
22	$Cu/ZnO@mSiO_2$[207]	270	50	11.9	61.8	0.15
23	Cu/ZnO_x@UiO-bpy[208]	250	40	3.3	100	0.003[d]

a: H_2:CO_2 = 10:1, b: H_2:CO_2 = 3.8:1. c: H_2:CO_2 = 4:1. d: STY based on per gram copper g_{MeOH}/g_{Cu}/h.

Most catalysts exhibit a space-time-yield (STY) of methanol below 0.7 g_{MeOH}/g_{cat}/h. The CO_2 conversion rate is generally low (< 20%), which is the main challenge for the high STY of

methanol.

The state-of-art CO_2 to methanol catalyst is a mixture of metallic Cu, ZnO and Al_2O_3 ($Cu/ZnO/Al_2O_3$), which shows high CO_2 conversion and methanol selectivity at elevated temperature (200–300 °C) and high pressure (5–360 bar).[75,190] For example, Bansode *et al.* reported a $Cu/ZnO/Al_2O_3$ catalyst that displays > 65.8% CO_2 conversion, >77.3% methanol selectivity and 7.7 $g_{MeOH}/g_{cat}/h$ methanol yield at 360 bar and 260 °C (Entry 1, Table 1.1).[190] However, the CO_2 conversion of $Cu/ZnO/Al_2O_3$ reduces intensively at low pressure. García-Trenco *et al.* reported that at 50 bar and 210 °C, the CO_2 conversion of the commercial $Cu/ZnO/Al_2O_3$ catalyst is below 3% (Entry 2).[191]

Moreover, this catalyst suffers from a short lifetime due to active site sintering and water poisoning during the reaction.[180,209] Lunkenbein *et al.* reported that the interface of Cu-ZnO promotes methanol synthesis. During the reaction, the nanocrystallite ZnO sinter to produce a more dense and bulky structure, leading to diminished catalytic performance (Figure 1.12).[210]

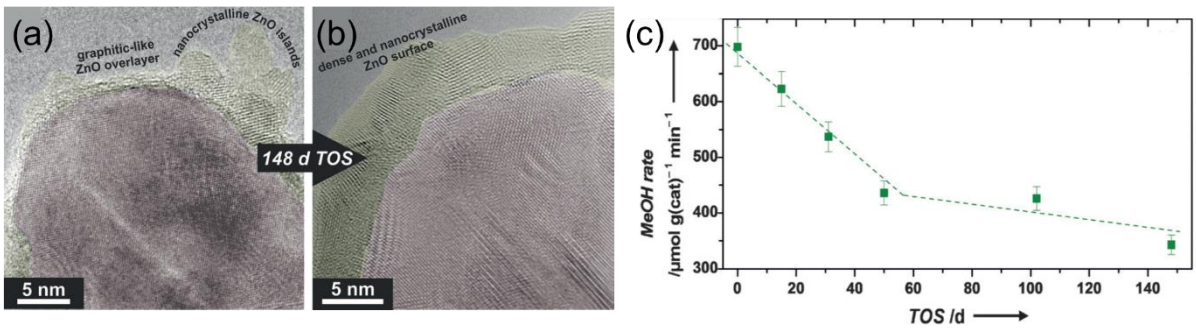


Figure 1.12 TEM images of Cu/ZnO catalyst after different time-on-stream (TOS) (a) 0 days and (b) 148 days. (c) Space-time-yield of methanol of Cu/ZnO catalyst against TOF. Reproduced with permission from literature.[210]

1.3.2.1.1. LDH-based catalysts for CO_2 to methanol

LDHs, especially those containing Cu, Zn and Al, is used as the precursor for CO_2 to methanol catalysts due to the uniform dispersion of metal cations within layers (Entry 17–19, Table 1.1).[37,204–206,211–213] The Sun group reported that CuZnAlZr catalyst derived from pure LDH shows better performance (0.087 $g_{MeOH}/g_{cat}/h$) than those derived from a mixture of LDH and zincian malachite (0.011 $g_{MeOH}/g_{cat}/h$); they attributed the superior activity to the improved dispersion of Cu in LDH structure which leads to smaller copper particle size and stronger Cu and ZnO interaction.[204,205]

The copper cation in the Cu-containing LDH is 6-coordinated and in most cases, has an oxidation state of +2 (d^9). According to the Jahn-Teller theorem, the non-linear $Cu(OH)_6$ octahedron with an orbitally degenerate ground state is unstable (electronic configuration has high energy); therefore, the octahedron will be distorted to remove the degeneracy and achieve a more stable structure (electronic configuration has lower energy).[214,215] Depending on the electronic configuration, there may be two possible distortions; a compressed octahedron appears when the d_{z^2} orbital is half-filled and has higher energy (than the $d_{x^2-y^2}$ orbital); an elongated octahedron occurs when the $d_{x^2-y^2}$ orbital is half-filled and has higher energy (thed_{z^2} orbital). [214,215] Li et al. reported that $Cu(OH)_6$ octahedrons are elongated in a CuAl-LDH.[216] Due to the Jahn-Teller effect, it is difficult to prepare pure CuAl-LDHs with high copper content, because impurity phases such as malachite and gerhardtite will be formed simultaneously.[217,218]

Apart from the Cu-containing LDH, LDHs with precious metals have been used in the catalytic hydrogenation of CO_2 to produce methanol. Ota *et al.* prepared a series of highly dispersed Pd

catalysts by adding 1 mol% Pd to the reaction mixture of LDH (Figure 1.13). They noted that Pd enters the framework of LDH to give PdZnAl-LDH and PdMgGa-LDH and proposed that embedding metal in a LDH framework is a facile way to obtain monometallic and intermetallic catalysts.[206]

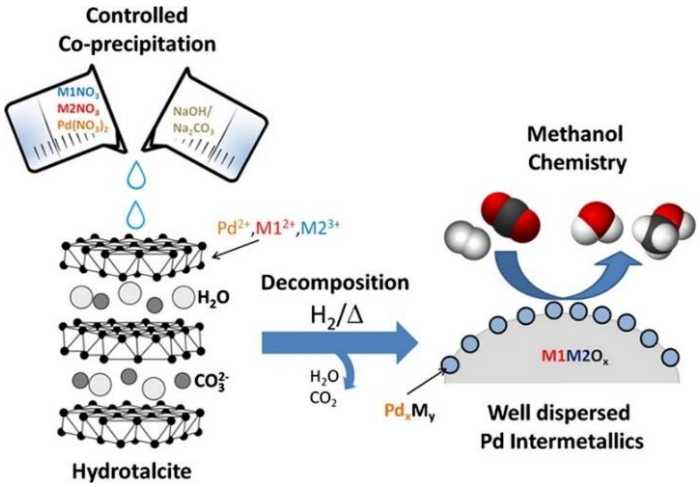


Figure 1.13 Illustration for the synthesis of Pd-doped LDH and corresponding catalysts. Reproduced with permission from literature.[206]

1.3.2.1.2. Core-shell catalysts for CO_2 to methanol

CO_2 hydrogenation to methanol is normally conducted above 200 °C for fast kinetics.[180,219] However, the sintering of the active sites is accelerated at such high temperature. Moreover, the formation of water as the by-product further exacerbates the sintering.[75,180,219] To protect the active sites, core-shell catalysts were investigated where active species such as metallic Cu and Pd are embedded in metal oxide or silica shell.[75]

Yang *et al.* prepared a Cu-embedded $mSiO_2$ core-shell (Cu@$mSiO_2$), a Cu/ZnO-embedded $mSiO_2$ core-shell (Cu/ZnO@$mSiO_2$) and the physical mixture of Cu and mesoporous silica (Cu/$mSiO_2$). The authors found that the core-shell shows much higher CO_2 conversion than the physical mixture (Entry 20–22, Table 1.1, Figure 1.14).[207] Moreover, the core-shell catalyst

exhibits high stability, i.e. the CO_2 conversion and MeOH selectivity of Cu/ZnO@mSiO_2 decreased by 1.6% and 1.0%, respectively, after reacting for 168 h. While Cu/mSiO_2 loses most of its activity in 100 h (Figure 1.14c). The authors believed that the superior catalytic activity and stability is due to the silica shell, which improves the copper dispersion and protects the active site from sintering.[207]

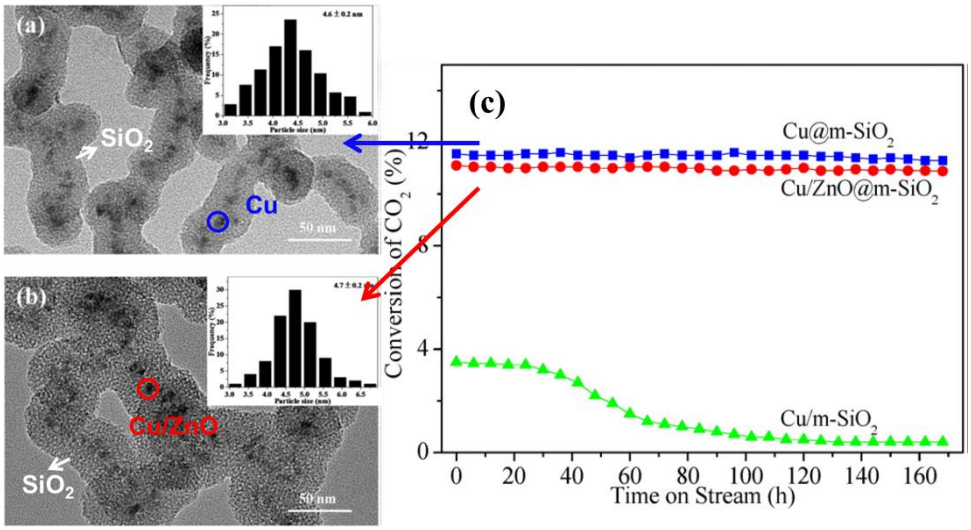


Figure 1.14 TEM images of (a) Cu@mSiO_2 and (b) Cu/ZnO@mSiO_2. (c) CO_2 conversion of catalysts over reaction time. Reproduced with permission from literature.[207]

An *et al.* prepared a core-shell with Cu/ZnO_x core and UiO-bpy shell (Figure 1.15).[208] They noted that the UiO-bpy shell not only prevents Cu/ZnO from sintering and phase separation, but the high spatial proximity between Cu/ZnO_x interface and Cu/ZrO_x interface also promotes the methanol selectivity.[208]

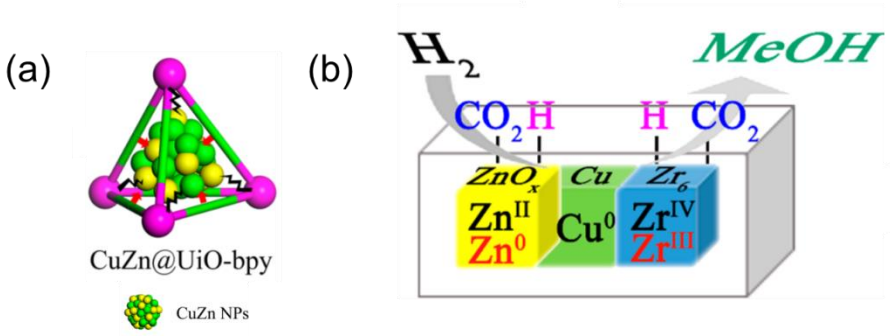


Figure 1.15 Schematic of (a) Cu/ZnO_x@UiO-bpy core-shell. (b) functions of interface for CO_2 hydrogenation to methanol in the core-shell. Reproduced with permission from literature.[208]

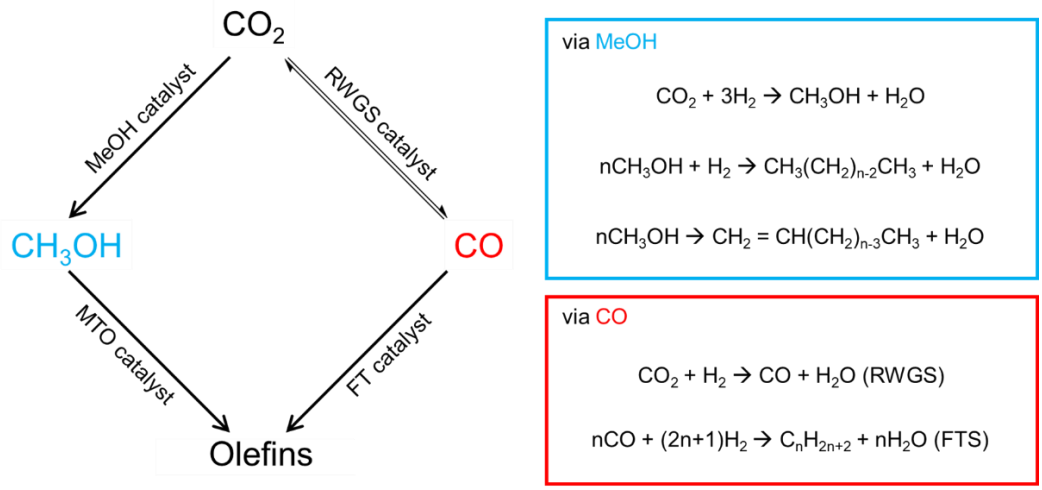
A literature survey was conducted in order to get the comprehensive information about the application of core@LDH in the CO_2 hydrogenation to methanol. However, no core@LDH materials that have been reported for the related study. The target reaction for core@LDH derived catalysts are typically CO_2 photoreduction to methane,[92] oxygen evolution reaction[94] and water-splitting.[89,90]

1.3.2.2. Catalytic CO_2 conversion to olefins

Olefins are another target product from CO_2 hydrogenation that have been extensively investigated. Because olefins are the essential chemical feedstock of plastics and solvents and can be used as energy sources.[175,220] Similar to methanol, olefins are generally produced from fossil fuels (via petroleum refinement or oil cracking).[221–224] Converting CO_2 to highly valuable C_{2+} olefins can not only recycle CO_2 but also provides a viable alternative to replenish the fossil fuel-based olefins market in the light of fossil fuel depletion.[224–226]

The chemically inert CO_2 needs to be converted into more active C_1 species before being further converted to olefins. Two synthetic routes are widely accepted for CO_2 to olefins conversion (Scheme 1.1) [174,227–230]: 1) methanol-mediated pathway, consisting of CO_2 hydrogenation to

methanol and methanol to olefin (MTO) conversion,[231,232] 2) carbon monoxide-mediated pathway involving the reverse water gas shift (RWGS) and Fischer-Tropsch (FT) reaction.[224,233,234]



Scheme 1.1 Methanol-mediated and carbon monoxide-mediated synthetic pathway for CO_2 to C_{2+} hydrocarbon conversion and examples of reactions involved.

Heterogeneous catalysts for olefins synthesis from CO_2 through both MeOH-mediated and CO-mediated routes has been comprehensively studied and reviewed (Table 1.2).[174,227–230] For MeOH-mediated pathway, the combination of the CO_2 to methanol catalysts (e.g. copper and indium-based catalysts) and MTO catalysts (e.g. zeolite and alumina) is intensively investigated (Entry 1–8).[174,227–230,235–238] Joen *et al.* developed a range of catalysts comprising $Cu/ZnO/Al_2O_3$ or Cu/ZnO/ZrO and zeolite (including SAPO-5, SAPO-44 and H-ZSM-5) for CO_2 to hydrocarbon conversion (Entry 2–3).[236] Dang *et al.* published using the physical mixture of In_2O_3/ZrO_2 (2:1 by molar) and SAPO-34 to reach 26.2% CO_2 conversion, 36.1% hydrocarbon selectivity and 74.5% $C_2^=$–$C_4^=$ selectivity (among hydrocarbon) (Entry 5).[237]

Iron and cobalt-based catalysts have been extensively studied for RWGS-FT catalysis due to

their excellent CO_2 activation ability and olefins selectivity (Entry 9–13).[174,239–242] Incorporation of promotors (such as alkali metal, copper, zinc, nickel and magnesium) and supports (including carbons, zeolites, silica and metal oxides) is found to boost the C_{2+} chemical production by improving the CO_2 conversion and facilitate the carbon chain growth (Entry 10–12).[174,227–230,242] Dai *et al.* reported using hierarchical porous carbon monolith (HPCM)-supported Fe–K catalyst to obtain 33.4% CO_2 conversion and 18.0% $C_2^=$–$C_4^=$ selectivity (Entry 10).[240] The author attributed the outstanding performance to the high dispersion of Fe-K active sites brought by the hierarchical porous morphology of the HPCM support and therefore an enhanced synergy (between Fe-K).[240]

Table 1.2 Summary of reaction conditions with CO_2 conversion and light olefins selectivity for selected catalyst. A H_2: CO_2 = 3:1 gas feed was used.

Entry	Catalyst	Press/bar	Temp/°C	CO_2 conv/%	$C_2^=$–$C_4^=$ selec/%
1	$Cu/ZnO/Al_2O_3$+SAPO-34[235]	30	400	53.5	62.1[a]
2	$Cu/ZnO/Al_2O_3$+SAPO-5[236]	28	340	24.3	70.8[b]
3	$Cu/ZnO/ZrO_2$+H-ZSM-5[236]	28	340	24.5	86.9[b]
4	In_2O_3+SAPO-34[c237]	30	380	15.3	81.9[a]
5	$In_2O_3ZrO_2$+SAPO-34[b237]	30	380	26.2	74.5[a]
6	CuZnZr+SAPO-34[238]	30	400	9.7	34.7[a]
7	CuZnZr@SAPO-34[238]	30	400	12.6	42.5[a]
8	CuZnZr@Zn-SAPO-34[238]	30	400	19.6	60.5[a]
9	Fe_3O_4[239]	20	350	43.0	41.5[a]
10	Fe-K+HPCMs-1[240]	30	400	33.4	18.0
11	$FeCo/K-Al_2O_3(152.3)$[241]	20	360	41.6	41.2
12	Na/Fe+H-ZSM-5[242]	10	340	30.9	3.2[a]
13	$Na/Fe+H-ZSM-5@SiO_2$[242]	10	340	30	24.5[a]

a: selectivity of $C_2^=$-$C_4^=$ within the hydrocarbon product. b: selectivity of C_2-C_4 within hydrocarbon. c: gas feed $H_2/CO_2/N_2$ = 73/24/3.

1.3.2.2.1. LDH-based catalysts for CO_2 to olefins

To the best of our knowledge, there is no report that using LDH-based materials to catalyse CO_2

to olefins conversion. It is possible that LDH is used as the precursor but the authors did not mention it in the main context. However, there have been reports of LDH-based materials for CO_2 conversion to hydrocarbons and gasoline. For example, the Zhang group investigated the effect of reduction temperature on the product selectivity of Co_2FeAl LDH derived catalyst for CO_2 photo-hydrogenation to C_{2+} hydrocarbon; they noted that at reduction temperature above 600 °C, the calcined Co_2FeAl LDH converted to Al_2O_3 supported CoFe nano-alloy and exhibits 79% CO_2 conversion with 60% CH_4 and 35% C_{2+} selectivity.[39]

1.3.2.2.2. Core-shell catalysts for CO_2 to olefins

Core-shell catalysts are regarded to have great potential in catalysing the CO_2 to olefins reaction because it allows more precise control than the single catalyst and exhibits more uniform microstructure than physical mixtures of catalysts.[75] Furthermore, the product selectivity of core-shells can be tuned by adjusting the spatial proximity between different active sites.[75]

Chen *et al.* reported that CuZnZr@SAPO-34 exhibits higher CO_2 conversion and olefin selectivity than the physical mixture CuZnZr+SAPO34 (Entry 6–7, Table 1.2).[238] The author proposed that when small CuZnZr species was mixed with large SAPO-34 particles, the interface is large which reduces the acidity of SAPO-34, slightly diminishes the hydrogenation ability of CuZnZr and leads to a low CO_2 conversion and olefins selectivity. By forming the CuZnZr@SAPO-34 core-shell, the interface becomes smaller so that SAPO-34 and CuZnZr are less affected by each other (Figure 1.16). Moreover, the core-shell structure allows a further modification of SAPO-34 shell without disturbing CuZnZr core. The author then prepared a core-shell with Zn decorated SAPO-34 (Zn-SAPO-34) to tune the acidity of the shell and

obtained a core-shell with even better catalytic performance (Entry 8).[238]

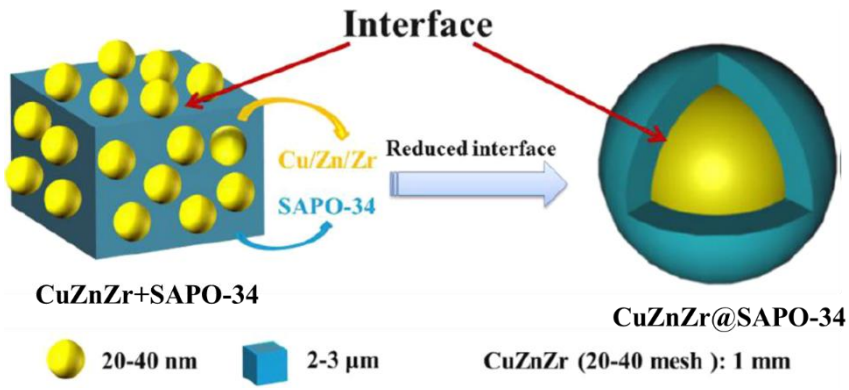


Figure 1.16 Schematic of the interface between CuZnZr species and SAPO-34. Reproduced with permission from literature.[238]

1.3.2.2.3. LDH-based core-shell catalysts for CO_2 to olefins

There is only one example of using LDH-based core-shell material to catalysing CO_2 to olefins conversion. Wang *et al.* developed nano-sized zeolite decorated CoAl layered double oxide (CoAl-LDO@NZ) for CO_2 to gasoline catalysis (Figure 1.17a).[243] Co in CoAl-LDO is responsible for catalysing CO to hydrocarbon conversion via the Fischer-Tropsch reaction. The core-shell catalyst shows better gasoline selectivity (70.5%) and lower long-chain hydrocarbon selectivity (3.9%) than the pure CoAl-LDO (43.1% and 15.9%, respectively). The author proposed that the nano-sized zeolite catalyses the hydrocracking of long-chain hydrocarbon and produce short-chain product (Figure 1.17b). Moreover, the small size of zeolite particles inhibits the over-cracking for C_1–C_4 hydrocarbon, resulting in a narrow product distribution.[243]

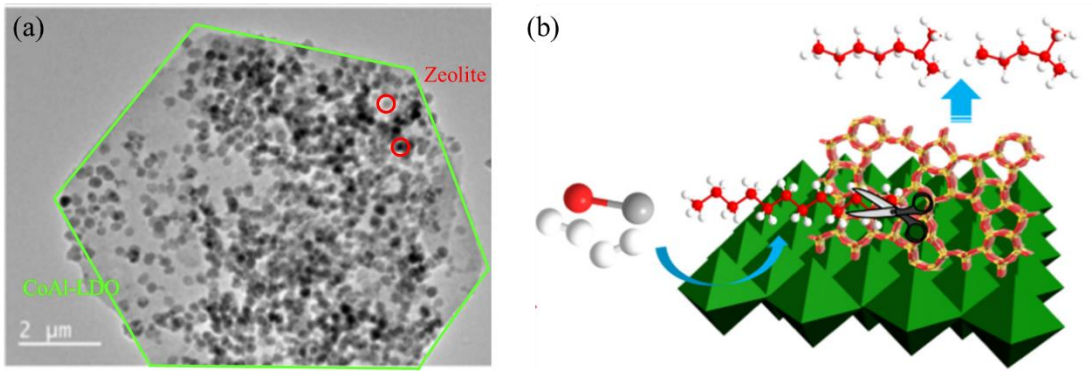


Figure 1.17 (a) TEM image of CoAl-LDO@NZ. (b) Scheme of the reaction mechanism of CoAl-LDO@NZ in the FT reaction. H, C and O are represented by white, red and grey, respectively.

1.4 Scope of thesis

The scope of this thesis is to develop a series of LDH-based core-shell materials and use them as efficient CO_2 sorbents or catalysts for CO_2 hydrogenation to methanol or olefins. In Chapter 2, the synthesis and characterisation of core-shells using zeolite-13X (the benchmark CO_2 adsorbent) as the core and Mg_2Al LDH as the shell are conducted and the CO_2 adsorption ability of the core-shell materials is examined. The effect of synthetic conditions and composition on the crystallinity, morphology and CO_2 capture ability of the core-shells are investigated. Chapter 3 focuses on the synthesis and characterisation of silica-supported CuZnAl-LDH core-shells. The effect of synthetic conditions, copper loading and property of silica core on the crystallinity, composition, morphology, and porosity of core-shell are investigated. Chapter 4 presents the catalyst evaluation of CO_2 hydrogenation to methanol using some core-shells prepared in Chapter 3. The effect of copper loading and the property of silica on the catalytic performance of core-shell are discussed. The application of CuZnAl-LDH based core-shell materials in CO_2 hydrogenation is further explored in Chapter 5 by changing the core from silica to H-ZSM-5, aiming to produce high value olefins. The preliminary catalytic results and

synthesis optimisation are presented, trying to modify the acidity of the core-shell and improve the catalytic activity.

1.5 References

1 H. Yan, X.-J. Zhao, Y.-Q. Zhu, M. Wei, D. G. Evans and X. Duan, in *The Periodic Table II: Catalytic, Materials, Biological and Medical Applications*, ed. D. M. P. Mingos, Springer International Publishing, Cham, 2019, pp. 89–120.

2 F. Cavani, F. Trifirò and A. Vaccari, *Catal. Today*, 1991, **11**, 173–301.

3 A. Garcia-Gallastegui, D. Iruretagoyena, M. Mokhtar, A. M. Asiri, S. N. Basahel, S. A. Al-Thabaiti, A. O. Alyoubi, D. Chadwick and M. S. P. Shaffer, *J. Mater. Chem.*, 2012, **22**, 13932–13940.

4 E. Manasse, *Atti Soc. Toscana Sci. Nat.*, 1915, **24**, 92–92.

5 W. Feitknecht, *Helv. Chim. Acta*, 1942, **27**, 131–137.

6 D. G. Evans and R. C. T. Slade, in *Layered Double Hydroxides (Structure and bonding)*, eds. D. G. Evans and X. Duan, Springer-Verlag, Berlin/Heidelberg, 1st edn., 2006, vol. 119, pp. 1–87.

7 F. Basile, G. Fornasari, M. Gazzano and A. Vaccari, *Appl. Clay Sci.*, 2000, **16**, 185–200.

8 X. Hou, A. G. Kalinichev and R. J. Kirkpatrick, *Chem. Mater.*, 2002, **14**, 2078–2085.

9 D. Srankó, A. Pallagi, E. Kuzmann, S. E. Canton, M. Walczak, A. Sápi, Á. Kukovecz, Z. Kónya, P. Sipos and I. Pálinkó, *Appl. Clay Sci.*, 2010, **48**, 214–217.

10 J. L. Milagres, C. R. Bellato, R. S. Vieira, S. O. Ferreira and C. Reis, *J. Environ. Chem. Eng.*, 2017, **5**, 5469–5480.

11 C. Depège, F. Z. El Metoui, C. Forano, A. De Roy, J. Dupuis and J. P. Besse, *Chem. Mater.*, 1996, **8**, 952–960.

12 A. I. Khan and D. O'Hare, *J. Mater. Chem.*, 2002, **12**, 3191–3198.

13 K. A. Carrado, A. Kostapapas and S. L. Suib, *Solid State Ionics*, 1988, **26**, 77–86.

14 S. P. Newman and W. Jones, *New J. Chem.*, 1998, **22**, 105–115.

15 Z. Li, Q. Zhang, X. Liu, L. Wu, H. Hu and Y. Zhao, *J. Mater. Sci.*, 2018, **53**, 12795–12806.

16 L. H. Chagas, G. S. G. De Carvalho, W. R. Do Carmo, R. A. S. San Gil, S. S. X. Chiaro, A. A. Leitão, R. Diniz, L. A. De Sena and C. A. Achete, *Mater. Res. Bull.*, 2015, **64**, 207–215.

17 S. Velu, N. Satoh, C. S. Gopinath and K. Suzuki, *Catal. Letters*, 2002, **82**, 145–152.

18 L. H. Zhang, F. Li, D. G. Evans and X. Duan, *J. Mater. Sci.*, 2010, **45**, 3741–3751.

19 C. Wang, DPhil thesis, University of Oxford, 2012.

20 F. Dionigi, Z. Zeng, I. Sinev, T. Merzdorf, S. Deshpande, M. B. Lopez, S. Kunze, I. Zegkinoglou, H. Sarodnik, D. Fan, A. Bergmann, J. Drnec, J. F. de Araujo, M. Gliech, D. Teschner, J. Zhu, W. X. Li, J. Greeley, B. R. Cuenya and P. Strasser, *Nat. Commun.*, 2020, **11**, 1–10.

21 A. V. Radha, P. V. Kamath and C. Shivakumara, *Acta Crystallogr. Sect. B Struct. Sci.*, 2007, **63**, 243–250.

22 S. Radha and P. V. Kamath, *Zeitschrift fur Anorg. und Allg. Chemie*, 2012, **638**, 2317–2323.

23 Z. P. Xu, J. Zhang, M. O. Adebajo, H. Zhang and C. Zhou, *Appl. Clay Sci.*, 2011, **53**, 139–150.

24 R. D. Shannon, *Acta Cryst.*, 1976, **A32**, 751–767.

25 H. Jing, M. Wei, L. Bo, K. Yu, D. G. Evans and X. Duan, in *Layered Double Hydroxides (Structure and bonding)*, eds. D. G. Evans and X. Duan, Springer-Verlag, Berlin/Heidelberg, 1st edn., 2006, vol. 119, pp.

89–119.
26 W. L. J. Kwok, University of Oxford, 2020.
27 H. H. Willard and N. K. Tang, *J. Am. Chem. Soc.*, 1937, **59**, 1190–1196.
28 Y. K. Lin, Y. H. Su, Y. H. Huang, C. J. Hsu, Y. K. Hsu, Y. G. Lin, K. H. Huang, S. Y. Chen, K. H. Chen and L. C. Chen, *J. Mater. Chem.*, 2009, **19**, 9186–9194.
29 O. O. Oluokun and I. O. Otunniyi, *Hydrometallurgy*, 2020, **193**, 105320–105326.
30 A. R. Johnson, T. M. McQueen and K. T. Rodolfa, *J. Chem. Educ.*, 2005, **82**, 408–414.
31 G. Hu and D. O'Hare, *J. Am. Chem. Soc.*, 2005, **127**, 17808–17813.
32 C. J. Wang, Y. A. Wu, R. M. J. Jacobs, J. H. Warner, G. R. Williams and D. O'Hare, *Chem. Mater.*, 2011, **23**, 171–180.
33 U. Costantino, F. Marmottini, M. Nocchetti and R. Vivani, *Eur. J. Inorg. Chem.*, 1998, 1439–1446.
34 F. Prinetto, G. Ghiotti, P. Graffin and D. Tichit, *Microporous Mesoporous Mater.*, 2000, **39**, 229–247.
35 M. Yang, G. Zhang, C. Wu, Z. Chang, X. Sun and X. Duan, *Chinese J. Chem.*, 2012, **30**, 2183–2188.
36 L. H. Zhang, C. Zheng, F. Li, D. G. Evans and X. Duan, *J. Mater. Sci.*, 2008, **43**, 237–243.
37 M. Behrens, I. Kasatkin, S. Kühl and G. Weinberg, *Chem. Mater.*, 2010, **22**, 386–397.
38 Y. Zhang, C. Li, C. Yu, T. Tran, F. Guo, Y. Yang, J. Yu and G. Xu, *Chem. Eng. J.*, 2017, **330**, 1082–1090.
39 G. Chen, R. Gao, Y. Zhao, Z. Li, G. I. N. Waterhouse, R. Shi, J. Zhao, M. Zhang, L. Shang, G. Sheng, X. Zhang, X. Wen, L. Z. Wu, C. H. Tung and T. Zhang, *Adv. Mater.*, 2018, **30**, 1–8.
40 Q. Wang, Z. Wu, H. H. Tay, L. Chen, Y. Liu, J. Chang, Z. Zhong, J. Luo and A. Borgna, *Catal. Today*, 2011, **164**, 198–203.
41 X. Zhu, C. Chen, H. Suo, Q. Wang, Y. Shi, D. O'Hare and N. Cai, *Energy*, 2019, **167**, 960–969.
42 Y. Gao, Z. Zhang, J. Wu, X. Yi, A. Zheng, A. Umar, D. O'Hare and Q. Wang, *J. Mater. Chem. A*, 2013, **1**, 12782–12790.
43 J. Rocha, M. Del Arco, V. Rives and M. A. Ulibarri, *J. Mater. Chem.*, 1999, **9**, 2499–2503.
44 Y. Zhao, B. Li, Q. Wang, W. Gao, C. J. Wang, M. Wei, D. G. Evans, X. Duan and D. O'Hare, *Chem. Sci.*, 2014, **5**, 951–958.
45 G. Fan, F. Li, D. G. Evans and X. Duan, *Chem. Soc. Rev.*, 2014, **43**, 7040–7066.
46 Y. Wei, X. Zhang, X. Wu, D. Tang, K. Cai and Q. Zhang, *RSC Adv.*, 2016, **6**, 39317–39322.
47 X. Li, D. Du, Y. Zhang, W. Xing, Q. Xue and Z. Yan, *J. Mater. Chem. A*, 2017, **5**, 15460–15485.
48 Q. Wang, Y. Gao, J. Luo, Z. Zhong, A. Borgna, Z. Guo and D. O'Hare, *RSC Adv.*, 2013, **3**, 3414–3420.
49 F. P. Jiao, Z. Di Fu, L. Shuai and X. Q. Chen, *Trans. Nonferrous Met. Soc. China*, 2012, **22**, 476–482.
50 X. Bi, H. Zhang and L. Dou, *Pharmaceutics*, 2014, **6**, 298–332.
51 D. Li, Y. T. Zhang, M. Yu, J. Guo, D. Chaudhary and C. C. Wang, *Biomaterials*, 2013, **34**, 7913–7922.
52 Q. Wang and D. O'Hare, *Chem. Commun.*, 2013, **49**, 6301–6303.
53 N. P. Funnell, Q. Wang, L. Connor, M. G. Tucker, D. O'Hare and A. L. Goodwin, *Nanoscale*, 2014, **6**, 8032–8036.
54 C. Chen, M. Yang, Q. Wang, J.-C. Buffet and D. O'Hare, *J. Mater. Chem. A*, 2014, **2**, 15102–15110.
55 Q. Wang, J. P. Undrell, Y. Gao, G. Cai, J. C. Buffet, C. A. Wilkie and D. O'Hare, *Macromolecules*, 2013, **46**, 6145–6150.
56 J. Yu, B. R. Martin, A. Clearfield, Z. Luo and L. Sun, *Nanoscale*, 2015, **7**, 9448–9451.
57 R. Ma, Z. Liu, L. Li, N. Iyi and T. Sasaki, *J. Mater. Chem.*, 2006, **16**, 3809–3813.
58 S. O'Leary, D. O'Hare and G. Seeley, *Chem. Commun.*, 2002, **2**, 1506–1507.

59 M. Adachi-Pagano, C. Forano and J. P. Besse, *Chem. Commun.*, 2000, **1**, 91–92.

60 F. Leroux, M. Adachi-Pagano, M. Intissar, S. Chauvière, C. Forano and J. P. Besse, *J. Mater. Chem.*, 2001, **11**, 105–112.

61 J. Yu, Q. Wang, D. O'Hare and L. Sun, *Chem. Soc. Rev.*, 2017, **46**, 5950–5974.

62 C. Chen, R. Felton, J.-C. Buffet and D. O'Hare, *Chem. Commun.*, 2015, **51**, 3462–3465.

63 W. L. J. Kwok, D.-G. Crivoi, C. Chen, J.-C. Buffet and D. O'Hare, *Dalton Trans.*, 2018, **47**, 143–149.

64 C. Chen, R. Felton, J. C. Buffet and D. O'Hare, *Chem. Commun.*, 2015, **51**, 3462–3465.

65 H. Suo, C. Chen, J.-C. Buffet and D. O'Hare, *Dalton Trans.*, 2018, **47**, 16413–16417.

66 J.-C. Buffet, C. F. H. Byles, R. Felton, C. Chen and D. O'Hare, *Chem. Commun.*, 2016, **52**, 4076–4079.

67 C. Chen, C. F. H. Byles, J.-C. Buffet, N. H. Rees, Y. Wu and D. O'Hare, *Chem. Sci.*, 2016, **7**, 1457–1461.

68 H. Suo, H. Duan, C. Chen, J. C. Buffet and D. O'Hare, *RSC Adv.*, 2019, **9**, 3749–3754.

69 M. Lyu, C. Chen, J. C. Buffet and D. O'Hare, *New J. Chem.*, 2020, **44**, 10095–10101.

70 Y. Zhang, L. Wen, X. Bai, N. Song, X. Huang and Y. Li, *Chem. Lett.*, 2019, **48**, 1148–1151.

71 H. Suo, H. Duan, C. Chen, J.-C. Buffet and D. O'Hare, *RSC Adv.*, 2019, **9**, 3749–3754.

72 C. Chen, P. Gunawan and R. Xu, *J. Mater. Chem.*, 2011, **21**, 1218–1225.

73 H. Zhang, G. Zhang, X. Bi and X. Chen, *J. Mater. Chem. A*, 2013, **1**, 5934–5942.

74 P. Li, Y. Yu, P. P. Huang, H. Liu, C. Y. Cao and W. G. Song, *J. Mater. Chem. A*, 2014, **2**, 339–344.

75 S. Das, J. Pérez-Ramírez, J. Gong, N. Dewangan, K. Hidajat, B. C. Gates and S. Kawi, *Chem. Soc. Rev.*, 2020, **49**, 2937–3004.

76 M. R. Othman, N. M. Rasid and W. J. N. Fernando, *Chem. Eng. Sci.*, 2006, **61**, 1555–1560.

77 R. Li, T. Xue, R. Bingre, Y. Gao, B. Louis and Q. Wang, *ACS Appl. Mater. Interfaces*, 2018, **10**, 34834–34839.

78 Z. Gu, J. J. Atherton and Z. P. Xu, *Chem. Commun.*, 2015, **51**, 3024–3036.

79 C. Chen, P. Wang, T. T. Lim, L. Liu, S. Liu and R. Xu, *J. Mater. Chem. A*, 2013, **1**, 3877–3880.

80 M. Shao, F. Ning, J. Zhao, M. Wei, D. G. Evans and X. Duan, *J. Am. Chem. Soc*, 2012, **134**, 1071–1077.

81 M. Shao, F. Ning, Y. Zhao, J. Zhao, M. Wei, D. G. Evans and X. Duan, *Chem. Mater.*, 2012, **24**, 1192–1197.

82 Y. Zhao, S. He, M. Wei, D. G. Evans and X. Duan, *Chem. Commun.*, 2010, **46**, 3031–3033.

83 L. Li, R. Ma, N. Iyi, Y. Ebina, K. Takada and T. Sasaki, *Chem. Commun.*, 2006, **2**, 3125–3127.

84 X. Liu, C. Wang, Y. Dou, A. Zhou, T. Pan, J. Han and M. Wei, *J. Mater. Chem. A*, 2014, **2**, 1682–1685.

85 X. Ge, Y. He, T. Plachy, N. Kazantseva, P. Saha and Q. Cheng, *Nanomaterials*, 2019, **9**, 527–541.

86 J. Cao, L. Li, Y. Xi, J. Li, X. Pan, D. Chen and W. Han, *Sustain. Energy Fuels*, 2018, **2**, 1350–1355.

87 C. Chen, L. K. Yee, H. Gong, Y. Zhang and R. Xu, *Nanoscale*, 2013, **5**, 4314–4320.

88 D. Park, J.-E. Kim, J.-M. Oh, Y.-G. Shul and J.-H. Choy, *J. Am. Chem. Soc.*, 2010, **132**, 16735–16736.

89 L. Yu, H. Zhou, J. Sun, F. Qin, D. Luo, L. Xie, F. Yu, J. Bao, Y. Li, Y. Yu, S. Chen and Z. Ren, *Nano Energy*, 2017, **41**, 327–336.

90 L. Yu, H. Zhou, J. Sun, F. Qin, F. Yu, J. Bao, Y. Yu, S. Chen and Z. Ren, *Energy Environ. Sci.*, 2017, **10**, 1820–1827.

91 G. Mendoza-Damián, F. Tzompantzi, A. Mantilla, R. Pérez-Hernández and A. Hernández-Gordillo, *Appl. Clay Sci.*, 2016, **121**–**122**, 127–136.

92 Q. Guo, Q. Zhang, H. Wang, Z. Liu and Z. Zhao, *Catal. Commun.*, 2016, **77**, 118–122.

93 S. Wu, K. S. Hui and K. N. Hui, *J. Phys. Chem. C*, 2015, **119**, 23358–23365.

94 Y. Ni, L. Yao, Y. Wang, B. Liu, M. Cao and C. Hu, *Nanoscale*, 2017, **9**, 11596–11604.

95 Y. Zhao, X. He, R. Chen, Q. Liu, J. Liu, J. Yu, J. Li, H. Zhang, H. Dong, M. Zhang and J. Wang, *Chem. Eng. J.*, 2018, **352**, 29–38.

96 D. Pan, H. Zhang, T. Fan, J. Chen and X. Duan, *Chem. Commun.*, 2011, **47**, 908–910.

97 Q. Yan, Z. Zhang, Y. Zhang, A. Umar, Z. Guo, D. O'Hare and Q. Wang, *Eur. J. Inorg. Chem.*, 2015, **25**, 4182–4191.

98 J.-C. Buffet, C. F. H. Byles, R. Felton, C. Chen and D. O'Hare, *Chem. Commun.*, 2016, **52**, 4076–4079.

99 C. Wang, B. Ma, S. Xu, D. Li, S. He, Y. Zhao, J. Han, M. Wei, D. G. Evans and X. Duan, *Nano Energy*, 2017, **32**, 463–469.

100 X. Li, Z. Yang, W. Qi, Y. Li, Y. Wu, S. Zhou, S. Huang, J. Wei, H. Li and P. Yao, *Appl. Surf. Sci.*, 2016, **363**, 381–388.

101 Y. Ni, L. Yao, Y. Wang, B. Liu, M. Cao and C. Hu, *Nanoscale*, 2017, **9**, 11596–11604.

102 M. Thommes, K. Kaneko, A. V. Neimark, J. P. Olivier, F. Rodriguez-Reinoso, J. Rouquerol and K. S. W. Sing, *Pure Appl. Chem.*, 2015, **87**, 1051–1069.

103 K. A. Cychosz and M. Thommes, *Engineering*, 2018, **4**, 559–566.

104 R. Bardestani, G. S. Patience and S. Kaliaguine, *Can. J. Chem. Eng.*, 2019, **97**, 2781–2791.

105 E. P. Barrett, L. G. Joyner and P. P. Halenda, *Vol. Area Distrib. Porous Subst.*, 1951, **73**, 373–380.

106 M. L. Ojeda, J. M. Esparza, A. Campero, S. Cordero, I. Kornhauser and F. Rojas, *Phys. Chem. Chem. Phys.*, 2003, **5**, 1859–1866.

107 F. J. Sotomayor, K. A. Cychosz and M. Thommes, *Acc. Mater. Surf. Res*, 2018, **3**, 34–50.

108 A. Baede, P. van der Linden and A. Verbruggen, *Annex to IPCC Fourth Assessment Report*, 2007, vol. 1.

109 D. Archer, in *Global Warming: understanding the forecast*, ed. D. Archer, Wiley-Blackwell, 1st edn., 2006, pp. 29–45.

110 M. Höpfner, M. Milz, S. Buehler, J. Orphal and G. Stiller, *Geophys. Res. Lett.*, 2012, **39**, 6–11.

111 M. Sai Bhargava Reddy, D. Ponnamma, K. K. Sadasivuni, B. Kumar and A. M. Abdullah, *RSC Adv.*, 2021, **11**, 12658–12681.

112 British Petroleum Company, *BP statistical review of world energy*, 2018.

113 J. Yu, L.-H. Xie, J.-R. Li, Y. Ma, J. M. Seminario and P. B. Balbuena, *Chem. Rev.*, 2017, **117**, 9674–9754.

114 J. R. Li, Y. Ma, M. C. McCarthy, J. Sculley, J. Yu, H. K. Jeong, P. B. Balbuena and H. C. Zhou, *Coord. Chem. Rev.*, 2011, **255**, 1791–1823.

115 S. C. Doney, V. J. Fabry, R. A. Feely and J. A. Kleypas, *Ann. Rev. Mar. Sci.*, 2009, **1**, 169–192.

116 Masson-Delmotte, P. Z. V., H.-O. Pörtner, D. Roberts, J. Skea, P. R. Shukla, A. Pirani, W. Moufouma-Okia, R. P. C. Péan, S. Connors, J. B. R. Matthews, Y. Chen, X. Zhou, M. I. Gomis, E. Lonnoy, T. Maycock, M. Tignor and T. Waterfield, *2018: Global Warming of 1.5°C. An IPCC Special Report on the impacts of global warming of 1.5°C above pre-industrial levels and related global greenhouse gas emission pathways, in the context of strengthening the global response to the threat of climate c*, 2018.

117 X. Shi, H. Xiao, H. Azarabadi, J. Song, X. Wu, X. Chen and K. S. Lackner, *Angew. Chem. Int. Ed.*, 2020, **59**, 6984–7006.

118 F. M. Baena-Moreno, M. Rodríguez-Galán, F. Vega, B. Alonso-Fariñas, L. F. Vilches Arenas and B. Navarrete, *Energy Sources, Part A Recover. Util. Environ. Eff.*, 2019, **41**, 1403–1433.

119 S. Choi, J. H. Drese and C. W. Jones, *ChemSusChem*, 2009, **2**, 796–854.

120 D. Aaron and C. Tsouris, *Sep. Sci. Technol.*, 2005, **40**, 321–348.

121 A. Mukherjee, J. A. Okolie, A. Abdelrasoul, C. Niu and A. K. Dalai, *J. Environ. Sci. (China)*, 2019, **83**, 46–63.

122 Y. Artanto, J. Jansen, P. Pearson, T. Do, A. Cottrell, E. Meuleman and P. Feron, *Fuel*, 2012, **101**, 264–275.

123 C. Song, W. Pan, S. T. Srimat, J. Zheng, Y. Li, Y. H. Wang, B. Q. Xu and Q. M. Zhu, *Stud. Surf. Sci. Catal.*, 2004, **153**, 315–322.

124 F. A. Rahman, M. M. A. Aziz, R. Saidur, W. A. W. A. Bakar, M. R. Hainin, R. Putrajaya and N. A. Hassan, *Renew. Sustain. Energy Rev.*, 2017, **71**, 112–126.

125 K. Sumida, D. L. Rogow, J. A. Mason, T. M. McDonald, E. D. Bloch, Z. R. Herm, T. H. Bae and J. R. Long, *Chem. Rev.*, 2012, **112**, 724–781.

126 G. T. Rochelle, *Science*, 2009, **325**, 1652–1654.

127 B. Seoane, J. Coronas, I. Gascon, M. E. Benavides, O. Karvan, J. Caro, F. Kapteijn and J. Gascon, *Chem. Soc. Rev.*, 2015, **44**, 2421–2454.

128 L. Zou, Y. Sun, S. Che, X. Yang, X. Wang, M. Bosch, Q. Wang, H. Li, M. Smith, S. Yuan, Z. Perry and H. C. Zhou, *Adv. Mater.*, 2017, **29**, 1–35.

129 J. Merel, M. Clausse and F. Meunier, *Ind. Eng. Chem. Res.*, 2008, **47**, 209–215.

130 R. Ben-Mansour, M. A. Habib, O. E. Bamidele, M. Basha, N. A. A. Qasem, A. Peedikakkal, T. Laoui and M. Ali, *Appl. Energy*, 2016, **161**, 225–255.

131 F. Brandani and D. M. Ruthven, *Ind. Eng. Chem. Res.*, 2004, **43**, 8339–8344.

132 Z. Zhang, Z. Yao, S. Xiang and B. Chen, *Energy Environ. Sci.*, 2014, **7**, 2868–2899.

133 C. Trickett, A. Helal, B. Al-Maythalony, Z. H. Yamani, K. E. Cordova and O. M. Yaghi, *Nat. Rev. Mater.*, 2017, **2**, 1–16.

134 P. Asiedu-Boateng, R. Legros and G. S. Patience, *Adv. Powder Technol.*, 2016, **27**, 786–795.

135 K. Ho, S. Jin, M. Zhong, A. T. Vu and C. H. Lee, *Mater. Chem. Phys.*, 2017, **198**, 154–161.

136 M. A. Camblor and S. B. Hong, in *Porous Materials*, eds. D. W. Bruce, D. O'Hare and R. I. Walton, John Wiley & Sons Ltd, 1st edn., 2011, pp. 265–325.

137 W. J. Roth, P. Nachtigall, R. E. Morris and J. Čejka, *Chem. Rev.*, 2014, **114**, 4807–4837.

138 F. Dreisbach, R. Staudt and J. U. Keller, *Adsorption*, 1999, **5**, 215–227.

139 A. I. Shirley, *Ind. Eng. Chem. Res.*, 1994, **33**, 2879–2880.

140 B. K. Na, K. K. Koo, H. M. Eum, H. Lee and H. K. Song, *Korean J. Chem. Eng.*, 2001, **18**, 220–227.

141 K. T. Chue, J. N. Kim, Y. J. Yoo, S. H. Cho and R. T. Yang, *Ind. Eng. Chem. Res.*, 1995, **34**, 591–598.

142 R. P. Davies, P. D. Lickiss, K. Robertson and A. J. P. White, *Aust. J. Chem.*, 2011, **64**, 1239–1246.

143 R. P. Davies, P. D. Lickiss, K. Robertson and A. J. P. White, *CrystEngComm*, 2012, **14**, 758–760.

144 P. D. C. Dietzel, R. Blom and H. Fjellvåg, *Eur. J. Inorg. Chem.*, 2008, **23**, 3624–3632.

145 Z. Bao, L. Yu, Q. Ren, X. Lu and S. Deng, *J. Colloid Interface Sci.*, 2011, **353**, 549–556.

146 A. C. Kizzie, A. G. Wong-Foy and A. J. Matzger, *Langmuir*, 2011, **27**, 6368–6373.

147 K. Sumida, D. L. Rogow, J. A. Mason, T. M. Mcdonald, E. D. Bloch, Z. R. Herm, T. Bae and R. Long, 2012, **112**, 724–781.

148 R. Barker, *J. appl. Chem. Biotechnol*, 1974, **24**, 221–227.

149 Z. S. Li, N. S. Cai and Y. Y. Huang, *Ind. Eng. Chem. Res.*, 2006, **45**, 1911–1917.

150 S. K. Bhatia and D. D. Perlmutter, *AIChE J.*, 1983, **29**, 79–86.

151 V. K. Singh and E. A. Kumar, *Energy Procedia*, 2016, **90**, 316–325.

152 X. Zhu, C. Chen, H. Suo, Q. Wang, Y. Shi, D. O'Hare and N. Cai, *Energy*, 2019, **167**, 960–969.

153 Q. Wang, H. H. Tay, D. J. W. Ng, L. Chen, Y. Liu, J. Chang, Z. Zhong, J. Luo and A. Borgna, *ChemSusChem*, 2010, **3**, 965–973.

154 N. D. Hutson and B. C. Attwood, *Adsorption*, 2008, **14**, 781–789.

155 P. W. Xiao, J. Y. Jun, J. Cheng, P. H. Zheng and P. X. Zhi, *Environ. Sci. Technol.*, 2008, **42**, 614–618.

156 N. D. Hutson, S. A. Speakman and E. A. Payzant, *Chem. Mater.*, 2004, **16**, 4135–4143.

157 M. K. Ram Reddy, Z. P. Xu, G. Q. Lu and J. C. Diniz Da Costa, *Ind. Eng. Chem. Res.*, 2008, **47**, 2630–2635.

158 D. A. Torres-Rodríguez, E. Lima, J. S. Valente and H. Pfeiffer, *J. Phys. Chem. A*, 2011, **115**, 12243–12250.

159 K. Coenen, F. Gallucci, G. Pio, P. Cobden, E. van Dijk, E. Hensen and M. van Sint Annaland, *Chem. Eng. J.*, 2017, **314**, 554–569.

160 M. J. Ramírez-Moreno, I. C. Romero-Ibarra, M. A. Hernández-Pérez and H. Pfeiffer, *Ind. Eng. Chem. Res.*, 2014, **53**, 8087–8094.

161 S. Cavenati, C. A. Grande and A. E. Rodrigues, *J. Chem. Eng. Data*, 2004, **49**, 1095–1101.

162 Y. Ding and E. Alpay, *Process Saf. Environ. Prot.*, 2001, **79**, 45–51.

163 X. Zhu, C. Chen, Q. Wang, Y. Shi, D. O'Hare and N. Cai, *Chem. Eng. J.*, 2019, **366**, 181–191.

164 X. Zhu, T. Ge, F. Yang, M. Lyu, C. Chen, D. O'Hare and R. Wang, *J. Mater. Chem. A*, 2020, **8**, 16421–16428.

165 X. Zhu, M. Lyu, T. Ge, J. Wu, C. Chen, F. Yang, D. O'Hare and R. Wang, *Cell Reports Phys. Sci.*, 2021, **2**, 1–14.

166 Q. Al-Naddaf, A. A. Rownaghi and F. Rezaei, *Chem. Eng. J.*, 2020, **384**, 1–9.

167 D. Iruretagoyena, M. S. P. Shaffer and D. Chadwick, *Ind. Eng. Chem. Res.*, 2015, **54**, 6781–6792.

168 F. Yang, J. Wu, X. Zhu, T. Ge and R. Wang, *Chem. Eng. J.*, 2021, **410**, 1–8.

169 Q. Al-Naddaf, H. Thakkar and F. Rezaei, *ACS Appl. Mater. Interfaces*, 2018, **10**, 29656–29666.

170 A. Schoedel, Z. Ji and O. M. Yaghi, *Nat. Energy*, 2016, **1**, 1–13.

171 B. Smit, *Faraday Discuss.*, 2016, **192**, 9–25.

172 J. Alcalde, S. Flude, M. Wilkinson, G. Johnson, K. Edlmann, C. E. Bond, V. Scott, S. M. V. Gilfillan, X. Ogaya and R. Stuart Haszeldine, *Nat. Commun.*, 2018, **8**, 1–13.

173 J. Artz, T. E. Müller, K. Thenert, J. Kleinekorte, R. Meys, A. Sternberg, A. Bardow and W. Leitner, *Chem. Rev.*, 2018, **118**, 434–504.

174 H. Yang, C. Zhang, P. Gao, H. Wang, X. Li, L. Zhong, W. Wei and Y. Sun, *Catal. Sci. Technol.*, 2017, **7**, 4580–4598.

175 Z. Ma and M. D. Porosoff, *ACS Catal.*, 2019, **9**, 2639–2656.

176 N. Podrojková, V. Sans, A. Oriňak and R. Oriňaková, *ChemCatChem*, 2020, **12**, 1802–1825.

177 B. deB. Darwent, *Bond Dissociation Energies in Simple molecules*, 1970, vol. 31.

178 V. I. Vedeneev, *Bond energies, ionization potentials and electron affinities*, New York: St. Martin's, 1966.

179 C. Song, *Catal. Today*, 2006, **115**, 2–32.

180 X. Jiang, X. Nie, X. Guo, C. Song and J. G. Chen, *Chem. Rev.*, 2020, **120**, 7984–8034.

181 K. Harris, R. G. Grim, Z. Huang and L. Tao, *Appl. Energy*, 2021, **303**, 117637.

182 M. Alvarado, *The changing face of the global methanol industry*, 2016.

183 M. Alvarado, *Methanol Industry Overview*, Stanford Natural Gas Initiative Stanford, CA, 2017.

184 C. F. Shih, T. Zhang, J. Li and C. Bai, *Joule*, 2018, **2**, 1925–1949.

185 M. J. Bos, S. R. A. Kersten and D. W. F. Brilman, *Appl. Energy*, 2020, **264**, 114672.

186 C. Hank, S. Gelpke, A. Schnabl, R. J. White, J. Full, N. Wiebe, T. Smolinka, A. Schaadt, H. M. Henning and C. Hebling, *Sustain. Energy Fuels*, 2018, **2**, 1244–1261.

187 G. J. Janz and S. C. Wait, *J. Chem. Phys.*, 1955, **23**, 1550–1551.

188 O. A. Ojelade and S. F. Zaman, *Catal. Surv. from Asia*, 2020, **24**, 11–37.

189 P. S. Murthy, W. Liang, Y. Jiang and J. Huang, *Energy Fuels*, 2021, **35**, 8558–8584.

190 A. Bansode and A. Urakawa, *J. Catal.*, 2014, **309**, 66–70.

191 A. García-Trenco, A. Regoutz, E. R. White, D. J. Payne, M. S. P. Shaffer and C. K. Williams, *Appl. Catal. B Environ.*, 2018, **220**, 9–18.

192 G. Wang, D. Mao, X. Guo and J. Yu, *Int. J. Hydrogen Energy*, 2019, **44**, 4197–4207.

193 A. Bansode, B. Tidona, P. R. Von Rohr and A. Urakawa, *Catal. Sci. Technol.*, 2013, **3**, 767–778.

194 T. Fujitani, M. Saito, Y. Kanai, T. Watanabe, J. Nakamura and T. Uchijima, *Appl. Catal. A, Gen.*, 1995, **125**, 199–202.

195 S. Bai, Q. Shao, Y. Feng, L. Bu and X. Huang, *Small*, 2017, **13**, 1–6.

196 J. Wang, G. Li, Z. Li, C. Tang, Z. Feng, H. An, H. Liu, T. Liu and C. Li, *Sci. Adv.*, 2017, **3**, 1–11.

197 J. Wang, C. Tang, G. Li, Z. Han, Z. Li, H. Liu, F. Cheng and C. Li, *ACS Catal.*, 2019, **9**, 10253–10259.

198 O. Martin, A. J. Martín, C. Mondelli, S. Mitchell, T. F. Segawa, R. Hauert, C. Drouilly, D. Curulla-Ferré and J. Pérez-Ramírez, *Angew. Chem. Int. Ed.*, 2016, **55**, 6261–6265.

199 C. Y. Chou and R. F. Lobo, *Appl. Catal. A Gen.*, 2019, **583**, 1–9.

200 F. Lin, X. Jiang, N. Boreriboon, Z. Wang, C. Song and K. Cen, *Appl. Catal. A Gen.*, 2019, **585**, 1–10.

201 I. Sharafutdinov, C. F. Elkjær, H. W. P. De Carvalho, D. Gardini, G. L. Chiarello, C. D. Damsgaard, J. B. Wagner, J. D. Grunwaldt, S. Dahl and I. Chorkendorff, *J. Catal.*, 2014, **320**, 77–88.

202 X. Li, G. Liu, D. Xu, X. Hong and S. C. Edman Tsang, *J. Mater. Chem. A*, 2019, **7**, 23878–23885.

203 B. Hu, Y. Yin, Z. Zhong, D. Wu, G. Liu and X. Hong, *Catal. Sci. Technol.*, 2019, **9**, 2673–2681.

204 P. Gao, R. Xie, H. Wang, L. Zhong, L. Xia, Z. Zhang, W. Wei and Y. Sun, *J. CO2 Util.*, 2015, **11**, 41–48.

205 S. Xiao, Y. Zhang, P. Gao, L. Zhong, X. Li, Z. Zhang, H. Wang, W. Wei and Y. Sun, *Catal. Today*, 2017, **281**, 327–336.

206 A. Ota, E. L. Kunkes, I. Kasatkin, E. Groppo, D. Ferri, B. Poceiro, R. M. Navarro Yerga and M. Behrens, *J. Catal.*, 2012, **293**, 27–38.

207 H. Yang, P. Gao, C. Zhang, L. Zhong, X. Li, S. Wang, H. Wang, W. Wei and Y. Sun, *Catal. Commun.*, 2016, **84**, 56–60.

208 B. An, J. Zhang, K. Cheng, P. Ji, C. Wang and W. Lin, *J. Am. Chem. Soc.*, 2017, **139**, 3834–3840.

209 M. B. Fichtl, D. Schlereth, N. Jacobsen, I. Kasatkin, J. Schumann, M. Behrens, R. Schlögl and O. Hinrichsen, *Appl. Catal. A Gen.*, 2015, **502**, 262–270.

210 T. Lunkenbein, F. Girgsdies, T. Kandemir, N. Thomas, M. Behrens, R. Schlögl and E. Frei, *Angew. Chem. Int. Ed.*, 2016, **55**, 12708–12712.

211 J. G. Nunan, P. B. Himelfarb, R. G. Herman, K. Klier, C. E. Bogdan and G. W. Simmons, *Inorg. Chem.*, 1989, **28**, 3868–3874.

212 M. M. J. Li, C. Chen, T. Ayvall, H. Suo, J. Zheng, I. F. Teixeira, L. Ye, H. Zou, D. O'Hare and S. C. E. Tsang, *ACS Catal.*, 2018, **8**, 4390–4401.

213 C. Busetto, G. Del Piero, G. Manara, F. Trifirò and A. Vaccari, *J. Catal.*, 1984, **85**, 260–266.

214 P. W. Atkins, T. L. Overton, J. P. Rourke, M. T. Weller and F. A. Armstrong, in *Shriver and Atkins' Inorganic Chemistry*, Oxford University Press, Oxford, 5th edn., 2010, pp. 473–506.

215 R. Janes and E. Moore, in *Metal-Ligand Bonding*, Royal Society of Chemistry, London, 1st edn., 2004, pp. 21–27.

216 J. Li, S. Zhang, Y. Chen, T. Liu, C. Liu, X. Zhang, M. Yi, Z. Chu and X. Han, *RSC Adv.*, 2017, **7**, 29051–29057.

217 M. Intissar, A. Seron, F. Giovannelli and F. Delorme, *J. Mater. Sci.*, 2015, **50**, 1427–1434.

218 A. Alejandre, F. Medina, X. Rodriguez, P. Salagre, Y. Cesteros and J. E. Sueiras, *Appl. Catal. B Environ.*, 2001, **30**, 195–207.

219 K. Stangeland, H. Li and Z. Yu, *Ind. Eng. Chem. Res.*, 2018, **57**, 4081–4094.

220 M. Ronda-Lloret, G. Rothenberg and N. R. Shiju, *ChemSusChem*, 2019, **12**, 3896–3914.

221 H. Li, P. Zhang, L. Guo, Y. He, Y. Zeng, M. Thongkam, J. Natakaranakul, T. Kojima, P. Reubroycharoen, T. Vitidsant, G. Yang and N. Tsubaki, *ChemSusChem*, 2020, **13**, 2060–2065.

222 S. M. Sadrameli, *Fuel*, 2016, **173**, 285–297.

223 X. Cui, P. Gao, S. Li, C. Yang, Z. Liu, H. Wang, L. Zhong and Y. Sun, *ACS Catal.*, 2019, **9**, 3866–3876.

224 J. Wei, Q. Ge, R. Yao, Z. Wen, C. Fang, L. Guo, H. Xu and J. Sun, *Nat. Commun.*, 2017, **8**, 1–8.

225 Y. H. Choi, Y. J. Jang, H. Park, W. Y. Kim, Y. H. Lee, S. H. Choi and J. S. Lee, *Appl. Catal. B-Environmental*, 2017, **202**, 605–610.

226 Y. Xu, C. Shi, B. Liu, T. Wang, J. Zheng, W. Li, D. Liu and X. Liu, *Catal. Sci. Technol.*, 2019, **9**, 593–610.

227 Z. Q. Ma and M. D. Porosoff, *ACS Catal.*, 2019, **9**, 2639–2656.

228 R.-P. Ye, J. Ding, W. Gong, M. D. Argyle, Q. Zhong, Y. Wang, C. K. Russell, Z. Xu, A. G. Russell and Q. Li, *Nat. Commun.*, 2019, **10**, 1–15.

229 Y. A. Daza and J. N. Kuhn, *Rsc Adv.*, 2016, **6**, 49675–49691.

230 M. D. Porosoff, B. Yan and J. G. Chen, *Energy Environ. Sci.*, 2016, **9**, 62–73.

231 P. Gao, S. Li, X. Bu, S. Dang, Z. Liu, H. Wang, L. Zhong, M. Qiu, C. Yang, J. Cai, W. Wei and Y. Sun, *Nat. Chem.*, 2017, **9**, 1019–1024.

232 D. L. S. Nieskens, A. Ciftci, P. E. Groenendijk, M. F. Wielemaker and A. Malek, *Ind. Eng. Chem. Res.*, 2017, **56**, 2722–2732.

233 F. Jiang, B. Liu, S. Geng, Y. Xu and X. Liu, *Catal. Sci. Technol.*, 2018, **8**, 4097–4107.

234 A. Ramirez, S. Ould-Chikh, L. Gevers, A. D. Chowdhury, E. Abou-Hamad, A. Aguilar-Tapia, J. L. Hazemann, N. Wehbe, A. J. Al Abdulghani, S. M. Kozlov, L. Cavallo and J. Gascon, *ChemCatChem*, 2019, **11**, 2879–2886.

235 H. Tian, J. Yao, F. Zha, L. Yao and Y. Chang, *Appl. Clay Sci.*, 2020, **184**, 105392–105401.

236 J.-K. Jeon, K.-E. Jeong, Y.-K. Park and S.-K. Ihm, *Appl. Catal. A Gen.*, 1995, **124**, 91–106.

237 S. S. Dang, P. Gao, Z. Y. Liu, X. Q. Chen, C. G. Yang, H. Wang, L. S. Zhong, S. G. Li and Y. H. Sun, *J. Catal.*, 2018, **364**, 382–393.

238 J. Chen, X. Wang, D. Wu, J. Zhang, Q. Ma, X. Gao, X. Lai, H. Xia, S. Fan and T. S. Zhao, *Fuel*, 2019, **239**, 44–52.

239 J. Jiang, C. Wen, Z. Tian, Y. Wang, Y. Zhai, L. Chen, Y. Li, Q. Liu, C. Wang and L. Ma, *Ind. Eng. Chem. Res.*, 2020, **59**, 2155–2162.

240 C. Dai, A. Zhang, M. Liu, J. Li, F. Song, C. Song and X. Guo, *RSC Adv.*, 2016, **6**, 10831–10836.

241 T. Numpilai, N. Chanlek, Y. Poo-Arporn, S. Wannapaiboon, C. K. Cheng, N. Siri-Nguan, T. Sornchamni, P. Kongkachuichay, M. Chareonpanich, G. Rupprechter, J. Limtrakul and T. Witoon, *Appl. Surf. Sci.*, 2019, **483**, 581–592.

242 Y. Xu, C. Shi, B. Liu, T. Wang, J. Zheng, W. Li, D. Liu and X. Liu, *Catal. Sci. Technol.*, 2019, **9**, 593–610.
243 Y. Wang, W. Gao, S. Kazumi, Y. Fang, L. Shi, Y. Yoneyama, G. Yang and N. Tsubaki, *Fuel*, 2019, **253**, 249–256.

Chapter 2. Synthesis and CO_2 capture of Zeolite@Mg_2Al CO_3 LDH core-shell materials

2.1. Introduction

LDHs and the derived calcined products have been used as CO_2 sorbents.[1–7] However, they suffer from low CO_2 capacity due to the aggregation between LDH platelets.[8] Shaffer *et al.* supported Mg_3Al-LDH on graphene oxide and achieved a hybrid material (LDH/GO) with higher surface area (149.9 m^2/g) than the parent materials (98.3 m^2/g and 0.1 m^2/g for Mg_3Al-LDH and graphene oxide respectively). Correspondingly, the CO_2 capacity increases, i.e. from 0.28 mmol/g for calcined Mg_3Al-LDH (Mg_3Al-LDO) to 0.45 mmol/g for calcined LDH/GO (LDO/GO).[9] Moreover, it was reported that adsorbents derived from LDH/GO show better durability than the ones from pure LDH; after 10 cycles of adsorption and desorption, the CO_2 capacity of Mg_3Al-LDO dropped to 55%, while for LDO/GO 76% capacity remains.[9] The same group also reported that water has a positive effect on CO_2 uptake by graphene oxide-supported LDO, i.e. the CO_2 capacity increases from 0.37 mmol/g under dry conditions to 0.52 mmol/g with 16% relative humidity (RH).

As stated in Chapter 1, Zeolite 13X is a benchmark CO_2 adsorbent, but the CO_2 capacity is diminished in a humid environment due to the competitive adsorption between water and CO_2.[10–12] Li *et al.* prepared a series of core-shell materials with zeolite as the core and Mg_2Al-LDH as the shell and noticed that core-shells show higher toluene vapour uptake under wet condition (50% RH) compared to the bare zeolite.[13]

It is anticipated that core-shells using a zeolite 13 core and Mg_2Al-LDH shell, may exhibit the

distinguishing features of both zeolite and LDH, and perform outstanding CO_2 adsorption, especially under increased humidity.

Herein, we describe the synthesis of zeolite 13X@Mg_2Al LDH using a low-cost and scalable co-precipitation method. The effect of addition time, ageing time and LDH fraction on the LDH shell growth, morphology and surface area of core-shell has been systematically studied and the carbon capture ability of prepared core-shell materials was evaluated.

2.2. Synthesis and characterisation of Z13X@Mg_2Al-CO_3-LDH

2.2.1. Synthesis and characterisation of Z13X@Mg_2Al-CO_3-LDH

The core-shell material, named Z13X@Mg_2Al-LDH, was prepared using the co-precipitation method. A Mg/Al (2:1 by molar) nitrate solution was added to the aqueous dispersion of zeolite 13X (Z13X) and Na_2CO_3 at pH 10 to grow LDH platelets onto the surface of Z13X. A control Mg_2Al-CO_3-LDH was synthesised using the same method as Z13X@Mg_2Al-LDH without adding Z13X, termed as Mg_2Al-LDH.

The powder X-ray diffraction (XRD) pattern of Z13X and Mg_2Al-LDH are shown in Figure A1. The commercial Z13X is highly crystalline material that gives a set of sharp Bragg reflections. Mg_2Al-LDH is a layered material with characteristic (00*l*) and (110) Bragg reflections. It is expected that a pure Z13X@Mg_2Al-LDH core-shell should contain no more than three phases: zeolite 13X phase, Mg_2Al-LDH phase and a phase for the zeolite-LDH interface. The XRD of Z13X@Mg_2Al-LDH contains both the diffraction features of Z13X and Mg_2Al LDH as confirmed by the two-phase Pawley refinement (Figure 2.1).[14] The details of

the refinement can be found in the Appendix (Figure A2, Table A1). No reflection associated with additional phases can be observed, indicating that the interface phase is either amorphous or is a minor phase (reflections of which is below the detection level). The *d*-spacing of the (003) plane is 7.65 Å, indicating that the LDH is carbonate-intercalated.[15]

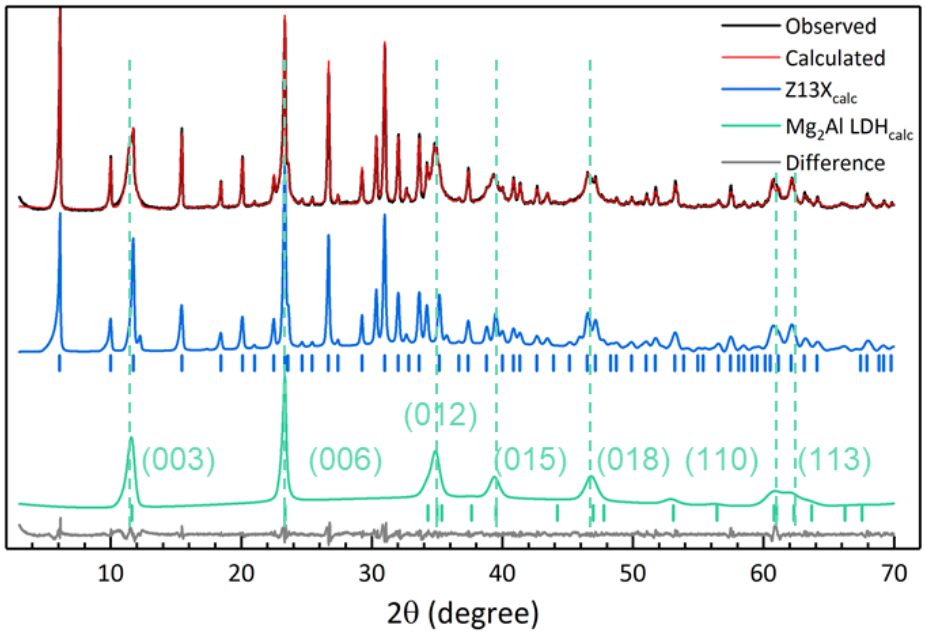


Figure 2.1 XRD pattern and two-phase Pawley refinement of Z13X@Mg_2Al-LDH. The observed, calculated, and difference plots are shown in black, red and grey, respectively. The calculated Z13X and Mg_2Al LDH single phases are shown in blow and green, respectively and their (*hkl*) planes are marked with short sticks.

The commercial Z13X adopts an octahedral particle morphology, with uniform size distribution (2–4 μm) and smooth edges (Figure 2.2a, d and Figure A3a). Mg_2Al-LDH forms clusters of nanoplatelets with particle diameter between 300–500 nm (Figure 2.2b), the agglomerate of which exhibits a random morphology and a rough surface (Figure 2.2e and Figure A3b). The TEM and SEM of Z13X@Mg_2Al-LDH show that LDH nanosheets grow hierarchically onto the surface of Z13X, forming uniform particles with a shell with a thickness of ~300 nm (Figure 2.3c, f and Figure A3c). Similar to what have been reported in the literature, some free LDH

(LDH platelets unbounded to zeolite core) present in the core-shell sample.[16,17]

The EDX mapping showed that Si from Z13X was mainly distributed in the inner core; Mg from the Mg_2Al-LDH was homogeneously dispersed over the whole particle. This further revealed the formation of core-shell structure with zeolite as the core and LDH as the shell (Figure 2.3).

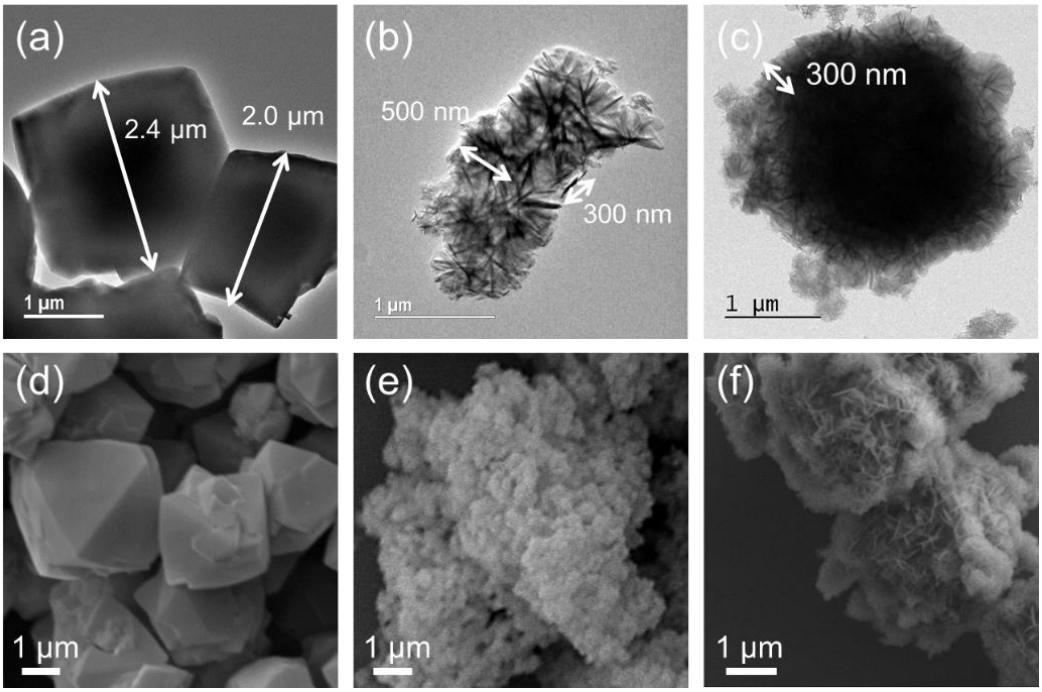


Figure 2.2 TEM images of (a) Z13X, (b) Mg_2Al-LDH and (c) Z13X@Mg_2Al-LDH. SEM images of (d) Z13X, (e) Mg_2Al-LDH and (f) Z13X@Mg_2Al-LDH

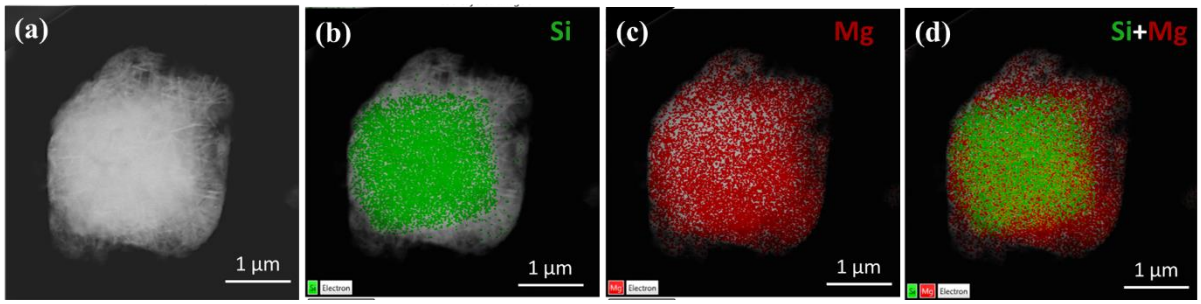


Figure 2.3 (a) STEM image and (b)-(d) EDX elemental mapping of Si (green), Mg (red) and Si+Mg for Z13X@Mg_2Al-LDH.

The ^{29}Si and ^{27}Al solid-state NMR (ssNMR) spectra of Z13X and Z13X@Mg_2Al-LDH were

recorded to study the Si and Al environment in the core-shell. Figure 2.4a shows that the Z13X core contains seven characteristic ^{29}Si resonances. Five of them, from the framework of zeolite, are at −84.2, −88.8, −93.5, −98.1 and −102.0 ppm which can be assigned to Q^4Si(4Al), Q^4Si(3Al), Q^4Si(2Al), Q^4Si(1Al) and Q^4Si(0Al), respectively (Table A2).[18] Two resonances at −111.2 and −117.7 ppm, assigned as Q^4Si(0Al), may come from amorphous silicates in the Z13X sample.[19,20]

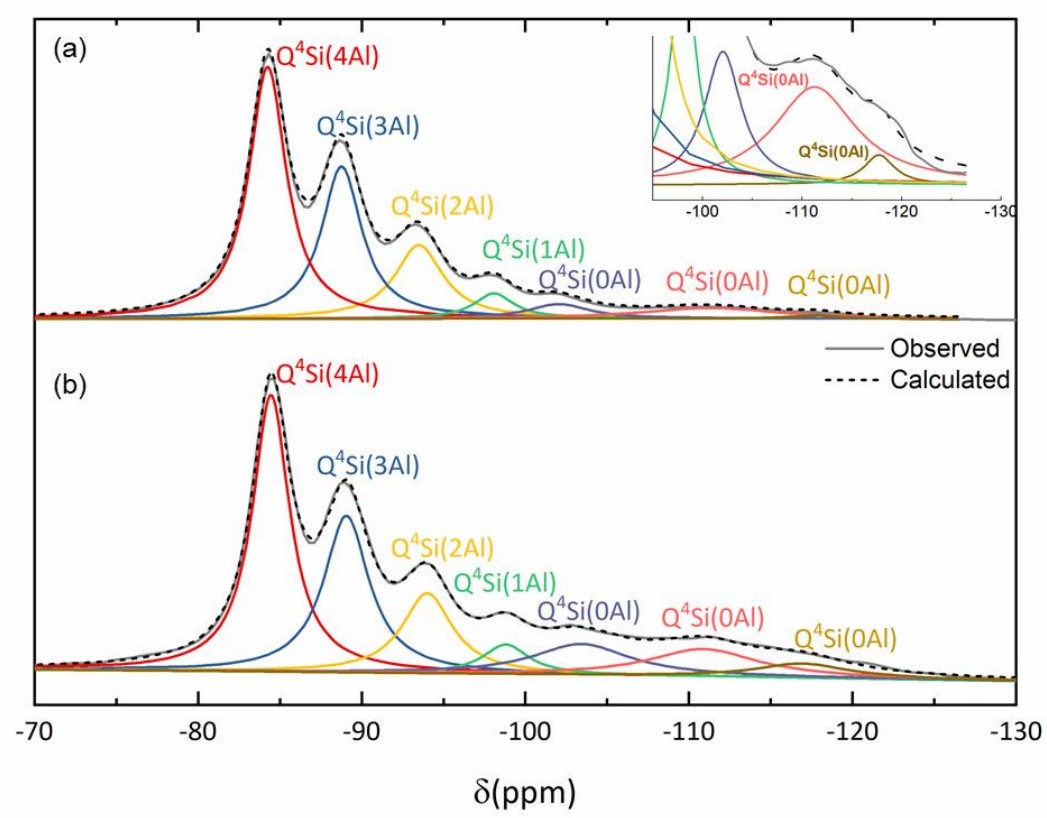


Figure 2.4 ^{29}Si solid-state DPMAS NMR (79.4 MHz) spectra of (a) Z13X and (b) Z13X@Mg_2Al-LDH. The observed and calculated plots are shown using solid grey line and black dash lines, respectively. The inserted graph is the zoom-in of Z13X.

The core-shell Z13X@Mg_2Al-LDH exhibits seven ^{29}Si resonances (Figure 2.4b, Table A2). Five of them are the corresponding resonance of Q^4Si(4Al), Q^4Si(3Al), Q^4Si(2Al), Q^4Si(1Al) and Q^4Si(0Al) of zeolite at −84.4, −89.1, −94.0, −98.8 and −103.4 ppm respectively. After co-precipitation, resonances corresponding to Si with neighbouring Al, Q^4Si(4Al), Q^4Si(3Al),

$Q^4Si(2Al)$, $Q^4Si(1Al)$, exhibit a lower relative intensity (from 90% to 76%), indicating the dealumination of the zeolite framework.[21–23] Resonances arising from amorphous silicates (−111.2 and −117.7 ppm) shift to a lower frequency and gain intensity after co-precipitation (from 6.4% to 14.2%, Table A2). It is likely that during the co-precipitation, the zeolite has dealuminated and more amorphous silicate were formed. The Si/Al ratio of zeolite was assumed using Loewenstein's rule (Equation A1). After coating with LDH, the Si/Al ratio of zeolite increased from 1.40 to 1.67, which is attributed to the dealumination of this Al-rich zeolite.

Z13X shows one characteristic ^{27}Al resonance at 60 ppm due to the tetrahedrally coordinated Al in zeolite framework (Figure A4).[24,25] Mg_2Al-LDH displays one resonance at 8 ppm from the octahedrally coordinated Al in the metal hydroxide layers (Figure A4).[26] Z13X@Mg_2Al-LDH possesses both resonances from zeolite and LDH. (Figure A4), indicating the presence of zeolite and LDH phases.

The FTIR spectra of Z13X, Z13X@Mg_2Al-LDH and Mg_2Al-LDH are shown in Figure 2.5a. Z13X displays a Si-O stretching band at 960 cm^{-1}, a T-O-T (T refers to tetrahedral site) stretching band at 750 $cm^{-1}$and a band due to Si-O-Si or Si-O-Na stretching at 675 cm^{-1}.[27–29] Mg_2Al-LDH possesses a M-O vibration band at 750 cm^{-1}, CO_3^{2-} stretching band at 1360 cm^{-1}, water bending band at 1600 cm^{-1} and O-H bending band at 3500 cm^{-1}.[15] Z13X@Mg_2Al-LDH exhibits all the characteristic bands from both core and shell materials; for example, CO_3^{2-} stretching and O-H bending bands from the LDH shell and Si-O stretching band from the Z13X core.

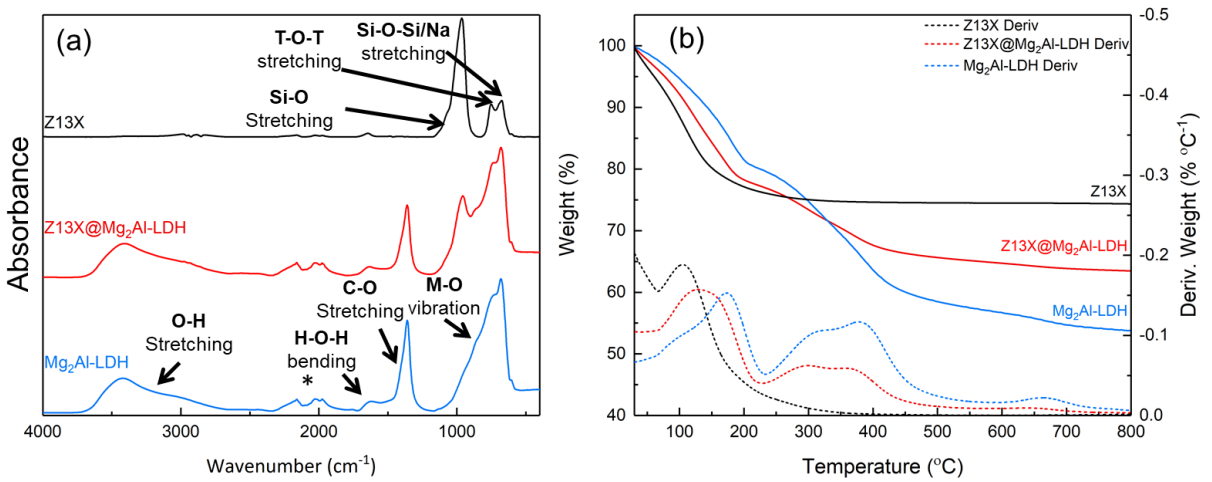


Figure 2.5 (a) FTIR absorbance spectra and (b) TGA and DTG plots of the Z13X (Black), Z13X@Mg_2Al-LDH (Red) and Mg_2Al-LDH (Blue). Features mark with * are signals from sample stage.

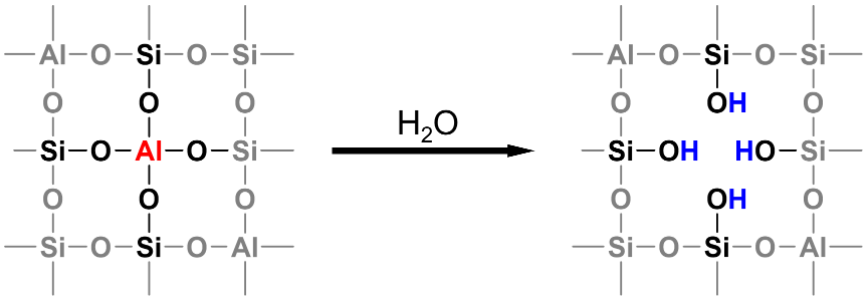
The thermal stability of the materials was studied using TGA (Figure 2.5b). Z13X shows one weight loss stage due to the removal of water.[30] Mg_2Al-LDH exhibits three weight loss events due to water removal (around 150 °C), dehydroxylation and partial decarboxylation (250–450 °C) and complete decarboxylation (above 550 °C) respectively.[31] Similarly, Z13X@Mg_2Al-LDH possesses three weight loss stages. When heated up to 200 °C, the core-shell loses about 20.0% weight due to water evaporation. At around 370 °C, the dehydroxylation of LDH completes and partial decarboxylation takes place. This leads to a 12.3% weight loss. The final stage gives a 4.1% weight loss which arises from the complete decarboxylation of LDH.[31,32] The residual weight of Z13X, Mg_2Al-LDH and Z13X@Mg_2Al-LDH suggests a 1:1 weight ratio between zeolite and LDH in the core-shell.

Based on the TGA, ssNMR spectroscopy and elemental analysis results, the chemical formula of Z13X, Z13X@Mg_2Al-LDH and Mg_2Al-LDH were worked out (Table 2.1). It is noted that the zeolite component of the core-shell has less Al than the original Z13X, which agrees with the loss of Al in zeolite framework during co-precipitation as suggested by ^{29}Si solid-state NMR

spectroscopy. The dealumination of zeolite is as shown in Scheme 2.1.[33,34] Charge balance is met by forming hydroxyl groups. Consequently, the stoichiometry of hydrogen in zeolite increases. The potential ion exchange in Z13X and the formation of the aluminosilicate interface was not able to be investigated based on current data; further studies are required to further refine the composition of Z13X@Mg_2Al-LDH.

Table 2.1 Chemical formula of Z13X, Z13X@Mg_2Al-LDH and Mg_2Al-LDH.

Sample name	Formula
Z13X	$H_{0.06}Na_{0.36}(AlO_2)_{0.43}(SiO_2)_{0.60}\cdot 1.04H_2O$
Z13X@Mg_2Al-LDH	$[H_{0.34}Na_{0.36}(AlO_2)_{0.36}(SiO_2)_{0.60}]\ [Mg_{0.64}Al_{0.35}(OH)_{1.98}(CO_3)_{0.18}]\cdot 1.5H_2O$
Mg_2Al-LDH	$Mg_{0.65}Al_{0.35}(OH)_2(CO_3)_{0.18}\cdot 0.9H_2O$



Scheme 2.1 Schematic of the dealumination of an aluminosilicate in water.

The surface area and pore structure were investigated based on the N_2 adsorption and desorption isotherm. Z13X displays a type I N_2 adsorption isotherm (Figure 2.6a) due to its microporous morphology (Figure 2.6b).[35] Mg_2Al-LDH exhibits a type II adsorption isotherm with a H3 hysteresis loop because of the slit-like pores from the aggregation of LDH platelets (Figure 2.6c).[31,35] Z13X@Mg_2Al-LDH shows typical type I isotherm at relative pressure below 0.3 due to the micropore from Z13X, as supported by the pore size distribution (Figure 2.6b).[35] At relative pressure above 0.3, the core-shell composite displays a type II isotherm with H3 loop because of the slit-like mesopore and macropore in Mg_2Al-LDH (Figure 2.6c).[35]

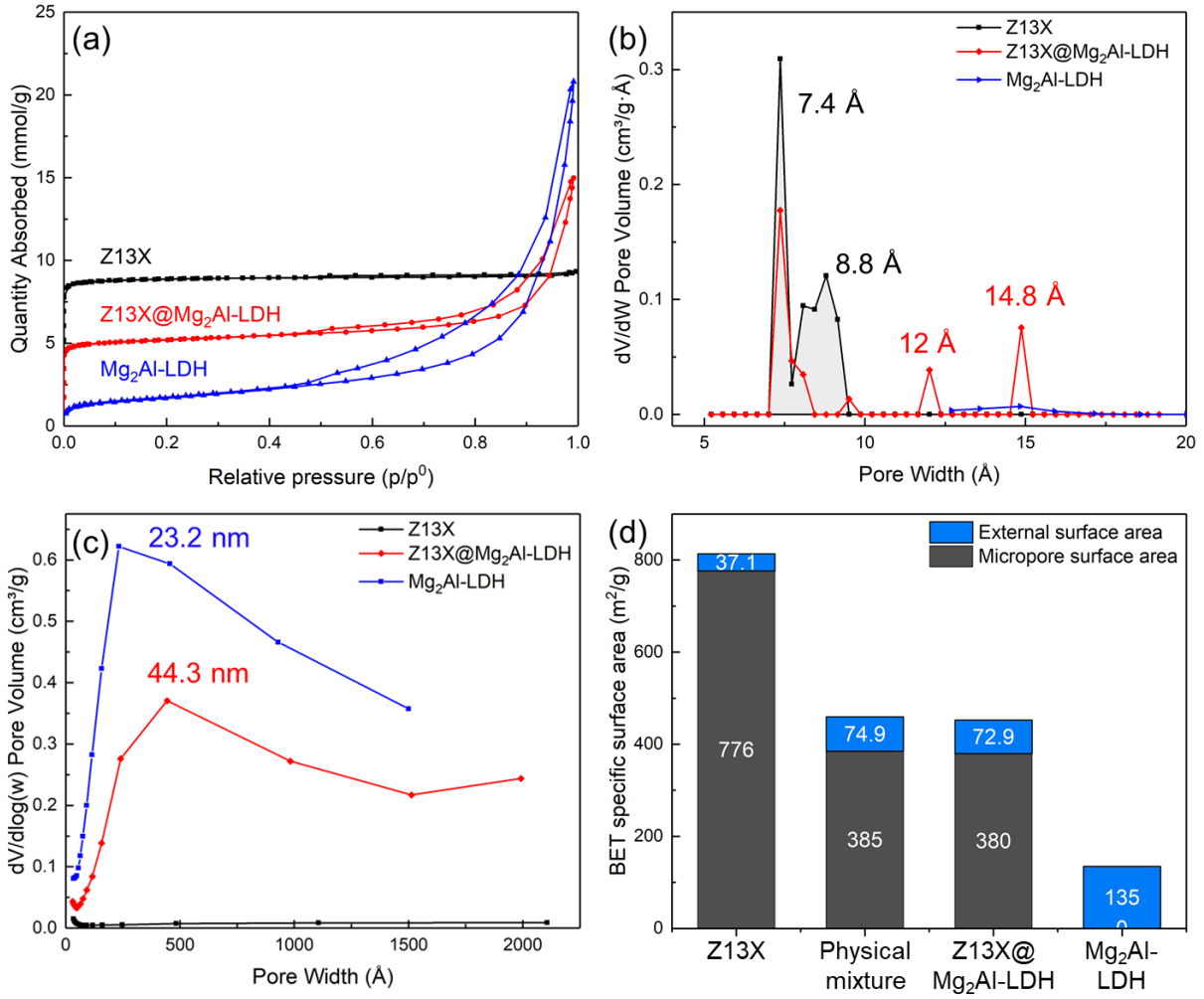


Figure 2.6 (a) N_2 adsorption-desorption isotherm (at 77K), (b) DFT pore size distribution, (c) BJH pore size distribution of the Z13X (black), Z13X@Mg_2Al-LDH (red) and Mg_2Al-LDH (blue). (d) BET specific surface area of materials.

Although a dramatic increase in BET specific surface area is observed on core@LDH hybrids with non-porous core, e.g. sphere silica[26], metal oxides[36,37], core@LDH hybrids with micro-/meso-porous core do not demonstrate the same increase.[13,38,39] Figure 2.6d shows that Z13X@Mg_2Al-LDH with the microporous Z13X core possesses less BET specific surface area (457.9 m^2/g) than Z13X itself (813.1 m^2/g). This is because of the addition of low surface area Mg_2Al-LDH to the core-shell hybrid.

A Z13X and Mg_2Al-LDH physical mixture with a 1:1 weight ratio was prepared, of which the

micropore surface area and micropore pore volume are about the same as Z13X@Mg_2Al-LDH (Figure 2.6d and Figure A5). This demonstrates that using co-precipitation to grow LDH shell might not block the micropore of zeolite. Pristine Z13X has a much lower external surface area (37.1 m^2/g) than pure LDH (135.0 m^2/g); the external surface area of core-shell is mainly determined by the surface area of LDH. It is anticipated that core-shell has higher external surface area and external pore volume than the physical mixture because the layer-by-layer stacking can be diminished as LDH platelets are radially grown on the zeolite surface. However, the external parameters of Z13X@Mg_2Al-LDH and the physical mixture are similar. The gained surface area and pore volume may be balanced by the loss of zeolite surface area and pore volume at the interface.[40] One option to achieve higher surface area and pore volume is to use aqueous miscible organic (AMO) solvent such as ethanol or acetone to treat the core-shell.[38,41] The AMO solvent treatment can further diminish the *ab*-face stacking of LDH and gain an overall higher surface area of core-shells.[11]

2.2.2. Effect of metal nitrate addition rate

The metal salt addition rate is one of the factors that determine the concentration of LDH nuclei in the reaction mixture and thus impacts the particle size and morphology of the LDH shell.[16,42,43] To investigate the effect of metal nitrate addition rate, Z13X@Mg_2Al-CO_3-LDH core-shells were prepared with the same concentration and amount of metal nitrate solution at different addition times (0, 0.5, 1, 1.5 and 2 h), i.e. addition rate varies from 270, 0.15, 0.07, 0.05 to 0.04 mM/h.

Figure A6 compares the XRD pattern of Z13X@Mg_2Al-CO_3-LDH core-shells synthesised with

different addition times (0–2 h). All samples exhibit typical Z13X and LDH Bragg reflections. The d_{003} of the LDH phase is between 7.65–7.70 Å in all cases, revealing that the LDH phase is intercalated by carbonate anions (Table 2.2 and Table A4 for details).

The expanded sections of the XRD pattern are shown in Figure 2.7. Core-shells prepared with addition time ≥ 0.5 h exhibit similar XRD pattern, d_{110} (1.52 Å) and crystallite size (8–11 nm). The LDH pattern from 0 h addition time is broader than rest samples (with longer addition time), indicating that adding all metal nitrates at once leads to a low crystallinity LDH. Correspondingly, the LDH crystallite size from 0 h addition time is less than half of that of the rest samples (Table 2.2), i.e. 3.97 nm comparing to7.87–11.04 nm. The d_{110} of sample from 0 h addition time is 1.54 Å which is larger than the 1.52 Å for the rest of the samples (Table 2.2), indicating a longer mean metal-metal distance in LDH. Considering the cationic radii of Mg^{2+} and Al^{3+} are 0.072 nm and 0.054 nm, respectively,[44] the actual Mg/Al ratio in the LDH matrix might be higher than 2 when metal salt was added at once (addition time = 0 h). It is possible that the extremely short addition time (0 h) leads to an abundant aluminium environment and thus boosts the formation of amorphous aluminium hydroxides. In the formation of the SiO_2@Mg_2Al-CO_3-LDH core-shell, Al interacts with surface Si to form aluminosilicate.[26,45] Another reason may be that the high concentration of aluminium hydroxide in the reaction mixture promotes the formation of aluminosilicate.

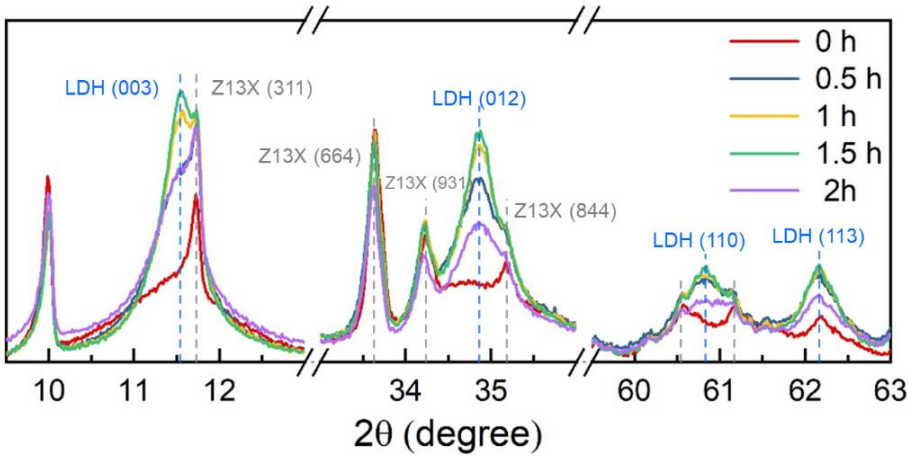


Figure 2.7 Sections of the powder XRD patterns of Z13X@Mg_2Al-CO_3-LDH core-shells prepared from different addition times (0–2 h). Ageing time = 1 h in all cases.

Table 2.2 The *d*-spacing and crystallite size of LDH phase in Z13X@Mg_2Al-LDH core-shells prepared from different addition times and 1 h ageing time.

Metal addition time (h)	d_{003} (Å)	d_{110} (Å)	D_{00l} (nm)[a]	D_{110} (nm)[a]
0	7.70	1.54	3.97	3.97
0.5	7.67	1.52	8.43	8.43
1	7.66	1.52	10.80	10.80
1.5	7.65	1.52	11.06	11.06
2	7.66	1.52	7.87	7.87

a: Calculated crystallite size of (00*l*) and (110) is an approximation of the average crystallite size and the value should only be used to indicate the trend in the crystallinity of LDH in this work.

The TGA plot of all core-shells exhibits Z13X and Mg_2Al-LDH characteristic weight loss stages (Figure A7). The residual weight of samples from addition time ≥ 0.5 h is around 62.9%–63.5%, revealing a 52–56 wt% LDH content. However, the residual weight for 0 h addition time is 65.6%, indicating a much lower LDH content (43 wt%).

The FTIR absorbance spectra of all core-shells are the combination of both pristine Z13X and Mg_2Al-LDH (Figure A8). Samples from addition time ≥ 0.5 h show CO_3^- stretching band and more intense M-O vibration band than the Si-O vibration band. While with addition time 0 h, the M-O vibration band is weaker than the Si-O vibration band. The FTIR and TGA results

suggest that there is less LDH than expected when the metal nitrate is added at once. One possible explanation is that the LDH particles are too small at this extremely short addition time and get washed out as free LDH particles during the filtration and washing process.[42]

TEM images in Figure 2.8a and b show that at addition time = 0 h, poor coverage of LDH and a thin shell thickness (50–100 nm) are observed; this is because, under high concentration of metal hydroxide, the nucleation of LDH is dominant, while the crystal growth of LDH and the formation of covalent bonds between the core and the LDH shell are inhibited.[46] Similar observations have been made for SiO_2@Mg_2Al-CO_3-AMO-LDH.[46] At addition time ≥ 0.5 h, the core-shell morphology is readily achieved and the thickness of LDH shell is around 350–550 nm (Figure 2.8c–f). The shell thickness is slightly increased when a longer addition time is used. At addition time = 0 h, most LDH are free LDH. With longer addition time (≥ 0.5 h), most LDH are bounded to zeolite and form the shell.

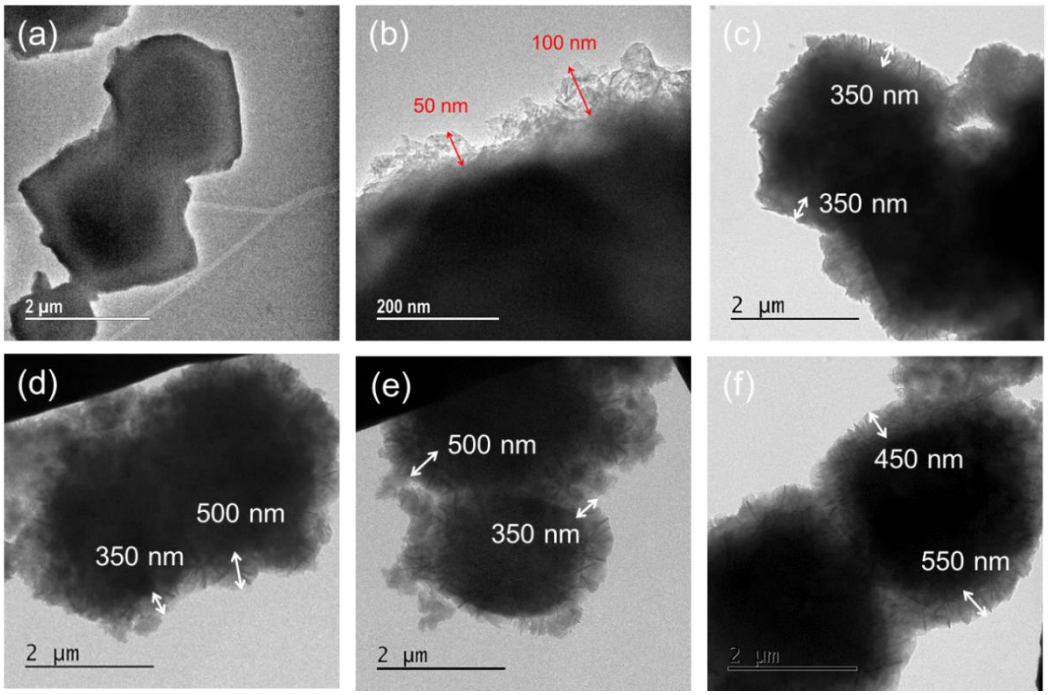


Figure 2.8 TEM image of Z13X@Mg_2Al-CO_3-LDH core-shell prepared from different addition time: (a) 0 h, (b) zoom-in of 0 h, (c) 0.5 h, (d) 1 h, (e) 1.5 h and (f) 2 h. The ageing time is fixed to 1 h.

The Z13X@Mg_2Al-CO_3-LDH core-shells prepared with moderate to long addition time (≥ 0.5 h) exhibit a combination of type I isotherm (relative pressure ≤ 0.3) and type II isotherm with a H3 hysteresis loop (relative pressure > 0.3) (Figure 2.9a), which is due to its microporous Z13X core (Figure A9) and mesoporous LDH shell (Figure 2.9b), respectively.[35] The core-shell obtained at 0 h addition time displays only the type I isotherm and has no mesopores (Figure 2.9b), consistent with the TEM result.

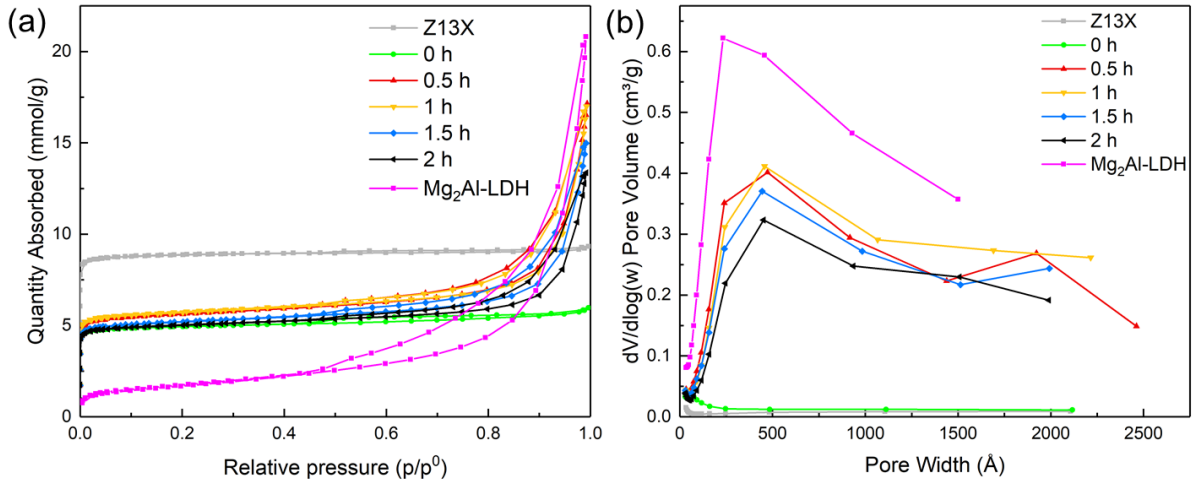


Figure 2.9 (a) N_2 adsorption-desorption isotherm (at 77K) and (b) BJH pore size distribution of the Z13X, Mg_2Al-LDH and Z13X@Mg_2Al-CO_3-LDH prepared from different addition times (ageing time = 1 h).

The external surface area and pore volume mainly come from Mg_2Al-LDH, and micropore related parameters are mainly due to Z13X.[38,47] The 0 h addition time sample exhibits the lowest external surface area and external pore volume because less LDH (43 wt% compared to 52–56 wt% for the remaining samples) is present in this sample and the aggregation between LDH nanosheets gets strengthened when the particles size reduces (Figure 2.10).[42] The 0.5 h addition time core-shell exhibits the highest N_2 BET specific surface area (495.0 m^2/g) and total pore volume (0.60 cm^3/g). Further increasing the addition time leads to more stacked LDHs and results in a decreased external surface area and pore volume.[16,17,42] Moreover, the micropore

surface area and pore volume is reduced at the longer addition time; it is possible that the aggregation between LDH platelets block the micropore at the interface.[40]

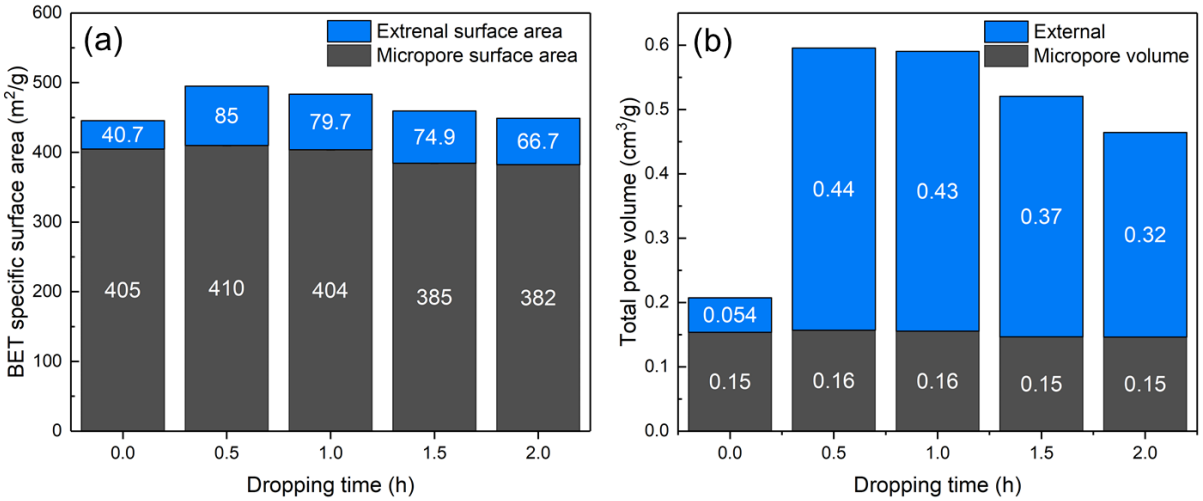


Figure 2.10 (a) BET specific surface area and (b) pore volume of Z13X@Mg_2Al-CO_3-LDH core-shells prepared from different addition times. Ageing time was fixed to 1 h.

2.2.3. Effect of ageing time

Ageing time is another factor that determines the particle size and particle shape of LDH and thus the shell morphology of Z13X@Mg_2Al-CO_3-LDH core-shells.[43,48] In this study, the ageing time of core-shells was varied (0.5–16 h) to study their effect. The metal nitrate addition time was fixed to 0.5 h to get appropriate LDH nucleation and high surface area.

Powder XRD patterns in Figure A10 show that all samples exhibit characteristic Z13X and LDH reflections. The crystallinity of the LDH phase is identical regardless of the ageing time (Figure 2.11). Correspondingly, the *d*-spacing of (003) and (110) planes and crystallite size are similar (Table A5). The d_{003} equals 7.66–7.67 Å in all core-shells, indicating they are carbonate-intercalated.[15] The d_{110} is 1.52 Å in all cases revealing that the Mg/Al molar ratio of all samples are similar.

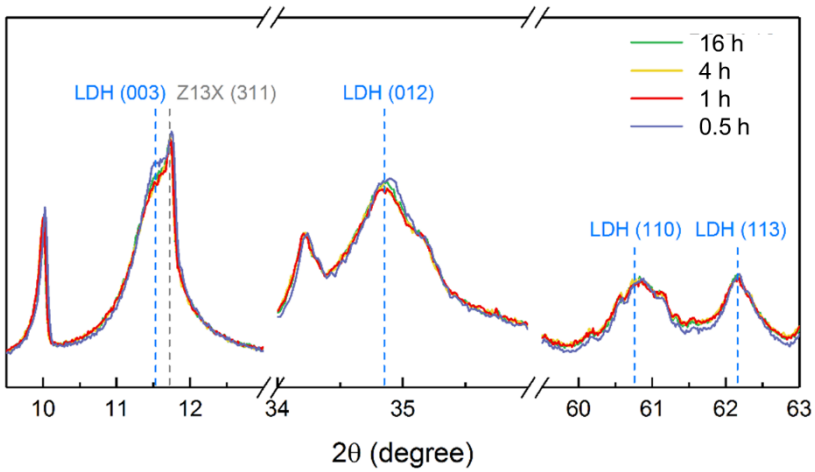


Figure 2.11 Sections of the powder XRD patterns of Z13X@Mg_2Al-CO_3-LDH core-shells prepared from different ageing times. Addition time = 0.5 h in all cases.

The FTIR spectra (Figure A11) and TGA curves (Figure A12) of all core-shells exhibit both LDH and Z13X features and are highly similar to each other, indicating that varying ageing time between 0.5–16 h does not affect the composition and thermal stability of core-shells. The residual weight of all core-shells after 800 °C is between 63.1% and 63.7%, suggesting a 45–48 wt% LDH content in the core-shell.

Core-shell morphology is obtained in all samples (Figure 2.12). The LDH coverage, shell thickness (270–540 nm) and the level of free LDH are similar regardless of ageing time.

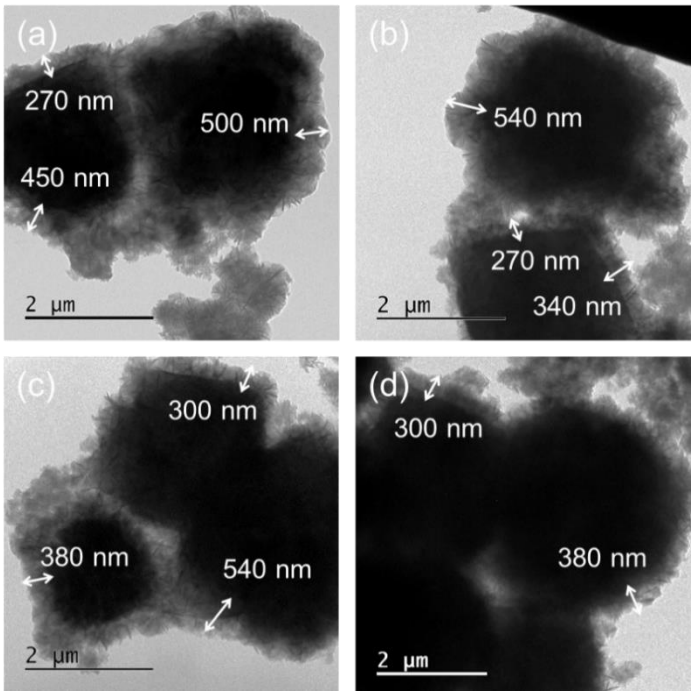


Figure 2.12 TEM image of Z13X@Mg_2Al-CO_3-LDH core-shell prepared from different ageing time: (a) 0.5 h, (b) 1 h, (c) 4 h and (d) 16 h. The addition time is fixed to 0.5 h.

As expected from the TEM results, the ageing time does not change the shape of the N_2 adsorption and desorption isotherm, i.e., all core-shells display the type I isotherm at relative pressure < 0.3 due to the microporous Z13X core and the type II isotherm with H3 hysteresis loop at higher relative pressure because of the LDH shell with slit-like pores (Figure A13, 14).[35] The surface area and pore volume vary slightly with the ageing time (Figure 2.13). Ageing for 0.5 hours provides a product with 517.3 m^2/g N_2 BET specific surface area. Extending the ageing time to one hour and four hours, the surface area decreases to 495.0 m^2/g and 467.0 m^2/g, respectively. Further increasing the ageing time to 16 h leads to an increase of the BET specific surface area to 518.9 m^2/g.

This variation in micropore surface area could be due to the crystal growth process and Ostwald ripening effect.[49] In the highly alkaline solution with the presence of LDH precursor (Mg^{2+} and

Al^{3+}), Si and Al at the surface of the zeolite became metastable, leading to a partial dealumination as proved by the ssNMR spectroscopy data. These metastable Al sites could act as the LDH nucleation sites. LDH nanosheets at the interface are small and are not able to block micropore with 0.5 h ageing time. When the ageing time reaches 1–4 hours, LDH nanosheets undergo crystal growth process and Ostwald ripening to form large particles which start to block the interface micropores (as supported by the loss of micropore in Figure 2.13b and Figure A14a). With ageing time being prolonged to 16 hours, LDHs experience a longer period of Ostwald ripening. The large nanosheets grow bigger at the expense of small LDH nanosheets nearby. Therefore, some of the blocked micropores can be released, resulting in an overall increase in BET-specific surface area.

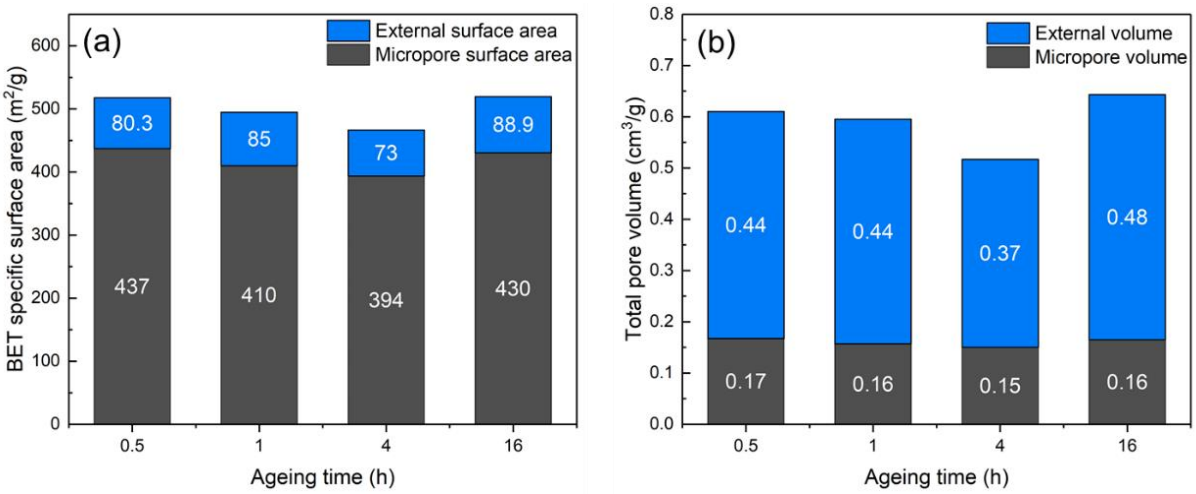


Figure 2.13 (a) BET specific surface area and (b) pore volume of Z13X@Mg_2Al-CO_3-LDH core-shells prepared from different ageing times (0.5–16 h). Addition time was fixed to 0.5 h.

2.2.4. Effect of LDH fraction

Studies in sections 2.2.3 and 2.2.4 reveal that using 0.5 h addition time (0.15 mM/h metal nitrate addition rate) and 0.5 h ageing time can produce Z13X@Mg_2Al-CO_3-LDH core-shell with

good crystallinity, high LDH coverage and uniform shell morphology. However, some unbound 'free' LDH was observed and cannot be avoided by modifying the addition time and ageing time. In order to minimise the amount of free LDH, the LDH content in core-shell was decreased (35, 20 and 5 wt% were used). The concentration of the metal salt solution for co-precipitation was kept constant, while the amount used is reduced. Correspondingly, the time required to add metal salt solution is reduced. In all syntheses, the metal nitrate addition rate is fixed at 0.15 mM/h (same rate as preparing core-shell with 50 wt% LDH with addition time 0.5 h), and ageing time is kept at 0.5 h to eliminate their effects on LDH nucleation and crystal growth.

The XRD pattern in Figure A15 shows that all samples exhibit reflections from Z13X. As expected, Bragg reflections from LDH reduce in intensity with the decreased LDH content in the core-shell (Figure 2.14). At LDH fraction ≤ 20 wt %, corresponding reflections become hard to observe.

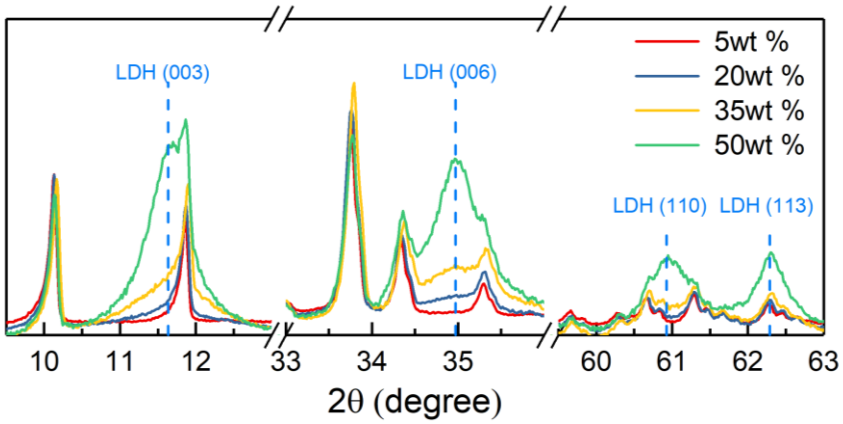


Figure 2.14 Sections of the powder XRD patterns of Z13X@Mg_2Al-CO_3-LDH core-shells prepared from different LDH content. Addition rate = 0.15 mM/h and ageing time = 0.5 h in all cases.

^{27}Al solid-state NMR spectroscopy was used to further check the composition of the core-shell

materials. As stated, resonances at 60 ppm and 8 ppm are ascribed to the tetrahedrally coordinated Al (AlO_4) in Z13X and the octahedrally coordinated Al (AlO_6) in Mg_2Al-LDH, respectively; the AlO_6 resonance is observed in all core-shells, suggesting the presence of LDH in all cases. Moreover, The O_h resonance is progressively reduced as the amount of LDH decreases, which is consistent with XRD results. Interestingly, the proportion of the AlO_6 resonance is close to the expected LDH content in the core-shell (Table 2.3).

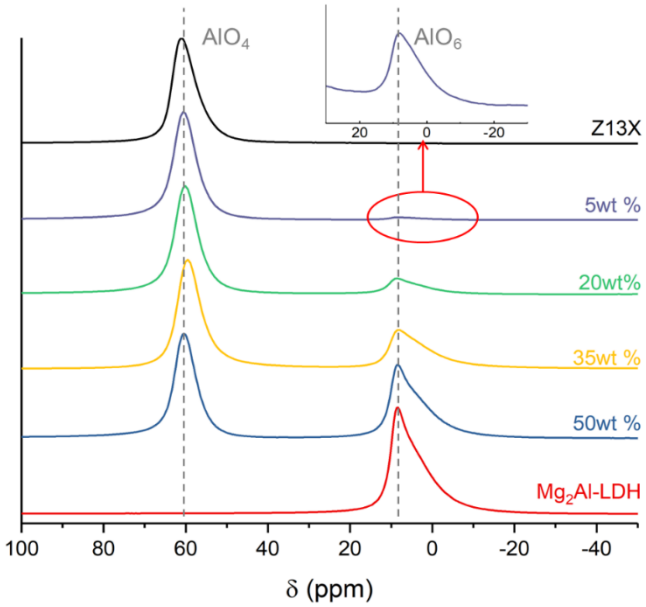


Figure 2.15 ^{27}Al solid-state DPMAS NMR (104.2 MHz) spectrum of Z13X@Mg_2Al-CO_3-LDH prepared with different LDH content. The insert is the zoom-in of the 5 wt% sample. Addition rate and ageing time is kept to 0.15 mM/h and 0.5 h, respectively.

The FTIR spectra in Figure 2.16a shows that the characteristic LDH absorbance band, C-O stretching at 1350 cm^{-1}, is present in all core-shells. This further supports the formation of LDH even though the LDH content is as low as 5 wt%, consistent with the ^{27}Al NMR spectroscopy results. The FTIR spectrum of each core-shell was normalised to their M-O vibration band. It is seen that the peak intensity of the Si-O stretching band increases with the decrease in LDH content, which agrees with the XRD and ^{27}Al NMR spectroscopy results.

As anticipated, the thermal stability of core-shells is similar when the LDH weight fraction is larger than 5 wt% (Figure 2.16b). When the amount of LDH is as low as 5 wt%, the dehydroxylation and decarboxylation weight loss stages that occur between 150–700 °C is too weak to be seen. The residual weight of core-shell increases as the LDH content decreases. The weight fraction of LDH is calculated from the residual weight and is listed in Table 2.3. The calculated values are close to the expected fraction with a 1.5–3.9 wt% deviation.

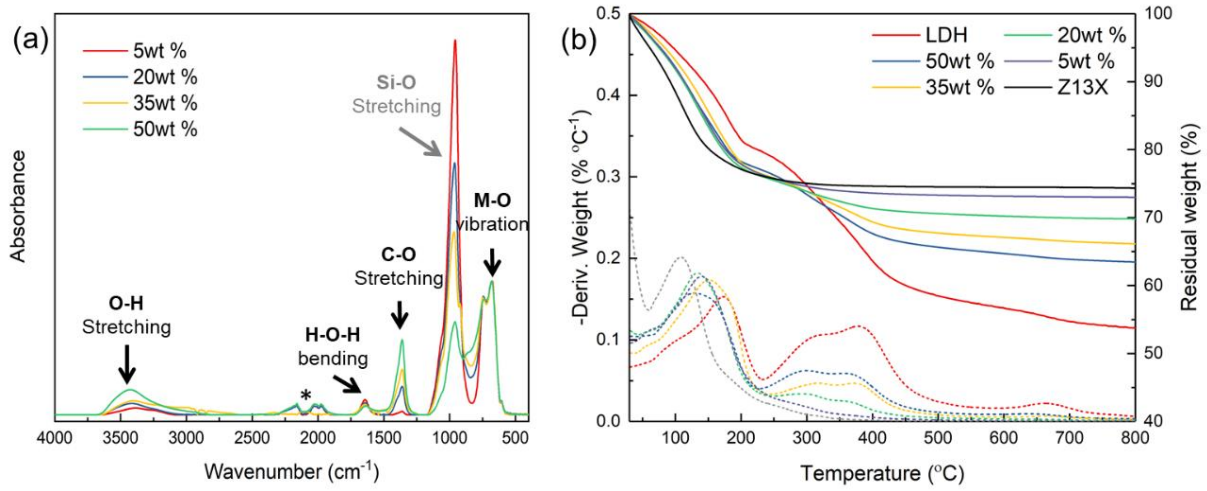


Figure 2.16 (a) FTIR spectra and (b) TGA and derivative TG (dTG) curves of Z13X@Mg_2Al-CO_3-LDH prepared with different LDH content. dTG curves were plotted with dashed lines. The addition rate is fixed to 0.15 mM/h and ageing time is fixed to 0.5 h.

Combining the TGA and elemental analysis results, the possible formulas of Z13X@Mg_2Al-CO_3-LDH core-shells with different LDH contents are worked out and listed in Table 2.3 (Details in Table A6).

Table 2.3 The expected LDH content (from reagent), the proportion of AlO_6 resonance (from integration of the ^{27}Al ssNMR spectrum), the calculated LDH content (from TGA results) and the possible formula of Z13X@Mg_2Al-CO_3-LDH core-shells prepared with different LDH weight fractions.

Theoretical LDH content (wt %)	Experimental LDH content (wt %)[b]	AlO_6 (%)[a]	Formula
5.0	6.5	7.1	$[H_{0.34}Na_{0.36}(AlO_2)_{0.36}(SiO_2)_{0.60}]$ $[Mg_{0.64}Al_{0.35}(OH)_{1.98}(CO_3)_{0.18}]_{0.13} \cdot 1H_2O$
20.0	22.1	17.4	$[H_{0.34}Na_{0.36}(AlO_2)_{0.36}(SiO_2)_{0.60}]$ $[Mg_{0.64}Al_{0.35}(OH)_{1.98}(CO_3)_{0.18}]_{0.44} \cdot 1H_2O$
35.0	38.9	33.7	$[H_{0.34}Na_{0.36}(AlO_2)_{0.36}(SiO_2)_{0.60}]$ $[Mg_{0.64}Al_{0.35}(OH)_{1.98}(CO_3)_{0.18}]_{0.80} \cdot 1.2H_2O$
50.0	53	47.6	$[H_{0.34}Na_{0.36}(AlO_2)_{0.36}(SiO_2)_{0.60}]$ $[Mg_{0.64}Al_{0.35}(OH)_{1.98}(CO_3)_{0.18}] \cdot 1.5H_2O$

TEM images in Figure 2.17 show that core-shell morphology has been obtained at LDH content as low as 5 wt%. The thickness of the LDH shell decreases from 270–540 nm (Figure 2.12a) to 80–100 nm when the quantity of LDH is reduced from 50 wt% to 20 wt%. A further decrease of the thickness to 70 nm is observed when only 5 wt% LDH is present in the core-shell. Unfortunately, the formation of free LDH cannot be avoided by reducing the amount of LDH. The study in Chapter 3 suggests that using a concentrated reaction conditions may be a good choice to eliminate this.

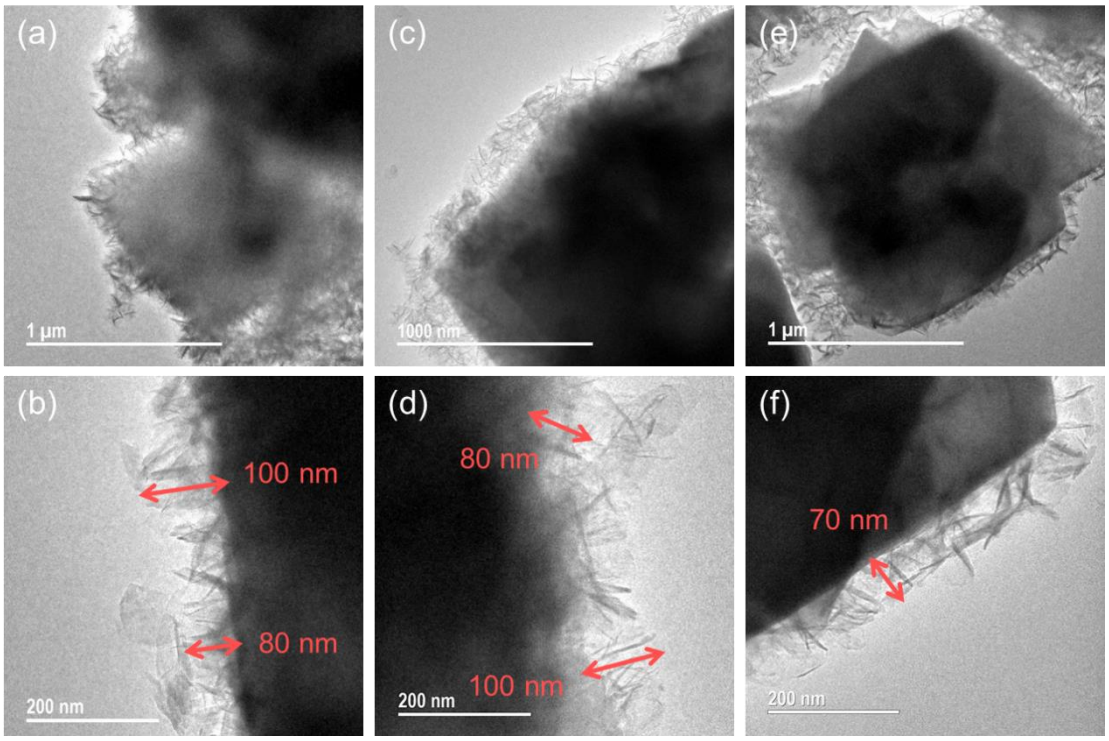


Figure 2.17 TEM images of Z13X@Mg_2Al-CO_3-LDH core-shell prepared with different LDH content: (a) and (b) 35 wt%, (c) and (d) 20 wt%, (e) and (f) 5 wt%. The addition rate is fixed to 0.15 mM/h and the ageing time is kept at 0.5 h.

Modifying the LDH content of Z13X@Mg_2Al-CO_3-LDH does not significantly change the shape of the N_2 isotherm; all core-shells possess a type I isotherm at relative pressure < 0.3 and a type IV isotherm with H_2 hysteresis loop at higher p/p^0 (Figure A16). The BET specific surface area is dominated by the micropore surface area. While the total pore volume is mainly determined by the external pore volume. As anticipated, the reduced LDH content in the core-shell leads to an increase in the total surface area and decreased pore volume (Figure 2.18).

Noteworthy, the core-shell with 5 wt% LDH exhibits higher BET specific surface area and total pore volume than the pristine Z13X due to the presence of more micropores (Figure 2.18 and Figure A17). Results in the following section demonstrate that heating Z13X at 200 °C (the pretreatment temperature used here) cannot remove chemisorbed water from the micropore and

the measured pore size (7.4 Å) is smaller than the actual size (11.3 Å). It is likely that dealumination and potential ion exchange alter the surface of micropores in Z13X, resulting in weakened binding with water and releasing more micropores under the same pretreatment conditions.[50]

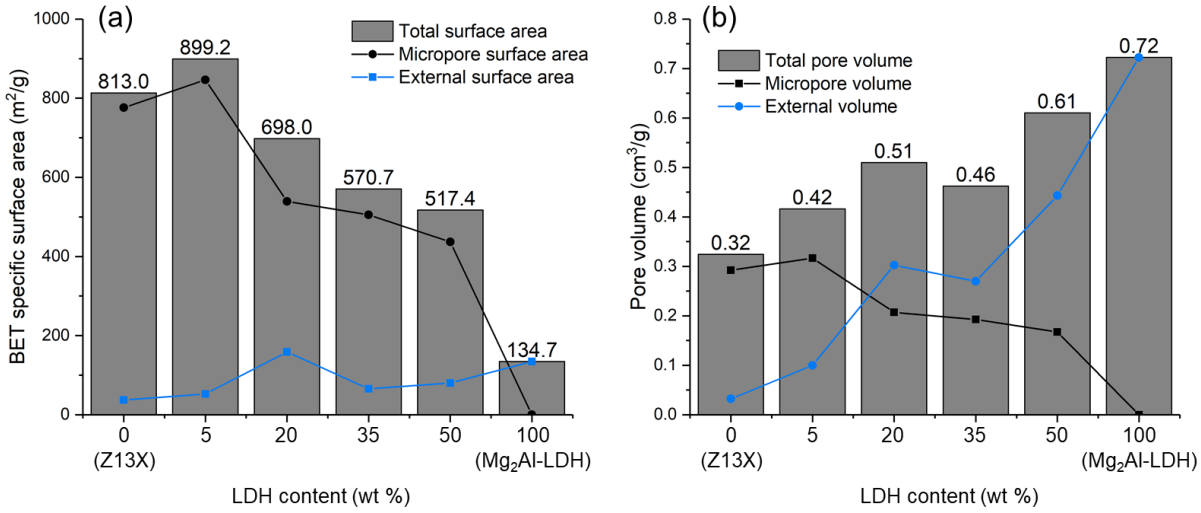


Figure 2.18 (a) N_2 BET specific surface area and (b) the total pore volume of Z13X@Mg_2Al-CO_3-LDH core-shells with varied LDH content. The addition rate and the ageing time are fixed to 0.15 mM/h and 0.5 h, respectively.

2.3. CO_2 capture performance of Z13X@Mg_2Al-LDH

After the successful synthesis of Z13X@Mg_2Al-CO_3-LDH precursors, the next step is to test their CO_2 capture ability. The literature has demonstrated that LDH or Zeolite 13X can be activated into CO_2 adsorbents by calcining at 350–550 °C.[4,51–55] In this work, Z13X@Mg_2Al-CO_3-LDH core-shells were calcined at 500 °C for 3 hours under static air. The Z13X@Mg_2Al-CO_3-LDH core-shell prepared from 0.5 h addition time, 0.5 h ageing time, and 50 wt% LDH is named Z13X@Mg_2Al-LDH-2 and its calcined product is called Z13X@Mg_2Al-LDO. Pristine Z13X and Mg_2Al-CO_3-LDH were activated at the same condition for comparison; Their calcined products are named Z13X-Cal and Mg_2Al-LDO,

respectively.

As expected, the calcination of Z13X does not change its XRD pattern (Figure 2.19); the relative intensity of some reflections are reduced due to dehydration.[56] Calcining MgAl-CO_3-LDH within a certain temperature window (300–600 °C) produces a layered double oxide (LDO) which is a solid solution of metal oxides. In Mg_2Al-LDO, the characteristic LDH Bragg reflections such as (00*l*) and (110) disappear and three peaks at 35.1°, 42.9° and 62.8° corresponding to the (111), (200) and (220) Bragg reflections of MgO appear indicating the formation of MgO. The cubic lattice parameter *a* (= *b* = *c*) of the MgO phase in Mg_2Al-LDO is 4.19 Å and is smaller than that of pure MgO (4.21 Å), revealing some insertion of small Al^{3+} (0.054 nm compared to 0.072 nm of Mg^{2+}) in the framework.[44,57,58] Aluminium oxide should also be formed in the Mg_2Al-LDO. However, it is amorphous and is unobservable in XRD.[58,59] Z13X@Mg_2Al-LDO possesses characteristic Bragg reflections of zeolite 13X; some broadening around 43° and 63° indicates the presence of MgO phase from Mg_2Al-LDO.

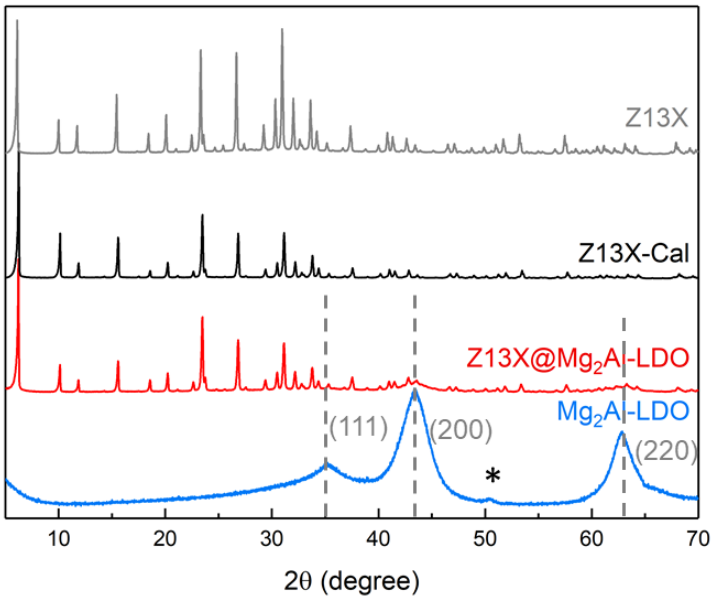


Figure 2.19 Powder-XRD patterns of Z13X, Z13X-Cal, Z13X@Mg_2Al-LDO and Mg_2Al-LDO. Peak marked with * is due to sample holder.

The ^{27}Al solid-state NMR spectrum in Figure 2.20a shows that Z13X@Mg$_2$Al-LDO has three resonances at 12.2, 55.8 and 74.4 ppm. The resonance at 12.2 ppm is undoubtedly ascribed to the octahedral (O_h) Al in the LDO structure and is consistent with the XRD result. The resonances at 55.8 and 74.4 ppm correspond to the tetrahedral (T_d) Al sites with different Si environments.[58] The resonance at 55.8 ppm is indexed as Al^4(4Si) and is due to the Al in the zeolite framework. The resonance at 74.4 ppm is assigned as Al^4(0Si) and results from the Al_2O_3 in the LDO phase.[60] During the calcination, some Al in the metal hydroxide layer migrates out and are coordinated with three oxygen atoms from the layer and one oxygen at the interlayer.[60,61]

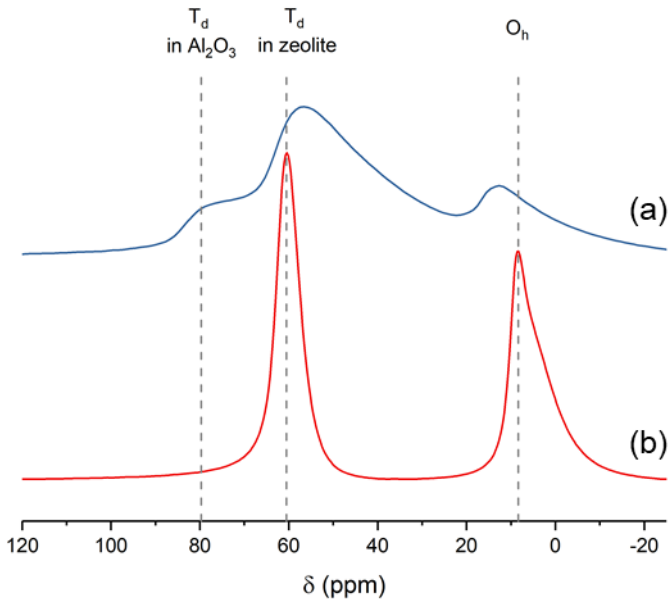


Figure 2.20 ^{27}Al solid-state DPMAS NMR spectrum (104.2 MHz) of (a) Z13X@Mg$_2$Al-LDO and (b) Z13X@Mg$_2$Al-LDH-2.

Z13X@Mg$_2$Al-LDO has a much broader spectrum than Z13X@Mg$_2$Al-LDH-2 (Figure 2.20) due to the loss of hydroxyl groups and thus the weakened quadrupolar interaction between Al atoms and protons from their neighbouring hydroxyl groups. Moreover, the dehydration and dehydroxylation (in the calcination) can lead to the shift of resonances and change in the relative intensity, which is observed in the ^{27}Al and ^{29}Si ssNMR spectra of Z13X@Mg$_2$Al-LDO (Figure

2.20a and Figure A18).[62] The proportion of O_h and T_d Al in fresh Z13X@Mg_2Al-LDH-2 is 48:52. While the proportion of O_h and T_d (zeolite) and T_d (Al_2O_3) Al in Z13X@Mg_2Al-LDO is 16: 66: 18. The increase in the T_d Al content of zeolite (from 52% to 66%) could be either due to the formation of interface aluminosilicate upon the calcination or the change of resonance due to dehydration.[62] Another possibility is that calcination of LDH shell produces some penta-coordinated Al, the signal of which overlaps with the broad T_d (zeolite) resonance and increases the relative intensity.

The ^{29}Si solid-state NMR spectrum of the calcined and fresh core-shell are highly similar (Figure A18), consistent with the TGA result that Z13X are stable at high temperatures.

On the calcination of Mg_2Al-LDH, dehydration, dehydroxylation and partial decarbonation occur, leading to the disappearance of H-O-H bending and O-H stretching bands and a weakening of the C-O stretching band (Figure 2.21a). Moreover, the carbonate stretching band transforms from a singlet to a doublet, revealing that the carbonate group in Mg_2Al-LDO has reduced symmetry. A similar change of the FTIR spectrum has been observed in Z13X@Mg_2Al-LDO (Figure 2.21a), indicating the successful conversion of the LDH shell to the mixed metal oxide shell. The existence of the H-O-H bending peak in Z13X@Mg_2Al-LDO is due to the highly hydrophilic Z13X core.[63]

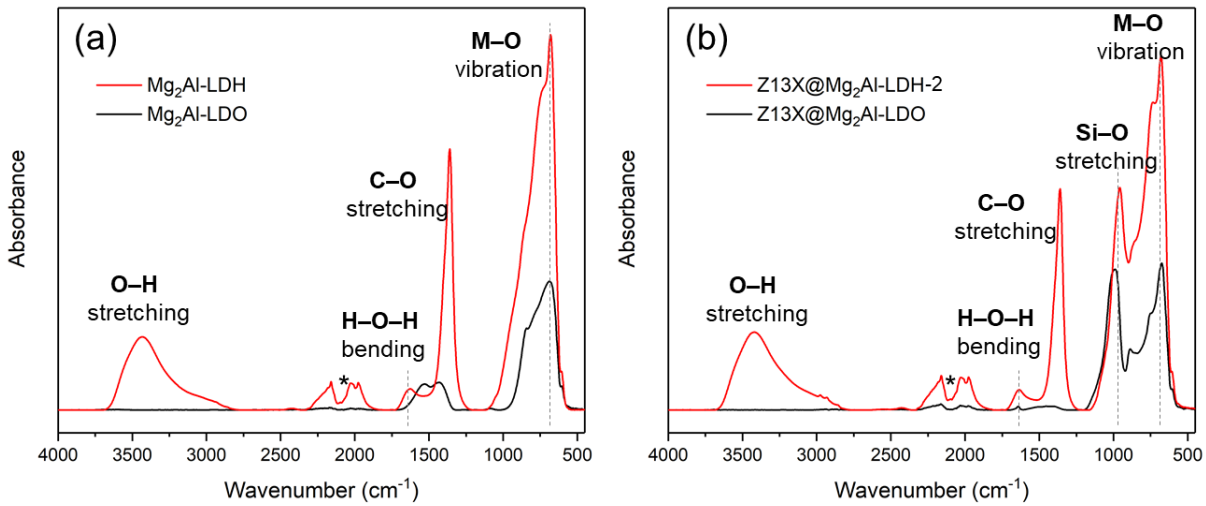


Figure 2.21 FTIR spectra of (a) Mg_2Al-LDH and Mg_2Al-LDO and (b) Z13X@Mg_2Al-LDH-2 and Z13X@Mg_2Al-LDO.

The TEM images in Figure 2.22a show that calcined Z13X (Z13X-Cal) has the same morphology as the pristine Z13X (smooth edges with no apparent defects). The LDO has a similar platelet-like morphology to the LDH precursor (Figure 2.22b and c). However, the removal of hydroxyl and carbonate groups leads to a more porous structure and thus a more porous morphology (small holes appear on the platelets).

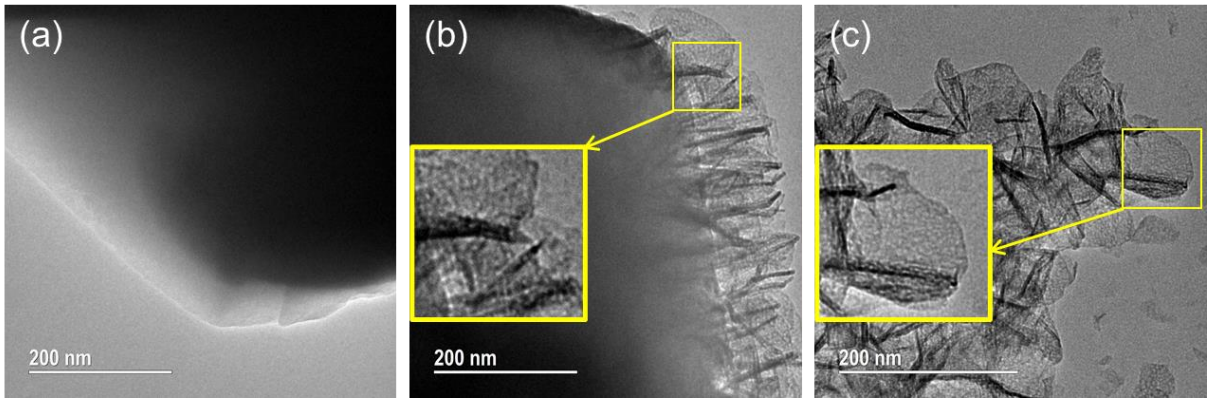


Figure 2.22 TEM images of (a) Z13X-Cal, (b) Z13X@Mg_2Al-LDO and (c) Mg_2Al-LDO.

The shape of the N_2 adsorption and desorption isotherm of Z13X@Mg_2Al-LDO is similar to its LDH precursor (Figure A19), indicating that calcination does not alter the pore structure intensively. The calcined samples tend to exhibit higher BET specific surface area and total

pore volume than the pristine samples (Figure 2.23). Surprisingly, the surface area of Z13X increased from 813.1 m^2/g to 1106.3 m^2/g after calcination. Moreover, the pore size of Z13X expanded from 7.4 Å to 11.3 Å (Figure A20a). It is possible that heating at 500 °C can remove the strongly physisorbed H_2O in zeolite and further empties the micropore.[64] Therefore, additional pore volume was gained (Figure 2.23b). Consistent with the TEM result, the more porous Mg_2Al-LDO (compared to Mg_2Al-LDH, Figure A20a) exhibits a higher surface area and the total pore volume (Figure 2.23).

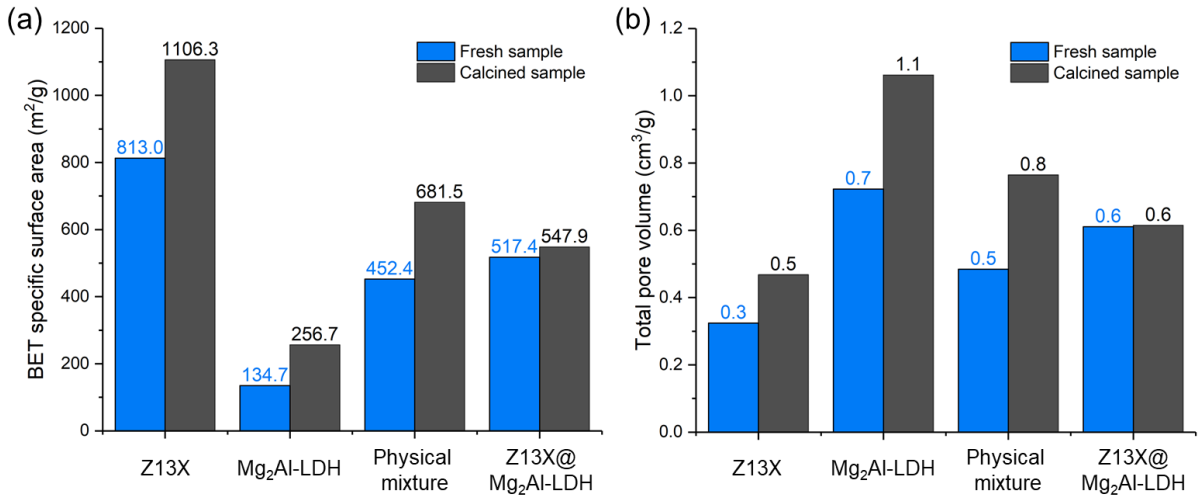


Figure 2.23 (a) the BET specific surface area and (b) the total pore volume of Z13X, Mg_2Al-LDH, physical mixture (Z13X: Mg_2Al-LDH = 1:1 by weight) and Z13X@Mg_2Al-LDH before and after the calcination. The value for physical mixture is a theoretical value worked out from the data of Z13X-cal and Mg_2Al-LDO.

However, the calcined core-shell shows lower BET specific surface area and pore volume than the calcined physical mixture (Figure 2.23); this is mainly due to the inferior micropore parameter arising from the micropore blocking (Figure 2.24). Rivera-Ramos *et al.* reported that substituting Si^{4+} or Al^{3+} by some lower valent metal cations (Mg^{2+}, Ca^{2+} etc.) requires more counterion (Na^+) in the framework and leads to a pore blockage of zeolite.[50] It is likely that ion exchange occurred during the co-precipitation, which causes the micropore of the zeolite to

narrow from 11.3 Å to 7.4 Å (Figure A20b). Unfortunately, due to the limit of characterisation, the change of zeolite structure was not able to be analysed. It is also noted that the core-shell has a smaller external surface area than the physical mixture; this is likely that the interface LDH decomposes differently from the bulk LDH and leads to different surface area and porosity.

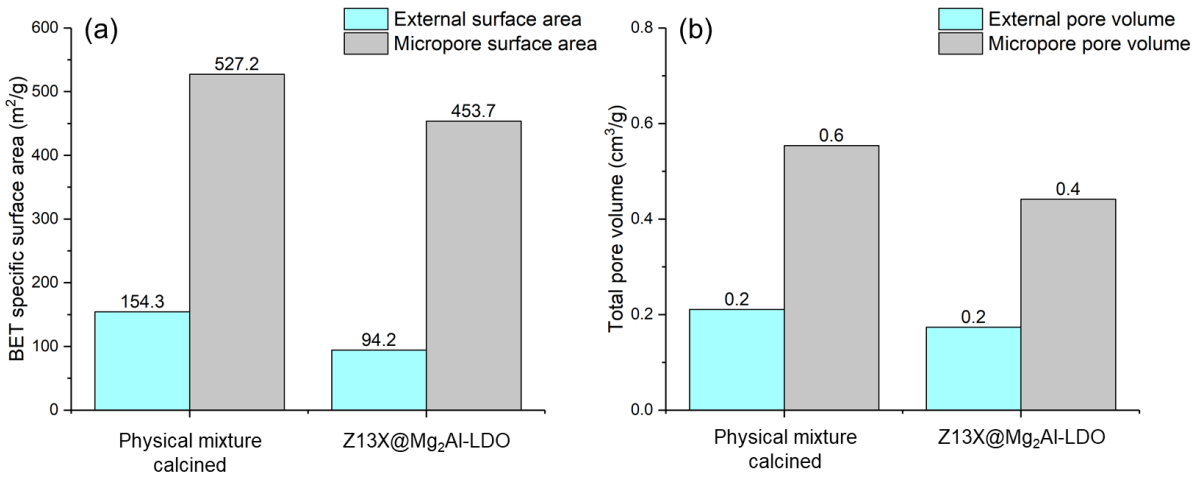


Figure 2.24 (a) the BET specific surface area and (b) the pore volume of the physical mixture (Z13X: Mg_2Al-LDO = 1:1 by weight) and Z13X@Mg_2Al-LDO.

The CO_2 capture ability of activated adsorbents at 35 °C and 1 bar CO_2 atmosphere is displayed in Figure 2.25a. The calcined Z13X shows the highest CO_2 adsorption capacity (6.23 mmol/g). A trend between the surface area and the carbon capture ability of adsorbent can be found; the adsorbent with the higher surface area presents the larger CO_2 capture capacity. Coating with LDO does not promote the CO_2 adsorption ability of Z13X. Instead, introducing the low-surface-area LDO leads to a reduced CO_2 capacity. The adsorbent derived from the physical mixture shows higher surface area than the one derived from core-shell. However, the core-shell adsorbent exhibits slightly higher CO_2 capacity than the physical mixture adsorbent.

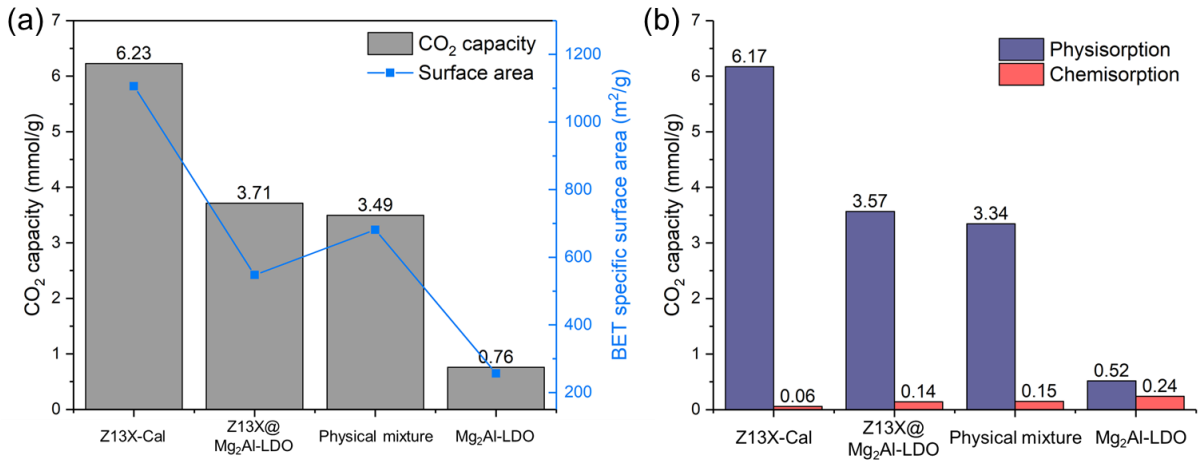


Figure 2.25 (a) The CO_2 capacity (at 35 °C, 1 bar CO_2 atmosphere) and N_2 BET specific surface area and (b) the CO_2 physisorption and chemisorption amount of Z13X-Cal, Z13X@Mg_2Al-LDO, physical mixture and Mg_2Al-LDO.

The CO_2-temperature programmed desorption (CO_2-TPD) was conducted at elevated temperature (over 100 °C) to investigate whether chemisorption of CO_2 has occurred. All adsorbents (Z13X-Cal, Mg_2Al-LDO and Z13X@Mg_2Al-LDOs) exhibit a peak over 100 °C (100–350 °C for Z13X-Cal and 100–450 °C for the rest samples), indicating that all adsorbents will chemisorb CO_2 (Figure A21).

The CO_2 capacity from physisorption and chemisorption was measured by conducting a repeated CO_2 adsorption isotherm at 35 °C. Between the measurement of two adsoption isotherms, the adsorbent was evacuated at 35 °C for 3 hours to remove all physisorbed CO_2. The CO_2 capacity obtained from the first isotherm is the total CO_2 capacity while the one obtained from the second adsorption isotherm is the CO_2 capacity due to physisorption. The difference between the two values is the amount of chemisorbed CO_2.

It is found that physisorption is dominant in all cases (Figure 2.25b) and the better performance of core-shell adsorbent than its physical mixture analogue is due to the enhanced physisorption.

There are two likely reasons for the higher CO_2 uptake of core-shell. Firstly, the additional Si-OH groups resulting from the dealumination of zeolite (Scheme 2.1) interact with CO_2 via H-bonding.[65] Secondly, the formation of interface generates some Al(T_d)-Metal(O_h) pairs(metal can be Mg or Al), which can interact with CO_2 via the tetrahedral Al and the adjacent oxygen.[66]

2.3.1. Effect of addition time and ageing time

The CO_2 adsorption abilities of core-shell adsorbents prepared using a range of addition times and ageing times are shown in Figure 2.26. The overall performance of adsorbents derived from Z13X@Mg_2Al-CO_3-LDH core-shells are similar as these adsorbents have similar surface area, pore volume and composition. The CO_2 uptake of theses core-shell adsorbents is 3.75 ± 0.31 mmol/g CO_2 at 1 bar CO_2 atmosphere.

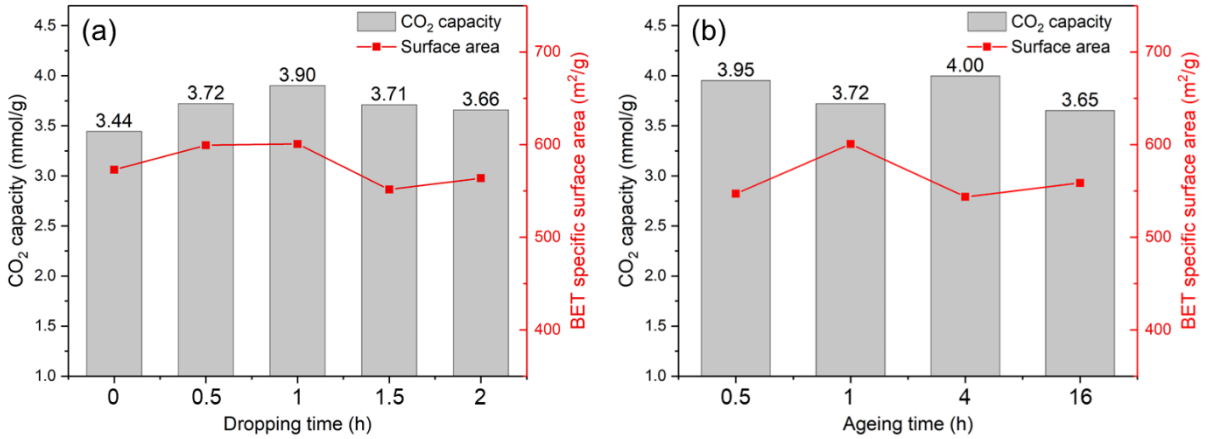


Figure 2.26 The CO_2 capacity and BET specific surface area of core-shell adsorbents derived from Z13X@Mg_2Al-CO_3-LDHs that are prepared from (a) different addition times (ageing time = 1 h) and (b) different ageing times (addition time = 0.5 h). The activation procedure: calcining at 500 °C for 3 h under static air condition.

2.3.2. Effect of LDH fraction in Z13X@Mg_2Al-CO_3-LDH

Figure 2.27 shows the CO_2 capacity of adsorbents derived from Z13X@Mg_2Al-CO_3-LDH with differing LDH contents. It is not surprising to find that the CO_2 capacity increases as the LDH

loading decreases, due to the increased surface area of adsorbents. The lowest LDH content in the precursor (5 wt%) gives the highest CO_2 uptake at 5.75 mmol/g. It is difficult to compare the performance of adsorbents prepared in this work with the performance of the adsorbents reported in the literature, because temperature and pressure have a significant effect on the CO_2 capacity, and the conditions used in the literature are always different from the one used in this work.

Here, the performance of several benchmark solid adsorbents that are tested under condition (22–30 °C and 1 bar) similar to the one adopted in this work (35 °C and 1bar) are listed. (Table 2.4), it is found that our Z13X@Mg_2Al-LDO adsorbents with 5–20 wt% LDH in the precursor show a moderate to high performance.[67,68] However, pristine Z13X possesses the highest CO_2 capacity (6.23 mmol/g) under dry conditions, better than all core-shell adsorbents developed in this work because of its high surface area.

Although Z13X performs better CO_2 uptake ability under dry condition, under humid environment, water will take competitive adsorption with CO_2 and lead to a diminished CO_2 adsorption performance of Z13X.[10–12] While, the CO_2 capacity of LDO increases with the presence of water, Li *et al.* reported that zeolite@LDO adsorbents exhibit superior toluene gas uptake under humid environment than pure zeolite. It is possible that Z13X@LDO would show better CO_2 adsorption ability than pure Z13X under humid environment.[13] Therefore, testing the CO_2 uptake ability under humid environment is planned as future work.[69,70]

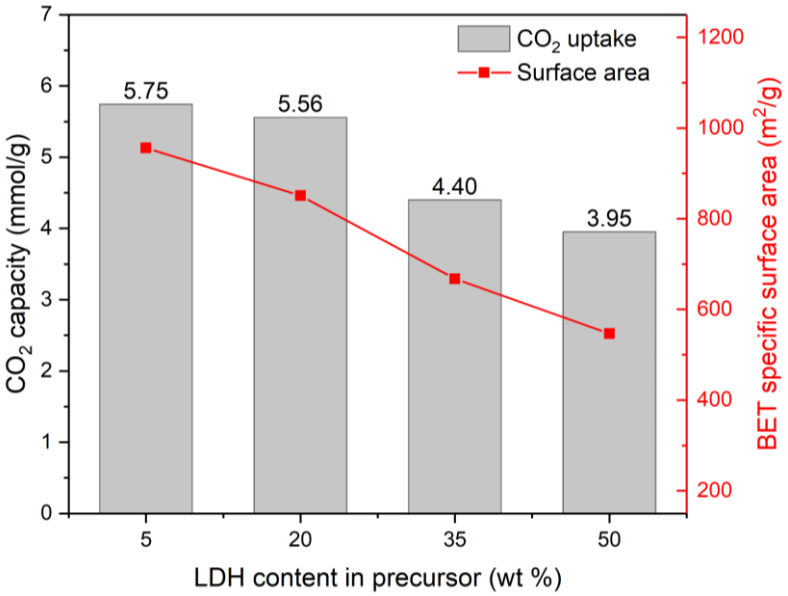


Figure 2.27 The CO_2 capacity and BET specific surface area of core-shell adsorbents derived from Z13X@Mg_2Al-CO_3-LDHs with various LDH content. The addition rate is fixed to 0.15 mM/h and the ageing time was kept at 0.5 h.

Table 2.4 CO_2 adsorption benchmarks of selected solid adsorbents at 1 bar and 0–35 °C.

Sample		Adsorption temperature (°C)	Adsorption pressure (bar)	CO_2 uptake (mmol/g)
Type	**Name**			
Core-shell	Z13X@Mg_2Al-LDO*	35	1	5.75
Zeolite	Zeolite 13X[55]	25	1	6.2
MOF	Mg-MOF-74[71]	25	1	8.4
MOF	Cu-BTC[72]	22	1	5
Porous carbon	Coconut shell[73]	25	1	4.8
Core-shell	CoAl-LDH@ZIF-67[74]	30	1	0.52
Core-shell	ZSM-5@CS[75]	30	1	2.4
Core-shell	Zeolite 5A@ZIF-8[76]	25	1	2.67

*: core-shell adsorbent developed in this work (with 5 wt% LDH in the precursor).

2.4. Conclusions

A series of Z13X@Mg_2Al-LDH core-shells have been synthesised via one-step co-precipitation. Dealumination and ion exchange occur during the core-shell preparation and leads to an increased Si/Al ratio (from 1.40 to 1.67) and partial blocking of micropores of the zeolite core respectively. Core-shells prepared from various addition times (0.5–2 h) and ageing times (0.5–

16 h) exhibit similar crystallinity, thermal stability and compositions. The highest BET specific surface area (518.9 m^2/g) was observed for the sample obtained from 0.5 h addition time and 16 hours ageing time. Moreover, a core-shell with high-surface-area (517.3 m^2/g) can be readily prepared with a 1 hour reaction time (0.5 hour addition time and 0.5 hour ageing time).

Reducing the LDH weight fraction in core-shell from 50% to 5% leads to the LDH shell thickness decreasing from 270–540 to 70 nm and the BET specific surface area increasing from 517.3 to 899.2 m^2/g. Unfortunately, free LDH cannot be removed by adjusting the addition time, ageing time or weight fraction of LDH in the core-shell. Modifying other synthetic conditions such as concentration should be considered.

Calcination removes the chemisorbed water in zeolite, transforms LDH to mixed metal oxide and provides the core-shell adsorbent with more porous morphology and higher BET specific surface area. Compared with the physical mixture, the core-shell adsorbent exhibits higher CO_2 uptake at a lower BET specific surface area, which may be due to the hydrogen bonding between Si-OH and CO_2 and interaction between the interface Al(T_d)-Metal(O_h) pairs with CO_2 via Al(T_d) and adjacent oxygen. CO_2 adsorption by core-shell adsorbents is dominated by physisorption, which is mainly determined by the surface area. Core-shell with the lowest LDH loading (5 wt%) in the precursor possesses the highest capacity (5.75 mmol/g at 1 bar CO_2 atmosphere and 35 °C), which could be a promising material for post-combustion carbon capture. In the future, it would be interesting to explore the CO_2 adsorption ability of Z13X@Mg_2Al-LDO under humid environment.

2.5. Reference

1 Q. Wang, Y. Gao, J. Luo, Z. Zhong, A. Borgna, Z. Guo and D. O'Hare, *RSC Adv.*, 2013, **3**, 3414–3420.

2 Q. Wang, Z. Wu, H. H. Tay, L. Chen, Y. Liu, J. Chang, Z. Zhong, J. Luo and A. Borgna, *Catal. Today*, 2011, **164**, 198–203.

3 X. Zhu, C. Chen, H. Suo, Q. Wang, Y. Shi, D. O'Hare and N. Cai, *Energy*, 2019, **167**, 960–969.

4 Q. Wang, H. H. Tay, D. J. W. Ng, L. Chen, Y. Liu, J. Chang, Z. Zhong, J. Luo and A. Borgna, *ChemSusChem*, 2010, **3**, 965–973.

5 Y. Gao, Z. Zhang, J. Wu, X. Yi, A. Zheng, A. Umar, D. O'Hare and Q. Wang, *J. Mater. Chem. A*, 2013, **1**, 12782–12790.

6 P. W. Xiao, J. Y. Jun, J. Cheng, P. H. Zheng and P. X. Zhi, *Environ. Sci. Technol.*, 2008, **42**, 614–618.

7 N. D. Hutson, S. A. Speakman and E. A. Payzant, *Chem. Mater.*, 2004, **16**, 4135–4143.

8 X. Zhu, C. Chen, H. Suo, Q. Wang, Y. Shi, D. O'Hare and N. Cai, *Energy*, 2019, **167**, 960–969.

9 A. Garcia-Gallastegui, D. Iruretagoyena, V. Gouvea, M. Mokhtar, A. M. Asiri, S. N. Basahel, S. A. Al-Thabaiti, A. O. Alyoubi, D. Chadwick and M. S. P. Shaffer, *Chem. Mater.*, 2012, **24**, 4531–4539.

10 J. Merel, M. Clausse and F. Meunier, *Ind. Eng. Chem. Res.*, 2008, **47**, 209–215.

11 R. Ben-Mansour, M. A. Habib, O. E. Bamidele, M. Basha, N. A. A. Qasem, A. Peedikakkal, T. Laoui and M. Ali, *Appl. Energy*, 2016, **161**, 225–255.

12 F. Brandani and D. M. Ruthven, *Ind. Eng. Chem. Res.*, 2004, **43**, 8339–8344.

13 R. Li, T. Xue, R. Bingre, Y. Gao, B. Louis and Q. Wang, *ACS Appl. Mater. Interfaces*, 2018, **10**, 34834–34839.

14 G. S. Pawley, *J. Appl. Crystallogr.*, 1981, **14**, 357–361.

15 F. Cavani, F. Trifirò and A. Vaccari, *Catal. Today*, 1991, **11**, 173–301.

16 W. L. J. Kwok, D.-G. Crivoi, C. Chen, J.-C. Buffet and D. O'Hare, *Dalton Trans.*, 2018, **47**, 143–149.

17 C. Chen, P. Wang, T.-T. Lim, L. Liu, S. Liu and R. Xu, *J. Mater. Chem. A*, 2013, **1**, 3877–3880.

18 S. Greiser, M. Hunger and C. Jäger, *Solid State Nucl. Magn. Reson.*, 2016, **79**, 6–10.

19 P. Pena, J. M. Rivas Mercury, A. H. de Aza, X. Turrillas, I. Sobrados and J. Sanz, *J. Solid State Chem.*, 2008, **181**, 1744–1752.

20 J. Huang, Y. Jiang, V. R. Reddy Marthala, Y. S. Ooi, J. Weitkamp and M. Hunger, *Microporous Mesoporous Mater.*, 2007, **104**, 129–136.

21 S. Lee, H. Kim and M. Choi, *J. Mater. Chem. A*, 2013, **1**, 12096–12102.

22 J. Klinowski, *Chem. Rev.*, 1991, **91**, 1459–1479.

23 C. A. Fyfe, Y. Feng, H. Grondey, G. T. Kokotailo and H. Gies, *Chem. Rev.*, 1991, **91**, 1525–1543.

24 S. F. Wong, H. Awala, A. Vincente, R. Retoux, T. C. Ling, S. Mintova, R. R. Mukti and E. P. Ng, *Microporous Mesoporous Mater.*, 2017, **249**, 105–110.

25 K. Góra-Marek, K. Tarach, J. Tekla, Z. Olejniczak, P. Kuštrowski, L. Liu, J. Martinez-Triguero and F. Rey, *J. Phys. Chem. C*, 2014, **118**, 28043–28054.

26 C. Chen, R. Felton, J.-C. Buffet and D. O'Hare, *Chem. Commun.*, 2015, **51**, 3462–3465.

27 M. Safak Boroglu and M. Ali Gurkaynak, *Polym. Bull.*, 2011, **66**, 463–478.

28 D. Nibou, S. Amokrane, H. Mekatel and N. Lebaili, *Phys. Procedia*, 2009, **2**, 1433–1440.

29 A. Zainal Abidin, N. H. H. Abu Bakar, E. P. Ng and W. L. Tan, *J. Taibah Univ. Sci.*, 2017, **11**, 1070–1079.

30 S. Pu, J. Wang, L. Li, Z. Zhang, Z. Bao, Q. Yang, Y. Yang, H. Xing and Q. Ren, *Ind. Eng. Chem. Res.*,

2018, **57**, 1645–1654.

31 C. Chen, M. Yang, Q. Wang, J.-C. Buffet and D. O'Hare, *J. Mater. Chem. A*, 2014, **2**, 15102–15110.

32 W. Yang, Y. Kim, P. K. T. Liu, M. Sahimi and T. T. Tsotsis, *Chem. Eng. Sci.*, 2002, **57**, 2945–2953.

33 J. Li, H. Liu, T. An, Y. Yue and X. Bao, *RSC Adv.*, 2017, **7**, 33714–33725.

34 M. Nielsen, A. Hafreager, R. Y. Brogaard, K. De Wispelaere, H. Falsig, P. Beato, V. Van Speybroeck and S. Svelle, *Catal. Sci. Technol.*, 2019, **9**, 3721–3725.

35 M. Thommes, K. Kaneko, A. V. Neimark, J. P. Olivier, F. Rodriguez-Reinoso, J. Rouquerol and K. S. W. Sing, *Pure Appl. Chem.*, 2015, **87**, 1051–1069.

36 Q. Yan, Z. Zhang, Y. Zhang, A. Umar, Z. Guo, D. O'Hare and Q. Wang, *Eur. J. Inorg. Chem.*, 2015, **25**, 4182–4191.

37 Q. Guo, Q. Zhang, H. Wang, Z. Liu and Z. Zhao, *Catal. Commun.*, 2016, **77**, 118–122.

38 C. Chen, C. F. H. Byles, J.-C. Buffet, N. H. Rees, Y. Wu and D. O'Hare, *Chem. Sci.*, 2016, **7**, 1457–1461.

39 H. Suo, H. Duan, C. Chen, J.-C. Buffet and D. O'Hare, *RSC Adv.*, 2019, **9**, 3749–3754.

40 D. K. Panchariya, R. K. Rai, E. Anil Kumar and S. K. Singh, *ACS Omega*, 2018, **3**, 167–175.

41 H. Suo, C. Chen, J.-C. Buffet and D. O'Hare, *Dalton Trans.*, 2018, **47**, 16413–16417.

42 C. Chen, A. Wangriya, J.-C. Buffet and D. O'Hare, *Dalton Trans.*, 2015, **44**, 16392–16398.

43 M. Ejgenberg and Y. Mastai, in *Advances in Crystallization Processes*, ed. Yitzhak Mastai, IntechOpen, Rijeka, 1st edn., 2012, pp. 39–58.

44 Z. P. Xu, J. Zhang, M. O. Adebajo, H. Zhang and C. Zhou, *Appl. Clay Sci.*, 2011, **53**, 139–150.

45 W. L. J. Kwok, D. G. Crivoi, C. Chen, J. C. Buffet and D. O'Hare, *Dalton Trans.*, 2018, **47**, 143–149.

46 W. L. J. Kwok, DPhil thesis, University of Oxford, 2020.

47 Y. Zhai, S. Zhang, Y. Shang, Y. Song, W. Wang, T. Ma, L. Zhang, Y. Gong, J. Xu and F. Deng, *Catal. Sci. Technol.*, 2019, **9**, 659–671.

48 X. Sun and S. K. Dey, *J. Colloid Interface Sci.*, 2015, **458**, 160–168.

49 X. Liu, C. Wang, Y. Dou, A. Zhou, T. Pan, J. Han and M. Wei, *J. Mater. Chem. A*, 2014, **2**, 1682–1685.

50 M. E. Rivera-Ramos, G. J. Ruiz-Mercado and A. J. Hernández-Maldonado, *Ind. Eng. Chem. Res.*, 2008, **47**, 5602–5610.

51 J. I. Di Cosimo, V. K. Díez, M. Xu, E. Iglesia and C. R. Apesteguía, *J. Catal.*, 1998, **178**, 499–510.

52 Y. Gao, Z. Zhang, J. Wu, X. Yi, A. Zheng, A. Umar, D. O'Hare and Q. Wang, *J. Mater. Chem. A*, 2013, **1**, 12782–12790.

53 S. H. Hong, M. S. Jang, S. J. Cho and W. S. Ahn, *Chem. Commun.*, 2014, **50**, 4927–4930.

54 Z. Zhao, X. Cui, J. Ma and R. Li, *Int. J. Greenh. Gas Control*, 2007, **1**, 355–359.

55 C. Chen, D. W. Park and W. S. Ahn, *Appl. Surf. Sci.*, 2014, **292**, 63–67.

56 M. M. J. Treacy and J. B. Higgins, *Collection of Simulated XRD Powder Patterns for Zeolites*, Elsevier Science, Netherland, 5th edn., 2001.

57 A. Vaitkus, A. Merkys and S. Gražulis, *J. Appl. Crystallogr.*, 2021, **54**, 661–672.

58 M. Haouas, F. Taulelle and C. Martineau, *Prog. Nucl. Magn. Reson. Spectrosc.*, 2016, **94–95**, 11–36.

59 P. Li, Y. Yu, P. P. Huang, H. Liu, C. Y. Cao and W. G. Song, *J. Mater. Chem. A*, 2014, **2**, 339–344.

60 Y. Gao, Z. Zhang, J. Wu, X. Yi, A. Zheng, A. Umar, D. O'Hare and Q. Wang, *J. Mater. Chem. A*, 2013, **1**, 12782–12790.

61 M. Bellotto, B. Rebours, O. Clause, J. Lynch, D. Bazin and E. Elkaïm, *J. Phys. Chem.*, 1996, **100**, 8535–8542.

62 J. Jiao, W. Wang, B. Sulikowski, J. Weitkamp and M. Hunger, *Microporous Mesoporous Mater.*, 2006, **90**, 246–250.

63 M. Miyamoto, Y. Fujioka and K. Yogo, *J. Mater. Chem.*, 2012, **22**, 20186–20189.

64 D.Coster, A. L. Blumenfeld and J. J. Fripiat, *J. Phy. Chem*, 1994, **98**, 6201–6211.

65 C. Chen, N. Zhang, W. Li and Y. Song, *Mol. Phys.*, 2016, **114**, 2924–2935.

66 C. Morter, A. Zecchin, S. C. A and A. Chiorin, *J. Chem. Soc., Faraday Trans. 1*, 1977, 1544–1560.

67 S. Kumar, R. Srivastava and J. Koh, *J. CO2 Util.*, 2020, **41**, 1–16.

68 R. Aniruddha, I. Sreedhar and B. M. Reddy, *J. CO2 Util.*, 2020, **42**, 1–27.

69 M. K. Ram Reddy, Z. P. Xu, G. Q. Lu and J. C. Diniz Da Costa, *Ind. Eng. Chem. Res.*, 2008, **47**, 2630–2635.

70 D. A. Torres-Rodríguez, E. Lima, J. S. Valente and H. Pfeiffer, *J. Phys. Chem. A*, 2011, **115**, 12243–12250.

71 A. O. Yazaydin, R. Q. Snurr, T.-H. Park, K. Koh, J. Liu, M. D. Levan, A. I. Benin, P. Jakubczak, M. Lanuza, D. B. Galloway, J. J. Low and R. R. Willis, *J. Am. Chem. Soc.*, 2009, **131**, 18198–18199.

72 R. Mohammadian, M. Karimi Alavijeh, N. Kamyar, M. M. Amini and A. Shaabani, *Polyhedron*, 2018, **156**, 174–187.

73 J. Chen, J. Yang, G. Hu, X. Hu, Z. Li, S. Shen, M. Radosz and M. Fan, *ACS Sustain. Chem. Eng.*, 2016, **4**, 1439–1445.

74 Y. Yang, X. Yan, X. Hu, R. Feng, M. Zhou and W. Cui, *Colloids Surfaces A Physicochem. Eng. Asp.*, 2018, **552**, 16–23.

75 S. Kumar, R. Bera, N. Das and J. Koh, *Carbohydr. Polym.*, 2020, **232**, 1–8.

76 F. Gao, Y. Li, Z. Bian, J. Hu and H. Liu, *J. Mater. Chem. A*, 2015, **3**, 8091–8097.

Chapter 3 Synthesis and characterisation of porous SiO_2@Cu_xZnAl-CO_3-LDH core-shell materials

3.1 Introduction

Enormous efforts have been put into developing stable and efficient Cu-based heterogeneous catalysts for CO_2 hydrogenation to methanol. Introducing promoters and supports are two ways that have been intensively studied.[1,2]

Promoters are added to adjust the electronic properties of the surface and thus tune both the catalytic activity and stability of catalysts.[1,3] Common promoters include alkali metals (e.g., K),[4] main group metals (e.g., Mg and Ba),[4,5] noble metals (e.g., Pt and Pd)[6,7] and metal oxides (e.g., MgO, ZnO, ZrO_2, Al_2O_3 and Cr_2O_3).[1,2,8–11] It has been demonstrated that one or a combination of promoters can be used at the same time to enhance the stability and activity of Cu-based catalysts. The Cu/ZnO/Al_2O_3 mixture is the state-of-art industrial catalyst for methanol production.[12] Gao *et al.* developed a Cu/ZnO/Al_2O_3/ZrO_2 (2/1/1.2/1 molar ratio) catalyst with excellent activity, showing 25.6% CO_2 conversion and 61.3% MeOH selectivity at 250 °C and 50 bar, with high stability (maintaining performance over 1000 h); they attributed the excellent catalytic activity and high stability to the increased copper surface area and improved Cu dispersion as a result of high Al_2O_3 content (Al occupies 27.9 mol%).[13]

Supports are used to immobilise active copper nanoparticles, increase the copper dispersion and avoid them from sintering. Metal oxides (e.g., Al_2O_3, ZrO_2, ZnO and CeO_2) can be used as both the promoters and supports.[1,2] It has been reported that a strong metal support interaction (SMSI) between the metallic copper and metal oxide promotes catalytic activity.[2,14] Other common

supports includes silica and carbon.[1,2] Koh *et al.* reported their work on the KIT-6, a mesoporous silica, supported Cu/ZnO/MnO catalyst (6/1.5/0.5 molar ratio) which displayed 8.2% CO_2 conversion, ≥ 99% MeOH selectivity and 3.37 $g_{MeOH}/g_{catalyst}$/h yield at 180 °C and 40 bar; this excellent performance was attributed to the porous morphology of KIT-6 which promotes the copper dispersion, achieves a high copper surface area, prevents the copper sintering and realises an efficient diffusion of reactant and product.[15]

Previously, our group has reported a Cu/ZnO/Ga_2O_3 catalyst derived from an aqueous miscible organic (AMO) solvent-treated layered double hydroxide (AMO-LDH) precursor that showed a 20% CO_2 conversion, 50% methanol selectivity and 0.59 $g_{MeOH}/g_{catalyst}$/h space time yield of methanol at 270 °C and 45 bar, higher than most of the previously reported catalysts.[16] This superior performance is due to the high copper surface area and well-dispersed metallic Cu crystallites obtained from the ultrathin layered morphology and homogeneous dispersion of Cu, Zn and Al in the cationic layer.[2,16] The goal of the AMO treatment is to reduce the stacking between LDH platelets and to expose more active site. Immobilising LDH on a core has been found to have the same effect, i.e., avoiding stacking.[17,18]

It is hypothesised that using an appropriate core, such as porous silica, to support LDH, can further improve the performance of an LDH-derived catalyst. In this chapter, a series of mesoporous silica supported CuZnAl-CO_3-LDH core-shell materials (*m*SiO_2@CuZnAl-CO_3-LDH) are prepared and characterised. The effects of synthetic conditions, the composition of core-shell and LDH, and the properties of the silica core on the characteristics of the core-shell materials are explored and evaluated in the context of their use as pre-catalysts for the

hydrogenation of CO_2 to methanol.

3.2 Synthesis and characterisation of MCM-48@Cu$_x$ZnAl-CO$_3$-LDH

3.2.1. Synthesis and characterisation of MCM-48@Cu$_{1.3}$ZnAl-CO$_3$-LDH

Core-shell with MCM-48 core and $Cu_{1.3}ZnAl$-CO_3-LDH shell was prepared using the co-precipitation method. An aqueous solution of copper, zinc and aluminium nitrate, with Cu: Zn: Al molar ratio = 1.3:1:1, was added to a dispersion of MCM-48 and $Na_2CO_{3(aq)}$ at pH 10. The pH of the reaction mixture was maintained at 10 using 1 M $NaOH_{(aq)}$ solution. After completing the addition of metal nitrate, the resulting mixture was stirred at 500 rpm for 1 hour. The solid product was collected by filtration and washed with DI water before drying under vacuum at 30 °C overnight to afford the core-shell material MCM-48@$Cu_{1.3}ZnAl$-LDH-pH10 as a blue powder. An analogous $Cu_{1.3}ZnAl$-CO_3-LDH was prepared under the same conditions as MCM-48@$Cu_{1.3}ZnAl$-LDH-pH10 without the MCM-48 core and was termed $Cu_{1.3}ZnAl$-LDH. In this core-shell (and $Cu_{1.3}ZnAl$-LDH) the oxidation state of copper, zinc and aluminium is +2, +2 and +3, respectively.

The MCM-48 used in this study is a commercial silica with highly-ordered mesopores which gives characteristic Bragg peak at 2θ lower than 3° in the powder X-Ray diffraction (XRD) pattern and an broad feature at 2θ *ca*. 24° (Appendix B, Figure B1).[19] Due to the limits of the instrument, only scattering between 2θ = 5–70° is recorded. MCM-48@$Cu_{1.3}ZnAl$-LDH-pH10 and $Cu_{1.3}ZnAl$-LDH exhibit the typical LDH Bragg reflections (Figure 3.1), such as (00*l*), (110) and (113) and no Bragg reflections associated with crystalline impurities are observed. Compared with $Cu_{1.3}ZnAl$-LDH, a weakened intensity and a broadening of LDH Bragg

reflections, especially the 00*l* harmonic series, are noticed in MCM-48@$Cu_{1.3}$ZnAl-LDH-pH10. The weakened intensity results from the reduced weight fraction of LDH in the core-shell (50 wt%) compared to pure LDH sample.[20] The broadening is due to the reduced LDH crystallinity.

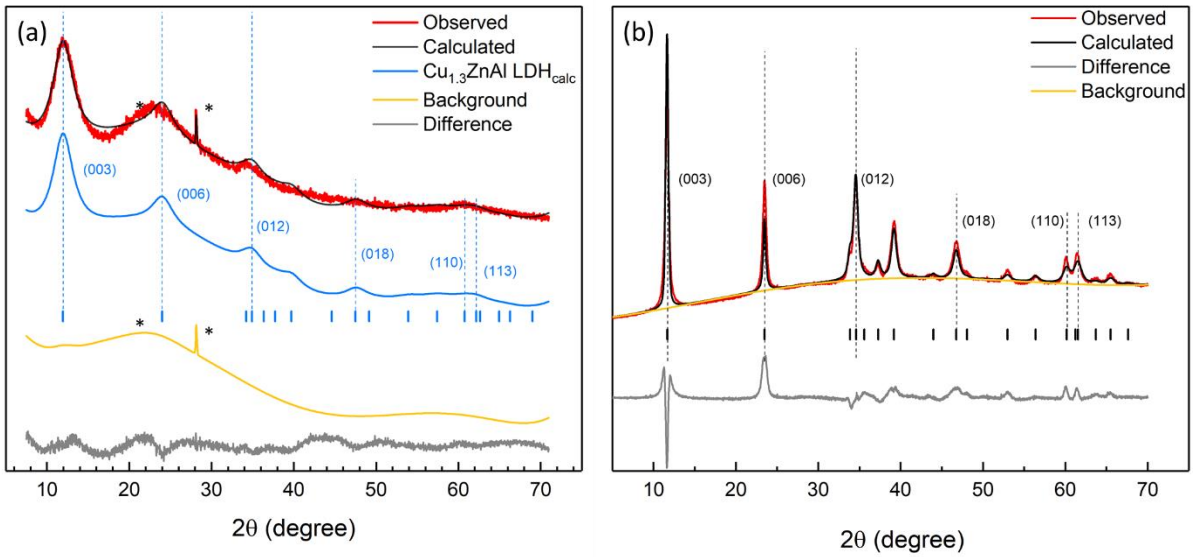


Figure 3.1 Powder XRD pattern and single-phase Pawley refinement results of (a) MCM-48@$Cu_{1.3}$ZnAl-LDH-pH10 and (b) $Cu_{1.3}$ZnAl-LDH. The observed, calculated, extracted $Cu_{1.3}$ZnAl LDH phase, background and difference are shown in red, black, blue, yellow and grey, respectively. (*hkl*) plane reflection of LDH was indicated with short sticks. Peak marked with * comes from grease and glass slide used in sample preparation.

In addition, a single-phase Pawley refinement based on the space group of LDH, *R-3m*, was carried out on both samples (Figure 3.1).[21,22] The details of refinement can be found in Table B1. The core-shell and LDH have similar d_{110} values (Table 3.1), corresponding to similar metal-metal distances, indicating the metallic composition of the LDH phase remained. $Cu_{1.3}$ZnAl-LDH has d_{003} equal to 7.59 Å, demonstrating that it is carbonate-intercalated.[23] MCM-48@$Cu_{1.3}$ZnAl-LDH-pH10 possesses a decreased d_{003} (7.39 Å). This reflects a change in the interlayer galley, which may be due to the loss of interlayer water molecules, partial substitution of carbonate anions with hydroxyl ions, or modified electrostatic interaction

between metal hydroxide layers and anions.[23]

Table 3.1 The *d*-spacing and crystallite size of $Cu_{1.3}$ZnAl-LDH and MCM-48@$Cu_{1.3}$ZnAl-LDH-pH10 obtained from the single-phase Pawley refinement.

Sample	d_{003} (Å)	d_{110} (Å)	D_{00l} (nm)	D_{110} (nm)
$Cu_{1.3}$ZnAl-LDH	7.59	1.54	12.48	9.86
MCM-48@$Cu_{1.3}$ZnAl-LDH-pH10	7.39	1.52	2.06	0.89

D_{00l} is the crystallite domain size perpendicular to (00*l*) planes. D_{110} is the crystallite domain size perpendicular to the (110) plane.

Reduced crystallite size, increased microstrain and stacking faults are three factors that contribute to the observed peak broadening.[24] Taking the stacking faults into account in refining the peak broadening of a layered material would provide a more precise and accurate model but it is a burdensome calculation for an LDH and was not included in the routine refinement; the low-symmetry interlayer carbonate positions produce about 200 atom positions that will participate in the refinement and the fourteen possible polytypes of stacking sequence for LDH could co-exist to afford even more complex stacking sequences.[25–27]

Using lab XRD data with a poor signal-to-noise ratio, e.g., the data of MCM-48@$Cu_{1.3}$ZnAl-LDH-pH10, refining crystallite size and microstrain broadening at the same time may lead to an over-parameterisation and end up with meaningless numbers. Therefore, only crystallite size is refined in this work, which is calculated from the integral breadth of peaks. Its value is an underestimation of the average crystallite size; the change of the value is used to indicate the change of the phase crystallinity.

D_{00l} represents an average of the crystallite-size distribution vertical to the (00*l*) planes.[24] The higher the value of D_{00l}, the more layers are stacking together in the LDH. Reduction of the D_{00l}

of core-shell (from 12.48 nm in control LDH to 2.06 nm) suggests that the stacking between LDH sheets get reduced once LDH is immobilised on a core. The value of D_{110} is related to the average crystal domain diameter of LDH platelets. The decreased D_{110} (from 9.86 nm of LDH to 0.89 nm of core-shell) indicates a less crystalline metal hydroxide layer in the composite.

Similar broadening of LDH Bragg reflections is observed in various LDH-based composites in the presence of carbon or silica;[18,20,28,29] Xiang *et al.* attributed the decreased LDH crystallite size in a LDH and carbon mixture to the confined effect of carbon nanotube on the growth of LDH.[20] It is likely that MCM-48 suspended in the reaction mixture interferes with the LDH growth.

Figure 3.2a shows the ^{27}Al solid-state NMR spectrum of the core-shell and LDH. Al^{3+} is octahedrally coordinated in $Cu_{1.3}$ZnAl-LDH and is expected to give a band at around 10 ppm.[30,31] However, the neighbouring paramagnetic Cu^{2+} leads to an expansion in chemical shift and a band broadening, which makes the 10.0 ppm resonance unobservable.[32,33] Two Al resonances are seen in the core-shell material. The 53.0 ppm resonance is assigned to tetrahedrally coordinated Al (AlO_4).[34] Si atoms are 4-coordinated in MCM-48.[35] The presence of AlO_4 is very likely due to the formation of aluminosilicate at the interface.[35] The other 8 ppm signal is associated with the octahedral Al (AlO_6).[24,25]

The presence of both AlO_4 and AlO_6 resonances in SiO_2@MgAl LDH core-shells has been reported within the research group;[17,18,36] the AlO_6 resonance is due to Al in LDH.[17,36] In this work, due to the paramagnetic Cu centres in the LDH, the AlO_6 resonance might not derive

from the LDH. Beardmore *et al.* illustrated a stable structure of hydroxyaluminosilicate which embeds both O_h and T_d Al (Figure 3.2b).[37] Romero *et al.* reported preparing aluminosilicate from MCM-48 and aluminium chloride hexahydrate; the author observed that the octahedral Al resonance appears at Si/Al ratio between 15 to 40.[29] Therefore, the AlO_6 resonance in core-shell may arise from the interface aluminosilicate which is likely has Si/Al ratio of around 15–40.[35,38,39]

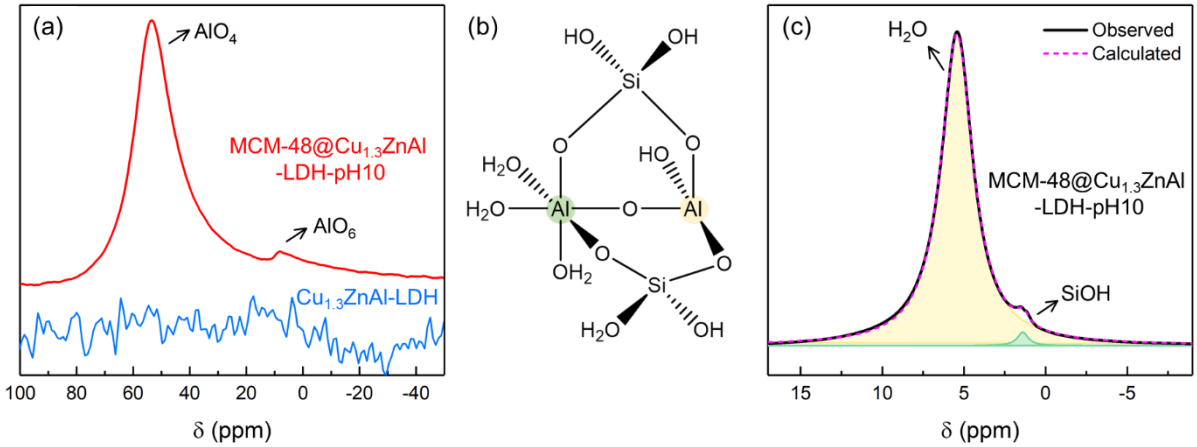


Figure 3.2 (a) ^{27}Al solid-state DPMAS NMR spectrum (104.2 MHz) of MCM-48@$Cu_{1.3}$ZnAl-LDH-pH10 and $Cu_{1.3}$ZnAl-LDH. Due to the presence of paramagnetic Cu(II) in the samples, the spectrum is not quantitative. (b) Structure of hydroxyaluminosilicate. (c) ^{1}H solid-state zgbs NMR spectrum of MCM-48@$Cu_{1.3}$ZnAl-LDH-pH10.

The ^{1}H NMR spectrum (Figure 3.2c) of the composite contains two features: one dominant resonance at 5.4 ppm due to the interlayer water and one at 1.4 ppm resulting from the silanol group, SiOH.[40,41] The hydroxyl group in the metal hydroxide layer will give ZnOH and ZnAlOH bands between 2.0–5.0 ppm, which overlap with the water resonance and are too weak to distinguish.[40,42]

The FTIR spectrum of MCM-48@$Cu_{1.3}$ZnAl-LDH-pH10 (Figure 3.3) exhibits both the characteristic IR absorbance bands of silica and LDH; the metal-oxygen (M-O) vibration at

700 cm^{-1} due to metal hydroxide, O-H stretching at 3440 cm^{-1} from the hydroxide group as well as interlayer water molecules in the LDH and the Si-O stretching at 1050 cm^{-1} from silica.[23,43] The C–O stretching band (1360 cm^{-1}) resulting from the interlayer carbonate anion is weaker in the core-shell than in pure LDH. One reason is the reduced LDH fraction (50 wt%). Moreover, the carbonate anions may be partially substituted by hydroxyl group (as revealed by reduced d_{003}).

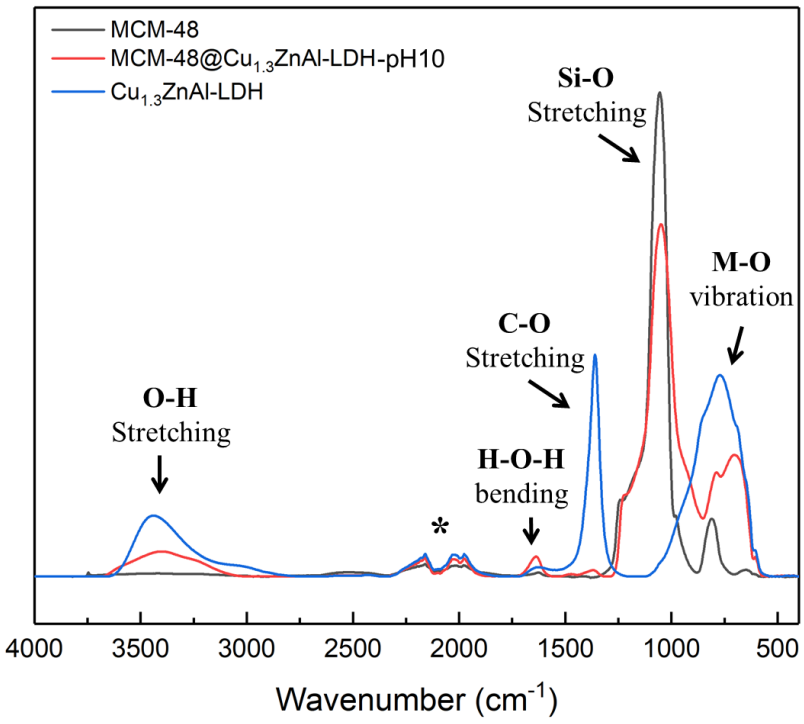


Figure 3.3 FTIR spectra of MCM-48, MCM-48@$Cu_{1.3}$ZnAl-LDH-pH10 and $Cu_{1.3}$ZnAl-LDH.

The thermostability of materials was studied using TGA (Figure 3.4). MCM-48 lost 10.5% of weight mainly due to water evaporation when heated up to 800 °C.[44] $Cu_{1.3}$ZnAl-LDH displays three distinguish weight loss stages: 1) The reversible removal of physisorbed water occurs up to 150 °C giving 14.1% weight loss;[45,46] 2) The reversible dehydroxylation and the decomposition of loosely bounded interlayer carbonate anions starts before 100 °C and finishes up to 400 °C, which causes 13.1% weight loss; [45–47] and 3) The full decarbonation of LDH

happens between 500–750 °C and leads to 6.0% loss.[47,48] The final stage exhibits two regions (Figure 3.4c). Velu *et al.* proposed that several oxycarbonate intermediates with the chemical composition $[M^{II}M^{III}_xO_y(CO_3)_z]$ were formed during the thermal decomposition of Cu-containing LDH.[47] It is possible that the distinct M^{II} (Cu^{2+} and Zn^{2+}) environments in the LDH and Jahn-Teller distortion of Cu give rise to $[M^{II}M^{III}_xO_y(CO_3)_z]$ species with different thermal stabilities which decompose at different rates.[49–51]

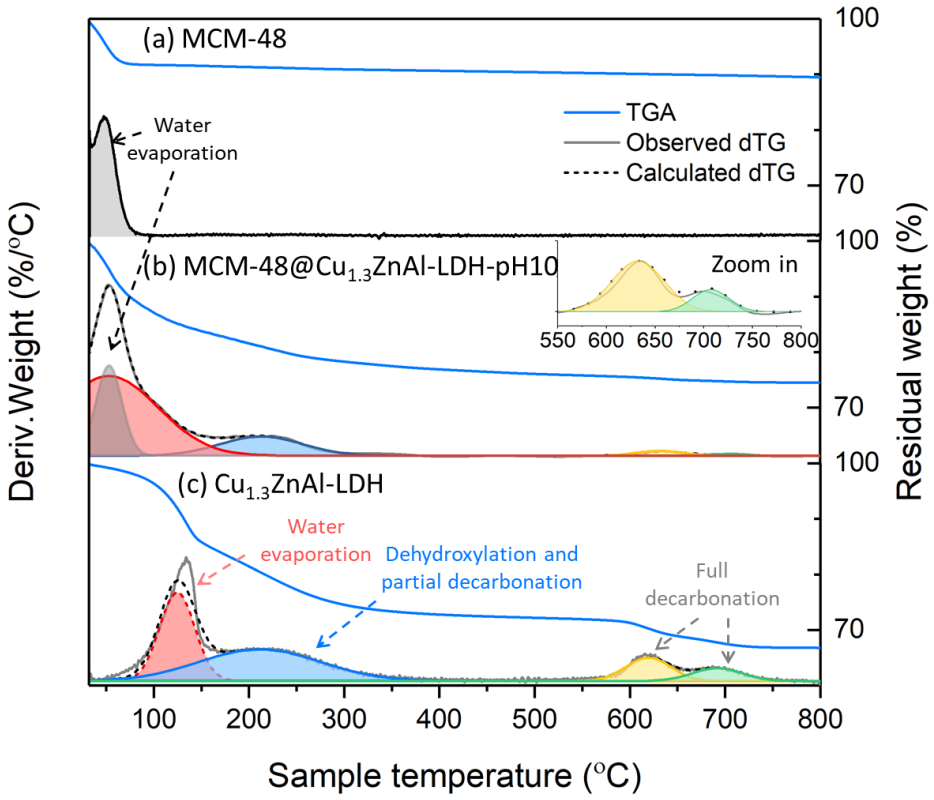


Figure 3.4 TGA and Derivative TGA (dTG) plots of (a) MCM-48, (b) MCM-48@$Cu_{1.3}$ZnAl-LDH-pH10 and (c) $Cu_{1.3}$ZnAl-LDH. The observed TGA, observed dTG and cumulative dTG are plotted with blue, grey, and grey dashed lines. The deconvoluted dTG peaks showing different weight loss stages are coloured in grey, red, blue, yellow and green, respectively.

MCM-48@$Cu_{1.3}$ZnAl-LDH-pH10 shows similar three weight loss events as pristine LDH (Figure 3.4b). However, the reversible water loss and dehydroxylation happen at a lower temperature than for a pure LDH, as demonstrated by the dTG curve. The ordered mesopore in

MCM-48 likely facilitates the water evaporation, and the less crystalline LDH is less stable, tending to decompose at low temperature.[52] The remaining weight (at 800 °C) for MCM-48, MCM-48@$Cu_{1.3}$ZnAl-LDH-pH10 and $Cu_{1.3}$ZnAl-LDH is 89.5%, 74.5% and 66.8%, respectively. This suggests a 34:66 weight ratio between silica and LDH which deviates from the expected 50:50. One possible explanation for this unexpected deviation is the hydrolysis/structure collapse of this high surface area silica in the basic environment.[53] The dissolved silica has then been removed in the subsequent filtration and washing process. The 66 wt% LDH content would give rise to the 3.9% weight loss in the full decarbonation step (500–750 °C). However, only 2.4% is observed. This inconsistency may be related to the partial substitution of carbonate by OH^- in the LDH interlayer gallery and is consistent with the XRD and FTIR result.

MCM-48 are spherical particles with a radius around 604 ± 159 nm (Figure 3.5a and Figure B2) and a pore size about 4.1 ± 0.7 nm as revealed by the TEM images (Figure 3.5b and Figure B3). $Cu_{1.3}$ZnAl-LDH is an agglomerate of hexagonal platelets with a diameter between 175 and 500 nm (Figure 3.5c). MCM-48@$Cu_{1.3}$ZnAl-LDH-pH10 displays a typical core-shell morphology with a spherical core and a seaweed-like shell of which the thickness varies from 8 nm to 226 nm (Figure 3.5d and e). A schematic illustration of the core-shell structure is given in Figure 3.5f based on the observed morphology. It is proposed that small LDH crystallites (positively charged) firstly wrap on the negatively charged surface of silica via electrostatic interaction, then radially grow from the interface to give non-rigid seaweed-like LDH shells.[18] The interface LDH (wrapping around silica) was not clear in SiO_2@Mg_2Al-CO_3-LDH and

MCM-48@AMO-Mg_3Al-CO_3-LDH core-shells previously prepared within the research group.[17,18,54] It is speculated that the formation of this interface LDH is not only related to the surface area of silica core but also depends on the dominant cations of LDH.

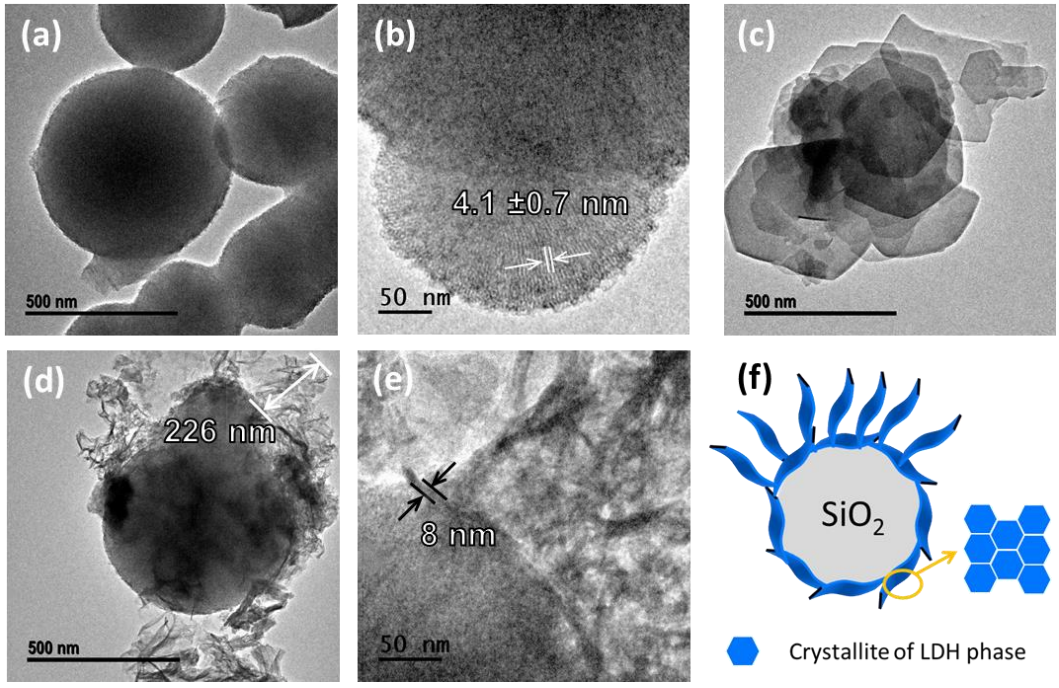


Figure 3.5 TEM images of (a) MCM-48 (b) MCM-48 at 50 nm scale, (c) $Cu_{1.3}$ZnAl-LDH, (d) MCM-48@$Cu_{1.3}$ZnAl-LDH-pH10 and (e) MCM-48@$Cu_{1.3}$ZnAl-LDH-pH10 at 50 nm scale. (f) The schematic illustration of MCM-48@$Cu_{1.3}$ZnAl-LDH-pH10.

MCM-48 that shows type a IVb N_2 adsorption isotherm with no hysteresis loop is mesoporous (Figure 3.6a).[55] $Cu_{1.3}$ZnAl-LDH that exhibits a type II N_2 adsorption isotherm with H3 hysteresis loop that can be ascribed to a non-rigid agglomerate of plate-like particles that gives slit-like pores,[55,56] which is consistent with the TEM images. MCM-48@$Cu_{1.3}$ZnAl-LDH-pH10 exhibits a type IV isotherm with H4 hysteresis loop, revealing the sample is aggregates of the micro- or meso-porous materials.[55]

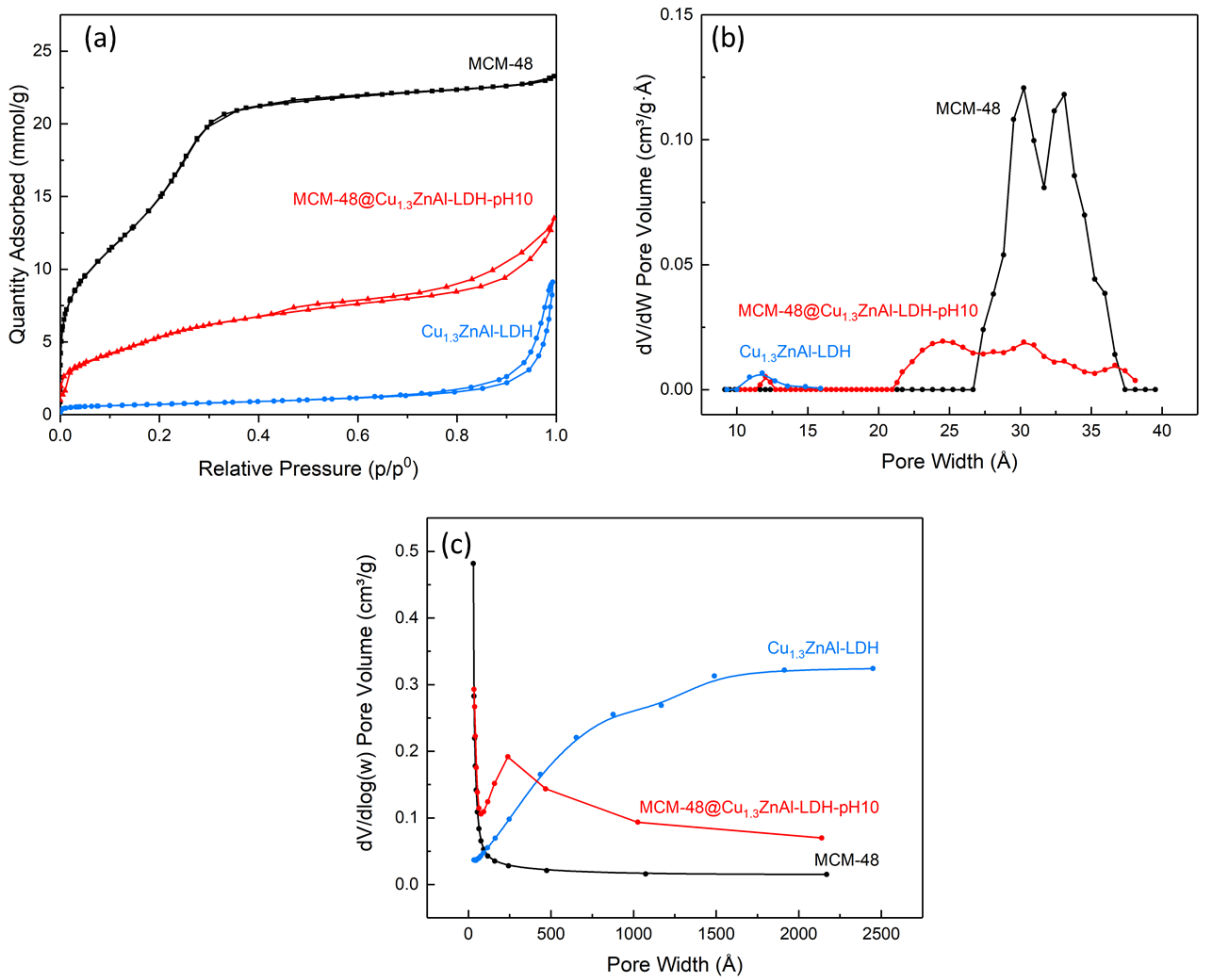


Figure 3.6 (a) The N_2 adsorption and desorption isotherm (at 77 K), (b) The density functional theory (DFT) pore size distribution and (c) The Barrett-Joyner-Halenda (BJH) pore size distribution of MCM-48, MCM-48@$Cu_{1.3}$ZnAl-LDH-pH10 and $Cu_{1.3}$ZnAl-LDH. DFT pore size distribution of $Cu_{1.3}$ZnAl-LDH is based on the kernels of slit-pore, the other two samples are based on the kernels for metal oxide with cylindrical pores.

The density functional theory (DFT) pore size distribution in Figure 3.6b confirms that MCM-48 has a narrow pore size distribution near diameter 3.0–3.3 nm. Compared to the pure mesoporous silica, MCM-48@$Cu_{1.3}$ZnAl-LDH-pH10 has wider pore size distribution and a lower pore volume. The distribution maxima dropped from 3.0–3.3 nm to 2.4–3.0 nm. Several published studies illustrated that incorporating metal atoms like Al, Co or Zn to the mesoporous silica can cause a reduction in the pore size and loss in both pore volume and surface area.[57–59] Doyle *et al.* reported a shrinkage of the mesopore (by 0.4 nm) as well as a less ordered pore

structure in MCM-48 after the silica was dispersed in pH 9 buffer solution at room temperature for 1.5 h.[53] It is assumed that the decrease in pore size could result from the metal atom (Cu, Zn and Al) incorporation and dispersion in the basic environment. LDH has 1.2 nm pore which is due to the micropore defects or aggregation of small LDH crystallites.[60] The micropore in the core-shell with a diameter around 1.2 nm (Figure 3.6b) could originate from either the silica core or the LDH shell.

The pore size distribution based on the Barrett-Joyner-Halenda (BJH) method in Figure 3.6c reveals that MCM-48 has no macropores. LDH possesses a wide distribution but no clear maxima in the mesopore and macropore range, indicating that the pore structure is not uniform. MCM-48@$Cu_{1.3}$ZnAl-LDH-pH10 has macropores at around 24.5 nm, which may be due to the pore-opening from the reduced layer-by-layer stacking of LDH or the formation of interparticle channel caused by the aggregation of core-shell particles.

Overall, MCM-48@$Cu_{1.3}$ZnAl-LDH-pH10 can be described as having a hierarchical pore structure; micro- and narrow meso-pores are present in the core, and large meso- and macro-pores exist in the LDH shell and the channel between particles.

The core-shell exhibits a lower N_2 BET specific surface area than its core, MCM-48 (Figure 3.7). This is consistent with the previous studies; a loss in the surface area and pore volume occurs when a micro/mesoporous core was employed as the substrate for LDH.[22,61–63] It is expected that the core-shell will have a higher BET specific surface area and total pore volume than the physical mixture (MCM-48/$Cu_{1.3}$ZnAl-LDH = 34/66 by weight) because that outer

LDH (not the interface) is radially grown on the silica surface and the layer-by-layer stacking is get diminished. However, Figure 3.7 shows that the core-shell (438.0 m^2/g) has a similar BET specific surface area as the physical mixture (440.1 m^2/g). It is possible that the gain in surface area from less-stacked LDH sheets is consumed by the loss in MCM-48 (pore shrinkage due to ion-exchange).[57–59] Moreover, the total pore volume of MCM-48@$Cu_{1.3}$ZnAl-LDH-pH10 (0.47 cm^3/g) and physical mixture (0.48 cm^3/g) are comparable. As revealed by the pore size distribution (Figure 3.6b and c), the additional pore volume from LDH shell and interparticle voids is balanced by the loss of mesopore in MCM-48.

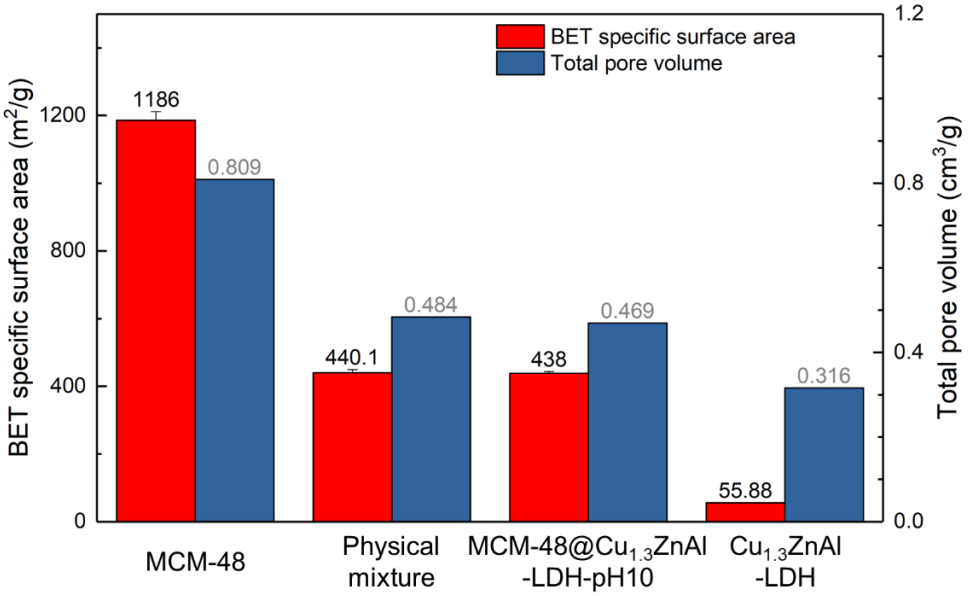


Figure 3.7 The BET specific surface areas and total pore volume of MCM-48, physical mixture, MCM-48@$Cu_{1.3}$ZnAl-LDH-pH10 and $Cu_{1.3}$ZnAl-LDH.

3.2.2. The effect of varying the reaction conditions

Although a core-shell material has been obtained, the uniformity of LDH on the core is not satisfactory. The effect of synthetic condition on the shell morphology were therefore studied. Core-shells prepared with increased amount of LDH (from 50wt % to 67wt %), dropped pH (from 10 to 9) and accelerated metal addition rate (from 0.05 mmol/min to 0.1 mmol/min) were

named MCM-48@$Cu_{1.3}$ZnAl-LDH-67wt, MCM-48@$Cu_{1.3}$ZnAl-LDH-pH9 and MCM-48@$Cu_{1.3}$ZnAl-LDH-0.1, respectively. A summary of the synthetic condition and their relevant samples are given in Table 3.2. More details can be found in Chapter 7. The actual LDH fraction was worked out from the TGA data, which shows a good agreement with the expected value apart from MCM-48@$Cu_{1.3}$ZnAl-LDH-pH10 (discussed in section 3.2.1).

Table 3.2 A summary of the varied synthetic condition, their relevant samples, the expected and the calculated LDH fraction in the composite.

Sample name	Reaction pH	Metal nitrate dropping rate (mmol/min)	LDH fraction (exp.)	LDH fraction (cal.)[a]
MCM-48@$Cu_{1.3}$ZnAl-LDH-pH10	10	0.05	50	66
MCM-48@$Cu_{1.3}$ZnAl-LDH-**67wt**	10	0.05	**67**	70
MCM-48@$Cu_{1.3}$ZnAl-LDH-**pH9**	**9**	0.05	50	55
MCM-48@$Cu_{1.3}$ZnAl-LDH-**0.1**	10	**0.1**	50	–[b]

a: the real LDH fraction in the composite is calculated from the TGA results. b: LDH fraction is not determined because the product is amorphous, no crystalline LDH phase was obtained.

The XRD pattern of MCM-48@$Cu_{1.3}$ZnAl-LDH-0.1 demonstrates that doubling the metal nitrate dropping rate results in an amorphous product rather than crystalline LDH (Figure B4). Reducing the reaction pH from 10 to 9 did not cause much change in the LDH phase (Figure 3.8a); samples from two pH exhibits similar *d*-spacing and crystallite size (Table 3.3).

The shoulder at the crest of the (00*l*) Bragg reflections, especially the (003) Bragg peak, of MCM-48@$Cu_{1.3}$ZnAl-LDH-67wt suggests the presence of a second LDH phase (Figure 3.8b). Rietveld refinement that considers the texture of LDH and restricts the peak intensity was performed using a two-phase model (Table B2). The refinement displays good fitting of the (00*l*) Bragg peaks. The d_{003} of two LDH phases are 7.53 Å and 8.17 Å, indicating the existence of a carbonate-intercalated and nitrate-intercalated LDH phase, respectively, where the

carbonate LDH is dominant (Table 3.3).[64,65]

On the other hand, it is likely that the interlayer gallery of the LDH in MCM-48@$Cu_{1.3}$ZnAl-LDH-67wt is filled with a mixture of carbonate and nitrate anions, i.e., $(CO_3^{2-})_x(NO_3^-)_{1-x}$ where $0 \leq x \leq 1$, rather than a clean segregation of carbonate and nitrate. The formation of nitrate LDH may be due to the insufficient carbonate concentration in the reaction mixture. The presence of the nitrate interlayer anion has been observed previously in Zn_3Al-CO_3-LDH prepared via co-precipitation.[66] Crystallite size at (00*l*) and (110) directions increase with the increase in the LDH content (67 wt% compared to 50 wt%), which is due to the Ostwald ripening; the longer reaction time for adding more metal nitrate (precursor of LDH) to the reaction mixture allows a longer Ostwald ripening process and leads to a larger crystallite size.[67–69]

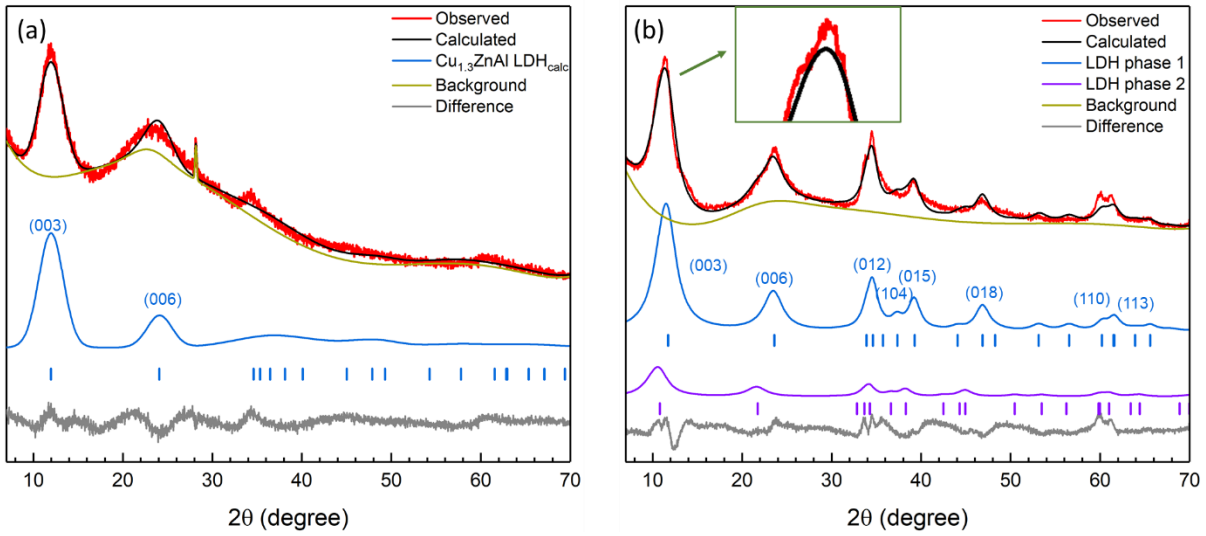


Figure 3.8 Powder XRD pattern and Rietveld refinement of (a) MCM-48@$Cu_{1.3}$ZnAl-LDH-pH9 and (b) MCM-48@$Cu_{1.3}$ZnAl-LDH-67wt. The observed, calculated, background, extracted LDH phase, and difference are shown in red, black, mustard yellow, blue (and purple), and grey, respectively. (*hkl*) reflections of LDH were indicated with short sticks.

Table 3.3 The *d*-spacing and crystallite size of LDH phase in MCM-48@$Cu_{1.3}$ZnAl-LDH core-shells obtained from the Rietveld refinement.

Sample	No. of LDH phase	d_{003} (Å)	d_{110} (Å)	D_{00l} (nm)	D_{110} (nm)
MCM-48@$Cu_{1.3}$ZnAl-LDH-pH10		7.39	1.52	2.06	0.89
MCM-48@$Cu_{1.3}$ZnAl-LDH-pH9		7.39	1.50	2.54	0.94
MCM-48@$Cu_{1.3}$ZnAl-LDH-67wt	1	7.53	1.53	2.39	5.86
	2	8.17	1.54		

The TGA and FTIR of MCM-48@$Cu_{1.3}$ZnAl-LDH-67wt and MCM-48@$Cu_{1.3}$ZnAl-LDH-pH9 displays typical LDH weight loss stages and characteristic IR absorbance bands (Figure B5). MCM-48@$Cu_{1.3}$ZnAl-LDH-67wt exhibits a more apparent LDH dehydroxylation and decarbonation weight loss and an enhanced carbonate stretching band comparing to MCM-48@$Cu_{1.3}$ZnAl-LDH-pH10, which is in line with the increased LDH amount.

A clear benefit of introducing more LDH in the composite is a better-defined platelet-like morphology of the shell rather than irregular shapes (Figure 3.9a–d). However, the shell coverage is not improved and a noticeable amount of free LDH appears as a consequence. Lowering the pH to 9, whilst keeping the LDH loading at 50 wt% realised an excellent shell that is thin and uniform, the thickness of which is 40 nm (Figure 3.9e and f). Moreover, no free LDH is observed.

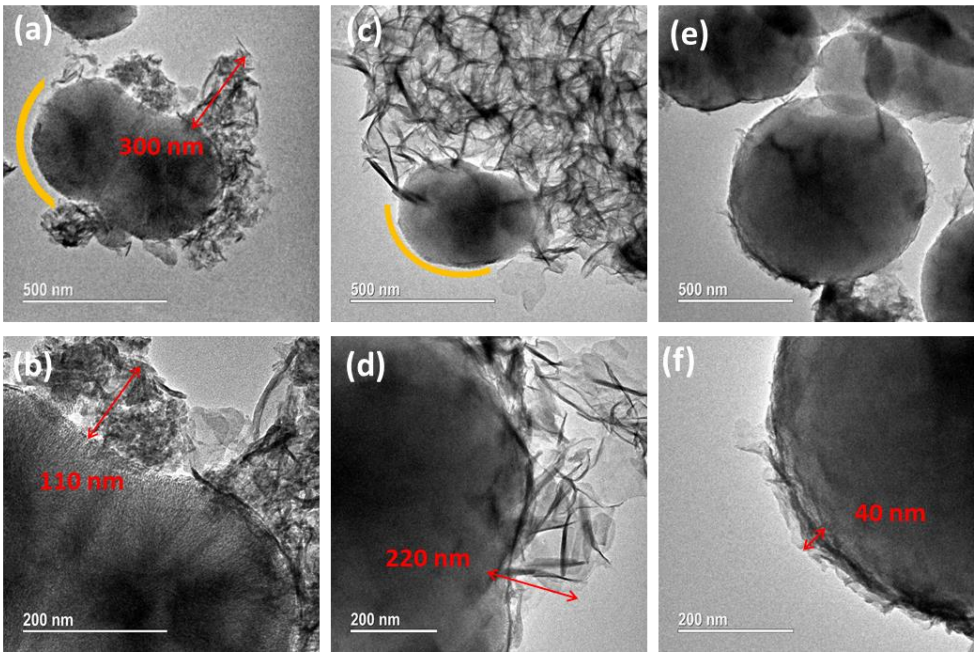


Figure 3.9 TEM images of (a) and (b) MCM-48@$Cu_{1.3}$ZnAl-LDH-pH10, (c) and (d) MCM-48@$Cu_{1.3}$ZnAl-LDH-67wt, (e) and (f) MCM-48@$Cu_{1.3}$ZnAl-LDH-pH9. The orange curves in the TEM images show the parts of silica that are not covered by LDH.

All three core-shells possesses a type IVb adsorption isotherm due to their mesoporous core (Figure 3.10a). Samples prepared at pH 10 and pH 9 possess a H3 hysteresis loop and a H4 hysteresis loop, respectively. Modifying the reaction pH and LDH content in the reaction mixture does not show an obvious effect on the size of small pores (< 4 nm) the in core-shells; all core-shells have micropore around 1.2 nm and small mesopore around 2.4–3.5 nm (Figure 3.10b).

MCM-48@$Cu_{1.3}$ZnAl-LDH-pH9 exhibits an almost flat N_2 adsorption isotherm at high relative pressure ($0.4 < p/p^0 \leq 1$), similar to that of MCM-48, indicating that both materials have low external surface area. This is consistent with TEM results that this core-shell has similar morphology as MCM-48 due to its thin LDH shell.[55] The BJH pore size distribution in Figure 3.10c reflects that MCM-48@$Cu_{1.3}$ZnAl-LDH-pH9 has a smaller mesopore (12.2 nm) and a

lower pore volume (peak integration) than the one prepared at pH 10 (24.5 nm). It is likely due to the difference in shell morphology. At pH 10, the radially growing LDH sheets afford additional pores (Figure 3.9a). MCM-48@$Cu_{1.3}$ZnAl-LDH-67wt shows a wide pore size distribution over meso- and macro-pore region and a high pore volume (Figure 3.10c), highly similar to that of pure LDH. Along with the TEM image (Figure 3.9c), it is believed that the substantial amount of free LDH in MCM-48@$Cu_{1.3}$ZnAl-LDH-67wt leads to this wide pore size distribution.

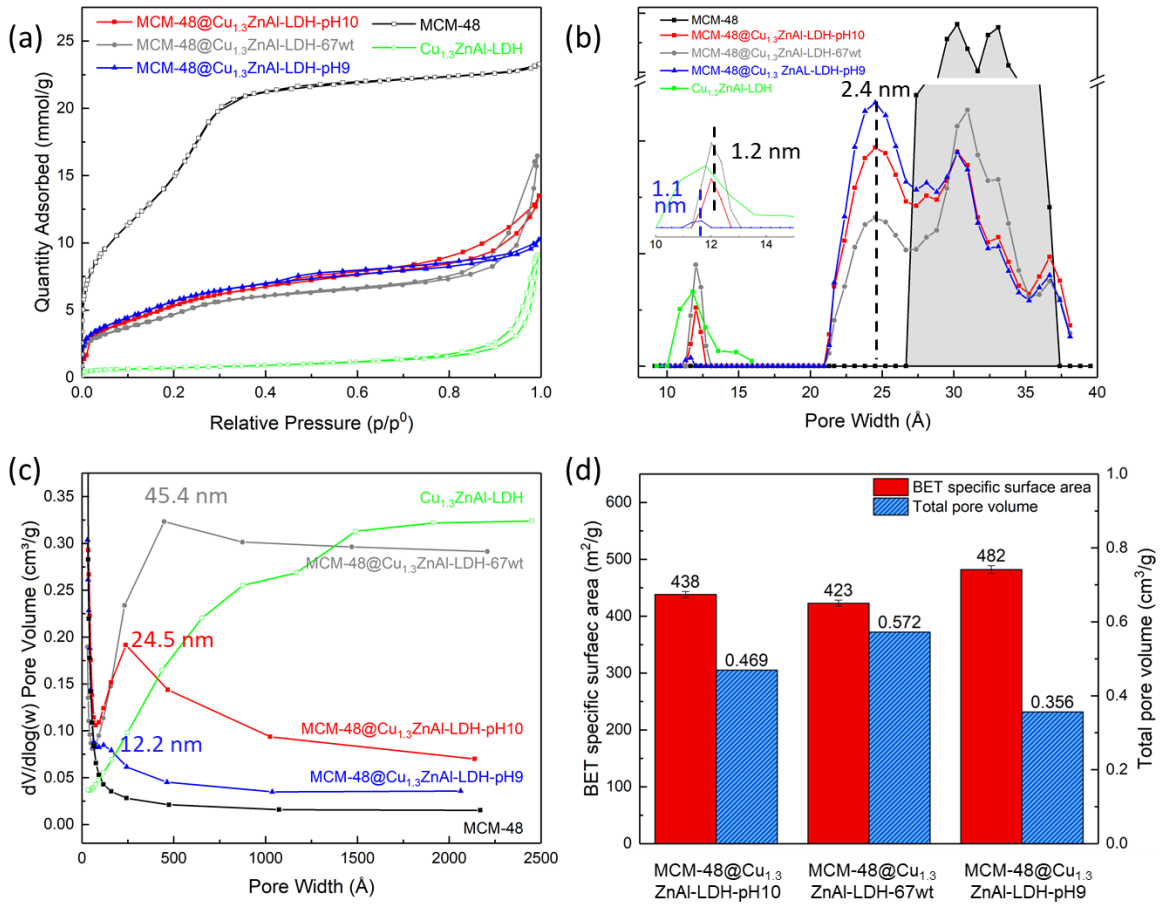


Figure 3.10 (a) The N_2 adsorption and desorption isotherm (at 77 K), (b) DFT pore size distribution based on the kernels for metal oxide with cylindrical pores, (c) The BJH pore size distribution, and (d) BET specific surface area and total pore volume of MCM-48@$Cu_{1.3}$ZnAl-LDH-pH10, -67 and -pH 9 core-shells.

The N_2 BET specific surface area and total pore volume are shown in Figure 3.10d.

MCM-48@$Cu_{1.3}$ZnAl-LDH-67wt has a similar surface area (423 m^2/g) as MCM-48@$Cu_{1.3}$ZnAl-LDH-pH10 (438 m^2/g) but a higher total pore volume. This enhancement could be attributed to the interplatelet void brought by the free LDH, as reflected by the BJH result. MCM-48@$Cu_{1.3}$ZnAl-LDH-pH9 exhibits the highest BET specific surface area (482 m^2/g) but the lowest total pore volume (0.356 cm^3/g). The latter, apart from two reasons as previously discussed (loss of pore volume due to metal incorporation and hydrolysis), could also be because of the absence of free LDH, giving no extra interplatelet void.

Based on the above characterisation results, a schematic illustration showing the effect of the synthetic conditions on the morphology of core-shells is given in Figure 3.11. It is known that metal cations interact with hydroxyl ion and anions to form LDH nuclei.[70] At pH 10, the sufficient amount of anions on the surface of the core and in the liquid phase of the reaction mixture leads to the formation of LDH nuclei at both the silica surface and in the liquid.[71,72] Some nuclei in the liquid moves to the silica surface due to the electrostatics interaction and aids the shell formation. The rest (free LDH nuclei) grow in the liquid phase and turn out to be the free LDH. The surface charge of silica sets an equilibrium/maximum loading of LDH nuclei. Once the neutral charge is met, the silica surface is less attractive to LDH nuclei. The total amount of LDH nuclei in the reaction mixture of MCM-48@$Cu_{1.3}$ZnAl-LDH-67wt is higher than that of MCM-48@$Cu_{1.3}$ZnAl-LDH-pH10, whilst the surface charge of silica is the same; this leads to an increase in the number of free LDH nuclei and thus more free LDH. Increasing LDH content is associated with longer reaction time and thus longer Ostwald ripening process, which explains larger LDH particles observed in MCM-48@$Cu_{1.3}$ZnAl-LDH-67wt.

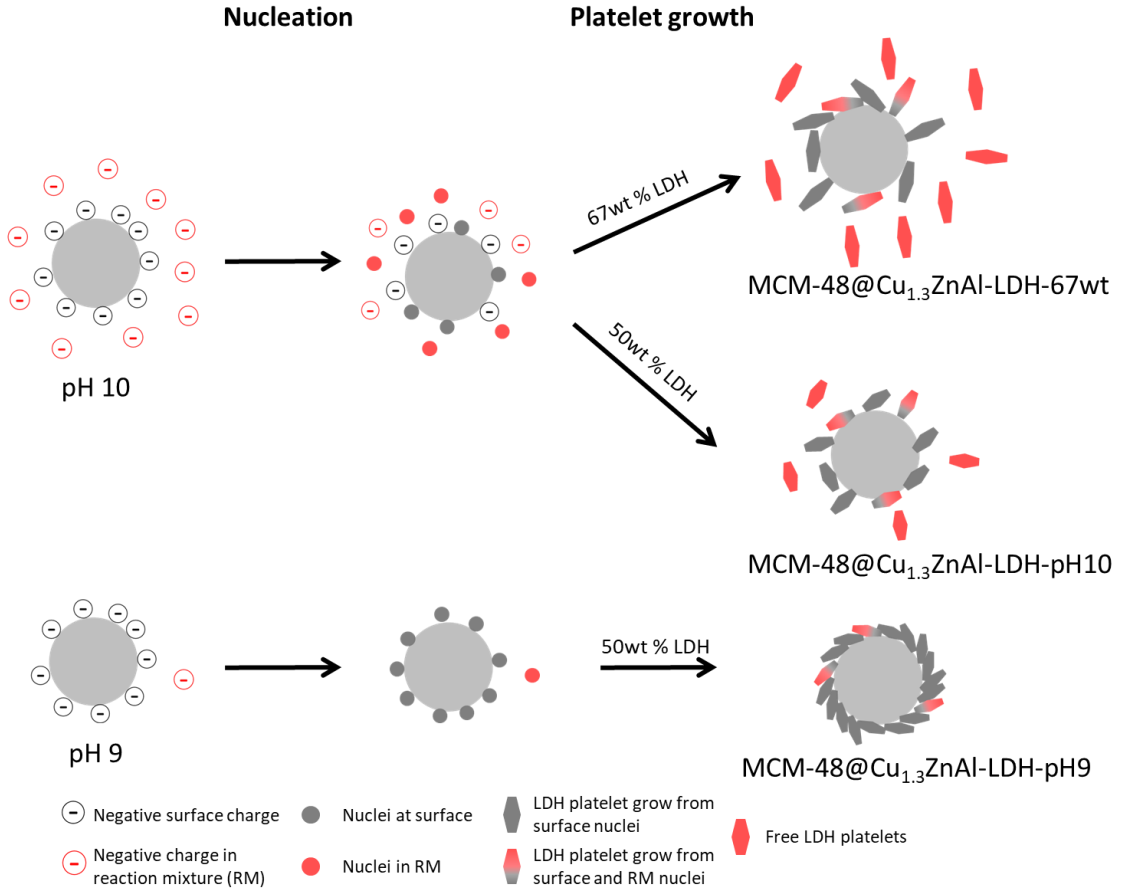


Figure 3.11 Schematic representation of the effect of increasing LDH fraction and reducing the reaction pH on the morphology of core-shells and the corresponding mechanisms.

Dropping the reaction pH from 10 to 9 reduces the OH^- concentration to one tenth and changes the mixture of metal species present; at pH 9, It is more likely to have neutral or even positive species such as $Zn(OH)_2$, $Al(OH)_3$ and $Zn(OH)^+$; at pH 10, negative species like $Zn(OH)_3^-$ and $Al(OH)_4^-$ are dominant.[73–76] Silica shows similar negative surface charge at pH 9 (−33.8 mV) and pH 10 (−35.4 mV).[72] The improved LDH shell coverage at pH 9 may be due to the better electrostatic attraction between positive metal hydroxide species and the negative silica surface. The densely packed nuclei at the surface causes the shell to wrap around the core rather than form radial sheets.

3.2.3. Variation of copper content

Following the success of core-shell generation, further tuning of the composition was carried out to ensure it would have a promising catalytic performance. Many of the reported $Cu/ZnO/Al_2O_3$ catalysts for methanol synthesis exhibit a Cu loading between18.0–63.5 wt% (Entry 1–5, Table 3.4).[16,77–80] It is also noticed that high Cu loading (between 30.0–50.0 wt%) seems to be related to good catalytic performance (Entry 2–4, Table 3.4).[16,78,79]

Table 3.4 Cu loading and the molar ratio of existing $Cu/ZnO/Al_2O_3$ methanol synthesis catalysts.

Entry	Cu loading (wt %)	Molar ratio			Precursor	STY[a]	Ref
		Cu	Zn	Al			
1	18.5[b]	3	1	1	LDH	–	77
2	32.7	1.9	1.4	1[c]	LDH	0.59	16
3	47.3	1.6	0.7	1	Oxides	1.41	78
4	51.2	8.5	3.2	1	Oxides	0.85	79
5	58.6–63.5[d]	3.8–8.4	1.2–1.4	1	Oxides	–	80

a: space time yield ($g_{MeOH}/g_{catalyst}/h$). b: value was calculated from the local EDX measurement of catalyst. c: Instead of Al, Ga was used in that study. d: calculated from the molar ratio provided.

However, the theoretical Cu content in the catalyst derived from MCM-48@$Cu_{1.3}$ZnAl-LDH-pH9 is only 12.3 wt%, which may be too low for excellent catalytic ability (Table 3.5, Entry 1). There are two alternatives for increasing Cu loading in the core-shell material. One is to increase the LDH fraction; by promoting the quantity of LDH from 50 wt% to 67 wt%, up to 16.5 wt% Cu loading can be achieved (Table 3.5, Entry 3). The other way is to increase the Cu density in the LDH. A 25.5 wt% Cu content (in the catalyst) can be obtained from a core-shell precursor where LDH shell occupies 60% weight, and its composition is Cu: Zn: Al = 4:1:1 by molar (Table 3.5, Entry 7).

Table 3.5 Theoretical Cu loading of MCM-48@CuZnAl-CO_3-LDH core-shells with different LDH fractions or different Cu density in LDH.

Entry	Theoretical Cu loading (wt%)*	LDH fraction (wt%)	The molar ratio in LDH		
			Cu	Zn	Al
1	12.3	**50**	1.3	1	1
2	14.8	**60**	1.3	1	1
3	16.5	**67**	1.3	1	1
4	18.9	60	**2**	1	1
5	22.8	60	**3**	1	1
6	24.2	60	**3.5**	1	1
7	25.5	60	**4**	1	1

*: Values are calculated from the theoretical formula of catalysts.

3.2.3.1. Variation of LDH content

Syntheses of MCM-48@$Cu_{1.3}$ZnAl-CO_3-LDH core-shells were conducted at pH 9 to get high LDH coverage and uniform shell morphology. In order to improve the LDH fraction in the composite, the total amount of the metal nitrate solution was raised; the concentration of nitrate solution and its addition rate is preserved to minimise the variation of the LDH nucleation.

Figure 3.3.12a and b show powder X-ray diffractograms of MCM-48@$Cu_{1.3}$ZnAl-CO_3-LDH core-shells with 60 wt% and 67 wt% LDH, respectively. In both samples, the characteristic LDH Bragg reflections are present. Pawley refinement based on the space group of LDH has been conducted on the XRD pattern, with the details being listed in Table B3; the *d*-spacing and crystallite size are similar regardless of the LDH content in core-shells (Table 3.6).

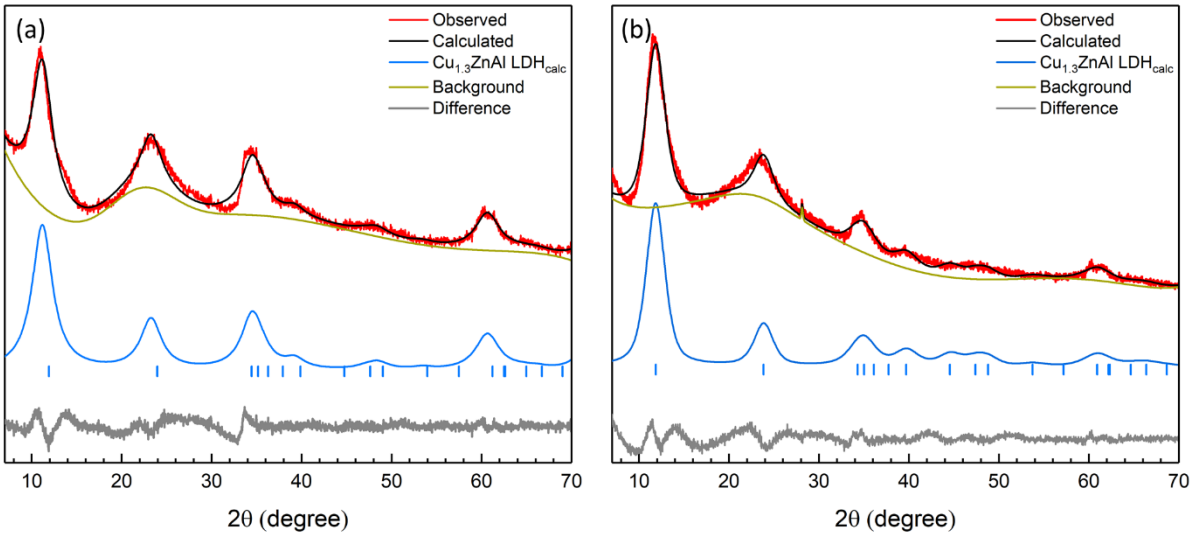


Figure 3.3.12 Powder XRD pattern and Pawley refinement of MCM-48@$Cu_{1.3}$ZnAl-CO_3-LDH core-shells prepared at pH 9 with (a) 60 wt% LDH and (b) 67 wt% LDH. The observed pattern, cumulative pattern, background, calculated LDH phase, and difference are shown in red, black, mustard yellow, blue (and purple), and grey. (*hkl*) plane reflection of LDH was indicated with short sticks.

Table 3.6 The theoretical and experimental LDH content of MCM-48@$Cu_{1.3}$ZnAl-LDH core-shells and the *d*-spacing and crystallite size of the relevant LDH phase (obtained from the Pawley refinement). Refinement details can be found in Table B3.

Theoretical LDH fraction (wt%)	Experimental LDH fraction (wt%)*	d_{003} (Å)	d_{110} (Å)	D_{00l} (nm)	D_{110} (nm)
50[a]	55	7.39	1.50	2.54	0.94[b]
60	62	7.43	1.52	2.07	2.70
67	75	7.46	1.52	2.69	2.15

*: Values were attained from the TGA results. a: sample MCM-48@$Cu_{1.3}$ZnAl-LDH-pH9. b: The (110) peak of core-shell with 50 wt% LDH is too weak to give a reliable D_{110} value.

TGA of all samples exhibits distinct LDH weight loss stages (Figure 3.13a). The increased amount of LDH in the core-shell leads to a more distinct dehydroxylation and decarboxylation stage and a higher weight loss. The actual LDH fractions were worked out based on the residual weight (Table 3.6), which is consistent with the theoretical value. Lower silica quantities are obtained due to the hydrolysis of silica in basic condition.[53]

The band intensity in FTIR spectra was normalised to the most intense band, Si-O stretching band at *ca* 1000 cm^{-1} (Figure 3.13b). Peaks related to the LDH, including the M-O vibration,

C-O stretching and O-H stretching, are enhanced with the raised LDH amount in the composite, which agrees with TGA results.

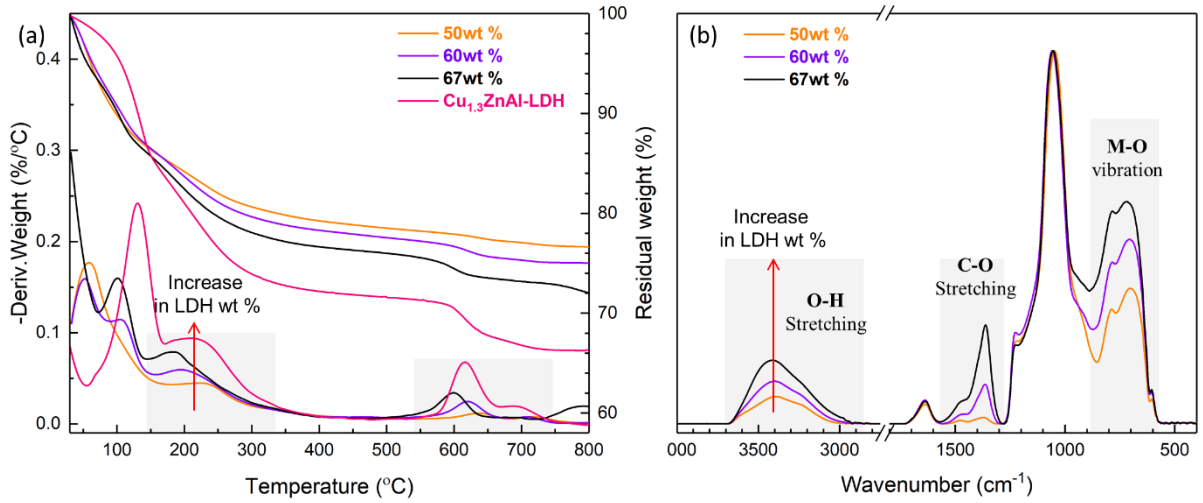


Figure 3.13 (a) TGA and –dTG plots, (b) FTIR spectra of MCM-48@$Cu_{1.3}$ZnAl-CO_3-LDH core-shells with 50 wt%, 60 wt% and 67 wt% LDH.

The thickness of the LDH shell shows an upward trend with the increase in the LDH amount, 40 nm for 50 wt%, 150–250 nm for 60 wt% and 250–350 nm for 67 wt% (Figure 3.14). Moreover, the amount of free LDH increases with the increased LDH content. Core-shells with the lowest amount of LDH (50 wt%) shows the highest uniformity. At 60 % LDH, small amount of free LDH appears. When the LDH amount reaches 67 wt%, a tremendous amount of free LDH shows up and leads to low uniformity (Figure B6).

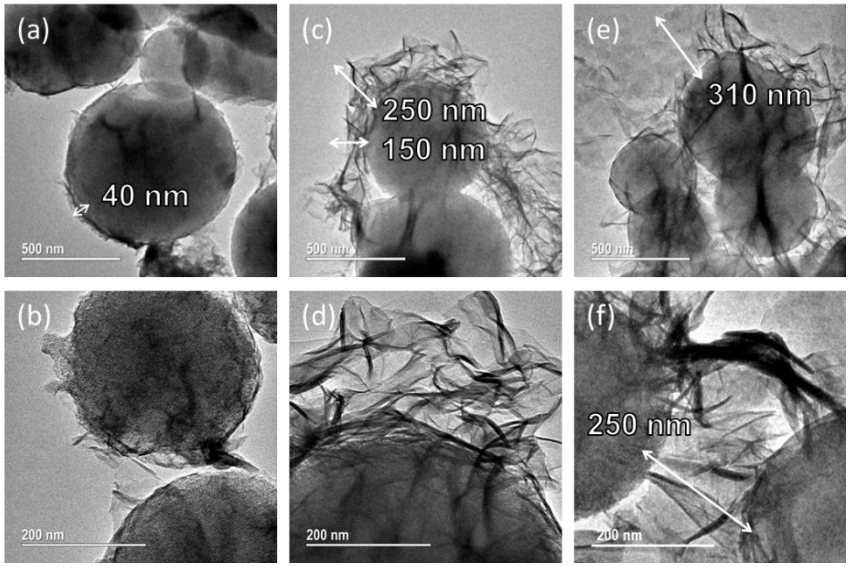


Figure 3.14 TEM images of MCM-48@$Cu_{1.3}$ZnAl-CO_3-LDH core-shells with (a) and (b) 50 wt% LDH, (c) and (d) 60 wt% LDH, (e) 67 wt% LDH.

All three samples possess a typical type IV adsorption isotherm at low relative pressure ($0 \leq p/p^0 \leq 0.4$) due to the micro and mesopore of MCM-48 (Figure 3.15a). The DFT pore size distribution (Figure B7) illustrates that these core-shells exhibit similar pore size distribution at pore widths below 4 nm, where 1.2 nm and 2.4–3.0 nm pores are detected. At higher relative pressure ($0.4 < p/p^0 \leq 1$), N_2 uptake increases with the increase in LDH content (Figure 3.15a). Adsorption in this region originates from the N_2 condensation in the interparticle voids due to particle–particle, particle–platelet, platelet–platelet aggregation.[55,81] As reflected by TEM images, increasing the LDH content in the core-shell leads to a thicker LDH shell and more free LDH and would give rise to interparticle voids. This explains the wider BJH pore size distribution and higher pore volume that is observed at the higher LDH loading (Figure 3.15b and Figure 3.16a). MCM-48@$Cu_{1.3}$ZnAl-LDH-pH9 (having 50 wt% LDH) displays a low N_2 uptake at high p/p^0 (Figure 3.15a), a narrow pore size distribution (Figure 3.15b) and the lowest pore volume (Figure 3.16a) because it has less free LDH and a hierarchical LDH shell with thin

thickness.

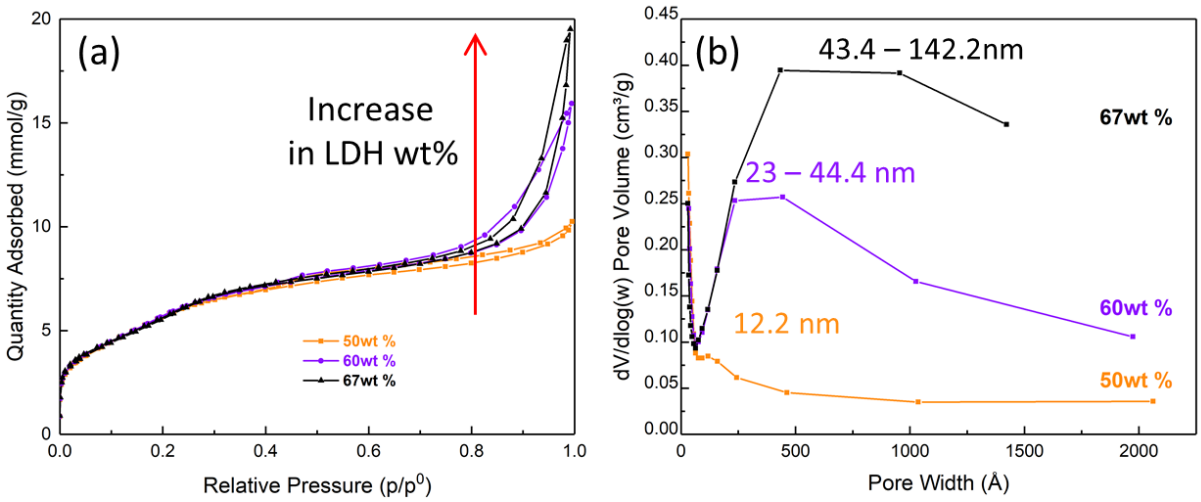


Figure 3.15 (a) The N_2 adsorption and desorption isotherm at 77 K and (b) The BJH pore size distribution of MCM-48@$Cu_{1.3}$ZnAl-CO_3-LDH core-shells with 50 wt%, 60 wt% and 67 wt% LDH.

The BET specific surface area is almost identical among the three samples regardless of the LDH loading (Figure 3.16b).

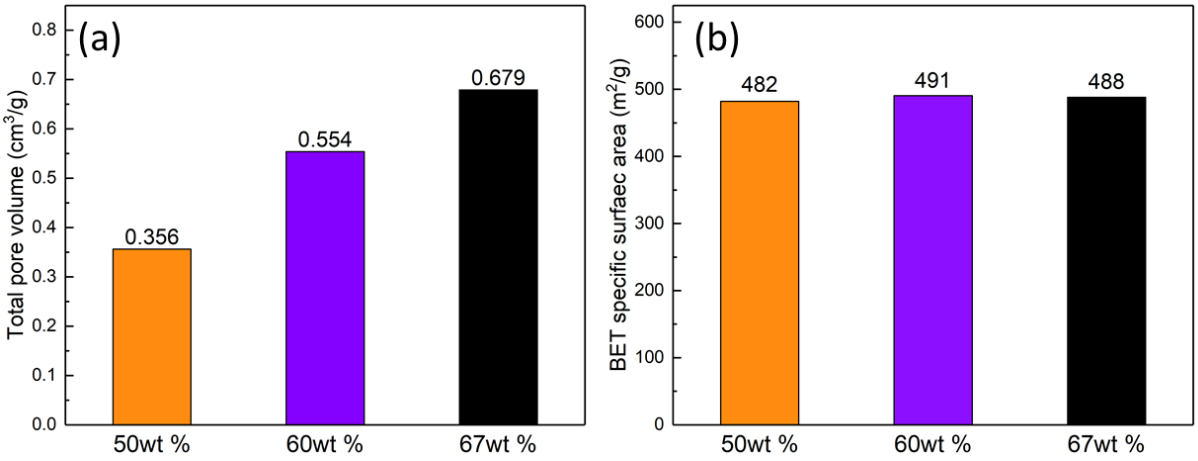


Figure 3.16 (a) The total pore volume and (b) the BET specific surface area of MCM-48@$Cu_{1.3}$ZnAl-CO_3-LDH core-shells with 50 wt%, 60 wt% and 67 wt% LDH.

3.2.3.2. Variation of Cu density in LDH

To further increase the Cu amount in the core-shell, the Cu/Al molar ratio was raised. The LDH fraction in the composite is fixed at 60 wt% to enable a moderate Cu loading, a well-defined

shell and a low level of free LDH. The total metal nitrate amount involved in the synthesis was kept constant while the metal ratio was varied. It is known that pure LDH can only form at M^{II}/M^{III} ratios between 1.5–5.[23] Setting the Zn/Al ratio to 1 in all cases, the Cu/Al molar ratio was varied from 1.3 to 4. The products are named as MCM-48@Cu$_x$ZnAl-LDH, where x is the Cu/Al molar ratio. Control LDHs are prepared under the same synthetic condition without MCM-48 and are termed Cu$_x$ZnAl-LDH. Full details about the sample preparation are described in Chapter 7.

Figure 3.17 shows the XRD diffractograms of Cu$_x$ZnAl-LDH and MCM-48@Cu$_x$ZnAl-LDH, x = 1.3, 2, 3, 3.5, and 4. All samples exhibit the characteristic LDH Bragg diffraction pattern without any reflections from impurities. Broadening in reflections at the increased Cu loading is noticed in both the pristine LDH and the core-shell material. This indicates that introducing more Cu to the LDH will decrease the crystallinity; crystallite size across the *ab*-plane and along the *c*-axis is reduced (Figure B8).

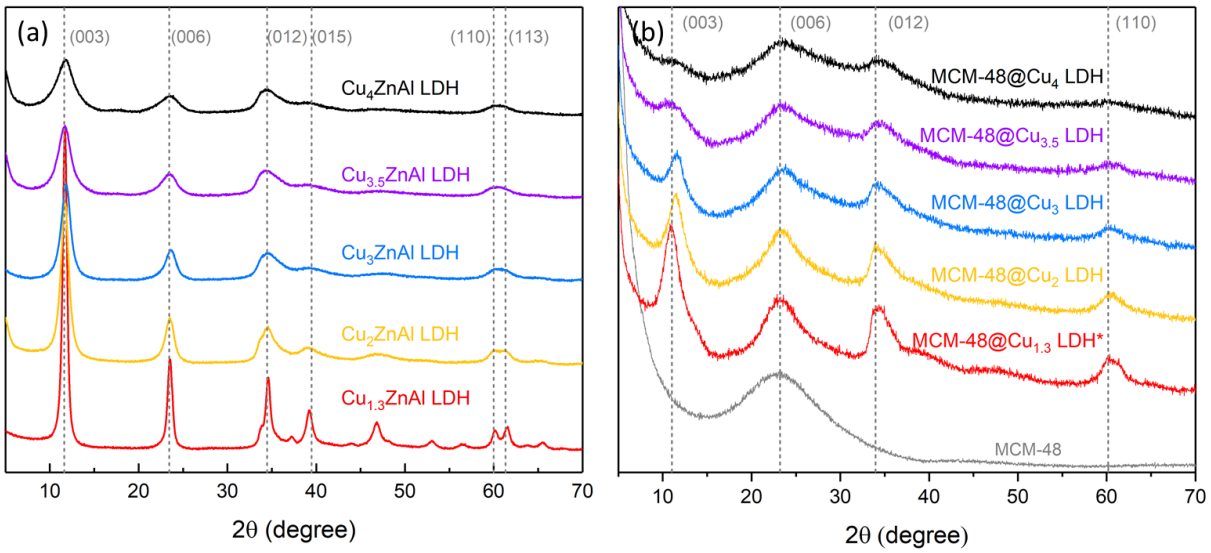


Figure 3.17 XRD patterns of (a) Cu$_x$ZnAl-LDH, (b) MCM-48@Cu$_x$ZnAl-LDH. x = 1.3, 2, 3, 3.5 and 4.

The *d*-spacing of samples are obtained from single-phase Pawley refinement. Details are shown in Table B4. The (003) basal spacing of LDHs and core-shells with Cu/Al = 2 and 3 are around 7.55 Å indicating carbonate is the interlayer anion (Figure 3.18a).[23] For core-shells with Cu/Al ≥ 3.5, the basal spacing reaches 7.80–7.90 Å, close to the spacing of a nitrate LDH.[65] As the nitrogen in these samples is below the detectable level (from elemental analysis data), it is more likely that abundant interlayer water contributes to this expansion. This assumption is proved by the TGA results, where a higher weight loss in the moisture evaporation stage is observed.

Both d_{003} and d_{110} of Cu_xZnAl LDH and core-shells increase as the Cu/Al ratio elevates (Figure 3.18). In a similar fashion, it has been reported serval times in the literature that the d_{003} and d_{110} of MgAl carbonate LDH progressively expand when the Mg/Al ratio raises.[82–85] The increase of d_{003} is due to the attenuated electrostatic interaction between the metal hydroxide layer and interlayer anion at reduced Al^{3+} density.[85,86] The Jahn-Teller distortion of Cu^{2+} causes the elongated octahedron,[87] and the higher density of Cu may lead to a severe distortion and give thicker metal hydroxide layers as well as a larger d_{003}. d_{110} of LDH is related to the metal-metal distance in the hydroxide layer. The ionic radii of 6-coordinated Cu^{2+}, Zn^{2+} and Al^{3+} are 0.073, 0.074 and 0.054 nm, respectively.[88,89] The increase of d_{110} at high copper loading is due to the raised proportion of large Cu^{2+} and Zn^{2+} cations.[82,90]

At the same Cu/Al ratio, core-shell generally shows larger d_{110} than pure LDH (Figure 3.18b); this suggests that the actual (Cu + Zn)/Al ratio of the LDH phase in the core-shell is larger than that of the pure LDH. Aluminosilicate was formed in all core-shells as evidenced by the presence of AlO_4 resonance in the ^{27}Al solid-state NMR spectra (Figure B9). Therefore, the

amount of Al in the LDH framework is less than expected. The larger d_{110} of core-shell compared to pure LDH is consistent with the Al involvement in an interface silicate formation.

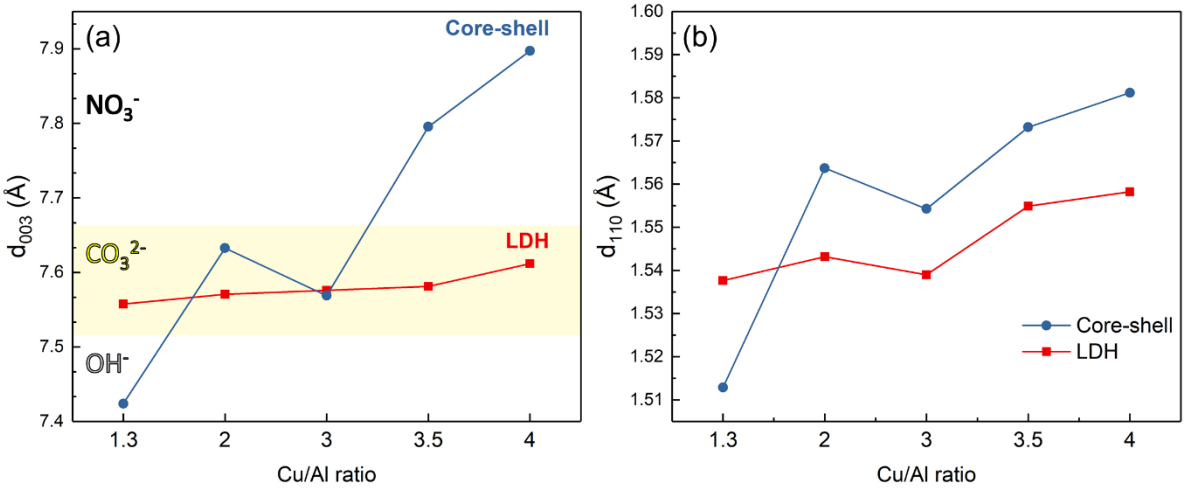


Figure 3.18 The *d*-spacing of (a) (003) plane and (b) (110) plane for Cu_xZnAl-LDHs and MCM-48@Cu_xZnAl-LDHs at different Cu/Al ratios (1.3–4).

The chemical composition and possible formula of Cu_xZnAl-LDH and MCM-48@Cu_xZnAl-LDH core-shells were investigated using elemental analysis. The theoretical formula of MCM-48 and $Cu_aZn_bAl_c$-LDH should be $[SiO_2 \cdot xH_2O]$ and $[Cu_aZn_bAl_c(OH)_{2(a+b+c)}(CO_3)_{c/2} \cdot nH_2O]$, respectively.[23] The molar amount of carbon in the LDH should be the half that of Al to meet the charge neutral. The Cu/Al ratios determined by ICP-OES agrees with the theoretical values in both cases of pristine LDHs and core-shells (Table 3.7 and Table 3.8, respectively). A noticeable excess amount of carbon was found in all LDH samples (C/Al > 0.5 by molar), which suggests carbonate impurity. During co-precipitation, Na^+ and CO_3^{2-} present at the same time and may form sodium carbonate or sodium bicarbonate. However, Na_2CO_3 and $NaHCO_3$ or a mixture of both are excluded as none of them gives a good match between the theoretical and actual composition. Copper hydroxide carbonates with formula $Cu_2(OH)_2CO_3$ could be possible as the calculated element content exhibits a good agreement

with the detected value, i.e., the difference between the calculated and the actual quantity of elements is within the error range (Table B5). The detailed calculation process is described in Appendix B, page B-9. A possible chemical formula of LDH can be given in Table 3.7. The amount of impurities increases with the increased Cu/Al ratio.

Minerals including malachite with formula $Cu_2(OH)_2CO_3$, rosasite with formula $(Cu,Zn)_2CO_3(OH)_2$ and aurichalcite $(Zn,Cu)_5(CO_3)_2(OH)_6$ are commonly found as crystalline impurities in the CuZnAl-CO_3-LDH.[23,91–94] Although the impurity is indexed as $Cu_2(OH)_2CO_3$, the impurity may also be the amorphous form of the aforementioned copper/zinc minerals or amorphous zinc-malachite.[23,91–96] The comparable atomic weight of Cu and Zn and the same divalent charge makes it hard to determine the exact composition of impurity simply from the ICP-OES and carbon, hydrogen and nitrogen (CHN) analysis.

Previous research has demonstrated that pure LDH can only be formed at $2.2 \leq (Cu + Zn)/Al$ ratio ≤ 3.2 and Cu/Zn ratio ≤ 1; outside this range, crystalline impurities will appear.[23,91–94] In this study, amorphous hydroxide carbonate species are generated at (Cu+Zn)/Al as low as 2.3 and Cu/Zn = 1.3. It is further confirmed that the formation of impurity in CuZnAl-CO_3-LDH is unavoidable at Cu/Zn > 1. The crystallinity of impurity would vary from the synthesis method. Besides XRD data, elemental analysis is also essential in studying the component of CuZnAl-LDH.

Table 3.7 The theoretical (Theo.) and experimental (Exp.) Cu: Al molar ratio in Cu_xZnAl-LDHs with their possible chemical formula and impurity.

Cu/Al ratio		Stoichiometry in LDH $[Cu_aZn_bAl_c(OH)_{2(a+b+c)}(CO_3)_{c/2}]\ nH_2O$						Impurity
Theo.[a]	Exp.	Cu	Zn	Al	OH	CO_3^{2-}	H_2O	$Cu_2CO_3(OH)_2$[b]
1.30	1.31	1.10	0.93	1.00	6.28	0.50	4.00	0.11
2.00	1.94	1.29	0.93	1.00	7.09	0.50	4.00	0.32
3.00	2.93	2.18	0.90	1.00	8.92	0.50	1.60	0.37
3.50	3.47	2.68	0.94	1.00	10.0	0.50	3.30	0.39
4.00	4.06	2.84	0.92	1.00	10.7	0.50	1.60	0.61

a: Theoretical Cu/Al ratio based on the amount of starting material in the co-precipitation. b: Impurity could be a mixture of zinc hydroxide carbonate and copper hydroxide carbonate.

The proposed chemical formula of MCM-48@Cu_xZnAl-LDHs is listed in Table 3.8. Details about the calculation process and deviation between the real and calculated elemental composition can be found in Appendix B, page 11 and Table B6.

Insufficient carbon was observed in core-shell with low Cu/Al ratio (1.3 and 2), where the amount of C is lower than half the amount of Al. This is in agreement with the XRD and ^{27}Al NMR spectroscopic results that Al partially migrates to SiO_2 to form interface aluminosilicate. Once there is less Al in the LDH, less carbonate counterion is required to meet the charge balance. The deficient carbon amount can be used to estimate the quantity of Al that shifted to SiO_2; 23% and 11% of the total Al interacts with silica to form aluminosilicate, respectively in MCM-48@$Cu_{1.3}$ZnAl-LDH and MCM-48@Cu_2ZnAl-LDH.

At Cu/Al ratio = 3–4, C/Al molar ratio is larger than 0.5. The proportion of Al that impregnated in SiO_2 cannot directly be worked out from the ICP-OES data and CHN analysis. Assuming that 20% Al migrates and the excess C is due to the hydroxide carbonate fragment, a possible formula of MCM-48@Cu_3, $Cu_{3.5}$, and Cu_4ZnAl-LDH can be provided (Table 3.8). On the other hand, the standard error in ICP and CHN are ± 1 wt% and ± 0.2wt%, respectively (from the

technician's experience). This significant error range leaves some uncertainty in the stoichiometry of the impurity and the metal composition of LDH.

It is proved in this study that the formation of aluminosilicate interface leads to an increased (Cu + Zn)/Al ratio of LDH in core-shell. It is also found that the higher Cu/Al ratio leads to larger amount of copper hydroxide carbonate (based on the change in the formula of LDH). However, the amount of $Cu_2(OH)_2CO_3$ is lower in core-shell than in the LDH having the same Cu/Al ratio. This conflict indicates that the proposed chemical formula for core-shells is inaccurate, which may result from not considering other impurities, such as layered metal silicate (as discussed in section 3.4), in the calculation.

Table 3.8 The theoretical (Theo.) and experimental (Exp.) Cu: Al molar ratio in MCM-48@Cu_xZnAl-LDHs with their possible chemical formula and impurity.

Cu/Al ratio		Stoichiometry in LDH $[Cu_aZn_bAl_c(OH)_{2(a+b+c)}(CO_3)_{c/2}]\ nH_2O$						SiO_2		$Cu_2CO_3(OH)_2$[b]
Theo.[a]	Exp.	Cu	Zn	Al	OH	CO_3^{2-}	H_2O	$NaAlO_2$	SiO_2	
1.30	1.37	1.37	0.96	0.77	6.20	0.39	1.50	0.23	3.50	0.00
2.00	2.04	2.04	0.92	0.89	7.70	0.45	1.00	0.11	4.40	0.00
3.00	3.04	2.81	0.92	0.80	9.10	0.4	2.10	0.20	5.50	0.12
3.50	3.38	3.07	0.96	0.80	9.60	0.40	1.80	0.20	6.00	0.15
4.00	4.04	3.05	0.98	0.80	9.70	0.40	1.80	0.20	6.50	0.49

a: Theoretical Cu/Al ratio based on the amount of starting material of co-precipitation. b: Impurity could be a mixture of zinc hydroxide carbonate and copper hydroxide carbonate.

FTIR spectra of Cu_xZnAl-LDHs are displayed in Figure B10a, where typical IR absorbance bands of the LDH material show up. In the case of core-shells, Si-O stretching band (~ 1000 cm^{-1}) appears in addition (Figure B10b). It is seen that the property of carbonate band varies with the Cu amount. Deconvolution of carbonate bands was carried out (Figure 3.19, details in Table B7) and five different types of peak are obtained. The one around 1640 cm^{-1} is

due to the H_2O bending.[97] The peak located at 1577 cm^{-1} in $Cu_{1.3}$ZnAl-LDH arises from the overlapping of H_2O bending and v_3-CO_3^{2-} mode. Three peaks centred at *ca.* 1360, 1390 and 1465 cm^{-1} all come from the asymmetric stretching of carbonate ions (also called v_3-CO_3^{2-} mode).[97–100] The splitting of v_3-CO_3^{2-} stretching band (appearance of peak at 1465 cm^{-1}) is also found in some MgAl-CO_3-LDH and ZnAl-CO_3-LDH and is due to the reduced symmetry of carbonate anions and thus a disordered nature of the interlayer.[23,101,102] The copper hydroxide carbonate impurity in LDHs and core-shell exhibit a similar v_3-CO_3^{2-} stretching band (Figure 3.19c). The raised intensity of the peak around 1465 cm^{-1} at high Cu loading is related to the more disordered interlayer environment due to the enhanced Jahn-Teller distortion and the increased amount of metal (Cu and/or Zn) hydroxide carbonate impurity. Generally, core-shells have a more prominent asymmetric carbonate stretching peak (the one at 1465 cm^{-1}) than LDH with the same Cu/Al ratio (Figure 3.19b). This is consistent with fact that the formation of aluminosilicate interface raises the Cu/Al ratio in the LDH phase.

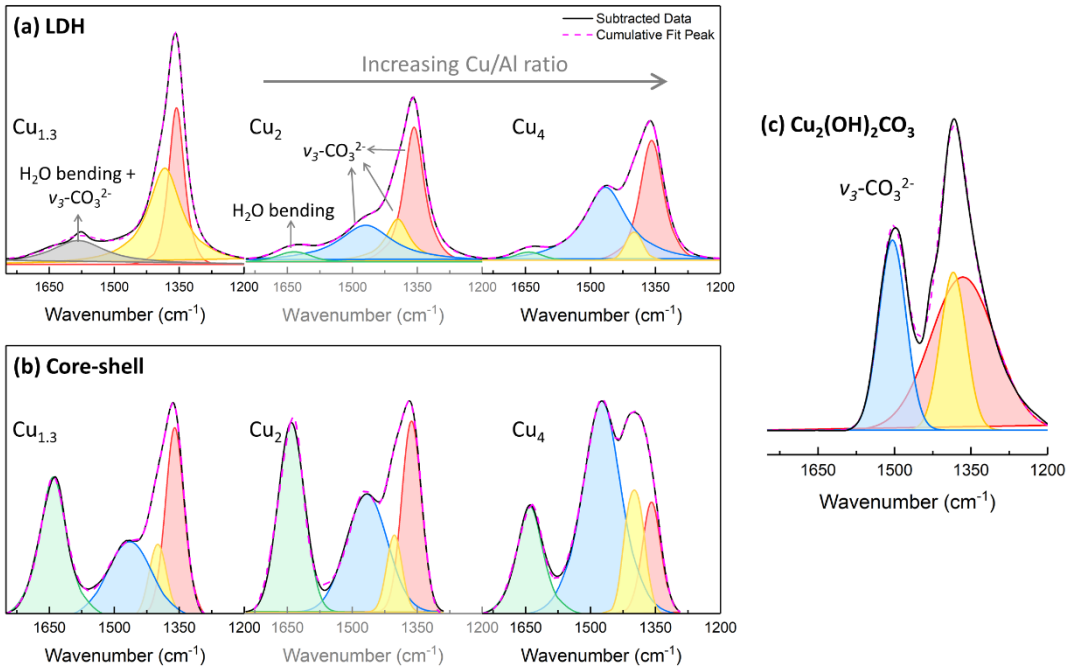


Figure 3.19 Section of FTIR spectra and the peak deconvolution of (a) $Cu_{1.3}$ZnAl-LDH, Cu_2ZnAl-LDH and Cu_4ZnAl-LDH, (b) corresponding core-shells, and (c) $Cu_2(OH)_2CO_3$. In $Cu_{1.3}$ZnAl-LDH, the peak located at 1577 cm^{-1} is coloured with grey. Peaks located at *ca.* 1640, 1465, 1390 and 1360 cm^{-1} are highlighted in green, blue, yellow and red, respectively.

TGA plots of LDHs and core-shells display distinct weight loss stages of LDH, indicating the LDH is the dominant phase (Figure B11). The water evaporation of core-shell starts at a lower temperature (60 °C) than LDH (120 °C) because the dehydration of MCM-48 occurs at low temperature. The increase in Cu/Al ratio draws the complete decarboxylation of LDH to a lower temperature, *i.e.*, 570 °C for $Cu_{1.3}$ZnAl-LDH and 450 °C for Cu_4ZnAl-LDH, signifying that the LDH phase with higher copper density is less stable. Higher residual weight is obtained from LDH with higher Cu loading. However, no noticeable trend between the residual weight of composite and their Cu density is observed. The SiO_2:LDH weight ratio estimated from the TGA data is consistent with the theoretical value (around 40:60).

TEM images in Figure 3.20 reflects that Cu_xZnAl-LDHs possess platelet-like morphology

irrespective of the Cu density. However, the particle size decreases with the raised copper population, where small fragments with irregular shapes are more common at high Cu loading than large hexagonal sheets.

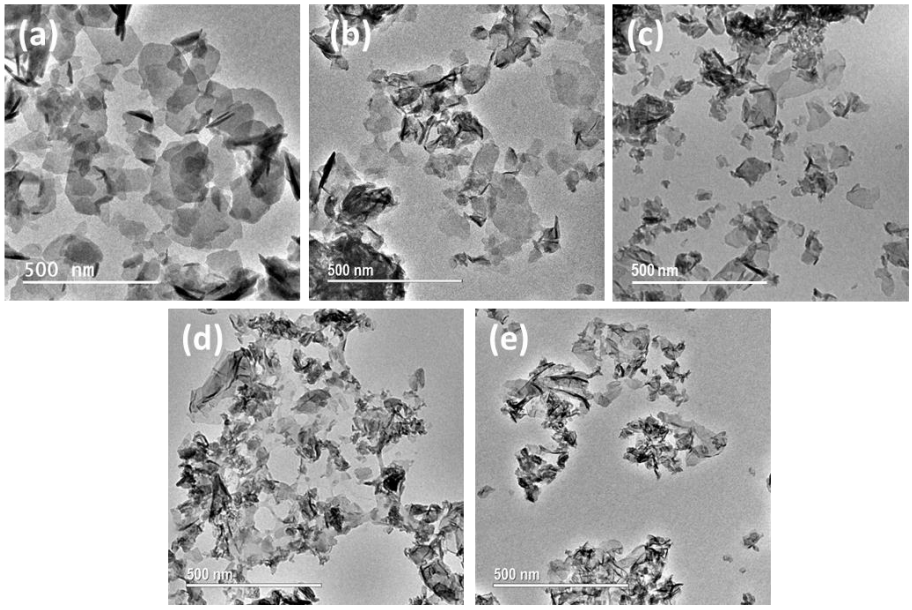


Figure 3.20 TEM images of (a) $Cu_{1.3}ZnAl$-LDH, (b) Cu_2ZnAl-LDH, (c) Cu_3ZnAl-LDH, (d) $Cu_{3.5}ZnAl$-LDH, and (e) Cu_4ZnAl-LDH

The core-shell morphology is obtained in all core-shells and almost no free LDH is observed (Figure 3.21). There is no clear trend between the thickness of the shell and the Cu density. A substantial amount of spherical debris is found when Cu/Al ratio reaches 3.5 and 4, which may be the copper (and/or zinc) hydroxide carbonate impurities.

The elemental mapping is further carried out to identify the distribution of each element in MCM-48@$Cu_{3.5}ZnAl$-LDH and MCM-48@Cu_4ZnAl-LDH (Figure 3.22 and Figure B12). A uniform distribution of elements over particles has been achieved in both samples. No apparent overabundance or deficiency appears. Line scan data of MCM-48@$Cu_{3.5}ZnAl$-LDH suggests that the composition of LDH is roughly consistent for interface LDH and external LDH (Figure

B13).

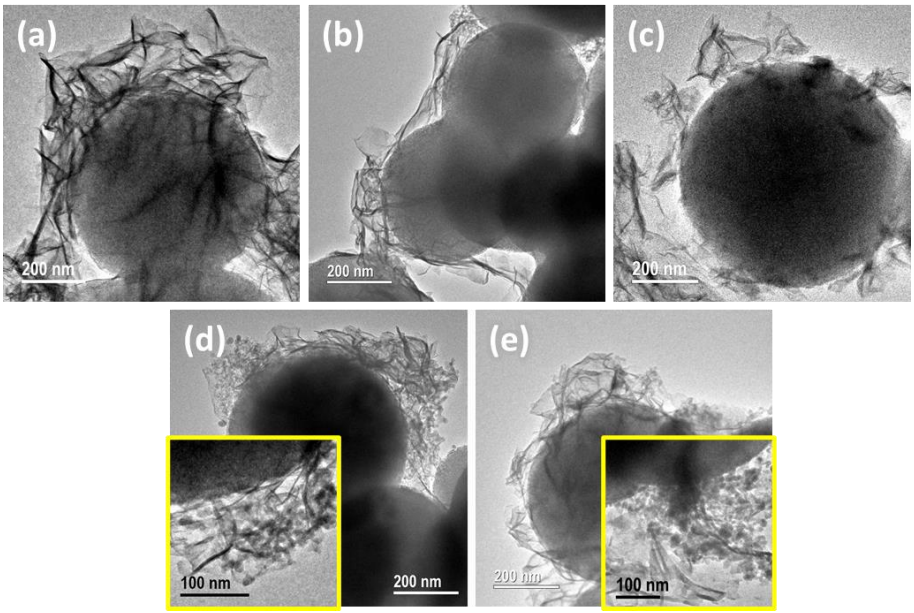


Figure 3.21 TEM images of (a) MCM-48@$Cu_{1.3}$ZnAl-LDH, (b) MCM-48@Cu_2ZnAl-LDH, (c) MCM-48@Cu_3ZnAl-LDH, (d) MCM-48@$Cu_{3.5}$ZnAl-LDH, and (e) MCM-48@Cu_4ZnAl-LDH.

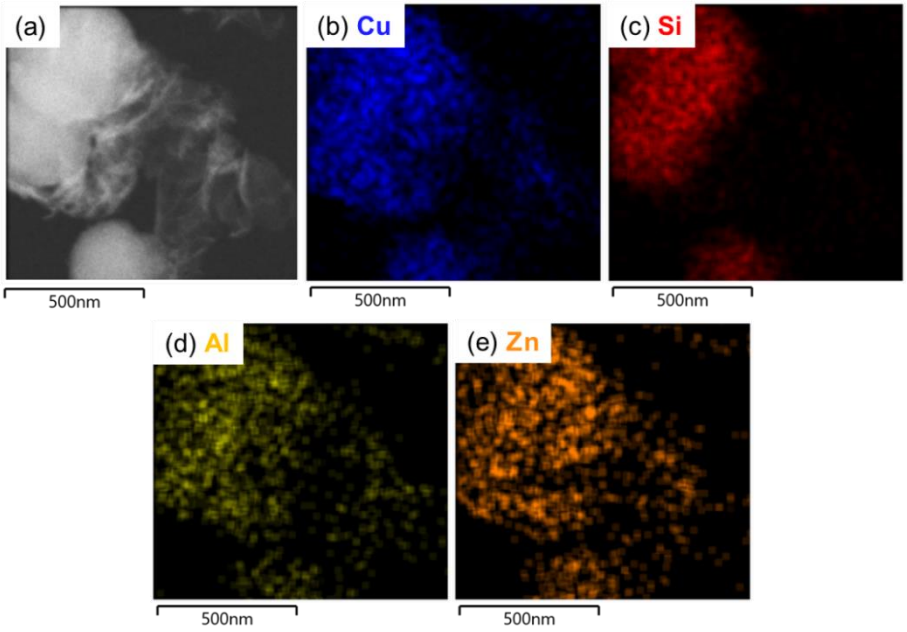


Figure 3.22 (a) Electron image of MCM-48@$Cu_{3.5}$LDH, and TEM-EDX elemental mapping of (b) Cu, (c) Si, (d) Al, and (e) Zn.

N_2 adsorption and desorption isotherm of Cu_xZnAl-LDH is shown in Figure B14a. All samples exhibit a type II isotherm accompany by a H3 loop, which agrees that they are agglomerate of platelets with slit-like pores. The DFT pore size distribution of Cu_xZnAl-LDHs are similar, in

which micropores around 1.0–1.2 nm are detected (Figure 3.23a). $Cu_{1.3}$ZnAl-LDH exhibits a wide pore size distribution with no clear maxima (Figure B15a); this is due to the intense interparticle aggregation.[103] Cu_xZnAl LDH with higher Cu/Al ratio shows a narrower pore size distribution and a clear maxima between 30–70 nm (Figure B15a). Chen *et al.* reported that meso- and macro-pores are generated when LDH start to exfoliate.[103] The narrow pore size distribution at increased copper loading should result from the reduced stacking along *c*-axis.

Moreover, the BET specific surface area and total pore volume of LDH show an upward trend as Cu/Al ratio increases (Figure 3.23b); this is in agreement with the BJH pore size distribution result, as the diminished interparticle aggregation can release additional surface area and pore volume. It is also possible that the metal hydroxide carbonate species disturb layer-by-layer stacking by interfering the electrostatic interaction between layers. The higher the amount of hydroxide carbonate, the less stacking of layers.

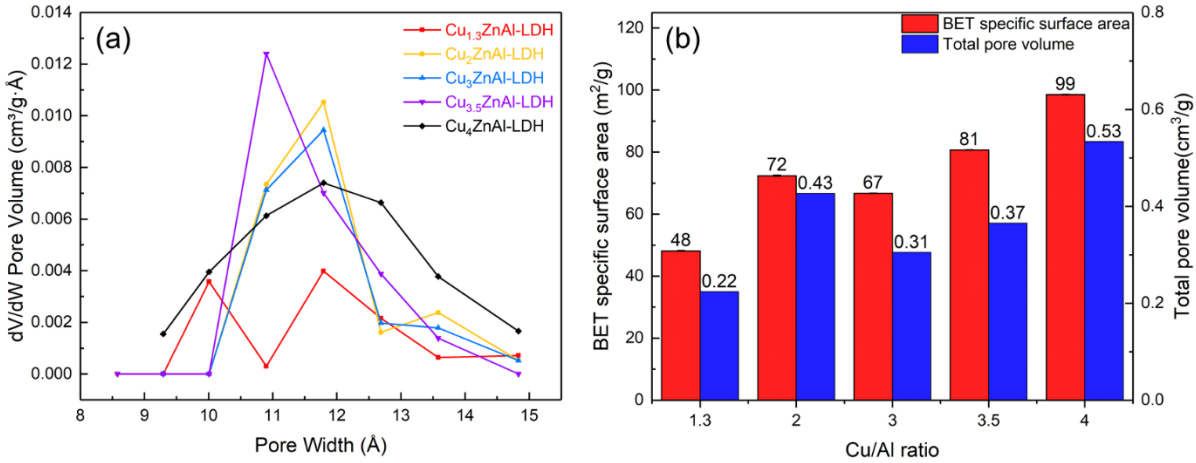


Figure 3.23 (a) the DFT pore size distribution (based on the kernels for slit pore) and (b) the BET specific surface area and total pore volume of Cu_xZnAl-LDH.

MCM-48@Cu_xZnAl-LDH possesses a combination of type IVb and type II adsorption isotherm with a H3 loop (Figure B14b) due to its hierarchical pore structure, where micro- and meso-

pores present in the inner core (Figure 3.24a) and large meso- and macro-pores occur in the shell and channel between composites (Figure B15b). In contrast to the trend in LDH, the surface area and total pore volume of core-shells decrease with an increased Cu/Al ratio (Figure 3.24b). An exception is MCM-48@Cu_2ZnAl-LDH (549.0 m^2/g) which shows a higher surface area than MCM-48@$Cu_{1.3}$ZnAl-LDH (491.0 m^2/g). The loss in both the surface area and pore volume should be due to the pore blocking of the mesoporous core (Figure 3.23b). Likely, the smaller LDH crystallites formed at higher Cu loading can easily enter the mesopore and cause a significant pore-blocking.

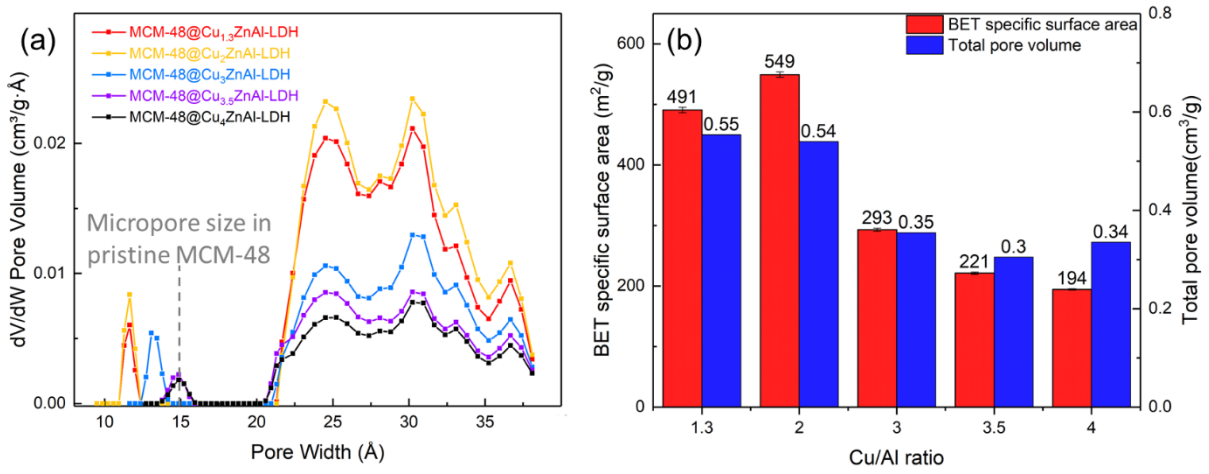


Figure 3.24 (a) the DFT pore size distribution (based on the kernels for metal oxide with cylindrical pore) and (b) the BET specific surface area and total pore volume of MCM-48@Cu_xZnAl-LDH.

3.3 Synthesis and characterisation of ES757@Cu_xZnAl-CO_3-LDH

The broader goal of this project is using various silica to develop SiO_2@Cu_xZnAl-LDH core-shells derived catalysts. ES757, a commercial silica, is one of the candidates because of its potential for scalable synthesis and industrial application.[104]

3.3.1. The effect of synthetic conditions on ES757@Cu_4ZnAl-CO_3-LDH

ES757-based core-shell was firstly prepared with the highest copper loading.

ES757@Cu_4ZnAl-LDH-Ori was obtained using the same condition as MCM-48@Cu_4ZnAl-LDH. To achieve enough sample for characterisation and catalyst evaluation from one batch, synthesis was attempted at an eight-times scale. A clean XRD pattern that only shows the typical LDH reflections proves the product's purity (Figure 3.26). ES757 are bulky spherical silica with a smooth surface (Figure B16a and Figure 3.25a). SEM image and EDX mapping of ES757@Cu_4ZnAl-LDH-Ori reveals that the LDH shell has formed on the surface of ES757 (Figure 3.25b–g). However, unlike MCM-48@Cu_4ZnAl-LDH, a significant amount of free LDH appears in ES757@Cu_4ZnAl-LDH-Ori (Figure B16c and d). It is assumed that the vast difference in the surface area (272.0 m^2/g for ES757 and 1185.8 m^2/g for MCM-48) leads to this change in the morphology. In ES757, there is less interface for LDH to grow on.

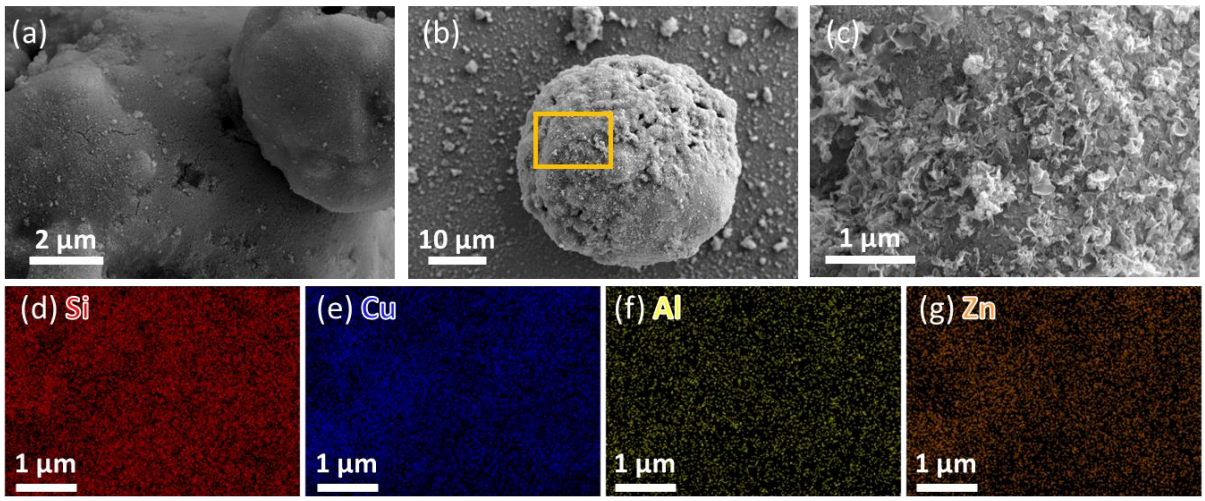
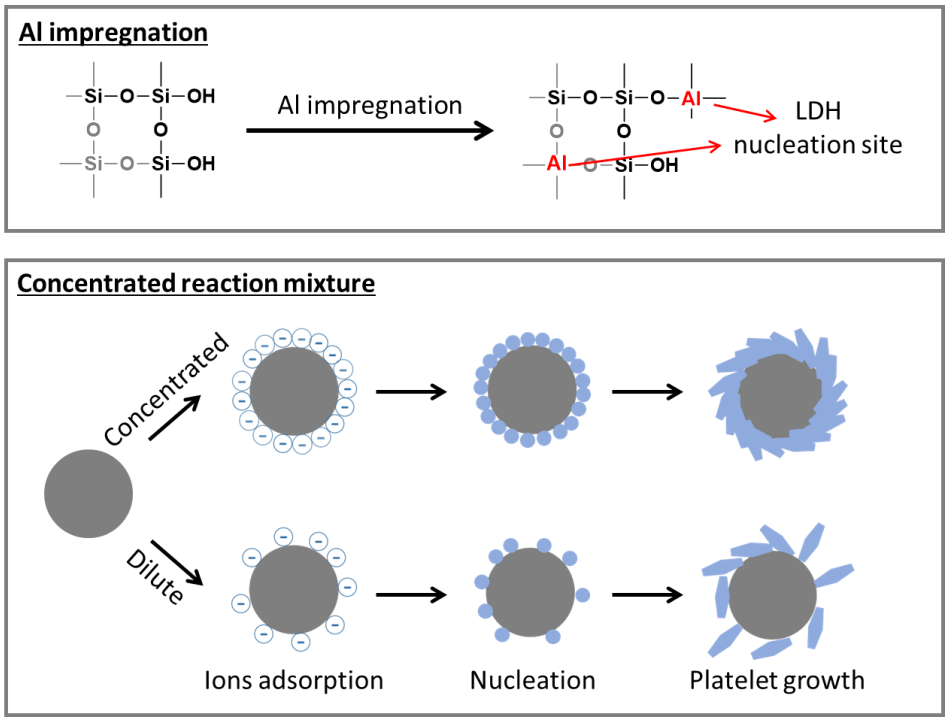


Figure 3.25 SEM images of (a) ES757, (b) ES757@Cu_4ZnAl-LDH-Ori. (c) The zoom-in image of the orange-box region in (b). (d)–(g) is the elemental mapping of Si, Cu, Al and Zn, respectively at the orange-box region.

Previous work in our group proved that using aluminium impregnation and concentrated reaction mixtures can improve the LDH coverage and reduce the proportion of free LDH in the large-scale SiO_2@LDH preparation.[36,105] Scheme 3.1 shows the process and possible effects. In

Al impregnation, silica was wet impregnated with $Al(NO_3)_3$ and then dried at 100 °C for 2 hours to anchor Al atoms on the surface of ES757. Those Al atoms would act as the nucleation site of LDH and facilitate the growth of LDH on the surface of SiO_2. In the concentrated reaction mixture, the LDH nuclei have a higher chance to contact with silica core, which would boost the formation of supported nuclei and gain better LDH coverage and a lower level of free LDH.



Scheme 3.1 The process and effect for Al impregnation and use concentrated reaction mixture.

To eliminate the free LDH, Al impregnation, concentrated condition, and a combination of both were attempted. The product prepared from the Al-impregnated silica is called ES757@Cu_4ZnAl-LDH-Al. For high concentration conditions, the amount of metal nitrate and silica involved in the synthesis remains the same. While the water in the metal nitrate solution is reduced to 38% of the original amount; for the silica dispersion, 15% of water was used. Accordingly, the metal nitrate dropping rate was adjusted to ensure metal cations were added at the same speed in both the original and concentrated condition. The sample that is prepared

from the high concentration conditions is termed ES757@Cu_4ZnAl-LDH-conc. The sample that results from the Al-impregnated silica at the condensed environment is named ES757@Cu_4ZnAl-LDH-Al + conc. Details about the preparation can be found in Chapter 7.

The XRD pattern in Figure 3.26 shows that LDH is the only crystalline phase observed in all samples. The *d*-spacing and crystallite sizes are similar within these composites (Table B8).

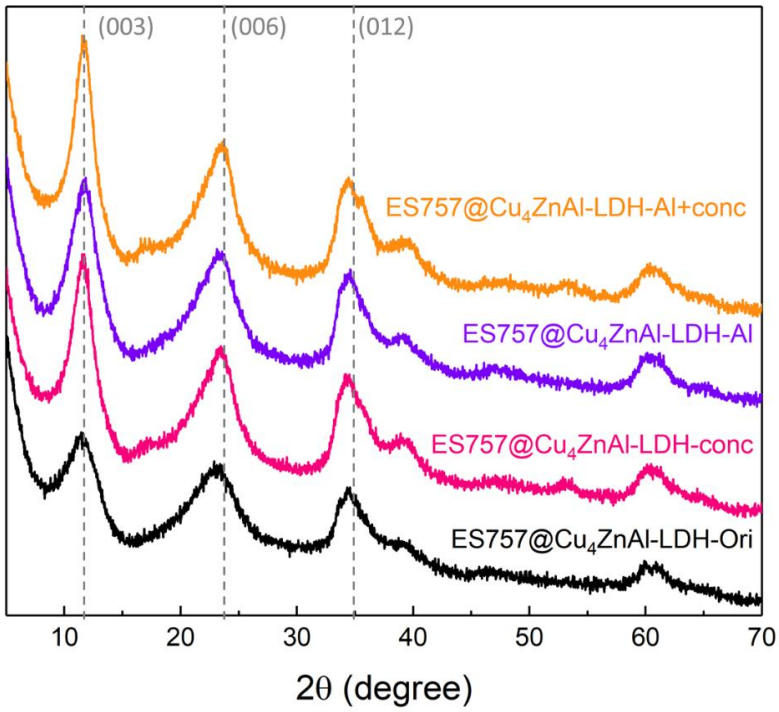


Figure 3.26 The XRD plots of ES757@Cu_4ZnAl-LDH core-shells from the different synthetic conditions.

High-resolution (HR) SEM images in Figure 3.27 reveals that a clean background is obtained when one of or both the Al impregnation and concentrated condition is applied. This indicates a successful elimination of free LDH. However, LDH coverage of ES757@Cu_4ZnAl-LDH-Al is inadequate (Figure 3.27a), i.e., most of the silica is uncovered.

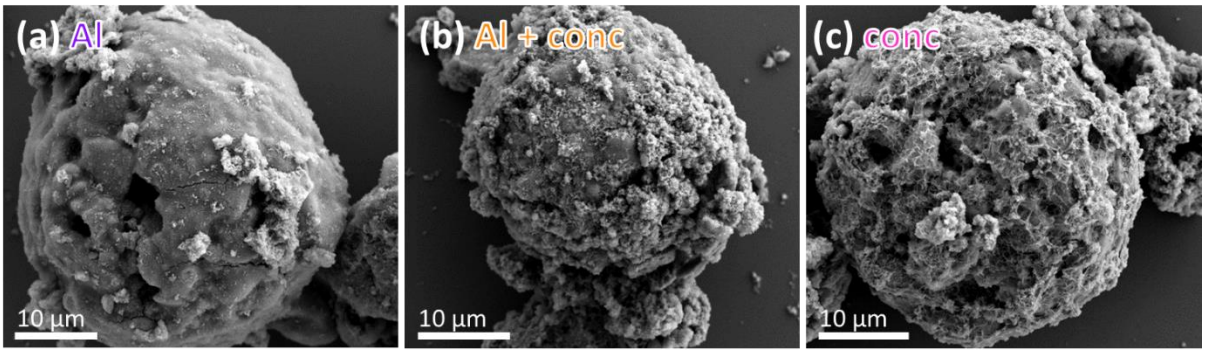


Figure 3.27 High-resolution (HR) SEM image of (a) ES757@Cu_4ZnAl-LDH-Al, (b) ES757@Cu_4ZnAl-LDH-Al + conc and (c) ES757@Cu_4ZnAl-LDH-conc.

Moreover, LDH distribution on the surface of the core is not uniform in ES757@Cu_4ZnAl-LDH-Al (Figure 3.28a); LDH aggregation and bare surface exist at the same time. A similar phenomenon has been found in ES757@Cu_4ZnAl-LDH-Al + conc (Figure 3.28b). The possible explanation is the uneven dispersion of interface Al atoms from the wet impregnation; the areas of abundant Al sites lead to a thick shell and LDH aggregation (region I), while the sparse areas cause the thin shell or, even worse, the bare coverage.

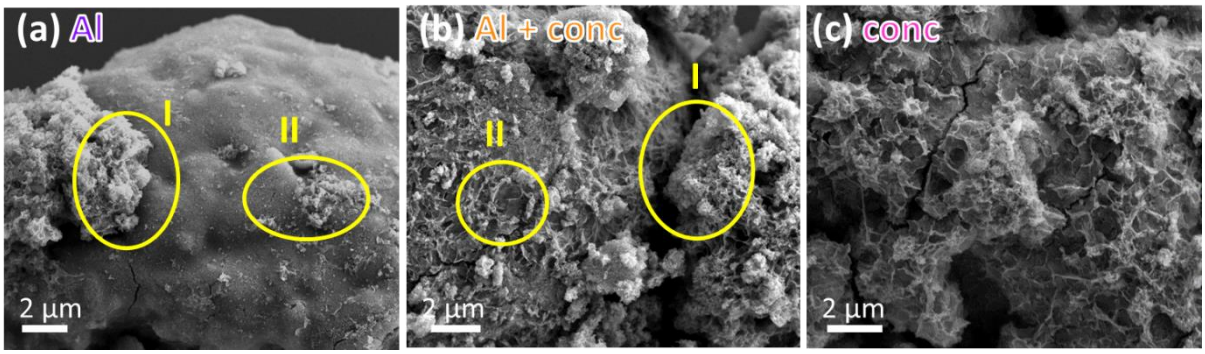


Figure 3.28 Zoom-in of the HR SEM image of (a) ES757@Cu4ZnAl-LDH-Al, (b) ES757@Cu4ZnAl-LDH-Al + conc and (c) ES757@Cu_4ZnAl-LDH-conc.

The high concentration conditions alone afford two core-shells with good coverage and a well-defined shell (Figure 3.28b and c). ES757@Cu_4ZnAl-LDH-conc has a uniform shell where LDH grows as a web arraying along the honeycomb grid (Figure 3.28c). The EDX elemental

mapping verifies the homogeneous allocation of Cu, Zn and Al over the particle (Figure 3.29).

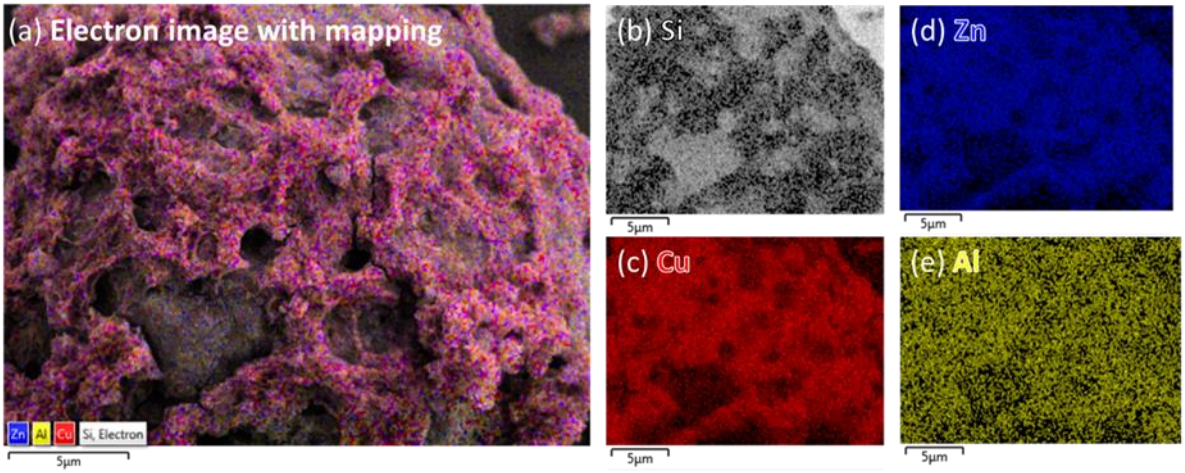


Figure 3.29 (a) HR-SEM image with elemental mapping and (b)–(e) Si, Cu, Zn and Al mapping of ES757@Cu_4ZnAl-LDH-conc.

FTIR spectra (Figure B17a) and TGA plots (Figure B17b) of all four samples show typical SiO_2@CuZnAl-CO_3-LDH IR absorbance bands and characteristic SiO_2@CuZnAl-CO_3-LDH weight loss stages, as previously discussed. The weight fraction of SiO_2 calculated from the TGA data is 36% for the dilute condition (ES757@Cu_4ZnAl-LDH-ori and ES757@Cu_4ZnAl-LDH-Al) and 40% for the condensed condition. It is possible that more silicate is formed under the high concentration conditions and leads to a higher value of residual weight of the core-shell.

ES757 exhibits a type II isotherm with H2b hysteresis loop (Figure 3.30a), indicating it is a macroporous material in which the pore body is slightly wider than the pore neck.[55] Cu_4ZnAl-LDH shows a type II isotherm with a H3 hysteresis loop. All core-shells possess a type II isotherm. Products prepared from high concentration conditions (ES757@Cu_4ZnAl-LDH-conc and -Al + conc) has a H2b dominant loop. In contrast, samples prepared from the dilute condition have H3 dominant loop. The shape of the hysteresis loop depends on the pore

structure. This suggests that products obtained from a condensed environment exhibit a pore structure close to the core ES757; the pore structure from the dilute condition is comparable to that of LDH.

BJH pore size distribution further confirmed the effect of the concentration of reaction mixture on the pore structure of core-shells (Figure 3.30b). Core-shells from the concentrated condition exhibits a narrow pore size distribution over 0–150 nm range, similar to that of ES757 core. However, core-shells from the dilute condition show a wider pore size distribution (ES757@Cu_4ZnAl-LDH-ori and -Al); moreover, the presence of macropore over 150 nm reflects the presence of free LDH.

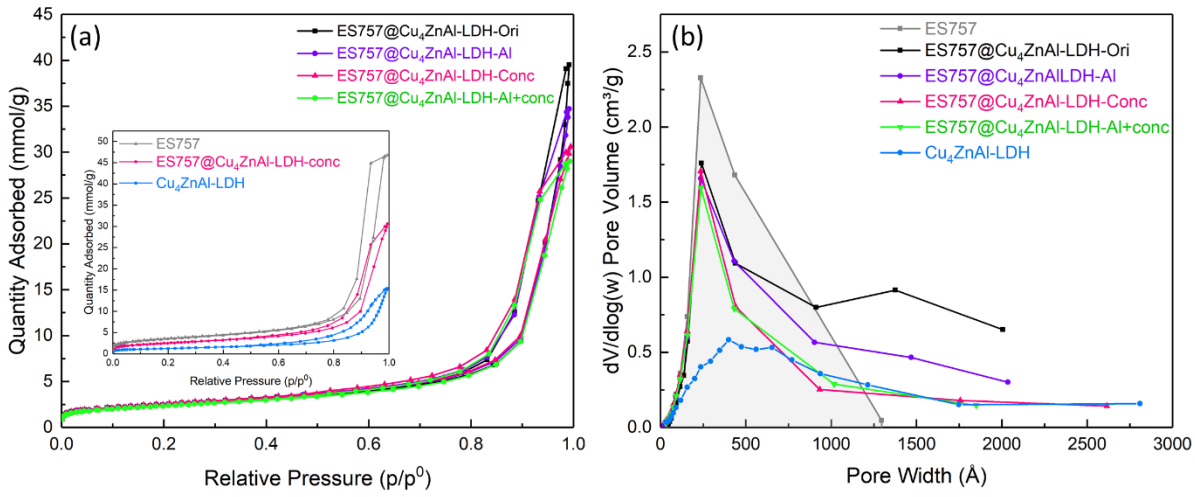


Figure 3.30 (a) The N_2 adsorption and desorption isotherm (at 77 K) and (b) the BJH pore size distribution of ES757, Cu_4ZnAl-LDH and ES757@Cu_4ZnAl-LDH core-shell prepared from different synthetic conditions. The insert plots in (a) are isotherms of ES757, ES757@Cu_4ZnAl-LDH-conc and Cu_4ZnAl-LDH.

The BET specific surface area is almost identical in all core-shells and is higher than that of the physical mixture (Figure 3.31a). This superior surface area maybe because that the extra surface area is gained from the less stacked LDH sheets in core-shells compared to the pristine LDH.[103]

The total pore volume of core-shells is higher than that of the physical mixture (Figure 3.31b), which is believed to be due to the formation of interparticle voids from the diminished stacking among LDH platelets. Samples from concentrated condition display smaller pore volume than those from dilute condition (Figure 3.31b), which is because the thick LDH shell from concentrated condition grows on the pore's inside wall and narrows the pore diameter more markedly (as proved by BJH pore size distribution). Moreover, core-shells prepared at dilute condition has more free LDH which provides additional pore volume.

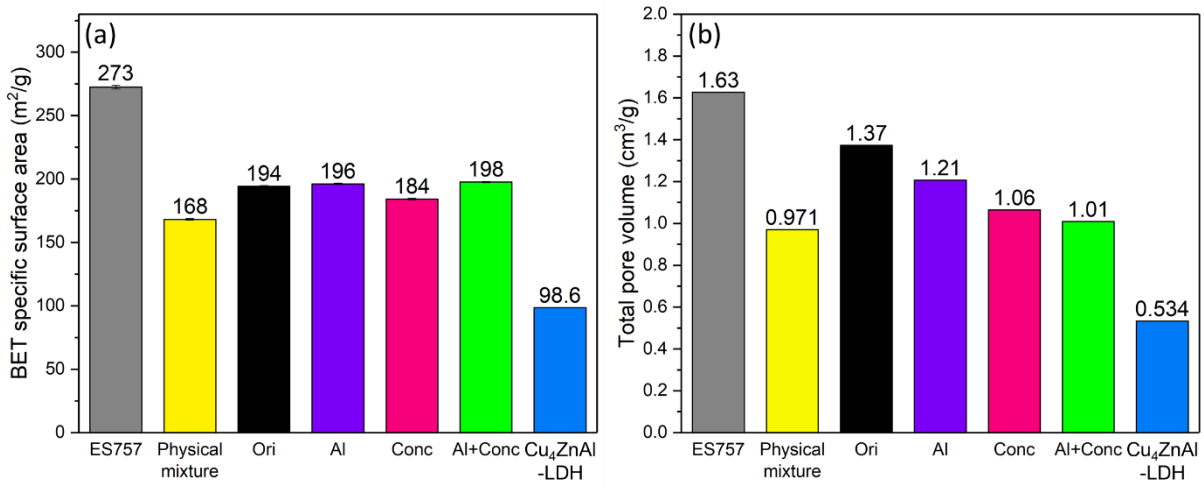


Figure 3.31 (a) the BET specific surface area and (b) the total pore volume of ES757, Cu_4ZnAl-LDH, their physical mixture with composition (SiO_2: LDH = 40:60) and ES757@Cu_4ZnAl-LDHs from various conditions. For clarity, the sample name was shorted to its suffix.

3.3.2. The effect of Cu content on ES757@Cu_xZnAl-CO_3-LDH

After the successful large-scale synthesis of ES757@Cu_4ZnAl-LDH-conc core-shell with uniform shell morphology and high LDH coverage. The next step is to prepare enough core-shell precursors with different copper loading for the following catalysis study.

Five core-shells were prepared under the same condition as ES757@Cu_4ZnAl-LDH-conc but the Cu/Al molar ratio in LDH varies from 0.8, 1.3, 2, 3 to 4. The expected Cu wt% from the

derived catalyst should exhibit a progressive increase (14, 19, 25, 29 and 33, respectively). The Zn/Al ratio remains at 1 and the total amount of metal nitrate is kept the same for all syntheses. Products are named as ES757@Cu_xZnAl-LDH, where x is the Cu/Al ratio.

The presence of LDH Bragg reflections in all ES757@Cu_xZnAl-LDHs proves the formation of LDH phase and the absence of crystalline impurity (Figure 3.32). As before, an increase in Cu/Al ratio leads to a decrease in the crystallinity of the LDH phase. Single-phase Pawley refinement based on the structural information of LDH has been carried out on all samples (Table B9). This set of materials possess a d_{003} between 7.5 and 7.6 Å, demonstrating they are carbonate-intercalated LDHs. The d_{110} expanded from 1.53 to 1.54 Å when Cu/Al ratio raises from 0.8 to 2. This could be because of the enlarged metal-metal distance as a result of replacing small Al^{3+} (0.054 nm) with bigger Cu^{2+}(0.073 nm).[88,89] The d_{110} of Cu/Al = 3 and 4 is 1.53 Å, slightly smaller than that of Cu/Al = 2 (1.54 Å). It may be due to the error in calculation arising from the broad and weak (110) Bragg reflection at high Cu loading. Another possibility is that at Cu/Al ratio = 3 and 4, certain amount of amorphous hydroxide carbonate forms (as discussed in section 3.2.3.2). Therefore, the actual Cu content in ES757@Cu_3ZnAl-LDH and ES757@Cu_4ZnAl-LDH is lower than expectation.

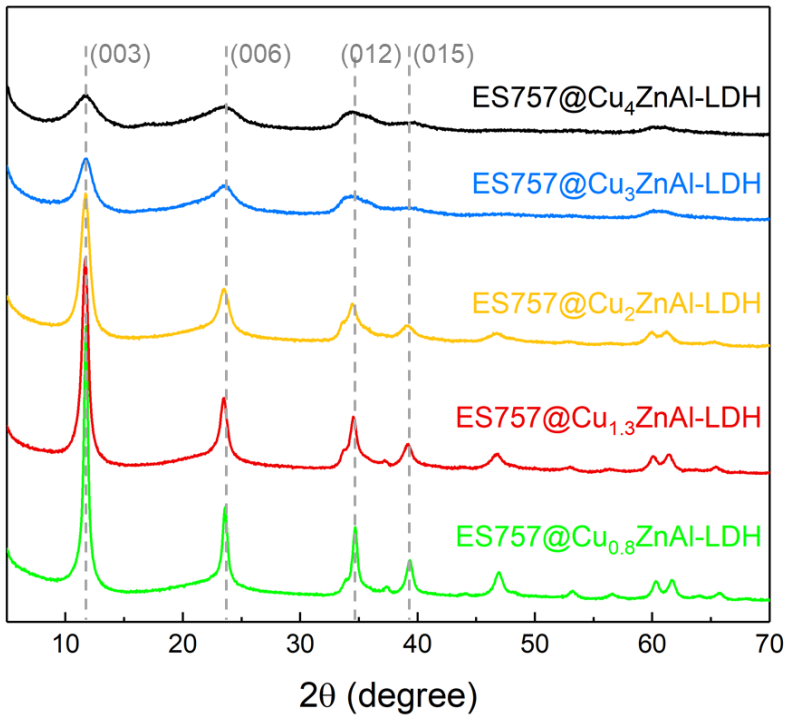


Figure 3.32 XRD profiles freshly prepared ES757@Cu_xZnAl-LDH.

The composition was determined by the ICP-OES and CHN analysis. The amount of element is normalised to the amount of Al. The detected Cu/Al ratio is closed to the expected value (Table 3.9). The C/Al molar ratio is ≥ 0.5 for ES757@Cu_xZnAl-LDHs indicating the presence of carbonate impurities. As discussed before, it is likely to be copper and/or zinc hydroxide carbonate.

Based on the discussion in the previous section, it is known that Al will partially move to silica during the co-precipitation. This phenomenon is corroborated by the presence of tetrahedral Al resonance in the ^{27}Al solid-state NMR spectra of MCM-48@Cu_xZnAl-CO_3-LDH core-shells and the deficient amount of carbon (C/Al < 0.5). The high carbon amount (C/Al ≥ 0.5) in ES757@Cu_xZnAl-LDHs may be related to the low surface area of ES757 (273.0 m^2/g) compared to MCM-48 (1185.8 m^2/g). Less migrated aluminium forms aluminosilicate at the interface due to less exposed Si.[22,105,106]

Without the deficiency in carbon, it is hard to estimate the proportion of $NaAlO_2$, the form of interface Al. Moreover, the paramagnetic Cu strongly weakens the signal of octahedral Al in the ^{27}Al NMR spectra of core-shell, making it impossible to quantify the amount of tetrahedral Al using the octahedral Al as the standard.

A possible chemical formula of ES757@Cu$_x$ZnAl-LDH assuming a negligible Al migration is listed in Table 3.9. The calculation process is the same as that is adopted for MCM-48@Cu$_x$ZnAl-LDH (Appendix B, page B-10). The elemental composition from this chemical formula is in agreement with the actual composition (Table B10). The impurity is tentatively assigned as $Cu_2(OH)_2CO_3$. It is seen that hydroxide carbonate impurities occur at Cu/Al ratio as low as 1.3. The quantity of impurity increases with the elevated copper density. Generally, ES757@Cu$_x$ZnAl-LDH has more hydroxide carbonate species than MCM-48@Cu$_x$ZnAl-LDH at the same copper loading. This could either due to the difference in the property of silica or the varied synthetic condition.

Table 3.9 The theoretical and experimental Cu: Al molar ratio in ES757@Cu$_x$ZnAl-LDHs with their possible chemical formula and impurity.

Cu/Al ratio		Stoichiometry in LDH $[Cu_aZn_bAl_c(OH)_{2(a+b+c)}(CO_3)_{c/2}]\ nH_2O$						SiO_2	$Cu_2CO_3(OH)_2$[b]
Theo.[a]	Exp.	Cu	Zn	Al	OH	CO_3^{2-}	H_2O		
0.8	0.84	0.84	1.05	1.00	5.78	0.50	1.40	3.35	0.00
1.3	1.34	1.29	1.03	1.00	6.64	0.50	1.49	3.85	0.02
2	2.05	1.86	1.02	1.00	7.77	0.50	1.63	4.50	0.09
3	3.24	2.65	0.98	1.00	9.25	0.50	1.95	5.50	0.30
4	4.14	2.80	1.03	1.00	9.67	0.50	2.28	6.50	0.67

a: theoretical Cu/Al ratio based on the amount of starting material in co-precipitation. B: Impurity could be a mixture of zinc hydroxide carbonate and copper hydroxide carbonate.

TGA plots of ES757@Cu$_x$ZnAl-LDHs show typical weight loss stages of SiO_2@CuZnAl-

CO_3-LDH (Figure B18). The SiO_2: CuZnAl LDH fraction calculated from the TGA data is similar in all samples and is approximately 40:60, in agreement with the expected number (Table B9). The start temperature for the complete decarboxylation (3rd weight loss stage) shifts to a lower value at raised Cu loading (650 °C for ES757@$Cu_{0.8}$ZnAl-LDH and 550 °C for ES757@Cu_4ZnAl-LDH), agrees with previous finding that the higher the copper content, the more unstable the LDH.

FTIR spectra of ES757@Cu_xZnAl-LDHs are similar, besides that high copper loading does have a more obvious asymmetric carbonate vibration band at around 1460 cm^{-1} due to the more disordered interlayer environment and the increased amount of hydroxide carbonate impurity (Figure B19). All samples possess typical LDH absorbance bands at 750 cm^{-1}, 1350 cm^{-1} and 3500 cm^{-1} due to the M-O vibration, carbonate vibration, and OH stretching, respectively. Additionally, a peak at around 1000 cm^{-1} is attributed to the Si-O vibration.[44]

HR-SEM images reveals that core-shell structure is obtained in ES757@Cu_xZnAl-LDHs regardless of the LDH composition (Figure B20). The elemental mapping proves the uniform Cu, Zn and Al dispersion over the particles (Figure B21–B24). However, the morphology of the shell changes with their composition. At Cu/Al ≤ 2, the shell consists of rigid platelets (Figure 3.33a–c). While at Cu/Al = 3 and 4, thinner platelets make up the seaweed-like shell (Figure 3.33d–e). Moreover, the HR-SEM image showing the cross-section region of a fragmented particle of ES757@Cu_2ZnAl-LDH (Figure 3.33f) proves that LDH firstly wrapped on the silica surface and then radially grew to build the thickness; this is consistent with the previous finding in MCM-48@Cu_xZnAl-CO_3-LDH.

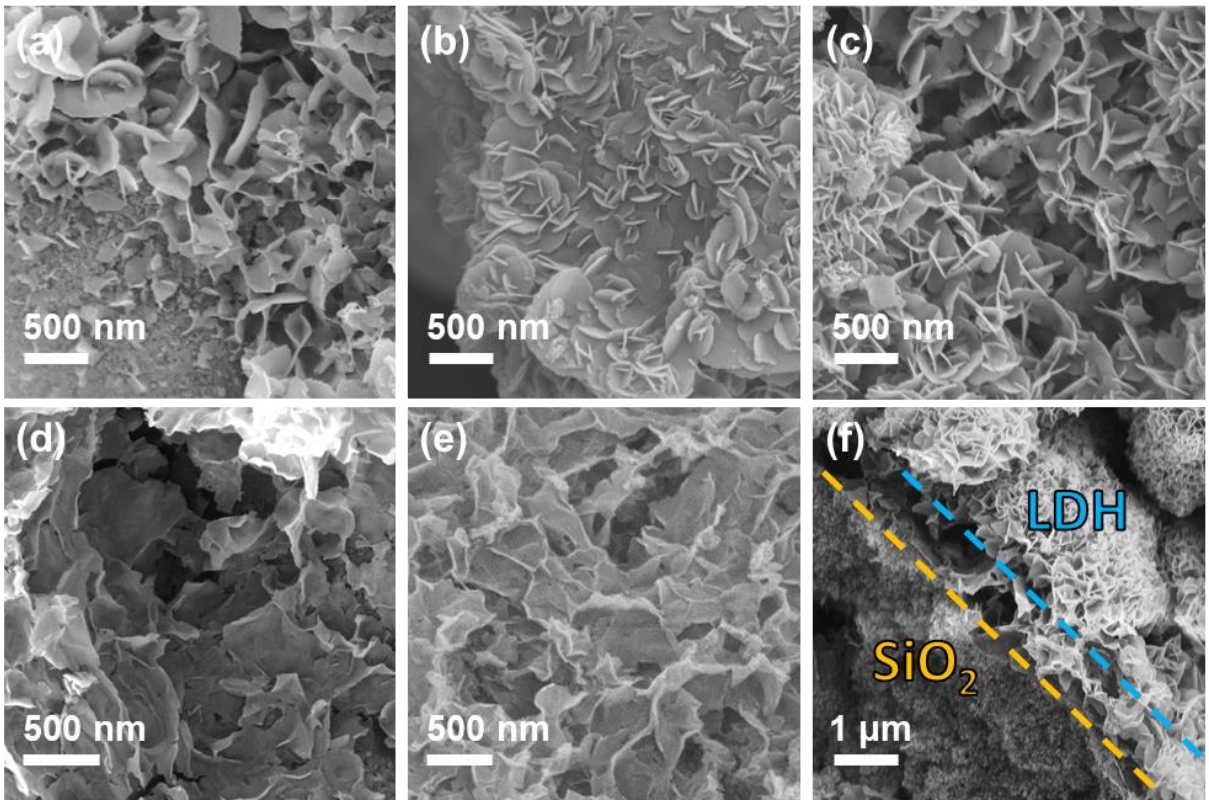


Figure 3.33 HR-SEM images showing the shell of (a) ES757@$Cu_{0.8}$ZnAl-LDH, (b) ES757@$Cu_{1.3}$ZnAl-LDH, (c) ES757@Cu_2ZnAl-LDH, (d) ES757@Cu_3ZnAl-LDH and (e) ES757@Cu_4ZnAl-LDH. (f) HR-SEM images shows the cross-section region of a fragmented particle of ES757@Cu_2ZnAl-LDH.

All ES757@Cu_xZnAl-LDH exhibit the type II N_2 adsorption and desorption isotherm with a H2b hysteresis loop, identical to that of ES757 (Figure B25). This demonstrates that the core-shell precursor are macroporous materials where the pore body is slightly larger than the pore neck. The pore structure of the mother silica survives after co-precipitation.

Contrary to the noticeable reduction in the surface area and total pore volume that occurs in MCM-48@Cu_xZnAl-LDH at elevated Cu/Al ratio (Figure 3.24), the BET specific surface area and the pore volume are similar in ES757@Cu_xZnAl-LDH regardless of the copper loading (Figure 3.34). The ES757 (24.2 nm from BJH and 1 µm from supplier) has much wider pores than MCM-48 (3.2 nm from DFT). Smaller LDH platelets (at high copper density) do not lead to the same level of pore plugging in ES757 as that in MCM-48.

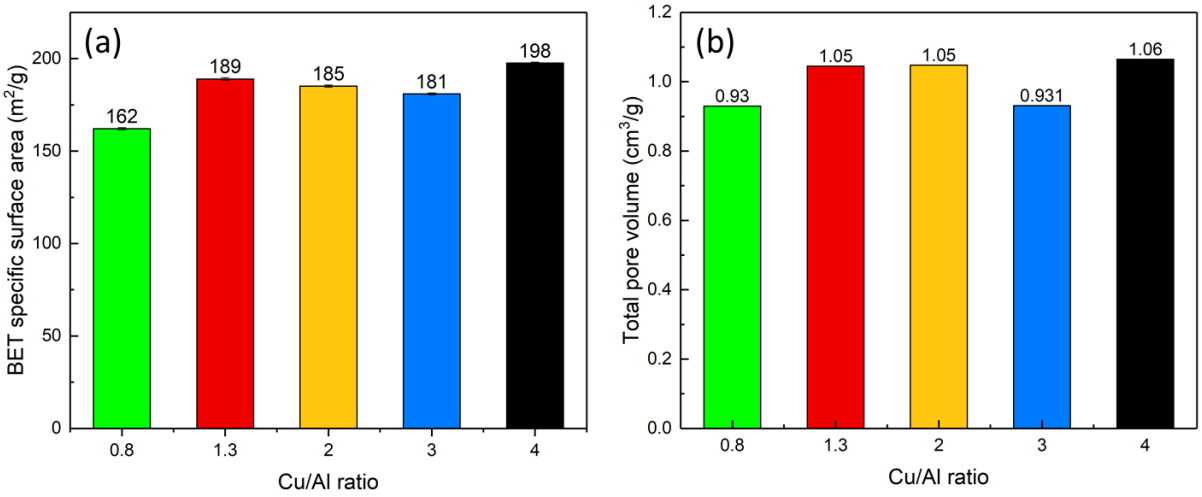


Figure 3.34 (a) The BET specific surface area and (b) the total pore volume of ES757@Cu$_x$ZnAl-LDH, where x = Cu/Al ratio.

3.4 Synthesis of mesoporous SiO_2@Cu_2ZnAl-CO_3-LDH

The dispersion of the active site and the mass transfer property of the material are closely associated with catalyst performance.[2] It is assumed that these two properties for catalysts derived from the mesoporous SiO_2@LDH, abbreviated as mSiO_2@LDH, core-shells are related to the surface area and pore structure of the silica support. To study this, a series of mSiO_2@Cu_2ZnAl-LDH composites are prepared using silica with different surface area and pore structure. Four mesoporous silica SBA-15, SBA-16, MCM-41 and MCM-48 were selected. The physical properties of those silica and ES757 are listed in Table 3.10. SBA-15 and MCM-41 have similar pore structures (2D pores arranged along a hexagonal grid) but different surface areas due to different pore sizes.[107,108] SBA-15 and SBA-16 have similar surface areas but different pore structures (2D pore structure in SBA-15 while 3D in SBA-16). MCM-41 and MCM-48 have similar particle shapes and pore sizes, but different surface areas and pore structures (2D pore structure in MCM-41 while 3D in MCM-48).

Table 3.10 Physical properties of silica used in this study.

Silica	Particle morphology[a]	Particle size (μm)[b]	BET specific surface area (m^2/g)[c]	Total pore volume (cm^3/g)[c]	Pore size (nm)[c]	Pore structure
ES757	Spherical	25	273.0	1.63	24.2	Unknown
SBA-15	Wire-like	30	536.7	0.56	1.1, 1.6, 6.8	2D round
SBA-16	Spherical	50	687.8	0.50	1.1, 2.1, 7	3D
MCM-41	Spherical	4.5	792.1	0.69	3.6	2D hexagonal
MCM-48	Spherical	3	1185.8	0.81	3.2	3D

a: The particle morphology is checked by the HR-SEM and is presented in Figure 3.39. b: The particle size is obtained from the supplier. c: The BET specific surface area, total pore volume and pore size is obtained from the N_2 adsorption and desorption isotherm at 77 K. DFT kernel based on the metal oxide with cylindrical pore was used to obtain the pore size.

Core-shells were prepared following the same conditions used for ES757@Cu_2ZnAl-LDH. Products are named after their core, for example, composite containing SBA-15 is called SBA-15@Cu_2ZnAl-LDH.

ES757@Cu_2ZnAl-LDH and SBA-15@Cu_2ZnAl-LDH exhibit a clean XRD pattern where only Bragg reflections from the LDH are observed (Figure 3.35). However, for the other three core-shells, an extra peak occurs near the LDH (003) Bragg reflection, indicating the presence of a crystalline impurity. The peak location for (003) is speculated from the (006) and (009) Bragg reflections based on the principle: $d_{003} = 2d_{006} = 3d_{009}$. The d_{003} of composites from SBA-15, SBA-16, MCM-41 and MCM-48 is around 7.5–7.8 Å, indicating a carbonate intercalated LDH phase (Table B11).

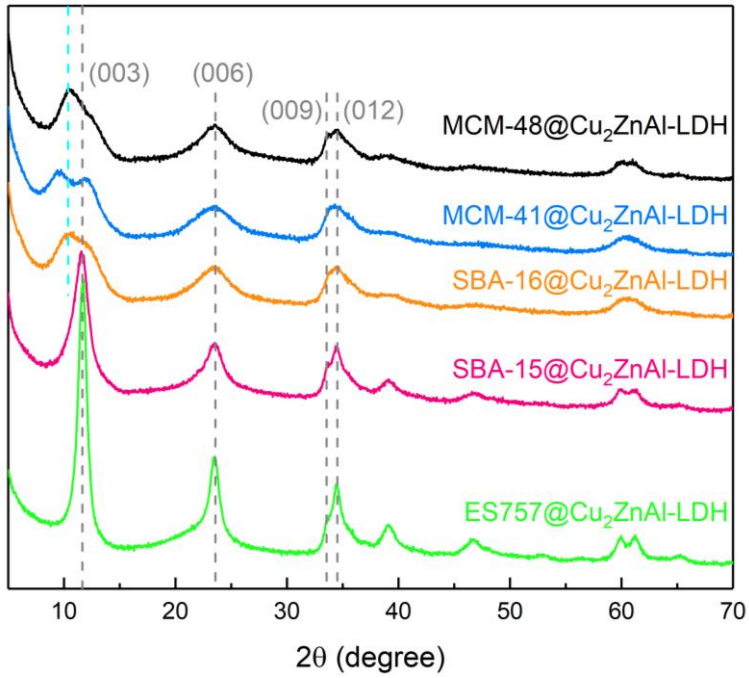


Figure 3.35 (a) XRD profiles of $mSiO_2$@Cu_2ZnAl-LDH core-shell materials.

It is hard to determine the impurity based on only one Bragg reflection peak. However, identification is required so that synthesis optimisation can be designed to eliminate the impurity in further synthesis.

The additional Bragg reflections in SBA-16@Cu_2ZnAl-LDH, MCM-41@Cu_2ZnAl-LDH and MCM-48@Cu_2ZnAl-LDH appear at 2θ = at 10.41°, 9.52° and 10.47°, respectively. Metal hydroxide nitrate and metal hydroxide carbonate are two possible impurities. Figure 3.36 reveals that, instead of being hydroxide carbonates (hydrozincite and aurichalcite) or copper hydroxide nitrate (gerhardtite), this crystalline impurity is more likely to be zinc hydroxide nitrate. However, the nitrogen content in these three composites are below the detectable level according to CHN analysis (Table 3.12). Therefore, zinc hydroxide nitrate might not present in these core-shells. Yurieva *et al.* reported that copper-zinc silicate shows a dominant peak at *ca.* 2θ = 8° and weak reflections at *ca.* 2θ = 35° in its XRD pattern,[109] suggesting that the impurity

phase could be copper-zinc silicate. While some researchers present their work on zinc silicate, none provide a detailed crystal structure.[110,111] Therefore, the powder XRD pattern of copper-zinc silicate cannot be computed. It is noticed that some silicates (talc or montmorillonite) shows a similar powder XRD pattern as copper-zinc silicates and have a similar structure (Figure 3.36).[109,110]

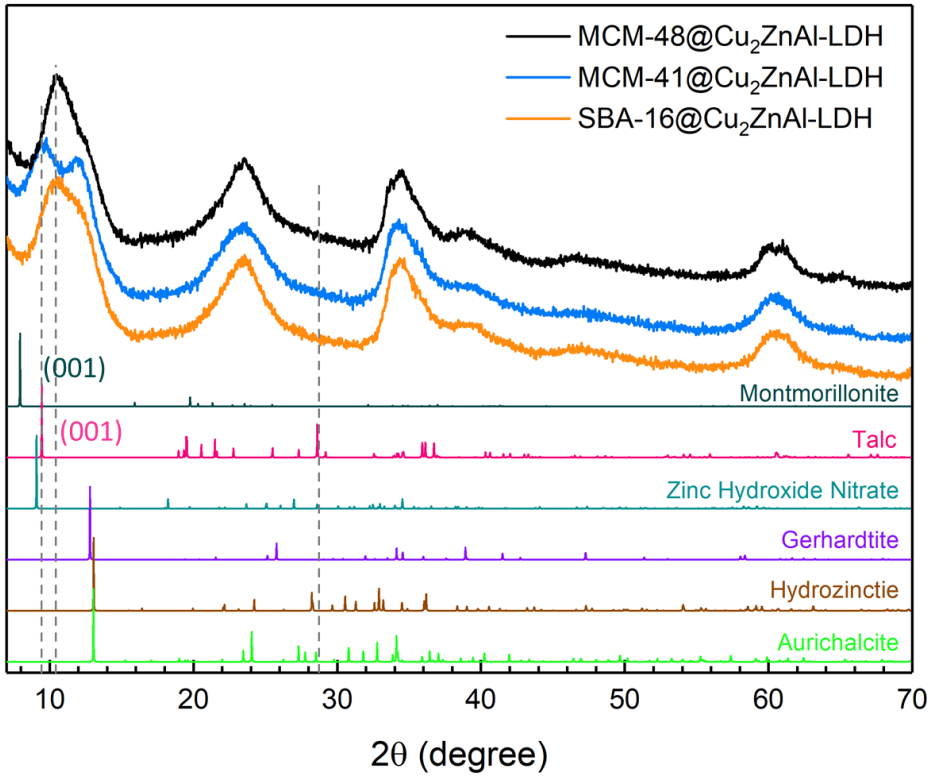


Figure 3.36 The XRD pattern of SBA-16@Cu_2ZnAl-LDH, MCM-41@Cu_2ZnAl-LDH, MCM-48@Cu_2ZnAl-LDH and the computed XRD pattern of the possible impurities at λ = 1.54059 Å.

The crystal structure and formula of talc and montmorillonite (MMT) are displayed in Figure 3.37.[112–114] Both minerals possess a layered structure.[109,110] The main component in them is the sandwich layer consisting of one sheet of linked $MO_4(OH)_2$ octahedra, where M = Mg or Al, and two sheets of linked SiO_4 tetrahedra. The metal atoms share oxygen atoms with adjacent Si to connect $MO_4(OH)_2$ sheets with SiO_4 sheet. In MMT, Si or Al are partly substituted by cations with lower valence, trivalent or divalent, respectively and the charge balance is met by

introducing counterions (*e.g.*, Li^+, Na^+, Ca^{2+}).[112,114] Accordingly, the d_{001} is expanded (d_{001} for MMT is 12.45 Å but 9.46 Å for talc).[112–114]

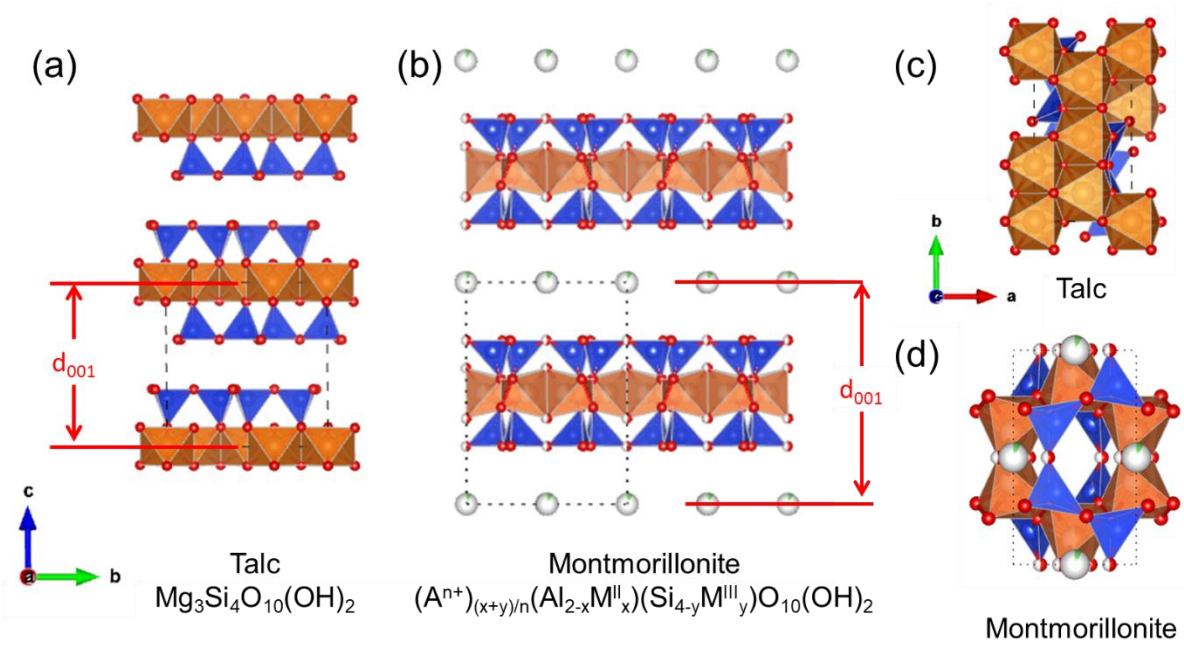


Figure 3.37 The crystal structure and formula of (a) Talc and (b) Montmorillonite (MMT) viewing from *a*-axis. The crystal structure of (c) Talc and (d) Montmorillonite viewing from the *c*-axis. SiO_4 is presented by blue tetrahedra, and $MO_4(OH)_2$ is presented by orange octahedra (M = Mg or Al). Counterion A^{n+} is presented by the white ball.

Refinement based on the space group and lattice parameter of MMT was carried out. Rietveld refinement was used to maintain the peak profile. Only lattice parameters *a*, *b* and *c* are refined. The results are listed in Table 3.11. The d_{001} (lattice parameter *c*) of SBA-16@Cu_2ZnAl-LDH and MCM-48@Cu_2ZnAl-LDH is close to that of Talc (Table 3.11) and the d_{001} of MCM-41@Cu_2ZnAl-LDH is approaching that of MMT; this indicates the impurity in these three core-shell is likely to be layered silicate where two sheets of linked SiO_4 tetrahedra sandwich one sheet of linked $MO_4(OH)_2$ octahedra. The Si/Metal ratio and thus the interlayer environment varies with the silica core.[112]

The atom arrangements in the *ab*-plane are very different in talc and MMT (Figure 3.37c and d) due to their different Si/Metal molar ratio.[114] The lattice parameters *a* and *b* of three $mSiO_2$@Cu_2ZnAl-LDH core-shells are larger than that for two layered silicates (Table 3.11), indicating that silicates in core-shells have different atomic arrangement in the *ab*-plane from two reference silicates.

Table 3.11 The lattice parameters of the impurity phase in $mSiO_2$@Cu_2ZnAl-LDH obtained from Rietveld refinement and lattice parameters of MMT and Talc.

Samples	*a*/Å	*b*/Å	*c* (= d_{001})/Å	α/°	β/°	γ/°
SBA-16@Cu_2ZnAl-LDH	7.00	9.99	9.53	90	99.69	90
MCM-41@Cu_2ZnAl-LDH	6.87	9.15	10.75	90	99.69	90
MCM-48@Cu_2ZnAl-LDH	7.05	10.19	9.23	90	99.69	90
Montmorillonite	5.18	8.90	12.45	90	99.69	90
Talc	5.29	9.18	9.46	90.5	98.7	90.1

Overall, the XRD results reveals that the impurity in of SBA-16@Cu_2ZnAl-LDH, MCM-41@Cu_2ZnAl-LDH and MCM-48@Cu_2ZnAl-LDH is likely to be layered metal silicate. As discussed in the previous section, growing LDH on the SiO_2 surface forms aluminosilicate at the interface. It is possible that the high surface area silica (SBA-16, MCM-41 and MCM-48) at high concentration condition is more active and forms more crystalline interface aluminosilicate (the layered metal silicate as observed in XRD). On the other hand, the layered metal silicate may be different from the interface aluminosilicate and is an undesired by-product. Further characterisation was required to study the core-shell and check the quantity and the chemistry of the layered silicate.

The FTIR spectra of $mSiO_2$@Cu_2ZnAl-LDH core-shells (with SBA-15, SBA-16, MCM-41 and MCM-48 core) exhibit typical silica and LDH absorbance bands (Figure B26). No band from

the impurities can be observed. This is consistent with XRD result, as the typical bands for layered metal silicate (M-O vibration, Si-O vibration and OH stretching) should overlap with silica and LDH bands. The TGA and dTG curves of those four composites displays characteristic silica and LDH weight loss stages (Figure B27). No distinct weight loss due to impurities is found. The silica to LDH weight fraction is around 42:58 in all composites, close to the theoretical 40:60. The high similarity between the TGA result (weight loss stages and composition) of SBA-15@Cu_2ZnAl-LDH and the rest three with layered metal silicate impurity indicates that the layered silicate impurity either is a minor component or has a similar thermal stability to Cu_2ZnAl-LDH.

ICP-OES and CHN analysis were used to investigate the elemental composition. The content of the element in the core-shells is normalised to the amount of Al. The Cu and Zn amounts agree with the expectation (Table 3.12). For SBA-15@Cu_2ZnAl-LDH, C/Al = 0.51, indicating a low level of aluminosilicate formation. While for the rest three samples, the C/Al ratio is lower than 0.5, especially for MCM-41, C/Al is 0.33. The intensity of the impurity peak in XRD shows a relationship with the C/Al ratio: the lower the C/Al, the more intense the peak. Formation of aluminosilicate consumes Al that is supposed to remain in the LDH framework and leads to a low C/Al ratio. The relationship between C/Al and XRD result reveals that formation of aluminosilicate promotes the crystallinity of layered metal silicate; this supported the assumption that layered metal silicate is the interface aluminosilicate. Divalent cations are essential for the sandwich layered structure, indicating that at least one of Cu^{2+} or Zn^{2+} is present in the silicate.

Previous study (section 3.2 and 3.3) shows that amorphous hydroxide carbonate species would form at this Cu/Zn ratio ≥ 2. The co-existence of layered metal silicate (contain Al and at least one of Cu or Zn), hydroxide carbonate and LDH makes it hard to work out the formula of these $mSiO_2$@Cu_2ZnAl-LDH core-shells.

Table 3.12 The content of elements in $mSiO_2$@Cu_2ZnAl-LDHs revealed by ICP-OES and CHN analysis and normalised by the molar amount of Al

Core	Cu	Zn	Al	Si*	Na	C	H	N
SBA-15	2.19	0.96	1.00	0.29	0.08	0.51	10.76	0.00
SBA-16	2.22	1.02	1.00	0.66	0.12	0.49	13.08	0.00
MCM-41	2.16	0.98	1.00	1.14	0.10	0.33	12.43	0.00
MCM-48	2.08	0.95	1.00	0.71	0.19	0.40	12.20	0.00

*: silica is partially dissolved in ICP-OES analysis. The obtained the value is lower than the actual value.

The ^{27}Al NMR spectra of $mSiO_2$@Cu_2ZnAl-LDH (Figure 3.38a) shows both the tetrahedral Al resonance (55.0 ppm) and octahedral resonance (9.0 ppm). As discussed in section 3.1, both resonances are due to the formation of aluminosilicate interface in the core-shell. MCM-41@Cu_2ZnAl-LDH exhibit a relative weak O_h resonance compared to SBA-15@Cu_2ZnAl-LDH which may be due to the insertion of trace amount of paramagnetic Cu in the silicate.

The ^{29}Si resonance of MCM-41@Cu_2ZnAl-LDH can be deconvoluted into three peaks at −110.0 ppm, −100.0 ppm and −91.0 ppm (Figure 3.38b). According to the literature, they should be ascribed to the tetrahedrally coordinated Si with zero, one and two neighbouring Al, respectively.[115] The existence of Q^4Si(2Al) and Q^4Si(1Al) resonances further confirmed the generation of aluminosilicate in $mSiO_2$@LDH core-shells. SBA-15@Cu_2ZnAl-LDH possesses two Q^4Si(0Al) resonances at −110.0 ppm and −105.0 ppm (Figure 3.38c). No signal from Al-surrounded Si was detected, indicating that less aluminosilicate is generated in core-shell with

SBA-15 than that with MCM-41, consistent with the elemental analysis result.

The Si resonance of MCM-41@Cu_2ZnAl-LDH is about ten times weaker than that of SBA-15@Cu_2ZnAl-LDH (Figure 3.38b and c), which may be due to the formation of Cu-containing metal silicate at the interface of MCM-41 and LDH. The paramagnetic Cu hindered the resonance of its neighbouring Si and leads to a much weaker Si NMR spectrum. In the SBA-15-based core-shell, much less metal silicate is formed (as reflected by XRD result) due to less exposed Si (smaller surface area) and therefore the Si signal is not affected.

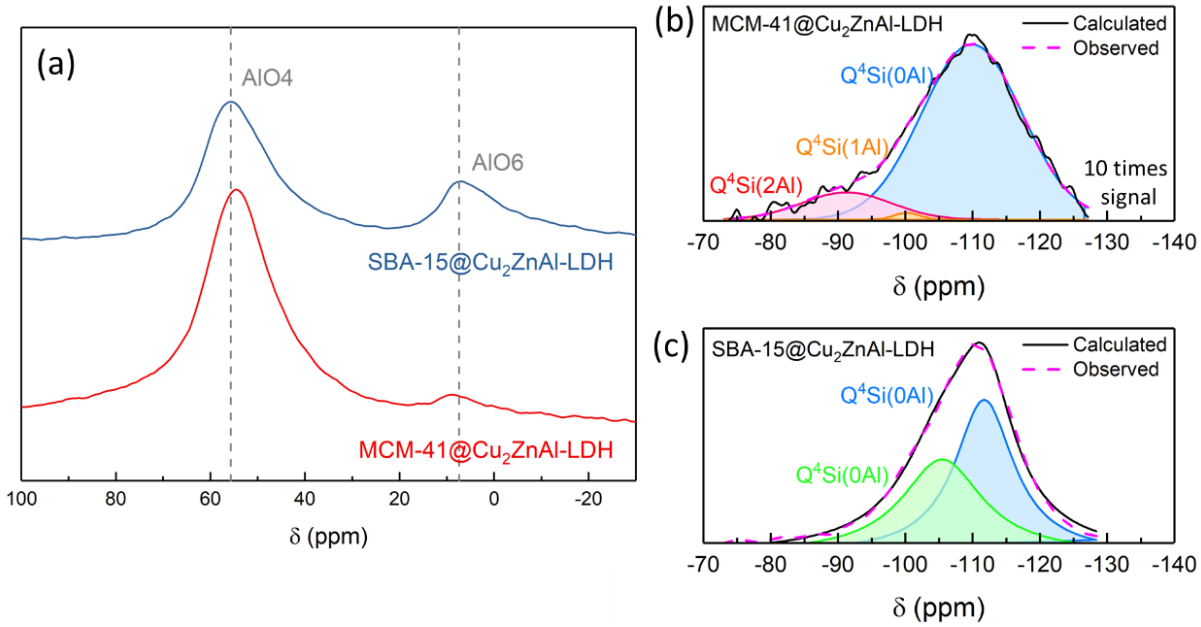


Figure 3.38 (a) the ^{27}Al NMR spectra of MCM-48@Cu_2ZnAl-LDH and SBA-15@Cu_2ZnAl-LDH. The observed and deconvoluted ^{29}Si NMR spectrum of (b) MCM-48@Cu_2ZnAl-LDH (signal was scaled-up by ten times) and (c) SBA-15@Cu_2ZnAl-LDH.

So far, the presence of additional peak in the XRD, elemental analysis result and diminished ^{29}Si ssNMR resonances suggest that in all mSiO_2@Cu_2ZnAl-LDH core-shells, the interface aluminosilicate is formed which is likely to have a layered structure. When SiO_2 with high surface area (SBA-16, MCM-41 and MCM-48) is used, large amount of aluminosilicate is

generated. Meanwhile, the composition of interface silicate changes, i.e., some Cu (and potentially Zn) is inserted. The increased amount and modified composition leads to the increased crystallinity of the interface silicate and thus a more evident Bragg reflection in the XRD.

No Bragg reflection from silicate is observed when silica with low surface area (ES757 and SBA-15) or a dilute synthetic condition (MCM-48@Cu_2ZnAl-LDH) is used. It is believed that the concentrated condition and high-surface-area silica leads to a high density of silicate ions in the reaction mixture and promotes the precipitation of metal silicate. Although current characterisation results suggest that silicate is formed at the interface, the chance of the presence of some undesirable free metal silicate is still possible.

The concentration of reaction mixture should be varied with the surface area of silica to limit the growth of silicate. For silica with low surface area ($\leq$ 500.0 m^2/g), the concentrated condition is required for high LDH coverage and low free LDH level. For silica with a high surface area (> 500.0 m^2/g), a dilute synthetic condition is preferred to minimised the content of free metal silicate.

HR-SEM images proves that core-shell morphology is obtained in all mSiO_2@Cu_2ZnAl-LDH composite (Figure 3.39b–i). EDX elemental mapping illustrates the uniform dispersion of Cu, Zn and Al over the particles (Figure B28–31).

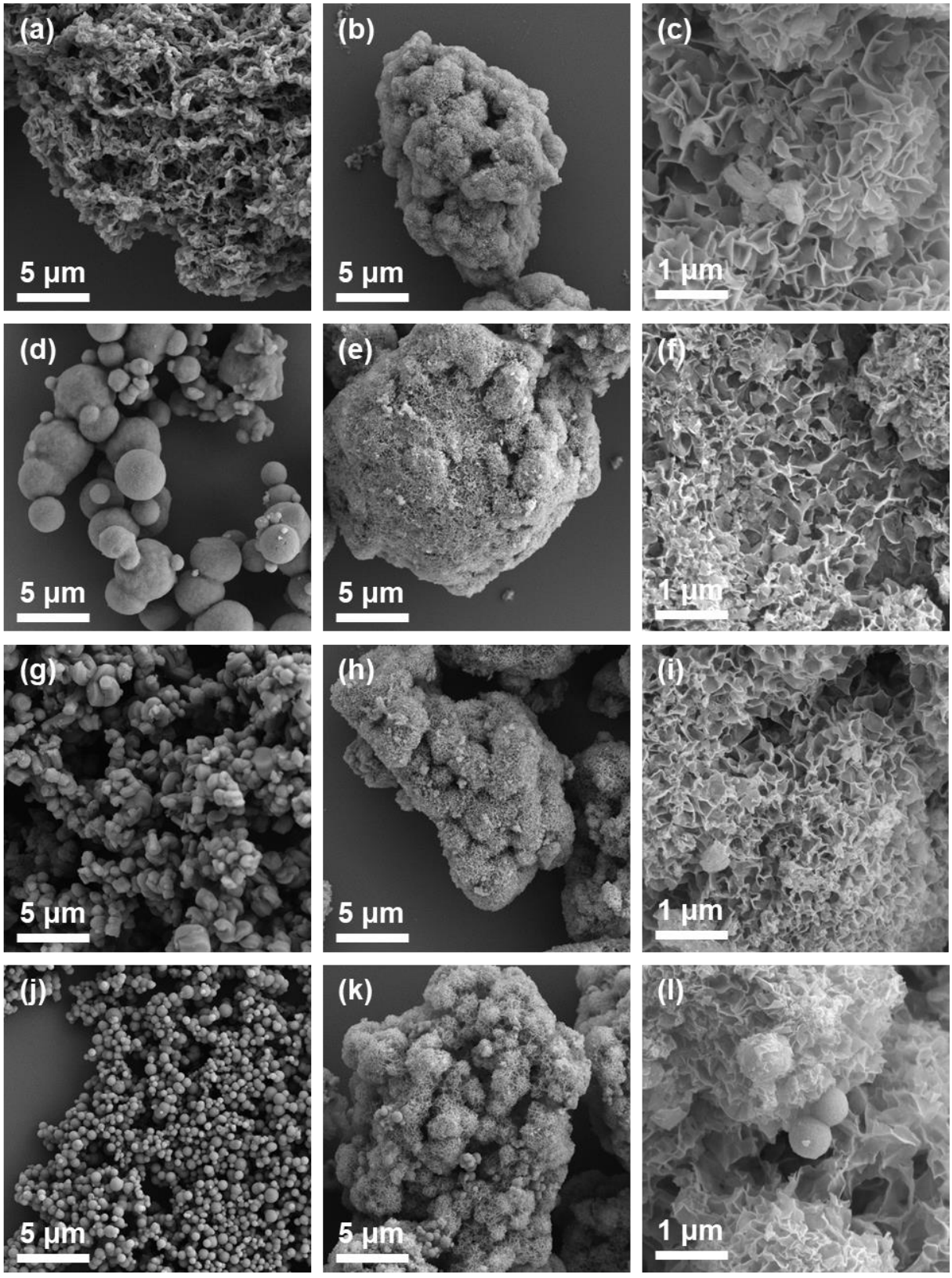


Figure 3.39 HR-SEM images of (a) SBA-15, (b) and (c) SBA-15@Cu_2ZnAl-LDH. (d) SBA-16, (e) and (f) SBA-16@Cu_2ZnAl-LDH. (g) MCM-41, (h) and (i) MCM-41@Cu_2ZnAl-LDH. (j) MCM-48, (k) and (l) MCM-48@Cu_2ZnAl-LDH.

Pore blockage of micro and mesopore in silica is observed in all $mSiO_2$@Cu_2ZnAl-LDH core-shells (Figure B32). Apart from the silica hydrolysis and metal doping factor that were previously discussed, the formation of metal silicate could also contribute to the plugging.

Figure 3.40 displays the N_2 BET specific surface area and total pore volume of silica, the corresponding $mSiO_2$@Cu_2ZnAl-LDH core-shells and physical mixture. As expected, all core-shells possess similar BET specific surface area as the physical mixture; no pronounced increase can be observed. The total pore volume of core-shells is higher than the physical mixture because of the extra volume brought by the LDH shell or free LDH.

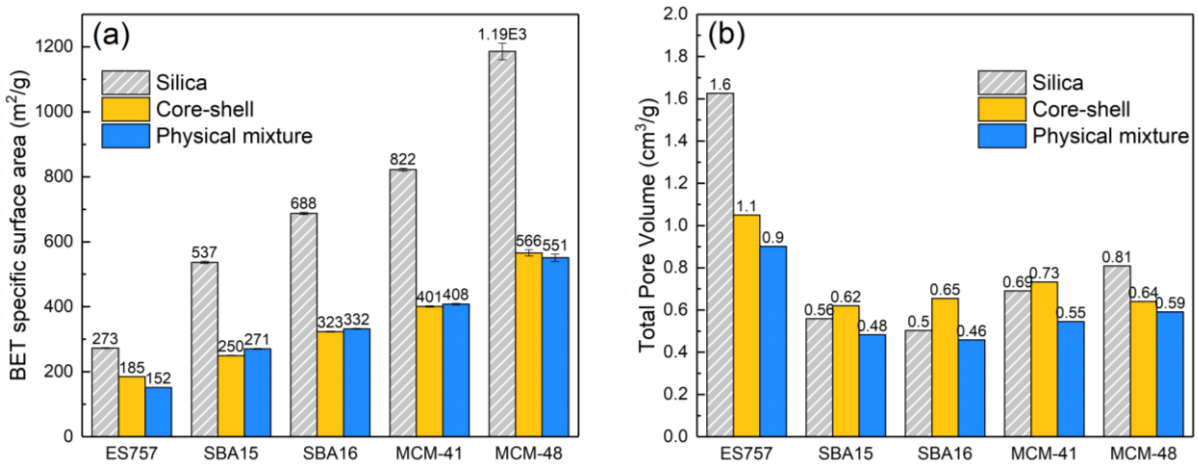


Figure 3.40 (a) The BET specific surface area and (b) total pore volume of silicas, their corresponding $mSiO_2$@Cu_2ZnAl-LDH core-shell and physical mixture ($mSiO_2$:Cu_2ZnAl-LDH = 40:60 by weight).

3.5 Conclusions

It has been shown that a wide variety of silica@CuZnAl core-shell composites can be synthesised with high purity and uniform morphology via the co-precipitation method, utilising various silicas such as ES757, SBA-15, SBA-16, MCM-41, MCM-48. Small LDH crystallites wrap the surface and then radially grow to afford a shell that consists of "seaweed-like" particles. Uniform core-shells can be obtained at pH 9 at SiO_2/LDH = 0.66–1 by weight. Further increases

in the LDH fraction lead to a substantial amount of free LDH. CuZnAl-CO_3-LDH can be synthesised between (Cu + Zn)/Al molar ratio 1.8–5. However, amorphous hydroxide carbonate impurity starts to form at (Cu + Zn)/Al ≥ 2.3 when Cu/Zn molar ratio is larger than 1. An increase in the copper loading leads to the generation of extensive amounts of impurity.

The synthetic conditions need to be varied depending on the silica core surface area to ensure the high uniformity of core-shell. When silica with a low surface area (≤ 500 m^2/g) is used, concentrated conditions should be applied to guarantee the high LDH coverage.

Preparing core-shell with high surface area silica (> 500 m^2/g) under high concentration condition leads to formation of large amount of layered silicate at the interface; this layered silicate contains aluminium and copper (and possibly zinc) and is likely to have a sandwich structure where one sheet of linked $MO_4(OH)_2$ octahedra insert between two sheets of linked SiO_4 tetrahedra. As the effect of the interface silicate on the core-shell is still unknown in this system, in the case of a high surface area (> 500 m^2/g), a dilute condition is desired to minimise the formation of metal silicate.

The de Jong group demonstrated the enhanced surface-specific activity of Cu towards methanol synthesis due to zinc silicate.[116] Wang *et al.* illustrated that the presence of copper phyllosilicate is responsible for the excellent stability of the silica-supported copper catalyst.[117] From previous reports, the presence of metal silicate seems to have a positive effect on the catalytic performance.[116,117] In the future, another set of mSiO_2@Cu_2ZnAl LDH core-shells with limited amount of meta silicate interface will be prepared to study the effect of metal silicate interface

on the catalytic ability toward CO_2 hydrogenation to methanol.

The ES757@Cu_xZnAl-LDH and mSiO_2@Cu_2ZnAl LDH core-shells will be taken into the further study of CO_2 hydrogenation to methanol catalysis. The effect of copper loading and the property of silica support will be explored in the next chapter.

3.6 References

1 P. S. Murthy, W. Liang, Y. Jiang and J. Huang, *Energy Fuels*, 2021, **35**, 8558–8584.

2 X. Jiang, X. Nie, X. Guo, C. Song and J. G. Chen, *Chem. Rev.*, 2020, **120**, 7984–8034.

3 S. Roy, A. Cherevotan and S. C. Peter, *ACS Energy Lett.*, 2018, **3**, 1938–1966.

4 A. Bansode, B. Tidona, P. R. Von Rohr and A. Urakawa, *Catal. Sci. Technol.*, 2013, **3**, 767–778.

5 I. U. Din, M. A. Alotaibi and A. I. Alharthi, *Sustain. Chem. Pharm.*, 2020, **16**, 100264.

6 K. Fujimoto and Y. Yu, *Elsevier Sci.*, 1993, **77**, 393–396.

7 T. Inui, H. Hara, T. Takeguchi and J. B. Kim, *Catal. Today*, 1997, **36**, 25–32.

8 S. K. Sharma, T. S. Khan, R. K. Singha, B. Paul, M. K. Poddar, T. Sasaki, A. Bordoloi, C. Samanta, S. Gupta and R. Bal, *Appl. Catal. A Gen.*, 2021, **623**, 118239.

9 N. Nomura, T. Tagawa and S. Goto, *React. Kinet. Catal. Lett.*, 1998, **63**, 21–25.

10 M. Behrens, S. Zander, P. Kurr, N. Jacobsen, J. Senker, G. Koch, T. Ressler, R. W. Fischer and R. Schlögl, *J. Am. Chem. Soc.*, 2013, **135**, 6061–6068.

11 S. Kuld, M. Thorhauge, H. Falsig, C. F. Elkjær, S. Helveg, I. Chorkendorff and J. Sehested, *Science*, 2016, **352**, 969–974.

12 J. Schittkowski, H. Ruland, D. Laudenschleger, K. Girod, K. Kähler, S. Kaluza, M. Muhler and R. Schlögl, *Chemie-Ingenieur-Technik*, 2018, **90**, 1419–1429.

13 P. Gao, R. Xie, H. Wang, L. Zhong, L. Xia, Z. Zhang, W. Wei and Y. Sun, *J. CO2 Util.*, 2015, **11**, 41–48.

14 D. Laudenschleger, H. Ruland and M. Muhler, *Nat. Commun.*, 2020, **11**, 3898–3907.

15 M. K. Koh, M. Khavarian, S. P. Chai and A. R. Mohamed, *Int. J. Hydrogen Energy*, 2018, **43**, 9334–9342.

16 M. M. J. Li, C. Chen, T. Ayvall, H. Suo, J. Zheng, I. F. Teixeira, L. Ye, H. Zou, D. O'Hare and S. C. E. Tsang, *ACS Catal.*, 2018, **8**, 4390–4401.

17 W. L. J. Kwok, D.-G. Crivoi, C. Chen, J.-C. Buffet and D. O'Hare, *Dalton Trans.*, 2018, **47**, 143–149.

18 C. Chen, R. Felton, J.-C. Buffet and D. O'Hare, *Chem. Commun.*, 2015, **51**, 3462–3465.

19 T. W. Kim, P. W. Chung and V. S. Y. Lin, *Chem. Mater.*, 2010, **22**, 5093–5104.

20 Z. Qiao, Z. Wang, C. Zhang, S. Yuan, Y. Zhu and J. Wang, *AIChE J.*, 2010, **56**, 2934–2945.

21 G. S. Pawley, *J. Appl. Crystallogr.*, 1981, **14**, 357–361.

22 C. Chen, C. F. H. Byles, J.-C. Buffet, N. H. Rees, Y. Wu and D. O'Hare, *Chem. Sci.*, 2016, **7**, 1457–1461.

23 F. Cavani, F. Trifirò and A. Vaccari, *Catal. Today*, 1991, **11**, 173–301.

24 R. E. Dinnebier, A. Leineweber and John S. O. Evans., *Rietveld Refinement Practical Powder Diffraction Pattern Analysis using TOPAS*, De Gruyter, 1st edn., 2018.

25 A. S. Bookin, V. I. Cherkashin and V. A. Drits, *Clays Clay Miner.*, 1993, **41**, 558–564.

26 A. S. Bookin and V. A. Drits, *Clays Clay Miner.*, 1993, **41**, 551–557.

27 A. V. Radha, P. V. Kamath and C. Shivakumara, *Acta Crystallogr. Sect. B Struct. Sci.*, 2007, **63**, 243–250.

28 B. Pradhan and S. K. Srivastava, *Compos. Part A Appl. Sci. Manuf.*, 2014, **56**, 290–299.

29 H. Suo, H. Duan, C. Chen, J.-C. Buffet and D. O'Hare, *RSC Adv.*, 2019, **9**, 3749–3754.

30 L. B. Staal, S. S. Charan Pushparaj, C. Forano, V. Prevot, D. B. Ravnsbæk, M. Bjerring and U. G. Nielsen, *J. Mater. Chem. A*, 2017, **5**, 21795–21806.

31 S. S. C. Pushparaj, C. Forano, V. Prevot, A. S. Lipton, G. J. Rees, J. V. Hanna and U. G. Nielsen, *J. Phys. Chem. C*, 2015, **119**, 27695–27707.

32 S. Ramadan, T. W. Hambley, B. J. Kennedy and P. A. Lay, *Inorg. Chem.*, 2004, **43**, 2943–2946.

33 A. J. Pell, G. Pintacuda and C. P. Grey, *Prog. Nucl. Magn. Reson. Spectrosc.*, 2019, **111**, 1–271.

34 S. K. Matam, A. J. O'Malley, C. R. A. Catlow, Suwardiyanto, P. Collier, A. P. Hawkins, A. Zachariou, D. Lennon, I. Silverwood, S. F. Parker and R. F. Howe, *Catal. Sci. Technol.*, 2018, **8**, 3304–3312.

35 A. A. Romero, M. D. Alba and J. Klinowski, *J. Phys. Chem. B*, 1998, **102**, 123–128.

36 Robert Strachan, Master thesis, University of Oxford, 2019.

37 J. Beardmore, X. Lopez, J. I. Mujika and C. Exley, *Sci. Rep.*, 2016, **6**, 1–8.

38 J. M. Campelo, D. Luna, R. Luque, J. M. Marinas, A. A. Romero, J. J. Calvino and M. P. Rodríguez-Luque, *J. Catal.*, 2005, **230**, 327–338.

39 G. A. Eimer, L. B. Pierella, G. A. Monti and O. A. Anunziata, *Catal. Letters*, 2002, **78**, 65–75.

40 N. D. Jensen, N. T. Duong, R. Bolanz, Y. Nishiyama, C. A. Rasmussen, J. Gottlicher, R. Steininger, V. Prevot and U. G. Nielsen, *Inorg. Chem.*, 2019, **58**, 6114–6122.

41 K. Chen, M. Abdolrhamani, E. Sheets, J. Freeman, G. Ward and J. L. White, *J. Am. Chem. Soc.*, 2017, **139**, 18698–18704.

42 M. Wang, G. Yu, W. Ji, L. Li, W. Ding and L. Peng, *Chem. Phys. Lett.*, 2015, **627**, 7–12.

43 R. P. Ye, L. Lin, C. C. Chen, J. X. Yang, F. Li, X. Zhang, D. J. Li, Y. Y. Qin, Z. Zhou and Y. G. Yao, *ACS Catal.*, 2018, **8**, 3382–3394.

44 S. O. Akpotu and B. Moodley, *J. Mol. Liq.*, 2018, **261**, 540–549.

45 L. Zhang, F. Li, D. G. Evans and X. Duan, *Mater. Chem. Phys.*, 2004, **87**, 402–410.

46 V. Rives and S. Kannan, *J. Mater. Chem.*, 2000, **10**, 489–495.

47 S. Velu and C.S.Swamy, *J. Mater. Sci. Lett.*, 1996, **15**, 1674–1677.

48 A. Alejandre, F. Medina, P. Salagre, X. Correig and J. E. Sueiras, *Chem. Mater.*, 1999, **11**, 939–948.

49 F. Jing, Y. Zhang, S. Luo, W. Chu and W. Qian, *Appl. Clay Sci.*, 2010, **48**, 203–207.

50 J. G. Nunan, P. B. Himelfarb, R. G. Herman, K. Klier, C. E. Bogdan and G. W. Simmons, *Inorg. Chem.*, 1989, **28**, 3868–3874.

51 P. J. Sideris, U. G. Nielsen, Z. Gan and C. P. Grey, *Science*, 2008, **321**, 113–117.

52 J. Wang, Y. Wei and J. Yu, *Appl. Clay Sci.*, 2013, **72**, 37–43.

53 A. Doyle and B. K. Hodnett, *Microporous Mesoporous Mater.*, 2003, **63**, 53–57.

54 H. Suo, H. Duan, C. Chen, J. C. Buffet and D. O'Hare, *RSC Adv.*, 2019, **9**, 3749–3754.

55 M. Thommes, K. Kaneko, A. V. Neimark, J. P. Olivier, F. Rodriguez-Reinoso, J. Rouquerol and K. S. W. Sing, *Pure Appl. Chem.*, 2015, **87**, 1051–1069.

56 J. B. Condon, in *Surface Area and Porosity Determinations by Physisorption*, ed. J. B. Condon, Elsevier Science, Amsterdam, 2006, pp. 1–27.

57 L. Wang, L. Xing, J. Liu, T. Qi, S. Zhang, Y. Ma and P. Ning, *Chem. Eng. J.*, 2021, **407**, 127210–127219.

58 P. M. Carraro, B. S. Goldani, D. Alves, A. Gabriel Sathicq, G. A. Eimer, G. P. Romanelli and R. Luque, *Catalysts*, 2019, **9**, 1–13.

59 J. T. Tompkins and R. Mokaya, *ACS Appl. Mater. Interfaces*, 2014, **6**, 1902–1908.

60 C. Ye, M. Q. Wang, S. J. Bao and C. Ye, *ACS Appl. Mater. Interfaces*, 2019, **11**, 30887–30893.

61 H. Suo, C. Chen, J.-C. Buffet and D. O'Hare, *Dalton Trans.*, 2018, **47**, 16413–16417.

62 M. Lyu, C. Chen, J. C. Buffet and D. O'Hare, *New J. Chem.*, 2020, **44**, 10095–10101.

63 R. Li, T. Xue, R. Bingre, Y. Gao, B. Louis and Q. Wang, *ACS Appl. Mater. Interfaces*, 2018, **10**, 34834–34839.

64 J. Labuschagn, D. Molefe, W. W. Focke and O. Ofosu, *Macromol. Symp.*, 2019, **384**, 1–10.

65 H. W. Olfs, L. O. Torres-Dorante, R. Eckelt and H. Kosslick, *Appl. Clay Sci.*, 2009, **43**, 459–464.

66 P. Kenyon and D O'Hare, unpublished work.

67 B. K. Kim, G. H. Gwak, T. Okada and J. M. Oh, *J. Solid State Chem.*, 2018, **263**, 60–64.

68 H. Chen, H. Zhang, Y. Zhang, Y. Wang, X. Su, L. Zhang and Z. Lin, *Chem. Eng. J.*, 2019, **375**, 1–8.

69 S. Kandula, K. R. Shrestha, G. Rajeshkhanna, N. H. Kim and J. H. Lee, *ACS Appl. Mater. Interfaces*, 2019, **11**, 11555–11567.

70 X. Sun and S. K. Dey, *J. Colloid Interface Sci.*, 2015, **458**, 160–168.

71 A. Benhamou, J. P. Basly, M. Baudu, Z. Derriche and R. Hamacha, *J. Colloid Interface Sci.*, 2013, **404**, 135–139.

72 J. Antonio, A. Júnior, J. B. Baldo, D. De Materiais, U. Federal, D. S. Carlos and S. Carlos, *New J. Glas. Ceram.*, 2014, **4**, 29–37.

73 K. Bensadok, S. Benammar, F. Lapicque and G. Nezzal, *J. Hazard. Mater.*, 2008, **152**, 423–430.

74 L. Hidmi and M. Edwards, *Environ. Sci. Technol.*, 1999, **33**, 2607–2610.

75 A. Degen and M. Kosec, *J. Eur. Ceram. Soc.*, 2000, **20**, 667–673.

76 A. Krężel and W. Maret, *Arch. Biochem. Biophys.*, 2016, **611**, 3–19.

77 M. Behrens, F. Studt, I. Kasatkin, S. Kühl, M. Hävecker, F. Abild-pedersen, S. Zander, F. Girgsdies, P. Kurr, B. Kniep, M. Tovar, R. W. Fischer, J. K. Nørskov and R. Schlögl, *Science*, 2012, **336**, 893–898.

78 F. Zhang, X. Xu, Z. Qiu, B. Feng, Y. Liu, A. Xing and M. Fan, *Green Energy Environ.*, , DOI:10.1016/j.gee.2020.11.027.

79 B. Hu, Y. Yin, Z. Zhong, D. Wu, G. Liu and X. Hong, *Catal. Sci. Technol.*, 2019, **9**, 2673–2681.

80 K. Xiao, Q. Wang, X. Qi and L. Zhong, *Catal. Letters*, 2022, **147**, 1581–1591.

81 F. J. Sotomayor, K. A. Cychosz and M. Thommes, *Acc. Mater. Surf. Res*, 2018, **3**, 34–50.

82 J. Kuljiraseth, A. Wangriya, J. M. C. Malones, W. Klysubun and S. Jitkarnka, *Appl. Catal. B Environ.*, 2019, **243**, 415–427.

83 Z. Shen, T. Ma, L. Fei, A. Li, J. Liu, Z. Xu, X. Hu and Y. Sun, *ACS EST Engg.*, 2021, **1**, 989–999.

84 O. B. Belskaya, N. N. Leont'Eva, T. I. Gulyaeva, S. V. Cherepanova, V. P. Talzi, V. A. Drozdov and V. A. Likholobov, *Russ. Chem. Bull.*, 2013, **62**, 2349–2361.

85 A. Azzouz, V. A. Aruş, N. Platon, K. Ghomari, I. D. Nistor, T. C. Shiao and R. Roy, *Adsorption*, 2013, **19**, 909–918.

86 D. Li, S. Xu, Y. Cai, C. Chen, Y. Zhan and L. Jiang, *Ind. Eng. Chem. Res.*, 2017, **56**, 3175–3183.

87 J. Li, S. Zhang, Y. Chen, T. Liu, C. Liu, X. Zhang, M. Yi, Z. Chu and X. Han, *RSC Adv.*, 2017, **7**, 29051–29057.

88 Z. P. Xu, J. Zhang, M. O. Adebajo, H. Zhang and C. Zhou, *Appl. Clay Sci.*, 2011, **53**, 139–150.

89 R. D. Shannon, *Acta Cryst.*, 1976, **A32**, 751–767.

90 P. Ma, Z. Xiao, S. Jin, C. Li and C. Liang, *J. Energy Chem.*, 2016, **25**, 782–792.

91 P. Gherardi, O. Ruggeri, F. Trifiro, A. Vaccari, G. Del Piero, G. Manara and A. Notari, *Stud. Surf. Sci. Catal.*, 1983, **16**, 723–733.

92 C. Busetto, G. Del Piero, G. Manara, F. Trifirò and A. Vaccari, *J. Catal.*, 1984, **85**, 260–266.

93 E. B. M. Doesburg, R. H. Höppener, B. De Koning, X. Xiaoding and J. J. F. Scholten, *Stud. Surf. Sci. Catal.*, 1987, **31**, 767–783.

94 S. Gusi, F. Pizzoli, F. Trifiro, A. Vaccari and G. Del Piero, *Stud. Surf. Sci. Catal.*, 1987, **31**, 753–765.

95 J. L. Jambor, *Can. Mineral.*, 1964, **8**, 92.

96 M. Behrens and F. Girgsdies, *Zeitschrift fur Anorg. und Allg. Chemie*, 2010, **636**, 919–927.

97 J. T. Kloprogge, L. Hickey and R. L. Frost, *J. Raman Spectrosc.*, 2004, **35**, 967–974.

98 T. Tanaka, Y. Kameshima, S. Nishimoto and M. Miyake, *Anal. Methods*, 2012, **4**, 3925–3927.

99 L. Berzina-Cimdina and N. Borodajenko, in *Infrared Spectroscopy - Materials Science, Engineering and Technology*, ed. T. Theophile, IntechOpen, 2012, pp. 123–148.

100 M. E. Böttcher, P.-L. Gehlken, H. Skogby and C. Reutel, *Mineral. Mag.*, 1997, **61**, 249–256.

101 R. C. Zeng, X. T. Li, Z. G. Liu, F. Zhang, S. Q. Li and H. Z. Cui, *Front. Mater. Sci.*, 2015, **9**, 355–365.

102 A. M. Cardinale, C. Carbone, S. Consani, M. Fortunato and N. Parodi, *Crystals*, 2020, **10**, 1–9.

103 C. Chen, A. Wangriya, J. C. Buffet and D. O'Hare, *Dalton Trans.*, 2015, **44**, 16392–16398.

104 Center Catalysts Group Business Office and R&D, *PQ Corporation-Silica support*, Conshohocken, 2018.

105 W. L. J. Kwok, DPhil thesis, University of Oxford, 2020.

106 C. Chen, R. Felton, J. C. Buffet and D. O'Hare, *Chem. Commun.*, 2015, **51**, 3462–3465.

107 M. Martínez-Carmona, Y. K. Gun'ko and M. Vallet-Regí, *Pharmaceutics*, 2018, **10**, 1–29.

108 L. Angiolini, B. Cohen and A. Douhal, *Int. J. Mol. Sci.*, 2019, **20**, 9–12.

109 T. M. Yurieva, G. N. Kustova, T. P. Minyukova, E. K. Poels, A. Bliek, M. P. Demeshkina, L. M. Plyasova, T. A. Krieger and V. I. Zaikovskii, *Mater. Res. Innov.*, 2001, **5**, 3–11.

110 G. Dong, G. Tian, L. Gong, Q. Tang, M. Li, J. Meng and J. Liang, *Microporous Mesoporous Mater.*, 2020, **305**, 110352–110361.

111 J. Qu, C. Y. Cao, Y. L. Hong, C. Q. Chen, P. P. Zhu, W. G. Song and Z. Y. Wu, *J. Mater. Chem.*, 2012, **22**, 3562–3567.

112 M. Segad, B. Jönsson, T. Åkesson and B. Cabane, *Langmuir*, 2010, **26**, 5782–5790.

113 M. Claverie, A. Dumas, C. Carême, M. Poirier, C. Le Roux, P. Micoud, F. Martin and C. Aymonier, *Chem. - A Eur. J.*, 2018, **24**, 519–542.

114 D. Gournis, A. Lappas, M. A. Karakassides, D. Többens and A. Moukarika, *Phys. Chem. Miner.*, 2008, **35**, 49–58.

115 S. Greiser, M. Hunger and C. Jäger, *Solid State Nucl. Magn. Reson.*, 2016, **79**, 6–10.

116 R. Van Den Berg, G. Prieto, G. Korpershoek, L. I. Van Der Wal, A. J. Van Bunningen, S. Lægsgaard-Jørgensen, P. E. De Jongh and K. P. De Jong, *Nat. Commun.*, 2016, **7**, 1–7.

117 Z. Q. Wang, Z. N. Xu, S. Y. Peng, M. J. Zhang, G. Lu, Q. S. Chen, Y. Chen and G. C. Guo, *ACS Catal.*, 2015, **5**, 4255–4259.

Chapter 4 Evaluation of porous SiO_2@Cu_xZnAl-CO_3-LDH for catalytic hydrogenation of CO_2 to methanol

4.1 Introduction

ZnO, Al_2O_3 and SiO_2 are widely used as the promoter and support for Cu-based catalyst for CO_2 hydrogenation to methanol.[1] It has been reported that these oxides can enhance the catalytic activity and catalyst stability by promoting the dispersion of active copper sites,[2–4] adjusting the surface acidity and basicity,[2,3,5] and establishing synergy.[1,6]

Robinson *et al.* reported an improved methanol selectivity of Cu/ZnO/Al_2O_3 catalyst at higher ZnO contents.[7] Zhang *et al.* reported that the CO_2 conversion and MeOH selectivity increases with increased (Cu + ZnO) content in the Cu/ZnO/Al_2O_3 catalyst and reaches the maximum at the highest (Cu + ZnO) content, e.g. methanol selectivity increase from 33.6 to 56.5% when (Cu + ZnO) content raises from 9.94 to 44.50 wt%.[8] It is believed that the proportion of Cu, ZnO and Al_2O_3 in the Cu/ZnO/Al_2O_3 catalysts will affect their catalytic performance.

Moreover, the morphology (e.g. pore structure) of SiO_2 or Al_2O_3 support has an impact on the property of catalyst.[7,9,10] Witoon *et al.* reported that supporting copper with a hierarchical meso-macroporous alumina achieves superior MeOH selectivity and much higher stability than the one supported on the unimodal mesoporous alumina. This enhancement was attributed to the more effective diffusion of reactants and products.[7]

In this chapter, catalysts derived from ES757@Cu_xZnAl-LDH and mSiO_2@Cu_2ZnAl-LDH are evaluated in order to study the effect of copper loading and morphology of silica support on the

catalytic performance. Techniques such as H_2 titration (of N_2O oxidised samples) and transmission electron microscopy (TEM) are used to investigate the correlation between the catalytic activity and structural parameters (such as copper surface area and size of copper particles). Finally, the performance of developed core-shell catalysts is compared with the industrial standard and some lab-scale benchmark catalysts.

4.2 The effect of Cu loading on ES757@Cu$_x$ZnAl-CO$_3$-LDH derived catalysts

4.2.1. Activation of ES757@Cu$_x$ZnAl-LDH

Activation of ES757@Cu$_x$ZnAl-LDH core-shells includes converting LDH into oxides via calcination and reducing the copper oxide to metallic copper with hydrogen.[11] Core-shells were calcined at 330 °C for 4 hours with 50 mL/min air flow under atmospheric pressure to remove hydroxyl group and carbonate anions. The obtained products are named as ES757@Cu$_x$ZnAl-LDO core-shell (x referring to the Cu/Al ratio) and are amorphous as confirmed by XRD (Figure 4.1a). The oxidation state of copper in ES757@Cu$_x$ZnAl-LDH and ES757@Cu$_x$ZnAl-LDO are the same (equal to +2).

FTIR was used to study the change of composition before and after calcination. All ES757@Cu$_x$ZnAl-LDO displays a similar FTIR spectra (Figure C1), exhibiting 750 cm^{-1} absorbance due to the M-O vibration and 1000 cm^{-1} absorbance arising from the Si-O vibration.[12] For clarity, only the spectra of ES757@Cu$_2$ZnAl-LDH and ES757@Cu$_2$ZnAl-LDO are shown in Figure 4.1b. In ES757@Cu$_2$ZnAl-LDO, the disappearance of the water bending absorbance (1600 cm^{-1}) and weakened O-H stretching band (3500 cm^{-1}) proves successful dehydration and dehydroxylation. Instead of a sharp band at 1350 cm^{-1}, the LDO composite

possesses a doublet at 1390 cm^{-1} and 1500 cm^{-1} due to the $\nu 3$ mode of carbonate with the reduced symmetry.[13,14] It is known that calcination at 330 °C only partly removes the carbonate in the LDH. The doublet confirms the presence of residual carbonate. Besides, a weak and broad shoulder at 2500 cm^{-1} occurs due to the adsorption of atmospheric CO_2 occurs during the measurement.[15]

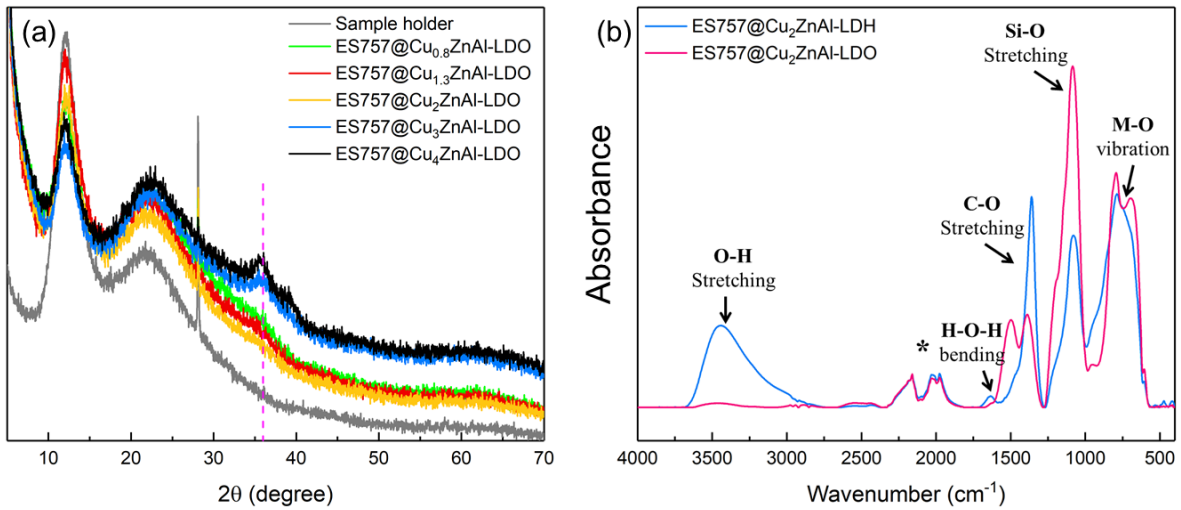


Figure 4.1 (a) XRD plots of ES757@Cu_xZnAl-LDO (calcined ES757@Cu_xZnAl-LDH at 330 °C for 4 h). Amorphous peak in XRD is highlighted with purple dash line. (b) FTIR absorbance spectra of ES757@Cu_2ZnAl-LDH and ES757@Cu_2ZnAl-LDO.

The temperature-programmed reduction with H_2 (H_2-TPR) was conducted on the fresh ES757@Cu_xZnAl-LDO to investigate the appropriate reduction temperature (for converting CuO to metallic Cu) and the dispersion of copper in the core-shell. It is known that even at temperature as high as 600 °C, ZnO and Al_2O_3 will not be reduced by H_2..[16,17] Signals recorded between 75–340 °C should correspond to the reduction of Cu moieties (Figure 4.2a). As expected, the amount of H_2 consumed (the peak integration) increases as the Cu/Al ratio increases. All composites finish their reduction below 280 °C, which is lower than the reduction temperature of bulk CuO (340–475 °C).[18] Many authors attributed the decreased reduction

temperature to well-dispersed CuO species.[11,16,18,19] For example, Shen *et al.* compared the reproducibility of CuO species from the decomposition of pure copper nitrate, copper nitrate that wet impregnated to ZnO and Al_2O_3 and CuZnAl LDH; they noted that well-dispersed CuO species requires lower reduction temperature, i.e., CuO species derived from CuZnAl LDH only need 230 °C while that from Cu impregnated ZnO/Al_2O_3 and pure copper nitrate need 327 °C and 475 °C, respectively.[19] They concluded that the LDH framework and core-shell structure facilitate the dispersion of copper.

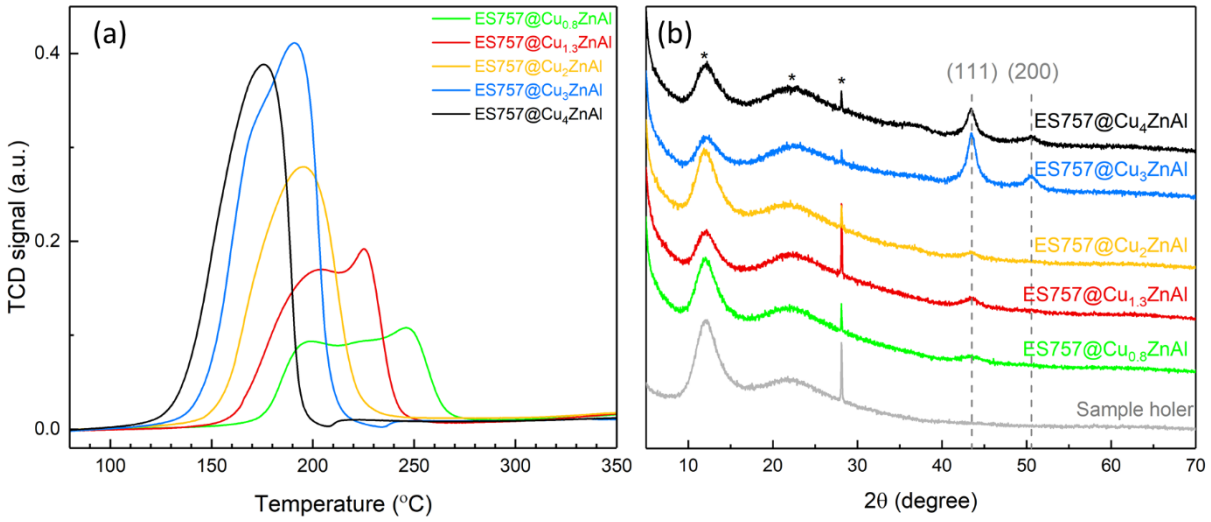


Figure 4.2 (a) Temperature-programmed reduction profile of ES757@Cu_xZnAl-LDO. (b) XRD profiles of ES757@Cu_xZnAl catalyst (hydrogen reduced ES757@Cu_xZnAl-LDO at 290 °C for 2 h), features marked with * are from the sample holder.

Interestingly, the reduction temperature shifts to a lower value as the Cu content increases. Several literature studies have reported that the smaller (or also called better dispersed) the copper particles, the lower the required reduction temperature.[11,16] Hajduk *et al.* calculated the crystallite size of metallic copper after hydrogen reduction and noted that larger copper crystallite requires higher reduction temperature.[16] The conclusion from the literature is in contrast to the observation in this study as the crystallite size of copper gets larger when the

overall copper loading raises (Table 4.1). It is possible that ZnO and Al_2O_3 stabilise surrounding copper and increase the reduction temperature;[18,20,21] when copper is dominant in the core-shell, this stabilising effect is negligible.

Noteworthy, core-shells with low copper loading exhibit more complex and broader H_2 reduction peaks (Figure 4.2a), indicating multiple Cu environments in the material or various particle sizes of copper. Sisani *et al.* suggested that copper may incorporate with alumina or zinc oxide in the Cu/ZnO/Al_2O_3 mixture to give multiple phases.[18] Schlőgl *et al.* presented that the Cu-ZnO_x species is formed under the reducing conditions due to the strong metal supporting interaction (SMSI) between Cu and ZnO.[22] It is possible that the Al and Zn abundant core-shell may have various copper environments, which is consistent with the high reduction temperature at low copper loading.

Based on the H_2-TPR result, ES757@Cu_xZnAl-LDO intermediates was reduced at 290 °C for 2 hours with 20 mL/min H_2/N_2 (10:90 by volume) flow at 1 bar to ensure a sufficient activation of the catalyst. The fresh catalyst is termed as ES757@Cu_xZnAl. The oxidation state of copper in ES757@Cu_xZnAl is zero.

XRD profiles in Figure 4.2b shows that Cu(111) and Cu(200) Bragg reflections are noticed in all catalysts indicating that metallic Cu are formed in all samples. The intensity of reflections increases as the Cu content raises. The crystallite domain size of copper is worked out via Rietveld refinement (details in Table C1). As expected, high copper loading leads to large copper crystallites (Table 4.1).

The ICP-OES results signify that the composition of core-shell catalyst is close to the expectation (Table 4.1). A minor amount of carbon is detected due to the incomplete decarbonation of LDH after calcining 330 °C and reducing at 290 °C. A trace amount of hydrogen is found because water was adsorbed/absorbed when the sample was exposed to the air.

Table 4.1 The theoretical Cu/Al ratio, the molar amount of elements in ES757@Cu_xZnAl obtained from ICP-OES and CHN (normalised by the molar amount of Al), the consumed H_2 amount during H_2-TPR measurement and the crystal domain size of copper in the catalysts.

Theo.[a]	Cu	Zn	Al	C	H	H_2 (mmol/g)	CDL of Cu (nm)[b]
0.80	0.89	1.04	1.00	0.32	1.72	2.01	1.24
1.30	1.43	1.03	1.00	0.39	2.05	3.16	1.82
2.00	2.16	1.02	1.00	0.40	2.56	4.10	2.24
3.00	3.10	0.94	1.00	0.27	2.70	4.85	5.79
4.00	4.14	0.91	1.00	0.41	3.56	5.07	5.73

a: the theoretical Cu/Al ratio based on the amount of copper and aluminium nitrate in the co-precipitation. b: the crystallite domain size (CDL) is obtained from the Rietveld refinement.

No significant difference associated with the different copper fractions is observed in the FTIR spectra of ES757@Cu_xZnAl (Figure C2). The spectrum of ES757@Cu_2ZnAl catalyst is almost the same as that of the LDO composite as reducing LDO at a low temperature (290 °C) cannot achieve a further decarboxylation. The appearance of carbonate stretching band is consistent with the fact that carbon element is detected in the elemental analysis.

After calcination, LDH was transformed to an amorphous layered double oxide with a more porous structure, as revealed by TEM images (Figure 4.3a, d and Figure C3a–c). However, this porous structure does not bring a significant increase in the BET specific surface area and the total pore volume; the enhancement in the surface area and total pore volume is within 4–14%

and 4–10%, respectively (Figure C4).

Once the ES757@Cu$_x$ZnAl-LDO is reduced to afford the ES757@Cu$_x$ZnAl catalyst, the surface area and total pore volume decrease due to the collapse of the porous oxide structure. Spherical particles, which should be copper and zinc oxide nanoparticles, are generated (Figure 4.3b, e and Figure C3d–f).[11,22] The core-shell structure remains in catalyst ES757@Cu$_x$ZnAl, and the shell morphology is identical to that of the LDH precursor (Figure 4.3c,f, Figure C3g–I and Figure C5).

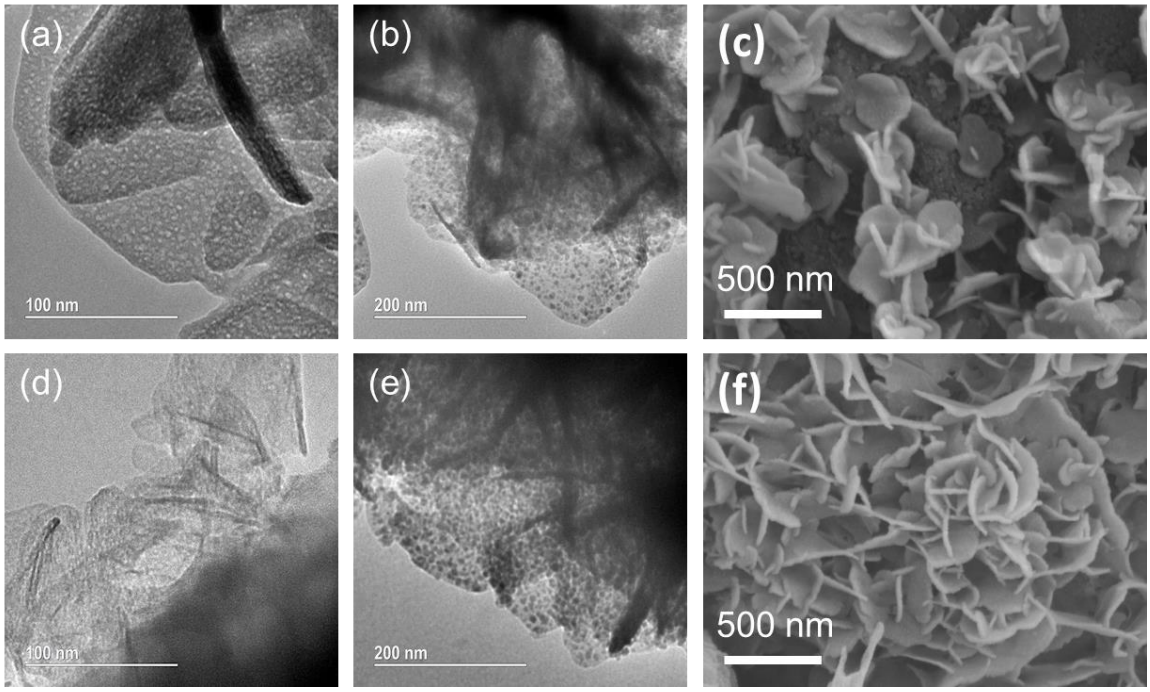


Figure 4.3 TEM images of (a) ES757@Cu$_{1.3}$ZnAl-LDO, (b) ES757@Cu$_{1.3}$ZnAl, (d) ES757@Cu$_2$ZnAl-LDO and (e) ES757@Cu$_2$ZnAl. HR-SEM images showing the shell of (c) ES757@Cu$_{1.3}$ZnAl and (f) ES757@Cu$_2$ZnAl.

ES757@Cu$_x$ZnAl catalysts exhibit the same N_2 isotherm as their precursor, type II adsorption isotherm with a H2b hysteresis loop, which is also identical to that of ES757 (Figure C6). BJH pore size distribution demonstrates that the catalyst also has similar pore structure as their LDH precursor (Figure C6). Except ES757@Cu$_4$ZnAl, ES757@Cu$_x$ZnAl catalysts have higher

surface area and larger pore volume than their LDH precursor due to a more defective structure after the calcination and hydrogen reduction (Figure 4.4).

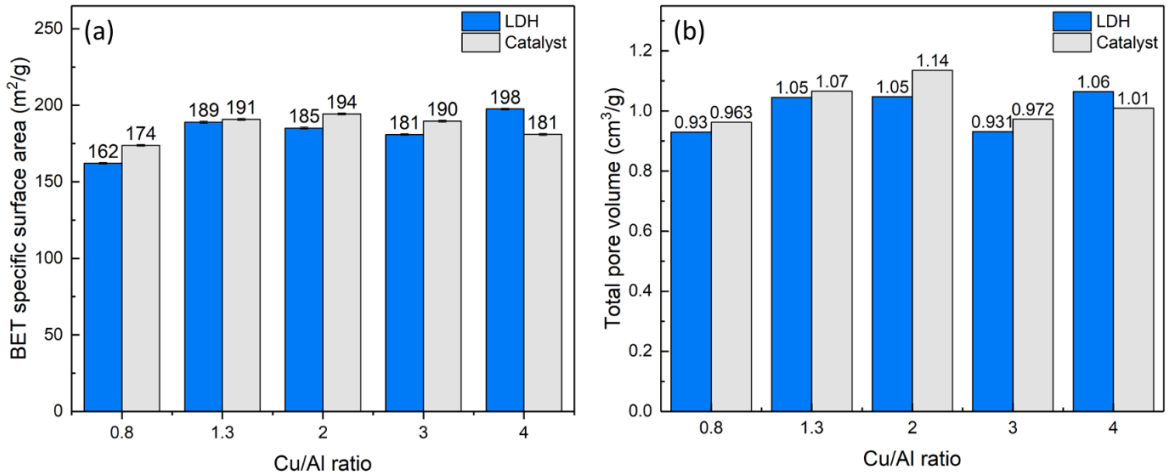


Figure 4.4 (a) The BET specific surface area and (b) the total pore volume of ES757@Cu$_x$ZnAl-LDH and ES757@Cu$_x$ZnAl catalyst, where x = Cu/Al ratio.

4.2.2. Catalytic performance and copper dispersion of ES757@Cu$_x$ZnAl

In the literature, the CO_2 to methanol catalyst evaluation is normally conducted at 150–320 °C under 25–50 bar with a mixture of H_2/CO_2 (molar ratio 3:1).[23] A previous work reported by our group shows that the Cu/ZnO/Ga_2O_3 catalyst derived from AMO-LDH displays an outstanding space time yield (STY) of methanol at 270 °C under 45 bar with a mixture of H_2/CO_2 (molar ratio 3:1). Therefore, the catalytic performance of ES757@Cu$_x$ZnAl (x = 0.8–4) towards MeOH production via CO_2 hydrogenation were evaluated between 230–350 °C under the same conditions (45 bar, H_2/CO_2 = 3:1).

The CO_2 conversion is displayed in Figure 4.5a. The CO_2 conversion of catalysts with different copper loading shows a similar trend between 230–350 °C: increasing to the maximum conversion at 270 °C before decreasing as the temperature is further increased. ES757@Cu$_{1.3}$ZnAl reaches its maximum conversion rate during 270–310 °C; the lower than

expected conversion rate at 290 °C may result from a measurement error.

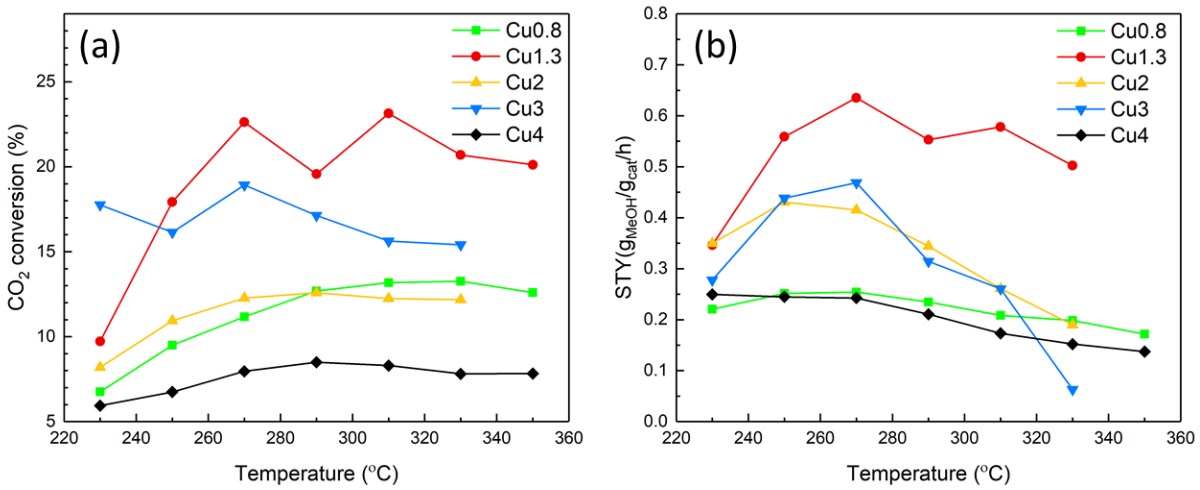


Figure 4.5 (a) CO_2 conversion and (b) space time yield of ES757@Cu_xZnAl catalyst, where x = Cu/Al molar ratio. Reaction condition: T = 230–350 °C, P = 45 bar, H_2: CO_2 (molar) = 3:1. WHSV = 18000 mL/$g_{catalyst}$/h. The name of catalyst is shortened to 'Cux' in the figure for clarity.

ES757@$Cu_{1.3}$ZnAl possesses the highest CO_2 conversion (23%) among all samples. It is noted that the highest transformation value between 230–350 °C following the order: ES757@$Cu_{1.3}$ZnAl > ES757@Cu_3ZnAl > ES757@$Cu_{0.8}$ZnAl ≥ ES757@Cu_2ZnAl > ES757@Cu_4ZnAl. No obvious relationship can be found between the copper content and the converted CO_2 amount. Stangeland *et al.* conducted a computational thermodynamic analysis on the CO_2 hydrogenation to methanol reaction; they proposed that the equilibrium conversion of CO_2 is around 25% under 50 bar and 22% under 30 bar between 275–300 °C.[24] The CO_2 conversion of ES757@$Cu_{1.3}$ZnAl at 270 °C under 45 bar should be very close to the equilibrium value at that condition.

Carbon monoxide is the only by-product that is found in the reaction. CO is generated via the reverse water gas shift (RWGS) that reaction,[24,25] the equation of which is shown in eq 3.1.

$$CO_2 + H_2 \rightleftharpoons CO + H_2O \qquad \Delta H^0_{273k} = 41.2 \text{ kJ/mol} \tag{3.1}$$

At 230 °C, the selectivity of methanol is over 50% for all ES757@Cu$_x$ZnAl catalysts and reaches up to 75% for ES757@Cu$_3$ZnAl (Figure C7a). However, the endothermic RWGS becomes more predominant at high temperatures which leads to an increased CO selectivity and a decreased methanol selectivity (Figure C7).[24] The falling slope seems to be steadier at low copper content. At Cu/Al = 0.8 and 1.3, the difference in the methanol selectivity between the lowest and highest reaction temperature is 24–30%, while for the other samples, the value reaches 40–70%. It is proposed that ES757@Cu$_x$ZnAl with Cu/Al ≥ 2 is less favoured to be used at high temperatures.

The space-time yield (STY) of methanol reaches a maximum at low temperature, 250–270 °C. Further raising the reaction temperature ends up with a lowered methanol yield (Figure 4.5b). This is mainly due to the dropped methanol selectivity at high temperatures. The highest STY (0.64 $g_{MeOH}/g_{catalyst}/h$) is obtained by using ES757@Cu$_{1.3}$ZnAl at 270 °C.

The catalytic performance at 270 °C of core-shell catalysts is compared and presented in Figure 4.6. As the Cu/Al ratio raises, the STY increases to its maximum at Cu/Al = 1.3 and then decreases. The trade-off between the CO_2 conversion and methanol selectivity results in ES757@Cu$_{0.8}$ZnAl and ES757@Cu$_4$ZnAl having a similar yield. Likewise, the STY of ES757@Cu$_2$ZnAl (0.43 $g_{MeOH}/g_{catalyst}/h$) and ES757@Cu$_3$ZnAl (0.47 $g_{MeOH}/g_{catalyst}/h$) are almost identical.

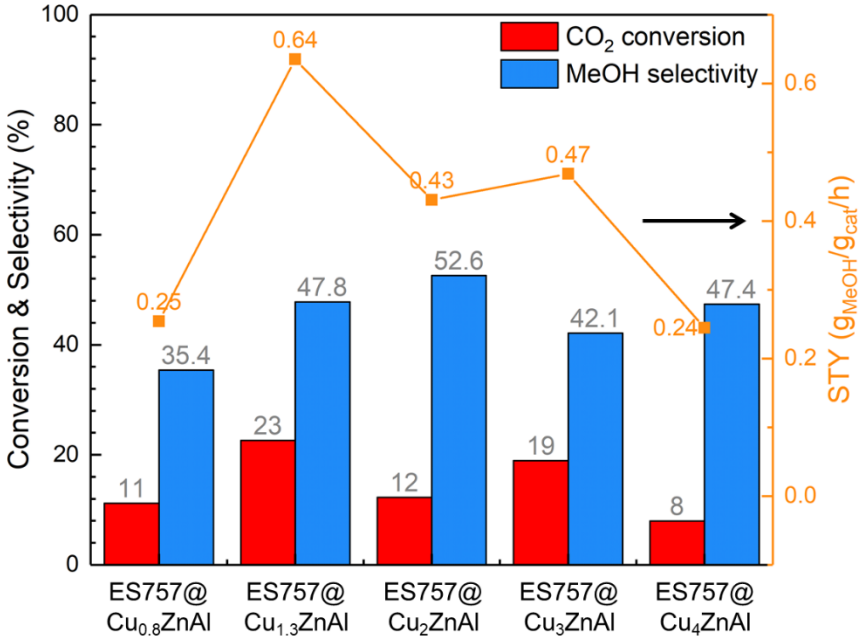


Figure 4.6 The CO_2 conversion, methanol selectivity and STY of ES757@Cu_xZnAl for CO_2 hydrogenation to methanol at 270 °C.

Figure 4.7 displays the catalytic performance of ES757@$Cu_{1.3}$ZnAl and the catalyst derived from unsupported $Cu_{1.3}$ZnAl-LDH (named as $Cu_{1.3}$ZnAl-catalyst). ES757@$Cu_{1.3}$ZnAl exhibits a better MeOH yield than unsupported catalyst due to its superior CO_2 transformation rate.

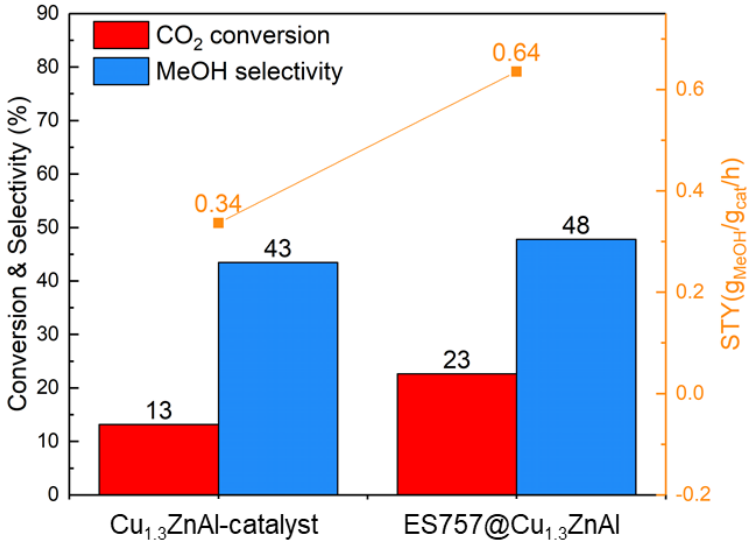


Figure 4.7 The CO_2 conversion, methanol selectivity and STY of $Cu_{1.3}$ZnAl-catalyst and ES757@$Cu_{1.3}$ZnAl for CO_2 hydrogenation to methanol at 270 °C.

Reasons behind the varied catalytic ability have been investigated. Copper dispersion and

copper surface area (S_{cu}) are two main factors that affect the catalytic performance of Cu-based catalysts in methanol synthesis.[23] It is widely accepted that well-dispersed copper and large S_{cu} are associated with outstanding methanol yield.[23] N_2O chemisorption accompanied with hydrogen reduction was used to determine copper dispersion and copper surface area. The exposed metallic Cu in the catalyst was firstly oxidised by N_2O then reduced by the hydrogen. The quantity of exposed copper can be calculated from the amount of consumed hydrogen. The dispersion of copper is the fraction of exposed copper among the total copper.[26] The S_{cu} is the surface area occupied by the metallic copper.[27,28]

Table 4.2 shows that the unsupported $Cu_{1.3}ZnAl$-catalyst has higher Cu loading (33.01 wt%) than the ES757 supported one (19.81 wt%). However, the *ab*-plane stacking of LDH leads to a lower S_{cu} (23.05 $m^2/g_{catalyst}$ comparing to 32.14 $m^2/g_{catalyst}$ of ES757@$Cu_{1.3}ZnAl$). It is believed that the core-shell structure promotes the LDH dispersion exposing more copper at an even lower copper loading and leads to an excellent catalytic performance.

ES757@$Cu_{1.3}ZnAl$ exhibits the largest copper surface area among all core-shells (Table 4.2), which may be the reason for its highest methanol yield. The trend of methanol STY follows the trend of S_{cu}. Low STY is associated with the low copper surface area. Noteworthy, apart from copper surface area, the electronic structure is also matters. ES757@Cu_2ZnAl and ES757@Cu_4ZnAl have a similar copper surface area, 18.05 $m^2/g_{catalyst}$ and 16.94 $m^2/g_{catalyst}$, respectively. While the STY of ES757@Cu_4ZnAl (0.24 $g_{MeOH}/g_{catalyst}/h$) is only about 55% of that of ES757@Cu_4ZnAl (0.43 $g_{MeOH}/g_{catalyst}/h$). The Al_2O_3 and ZnO are the acidic and basic promoter in Cu/ZnO/Al_2O_3 catalyst, respectively.[9,23] The varied proportion of Al_2O_3 and ZnO

in ES757@Cu$_x$ZnAl catalysts will lead to different electronic structures.[9,23] On the other hand, it has been demonstrated that the reduction of ZnO_{1-x} moieties in Cu/ZnO/Al_2O_3 catalyst occurs during the S_{cu} measurement.[29–32] It is possible that the detected copper surface area has different composition at Cu/Al = 2 and 4, i.e., the fraction of Cu and ZnO_{1-x} changes.

Table 4.2 The Cu loading, crystallite domain length (CDL), Cu dispersion and Cu surface area of ES757@Cu$_x$ZnAl catalysts.

Sample	Cu loading (wt%)[a]	CDL of Cu (nm)[b]	Cu dispersion (%)[c]	S_{Cu} ($m^2/g_{catalyst}$)[c]	TOF[d] ($mol_{MeOH}/mol_{Cu}/s$)	STY ($g_{MeOH}/g_{catalyst}/h$)
ES757@$Cu_{0.8}$ZnAl	15.57	1.24	17.13	17.32	0.0052	0.25
ES757@$Cu_{1.3}$ZnAl	19.81	1.82	25.00	32.14	0.0071	0.64
ES757@Cu_2ZnAl	24.98	2.24	11.13	18.05	0.0085	0.43
ES757@Cu_3ZnAl	32.21	5.79	9.93	20.76	0.0080	0.47
ES757@Cu_4ZnAl	37.40	5.73	6.98	16.94	0.0052	0.24
$Cu_{1.3}$ZnAl-catalyst	33.01*		10.76	23.05	0.0053	0.34

*: Cu content is calculated from that of ES757@$Cu_{1.3}$ZnAl. a: Determined by the ICP-OES (except $Cu_{1.3}$ZnAl-catalyst). b: Obtained from the Rietveld refinement of the XRD pattern. c: Dispersion and specific surface area of metallic Cu is obtained from N_2O chemisorption results.[26–28] d: The turnover frequency for methanol production against the surface copper amount.

Recently, the de Jongh group has demonstrated the importance of the size of copper nanoparticles on the surface-specific catalytic ability towards methanol synthesis.[33] The surface-specific catalytic ability refers to the turnover frequency (TOF), representing the number of methanol molecules formed per surface copper atom per second.[11,33] The TOF of core-shell catalysts are listed in Table 4.2. ES757@Cu_2ZnAl has the highest TOF at 0.0085 $mol_{MeOH}/mol_{Cu}/s$. The TOF for CuZn-LDH derived methanol catalyst ranging from 0.0021–0.0083 $mol_{MeOH}/mol_{Cu}/s$.[6,14] Behrens *et al.* reported that Cu-based catalyst possesses a TOF between 0.0013 to 0.006 $mol_{MeOH}/mol_{Cu}/s$.[22,34–36] ES757@Cu$_x$ZnAl exhibits a moderate to high TOF value among the reported Cu-based catalysts.

The size of copper nanoparticles is always linked with the TOF. Van den Berg *et al.* noted that the TOF significantly dropped when the size of copper particles is below 8 nm because that small particles have no space to embed step-edge active sites.[33] This is consistent with the finding in this study. Figure 4.8 and Figure C8 shows the TEM images of core-shell catalysts and particle size distribution of copper, respectively. It is observed that ES757@Cu_2ZnAl has the largest copper particles (9.31 ± 2.48 nm). Particles in other catalysts are smaller than 8 nm. The outstanding TOF value of ES757@Cu_2ZnAl should be related to its large particle size.

It is seen that the uniformity of nanoparticles reduces at Cu/Al ≥ 3. Particle aggregation may be the cause of the diminished methanol yield at a high copper population. The superior catalytic performance of ES757@$Cu_{1.3}$ZnAl could be also due to the uniform and densely packed copper particles.

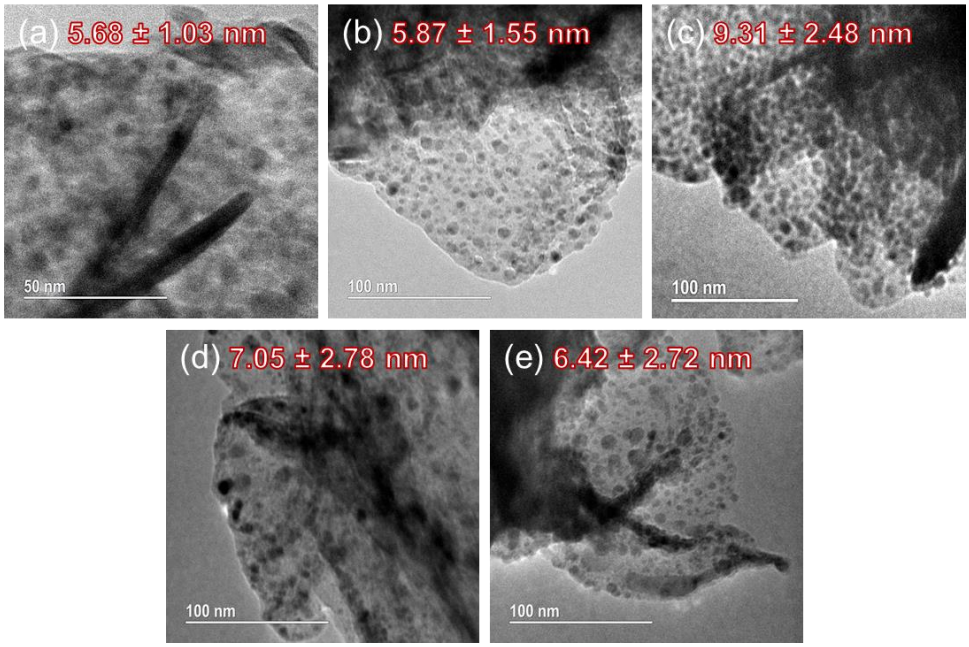


Figure 4.8 TEM images of (a) ES757@$Cu_{0.8}$ZnAl, (b) ES757@$Cu_{1.3}$ZnAl, (c) ES757@Cu_2ZnAl, (d) ES757@Cu_3ZnAl and (e) ES757@Cu_4ZnAl.

4.3 The effect of silica core on catalytic performance

To investigate the effect of silica property, the catalytic performance of catalysts derived from $mSiO_2$@Cu_2ZnAl-LDH ($mSiO_2$ = SBA-15, SBA-16, MCM-41 and MCM-48) were evaluated under 45 bar with a mixture of H_2/CO_2 (molar ratio 3:1) at 230–350 °C. The catalysts were obtained from the calcination (330 °C for 4 hours) and *in-situ* hydrogen reduction (290 °C for 2 hours) of $mSiO_2$@Cu_2ZnAl-LDH precursor and were named as $mSiO_2$@Cu_2ZnAl, where $mSiO_2$ is the precursor silica type.

The CO_2 conversion of all catalysts shows a clear increasing trend when the temperature is elevated from 230 °C to about 290 °C (Figure 4.9a). Further raising the reaction temperature does not change (either enhance or diminish) the CO_2 conversion significantly. The RWGS side reaction becomes more favourable at high temperature, leading to a dramatically reduced methanol selectivity at high temperature (Figure C9). Variation in the CO_2 conversion and product selectivity leads to the reduced methanol STY at a temperature higher than 290 °C (Figure 4.9b). The highest methanol STY is obtained by SBA-15@Cu_2ZnAl at 270 °C and is 0.76 $g_{MeOH}/g_{catalyst}/h$.

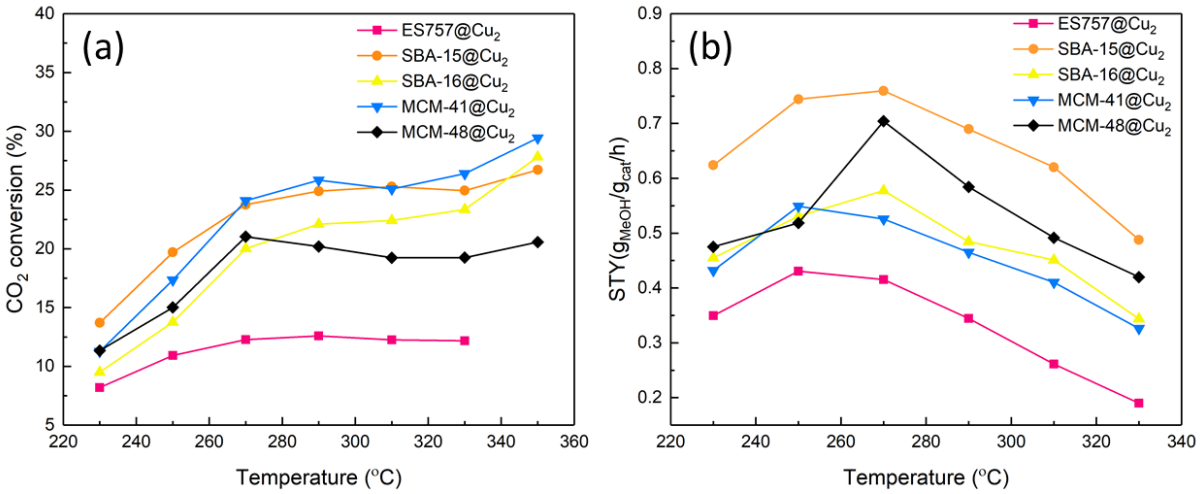


Figure 4.9 (a) CO_2 conversion and (b) space time yield of $mSiO_2@Cu_2ZnAl$. Reaction condition: T = 230–350 °C, P = 45 bar, H_2: CO_2 (molar) = 3:1. WHSV = 18000 mL/$g_{catalyst}$/h. The name of catalyst is shortened in the figure for clarity.

The CO_2 conversion and methanol selectivity at 270 °C are compared in Figure 4.10. It is seen that core-shell catalysts with SBA-15, SBA-16, MCM-41 and MCM-48 core have a similar CO_2 conversion rate which is 20–24%. In comparison, the methanol selectivity varies with the silica and determine the final yield of methanol. The difference in product selectivity could be due to several factors. Firstly, is the formation of metal silicates. The de Jongh group has demonstrated the enhanced surface-specific activity of Cu towards methanol synthesis due to the formation of zinc silicate.[33] As discussed in section 3.4, the chemical structure and quantity of metal/alumina-silicate formed in $mSiO_2@Cu_2ZnAl$ LDH varies with the surface area of silica core. It is possible that the amount and composition of metal silicate affect the catalyst's acidity and basicity and modify the product selectivity.[1]

Secondly, the dispersion of copper may get enhanced when silica with higher surface area is used;[1,10] this results in a smaller copper particle size and a reduced methanol selectivity due to the absence of active sites in tiny particles.[8] MCM-41 and SBA-15 have similar pore structure

but different surface area due to different pore size (MCM-41 has smaller pore and higher surface area). It is possible that copper particles are smaller in MCM-41@Cu_2ZnAl than in SBA-15@Cu_2ZnAl and that leads to a lowered MeOH selectivity (37.1% with MCM-41 core and 54.4% with SBA-15, Figure 4.10). Moreover, different pore structures may end up with different mass transfer and different size of copper crystallite.[28] Koh *et al.* noted that the unique pore structure of KIT-6 leads to an efficient mass transfer (of CO_2 and product), a small copper crystallite and thus a superior STY yield of MeOH for the KIT-6 supported Cu/ZnO/MnO catalyst.[28]

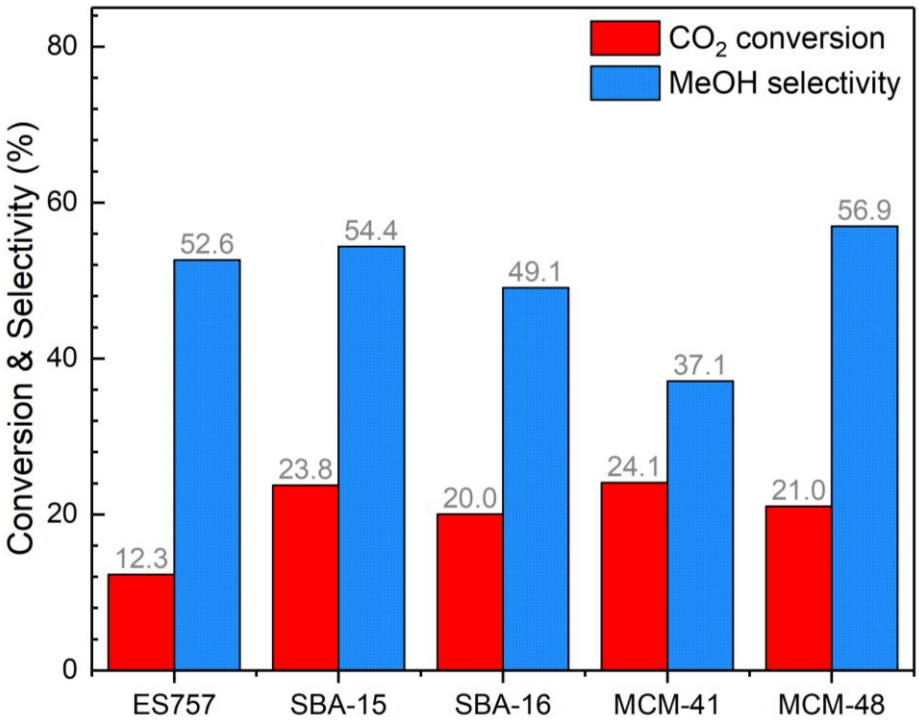


Figure 4.10 The CO_2 conversion and methanol selectivity mSiO_2@Cu_2ZnAl for CO_2 hydrogenation to methanol at 270 °C. The sample name was shorted to the name of their silica core for clarity.

The correlation between the surface area and methanol STY at 270 °C is plotted in Figure 4.11. No apparent relationship can be found between the surface area and the yield. The enhanced catalytic performance of SBA-15@Cu_2ZnAl compared to ES757@Cu_2ZnAl may be attributed

to the increased surface area. However, SBA-16@Cu_2ZnAl and MCM-41@Cu_2ZnAl, having a higher surface area in their precursor, shows a much lower methanol yield than SBA-15@Cu_2ZnAl due to their low MeOH selectivity. MCM-48@Cu_2ZnAl, of which the precursor possesses the highest surface area, exhibits the second-highest methanol yield (0.70 $g_{MeOH}/g_{catalyst}/h$). The effect of layered metal silicate formed in the mSiO_2@Cu_2ZnAl LDH precursor on the catalytic performance makes it difficult to distinguish the influence of the physical property of silica.

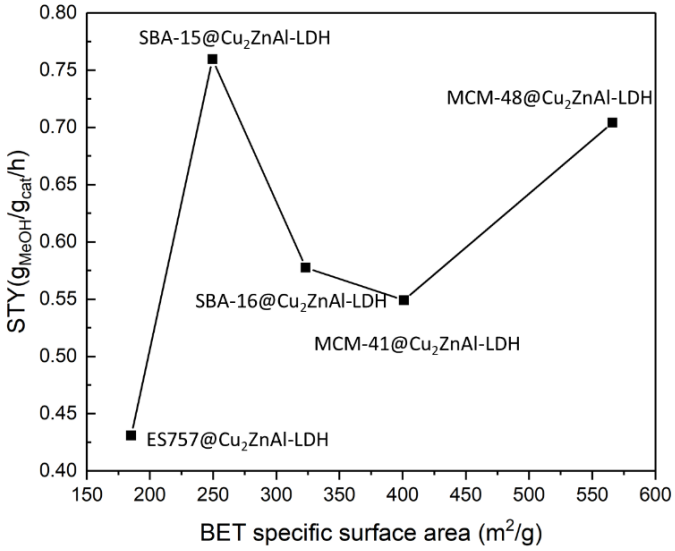


Figure 4.11 The correlation of the BET specific surface area of mSiO_2@Cu_2ZnAl-LDH and the STY of methanol (at 270 °C) from the corresponding catalyst.

The success in using silica with large pores such as ES757 and SBA-15 rather than the small pore MCM-41 indicates that substrate with wide pore shows good potential in developing an outstanding catalyst that is derived from core@LDH

Due to the limit of time, N_2O chemisorption was not able to be carried out.

4.4 Benchmarking studies of catalytic performance

The developed core-shell catalysts were compared with an industrial $Cu/ZnO/Al_2O_3$ catalyst (JM-HiFuel) and a benchmark Cu-catalyst derived from the exfoliated CuZnGa LDH precursor ($Cu_{1.3}ZnGa$).[11] The values of the two reference catalyst were taken from the literature.[11] The CO_2 to methanol reaction condition of two reference catalysts is the same as what is used in this study.

ES757@$Cu_{1.3}$ZnAl, SBA-15@Cu_2ZnAl and MCM-48@Cu_2ZnAl displayed superior catalytic performances than both the $Cu_{1.3}ZnGa$ and the industrial catalyst (Figure 4.12a) mainly due to their high MeOH selectivity (Figure 4.12b). Moreover, the copper loading in core-shell catalysts (19.81–24.5 wt%) is lower than that of $Cu_{1.3}ZnGa$ (33.5 wt%) and JM-HiFuel (50.0 wt%), making these $mSiO_2@Cu_xZnAl$ (x = 1.3 or 2) catalyst more cost-effective.

Interestingly, ES757@$Cu_{1.3}$ZnAl displays a better catalytic ability than $Cu_{1.3}ZnGa$ which possesses a lower copper surface area (32.1 and 99.2 $m^2/g_{catalyst,}$ respectively). This suggests that high copper surface area itself is not the only factor resulting in high catalytic ability. Other factors such as the interaction between metals and mass transfer property of the catalyst should be considered.

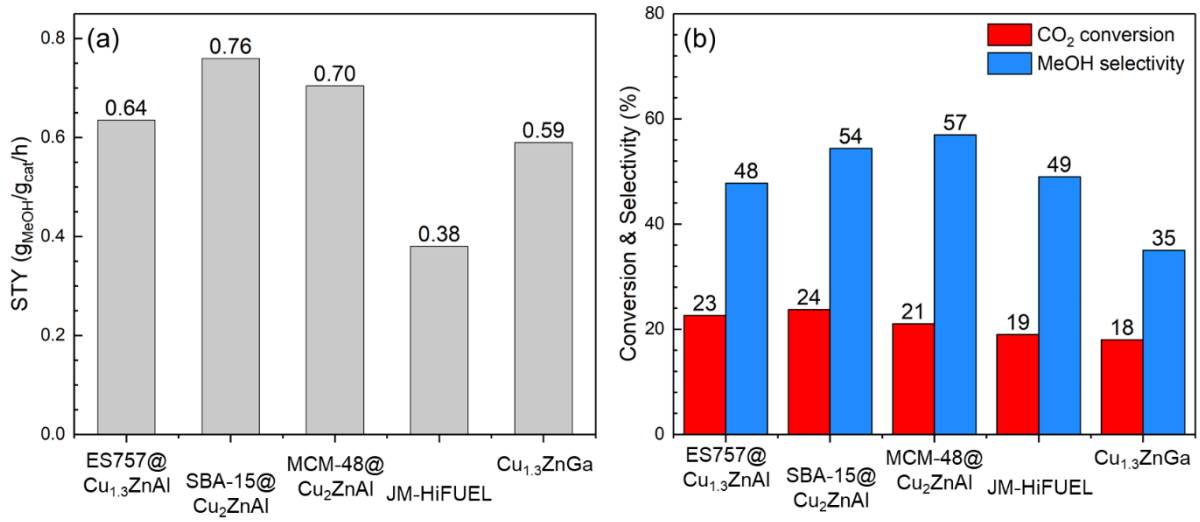


Figure 4.12 Comparison of (a) methanol STY and (b) CO_2 conversion and MeOH selectivity of ES757@$Cu_{1.3}ZnAl$. SBA-15@Cu_2ZnAl, MCM-48@Cu_2ZnAl, an industrial sample (JM-HiFuel) and $Cu_{1.3}ZnGa$ for the CO_2 hydrogenation to methanol at 270 °C, 45 bar with a H_2/CO_2 feed (3:1 by molar). The catalytic performance of JM-HiFuel and $Cu_{1.3}ZnGa$ is obtained from the literature.[11]

Compared with the 158 catalysts for CO_2 hydrogenation to methanol reviewed in 2020 by Jiang et *al*., these three core-shell catalysts rank in the top 12%.[23]

The best heterogeneous catalyst for CO_2 hydrogenation to methanol including KIT-6@Cu/ZnO/MnO, Pt_4Co/C and NiCo LDH which shows a STY of methanol between 3.37–10.74 $g_{MeOH}/g_{catalyst}$/h (Entry 1–3, Table 4.3).[10,37–39] The reported NiCo LDH should be the best CO_2 to methanol catalyst derived from LDH. Unfortunately, no characterisation data was provided to explain the superior performance. Other CO_2 to methanol catalysts that possess a similar or slightly better performance than SBA-15@Cu_2ZnAl exhibit different compositions such as Cu/ZnO/ZrO_2 and Pd-doped Ga_2O_3 (Entry 4–5, Table 4.3).[40,41]

SBA-15@Cu_2ZnAl, MCM-48@Cu_2ZnAl and ES757@$Cu_{1.3}ZnAl$ ranked second to fourth compared to the 67 catalysts in the review that were tested at the similar reaction condition (30–50 bar, 255–295 °C) as in this work;[23] the best performance was exhibited by Pd-dopped In_2O_3

with a MeOH STY of 1.00 $g_{MeOH}/g_{catalyst}/h$ at 280 °C, 50 bar (Entry 6, Table 4.3).[42]

The exact mechanism behind the excellent catalytic ability is still unknown. However, it is believed that the improvement could be due to the efficient mass transfer from porous silica core and better dispersion of active site from the core-shell structure.

Table 4.3 Summary of some best catalysts in the literature including the reaction conditions, CO_2 conversion, MeOH selectivity and STY of methanol. A mixture of H_2/CO_2 (3:1 by molar) gas feed were used in all cases.

Entry	Sample	Reaction temp. (°C)	Reaction press. (bar)	CO_2 conv. (%)	MeOH selec. (%)	Methanol STY ($g_{MeOH}/g_{catalyst}$ /h)
1	KIT-6@Cu/ZnO/MnO[10]	180	40	8.2	> 99.0	3.37
2	Pt_4Co nanowire/C[38]	150	32	–	–	7.66
3	NiCo LDH[39]	150	32	–	–	10.74
4	$CuZnOZrO_2$[40]	240	50	9.7	62.0	1.19
5	Pd/Ga_2O_3[41]	250	50	19.6	51.5	0.65
6	$Pd\text{-}In_2O_3$[42]*	280	50	–	78	1.00
7	ES757@$Cu_{1.3}$ZnAl	270	45	23	48	0.64
8	SBA-15@Cu_2ZnAl	270	45	24	54	0.76
9	MCM-48@Cu_2ZnAl	270	45	21	57	0.70

*Gas feed is H_2/CO_2 = 4:1 molar ratio.

4.5 Conclusions and outlook

The ES757@Cu_xZnAl-LDH and mSiO_2@Cu_2ZnAl-LDH core-shells, that were synthesised and characterised in Chapter 3, were tested for their catalytic ability towards CO_2 hydrogenation to methanol. Meanwhile, the relationship between the catalytic performance and the structural property of ES757@Cu_xZnAl was also investigated.

Among the ES757@Cu_xZnAl catalysts (x = 0.8–4), ES757@$Cu_{1.3}$ZnAl exhibits the highest CO_2 conversion (23%) and methanol STY (0.64 $g_{MeOH}/g_{catalyst}/h$) due to its superior copper surface area and uniform dispersion of copper particles. The core-shell ES757@$Cu_{1.3}$ZnAl also

possesses higher CO_2 conversion and better STY than the catalyst derived from unsupported $Cu_{1.3}ZnAl$-LDH (0.34 $g_{MeOH}/g_{catalyst}/h$) due to its higher copper surface area (32.1 m^2/g compared to 23.1 m^2/g of the unsupported catalyst). It is believed that the hierarchical core-shell structure promotes the dispersion of copper and achieves a higher copper surface area at a lower copper loading (Cu loading of ES757@$Cu_{1.3}ZnAl$ is 60% of $Cu_{1.3}ZnAl$-catalyst).

SBA-15@Cu_2ZnAl catalyst displays the highest methanol production (0.74 $g_{MeOH}/g_{catalyst}/h$) among all catalysts developed in this work. The catalytic performance of SBA-15@Cu_2ZnAl, MCM-48@Cu_2ZnAl (STY = 0.70 $g_{MeOH}/g_{catalys}/h$) and ES757@$Cu_{1.3}ZnAl$ are better than the industrial JM-HiFuel $Cu/ZnO/Al_2O_3$ catalyst and 88% of the reported CO_2 hydrogenation catalysts in the literature.

In the future, the reproducibility of the catalytic performance and the long-term stability of these core-shell catalysts should be tested. The reason behind the outstanding performance of these core-shell catalysts remains to be comprehensively studied. Techniques such as XPS, EXAFS, high-resolution TEM and simulation (DFT) can be used to further investigate the catalyst properties. Moreover, ES757@$Cu_{1.3}ZnAl$ shows superior performance than ES757@Cu_2ZnAl. It would be interesting to prepare SBA-15@$Cu_{1.3}ZnAl$ and MCM-48@$Cu_{1.3}ZnAl$ catalysts to see if the enhanced catalyst performance of this LDH composition is general on several core materials.

The facile and scalable synthesis of ES757@$Cu_{1.3}ZnAl$ shows great potential in industrial applications. There are several commercial silicas with similar pore sizes and surface areas as

ES757. In the future, it would be meaningful to explore SiO_2@CuZnAl catalysts synthesised using those silicas to further optimise the cost of CO_2 to methanol catalysts.

4.6 References

1 P. S. Murthy, W. Liang, Y. Jiang and J. Huang, *Energy Fuels*, 2021, **35**, 8558–8584.

2 M. Behrens, S. Zander, P. Kurr, N. Jacobsen, J. Senker, G. Koch, T. Ressler, R. W. Fischer and R. Schlögl, *J. Am. Chem. Soc.*, 2013, **135**, 6061–6068.

3 T. Phongamwong, U. Chantaprasertporn, T. Witoon, T. Numpilai, Y. Poo-arporn, W. Limphirat, W. Donphai, P. Dittanet, M. Chareonpanich and J. Limtrakul, *Chem. Eng. J.*, 2017, **316**, 692–703.

4 H. Guo, Q. Li, H. Zhang, F. Peng, L. Xiong, S. Yao, C. Huang and X. Chen, *Mol. Catal.*, 2019, **476**, 1–14.

5 N. Nomura, T. Tagawa and S. Goto, *React. Kinet. Catal. Lett.*, 1998, **63**, 21–25.

6 C. Tisseraud, C. Comminges, S. Pronier, Y. Pouilloux and A. Le Valant, *J. Catal.*, 2016, **343**, 106–114.

7 T. Witoon, S. Bumrungsalee, M. Chareonpanich and J. Limtrakul, *Energy Convers. Manag.*, 2015, **103**, 886–894.

8 C. Zhang, H. Yang, P. Gao, H. Zhu, L. Zhong, H. Wang, W. Wei and Y. Sun, *J. CO2 Util.*, 2017, **17**, 263–272.

9 S. Das, J. Pérez-Ramírez, J. Gong, N. Dewangan, K. Hidajat, B. C. Gates and S. Kawi, *Chem. Soc. Rev.*, 2020, **49**, 2937–3004.

10 M. K. Koh, M. Khavarian, S. P. Chai and A. R. Mohamed, *Int. J. Hydrogen Energy*, 2018, **43**, 9334–9342.

11 M. M. J. Li, C. Chen, T. Ayvall, H. Suo, J. Zheng, I. F. Teixeira, L. Ye, H. Zou, D. O'Hare and S. C. E. Tsang, *ACS Catal.*, 2018, **8**, 4390–4401.

12 S. O. Akpotu and B. Moodley, *J. Mol. Liq.*, 2018, **261**, 540–549.

13 M. Smyrnioti, C. Tampaxis, T. Steriotis and T. Ioannides, *Catal. Today*, 2020, **357**, 495–502.

14 J. C. Lavalley, *Catal. Today*, 1996, **27**, 377–401.

15 C. Rodriguez-Navarro, A. Suzuki and E. Ruiz-Agudo, *Langmuir*, 2013, **29**, 11457–11470.

16 Š. Hajduk, V. D. B. C. Dasireddy, B. Likozar, G. Dražić and Z. C. Orel, *Appl. Catal. B Environ.*, 2017, **211**, 57–67.

17 O. Braaten, A. Kjekshus and H. Kvande, *Jom*, 2000, **52**, 47–53.

18 M. Turco, G. Bagnasco, C. Cammarano, P. Senese, U. Costantino and M. Sisani, *Appl. Catal. B Environ.*, 2007, **77**, 46–57.

19 J. P. Shen and C. Song, *Catal. Today*, 2002, **77**, 89–98.

20 H. Yahiro, K. Nakaya, T. Yamamoto, K. Saiki and H. Yamaura, *Catal. Commun.*, 2006, **7**, 228–231.

21 S. Velu, K. Suzuki, M. Okazaki, M. P. Kapoor, T. Osaki and F. Ohashi, *J. Catal.*, 2000, **194**, 373–384.

22 M. Behrens, F. Studt, I. Kasatkin, S. Kühl, M. Hävecker, F. Abild-pedersen, S. Zander, F. Girgsdies, P. Kurr, B. Kniep, M. Tovar, R. W. Fischer, J. K. Nørskov and R. Schlögl, *Science*, 2012, **336**, 893–898.

23 X. Jiang, X. Nie, X. Guo, C. Song and J. G. Chen, *Chem. Rev.*, 2020, **120**, 7984–8034.

24 K. Stangeland, H. Li and Z. Yu, *Ind. Eng. Chem. Res.*, 2018, **57**, 4081–4094.

25 P. Gao, L. Zhong, L. Zhang, H. Wang, N. Zhao, W. Wei and Y. Sun, *Catal. Sci. Technol.*, 2015, **5**, 4365–4377.

26 G. V. Sagar, P. V. R. Rao, C. S. Srikanth and K. V. R. Chary, *J. Phys. Chem. B*, 2006, **110**, 13881–13888.

27 D. S. Brands, E. K. Poels, T. A. Krieger, O. V. Makarova, C. Weber, S. Veer and A. Bliek, *Catal. Letters*, 1996, **36**, 175–181.

28 W. R. A. M. Robinson and J. C. Mol, *Appl. Catal.*, 1990, **63**, 165–179.

29 S. Kuld, M. Thorhauge, H. Falsig, C. F. Elkjær, S. Helveg, I. Chorkendorff and J. Sehested, *Science*, 2016, **352**, 969–974.

30 M. B. Fichtl, J. Schumann, I. Kasatkin, N. Jacobsen, M. Behrens, R. Schlögl, M. Muhler and O. Hinrichsen, *Angew. Chem. Int. Ed.*, 2014, **53**, 7043–7047.

31 T. Lunkenbein, F. Girgsdies, T. Kandemir, N. Thomas, M. Behrens, R. Schlögl and E. Frei, *Angew. Chem. Int. Ed.*, 2016, **55**, 12708–12712.

32 B. Liang, J. Ma, X. Su, C. Yang, H. Duan, H. Zhou, S. Deng, L. Li and Y. Huang, *Ind. Eng. Chem. Res.*, 2019, **58**, 9030–9037.

33 R. Van Den Berg, G. Prieto, G. Korpershoek, L. I. Van Der Wal, A. J. Van Bunningen, S. Lægsgaard-Jørgensen, P. E. De Jongh and K. P. De Jong, *Nat. Commun.*, 2016, **7**, 1–7.

34 J. Szanyi and D. W. Goodman, *Catal. Letters*, 1991, **10**, 383–390.

35 P. B. Rasmussen, P. M. Holmblad, T. Askgaard, C. V. Ovesen, P. Stoltze, J. K. Nørskov and I. Chorkendorff, *Catal. Letters*, 1994, **26**, 373–381.

36 J. Yoshihara and C. T. Campbell, *J. Catal.*, 1996, **161**, 776–782.

37 Z. Q. Wang, Z. N. Xu, S. Y. Peng, M. J. Zhang, G. Lu, Q. S. Chen, Y. Chen and G. C. Guo, *ACS Catal.*, 2015, **5**, 4255–4259.

38 S. Bai, Q. Shao, Y. Feng, L. Bu and X. Huang, *Small*, 2017, **13**, 1–6.

39 Y. Peng, L. Wang, Q. Luo, Y. Cao, Y. Dai, Z. Li, H. Li, X. Zheng, W. Yan, J. Yang and J. Zeng, *Chem*, 2018, **4**, 613–625.

40 F. Arena, G. Mezzatesta, G. Zafarana, G. Trunfio, F. Frusteri and L. Spadaro, *Catal. Today*, 2013, **210**, 39–46.

41 T. Fujitani, M. Saito, Y. Kanai, T. Watanabe, J. Nakamura and T. Uchijima, *Appl. Catal. A, Gen.*, 1995, **125**, 199–202.

42 M. S. Frei, C. Mondelli, R. García-Muelas, K. S. Kley, B. Puértolas, N. López, O. V. Safonova, J. A. Stewart, D. Curulla Ferré and J. Pérez-Ramírez, *Nat. Commun.*, 2019, **10**, 1–11.

Chapter 5. Studies of CO_2 to olefins conversion using a ZSM-5@$Cu_{1.3}$ZnAl-CO_3-LDH core-shell catalyst precursor

5.1. Introduction

Studies in Chapter 4 have shown that ES757@$Cu_{1.3}$ZnAl-LDH core-shell derived catalyst exhibits outstanding catalytic activity towards CO_2 to methanol due to the generation of well-exposed copper metal active sites. CO_2 can be converted to olefins by initial hydrogenation to methanol, followed by methanol-to-olefins (MTO) conversion.[1,2] By replacing the ES757 silica core with a MTO catalyst, a potential CO_2 to olefins catalyst with excellent performance can be obtained.

H-ZSM-5 (the proton-exchanged form of zeolite ZSM-5) has been shown in literature to be one of the most efficient catalyst for methanol to olefin (MTO) conversion.[3] Ahouari *et al.* have shown that the physical mixture of Cu/ZnO/Al_2O_3 and H-ZSM-5 exhibits outstanding catalytic activity for CO_2 hydrogenation (39.8% CO_2 conversion and 16.8% hydrocarbon selectivity at 350 °C and 30 bar).[4] It is anticipated that the core-shell composites with H-ZSM-5 as the core and CuZnAl LDH as the shell would show bifunctional catalytic activity towards CO_2 to olefin conversion. Moreover, the core-shell hierarchical structure may bring some synergistic effects.[5,6]

In this chapter, a series of core-shells using a H-ZSM-5 core and a $Cu_{1.3}$ZnAl-LDH shell has been prepared and fully characterised. The effect of the acidity on the catalytic ability has been discussed. Various synthetic condition and methods are used to explore their effect on the acidity of the core-shell nanostructures.

5.2. Synthesis and characterisation of ZSM-5@$Cu_{1.3}ZnAl$-CO_3-LDH

The core-shell composite was prepared using the conventional co-precipitation method in which LDH platelets were grown on the surface of H-ZSM-5 zeolite.[7] An aqueous solution of Cu, Zn and Al nitrate solutions with a 1.3:1:1 molar ratio was added to an aqueous dispersion of H-ZSM-5 and Na_2CO_3 at pH 10 over the course of 1 hour. The pH of the mixture was controlled at 10 using 1 M NaOH solution. The resulting mixture was aged for 0.5 hour before being collected by filtration and washed with water. The obtained solid was dried under vacuum at 30 °C overnight to afford ZSM@$Cu_{1.3}ZnAl$-LDH as a pale blue powder. A control sample of the layered double hydroxide $Cu_{1.3}ZnAl$-CO_3-LDH, was prepared following the same synthesis method as ZSM@$Cu_{1.3}ZnAl$-LDH without the addition of H-ZSM-5. The obtained sample will be referred to as $Cu_{1.3}ZnAl$-LDH. The oxidation state of copper, zinc and aluminium in this core-shell (and $Cu_{1.3}ZnAl$-LDH) is +2, +2 and +3, respectively.

The powder X-ray diffraction (XRD) pattern of ZSM@$Cu_{1.3}ZnAl$-LDH possesses both the characteristic Bragg diffraction features of H-ZSM-5 and LDH, suggesting the presence of both phases in the core-shell; no crystalline impurity is observed (Figure 5.1). The intensity of zeolite reflections is weaker than that in pristine zeolite as zeolite only occupies half of the composite's mass.

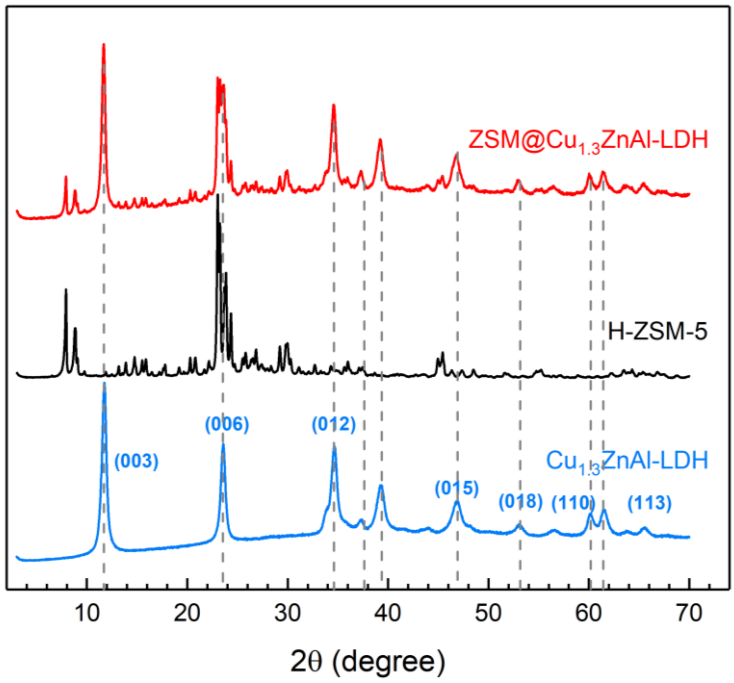


Figure 5.1 Powder XRD patterns of ZSM@$Cu_{1.3}$ZnAl-LDH, H-ZSM-5 and $Cu_{1.3}$ZnAl-LDH.

XRD patterns of zeolite, LDH and core-shell have been analysed by the Pawley method for ZSM-5, a Rietveld for the LDH and a combination of both, respectively (Table D1). The *d*-spacing and crystallite size are listed in Table 5.1. The d_{003} and d_{110} between the pristine LDH and core-shell are almost identical, indicating these two LDH phases have similar composition. The d_{003} is around 7.6 Å, indicating that the LDH phase is carbonate-intercalated.[8] The crystallite sizes of the LDH phase (D_{00l} and D_{110}) in the original $Cu_{1.3}$ZnAl-LDH and the core-shell are very similar.

However, in MCM-48@$Cu_{1.3}$ZnAl-LDH-pH10, the LDH phase is less crystalline, i.e. smaller crystallite domain size (Entry 4, Table 5.1). Comparing H-ZSM-5 with MCM-48, the only chemical difference is that zeolite has Al on the surface but silica does not. The difference in the LDH crystallinity of ZSM@$Cu_{1.3}$ZnAl-LDH and MCM-48@$Cu_{1.3}$ZnAl-LDH-pH10 demonstrates that aluminium in the core material participates in and facilitates the LDH

formation. This further supported the previous result reported by our group that aluminium at the interface acts as the nuclei site of LDH.[7,9–13] The crystallite size of zeolite slightly reduces after the co-precipitation (from 57.44 to 48.00 nm), possibly due to the hydrolysis of Si-O-Al bridge and of Si-O-Si bond in water.[14–17]

Table 5.1 The *d*-spacing and crystallite size of $Cu_{1.3}$ZnAl-LDH, ZSM@$Cu_{1.3}$ZnAl-LDH, H-ZSM-5 and MCM-48@ $Cu_{1.3}$ZnAl-LDH-pH10.

Entry	Sample	d_{003} (Å)	d_{110} (Å)	D_{00l} (nm)[a]	D_{110} (nm)[a]	$D_{zeolite}$ (nm)[b]
1	$Cu_{1.3}$ZnAl-LDH	7.59	1.54	12.48	9.86	–
2	ZSM@$Cu_{1.3}$ZnAl-LDH	7.57	1.54	14.71	12.33	48.00
3	H-ZSM-5	–	–	–	–	57.44
4	MCM-48@$Cu_{1.3}$ZnAl-LDH-pH10	7.39	1.52	2.06	0.89	–

a: the crystallite size of LDH along the (00l) or (110) direction calculated from Rietveld refinement. b: the crystallite size of zeolite worked out from Pawley refinement.

Commercial samples of H-ZSM-5 possess irregular shaped particles (Figure 5.2a). TEM images of the control LDH and composite indicate that hexagonal LDH platelets with particle size around 145–400 nm (Figure 5.2b) radially grow on the surface of zeolite to form a shell with a thickness between 250–500 nm (Figure 5.2c).

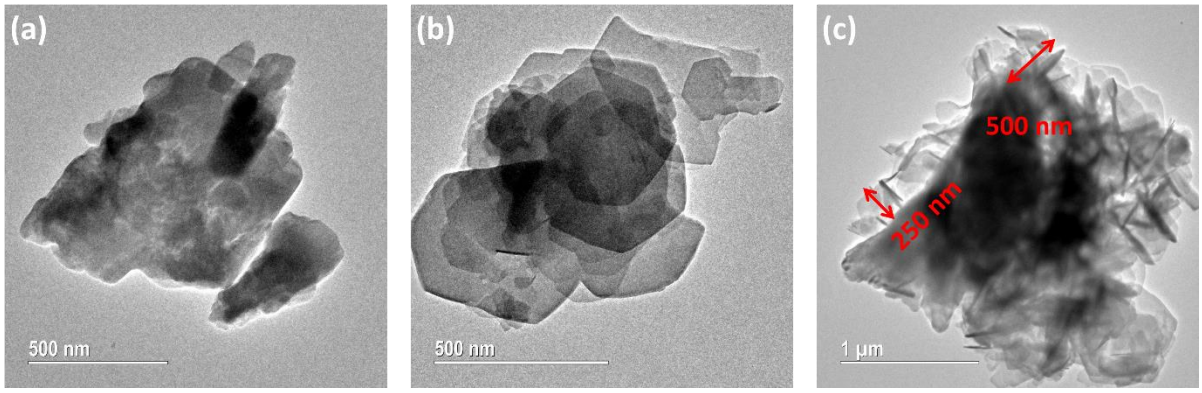


Figure 5.2 TEM images of (a) H-ZSM-5, (b) $Cu_{1.3}$ZnAl-LDH and (c) ZSM@$Cu_{1.3}$ZnAl-LDH.

Thermogravimetric analysis (TGA) was used to check the thermal stability and phase fraction. H-ZSM-5 shows two weight loss events (Figure 5.3a). The first one below 150 °C is due to the

water evaporation. The second one occurs over 200 °C and is ascribed to the removal of strongly bonded water and condensation of surface hydroxyl groups.[18,19] ZSM@$Cu_{1.3}$ZnAl-LDH exhibits three distinct weight loss events (Figure 5.3a). The first one giving 12.4 wt% weight loss between 100–150 °C arises from the reversible removal of physisorbed water in LDH and zeolite.[20–22] The second one ending at 400 °C with 6.9 wt% weight loss corresponds to the dehydroxylation of LDH and the decomposition of loosely bound interlayer carbonate anions in LDH.[20–23] At this stage, LDH transformed into amorphous mixed metal oxide, also referred as layered double oxide (LDO).[24] The final stage happens between 550 and 750 °C due to the full decarbonation of LDH and ends up with 3.1 wt% loss.[23,25] Velu *et al.* proposed that some oxycarbonate intermediates with the chemical formula $[M^{II}M^{III}_xO_y(CO_3)_z]$ develop during the decomposition of Cu-containing LDH.[23] The decomposition of those oxycarbonate species give rise to the full decarbonation of LDH. Two distinguishing regions are observed during the final complete decarbonisation stage of ZSM@$Cu_{1.3}$ZnAl-LDH; it is possible that the distinct M^{II} (Cu^{2+} and Zn^{2+}) environments and Jahn-Teller distortion of Cu in the LDH gave rise to $[M^{II}M^{III}_xO_y(CO_3)_z]$ species with different thermal stability.[22,26,27] The residual weight for H-ZSM-5, ZSM@$Cu_{1.3}$ZnAl-LDH and $Cu_{1.3}$ZnAl-LDH are 88.7%, 77.6% and 66.6% respectively, suggesting a 44:56 weight ratio between zeolite and LDH in ZSM@$Cu_{1.3}$ZnAl-LDH.

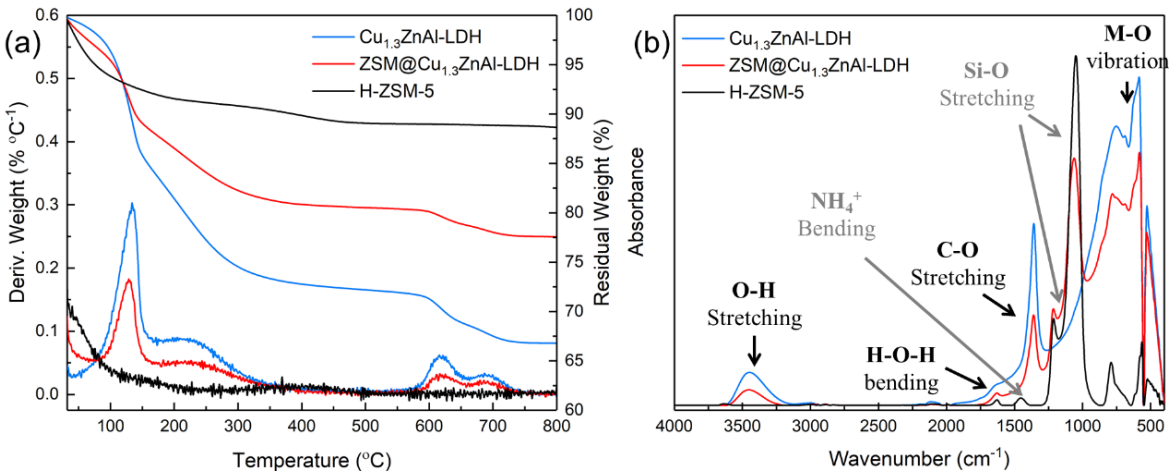


Figure 5.3 (a) TGA and derivative TGA (dTG) curves and (b) FTIR spectra of ZSM@$Cu_{1.3}$ZnAl-LDH, H-ZSM-5 and $Cu_{1.3}$ZnAl-LDH.

The FTIR spectrum of H-ZSM-5 in Figure 5.3b shows the NH_4^+ bending absorbance at 1450 cm^{-1} confirming the presence of ammonia counterion in the original zeolite (Figure 5.3b).[28,29] ZSM@$Cu_{1.3}$ZnAl-LDH exhibits both the LDH and zeolite features (Figure 5.3b); the metal-oxygen vibration band at 700 cm^{-1}, carbonate stretching band at 1370 cm^{-1}, and OH stretching band at 3500 cm^{-1} are from LDH;[8,30] two Si-O stretching bands located at around 1150 cm^{-1} from the zeolite.[7,13,31] An NH_4^+ absorption band is no longer observed in the core-shell due to counterion exchange (replacing NH_4^+ to Na^+) which takes place during the co-precipitation and this is supported by ICP-MS data (see below). No functional groups from impurities are observed.

The composition of materials was analysed by the inductively coupled plasma mass spectrometry (ICP-MS) and CHN analysis (Table 5.2). In $Cu_{1.3}$ZnAl-LDH, the molar amount of carbon is higher than the theoretical value (Table D2), which is half of the Al, indicating that there is carbonate impurity. Referring to the discussion in Chapter 3, the impurity is likely to be copper (and/or zinc) hydroxide carbonate. Assuming the impurity to be copper hydroxide

carbonate ($Cu_2(OH)_2CO_3$), a possible formula of $Cu_{1.3}$ZnAl-LDH can be given: $Cu_{1.12}Zn_{1.1}Al_1(OH)_{6.44}(CO_3)_{0.5}\cdot[Cu_2(OH)_2CO_3]_{0.19}\cdot 2.95H_2O$ (Details in Table D2).

The supplier indicates the Si: Al ratio of the as supplied H-ZSM-5 is 23:1. Since, the general formula of ZSM-5 is $A_nAl_nSi_{96-n}O_{192}\cdot 16H_2O$, where A is the counterion (Na^+ or NH_4^+). H-ZSM-5 used in this study should have a formula of $(NH_4)_4Al_4Si_{92}O_{192}\cdot 16H_2O$. However, the expected elemental composition from this formula is markedly different from the detected value (Table D2). The detected Si and Al content are much lower than the expected value due to the incomplete dissolution of zeolite during ICP-MS. In comparison, the measured Na, C, H and N amounts are higher than the expectation. Tetrapropylammonium (TPA) bromide and sodium chloride are used in the synthesis of H-ZSM-5.[32] Reagent residual may lead to excess elements. Adsorption of air may also contribute to the fluctuation in C, H and N.

Table 5.2 Elemental composition (wt%) of H-ZSM-5, $Cu_{1.3}$ZnAl-LDH, physical mixture and ZSM@$Cu_{1.3}$ZnAl-LDH.

Sample	Cu	Zn	Al	Na	Si	C	H	N
H-ZSM-5	0	0	0.62[a]	0.47	0.41[a]	0.08	1.25	1.62
ZSM@$Cu_{1.3}$ZnAl-LDH	12.58	9.56	3.98	4.11	–	1.22	2.03	0.06
Physical mixture[b]	12.68	9.62	3.86	0.42	0.18	1.14	2.26	0.71
$Cu_{1.3}$ZnAl-LDH	22.63	17.18	6.41	0.38	0	1.98	3.05	0

a: zeolite was not completely dissolved. The detected Al and Si amount should be much lower than the actual value. b: The 1:1 by weight physical mixture of H-ZSM-5 and $Cu_{1.3}$ZnAl-LDH.

As shown in Table 5.2, the elemental composition of ZSM@$Cu_{1.3}$ZnAl-LDH is almost identical to the composition of the physical mixture (calculated from the experimental value of H-ZSM-5 and $Cu_{1.3}$ZnAl-LDH), except Na and N. The Na content of core-shell is higher than that in the physical mixture. In contrast, the N amount in core-shell is lower. This variation indicates

that the ion exchange, Na^+ replacing NH_4^+, occurred during the co-precipitation. The chemical formula of ZSM@$Cu_{1.3}$ZnAl-LDH is likely to be $[Na_4Al_4Si_{92}O_{192}]_{0.05}[Cu_{1.12}Zn_{1.1}Al_1(OH)_{6.44}(CO_3)_{0.5}]$ $[Cu_2(OH)_2CO_3]_{0.19}\cdot 3.79H_2O$.

The ^{29}Si solid-state magic angle spinning (MAS) nuclear magnetic resonance (NMR) spectra of the pure zeolite and ZSM@$Cu_{1.3}$ZnAl-LDH are shown in Figure 5.4, with the details being presented in Table D3. H-ZSM-5 possesses two characteristic Si resonances. The resonance at −111.3 ppm can be unequivocally assigned to $Si(OSi)_4$.[3,33–36] Rather than from a single $Si(OSi)_3(OAl)$ resonance, the band at −104.7 ppm is more likely to arise from a combination of $Si(OSi)_3(OAl)$ and $Si(OSi)_3(OH)$ environments.[33,36] The Si/Al molar ratio of H-ZSM-5 can be estimated using Loewenstein's equation (Equation D1) from integration of the NMR spectrum.[3,37–39] If the resonance at −104.7 ppm solely represents $Si(OSi)_3(OAl)$, the Si/Al ratio in the commercial zeolite would be 16, significantly lowering than the value 23 provided by the supplier. Instead, if $Si(OSi)_3(OH)$ occupies 32% of the resonance at −104.7 ppm, the actual Si/Al ratio would be closer to the theoretical 23.

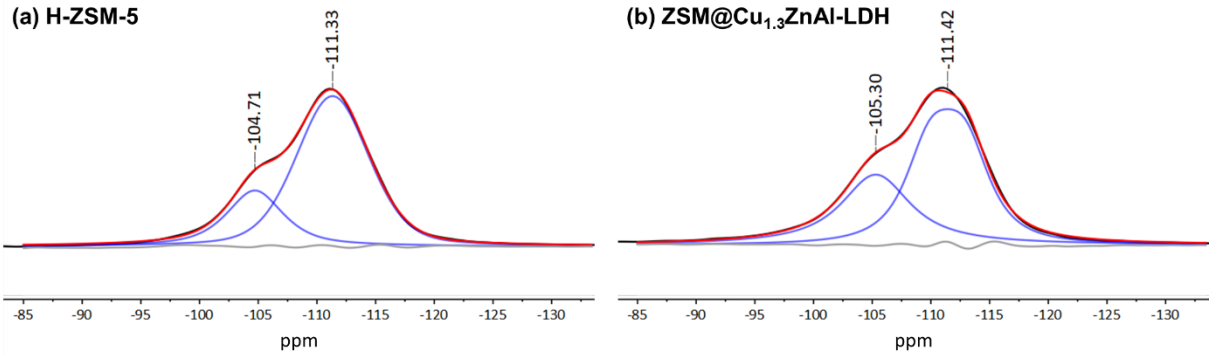


Figure 5.4 ^{29}Si solid-state MAS NMR spectra and peak fitting results of (a) H-ZSM-5 and (b) ZSM@$Cu_{1.3}$ZnAl-LDH. The observed, cumulative, deconvoluted peaks and differences are shown in black, red, blue, and grey, respectively.

ZSM@$Cu_{1.3}$ZnAl-LDH exhibits two characteristic Si resonances at −105.3 and −111.4 ppm that are derived from the ZSM5 core. Compared to the pristine ZSM-5, the core-shell shows a lower fraction of $Si(OSi)_4$ at −111.4 ppm (relative intensity reduces from 74.6% to 61.2%), undoubtedly due to the desilication of zeolite in the alkaline media.[40,41] As a result, an increased relative intensity of −105.3 ppm resonance was observed (from 25.4% to 38.8%); meanwhile, with respect to ZSM-5, this resonance shifted to higher frequency, which is possibly due to the dealumination of zeolite.

The ^{27}Al MAS NMR spectra of pristine zeolite and ZSM@$Cu_{1.3}$ZnAl-LDH are shown in Figure 5.5, and the details are summarised in Table D4. H-ZSM-5 exhibits one resonance at 56.4 ppm corresponding to the tetrahedrally coordinated Al, also referred to as AlO_4, in the zeolite.[42] No band is observed in 0–50 ppm region, indicating that there is no 5- nor 6-coordinated extra-framework Al in the pristine zeolite.[33,36]

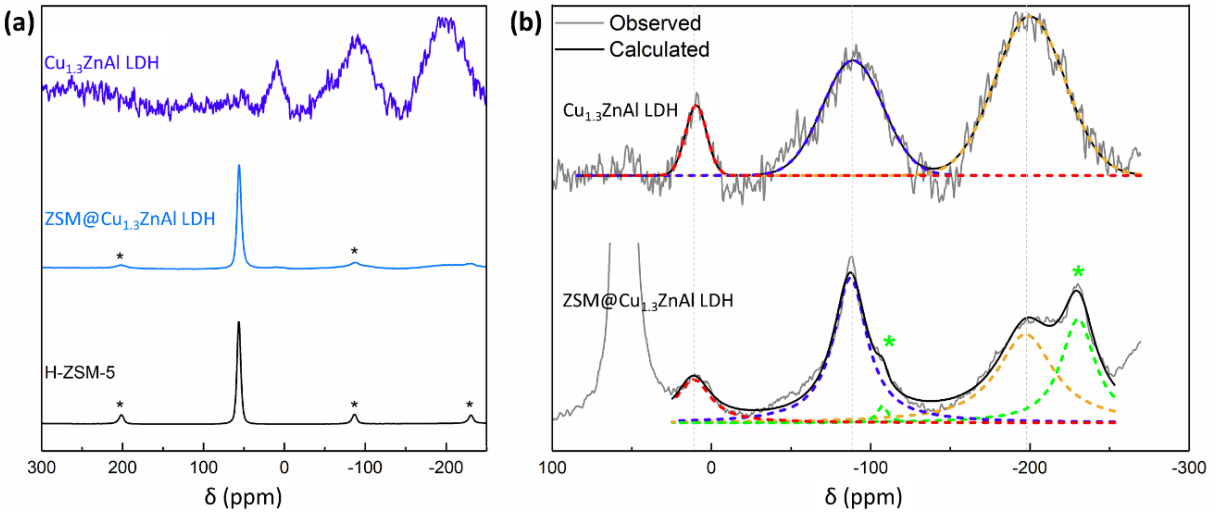


Figure 5.5 (a) ^{27}Al solid-state DPMAS NMR spectra of CuZnAl-LDH, ZSM@$Cu_{1.3}$ZnAl-LDH and H-ZSM-5. * indicate the spinning sidebands; (b) Section of ^{27}Al solid-state MAS NMR spectra of CuZnAl-LDH, ZSM@$Cu_{1.3}$ZnAl-LDH and H-ZSM-5. The observed and calculated plots are shown in grey and black. The deconvoluted peaks are plotted with red, blue and yellow dash lines. The spinning sidebands are marked with * and indicated with green dash line.

Due to the presence of paramagnetic Cu within the metal hydroxide layer, ^{27}Al resonances in LDH exhibits a very broad signal and large chemical shift.[43,44] $Cu_{1.3}$ZnAl-LDH displays three weak resonances at 9.7, −88.8 and −199.9 ppm (Figure 5.5). Consistent with the literature, the 9.7 ppm band arises from the octahedrally coordinated Al (AlO_6) in the LDH.[45–48] It is proposed that the two other resonances also result from AlO_6. The presence of Cu^{2+} introduces a distortion within the LDH layers, which significantly alters the electric field gradient measured at the Al sites and leads to multiple Al environments.[47] Similar result has been reported by Nielsen and co-workers: five different Al resonances were observed for MgNiAl-LDH due to various Ni^{2+} environments with respect to the Al ions meanwhile, the chemical shift of Al dramatically expands to nearly −1800 ppm due to the induction of paramagnetic shift caused by Ni^{2+}.[48] Furthermore, unpublished result from our group has demonstrated that three octahedral Al resonances were observed in MgAlTi LDH due to different Ti surroundings.[49]

Sideris *et al.* reported that cations (M^{2+} and M^{3+}) are highly ordered in Mg_xAl CO_3 LDH ($2.0 \leq x \leq 4.2$); each Al atom is surrounded by six Mg^{2+} cations without any Al^{3+}-Al^{3+} close contact.[27] It is theoretically likely that the CuZnAl-LDH (with Cu:Zn:Al molar ratio = 1.3:1:1) possesses seven local Al environments (Figure 5.6). Considering that more Cu^{2+} cations would initiate a stronger distortion and ends up with a more significant variation in the Al chemical shift, the three observed resonances, 9.7, −88.8 and −199.9 ppm, may be attributed to $Al(OCu)_0$, $Al(OCu)_1$ and $Al(OCu)_2$, respectively.

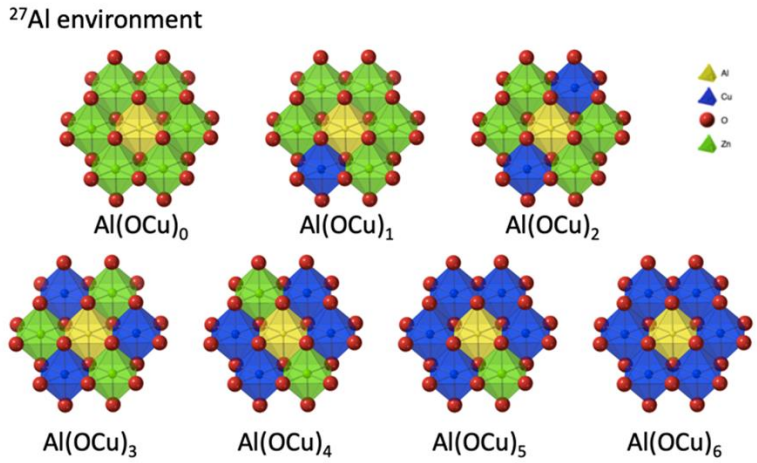


Figure 5.6 The illustration of the seven possible Al environments in $Cu_{1.3}$ZnAl-LDH. Cu, Zn, and Al are indicated in blue, green and yellow, respectively. Only one of the possible examples for two, three and four Cu^{2+} cations is shown.

Based on the deconvoluted spectra (Figure 5.5b), ZSM@$Cu_{1.3}$ZnAl-LDH was found to exhibit both the characteristic Al resonance bands from H-ZSM-5 and $Cu_{1.3}$ZnAl-LDH; the AlO_4 resonance at 56.0 ppm is derived from the zeolite core; AlO_6 resonances at 13.7, −86.7 and −195.8 ppm are from the $Cu_{1.3}$ZnAl-LDH shell. The AlO_4 resonance shifts by 0.4 ppm to lower frequency after co-precipitation. It is possible that a small amount of Cu (and/or Zn) enters the H-ZSM-5 framework via ion exchange during the co-precipitation and causes a slight distortion of Al local environment in the zeolite.[50] AlO_6 bands of ZSM@$Cu_{1.3}$ZnAl shift by 2–4 ppm to higher frequency compared to CuZnAl-LDH. Meanwhile, the percentage integration of Al(OCu)$_0$ and Al(OCu)$_1$ resonances increases with a decrease in the Al(OCu)$_2$ peak. It is believed that the alteration of the AlO_6 bands is related to the distribution of Cu^{2+} in the core-shell and the interface formation between zeolite and $Cu_{1.3}$ZnAl-LDH.

The pore structure and surface area were investigated by N_2 adsorption and desorption isotherm. H-ZSM-5 exhibits a type I isotherm with a H4 hysteresis loop (Figure 5.7a), indicating clusters

of microporous particles.[51] $Cu_{1.3}$ZnAl-LDH displays a type II isotherm with a H3 hysteresis loop, suggesting it is agglomerates of platelet-like particles which give slit-like macropores (Figure 5.7a).[51,52] ZSM@$Cu_{1.3}$ZnAl-LDH possesses a type I isotherm at low relative pressure and type II isotherm with H3 hysteresis loop at high relative pressure, which is a combination of zeolite and LDH.[51] The N_2 uptake at the micropore filling region (p/p^0 < 0.05) of the composite is about half of that for the original zeolite (Figure 5.7a), which indicates micropore loss; the DFT pore size distribution further supports this. Original H-ZSM-5 has micropores with pore diameter at 7.4, 15.6 and 18.4 Å (Figure 5.7b). However, after co-precipitation, most of the micropores in the zeolite disappear (Figure 5.7b). It is known that pores in zeolite will expand in basic environments, especially with the presence of Na^+.[53,54] Disappearance of micropores should be due to pore plugging resulting from the growth of LDH platelets inside the pore.

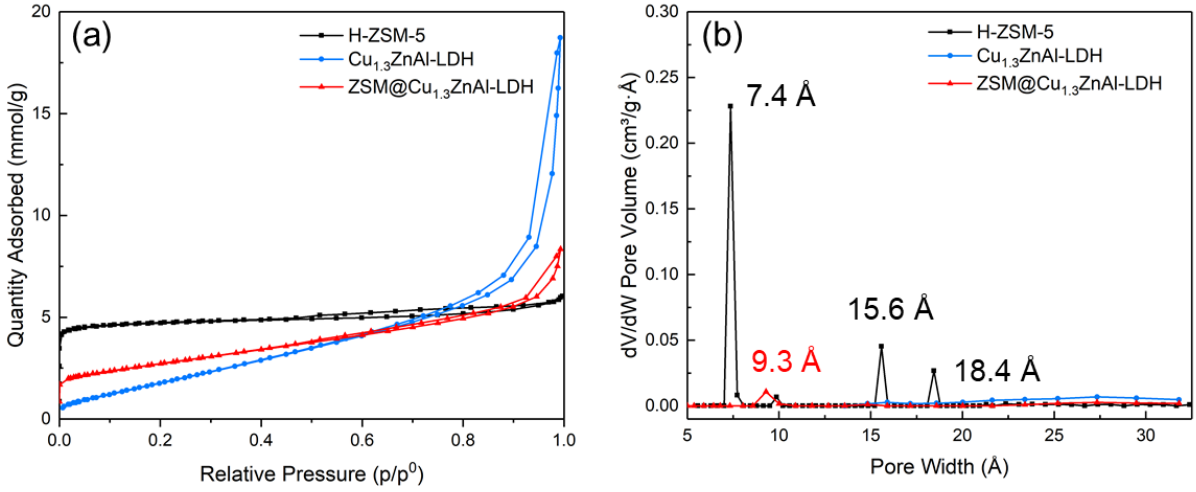


Figure 5.7 (a) The N_2 adsorption and desorption isotherm (77 K) and (b) DFT pore size distribution of H-ZSM-5, ZSM@$Cu_{1.3}$ZnAl-LDH and $Cu_{1.3}$ZnAl-LDH. DFT pore size distribution of LDH is calculated based on the kernels of slit pore; the others are obtained based on the kernels for metal oxide with cylindrical pore.

The N_2 BET specific surface area and pore volume of zeolite core predominantly come from the microporous structure (Figure 5.8a and b). In ZSM@$Cu_{1.3}$ZnAl-LDH, the micropore blockage leads to a dramatic reduction in the corresponding surface area and pore volume. The external surface area of this composite mainly depends on LDH surface area. ZSM@$Cu_{1.3}$ZnAl-LDH has a higher external surface area than the physical mixture. Considering that the platelet size of LDH is similar in the core-shell and the control LDH, the enhanced external surface area may be due to the reduced accumulation of LDH lamellae in ZSM@$Cu_{1.3}$ZnAl-LDH.

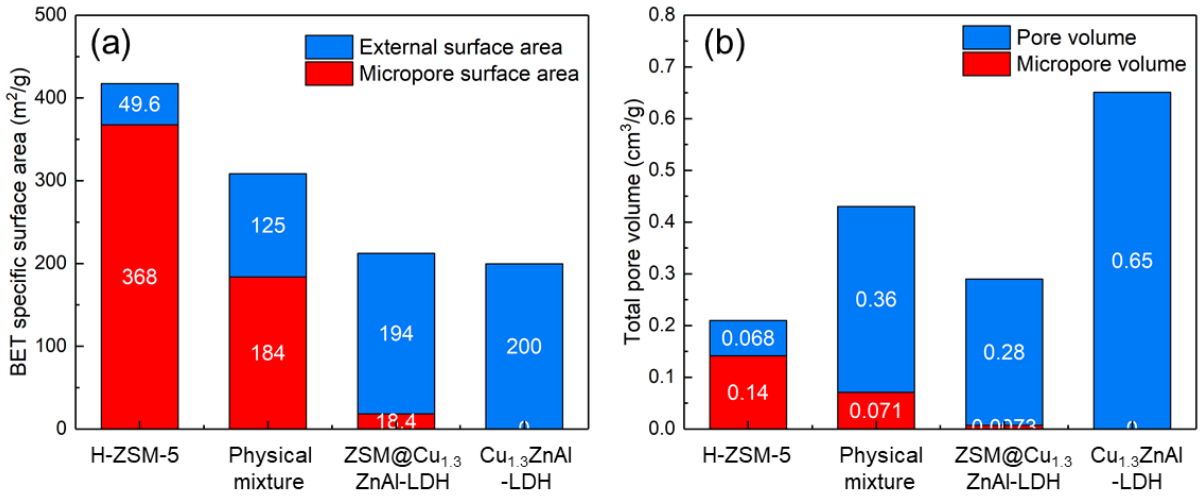


Figure 5.8 (a) The N_2 BET specific surface area and (b) total pore volume of H-ZSM-5, physical mixture of H-ZSM-5 and $Cu_{1.3}$ZnAl-LDH (weight ratio 44:56), ZSM@$Cu_{1.3}$ZnAl -LDH and $Cu_{1.3}$ZnAl-LDH.

5.3. Preliminary studies of CO_2 to olefins conversion using ZSM@$Cu_{1.3}$ZnAl-LDH

5.3.1. Reaction conditions and setup

After the successful synthesis of ZSM@$Cu_{1.3}$ZnAl-LDH, the next step is to test the catalytic ability towards CO_2 conversion to olefins for catalysts derived from core-shell. The reaction conditions used for CO_2 to olefin conversion, both from previous reports and for this work, are collated in Table 5.3. CO_2 hydrogenation requires a low temperature and high pressure, while

the methanol dehydration reaction requires moderate temperature and low reaction pressure. The catalyst derived from ZSM@$Cu_{1.3}$ZnAl-LDH was evaluated at high pressure over a wide range of reaction temperatures (Entry 7, Table 5.3) using a tubular fixed bed reactor. An illustration of the setup is shown in Figure D1.

Table 5.3 Reaction conditions for CO_2 to methanol, methanol to olefins and CO_2 to olefins conversion.

Entry	Product	Catalyst	T (°C)	Press. (bar)	Gas input (and volume ratio)	Total gas flow (sccm)
1	MeOH	CuZnGa oxides[55]	190–310	45	H_2/CO_2 =3	30
2	MeOH	CuZnAl oxides[56]	200	30	H_2/CO_2 =3	[a]
3	Olefins	H-ZSM-5[3]	325	1	MeOH/Ar [b]	40
4	Olefins	H-ZSM-5[57]	370	1	MeOH/He[c]	35
5	Olefins	SAPO-34 & CuZnAl oxides[2]	380	50	H_2/CO =3[d]	100
6	Olefins	MnNaFe oxide[58]	320	30	H_2/CO_2/Ar=7/2/1	34[e]
7	Olefins	ZSM@$Cu_{1.3}$ZnAl*	210–420	45	H_2/CO_2 =3	30
8	Olefins	H-ZSM-5*	400	1	MeOH/N_2[f]	30

*: This work. a: The gas hourly space velocity (GHSV)of the reaction is 9000 mL/$g_{catalyst}$/h. **b**: MeOH was feed with liquid volume flow at 0.04 mL/h with the Ar flow at 40 mL/min. **c**: MeOH was feed at 110 mbar saturation evaporator by He. **d**: 10% He by volume was used as internal standard. **e**: gas flow was calculated from GHSV = 2040 mL/$g_{catalyst}$/h. **f**: MeOH was feed by N_2 at 30 mL/min flow rate at 25 °C

5.3.2. Catalytic results for ZSM@$Cu_{1.3}$ZnAl

The ZSM@$Cu_{1.3}$ZnAl-LDH precursor was calcined at 500 °C for 3 h under air flow and reduced *in-situ* with H_2 at 290 °C for 2 h at atmospheric pressure to afford the fresh catalyst ZSM@$Cu_{1.3}$ZnAl. Similarly, the activated catalysts from $Cu_{1.3}$ZnAl-LDH as well as the 1:1 wt physical mixture of H-ZSM-5 and $Cu_{1.3}$ZnAl-LDH were prepared and were named $Cu_{1.3}$ZnAl-catalyst and PM-catalyst, respectively. The oxidation state of copper in all catalysts are the same and equal to zero.

Overall, the catalytic ability of ZSM@$Cu_{1.3}$ZnAl towards CO_2 conversion to olefins is not

satisfactory. The highest CO_2 conversion is obtained at 330 °C and is 4.8% (under 45 bar), far from the 27.4% CO_2 conversion equilibrium at 325 °C and 50 bar.[59] Importantly, ZSM@$Cu_{1.3}$ZnAl gives significant selectivity towards carbon monoxide (63.5%), methanol (14.2%), and dimethyl ether (14.0%). Only trace amounts of ethane and ethylene were formed (< 3%). The dominant selectivity for CO is due to the reversible water gas shift (RWGS) reaction becoming more predominant at high temperature.[59]

By comparison, the selectivity of activated $Cu_{1.3}$ZnAl-catalyst, H-ZSM-5 and PM-catalyst at 330 °C were tested and the results are summarised in

Table 5.4. Considering that H-ZSM-5 is not active for converting CO_2 to methanol,[60] the selectivity of H-ZSM-5 was evaluated using a methanol feed. Paraffins are presented as C_n; olefins are indicated by $C_{n=}$, where n = carbon number. Products of the $Cu_{1.3}$ZnAl-catalyst are CO (> 75%) and methanol (<25%). No olefin, paraffin, and dimethyl ether (DME) was produced.

Due to the instrument limit, methanol vapour cannot be pressurised; the catalytic test on H-ZSM-5 was conducted at 1 bar with a partial pressure of MeOH at 0.13 bar (Entry 8, Table 5.3). The commercial H-ZSM-5 used in this work achieves 100% methanol conversion at a reaction temperature above 370 °C and gives dominant selectivity towards light paraffins and olefins; trace amounts of C_1, DME, heavy paraffins and heavy olefins are also observed (Entry 2,

Table 5.4).

Contrary to the core-shell ZSM@$Cu_{1.3}$ZnAl, the PM-catalyst exhibits no selectivity towards

methanol but does show moderate selectivity towards light paraffins (C_1–C_3) due to the high MeOH conversion ability from H-ZSM-5 (Entry 3,

Table 5.4), i.e. the catalytic ability of H-ZSM-5 maintains in physical mixture. Unfortunately, due to the low CO_2 conversion (< 3%), a precise distribution of products cannot be given. The improved CO_2 conversion of ZSM@$Cu_{1.3}$ZnAl compared to the PM-catalyst demonstrates that the core-shell structure does, in some capacity, facilitate the CO_2 conversion; this is likely due to the diminished LDH platelet aggregation in core-shell compared to the physical mixture, as proven by the enhanced external surface area, or the LDH decorated diffusion channel (micropore) in zeolite as supported by the pore blocking in zeolite.

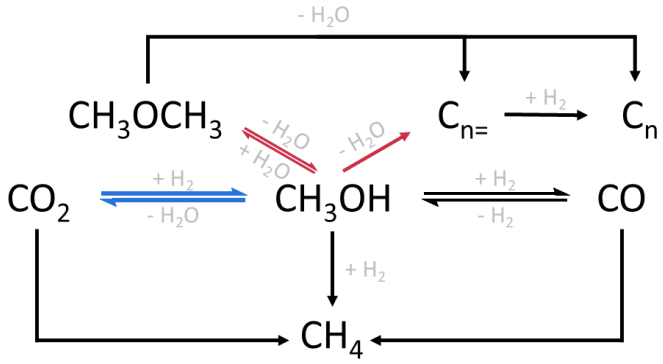
Table 5.4. The selectivity of $Cu_{1.3}$ZnAl-catalyst, H-ZSM-5, PM-catalyst and ZSM@$Cu_{1.3}$ZnAl at 330 °C (reaction condition for H-ZSM-5: MeOH feed, 1 bar; for the rest catalysts: H_2/CO_2 = 3 by mole, 45 bar, GHSV = 1800 mL/$g_{catalyst}$/h.)

Entry	Catalyst	Products		
		Dominant (>50%)	Moderate (total 10–30%)	Trace amount (< 3%)
1	$Cu_{1.3}$ZnAl-catalyst	CO	MeOH	
2	H-ZSM-5	C_2, $C_{2=}$, C_3, $C_{3=}$	C_4, C_5, C_6, C_7	C_1, DME, $C_{5=}$, $C_{6=}$, heavy parafins and olefins
3	PM-catalyst*	CO	C_1, C_2, C_3	$C_{2=}$, $C_{3=}$
4	ZSM@$Cu_{1.3}$ZnAl	CO	MeOH, DME	C_2, $C_{2=}$

*: Catalyst derived from the 1:1 wt physical mixture of H-ZSM-5 and CuZnAl-LDH.

Products and related reactions involved in the CO_2 to olefins conversion have been proposed in Scheme 5.1.[2,56,61–64] Prior studies have revealed that CO_2 to methanol reaction is catalysed by CuZnAl oxides derived from LDH;[65,66] methanol to DME (CH_3OCH_3) and olefins reaction is catalysed by acidic sites in H-ZSM-5.[56,61,62,67] It is proposed that the absence of olefins and paraffins selectivity of ZSM@$Cu_{1.3}$ZnAl could be due to the modification of acidic sites in

H-ZSM-5 arising from the ion-exchange during the co-precipitation synthesis step (NH_4^+ is replaced by Na^+).



Scheme 5.1 Proposed reaction network for the CO_2 to olefins conversion. Reactions highlight in blue and red are catalysed by CuZnAl oxides and H-ZSM-5, respectively.[2,56,61–64]

5.4. Variations of acidity of ZSM@$Cu_{1.3}$ZnAl-LDH via post-treatment methods

5.4.1. Post-treatment with ammonium salts

Preliminary catalytic CO_2 to olefins studies indicate that the ion exchange during the co-precipitation (Na^+ replacing NH_4^+) affects the acidity of ZSM@$Cu_{1.3}$ZnAl catalyst and leads to a lower hydrocarbon selectivity of core-shell comparing to the physical mixture. To tune the selectivity towards hydrocarbons (especially olefins), the acidity of ZSM@$Cu_{1.3}$ZnAl-LDH was modified by replacing the counterion, Na^+ for ZSM@$Cu_{1.3}$ZnAl-LDH, with NH_4^+ cation.

Normally, Na-templated ZSM-5 is dispersed in 0.5–2 M NH_4NO_3 aqueous solution at room temperature or elevated temperature for several hours to achieve a complete NH_4^+ exchange and obtain NH_4-formed ZSM-5.[68–72] To prevent LDH from dissolving, a neutral to slightly basic solution is desired. The NH_4^+ treatment procedure has been illustrated in Figure 5.9a. In the synthesis, after ageing, filtration and washing, the obtained ZSM@$Cu_{1.3}$ZnAl-LDH wet cake

was dispersed in an aqueous solution of NH_4HCO_3 at room temperature for 3 h to accomplish the NH_4^+ exchange. Although the XRD revealed no collapse of the LDH phase (Figure D2), an intense Cu leaching is observed when 1 M $(NH_4)HCO_3$ solution was used (Figure 5.9b). Further attempts were conducted at the same solid-to-solution ratio with lowered NH_4HCO_3 concentration: 0.5, 0.2, 0.1 and 0.01 M (Figure 5.9b). Based on visual inspection, no Cu leaching occurred when 0.01 M NH_4HCO_3 was used. The obtained sample was named ZSM@$Cu_{1.3}$ZnAl-LDH-10mM. The high similarity of the IR absorbance bands between the processed sample and the pristine core-shell proves the purity of ZSM@$Cu_{1.3}$ZnAl-LDH-10mM (Figure D3).

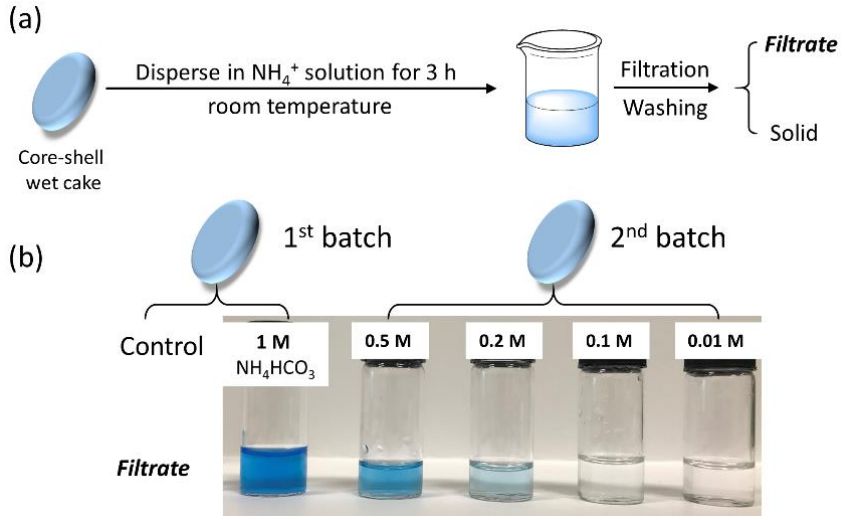


Figure 5.9 (a) Illustration of post-treatment for ZSM@$Cu_{1.3}$ZnAl-LDH and (b) filtrates from different concentrations of NH_4HCO_3 solution.

The ICP-MS result reveals that the treated sample exhibits an almost identical composition as the original core-shell, demonstrating that no metal leaching occurs (Table 5.5). It has been proved that this post-treatment is efficient in removing sodium as over 80% of Na^+ has been washed out. However, it is still possible that the residual sodium acts as the counterion of zeolite and hinders its acidity.

Table 5.5. ICP-MS and CHN analysis results for ZSM@$Cu_{1.3}$ZnAl-LDH and ZSM@$Cu_{1.3}$ZnAl-LDH-10mM.

Sample	Cu[a]	Zn[a]	Al[a]	**Na[a]**	Si[b]	C[c]	H[c]	**N[c]**
ZSM@$Cu_{1.3}$ZnAl-LDH	12.58	9.56	3.98	**4.11**	0.00	1.22	2.03	**0.06**
ZSM@$Cu_{1.3}$ZnAl-LDH-10mM	12.59	9.26	3.92	**0.82**	0.00	1.18	2.12	**0.16**

[a] The elemental weight percentage from ICP-MS analysis. [b] Si amount is below the detectable level in two samples [c] Element concentration obtained from elemental analysis.

The treated product exhibits a similar N_2 isotherm as the original one (Figure 5.10a), though adsorbs much less N_2 at the multilayer formation region ($p/p^0 > 0.05$); this suggests that ZSM@$Cu_{1.3}$ZnAl-LDH-10mM is microporous material that has less external surface area than the original composite. Consistently, the measured external surface area reduces from 194.0 m^2/g to 60.7 m^2/g after the ammonium modification (Figure 5.10b). However, the micropore surface area increases after the treatment, indicating a gain in the micropore; this is consistent with the DFT pore size distribution (Figure 5.11a) that 11.3 Å and 18.4 Å micropores are obtained after the treatment. Accordingly, the micropore pore volume increases (Figure 5.11b).[13,73] The reduction in the external surface area and external pore volume suggests that it is the change in the texture of LDH rather than zeolite that contributes to the micropore releasing (Figure 5.11). It is known that the formation of LDH is a dynamic dissolving-precipitate process conducted in aqueous media under neutral or basic condition.[74–76] During the post-treatment, small LDH platelets may undergo the Ostwald ripening, dissolving and settling out in a larger size. Therefore, some micropores that were previously blocked by those small particles get released.

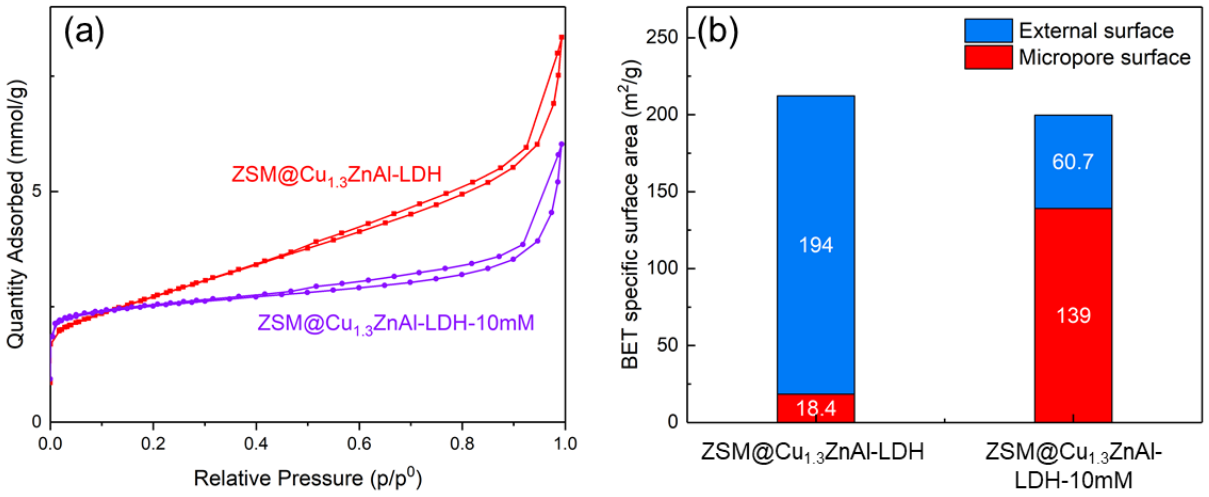


Figure 5.10 (a) The N_2 adsorption and desorption isotherm at 77 K and (b) the BET specific surface area of ZSM@$Cu_{1.3}$ZnAl-LDH and ZSM@$Cu_{1.3}$ZnAl-LDH-10mM.

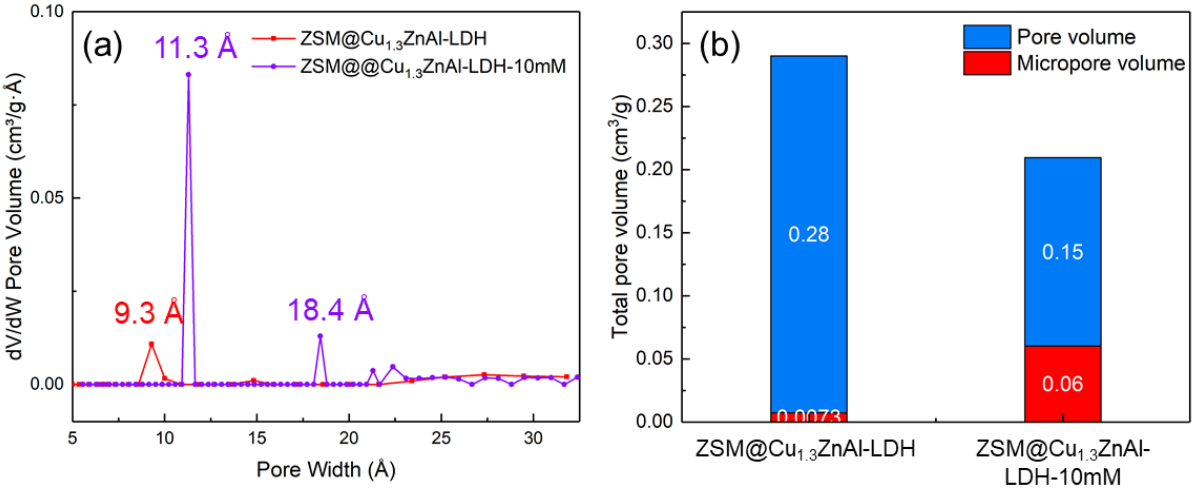


Figure 5.11 (a) the DFT pore size distribution based on the kernels for metal oxide with cylindrical pore and (b) total pore volume of ZSM@$Cu_{1.3}$ZnAl-LDH and ZSM@$Cu_{1.3}$ZnAl-LDH-10mM.

5.4.2. Studies of catalyst acidity

The acidity of the freshly prepared catalysts was studied using NH_3 temperature-programmed desorption (NH_3-TPD). A control sample of H-ZSM-5 was prepared following the same synthetic pathway as that for ZSM@$Cu_{1.3}$ZnAl-LDH without the addition of metal nitrates and was activated in the same way as other catalysts. The sample was termed ZSM-5-control.

The NH_3-TPD curves of H-ZSM-5 and ZSM-5-control are shown in Figure 5.12 with the number of acidic sites listed in Table 5.6, Entry 1–2. H-ZSM-5 possesses weak acidic sites (NH_3

desorbs below 250 °C) and strong acidic sites (NH_3 desorbs in the range 250–450 °C) (2.59 mmol/g and 1.23 mmol/g respectively). The weak acidic site is due to the physically adsorbed or weakly held NH_3, which is less likely correlated to the catalytic activity towards olefin production.[3,77,78] The strongly Brønsted acidic site in H-ZSM-5 results from the decomposition of NH_4^+ charge balancing cations during the catalyst activation and is responsible for the selectivity towards olefins.[72,79]

The control sample exhibits an almost identical amount of weak acidic sites as the original sample (2.51 mmol/g) while there are no strongly acidic sites. The absence of strong acidic sites is due to the substitution of NH_4^+ with Na^+, which is supported by the variation in Na and N amount of H-ZSM-5 and ZSM@$Cu_{1.3}$ZnAl-LDH.[18,72,80]

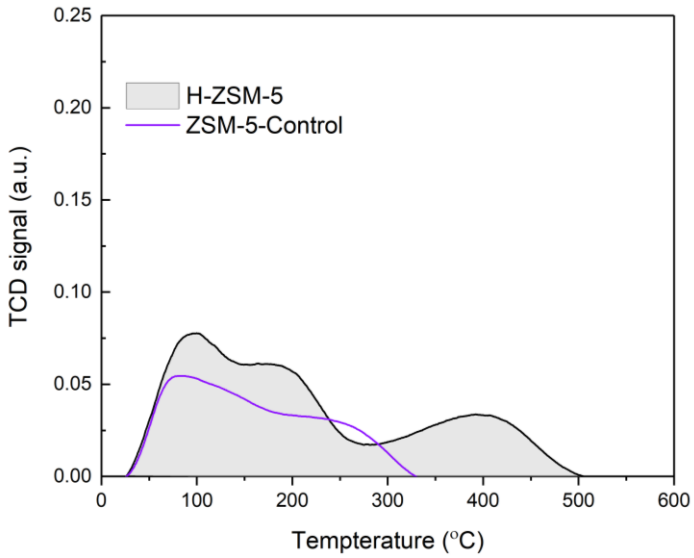


Figure 5.12 The NH_3-TPD curves of H-ZSM-5 and ZSM-5-control.

As shown in Figure 5.13, $Cu_{1.3}$ZnAl-catalyst has 1.49 mmol/g of very strong acidic sites (NH_3 desorbs above 450 °C), which could be Lewis acid sites arising from the interaction between the nitrogen of the NH_3 and the acid-base pairing (Al^{3+}-O^{2-}-Cu or Al^{3+}-O^{2-}-Zn^{2+}) in the material.[77,81,82] On the other hand, the catalyst is the incomplete decarbonation product of its

LDH precursor because the calcination temperature (500 °C) and reduction temperature (290 °C) is lower than the full decarbonation temperature (600–700 °C). Some gases detected between 500–600 °C may be CO_2 that is released due to the further decarbonisation of LDH. ZSM@$Cu_{1.3}$ZnAl possesses all three types of acidity while none of them are located near 400 °C, the position of the Brønsted acidic site in H-ZSM-5 (Figure 5.13). The absence of this strong acidic site may be responsible for the low olefin (and paraffin) selectivity.

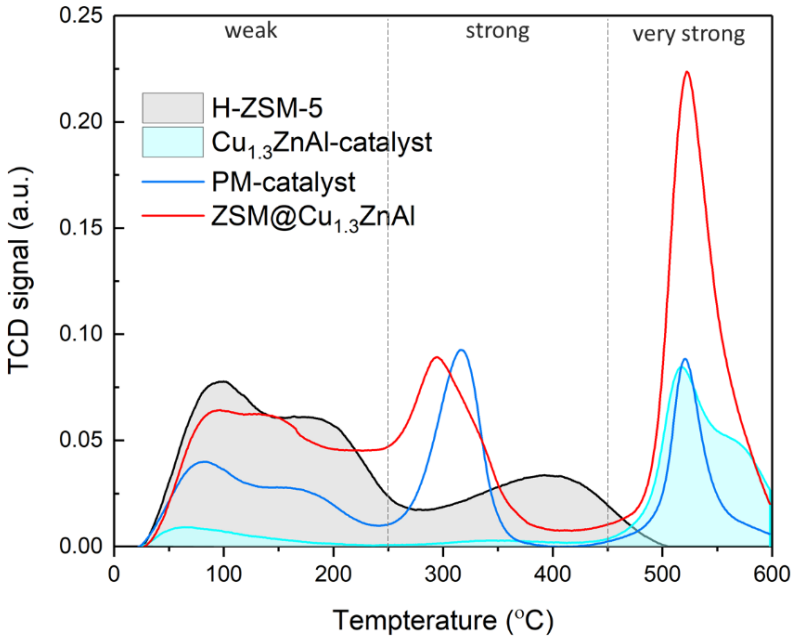


Figure 5.13 The NH_3-TPD profiles of H-ZSM-5, $Cu_{1.3}$ZnAl-catalyst, PM-catalyst and ZSM@$Cu_{1.3}$ZnAl. The oxidation state of copper in all Cu-containing catalysts is zero.

The acidity of PM-catalyst was considered to be a combination of those of H-ZSM-5 and $Cu_{1.3}$ZnAl-catalyst. As expected, the amount of the strong acidic site and the very strong acidic site of PM-catalyst is similar to the sum of H-ZSM-5 and $Cu_{1.3}$ZnAl-catalyst. However, the desorption temperature of NH_3 for strong acidic sites of PM-catalyst is lowered by 100 °C comparing to H-ZSM-5 (Figure 5.13 and Table 5.6, Entry 4–5). Several journal articles have demonstrated that decorating ZSM-5 with Cu or Zn or changing the Si/Al ratio will modify the

Brønsted acidity.[54,83,84] Presumably, the interface between Cu/ZnO/Al_2O_3 reduces the Brønsted acid strength of H-ZSM-5.[85]

The core-shell catalyst has over double the acidity of the one derived from the physical mixture. Moreover, the very strong acidic site is about four times that of PM-catalyst. The outstanding acid amount of ZSM@$Cu_{1.3}$ZnAl should result from the better dispersion of LDH due to the core-shell structure and could be the reason for the improved CO_2 conversion rate compared with PM-catalyst.

The strength of acid sites for PM-catalyst and ZSM@$Cu_{1.3}$ZnAl are similar, i.e., NH_3 desorption temperatures is similar. However, the difference in the product selectivity, ZSM@$Cu_{1.3}$ZnAl is MeOH and DME dominant while PM-catalyst is paraffin dominant, suggests that those two catalysts have different types of acidity. Yarulina *et al.* demonstrated that Brønsted and Lewis acid sites are both present in ZSM-5; the former is responsible for the olefin selectivity, and the latter prevents the generation of coke.[86] It is possible the strong acidic site (from zeolite core) in the PM-catalyst is mainly Brønsted acidity, while in ZSM@$Cu_{1.3}$ZnAl is mainly Lewis acidity. It has been reported that Na^+ in Na-ZSM-5 provides Lewis acidity.[87] The presence of sodium in the precursor of ZSM@$Cu_{1.3}$ZnAl supports this assumption. However, further characterisation is needed to clearly identify the acid type.

The catalyst derived from ZSM@$Cu_{1.3}$ZnAl-LDH-10mM is termed ZSM@$Cu_{1.3}$ZnAl-10mM. The post-treatment by ammonium bicarbonate does help to recover the acidity of zeolite as evidenced by a signal around 370 °C (Figure 5.14). However, the overall acid amount drops

sharply after the treatment (losing about 80% of acidity), which is unwanted; other methods to develop sodium-free core-shell will be required.

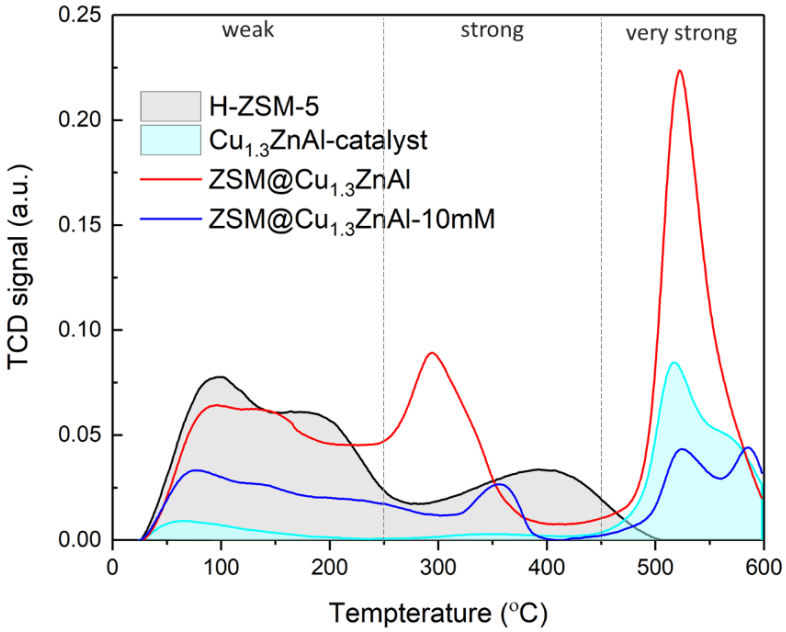


Figure 5.14 The NH_3-TPD profiles of ZSM@$Cu_{1.3}$ZnAl and ZSM@$Cu_{1.3}$ZnAl-10mM. The oxidation state of copper in all Cu-containing catalysts is zero.

Table 5.6 Acidity of catalysts.

Entry	Sample	Total acidity (mmol/g)*	Weak acidity (mmol/g)*	Strong acidity (mmol/g)*	Very strong acidity (mmol/g)*
1	H-ZSM-5	3.82	2.59	1.23	–
2	ZSM-5-control	2.51	2.51	–	–
3	$Cu_{1.3}$ZnAl-catalyst	1.49	–	–	1.49
4	ZSM@$Cu_{1.3}$ZnAl	10.33	4.33	2.00	4.00
5	PM-catalyst	4.09	1.62	1.45	1.11
6	ZSM@$Cu_{1.3}$ZnAl-10 mM	2.31	1.43	0.26	0.61

*: the amount is obtained directly from the measurement. However, due to the out-of-date calibration, the value is not comparable to the literature.

5.5. Sodium-free synthesis of ZSM@$Cu_{1.3}$ZnAl-LDH

5.5.1. Homogeneous precipitation

Apart from co-precipitation, homogeneous precipitation is another traditional LDH synthesis method, in which the aqueous solution of urea and metal salts undergoes the thermal treatment

to produce the LDH precipitates. The hydrolysis of urea provides the basic conditions and carbonate anions that are essential for LDH-CO_3 formation.[88] Before preparing core-shell via homogeneous precipitation, attempts were made to synthesise pure $Cu_{1.3}$ZnAl LDH.

Table D5 shows the synthesis conditions of CuZnAl LDH prepared via homogeneous precipitation. However, in all cases, impurities such as copper/zinc hydroxide chloride and copper/zinc ammonium chloride are present.[22,89,90] Previously within the group, it has been found that using urea/aluminium = 20 and refluxing the reaction mixture at 90 °C for 24 hours would provide highly crystalline MgAl-CO_3-LDH.[91] The first synthesis of $Cu_{1.3}$ZnAl LDH was conducted using the same synthesis conditions. The product is named $Cu_{1.3}$ZnAl-LDH-20Al and is a pale blue powder (Figure 5.15b).

The XRD pattern of $Cu_{1.3}$ZnAl-LDH-20Al in Figure 5.15a shows that the LDH phase and a trace amount of gerhardtite, one type of copper nitrate hydroxide, present in the sample. Meanwhile, the deep blue colour of the filtrate indicates that significant copper leaching occurs during the synthesis (Figure 5.15b). It is known that urea hydrolysis releases ammonia which would interact with Cu^{2+} and Zn^{2+} to generate water-soluble metal amine complexes in aqueous solution.[88,92,93]

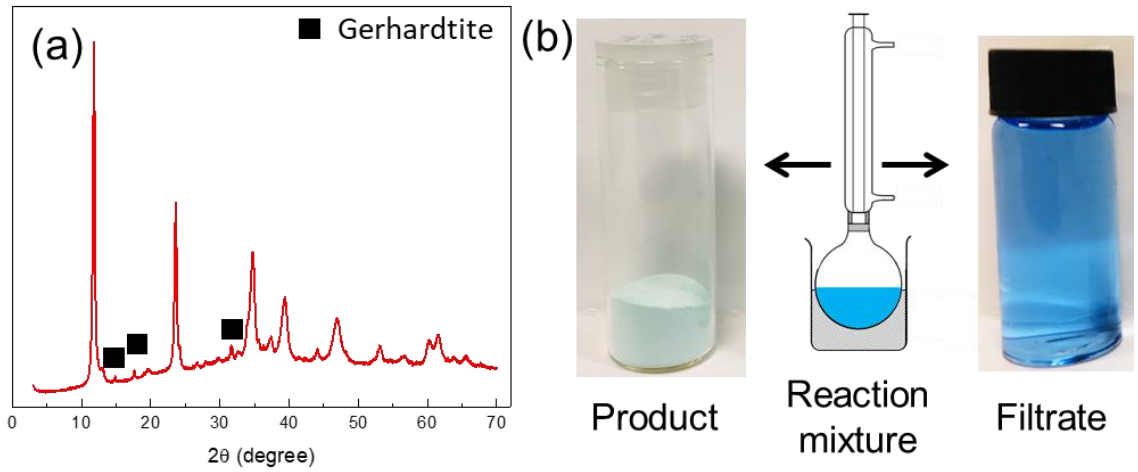


Figure 5.15 (a) XRD profile of $Cu_{1.3}$ZnAl-LDH-20Al. (b) Photo of $Cu_{1.3}$ZnAl-LDH-20Al and its filtrate.

In the literature, the urea/Al molar ratio in homogeneous precipitation varies from 6–20.[22,89,90] To eliminate the metal leaching, especially copper leaching, urea usage was reduced to 10 times and 6 times that of aluminium. Supported by the filtrate colour change, the metal leaching is reduced when less urea was used (Figure 5.16b). However, significant impurities were formed under the weak basic conditions and carbonate deficient environment (Figure 5.16b). When urea/Al = 6, no LDH phase was generated; gerhardtite and scarbroite ($Al_5CO_3(OH)_{13}\cdot 5H_2O$) were formed instead.

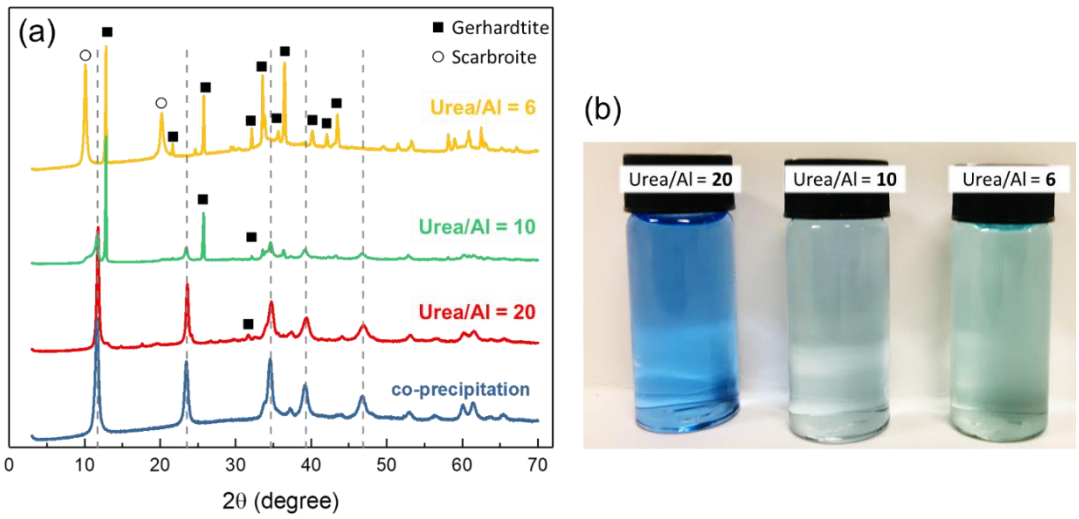


Figure 5.16 (a) XRD patterns and (b) photos of filtrate of $Cu_{1.3}$ZnAl-LDH prepared via homogeneous precipitation method with different urea/Al molar ratios (20, 10 and 6). The reaction temperature and time are fixed at 90 °C and 24 h. XRD pattern of $Cu_{1.3}$ZnAl-LDH obtained from the co-precipitation method was shown as a reference (blue).

At urea/Al = 10, the LDH phase is formed, and the copper leaching is acceptable. It is expected that the formation of impurity is due to the incomplete hydrolysis of urea, which can be avoided by elevating the reaction temperature. The synthesis was then repeated at an elevated temperature, 110 °C. The obtained product is called $Cu_{1.3}$ZnAl-LDH-10Al-110.

A highly crystalline LDH phase and a reduced amount of cuprite impurity were generated at elevated temperature, 110 °C (Figure 5.17a); the pale blue colour of the corresponding filtrate demonstrates that the copper leaching is minimal (Figure 5.17b). However, the product prepared at 110 °C mainly consists of a brown powder with small amount of green powder, the appearance of which is quite different from the typical look of $Cu_{1.3}$ZnAl LDH (a blue powder). Moreover, the FTIR reveals that $Cu_{1.3}$ZnAl-LDH-10Al-110 has far less carbonate than is expected in a $Cu_{1.3}$ZnAl-LDH (Figure D4). Therefore, the purity of this sample is in doubt.

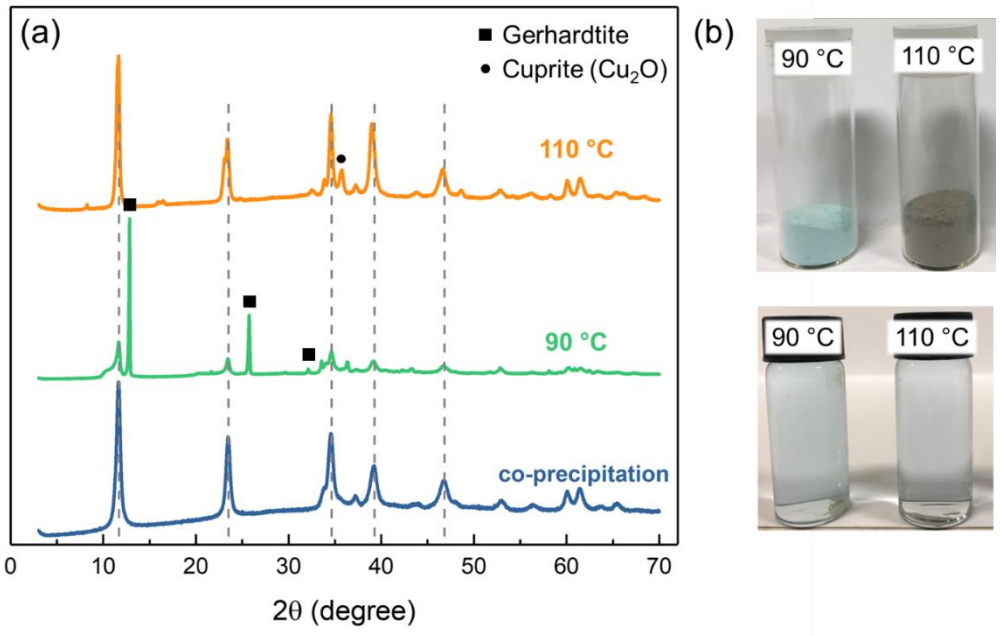


Figure 5.17 (a) XRD patterns and (b) photos of filtrate of $Cu_{1.3}$ZnAl-LDH prepared via homogeneous precipitation method with different reaction temperatures (90 °C and 110 °C).The urea/Al molar ratio and reaction time are fixed at 10 and 24 h. XRD pattern of CuZnAl-LDH obtained from the co-precipitation method was shown as a reference.

So far, metal leaching and impurity formation in synthesising $Cu_{1.3}ZnAl$ LDH via homogeneous precipitation cannot be avoided at the same time. Furthermore, the prolonged thermal treatment in aqueous solution is likely to change the properties of the zeolite.[53,54,94] Therefore, the homogeneous precipitation method is not optimal for preparing ZSM-5@CuZnAl-LDH core-shell. Other synthesis methods should be considered.

5.5.2. Co-precipitation with organic base

In synthesis of ZSM@$Cu_{1.3}ZnAl$-LDH via co-precipitation, the utilisation of sodium hydroxide and sodium carbonate initiates the counterion replacement. The former provides the necessary hydroxide group and acts as the pH control agent. The latter affords the essential interlayer carbonate anion for LDH generation. Sodium itself does not participate in building the LDH framework. Replacing those two chemicals with sodium-free reagents should prevent the altering of zeolite acidity through the counterion exchange.

Tetrapropylammonium hydroxide (TPAOH) was chosen as an organic base with low toxicity and a bulky cation group. It can not only avoid the ion exchange but also achieve a green synthesis. Basic copper carbonate, $Cu_2(OH)_2CO_3$, was used to provide carbonate and copper source.

The synthetic procedure was the same as that for ZSM@$Cu_{1.3}ZnAl$-LDH; apart from that small amount of concentrated nitric acid (HNO_3: $Cu_2(OH)_2CO_3$: = 2:1 by molar) was added to the metal salt solution to accomplish the complete dissolution of carbonate. Moreover, interlayer anion CO_3^{2-} presents in the metal salt solution rather than in the zeolite dispersion. The product

is a pale blue powder called ZSM@$Cu_{1.3}$ZnAl-LDH-TPA. A control LDH sample, $Cu_{1.3}$ZnAl-LDH-TPA, was prepared following the same synthesis method without the addition of H-ZSM-5.

The XRD pattern reveals that an LDH phase has been successfully formed using TPAOH base and copper carbonate (Figure 5.18). No crystalline impurity is found. The d_{003} for $Cu_{1.3}$ZnAl-LDH-TPA and ZSM@$Cu_{1.3}$ZnAl-LDH-TPA is 7.58 Å, indicating that the relevant LDH phase is carbonate-intercalated.[8]

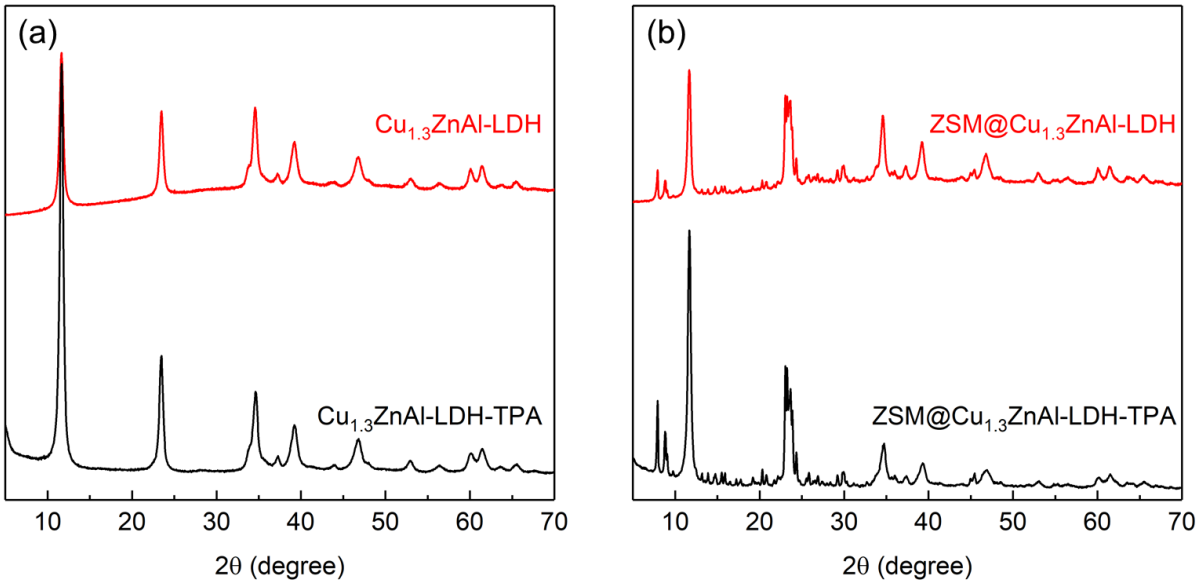


Figure 5.18 Powder XRD patterns of (a) $Cu_{1.3}$ZnAl-LDH and $Cu_{1.3}$ZnAl-LDH-TPA, (b) ZSM@$Cu_{1.3}$ZnAl-LDH and ZSM@$Cu_{1.3}$ZnAl-LDH-TPA.

The TEM image shows that $Cu_{1.3}$ZnAl-LDH-TPA are platelets with irregular shapes and a size of 152 ± 54 nm (Figure 5.19a), which is smaller than that of $Cu_{1.3}$ZnAl-LDH, 142–500 nm (Figure 5.19c). This observation demonstrates that changing the base and the carbonate source modifies the particle size of LDH. A core-shell structure is achieved in ZSM@$Cu_{1.3}$ZnAl-LDH-TPA; the thickness of the shell is 100–450 nm, slightly smaller than that of ZSM@$Cu_{1.3}$ZnAl-

LDH (250–500 nm) as a result of smaller LDH platelets (Figure 5.19d).

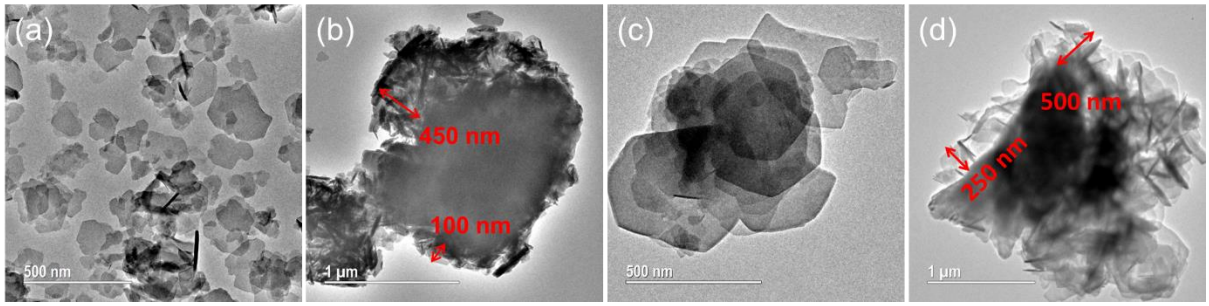


Figure 5.19 TEM image of (a) $Cu_{1.3}$ZnAl-LDH-TPA, (b) ZSM@$Cu_{1.3}$ZnAl-LDH-TPA, (c) $Cu_{1.3}$ZnAl-LDH and (d) ZSM@$Cu_{1.3}$ZnAl-LDH.

FTIR spectra and TGA plots of ZSM@$Cu_{1.3}$ZnAl-LDH-TPA show both the zeolite and LDH features (Figure D5 and D6). No obvious impurity can be found. LDHs and core-shells prepared from different base and carbonate sources exhibit similar thermal stability (Figure D6).

N_2 isotherm of CuZnAl-LDH-TPA is a type II isotherm with H3 hysteresis loop, indicating this material is macroporous and consists of cluster of plate-like particles (Figure 5.20b).[51] ZSM@$Cu_{1.3}$ZnAl-LDH-TPA exhibits type II isotherm with a H3 hysteresis loop (Figure 5.20a). The sharp N_2 uptake at ultra-low pressure ($p/p^0 < 0.05$) proves the presence of micropore from zeolite.[51] The steady N_2 adsorption over the multilayer formation range (p/p^0 = 0.1–0.8) suggests that this material has a low external surface area.[51] ZSM@$Cu_{1.3}$ZnAl-LDH displays a steeper N_2 uptake in the multilayer formation range than ZSM@$Cu_{1.3}$ZnAl-LDH-TPA, indicating the former has a larger external surface area than the latter.

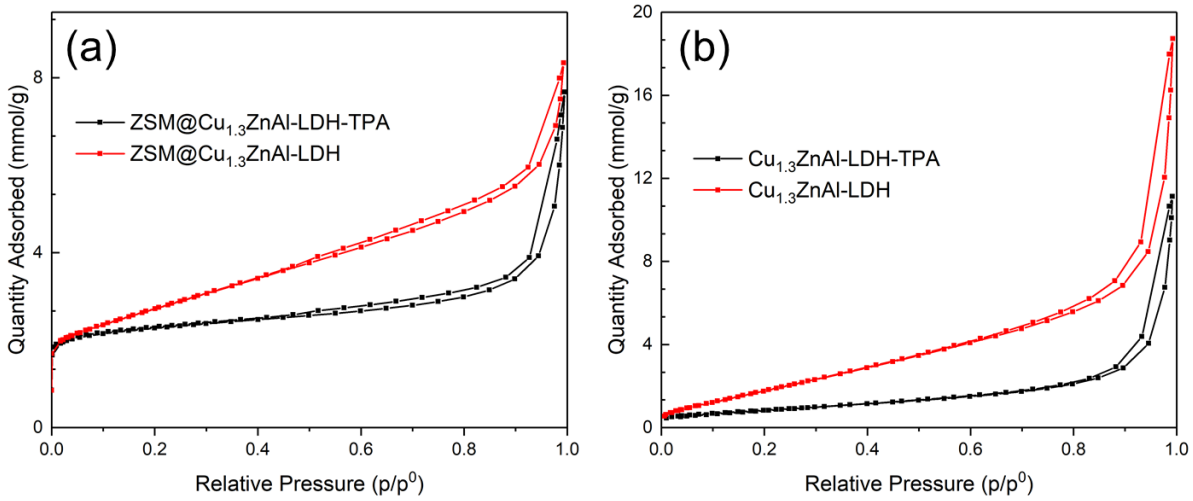


Figure 5.20 N_2 adsorption and desorption isotherm at 77 K of (a) CuZnAl-LDH and CuZnAl-LDH-TPA, and (b) ZSM@$Cu_{1.3}$ZnAl-LDH and ZSM@$Cu_{1.3}$ZnAl-LDH-TPA.

Correspondingly, ZSM@$Cu_{1.3}$ZnAl-LDH has 194.0 m^2/g external surface area, while ZSM@$Cu_{1.3}$ZnAl-LDH-TPA only has 59.2 m^2/g (Figure 5.21a). $Cu_{1.3}$ZnAl-LDH-TPA has lower BET specific surface area and total pore volume than the LDH prepared with the sodium reagent (Figure 5.21). Platelet-platelet aggregation may be more intense in the sodium-free condition, resulting in the loss of surface area and slit-like pores. Accordingly, the core-shell prepared from the sodium-free condition possesses lower external surface area. Consistent with the observation of BET specific surface area, ZSM@$Cu_{1.3}$ZnAl-LDH-TPA has a smaller external pore volume than the core-shell prepared with sodium.

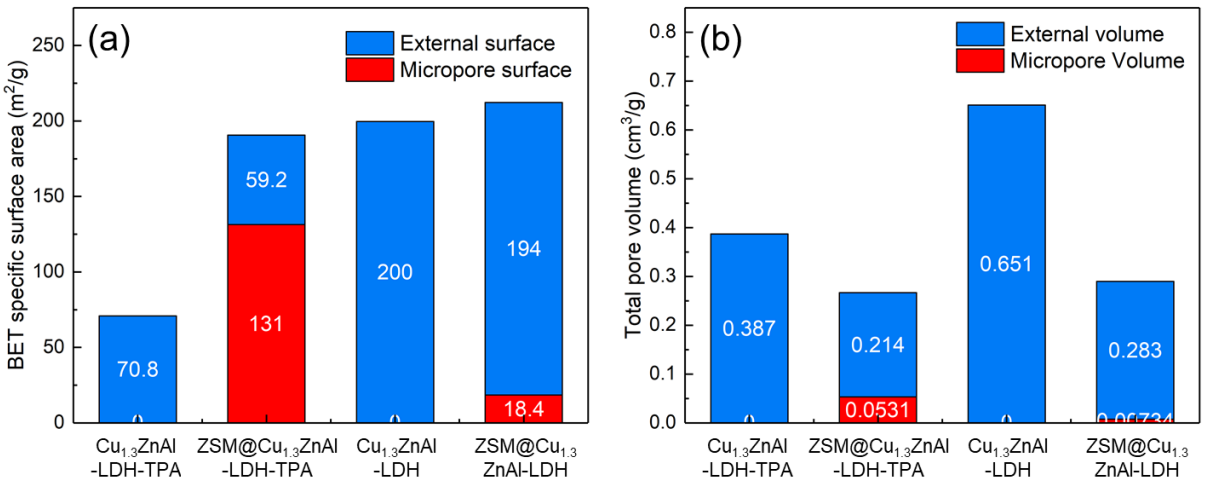


Figure 5.21 (a) BET specific surface area and (b) total pore volume of $Cu_{1.3}$ZnAl-LDH-TPA, ZSM@$Cu_{1.3}$ZnAl-LDH-TPA, $Cu_{1.3}$ZnAl-LDH and ZSM@$Cu_{1.3}$ZnAl-LDH.

The micropore size in pristine H-ZSM-5 is 7.4 Å and 18.4 Å, and the micropore volume reaches 0.14 cm^3/g (Figure 5.22a). When NaOH was used as the base, changes in the surface area and pore volume demonstrates that over 99% micropore is lost. However, in the case of using TPAOH, the loss in micropore is alleviated. The high micropore surface area (131.0 m^2/g) and evident micropore volume (0.053 cm^3/g) illustrate the presence of micropores in ZSM@$Cu_{1.3}$ZnAl-LDH-TPA. DFT pore size distribution reveals that the size of micropore is slightly expanded, 12.0 Å and 18.4 Å, compared to the original H-ZSM-5 (Figure 5.22a). The pore expansion could be due to dispersing zeolite at basic environment.[53,54]

TPA bromide is utilised as the template in the synthesis of commercial H-ZSM-5 used in this work, which means TPA^+ cation can perfectly sit in the pore of H-ZSM-5.[32] Before the metal nitrate addition, a certain amount of TPAOH was added to the aqueous dispersion of H-ZSM-5 to adjust the pH to 10. It is very likely that TPA^+ cations partially occupy the pore of H-ZSM-5 which hinders the entrance of metal cation and diminishes pore blockage due to LDH growth.

BJH pore size distribution shows that LDHs, $Cu_{1.3}$ZnAl-LDH and $Cu_{1.3}$ZnAl-LDH-TPA are macroporous, which agrees with the fact that LDH is composed of clusters of platelets (Figure 5.22b). Core-shells have some macropores as a result of interparticle aggregation.

The difference between the texture of core-shell prepared with TPAOH and NaOH indicates that the pore structure of the composite can be tuned by modifying the type of base used, and that pore blocking can be avoided.

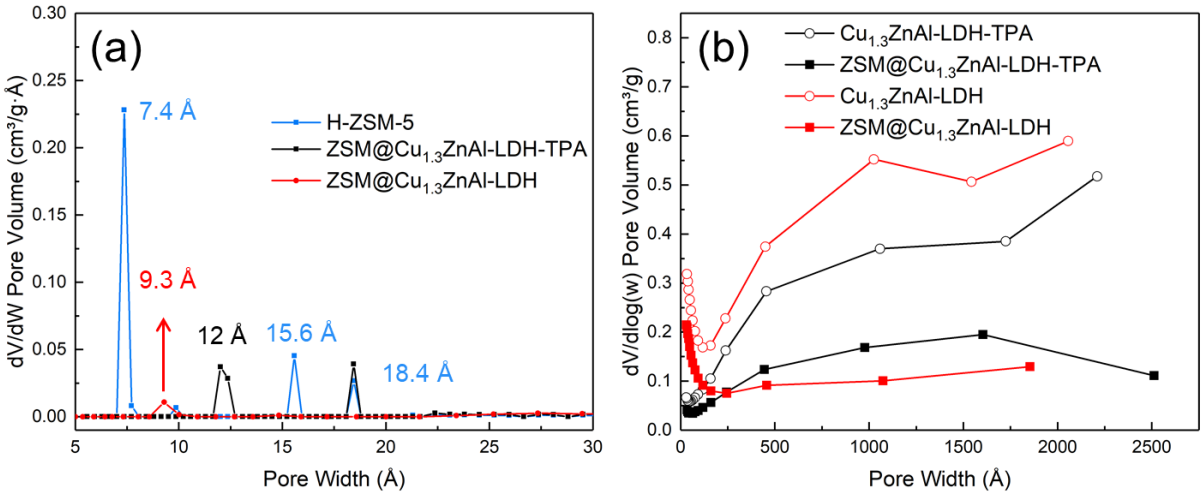


Figure 5.22 (a) DFT pore size distribution and of H-ZSM-5, ZSM@$Cu_{1.3}$ZnAl-LDH-TPA and ZSM@$Cu_{1.3}$ZnAl-LDH. (b)BJH pore size distribution of $Cu_{1.3}$ZnAl-LDH, $Cu_{1.3}$ZnAl-LDH-TPA, ZSM@$Cu_{1.3}$ZnAl-LDH-TPA and ZSM@$Cu_{1.3}$ZnAl-LDH.

5.6. Conclusions and Outlook

ZSM@$Cu_{1.3}$ZnAl-LDH core-shell has been successfully synthesised via the co-precipitation method. Unlike SiO_2@$Cu_{1.3}$ZnAl-LDH, the LDH shell on the zeolite core exhibits high crystallinity. Catalyst derived from this core-shell shows better CO_2 conversion (4.8%) towards CO_2 to olefins conversion compared to the one derived from the physical mixture (< 3%), which is likely due to its superior acid amount. Mobilising LDH on the zeolite core diminishes the interplatelet aggregation and releases acidic sites. However, the counterion exchange in the core-shell synthesis modifies the acidity of zeolite core and leads to a low olefin selectivity from this core-shell catalyst. The ammonium salt post-treatment restored the acidity to some extent while resulting in an overall reduction in the total acid sites.

Sodium-free core-shell syntheses were attempted to avoid the modification of zeolite acidity via ion exchange. The homogeneous precipitation method is not suitable for preparing $Cu_{1.3}$ZnAl LDH as metal leaching and impurity formation cannot be avoided. Co-precipitation using organic base TPAOH and basic copper carbonate can successfully generate pure CuZnAl LDH and relevant core-shell composite. LDH prepared with TPAOH shows more intense interplatelet aggregation than the one prepared with NaOH, though micropore blockage due to the LDH growth was prevented. This is the first time that pore blockage has been prevented in the LDH-based core-shell composite.

Future work on this area can focus on the evaluation of the catalytic performance for CO_2 to olefins using ZSM@$Cu_{1.3}$ZnAl-LDH-TPA, including correlating the material properties like acidity to the results. The effect of TPAOH usage on the texture (pore structure and LDH

morphology) of core-shells should be investigated further; abundant pores in catalysts promotes the mass transfer, regulates the selectivity and has a positive effect on the productivity.[95,96] Utilising TAPOH provides the opportunity to develop core-shell catalysts with abundant micropores and promising catalytic ability.

5.7. References

1 P. Gao, S. Li, X. Bu, S. Dang, Z. Liu, H. Wang, L. Zhong, M. Qiu, C. Yang, J. Cai, W. Wei and Y. Sun, *Nat. Chem.*, 2017, **9**, 1019–1024.

2 D. L. S. Nieskens, A. Ciftci, P. E. Groenendijk, M. F. Wielemaker and A. Malek, *Ind. Eng. Chem. Res.*, 2017, **56**, 2722–2732.

3 T. Liang, J. Chen, Z. Qin, J. Li, P. Wang, S. Wang, G. Wang, M. Dong, W. Fan and J. Wang, *ACS Catal.*, 2016, **6**, 7311–7325.

4 Z. Al, O. H.- De, A. Le and L. Pinard, 2015, **18**, 6–11.

5 Y. Wang, W. Gao, S. Kazumi, Y. Fang, L. Shi, Y. Yoneyama, G. Yang and N. Tsubaki, *Fuel*, 2019, **253**, 249–256.

6 S. Das, J. Pérez-Ramírez, J. Gong, N. Dewangan, K. Hidajat, B. C. Gates and S. Kawi, *Chem. Soc. Rev.*, 2020, **49**, 2937–3004.

7 C. Chen, C. F. H. Byles, J.-C. Buffet, N. H. Rees, Y. Wu and D. O'Hare, *Chem. Sci.*, 2016, **7**, 1457–1461.

8 F. Cavani, F. Trifirò and A. Vaccari, *Catal. Today*, 1991, **11**, 173–301.

9 C. Chen, R. Felton, J.-C. Buffet and D. O'Hare, *Chem. Commun.*, 2015, **51**, 3462–3465.

10 W. L. J. Kwok, D.-G. Crivoi, C. Chen, J.-C. Buffet and D. O'Hare, *Dalton Trans.*, 2018, **47**, 143–149.

11 H. Suo, H. Duan, C. Chen, J. C. Buffet and D. O'Hare, *RSC Adv.*, 2019, **9**, 3749–3754.

12 C. Chen, R. Felton, J. C. Buffet and D. O'Hare, *Chem. Commun.*, 2015, **51**, 3462–3465.

13 M. Lyu, C. Chen, J. C. Buffet and D. O'Hare, *New J. Chem.*, 2020, **44**, 10095–10101.

14 A. Vjunov, J. L. Fulton, D. M. Camaioni, J. Z. Hu, S. D. Burton, I. Arslan and J. A. Lercher, *Chem. Mater.*, 2015, **27**, 3533–3545.

15 D. W. Gardner, J. Huo, T. C. Hoff, R. L. Johnson, B. H. Shanks and J. P. Tessonnier, *ACS Catal.*, 2015, **5**, 4418–4422.

16 T. Ennaert, J. Geboers, E. Gobechiya, C. M. Courtin, M. Kurttepeli, K. Houthoofd, C. E. A. Kirschhock, P. C. M. M. Magusin, S. Bals, P. A. Jacobs and B. F. Sels, *ACS Catal.*, 2015, **5**, 754–768.

17 C. Auepattana-aumrung, V. Márquez, S. Wannakao, B. Jongsomjit, J. Panpranot and P. Praserthdam, *Sci. Rep.*, 2020, **10**, 1–11.

18 S. Hassanpour, M. Taghizadeh and F. Yaripour, *Ind. Eng. Chem. Res.*, 2010, **49**, 4063–4069.

19 O. B. Ayodele, *Sci. Rep.*, 2017, **7**, 1–14.

20 L. Zhang, F. Li, D. G. Evans and X. Duan, *Mater. Chem. Phys.*, 2004, **87**, 402–410.

21 V. Rives and S. Kannan, *J. Mater. Chem.*, 2000, **10**, 489–495.

22 F. Jing, Y. Zhang, S. Luo, W. Chu and W. Qian, *Appl. Clay Sci.*, 2010, **48**, 203–207.

23 S. Velu and C.S.Swamy, *J. Mater. Sci. Lett.*, 1996, **15**, 1674–1677.

24 M. Behrens, I. Kasatkin, S. Kühl and G. Weinberg, *Chem. Mater.*, 2010, **22**, 386–397.

25 A. Alejandre, F. Medina, P. Salagre, X. Correig and J. E. Sueiras, *Chem. Mater.*, 1999, **11**, 939–948.

26 J. G. Nunan, P. B. Himelfarb, R. G. Herman, K. Klier, C. E. Bogdan and G. W. Simmons, *Inorg. Chem.*, 1989, **28**, 3868–3874.

27 P. J. Sideris, U. G. Nielsen, Z. Gan and C. P. Grey, *Science*, 2008, **321**, 113–117.

28 J. Pironon, M. Pelletier, P. De Donato and R. Mosser-Ruck, *Clay Miner.*, 2003, **38**, 201–211.

29 F. Milella and M. Mazzotti, *React. Chem. Eng.*, 2019, **4**, 1284–1302.

30 R. P. Ye, L. Lin, C. C. Chen, J. X. Yang, F. Li, X. Zhang, D. J. Li, Y. Y. Qin, Z. Zhou and Y. G. Yao, *ACS Catal.*, 2018, **8**, 3382–3394.

31 J. Huang, Y. Jiang, V. R. Reddy Marthala, Y. S. Ooi, J. Weitkamp and M. Hunger, *Microporous Mesoporous Mater.*, 2007, **104**, 129–136.

32 B. S. Mojarad, A. Nourbakhsh, R. E. Kahrizsangi, M. Masoud and K. J. D. Mackenzie, *Ceram. Int.*, 2015, **41**, 5287–5293.

33 E. Epelde, J. I. Santos, P. Florian, A. T. Aguayo, A. G. Gayubo, J. Bilbao and P. Castaño, *Appl. Catal. A Gen.*, 2015, **505**, 105–115.

34 S. Sklenak, J. Dědeček, C. Li, B. Wichterlová, V. Gábová, M. Sierka and J. Sauer, *Phys. Chem. Chem. Phys.*, 2009, **11**, 1237–1247.

35 S. K. Matam, A. J. O'Malley, C. R. A. Catlow, Suwardiyanto, P. Collier, A. P. Hawkins, A. Zachariou, D. Lennon, I. Silverwood, S. F. Parker and R. F. Howe, *Catal. Sci. Technol.*, 2018, **8**, 3304–3312.

36 J. Valecillos, E. Epelde, J. Albo, A. T. Aguayo, J. Bilbao and P. Castaño, *Catal. Today*, 2020, **348**, 243–256.

37 F. Dogan, K. D. Hammond, G. A. Tompsett, H. Huo, W. C. Conner, S. M. Auerbach and C. P. Grey, *J. Am. Chem. Soc.*, 2009, **131**, 11062–11079.

38 W. Loewenstein and M. Lowensterin, *Am. Mineral.*, 1954, **39**, 92–96.

39 C. A. Fyfe, Y. Feng, H. Grondey, G. T. Kokotailo and H. Gies, *Chem. Rev.*, 1991, **91**, 1525–1543.

40 J. C. Groen, J. A. Moulijn and J. Pérez-Ramírez, *J. Mater. Chem.*, 2006, **16**, 2121–2131.

41 D. Verboekend and J. Pérez-Ramírez, *Catal. Sci. Technol.*, 2011, **1**, 879–890.

42 S. J. You and E. D. Park, *Microporous Mesoporous Mater.*, 2014, **186**, 121–129.

43 S. Ramadan, T. W. Hambley, B. J. Kennedy and P. A. Lay, *Inorg. Chem.*, 2004, **43**, 2943–2946.

44 A. J. Pell, G. Pintacuda and C. P. Grey, *Prog. Nucl. Magn. Reson. Spectrosc.*, 2019, **111**, 1–271.

45 S. S. C. Pushparaj, C. Forano, V. Prevot, A. S. Lipton, G. J. Rees, J. V. Hanna and U. G. Nielsen, *J. Phys. Chem. C*, 2015, **119**, 27695–27707.

46 L. B. Staal, S. S. Charan Pushparaj, C. Forano, V. Prevot, D. B. Ravnsbæk, M. Bjerring and U. G. Nielsen, *J. Mater. Chem. A*, 2017, **5**, 21795–21806.

47 L. H. Chagas, G. S. G. De Carvalho, W. R. Do Carmo, R. A. S. San Gil, S. S. X. Chiaro, A. A. Leitão, R. Diniz, L. A. De Sena and C. A. Achete, *Mater. Res. Bull.*, 2015, **64**, 207–215.

48 N. D. Jensen, C. Forano, S. S. C. Pushparaj, Y. Nishiyama, B. Bekele and U. G. Nielsen, *Phys. Chem. Chem. Phys.*, 2018, **20**, 25335–25342.

49 K. Cermelj, D.Phil thesis, University of Oxford, 2020.

50 M. Moreno-Recio, J. Santamaría-González and P. Maireles-Torres, *Chem. Eng. J.*, 2016, **303**, 22–30.

51 M. Thommes, K. Kaneko, A. V. Neimark, J. P. Olivier, F. Rodriguez-Reinoso, J. Rouquerol and K. S. W. Sing, *Pure Appl. Chem.*, 2015, **87**, 1051–1069.

52 J. B. Condon, in *Surface Area and Porosity Determinations by Physisorption*, ed. J. B. Condon, Elsevier Science, Amsterdam, 2006, pp. 1–27.

53 T. Suzuki and T. Okuhara, *Microporous Mesoporous Mater.*, 2001, **43**, 83–89.

54 X. Shen, J. Kang, W. Niu, M. Wang, Q. Zhang and Y. Wang, *Catal. Sci. Technol.*, 2017, **7**, 3598–3612.

55 M. M. J. Li, C. Chen, T. Ayvall, H. Suo, J. Zheng, I. F. Teixeira, L. Ye, H. Zou, D. O'Hare and S. C. E. Tsang, *ACS Catal.*, 2018, **8**, 4390–4401.

56 B. Liang, J. Ma, X. Su, C. Yang, H. Duan, H. Zhou, S. Deng, L. Li and Y. Huang, *Ind. Eng. Chem. Res.*, 2019, **58**, 9030–9037.

57 M. Bjorgen, F. Joensen, M. S. Holm, U. Olsbye, K. P. Lillerud and S. Svelle, *Appl. Catal. A Gen.*, 2008, **345**, 43–50.

58 B. Liang, T. Sun, J. Ma, H. Duan, L. Li, X. Yang, Y. Zhang, X. Su, Y. Huang and T. Zhang, *Catal. Sci. Technol.*, 2019, **9**, 456–464.

59 K. Stangeland, H. Li and Z. Yu, *Ind. Eng. Chem. Res.*, 2018, **57**, 4081–4094.

60 Z. Li, Y. Qu, J. Wang, H. Liu, M. Li, S. Miao and C. Li, *Joule*, 2019, **3**, 570–583.

61 P. Dejaifve, J. C. Védrine, V. Bolis and E. G. Derouane, *J. Catal.*, 1980, **63**, 331–345.

62 U. Olsbye, S. Svelle, M. Bjrgen, P. Beato, T. V. W. Janssens, F. Joensen, S. Bordiga and K. P. Lillerud, *Angew. Chem. Int. Ed.*, 2012, **51**, 5810–5831.

63 A. García-Trenco, A. Vidal-Moya and A. Martínez, *Catal. Today*, 2012, **179**, 43–51.

64 S. Velu, K. Suzuki and T. Osaki, *Catal. Letters*, 1999, **62**, 159–167.

65 M. Behrens, F. Studt, I. Kasatkin, S. Kühl, M. Hävecker, F. Abild-pedersen, S. Zander, F. Girgsdies, P. Kurr, B. Kniep, M. Tovar, R. W. Fischer, J. K. Nørskov and R. Schlögl, *Science*, 2012, **336**, 893–898.

66 T. Lunkenbein, F. Girgsdies, T. Kandemir, N. Thomas, M. Behrens, R. Schlögl and E. Frei, *Angew. Chem. Int. Ed.*, 2016, **55**, 12708–12712.

67 I. M. Dahl and S. Kolboe, *Catal. Letters*, 1993, **20**, 329–336.

68 L. Shirazi, E. Jamshidi and M. R. Ghasemi, *Cryst. Res. Technol.*, 2008, **43**, 1300–1306.

69 Y. Zhang, I. J. Drake and A. T. Bell, *Chem. Mater.*, 2006, **18**, 2347–2356.

70 M. Rostamizadeh and A. Taeb, *Synth. React. Inorganic, Met. Nano-Metal Chem.*, 2016, **46**, 665–671.

71 L. Tao, G. S. Li, S. F. Yin, O. Y. Qiang, S. L. Luo, X. P. Zhou and C. T. Au, *React. Kinet. Mech. Catal.*, 2011, **103**, 191–207.

72 R. Wei, C. Li, C. Yang and H. Shan, *J. Nat. Gas Chem.*, 2011, **20**, 261–265.

73 X. Liu, C. Wang, Y. Dou, A. Zhou, T. Pan, J. Han and M. Wei, *J. Mater. Chem. A*, 2014, **2**, 1682–1685.

74 A. J. Marchi and C. R. Apesteguía, *Appl. Clay Sci.*, 1998, **13**, 35–48.

75 C. Chen, P. Wang, T.-T. Lim, L. Liu, S. Liu and R. Xu, *J. Mater. Chem. A*, 2013, **1**, 3877–3880.

76 X. Sun and S. K. Dey, *J. Colloid Interface Sci.*, 2015, **458**, 160–168.

77 J. Hou, W. Luo, S. Luo, C. Lin, P. Liu, X. Liao, F. Jing and X. Li, *RSC Adv.*, 2017, **7**, 48662–48669.

78 F. Lónyi and J. Valyon, *Microporous Mesoporous Mater.*, 2001, **47**, 293–301.

79 F. Gorzin and F. Yaripour, *Res. Chem. Intermed.*, 2019, **45**, 261–285.

80 M. Dyballa, U. Obenaus, M. Blum and W. Dai, *Catal. Sci. Technol.*, 2018, **8**, 4440–4449.

81 L. J. I. Coleman, W. Epling, R. R. Hudgins and E. Croiset, *Appl. Catal. A Gen.*, 2009, **363**, 52–63.

82 H. Metiu, S. Chrétien, Z. Hu, B. Li and X. Sun, *J. Phys. Chem. C*, 2012, **116**, 10439–10450.

83 P. Parthasarathy and S. K. Narayanan, *Environ. Prog. Sustain. Energy*, 2014, **33**, 676–680.

84 E. H. Yuan, W. Han, G. Zhang, K. Zhao, Z. Mo, G. Lu and Z. Tang, *Catal. Surv. from Asia*, 2016, **20**, 41–

52.

85 J. Chen, X. Wang, D. Wu, J. Zhang, Q. Ma, X. Gao, X. Lai, H. Xia, S. Fan and T. S. Zhao, *Fuel*, 2019, **239**, 44–52.

86 I. Yarulina, K. De Wispelaere, S. Bailleul, J. Goetze, M. Radersma, E. Abou-Hamad, I. Vollmer, M. Goesten, B. Mezari, E. J. M. Hensen, J. S. Martínez-Espín, M. Morten, S. Mitchell, J. Perez-Ramirez, U. Olsbye, B. M. Weckhuysen, V. Van Speybroeck, F. Kapteijn and J. Gascon, *Nat. Chem.*, 2018, **10**, 804–812.

87 S. Bordiga, E. Escalona Platero, C. Otero Areán, C. Lamberti and A. Zecchina, *J. Catal.*, 1992, **137**, 179–185.

88 Y. K. Lin, Y. H. Su, Y. H. Huang, C. J. Hsu, Y. K. Hsu, Y. G. Lin, K. H. Huang, S. Y. Chen, K. H. Chen and L. C. Chen, *J. Mater. Chem.*, 2009, **19**, 9186–9194.

89 M. Turco, G. Bagnasco, U. Costantino, F. Marmottini, T. Montanari, G. Ramis and G. Busca, *J. Catal.*, 2004, **228**, 43–55.

90 S. Murcia-Mascarós, R. M. Navarro, L. Gómez-Sainero, U. Costantino, M. Nocchetti and J. L. G. Fierro, *J. Catal.*, 2001, **198**, 338–347.

91 K. Cermelj, Master thesis, University of Oxford, 2016.

92 O. O. Oluokun and I. O. Otunniyi, *Hydrometallurgy*, 2020, **193**, 105320–105326.

93 A. R. Johnson, T. M. McQueen and K. T. Rodolfa, *J. Chem. Educ.*, 2005, **82**, 408–414.

94 L. Han, Y. Ouyang, E. Xing, Y. Luo and Z. Da, *Chinese J. Chem. Eng.*, 2020, **28**, 3052–3060.

95 H. Becker, R. Güttel and T. Turek, *Catal. Sci. Technol.*, 2016, **6**, 275–287.

96 Y. He, W. J. Jiang, Y. Zhang, L. B. Huang and J. S. Hu, *J. Mater. Chem. A*, 2019, **7**, 18428–18433.

Chapter 6 Conclusions and Outlook

The work outlined in this thesis has focused on developing layered double hydroxide-based (LDH-based) core-shell materials and exploring their applications in CO_2 adsorption, and the catalytic conversion of CO_2 to methanol and olefins.

Initially, LDH-based core-shell materials as CO_2 adsorbents were studied. A series of core-shells using zeolite 13X (Z13X, the benchmark CO_2 adsorbent) as the core and Mg_2Al-CO_3-LDH as the shell were prepared via co-precipitation. The effects of metal salt solution addition rate, reaction ageing time and LDH fraction were studied. It was found that the crystallinity, thermal stability and composition of Z13X@Mg_2Al-CO_3-LDH core-shells prepared from various addition rates (0.5–2 h) and ageing times (0.5–16 h) were similar. A core-shell with high-N_2 BET surface-area (517.3 m^2/g) can be readily prepared within a 1-hour reaction time (0.5 hour addition time and 0.5 hour ageing time). Reducing the LDH content in the core-shell from 50 wt% to 5 wt% led to a reduction in the thickness of LDH shell (from 270–540 to 70 nm) and an increase of the N_2 BET specific surface area (517.3 to 899.2 m^2/g).

Z13X@Mg_2Al-CO_3-LDH core-shells were then calcined to produce the core-shell CO_2 adsorbents, Z13X@Mg_2Al-LDO, which were more porous and possessed higher N_2 BET specific surface areas than the precursors. CO_2 capture using core-shell adsorbents was dominated by physisorption, which is mainly attributed to the surface area, i.e. core-shell adsorbents with higher surface area showed higher CO_2 capacity. Core-shell samples with the lowest LDH loadings (5 wt%) in the precursor possessed the optimal capacity (5.75 mmol/g at 1 bar CO_2 atmosphere and 35 °C), which could be a promising material for post-combustion

carbon capture.

In the 2nd part of the thesis, the use of LDH-based core-shells for CO_2 hydrogenation to methanol catalysts were investigated. Mesoporous silica ($mSiO_2$) supported CuZnAl-CO_3-LDH core-shells ($mSiO_2$@CuZnAl-CO_3-LDH) were prepared via co-precipitation method. The effect of synthetic conditions (e.g., metal salt solution addition rate, pH, reaction concentration), LDH content, copper loading and property of silica were studied. Uniform core-shells could be obtained at pH 9 with a SiO_2/LDH ratio = 0.66–1 by weight with 0.05 mmol/min metal salt solution addition rate. Increasing the solution addition rates resulted in failure to generate crystalline LDHs. Further increase in the LDH fraction leads to a substantial amount of free LDH.

It was found that the surface area and pore size of silica was of great importance in determining the crystallinity, purity and uniformity of core-shells. When silica with a low surface area ($\leq$ 500 m^2/g), e.g. ES757 and SBA-15, is used, a high concentration condition should be applied to guarantee the high LDH coverage and low amount of free LDH. However, for the silica with high surface area ($>$ 500 m^2/g), e.g., SBA-16, MCM-41 and MCM-48, core-shell material prepared under high concentration condition possessed a large amount of layered silicate at the interface. As the effect of the interface silicate on the core-shell is still unknown, a dilute condition is desired for preparing core-shell with high surface area ($>$ 500 m^2/g) silica to minimise the formation of metal silicate. Besides, it is found that pure CuZnAl-CO_3-LDH phases can be synthesised between (Cu + Zn)/Al molar ratio 1.8–5. Amorphous hydroxide carbonate impurity starts to form at (Cu + Zn)/Al $\geq$ 2.3 when Cu/Zn molar ratio is larger than

1. An increase in the copper loading led to the generation of significant amounts of impurities.

After the systematic investigation of the synthesis of $mSiO_2@Cu_xZnAl$-LDH. The catalytic ability of these hybrid materials were tested for CO_2 hydrogenation to methanol. The effect of copper loading and the property of silica on the catalytic performance were explored using catalysts derived from ES757@Cu_xZnAl-LDHs (x = 0.8–4) and $mSiO_2@Cu_2$ZnAl-LDH respectively.

In ES757@Cu_xZnAl (x = 0.8–4), as the copper loading in core-shell catalysts increases, the space-time yield (STY) of methanol firstly increased to the maxima and then decreased. ES757@$Cu_{1.3}$ZnAl exhibited the highest CO_2 conversion (23%) and methanol STY (0.64 $g_{MeOH}/g_{catalyst}/h$) due to its superior copper surface area and uniform dispersion of copper particles. Further increasing the copper loading led to the aggregation of metallic copper particles and low copper surface area.

The ES757@$Cu_{1.3}$ZnAl core-shell catalyst also possesses higher CO_2 conversion and better STY than the catalyst derived from unsupported $Cu_{1.3}$ZnAl-LDH (0.34 $g_{MeOH}/g_{catalyst}/h$) due to its higher copper surface area (32.1 m^2/g compared to 23.1 m^2/g of the unsupported catalyst). It is believed that the hierarchical core-shell structure promotes the dispersion of copper and achieves a higher copper surface area at a lower copper loading (Cu loading of ES757@$Cu_{1.3}$ZnAl is 60% of $Cu_{1.3}$ZnAl-catalyst).

Among core-shell catalysts with different silica cores (ES757, SBA-15, SBA-16, MCM-41 and MCM-48), SBA-15@Cu_2ZnAl catalyst displayed the highest methanol production

(0.74 $g_{MeOH}/g_{catalyst}/h$). The catalytic performance of SBA-15@Cu_2ZnAl, MCM-48@Cu_2ZnAl (STY = 0.70 $g_{MeOH}/g_{catalys}/h$) and ES757@$Cu_{1.3}$ZnAl displayed a significant productivity improvement compared to a commercial catalyst (JM-HiFuel Cu/ZnO/Al_2O_3) and at least 88% of the reported CO_2 hydrogenation catalysts in the literature.

The success of using mSiO_2@CuZnAl-LDH derived catalysts for CO_2 hydrogenation to methanol inspired the further study of supporting the CuZnAl-LDH on methanol-to-olefins (MTO) catalysts, e.g. H-ZSM-5, and developing core-shells catalyst for CO_2 conversion to olefins.

ZSM@$Cu_{1.3}$ZnAl-LDH core-shell has been prepared via the co-precipitation method. Unlike mSiO_2@$Cu_{1.3}$ZnAl-LDH, the LDH shell on the zeolite core exhibits high crystallinity. Catalyst derived from this core-shell materials show better CO_2 conversion (4.8%) towards CO_2 to olefins conversion compared to the one derived from the physical mixture (< 3%), which is likely due to its superior acidic sites. Mobilising and orientating LDH nanosheets on the zeolite core surface diminished the interplatelet aggregation and released acidic sites. However, the counterion exchange (NH_4^+ by Na^+) in the core-shell synthesis modified the acidity of zeolite core and led to a low olefin selectivity from this core-shell catalyst.

To avoid the counterion exchange, several methods were employed. Firstly, the ammonium salt post-treatment was conducted to remove the Na^+ from core-shell material. This method restored the zeolite acidity to some extent while resulting in an overall reduction in the total acid sites. Secondary, the sodium-free core-shell syntheses via homogeneous precipitation method were attempted to avoid modifying the zeolite acidity via ion exchange. However, it was not suitable

for preparing pure $Cu_{1.3}ZnAl$ LDH as metal leaching and impurity formation could not be avoided. Lastly, the co-precipitation using organic base TPAOH and basic copper carbonate generated pure $Cu_{1.3}ZnAl$ LDH and relevant core-shell. In addition, due to the use of TPAOH, the micropore blockage of zeolite arising from the LDH growth has been avoided for the first time.

Future work can focus on several aspects. The first is to complete the study of $mSiO_2@Cu_xZnAl$-LDH, including testing the lifetime of core-shell catalysts, investigating the mechanism behind the outstanding performance of three core-shell catalysts (ES757@$Cu_{1.3}ZnAl$, SBA-15@Cu_2ZnAl and MCM-48@Cu_2ZnAl) using advanced characterisation such as XPS, EXAFS and HR-TEM and study the deactivation mechanism of the catalysts. To further reduce the cost of the core-shell catalysts and make them more suitable for industrial application, commercial silicas with porosities and surface areas similar to ES757, MCM-48 and SBA-15 can be good candidates for the cores.

For converting CO_2 to olefins using LDH-based core-shells, the catalytic ability of catalyst derived from sodium-free ZSM@$Cu_{1.3}ZnAl$-LDH should be evaluated. In addition to using catalysts derived from zeolite@CuZnAl-LDHs, a combination of $mSiO_2$ and Fe-based LDH, such as $mSiO_2$@Fe-LDH, may be a good choice.[1,2]

The success in using $mSiO_2$@CuZnAl core-shells to catalyse CO_2 hydrogenation to methanol has proven that the core-shell structure and appropriate core are beneficial to achieve better metal dispersion, thereby improving the catalytic performance. Therefore, it will be of interest

to explore the application of porous core@LDH core-shells as catalysts or catalysts precursors in other gaseous reactions.

Reference

1 S. Das, J. Pérez-Ramírez, J. Gong, N. Dewangan, K. Hidajat, B. C. Gates and S. Kawi, *Chem. Soc. Rev.*, 2020, **49**, 2937–3004.

2 X. Jiang, X. Nie, X. Guo, C. Song and J. G. Chen, *Chem. Rev.*, 2020, **120**, 7984–8034.

Chapter 7. Experimental Details

7.1. Analytical techniques for characterisation

Standard powder X-ray diffraction (PXRD) analysis was carried out on a PanAnalytical X'Pert Pro Diffractometer in scanning mode using Cu Kα radiation (40 kV, 40 mA). The sample was packed on a stainless-steel holder which resulted in peaks at 43.36, 44.29, and 50.51° which did not interfere with the analysis. Signals between 2θ = 3–70° were recorded with step size 0.0167°. PXRD patterns of fluorescent samples were collected on a Bruker D8 ECO diffractometer with Cu Kα radiation (45 kV, 40 mA). Signals between 2θ = 3–70° were gathered with step size 0.0298°. Pawley and Rietveld refinement were performed adopting TOPAS-Academic V6.[1] For lab XRD data with poor signal-to-noise ratio, e.g., the data of MCM-48@$Cu_{1.3}$ZnAl-LDH-pH10, refining crystallite size and microstrain broadening at the same time may lead to an over-parameterisation and end up with meaningless numbers. Therefore, only crystallite size is refined, which is calculated from the integral breadth of peaks. Its value is an underestimation of the average crystallite size; a change of the value indicates a change in the phase crystallinity.

Standard scanning electron microscopy (SEM) images and Energy dispersive X-ray spectroscopy (EDX) were obtained from a JOEL JSM-6610LV low vacuum scanning electron microscope at the Harwell Research Complex with an accelerating voltage of 10 kV or a Zeiss EVO scanning electron microscope with an accelerating voltage of 10 kV at the David Cockayne Centre for Electron Microscopy (DCCEM) within the Department of Materials, University of Oxford. Samples were mounted on aluminium stubs with adhesive carbon tape or

silver electrodag then sputter-coated with a 5–10 nm layer of gold or platinum using a Quorum Q150T ES Sputter Coater or Leica EM ACE 600 to facilitate imaging.

High resolution SEM (HR-SEM) images and EDX was achieved using a Zeiss Merlin high-resolution scanning electron microscope at an accelerating voltage of 5 kV, at DCCEM within the Department of Materials, University of Oxford.

Transmission electron microscopy (TEM) images and EDX were obtained from a JEOL-2100 electron microscope with an accelerating voltage of 200 kV using a single tilt specimen at the Harwell Research Complex (Chapter 2) or DCCEM within the Department of Materials, University of Oxford (Chapter 3–5).

Fourier transform Infrared spectroscopy (FTIR) was conducted utilizing a ThermoScientific Nicolet iS5 spectrometer fitted with an iD3 attenuated total reflection stage. Signals between 4000–700 cm^{-1} wavelengths were recorded at 4 cm^{-1} resolution.

Solid-state nuclear magnetic resonance (ssNMR) spectra (zgbs ^{1}H, direct-polarization magic angle spinning (DPMAS) ^{27}Al and DPMAS ^{29}Si) were obtained on a Bruker Advance IIIHD spectrometer in 4.0 mm O.D zirconia rotors (air-sensitive samples were packed with 3.2 mm O.D zirconia rotors) by Dr Nick Rees, University of Oxford.

The ^{27}Al NMR spectroscopy was collected at 104.2 MHz (9.4 T) with a MAS rate of 10 kHz. A single pulse excitation was applied adopting a short pulse width (0.23 μs) to get the quantitative MAS spectra. Typically, 16725 scans were acquired with a 0.1 s delay. All ^{27}Al chemical shifts in the spectroscopy are referenced to an aqueous solution of $Al(NO_3)_3$ (0 ppm).

The ^{29}Si NMR spectroscopy was gathered at 79.4 MHz (9.4 T) at a 10 kHz spinning. A one-pulse sequence and spinal 64 proton decoupling was applied to get the quantitative MAS spectra. Typically, 2619 transients were acquired with a 30 s delay. All ^{29}Si chemical shifts are referenced to kaolinite with chemical shift $\delta = -91.7$ ppm on a scale where δ (Tetramethylsilane) = 0 ppm as a secondary reference.

Thermogravimetric analysis (TGA) was carried out under a nitrogen atmosphere utilizing Mettler Toledo TGA/DSC 1 system or PerkinElmer TGA 8000. The weight change between 30–800 °C was collected with 5 °C/min ramp rate.

Elemental C, H, N analysis (EA) in Chapter 2 was performed by Mr. Stephen Boyer at the Science Centre, London Metropolitan University. The quantitative oxidative combustion technique was applied to test the carbon, hydrogen, nitrogen weight percent in the sample. Two measurements were taken, and the average value was reported. EA in Chapter 3–5 was conducted by Dr Nigel Howard at Microanalysis, University of Cambridge.

Inductively coupled plasma mass spectrometry (ICP-MS) analyses were performed by Dr. Alaa Abdul-Sada at University of Sussex using an Agilent 7500 series ICP-MS in helium collision mode to obtain the weight percent of individual elements in the sample. Approximately 10 mg of sample was digested in concentrated nitric acid. The mixture was then diluted by a factor of 10 with dilute nitric acid before the analysis. Each mixture was analysed three times and the average value was reported.

Inductively coupled plasma atomic emission spectroscopy (ICP-OES) analysis was

conducted by Dr Nigel Howard at Microanalysis, University of Cambridge.

N_2 adsorption/desorption isotherms of mesoporous (as well as macro-porous) and microporous materials were collected employing Micrometric Tristar II Plus and Micrometric 3Flex respectively at 77 K. All sample were *ex-situ* degassed on Micromeritics VacPrep overnight before the measurement. For microporous or core-shell samples, *in-situ* degas were applied subsequently. Z13X@Mg_2Al-CO_3-LDH and Mg_2Al-LDH samples were *ex-situ* degassed at 200 °C and *in-situ* degassed at 200 °C for 3 hours. Z13X@Mg_2Al-CO_3-LDH and Mg_2Al-LDH samples were *ex-situ* degassed at 200 °C and then *in-situ* degassed/calcined at 500 °C for 3 hours to get Z13X@Mg_2Al-LDO and Mg_2Al-LDO samples. ES757@Cu_xZnAl-CO_3-LDH core-shells were *ex-situ* degassed overnight at 110 °C and *in-situ* degassed at 110 °C for 1 hour. ES757@Cu_xZnAlLDOs and ES757@Cu_xZnAl catalysts was *ex-situ* degassed at 35 °C and *in-situ* degassed at 100 °C for 1 hour. Mesoporous SiO_2@Cu_2ZnAl-CO_3-LDHs were *ex-situ* degassed overnight at 150 °C and *in-situ* degassed at 150 °C for 3 hours. ZSM-5@$Cu_{1.3}$ZnAl-CO_3-LDH complex were *ex-situ* degassed at 150 °C and *in-situ* degassed at 150 °C for 3 hours.

The pore structure is investigated by the N_2 adsorption and desorption isotherm at 77 K. Specific surface area is estimated using the Brauner-Emmett-Teller (BET) method.[2] Pore size distribution within the micropore (< 2 nm) and mesopore (2–50 nm) is calculated by applying an appropriate DFT kernel to the adsorption isotherm. For silica and core-shell composite, the adsorption of N_2 at 77 K on metal oxide with cylindrical pore kernel was selected.[3] For LDH, the adsorption of N_2 at 77 K with slit-pore kernel was adopted.[4] Macropore (> 50 nm) size

distribution is determined utilising Barrett-Joyner-Halenda (BJH) method.[2]

7.2. Experimental details for Chapter 2

7.2.1. Materials

Zeolite 13X (Si/Al 1.23:1, Alfa Aesar); magnesium nitrate hexahydrate ($Mg(NO_3)_2 \cdot 6H_2O$, AR, Sigma-Aldrich); aluminium nitrate nonahydrate ($Al(NO_3)_3) \cdot 9H_2O$, AR, Sigma-Aldrich); sodium hydroxide (NaOH, AR, Sigma-Aldrich); sodium carbonate (Na_2CO_3, AR, Sigma-Aldrich). All chemicals and materials were used without further purification. All reference to 'water' or 'H_2O' refers to deionised water.

7.2.2. Synthesis procedure of Z13X@Mg_2Al-LDH

Core-shell Zeolite 13X@Mg_2Al-CO_3-LDHs were prepared using a modified published method.[5] Zeolite 13X (0.50 g) was dispersed in de-ionised (DI) water (100 mL) by sonication for thirty minutes. Na_2CO_3 (0.53 g, 5.00 mmol) was then added to the dispersion which was sonicated for five minutes. The achieved mixture was named as solution A. The pH value of solution A was adjusted to 10 with 10wt% nitric acid. An aqueous solution (96 mL) of $Mg(NO_3)_2 \cdot 6H_2O$ (1.23 g, 4.80 mmol) and $Al(NO_3)_3 \cdot 9H_2O$ (0.90 g, 2.40 mmol) was added to solution A within one and half hours (dropping rate 64 mL/h). The pH value of the reacting mixture was kept at 10 using 1 M NaOH aqueous solution. The resulting mixture was allowed to age for one hour under stirring after the completion of addition. The product was collected by Buchner filtration and washed with water till the pH of filtrate was equal to 7 before being dried under vacuum at 30 °C overnight. The product is white powder and is called Z13X@Mg_2Al-LDH.

7.2.3. Synthesis procedure of Z13X@Mg_2Al-CO_3-LDH with different dropping time or ageing time

Effect of dropping time: four different dropping times (0, 0.5, 1 and 2 hours) of metal nitrate solution were used. The procedure is the same as Z13X@Mg_2AlLDH mentioned above except the dropping time.

Effect of ageing time: four different ageing times (0, 0.5, 4 and 24 hours) of reaction mixture were used. The procedure is the same as Z13X@Mg_2Al-LDH mentioned above except using 0.5 hour dropping time and various ageing times.

7.2.4. Synthesis procedure of Z13X@Mg_2Al-CO_3-LDH with different LDH content

Effect of LDH content: three different LDH contents (5wt%, 20wt% and 35wt%) were used. The synthesis procedure is the same as Z13X@Mg_2Al LDH mentioned above except the total amount of metal nitrate solution added being different. The detail of metal nitrate solution used in the synthesis of different products are summarised in Table 7.1.The addition rate of metal nitrate solution is fixed at 0.15 mM/h with the ageing time being kept at half an hour. Products were named after their LDH content in the composite, for example, a sample with 35 wt% LDH was called Z13X@Mg_2Al-LDH-35.

Table 7.1 The composition of metal nitrate solution in the synthesis of Z13X@Mg_2Al-CO_3-LDH with different LDH content.

Sample name	Amount of metal nitrate (g)		Amount of water (mL)
	$Mg(NO_3)_2 \cdot 6H_2O$	$Al(NO_3)_3 \cdot 9H_2O$	
Z13X@Mg_2Al-LDH-5	0.065	0.047	52
Z13X@Mg_2Al-LDH-20	0.308	0.225	24
Z13X@Mg_2Al-LDH-35	0.663	0.485	5

7.2.5. Synthesis of Z13X@Mg_2Al layered double oxide (LDO) core-shells

Fresh Z13X@Mg_2Al-CO_3-LDH materials were calcined at 500 °C for 3 hours at a 10 °C/min ramp under static air to provide Z13X@Mg_2Al-LDOs. Calcined samples were transferred to a desiccator immediately to avoid any rehydration and intercalation of impurities. Calcined core-shells were named following from their parent, e.g., Z13X@Mg_2Al-LDO-5.

7.2.6. CO_2 adsorption ability test

Carbon dioxide adsorption ability tests were performed on a Micromeritics 3Flex with a chemisorption attachment. Fresh Z13X@Mg_2Al-CO_3-LDH core-shells and their parent materials zeolite 13X and Mg_2Al LDH were *in-situ* calcined at 500 °C for 3 hours at 10 °C/min ramp; About 120–200 mg fresh samples were loaded to make sure more than 100 mg of calcined materials would be left after the *in-situ* calcination. Subsequently, the sample was cooled to 35 °C at a ramp of 30 °C /min and left to evacuate to a vacuum at 35 °C for 3 hours. The CO_2 capacity measurement were then carried out twice at 35°C. The first round provides the total adsorption value, the second gives the physisorption. The difference between the two values provides the chemisorption value.

7.2.7. CO_2 temperature programmed desorption (TPD)

CO_2-TPD curves were recorded on a Micromeritics AutoChem II 2920 Chemisorption Analyser equipped with a thermal conductivity detector (TCD). Around 150 mg of fresh Z13X@Mg_2Al-CO_3-LDHs was loaded in a quartz U-tube and first purged in a flow of He (50 cm^3/min) at room temperature for 10 min to remove impurities. Subsequently, the sample was *in-situ* calcined at 500 °C for 3 hours at a ramp rate of 10 °C/min under a He stream

(50 cm^3/min). The temperature was then held at 100 °C to avoid any absorption and adsorption of moisture. CO_2 abundant flow (30 cm^3/min CO_2, 50 cm^3/min He) was then purged over the sample for 1 h. Physically adsorbed CO_2 was removed by flowing He (50 cm^3/min) over the sample for 1 h. For the desorption step, the sample was heated from 100 to 500 °C at a rate of 10 °C/min under a He flow (50 cm^3/min) with a sampling rate of 1 measurement per second.

7.3. Experimental details for Chapter 3

7.3.1. Materials

Copper (II) nitrate trihydrate ($Cu(NO_3)_2)\cdot 3H_2O$, P.A., Sigma-Aldrich); Zinc nitrate hexahydrate ($Zn(NO_3)_2)\cdot 6H_2O$, AR, Sigma-Aldrich); aluminium nitrate nonahydrate ($Al(NO_3)_3)\cdot 9H_2O$, AR, Sigma-Aldrich); MCM-48 (mesoporous SiO_2, 99.9% trace metals basis, Sigma-Aldrich); ES757 (synthetic amorphous SiO_2, PQ corporation); MCM-41 (mesoporous SiO_2, Sigma-Aldrich); SBA-15 (mesoporous SiO_2, 99.9% trace metals basis, Sigma-Aldrich); SBA-16 (mesoporous SiO_2, 99.9% trace metals basis, Sigma-Aldrich); sodium hydroxide (NaOH, AR, Sigma-Aldrich); sodium carbonate (Na_2CO_3, AR, Sigma-Aldrich). All chemicals and materials were used without further purification. All reference to 'water' or 'H_2O' refers to deionised water.

7.3.2. General synthesis procedure of MCM-48@$Cu_{1.3}$ZnAl-CO_3-LDH

Core-shell MCM-48@$Cu_{1.3}$ZnAl-CO_3-LDHs were prepared using a modified published method.[6,7] MCM-48 (0.10 g) was dispersed in de-ionised (DI) water (20.00 mL) by thirty-minute sonication. Na_2CO_3 (0.10 g, 0.94 mmol) was then added to the dispersion which was sonicated for five minutes. The achieved mixture was named as solution A. The pH value of

solution A was adjusted to 10 with 10wt% nitric acid. An aqueous solution (14 mL) of $Cu(NO_3)_2 \cdot 3H_2O$ (0.10 g, 0.43 mmol), $Zn(NO_3)_2 \cdot 6H_2O$ (0.10 g, 0.32 mmol) and $Al(NO_3)_3 \cdot 9H_2O$ (0.12 g, 0.32 mmol) was added to solution A within thirty minutes (dropping rate 0.05 mmol metal nitrate/min). The pH value of the reacting mixture was kept at 10 using 1 M NaOH aqueous solution. The resulting mixture was aged for one hour under stirring after the completion of addition. The product was collected by Buchner filtration and washed with water till the pH of filtrate was equal to 7 before being dried under vacuum at 30 °C overnight. The product is blue powder and is called MCM-48@$Cu_{1.3}$ZnAl-LDH-pH10.

7.3.3. Synthesis of MCM-48@$Cu_{1.3}$ZnAl-CO_3-LDH with varied synthetic condition

Increased dropping rate: The synthetic procedure is the same as MCM-48@$Cu_{1.3}$ZnAl-CO_3-LDH mentioned above, except that the dropping rate of metal nitrate was increased to 0.10 mmol/min, i.e., total dropping time reduced to 10 minutes. Product was named MCM-48@$Cu_{1.3}$ZnAl-LDH-0.1mmol.

Increased LDH content: The synthetic procedure is the same as MCM-48@$Cu_{1.3}$ZnAl-CO_3-LDH mentioned above, except that double amount of metal nitrate solution was added, i.e., an aqueous solution (24 mL) of $Cu(NO_3)_2 \cdot 3H_2O$ (0.21 g, 0.85 mmol), $Zn(NO_3)_2$ $6H_2O$ (0.19 g, 0.65 mmol) and $Al(NO_3)_3 \cdot 9H_2O$ (0.24 g, 0.64 mmol) was added. Product was termed MCM-48@$Cu_{1.3}$ZnAl-LDH-67wt.

Reduce synthetic pH to 9: The synthetic procedure is the same as MCM-48@$Cu_{1.3}$ZnAl-CO_3-LDH mentioned above, except that the synthetic pH was reduced from 10 to 9. Product was

denomiated MCM-48@$Cu_{1.3}$ LDH-pH9.

7.3.4. Synthesis of MCM-48@CuZnAl-CO_3-LDH with varied Cu content

Varied LDH content: The synthetic procedure is the same as that of MCM-48@$Cu_{1.3}$ZnAl-LDH-pH9 mentioned above, except that a different amount of metal nitrate solution was used. Products were termed MCM-48@$Cu_{1.3}$ZnAl-LDH-pH9-60wt and MCM-48@$Cu_{1.3}$ZnAl-LDH-pH9-67wt respectively according to the LDH content in the composite. Details of metal nitrate solution used in the synthesis are summarised in Table 7.2.

Varied Cu content in LDH: Four different Cu: Al molar ratios in LDH were attempted (2, 3, 3.5 and 4). The synthetic procedure is the same as MCM-48@$Cu_{1.3}$ZnAl-LDH-pH9-60wt mentioned above, apart from the composition of metal nitrate solution. The total metal nitrate amount was fixed at 1.6 mmol. Zn: Al molar ratio was kept at 1: 1. Products were titled after their Cu: Al ratio, for example, product with Cu: Al ratio = 2 was called MCM-48@Cu_2ZnAl-LDH. Details of metal nitrate solution are summarised in Table 7.2.

Table 7.2 The composition of metal nitrate solution in the synthesis of different MCM-48 core-shells.

Sample name	Amount of metal nitrate (g)			Amount of water (mL)
	$Cu(NO_3)_2)\cdot 3H_2O$	$Zn(NO_3)_2)\cdot 3H_2O$	$Al(NO_3)_3)\cdot 9H_2O$	
MCM-48@$Cu_{1.3}$ZnAl-LDH-pH9-60wt	0.155	0.144	0.180	21
MCM-48@$Cu_{1.3}$ZnAl-LDH-pH9-66wt	0.206	0.192	0.240	28
MCM-48@Cu_2ZnAl-LDH	0.194	0.119	0.150	21
MCM-48@Cu_3ZnAl-LDH	0.232	0.095	0.120	21
MCM-48@$Cu_{3.5}$ZnAl-LDH	0.246	0.087	0.109	21
MCM-48@Cu_4ZnAl-LDH	0.258	0.079	0.100	21

7.3.5. General synthesis procedure of ES757@Cu_4ZnAl-CO_3-LDH

Core-shell ES757@Cu_4ZnAl-CO_3-LDHs were prepared using a scale-up condition of MCM-48@Cu_4ZnAl-CO_3-LDH. ES757 (0.80 g) was dispersed in de-ionised (DI) water (160.00 mL) associated with thirty-minute sonication. Na_2CO_3 (0.24 g, 2.30 mmol) was then added to the dispersion which was sonicated for five minutes. The achieved mixture was named as solution A. The pH value of solution A was adjusted to 9 with 10wt% nitric acid. An aqueous solution (168.00 mL) of $Cu(NO_3)_2 \cdot 3H_2O$ (2.10 g, 8.50 mmol), $Zn(NO_3)_2 \cdot 6H_2O$ (0.64 g, 2.10 mmol) and $Al(NO_3)_3 \cdot 9H_2O$ (0.80 g, 2.10 mmol) was added to solution A within thirty minutes. The pH value of the reacting mixture was kept at 9 using 1 M NaOH aqueous solution. The resulting mixture was allowed to age for one hour under stirring after the completion of the addition step. The product was collected by Buchner filtration and washed with water till the pH of the filtrate was equal to 7 before being dried under vacuum at 30 °C overnight. The product is blue powder and is called ES757@Cu_4ZnAl-LDH-Ori.

7.3.6. Synthesis of ES757@Cu_4ZnAl-CO_3-LDH with varied synthetic condition

Aluminium impregnation: The synthetic procedure is the same as that of ES757@Cu_4 LDH-Ori, except that a wet impregnation of ES757 with aluminium nitrate is carried out before the synthesis. ES757 was mixed together with $Al(NO_3)_3 \cdot 6H_2O$ (60.00 mg, 0.16 mmol) and P cm^3 water, where P is the total pore volume of ES757. The wet solid was then dried at 120 °C for 1 hour. The obtained product was called ES757@Cu_4ZnAl-LDH-Al.

Concentrated condition: The synthetic procedure is the same as that of ES757@Cu_4 LDH-Ori, except that a concentrated ES757 dispersion and metal nitrate solution are used. The nucleation

and crystallinity of LDH is related to the concentration of metal nitrate solution and addition rate of metal nitrate solution.[8] The dropping rate was adjusted to make sure the same concentration of metal nitrate solution was added per unit time as ES757@Cu_4ZnAl-LDH-Ori, which is 0.15 mM/h. Detailed information are listed in Table 7.3. The product is denominated ES757@Cu_4ZnAl-LDH-Conc.

Aluminium impregnation and concentrated conditions: The synthesis procedure is the same as that of ES757@Cu_4 LDH-Al, apart from that a concentrated ES757 dispersion and metal nitrate solution are used. Details are listed in Table 7.3. The product is named ES757@Cu_4ZnAl-LDH-Al + Conc.

Table 7.3 The details of the metal nitrate solution, core dispersion and dropping rate for ES757@Cu_4ZnAl LDHs under varied synthetic conditions. For simplicity, only suffix of the sample name is shown in the table.

Sample name	Ori	Al	Conc.	Al + Conc.
Total metal nitrate amount (mmol)	12.8	12.8	12.8	12.8
H_2O in metal nitrate solution (mL)	168	168	64	64
Metal nitrate concentration (M)	0.08	0.08	0.20	0.20
H_2O amount in ES757 dispersion (mL)	160	160	24	24
Concentration of ES757 dispersion (g/mL)	0.005	0.005	0.030	0.030
Dropping rate (mL/h)	42	42	48	48

7.3.7. Synthesis of ES757@Cu_xZnAl-CO_3-LDH with varied Cu content

Four different Cu: Al molar ratios of LDH were attempted (0.8, 1.3, 2 and 3). The synthetic procedure is the same as ES757@Cu_4ZnAl-LDH-Conc mentioned above, apart from the

composition of metal nitrate solution being used. Total metal nitrate amount was fixed at 12.8 mmol. Zn: Al molar ratio was kept at 1: 1. Products were named after their Cu: Al ratio, for example, product with Cu: Al ratio = 2 was called ES757@Cu_2ZnAl-LDH. Details of metal nitrate solution are summarised in Table 7.4.

Table 7.4 The composition of metal nitrate solution for ES757@Cu_xZnAl-CO_3-LDH.

Sample name	Amount of metal nitrate (g)			Amount of water (mL)
	$Cu(NO_3)_2)\cdot 3H_2O$	$Zn(NO_3)_2)\cdot 3H_2O$	$Al(NO_3)_3)\cdot 9H_2O$	
ES757@$Cu_{0.8}$ LDH	0.885	1.363	1.718	64
ES757@$Cu_{1.3}$ LDH	1.221	1.156	1.458	64
ES757@Cu_2 LDH	1.549	0.954	1.203	64
ES757@Cu_3 LDH	1.859	0.763	0.962	64

7.3.8. Synthesis of mesoporous mSiO_2@Cu_2ZnAl-LDH

Mesoporous SiO_2@Cu_2ZnAl-CO_3-LDHs core-shell, adopting cores such as MCM-48, MCM-41, SBA-16 and SBA-15, were prepared using a co-precipitation method. SiO_2 aqueous dispersion was prepared by dispersing 0.8 g mesoporous SiO_2 in DI water (24.00 mL) via a thirty-minute sonication. Na_2CO_3 (0.24 g, 2.30 mmol) was then added to the dispersion which was sonicated for five minutes. The pH value of SiO_2 aqueous dispersion was adjusted to 9 with 10wt% nitric acid. An aqueous solution (64.00 mL) of $Cu(NO_3)_2\cdot 3H_2O$ (1.50 g, 6.40 mmol), $Zn(NO_3)_2\cdot 6H_2O$ (0.95 g, 3.20 mmol) and $Al(NO_3)_3\cdot 9H_2O$ (1.20 g, 3.20 mmol) was added to SiO_2 dispersion within eighty minutes. The pH value of the reacting mixture was kept at 9 using 4 M NaOH aqueous solution. The resulting mixture aged for one hour under stirring after the completion of the addition. The product was collected by Buchner filtration and washed with water till the pH of filtrate equalled 7 before being dried under vacuum at 30 °C overnight. The

product is blue powder and is termed after their core, e.g., composite using SBA-16 as core was called SBA-16@Cu_2ZnAl-LDH.

7.4. Experimental details for Chapter 4

7.4.1. Activation of catalyst precursors (mSiO_2@Cu_xZnAl-CO_3-LDH)

Calcination: All precursor materials were calcined at 330 °C for 4 hours at a 2 °C/min ramp rate under constant air flow at 50 mL_n/min. During the process, the sample was held at 80 °C and 150 °C for one hour dwell time respectively. All materials were titled after their parent with the suffix 'LDH' being replaced by 'LDO', e.g., calcined ES757@Cu_2ZnAl-LDH was called ES757@Cu_2ZnAl-LDO.

Hydrogen reduction: Calcined samples were reduced at 290 °C for 2 hours at 2 °C/min ramp rate under constant gas flow (5% H_2/N_2) at 50 stp mL/min (stp = standard temperature and pressure: P = 101.3 kPa, T = 298 K). Reduced composites are fresh catalyst which are called after their parents without suffix, namely, reduced ES757@Cu_2ZnAl-LDO was denominated ES757@Cu_2ZnAl.

7.4.2. Hydrogen temperature programmed reduction (H_2-TPR)

H_2-TPR curves were recorded on a Micromeritics AutoChem II 2920 Chemisorption Analyser equipped with a thermal conductivity detector (TCD). Around 120 mg of calcined core-shell was loaded in a quartz U-tube and purged with He (10 cm^3/min) for 5 minutes at room temperature. This He flow was maintained while the sample was heated to 150 °C (10 °C/min) and hold for 5 minutes to remove moisture and impurities. After cooling to 40 °C, the reduction

step started. The sample was heated from 40 to 600 °C at a rate of 5 °C/min under a H_2 flow (10% H_2 in N_2 at 50 cm^3/min) with a sampling rate of 1 measurement per second.

7.4.3. Catalytic tests for CO_2 hydrogenation reaction

Catalytic tests for CO_2 hydrogenation to produce methanol were conducted utilizing a tubular fixed bed reaction (12.7 mm outside diameter). Typically, 0.1 g of calcined sample was loaded which was then *in-situ* reduced at 290 °C for 2 hours at 2 °C/min ramp rate with a constant gas flow (5% H_2/N_2) at 50 stp mL/min. Subsequently, the reactor was pressurised to 4.5 MPa with CO_2/H_2 (volume ratio 1:3) once the temperature was cooled to below 50 °C. The activities of the catalysts were determined with a constant flow of CO_2 and H_2 gas mixture through the catalyst bed (30 stp mL/min) at desired temperature (230–350 °C). The activity measurements were taken after at least 2 hours on the stream at each selected reaction temperature. Products were quantitatively analysed by an Agilent 7890B gas chromatograph equipped with calibrated thermal conductivity detector (TCD) and flame ionization detector (FID).

7.4.4. Nitrous oxide (N_2O) reduction of ES757@Cu_xZnAl catalysts

The dispersion (D_{Cu}) and exposed surface area (S_{Cu}) of Cu were determined by dissociative N_2O chemisorption followed by hydrogen pulse reduction. N_2O chemisorption was carried out on a Micromeritics AutoChem II 2920 instrument. Before the measurement, 100 mg of calcined sample was reduced at 290 °C in a 10% H_2/Ar mixture (50 mL/min) for 2 h. After cooling to 60 °C, the sample was exposed to N_2O (20 mL/min) for 1 h to ensure complete oxidation of surface metallic copper to Cu_2O. Subsequently, the sample was flowed by N_2 (50 mL/min) to remove residual N_2O in the sample tube and physisorbed N_2O on the surface. Finally, a

calibrated hydrogen pulse reduction at 290 °C was conducted to determine the amount of surface Cu_2O species. D_{Cu} and S_{Cu} were then calculated by dividing the amount of surface copper by the actual Cu loading determined by ICP-OES.

7.5. Experimental details for Chapter 5

7.5.1. Materials

Copper (II) nitrate trihydrate ($Cu(NO_3)_2)\cdot 3H_2O$, P.A., Sigma-Aldrich); Zinc nitrate hexahydrate ($Zn(NO_3)_2)\cdot 6H_2O$, AR, Sigma-Aldrich); aluminium nitrate nonahydrate ($Al(NO_3)_3)\cdot 9H_2O$, AR, Sigma-Aldrich); Zeolite ZSM-5, ammonium (H-ZSM-5, Alfa Aesar); sodium hydroxide (NaOH, AR, Sigma-Aldrich); sodium carbonate (Na_2CO_3, AR, Sigma-Aldrich); Ammonium bicarbonate (NH_4HCO_3, 99%, Sigma Aldrich); Urea (NH_2CONH_2, Purity, Sigma Aldrich); Fumed silica (SiO_2, Sigma Aldrich); Copper(II) carbonate basic ($CuCO_3 \cdot Cu(OH)_2$, AR, Sigma Aldrich); 70% nitric acid (HNO_3, ACS reagent, Sigma Aldrich); Tetrapropylammonium hydroxide ($C_{12}H_{29}NO$, 25% in water, Acros Organics) All chemicals and materials were used without further purification. All reference to 'water' or 'H_2O' refers to deionised water.

7.5.2. Synthesis procedure of ZSM-5@$Cu_{1.3}$ZnAl-CO_3-LDH

Core-shell ZSM-5@$Cu_{1.3}$ZnAl-CO_3-LDHs were prepared using a reported method with adjustment.[5,7] H-ZSM-5 (1.20 g) was dispersed in de-ionised (DI) water (240 mL) associated with thirty-minute sonication. Na_2CO_3 (1.20 g, 11.30 mmol) was then added to the dispersion which was sonicated for five minutes. The achieved mixture was named as solution A. The pH value of solution A was adjusted to 10 with 10wt% nitric acid. An aqueous solution (256 mL) of $Cu(NO_3)_2\cdot 3H_2O$ (1.20 g, 5.10 mmol), $Zn(NO_3)_2\cdot 6H_2O$ (1.10 g, 3.80 mmol) and

$Al(NO_3)_3 \cdot 9H_2O$ (1.40 g, 3.80 mmol) was added to solution A over one hour. The pH value of the reacting mixture was kept at 10 using 1 M NaOH aqueous solution. Afterwards, the resulting mixture was aged for one hour under stirring. The wet cake of the product was obtained by Buchner filtration and washed with water till the pH of the filtrate equalled to 7, which after drying under vacuum at 30 °C for overnight, gives 2.4 g of blue powder. The product is called ZSM@$Cu_{1.3}$ZnAl-LDH.

Pristine $Cu_{1.3}$ZnAl-CO_3-LDH was prepared using the same method without the addition of H-ZSM-5 and was named $Cu_{1.3}$ZnAl-LDH.

7.5.3. Ammonium bicarbonate treated ZSM-5@$Cu_{1.3}$ZnAl-CO_3-LDH

The synthetic procedure is the same as described in 7.5.2., besides that the wet cake of product was treated with ammonium bicarbonate before drying.

The wet cake of product was dispersed in NH_4HCO_3 aqueous solution at the solution to solid ratio = 10 mL/g for 3 hours at room temperature, where 'solid' refers to the dried product. The weight of solid can be estimated from the fraction of wet cake, for example, ¼ of the wet cake, after drying, should provide 0.60 g solid which will need to be dispersed with 6 mL ammonium bicarbonate solution. Subsequently, the treated product was collected by Buchner filtration and washed with water till the pH of the filtrate equalled to 7 before being dried under vacuum at 30 °C overnight.

Five different concentrations of ammonium bicarbonate solution were used (1 M, 0.5 M, 0.2 M, 0.1 M and 0.01 M). The product is termed after the concentration of the bicarbonate solution

used, e.g., composite treated with 0.01 M bicarbonate solution was called ZSM@$Cu_{1.3}$ZnAl-LDH-10mM.

7.5.4. Homogeneous precipitation synthesis of $Cu_{1.3}$ZnAl-CO_3-LDH

An aqueous solution (50 mL) of $Cu(NO_3)_2 \cdot 3H_2O$ (1.10 g, 4.70 mmol), $Zn(NO_3)_2 \cdot 6H_2O$ (1.00 g, 3.50 mmol), $Al(NO_3)_3 \cdot 9H_2O$ (1.30 g, 3.50 mmol) and urea was refluxed at a certain temperature for a certain time to afford a suspension. The solid was then collected by Buchner filtration and washed with water till the pH of the filtrate equalled to 7 before being dried under vacuum at 30 °C overnight. The detailed synthesis conditions and the name of corresponding products are listed in Table 7.5. Generally, the product is termed after the amount of urea used, the reaction temperature and time.

Table 7.5 The synthesis conditions and names of corresponding samples for the homogeneous precipitation of $Cu_{1.3}$ZnAl-CO_3-LDH.

Sample name	Urea amount (g)	Urea: Al molar ratio	Reaction temperature (°C)	Reaction time (h)
$Cu_{1.3}$ZnAl-LDH-20Al	4.23	20	90	24
$Cu_{1.3}$ZnAl-LDH-10Al	2.11	10	90	24
$Cu_{1.3}$ZnAl-LDH-6Al	1.27	6	90	24
$Cu_{1.3}$ZnAl-LDH-10Al-110	2.11	10	110	24

7.5.5. Sodium-free co-precipitation of H-ZSM-5@$Cu_{1.3}$ZnAl-CO_3-LDH

$CuCO_3 \cdot Cu(OH)_2$ (0.57 g, 2.56 mmol), $Zn(NO_3)_2 \cdot 6H_2O$ (1.1 g, 3.79 mmol) and $Al(NO_3)_3 \cdot 9H_2O$ (1.4 g, 3.8 mmol) was dissolved in water (256.00 mL) with the assistance of 70% nitric acid (0.82 mL). H-ZSM-5 (1.2 g) was dispersed in de-ionised (DI) water (240.00 mL) via thirty-minute sonication. The pH value of H-ZSM-5 dispersion was adjusted to 10

using 25wt% TPAOH solution. The metal salt solution was then added to zeolite dispersion within one hour. The pH value of the reacting mixture was kept at 10 using 25wt% TPAOH solution. Subsequently, the resulting mixture was aged for one hour under stirring. The wet cake of the product was obtained by Buchner filtration and washed with water till the pH of the filtrate equalled 7, which after drying under vacuum at 30 °C for overnight, gives 2.40 g of blue powder. The product is called ZSM@$Cu_{1.3}$ZnAl-LDH-TPA. A control CuZnAl LDH was prepared under the same condition without H-ZSM-5 and is named $Cu_{1.3}$ZnAl-LDH-TPA.

7.5.6. Activation of catalyst precursors

Calcination: All precursor materials were calcined at 500 °C for 3 hours with a 2 °C/min ramp rate under constant air flow at 50 mL_n/min. During the process, the sample was held at 80 °C and 150 °C for one hour dwell time respectively. All materials were titled after their parent with the suffix 'LDH' being replaced by 'LDO', e.g., calcined ZSM@$Cu_{1.3}$ZnAl-LDH was called ZSM@$Cu_{1.3}$ZnAl-LDO.

Hydrogen reduction: Calcined samples were reduced at 290 °C for 2 hours at 2 °C/min ramp rate under constant gas flow (5% H_2/N_2) at 50 stp mL/min (stp = standard temperature and pressure: P = 101.3 kPa, T = 298 K). Reduced composites are fresh catalyst which are called after their parents without suffix, namely, reduced ZSM@$Cu_{1.3}$ZnAl-LDO was denominated ZSM@$Cu_{1.3}$ZnAl.

7.5.7. NH_3 temperature programmed desorption (TPD) traces

NH_3-TPD curves were recorded on a Micromeritics AutoChem II 2920 Chemisorption Analyser

equipped with a thermal conductivity detector (TCD). Around 120 mg of calcined core-shell was loaded in a quartz U-tube and purged with 10% H_2 in N_2 (50 cm^3/min) at room temperature for 5 min. The flow of H_2 and N_2 mixture was maintained while the sample was *in-situ* reduced at 290 °C for 2 hours with a ramp rate of 2 °C/min, before cooling to 40 °C. 10% NH_3 in He gas (25 cm^3/min) and He (25 cm^3/min) was then purged over the sample for 1 h. Physically adsorbed NH_3 was removed by flowing N_2 (20 cm^3/min) and He (20 cm^3/min) over the sample for 1 h. For the desorption step, the sample was heated from 40 to 600 °C at a rate of 4 °C/min under a He flow (25 cm^3/min) with a sampling rate of 1 measurement per second.

7.5.8. Catalytic test for CO_2 hydrogenation reaction

Catalytic tests for CO_2 hydrogenation to produce olefins were conducted utilizing a tubular fixed bed reaction (12.70 mm outside diameter). Typically, 0.10 g of calcined sample was loaded which was then *in-situ* reduced at 290 °C for 2 hours at 2 °C/min ramp rate with a constant gas flow (5% H_2/N_2) at 50 stp mL/min. Afterwards, the reactor was pressurised to 4.5 MPa with CO_2/H_2 (volume ratio 1:3) once the temperature was cooled to below 50 °C. The activities of the catalysts were determined with a constant flow of CO_2 and H_2 gas mixture through the catalyst bed (30 stp mL/min) at the desired temperature (210–420 °C). The activity measurements were taken after at least 2 hours on the stream at each selected reaction temperature. The products were quantitatively analysed by an Agilent 7890B gas chromatograph equipped with calibrated thermal conductivity detector (TCD) and flame ionization detector (FID).

7.5.9. Catalytic test for methanol to olefins (MTO) reaction on H-ZSM-5

The catalytic test was conducted utilizing a tubular fixed bed reaction (12.7 mm outside diameter). Typically, 0.10 g of calcined H-ZSM-5 was loaded which was then *in-situ* reduced at 290 °C for 2 hours at 2 °C/min ramp rate with a constant gas flow (5% H_2/N_2) at 50 stp mL/min. Once the temperature was cooled to below 50 °C, the input gas was switched to a methanol vapour (bubbling N_2 through methanol at 30 stp mL/min under atmospheric pressure). The partial pressure of methanol should be 0.13 bar. The activities of the catalysts were determined with this methanol feed which went through the catalyst bed at the desired temperature (210–420 °C). The activity measurements were taken after at least 2 hours on the stream at each selected reaction temperature. Products were quantitatively analysed by an Agilent 7890B gas chromatograph equipped with calibrated thermal conductivity detector (TCD) and flame ionization detector (FID).

7.6. Reference

1 A. A. Coelho, TOPAS-Academic (Version 6), Coelho Software, Brisbane, Australia, 2016.

2 M. Thommes, K. Kaneko, A. V. Neimark, J. P. Olivier, F. Rodriguez-Reinoso, J. Rouquerol and K. S. W. Sing, *Pure Appl. Chem.*, 2015, **87**, 1051–1069.

3 K. Schumacher, P. I. Ravikovitch, A. Du Chesne, A. V Neimark and K. K. Unger, 2000, 4648–4654.

4 C. Chen, A. Wangriya, J.-C. Buffet and D. O'Hare, *Dalton Trans.*, 2015, **44**, 16392–16398.

5 C. Chen, C. F. H. Byles, J.-C. Buffet, N. H. Rees, Y. Wu and D. O'Hare, *Chem. Sci.*, 2016, **7**, 1457–1461.

6 C. Chen, R. Felton, J.-C. Buffet and D. O'Hare, *Chem. Commun.*, 2015, **51**, 3462–3465.

7 M. M. J. Li, C. Chen, T. Ayvall, H. Suo, J. Zheng, I. F. Teixeira, L. Ye, H. Zou, D. O'Hare and S. C. E. Tsang, *ACS Catal.*, 2018, **8**, 4390–4401.

8 H. Jing, M. Wei, L. Bo, K. Yu, D. G. Evans and X. Duan, in *Layered Double Hydroxides (Structure and bonding)*, eds. D. G. Evans and X. Duan, Springer-Verlag, Berlin/Heidelberg, 1st edn., 2006, vol. 119, pp. 89–119.

Appendix A. Appendices to Chapter 2

A.1 Characterisation for Z13X@Mg_2Al LDH

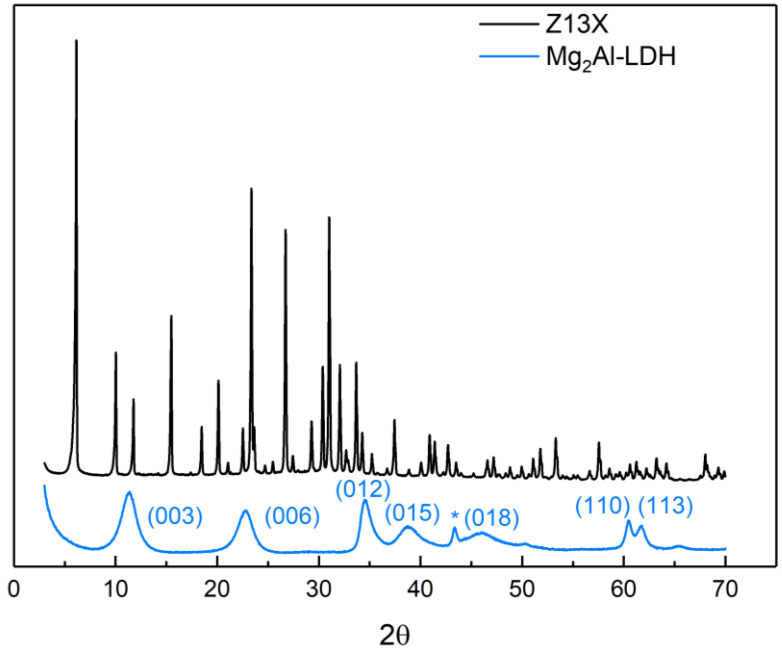


Figure A.1 The PXRD pattern of the original Z13X and Mg_2Al-LDH.

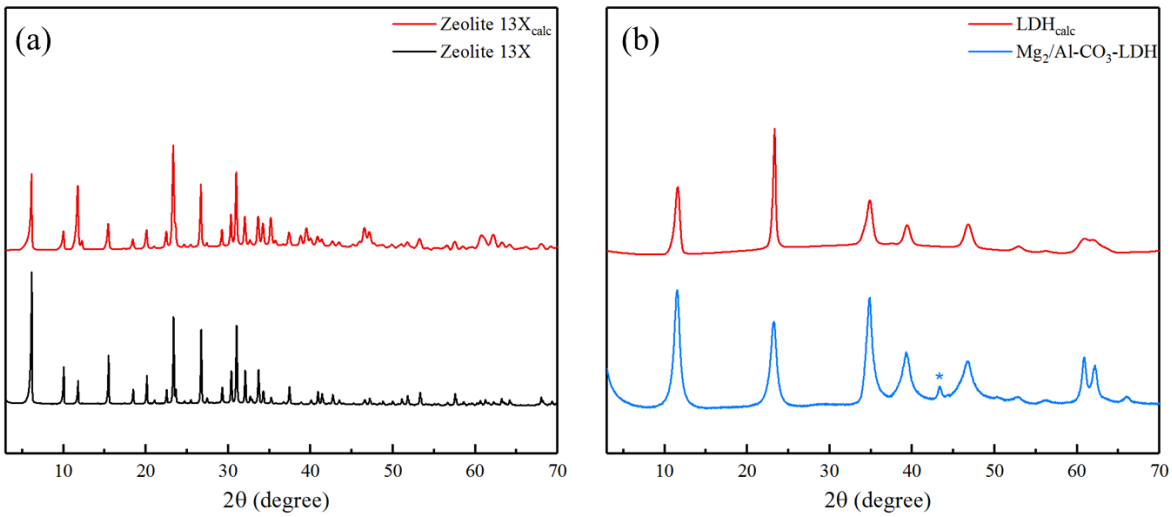


Figure A.2 XRD patterns of (a) the commercial Z13X (black) and the extracted individual phase of Z13X in Z13X@Mg_2Al-LDH from the Pawley refinement (red) and (b) Mg_2Al-LDH (blue) and the extracted individual phase of LDH in Z13X@Mg_2Al-LDH from the Pawley refinement (red). Peak arising from sample holder is marked with *.

Table A.1 Pawley refinement details for Z13X@Mg_2Al-LDH PXRD.

Single phase component	**Zeolite 13X**	**LDH**
Crystal system	Cubic	Rhombohedral (Hexagonal setting)
Space group	Fd -3	R -3m :H
a / Å	24.970	3.046
b / Å	24.970	3.046
c / Å	24.970	22.96
α/ °	90	90
β/ °	90	90
γ/ °	90	120
λ/ Å	1.5406	
Refinement type	Pawley	
Rp / %	4.682	
Rwp / %	6.578	
Rp' /%	8.989	
Rwp' / %	10.720	
Software	TOPAS-Academic V6	

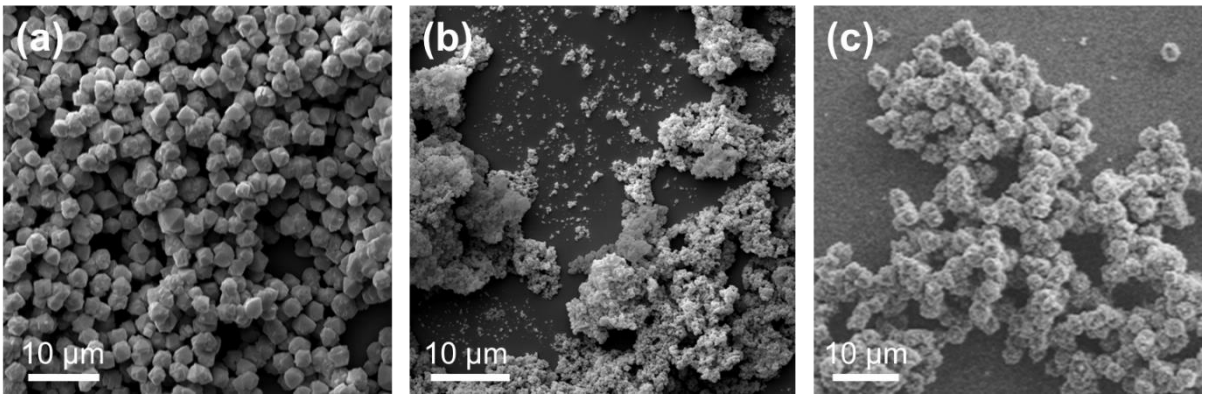


Figure A.3 The SEM image of (a) the commercial Zeolite 13X, (b) Mg_2Al-LDH and (c) Z13X@Mg_2Al-LDH at the 10 µm scale.

Table A.2 Silicon environment in Z13X and Z13X@Mg_2Al-LDH from ^{29}Si MAS solid-state NMR spectroscopy.

Assignment	Z13X		Z13X@Mg_2Al-LDH	
	Position	Integration	Position	Integration
$Q^4Si(4Al)$	-84.2	41.96%	-84.4	34.43%
$Q^4Si(3Al)$	-88.8	27.38%	-89.1	23.68%
$Q^4Si(2Al)$	-93.5	15.82%	-94.0	13.33%
$Q^4Si(1Al)$	-98.1	4.51%	-98.8	4.51%
	-102.0	3.88%	-103.4	9.86%
$Q^4Si(0Al)$	-111.2	5.75%	-110.9	9.74%
	-117.7	0.69%	-116.9	4.44%

Equation A1. Loewenstein's rule equation.[1–3]

$$\frac{Si}{Al} = \frac{\sum_{x=0}^{4} I_{Si(xAl)}}{0.25 \sum_{x=0}^{4} x I_{Si(xAl)}}$$

Loewenstein's rule states that Al-O-Al linkage in the zeolite framework is forbidden and is generally accepted to be inviolate in zeolites.[1–3]

Complying with the principle of Loewenstein's rule, the Si/Al ratio in the zeolite framework can be obtained from the Si(xAl) peak intensity using the above equation.[1]

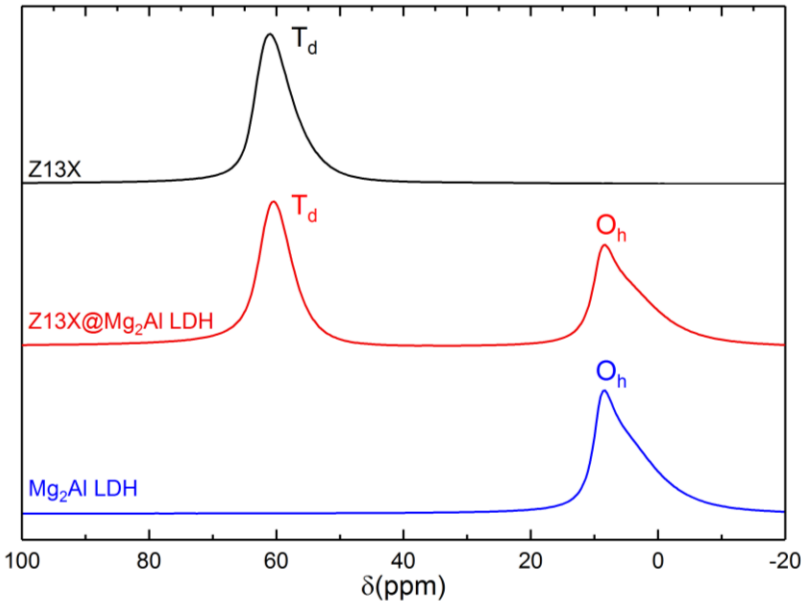


Figure A.4 ^{27}Al ssNMR DPMAS spectra (at 104.2 MHz) of the Z13X (Black), Z13X@Mg_2Al-LDH (Red) and Mg_2Al-LDH (blue). Two overlapped octahedral Al peaks can be observed from the Mg_2Al-LDH and Z13X@Mg_2Al-LDH ^{27}Al NMR spectra which is possible because of the different Mg

neighbouring environemt.[4]

Table A.3 The elemental analysis (C, H, N) and ICP analysis (Na, Mg, Al, Si) result of Z13X, Z13X@Mg_2Al LDH and Mg_2Al LDH and the calculated element weight percent from.

Element	Z13X		Z13X@Mg_2Al LDH		Mg_2Al LDH	
	Real (wt%)	From formula (wt%)	Real (wt%)	From formula (wt%)	Real (wt%)	From formula (wt%)
Na	9.48	9.35	3.68	5.10	0.02	0
Mg	0	0	9.66	9.58	18.27	18.46
Al	12.62	13.11	11.62	11.80	11.07	11.04
Si	7.02*	19.04*	7.32*	10.38*	0	0
C	0	0	1.32	1.33	2.65	2.53
H	2.43	2.43	3.22	3.30	3.85	4.38
N	0	0	0	0	0	0

*: Z13X and Z13X@Mg_2Al LDH did not completely digested in ICP analysis, Si content from formula should be higher than the detected value.

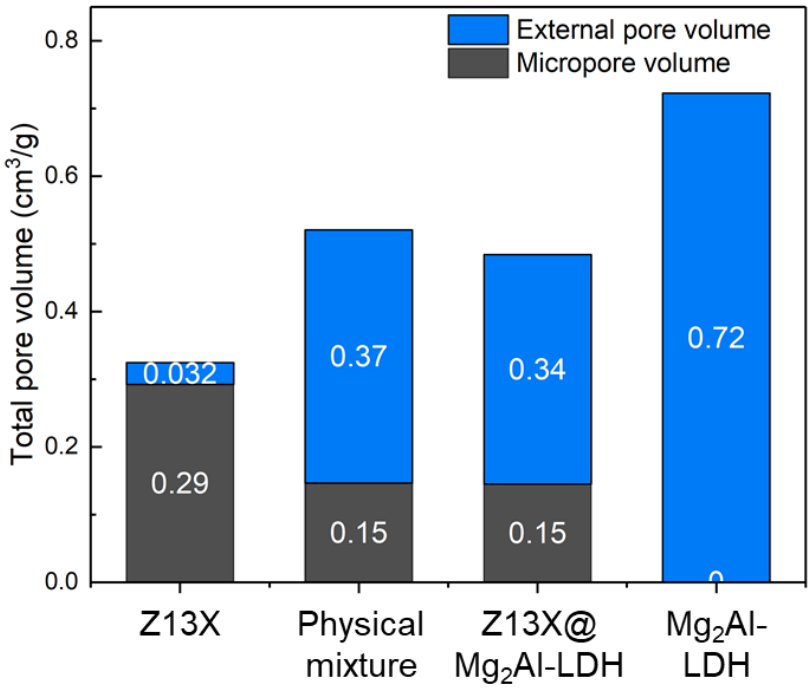


Figure A.5 Total pore volume of Z13X, physical mixture, Z13X@Mg_2Al-LDH and Mg_2Al-LDH.

A.2 Z13X@Mg_2Al LDHs with varied metal addition time

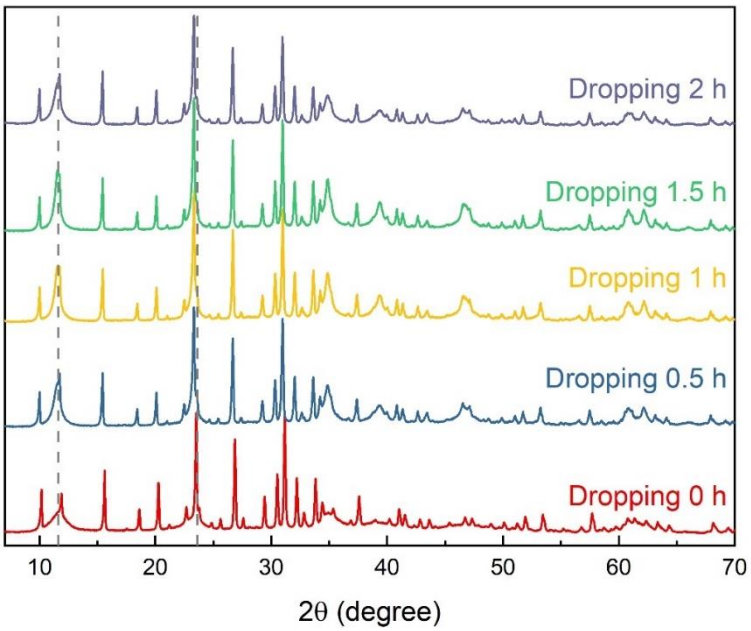


Figure A.6 XRD spectra of Z13X@Mg_2Al-CO_3-LDHs prepared from different addition time. Ageing time = 1 hour.

Table A.4 Details of Pawley refinement for Z13X@Mg_2Al-CO_3-LDHs prepared from different addition time. Ageing time was fixed to 1 h.

Addition time (h)	0	0.5	1	2
R_{wp}	6.22353177	7.17910178	7.0888238	6.86064395
GOF (Goodness of fit)	3.62176567	3.63340974	3.554455	3.74831933
Phase component	LDH	LDH	LDH	LDH
Space group	R-3m:H	R-3m:H	R-3m:H	R-3m:H
a (=b) /Å	3.079204	3.046216	3.046129	3.045841
c /Å	23.097973	22.997917	22.978657	22.993504
Phase component	Z13X	Z13X	Z13X	Z13X
Space group	Fd-3	Fd-3	Fd-3	Fd-3
a/Å	24.955435	24.984337	24.980842	24.990165

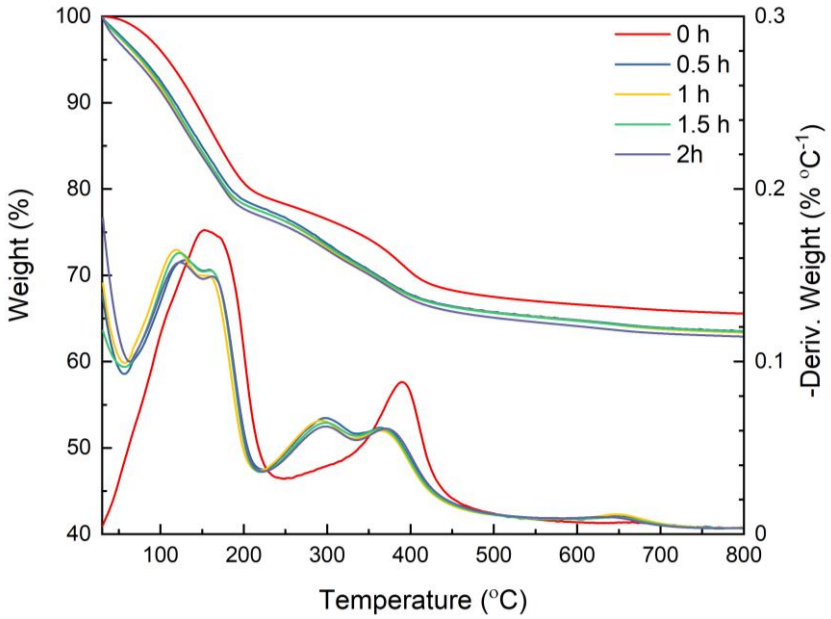


Figure A.7 TGA plots of Z13X@Mg_2Al-LDH core-shells with different addition time. Ageing time was fixed to 1 h.

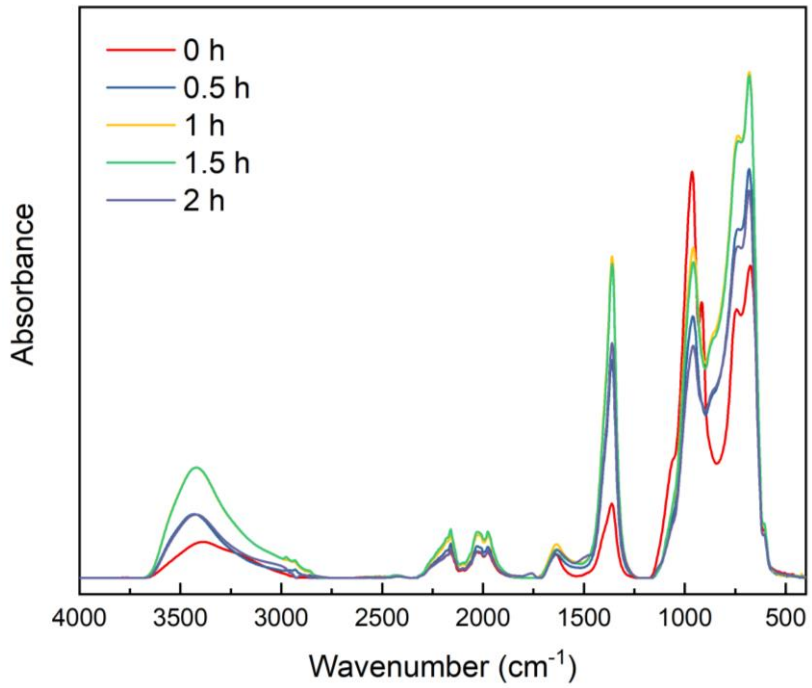


Figure A.8 FTIR absorbance spectra of Z13X@Mg_2Al-CO_3-LDH core-shells with different addition time. Ageing time was fixed to 1 h.

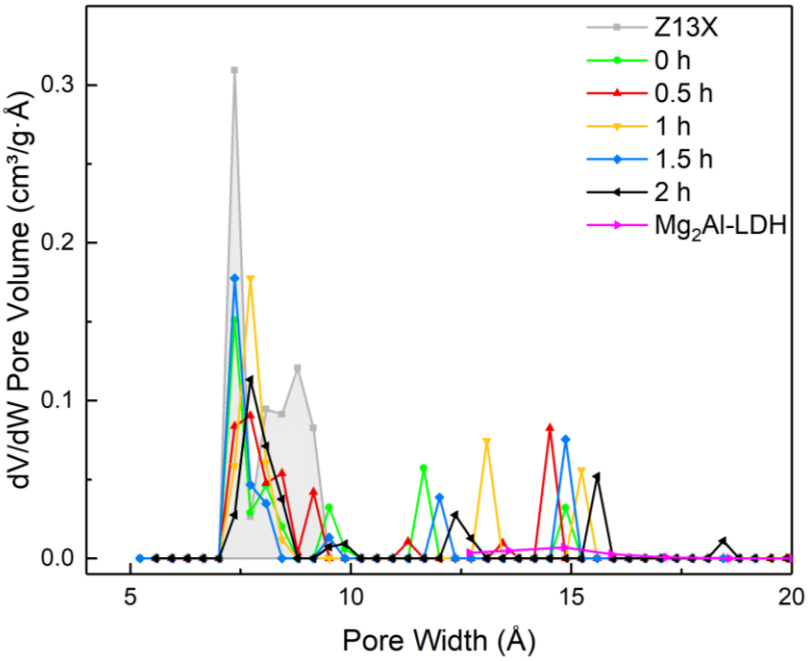


Figure A.9. The DFT pore size distribution of Z13X@Mg_2Al-CO_3-LDH core-shells prepared with different addition time. Ageing time was fixed to 1 h.

A.3 Z13X@Mg_2Al LDHs with varied ageing time

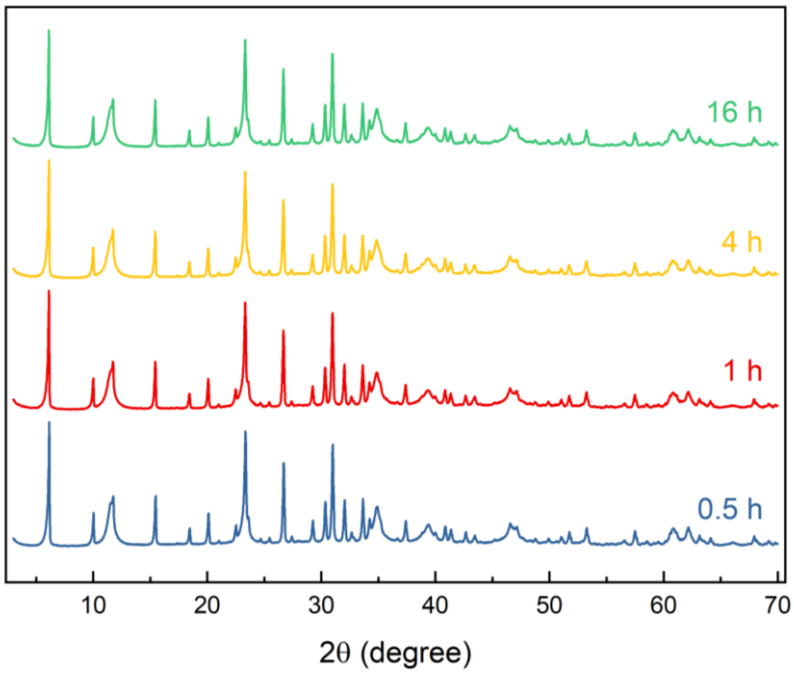


Figure A.10 XRD patterns of Z13X@Mg_2Al-CO_3-LDHs prepared from different ageing time. Addition time = 0.5 h.

Table A.5 Details of Pawley refinement for Z13X@Mg_2Al-CO_3-LDHs prepared from different ageing time. Addition time was fixed to 0.5 h.

Ageing time (h)	0.5	1*	4	16
R_{wp}	7.517234	7.17910178	7.32958785	7.03274208
GOF (goodness of fit)	3.20507518	3.63340974	3.71968382	3.54864984
Phase component	LDH	LDH	LDH	LDH
Space group	R-3m:H	R-3m:H	R-3m:H	R-3m:H
a (=b) /Å	3.046076	3.046216	3.046184	3.045710
c /Å	22.995574	22.997917	22.997639	22.985410
d_{003} (Å)	1.52	1.52	1.52	1.52
d_{110} (Å)	7.67	7.67	7.67	7.66
D_{00l} (nm)[a]	9.45	8.43	8.51	8.73
D_{110} (nm)[a]	9.45	8.43	8.51	8.73
Phase component	Z13X	Z13X	Z13X	Z13X
Space group	Fd-3	Fd-3	Fd-3	Fd-3
a/Å	24.976829	24.984337	24.984041	24.982011

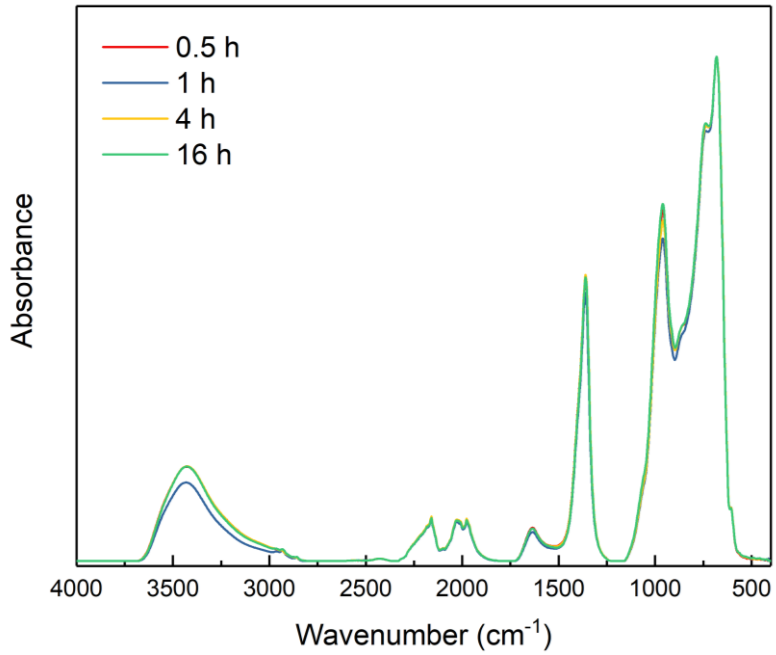


Figure A.11 FTIR absorbance spectra of Z13X@Mg_2Al-CO_3-LDH core-shells with different ageing time. Addition time was fixed to 1 h. Signal was normalized by the maximum value within each spectrum, i.e., the maximum value in all spectra = 1.

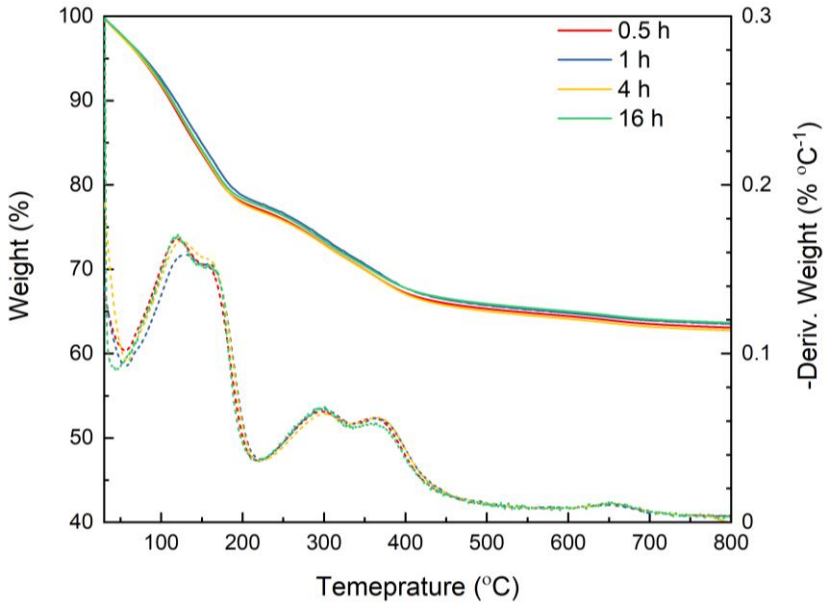


Figure A.12 TGA plots of Z13X@Mg_2Al LDH core-shells with different ageing time. Addition time was fixed to 0.5 h.

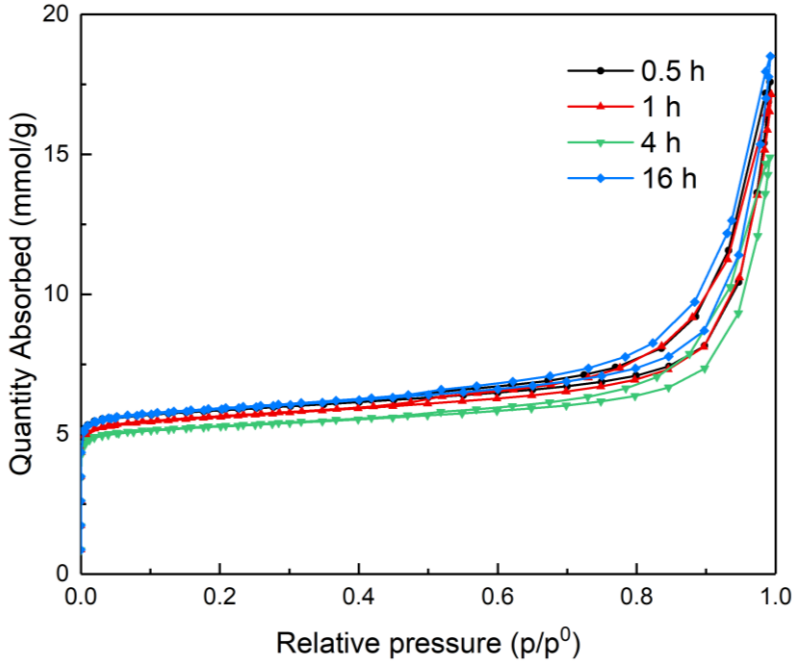


Figure A.13 N_2 adsorption-desorption isotherm (at 77K) of Z13X@Mg_2Al-CO_3-LDH core-shells prepared from different ageing time (addition time = 0.5 h).

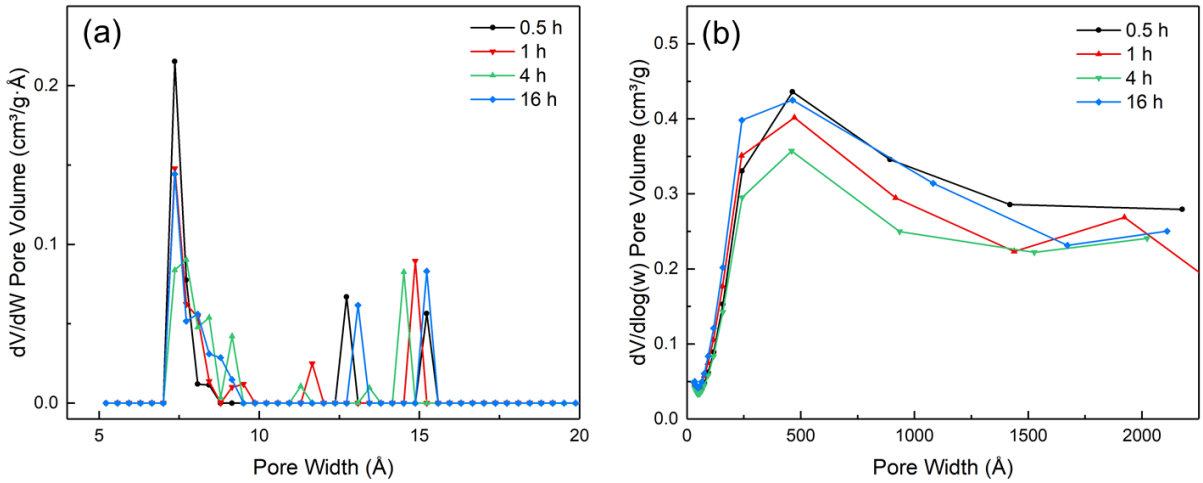


Figure A.14 (a) The DFT pore size distribution and (b) the BJH pore size distribution of Z13X@Mg_2Al-CO_3-LDH core-shells prepared with different ageing time. Addition time was fixed to 0.5 h.

A.4 Z13X@Mg_2Al LDHs with varied LDH content

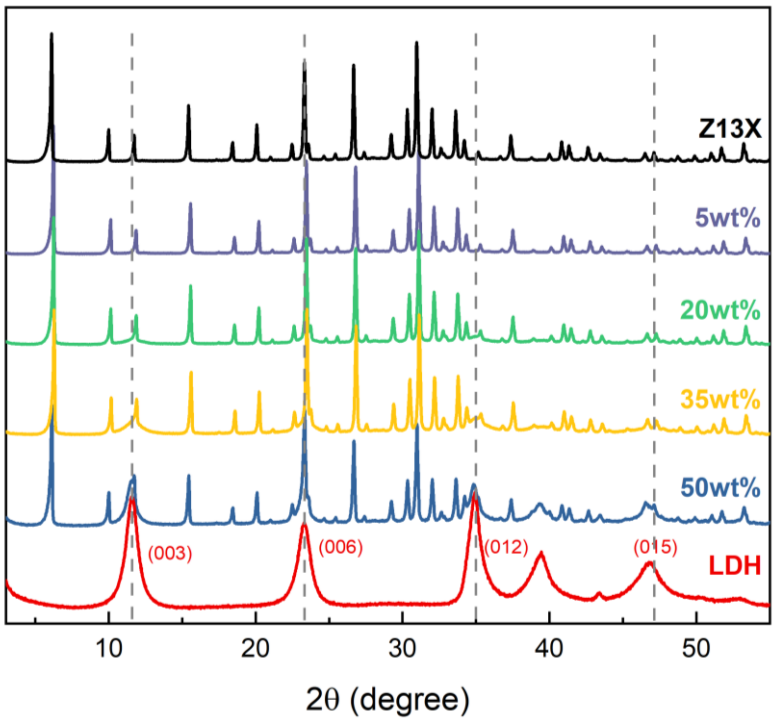


Figure A.15 XRD patterns of Z13X@Mg_2Al-CO_3-LDHs prepared from with varied LDH content. The addition rate and the ageing time are fixed to 0.15 mM/h and 0.5 h, respectively.

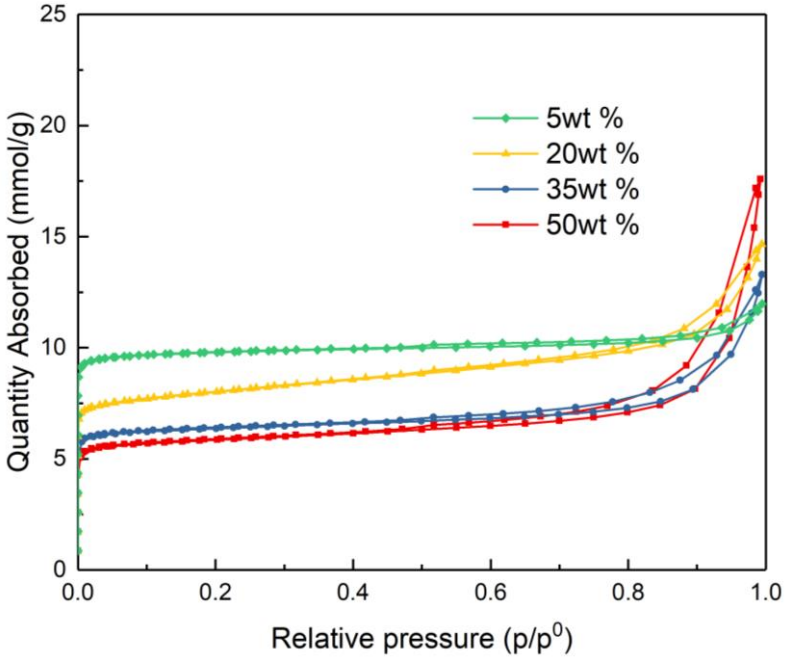


Figure A.16 The N_2 adsorption and desorption isotherm of Z13X@Mg_2Al-CO_3-LDH with different LDH content. The addition rate and the ageing time are fixed to 0.15 mM/h and 0.5 h, respectively.

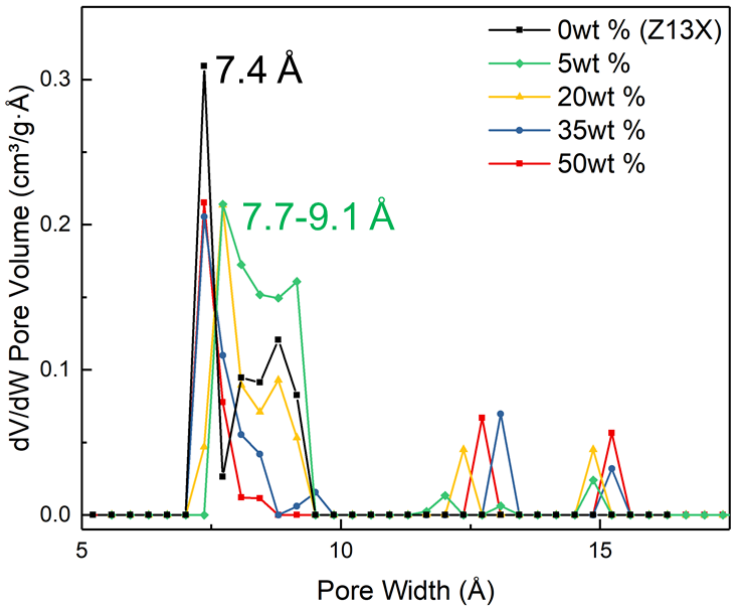


Figure A.17 The DFT pore size distribution of Z13X@Mg_2Al-CO_3-LDH with varied LDH content. The addition rate and the ageing time are fixed to 0.15 mM/h and 0.5 h, respectively. Sample with 0wt % LDH is the pristine Z13X.

Table A.6 The elemental analysis (C, H, N) and ICP-OES analysis (Na, Mg, Al, Si) result of Z13X@Mg_2Al-CO_3-LDH core-shells prepared with different LDH content and the calculated element weight percent from.

LDH content (wt %)		35	20	5
Na	Exp	4.89	6.01	7.56
	Real	4.10	5.61	8.34
	Δ	-0.79	-0.40	0.78
Mg	Exp	8.78	5.99	2.22
	Real	8.28	4.08	1.40
	Δ	-0.50	-1.91	-0.82
Al	Exp	12.22	12.10	11.99
	Real	13.46	12.68	14.39
	Δ	1.24	0.58	2.40
Si	Exp	11.95	14.68	18.46
	Real	10.18	11.76	16.78
	Δ	-1.77	-2.92	-1.68
C	Exp	1.22	0.83	0.31
	Real	0.86	0.50	0.27
	Δ	-0.37	-0.33	-0.04
H	Exp	2.88	2.75	2.56
	Real	2.84	2.57	2.62
	Δ	-0.04	-0.19	0.06
N	Exp	0	0	0
	Real	0	0	0
	Δ	0	0	0

*: Z13X@Mg_2Al-CO_3-LDH did not completely digested in ICP-OES analysis, actual Si ratio should be higher than reported value.

A.5 Z13X@Mg_2Al LDOs

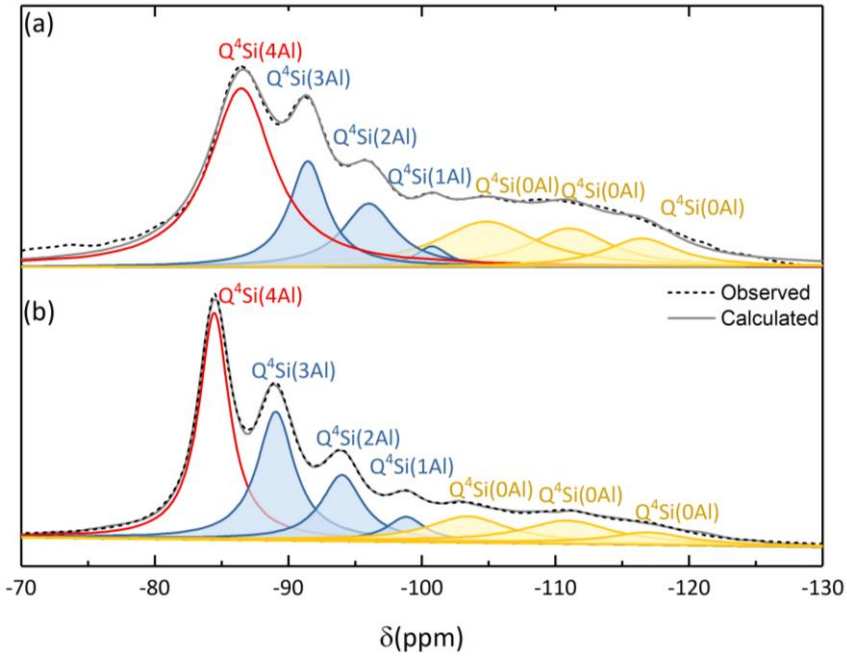


Figure A.18 ^{29}Si solid-state DPMAS NMR of (a) Z13X@Mg_2Al-LDO and (b) Z13X@Mg_2Al-LDH.

Due to the dehydration and potential dehydroxylation, resonances of Z13X@Mg_2Al-LDO are shifted by −2 ppm and their relative intensity changes a bit.[5,6]

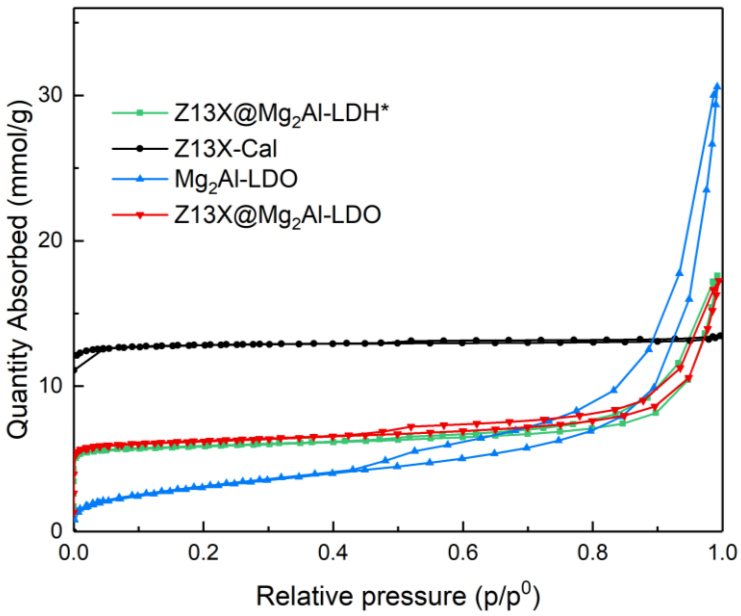


Figure A.19 N_2 adsorption and desorption isotherm at 77 K for Z13X-Cal, Mg_2Al-LDO, Z13X@Mg_2Al-LDH* and Z13X@Mg_2Al-LDO.

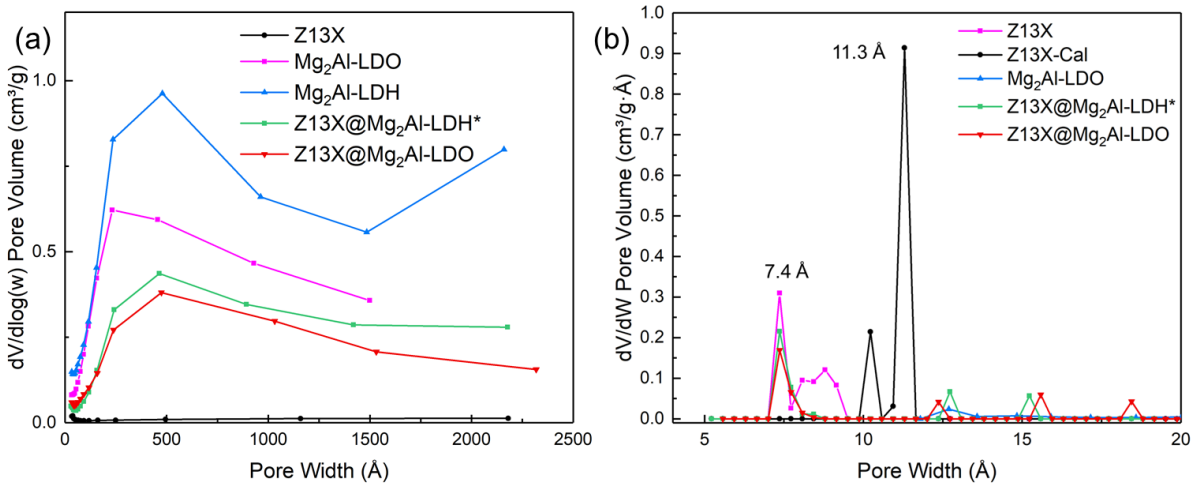


Figure A.20 (a) The BJH pore size distribution and (b) the DFT pore size distribution of materials (as shown by the legend).

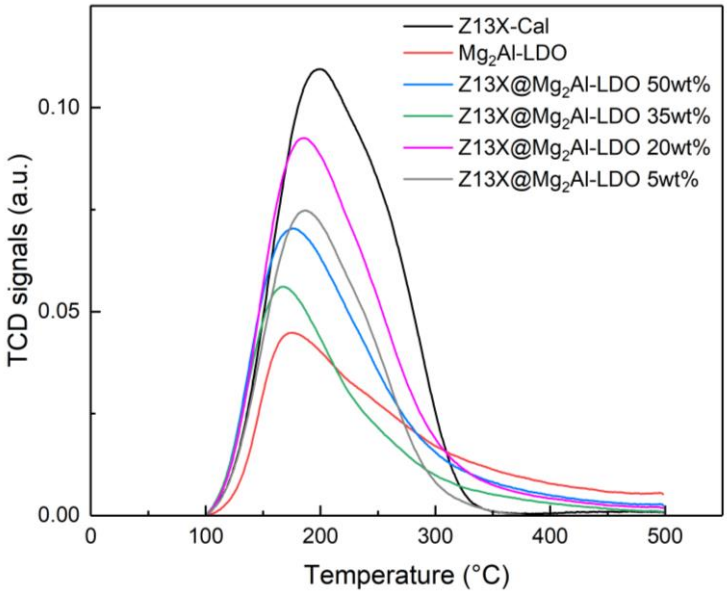


Figure A.21 CO_2-temperature programmed desorption (CO_2-TPD) curves for adsorbents. Peak integration was not normalized and calibrated and cannot be used to quantify the CO_2 capacity.

A.6 Reference

1 F. Dogan, K. D. Hammond, G. A. Tompsett, H. Huo, W. C. Conner, S. M. Auerbach and C. P. Grey, *J. Am. Chem. Soc.*, 2009, **131**, 11062–11079.

2 W. Loewenstein and M. Lowensterin, *Am. Mineral.*, 1954, **39**, 92–96.

3 C. A. Fyfe, Y. Feng, H. Grondey, G. T. Kokotailo and H. Gies, *Chem. Rev.*, 1991, **91**, 1525–1543.

4 P. J. Sideris, U. G. Nielsen, Z. Gan and C. P. Grey, *Science*, 2008, **321**, 113–117.

5 J. Jiao, W. Wang, B. Sulikowski, J. Weitkamp and M. Hunger, *Microporous Mesoporous Mater.*, 2006, **90**, 246–250.

6 Z. Li, C. Rieg, A. K. Beurer, M. Benz, J. Bender, C. Schneck, Y. Traa, M. Dyballa and M. Hunger, *Adsorption*, 2021, **27**, 49–68.

Appendix B: Appendix for Chapter 3

B.1. Synthesis and characterisation of MCM-48@Cu_xZnAl-CO_3-LDH

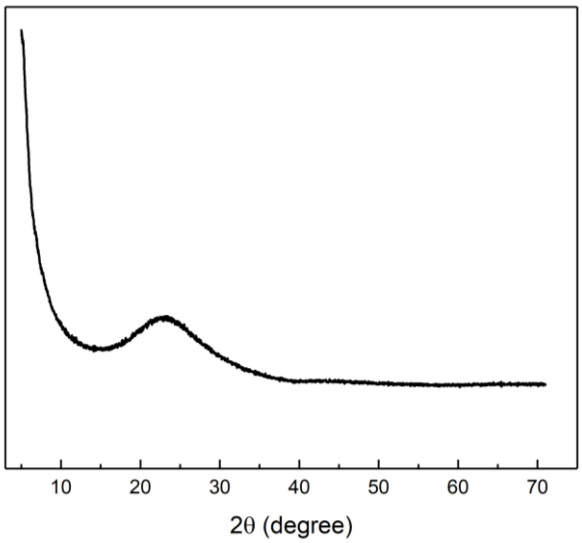


Figure B1 Powder XRD pattern of MCM-48.

Table B1. Details of single-phase Pawley refinement for MCM-48@$Cu_{1.3}$ LDH-pH10 and $Cu_{1.3}$ZnAl-LDH corresponding to the fits shown in Figure 3.1.

Sample name	MCM-48@$Cu_{1.3}$ZnAl-LDH-pH10	$Cu_{1.3}$ZnAl-LDH
Phase component	LDH	LDH
Space group	R-3*m*H	R-3*m*H
R_{wp}/%	3.8209933	3.14
GOF (goodness of fit)	1.8673174	2.49
a (=b) /Å	3.046(3)	3.079(0)
c /Å	22.193(20)	22.780(3)

Relationship between d_{003}, d_{110} and lattice parameter:

The d-spacing of (003) and (110) can be directly obtained from the position of peak by applying the Bragg equation; The lattice parameters are calculated from the d-spacing ($a = 2d_{110}$, $c = 3d_{003}$).[1,2]

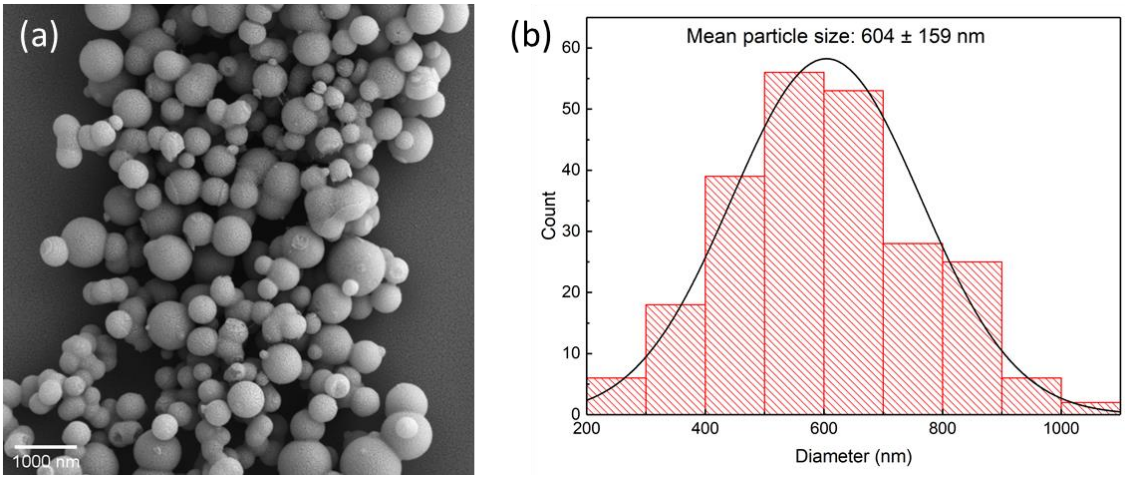


Figure B2 (a) SEM image of MCM-48, (b)Average particle size distribution plot of MCM-48 (counts vs diameter).

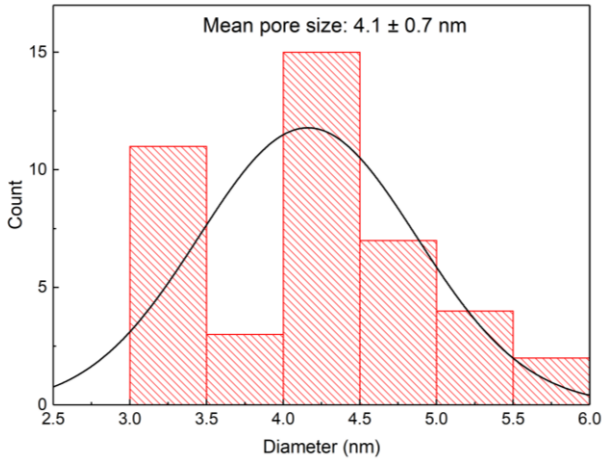


Figure B3 Average pore size distribution of the pore of MCM-48 from TEM images (counts vs diameter).

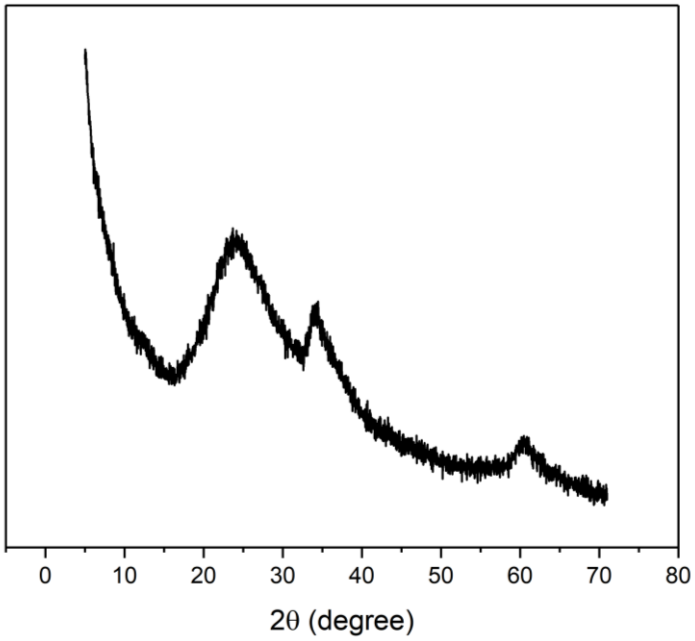


Figure B4 Powder XRD pattern of MCM-48@$Cu_{1.3}$ZnAl-LDH-0.1.

Table B2. Details of Rietveld Refinement and structural parameters for MCM-48@$Cu_{1.3}$ZnAl-LDH-67wt and MCM-48@$Cu_{1.3}$ZnAl-LDH-pH9

Sample name	MCM-48@$Cu_{1.3}$ZnAl-LDH-67wt%	MCM-48@$Cu_{1.3}$ZnAl-LDH-pH9
Phase component	LDH	LDH
Space group	R-3*m*H	R-3*m*H
R_{wp}/%	4.41561446	3.44642952
GOF (goodness of fit)	3.05940921	1.69641266
a (=b) /Å	3.072(2)/3.088(5)	3.011(198)
c /Å	22.608(25)/24.542(101)	22.163(22)

Structure parameter

Sample: MCM-48@$Cu_{1.3}$ZnAl-LDH-67wt			LDH phase 1		
Atom	x	y	z	Occupancy	beq[a]
Cu	0	0	0	0.41981	1
Zn	0	0	0	0.3001	1
Al	0	0	0	0.28009	1
O1	0	0	0.37318	0.81425	5
O2	0.125	-0.125	0.50503	0.16028	5
C	1/3	2/3	0.5	0.01863	5
Sample: MCM-48@$Cu_{1.3}$ZnAl-LDH-67wt			LDH phase 2		
Atom	x	y	z	Occupancy	beq[a]
Cu	0	0	0	0.41981	5
Zn	0	0	0	0.30000	5
Al	0	0	0	0.28019	5
O1	0	0	0.37318	0.81425	1.796
O2	0.125	-0.125	0.5	0.16028	1.796
C	1/3	2/3	0.5	0.01863	1.796
Sample: MCM-48@$Cu_{1.3}$ZnAl-LDH-pH9					
Atom	x	y	z	Occupancy	beq[a]
Cu	0	0	0	0.41981	5
Zn	0	0	0	0.30000	5
Al	0	0	0	0.28019	5
O1	0	0	0.37318	0.81425	1
O2	0.125	-0.125	0.5	0.16028	1
C	1/3	2/3	0.5	0.01863	1

[a]beq: atomic displacement parameters

- Considering the low crystallinity of the sample, **the atom position was not altered**.
- The **mismatch of (110) and (113) peaks** should because that **the stacking fault is not included** in the refinement.

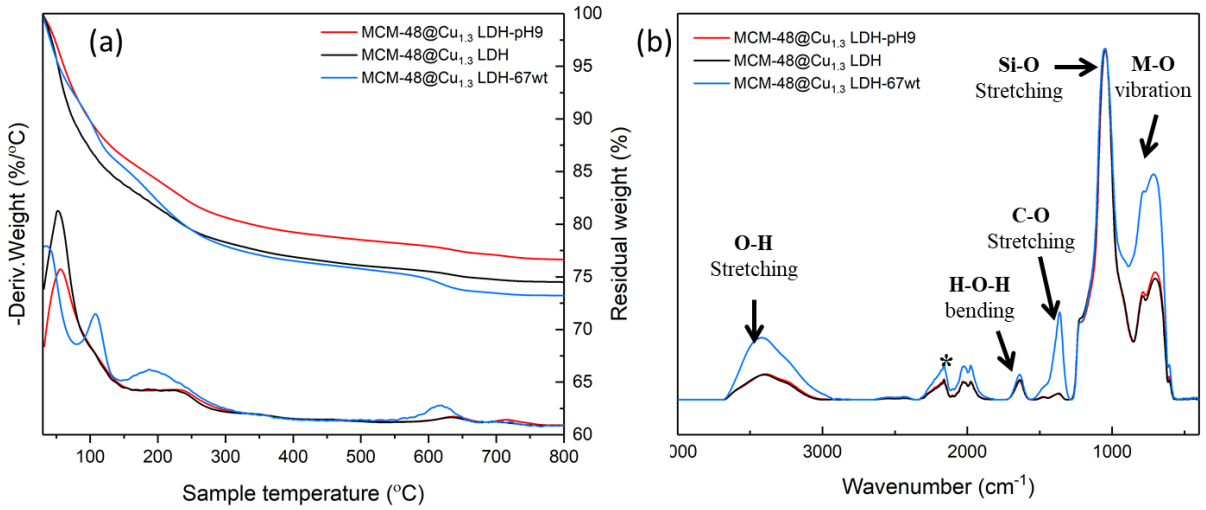


Figure B5 (a) TGA and Derivative TGA (dTGA) plots, and (b) FTIR spectra of MCM-48@$Cu_{1.3}$ZnAl-LDH, MCM-48@$Cu_{1.3}$ZnAl-LDH-67wt and MCM-48@$Cu_{1.3}$ZnAl-LDH-pH9.

Table B3 Details of Pawley Refinement and structural parameters for MCM-48@$Cu_{1.3}$ZnAl-CO_3-LDH core-shells prepared at pH 9 with various LDH fraction, 60 wt% and 67 wt%.

LDH content	60 wt%	67 wt%
Phase component	LDH	LDH
Space group	R-3*m*H	R-3*m*H
R_{wp}/%	2.8594738	3.44642952
GOF (goodness of fit)	1.95634139	1.69641266
a (=b) /Å	3.026(3)	3.058(4)
c /Å	22.272(61)	22.401(21)

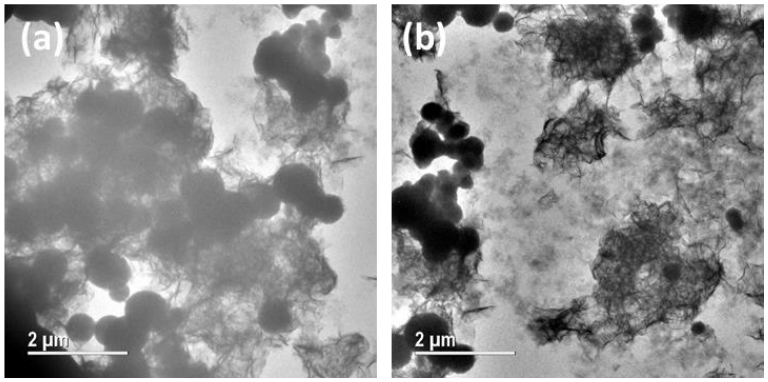


Figure B6 TEM images showing the free LDH in MCM-48@$Cu_{1.3}$ZnAl-CO_3-LDH with 67 wt% LDH.

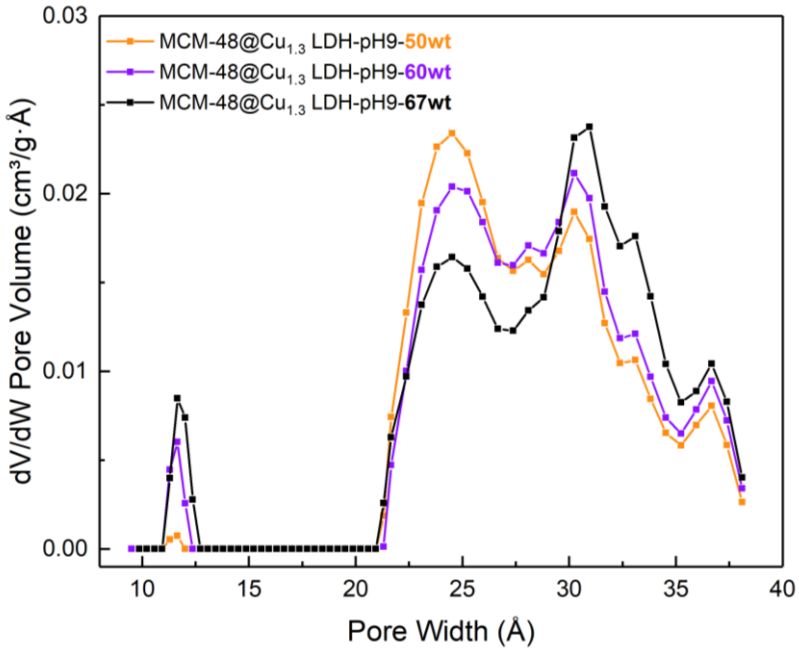


Figure B7 DFT pore size distribution of MCM-48@$Cu_{1.3}$ZnAl-CO_3-LDH core-shells with 50–67wt% LDH based on the kernel of N_2 adsorption at 77K on metal oxide with cylinder pore.

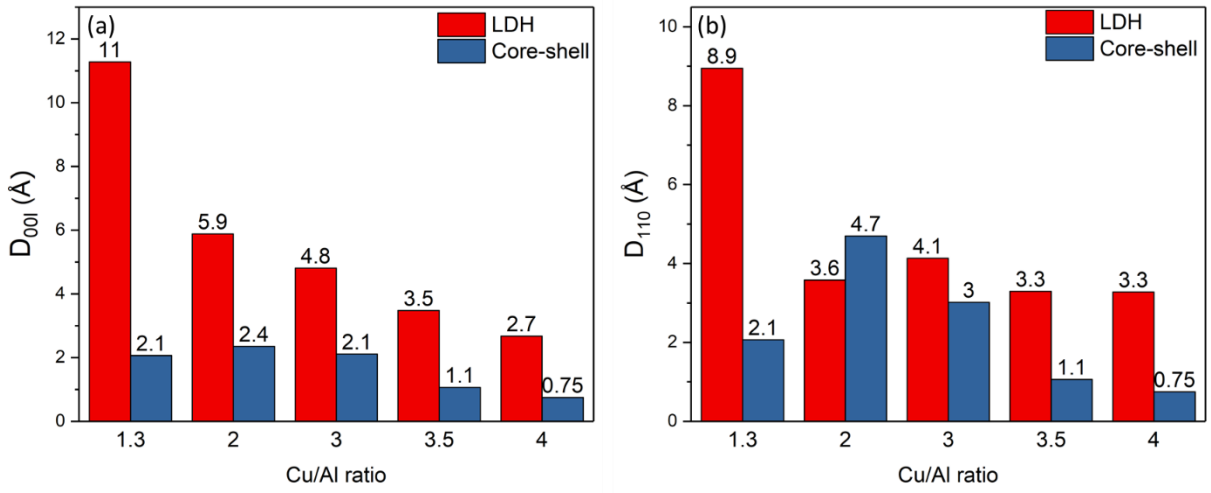


Figure B8 The crystallite size of Cu_xZnAl-LDH and MCM-48@Cu_xZnAl-LDH along (a) the (00*l*) direction and (b) the (110) direction. Values were obtained from the Pawley refinement.

Table B4 Details of Pawley Refinement and structural parameters for Cu_xZnAl-LDH and MCM-48@Cu_xZnAl-LDH.

Sample	Cu_xZnAl-LDH				
Cu/Al ratio	1.3	2	3	3.5	4
Phase component			LDH		
Space group			R-3*m*H		
R_{wp}/%	3.760724	2.799836	1.84086	1.682275	1.596393
GOF (goodness of fit)	2.891982	2.258434	1.477948	1.393962	1.338121
a (=b) /Å	3.075(0)	3.086(1)	3.078(1)	3.110(2)	3.116(3)
c /Å	22.673(3)	22.712(6)	22.728(7)	22.744(12)	22.835(18)
Sample	MCM-48@Cu_xZnAl-LDH				
Cu/Al ratio	1.3	2	3	3.5	4
Phase component			LDH		
Space group			R-3*m*H		
R_{wp}/%	2.859474	1.869015	1.595736	1.535628	1.469313
GOF (goodness of fit)	1.956341	1.314242	1.155222	1.135648	1.097282
a (=b) /Å	3.026(3)	3.127(3)	3.109(4)	3.146(16)	3.162(181)
c /Å	22.272(61)	22.898(10)	22.707(19)	26.248(50)	26.265(781)

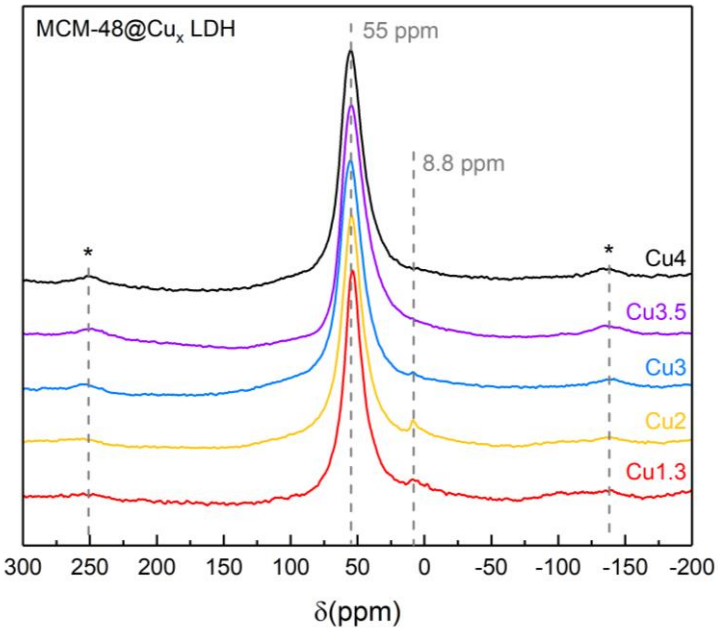


Figure B9. The ^{27}Al solid state NMR spectra for MCM-48@Cu_xZnAl-LDH, x = 1.3, 2, 3, 3.5,4. Peaks marked with star are spinning sidebands.

Details about chemical formula calculation

ICP-OES provides the weight percentage of elements in the sample. The wt% of elements are firstly divided by the corresponding atomic weight to give mol%. The mol% was then normalised by the mol% of Al to give the molar ratio between elements, *i.e.*, the molar amount of Al is 1 after normalisation.

For LDH

It is assumed all Cu, Zn and Al goes into LDH; H goes into hydroxide group, the stoichiometry of which should be double of the sum of metals, and water; C should come from carbonate. Due to the charge balance, the molar amount of C should be around 0.5. However, the actual C in LDH samples is between 0.6-1.14. This excess amount of C is expected to come from carbonate impurities like Na_2CO_3 and $NaHCO_3$ due to insufficient washing during synthesis or metal hydroxide carbonate impurities such as $Cu_2(OH)_2CO_3$.

In the case of impurities being Na_2CO_3 and $NaHCO_3$, the calculated and detected amount of Cu, Na and C cannot match at the same time, where 'match' means the difference between the expected and real value is less than ± 1wt% for Cu and Na and less than ± 0.2wt% for C.

Set the impurities to basic copper carbonate or so-called malachite ($Cu_2(OH)_2CO_3$) can give good fit between the theoretical and real value.

HCO_3^- as the interlayer anion rather than CO_3^{2-} is not considered in the case of pure LDH because the d_{003} of all CuZnAl-LDHs are around 7.6 Å indicating the interlayer region is occupied by carbonate anions.

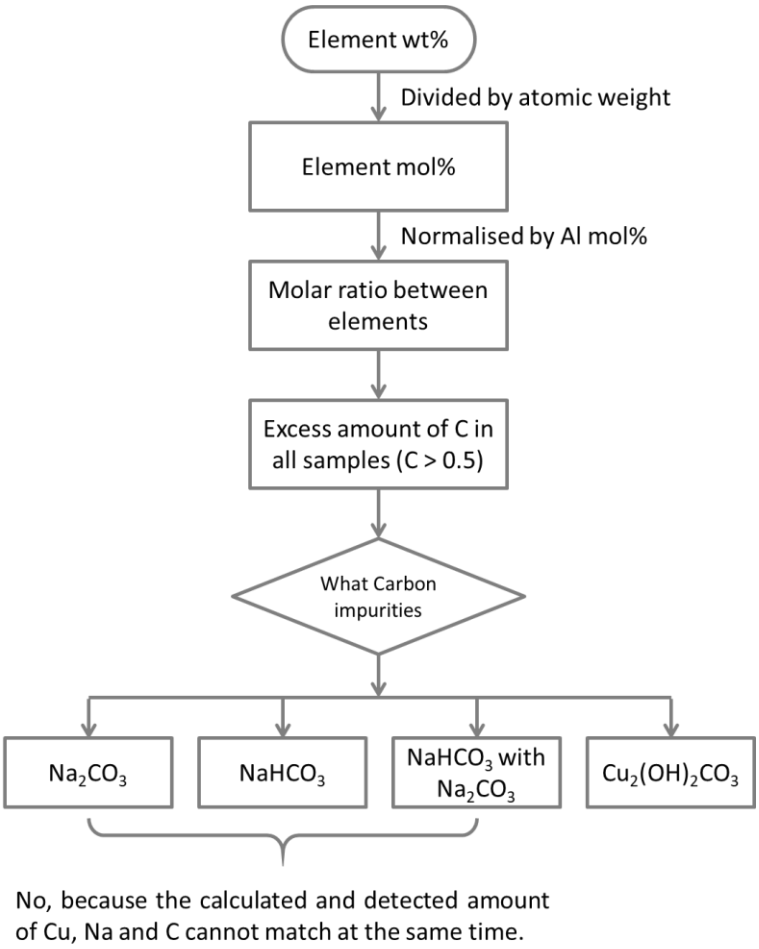
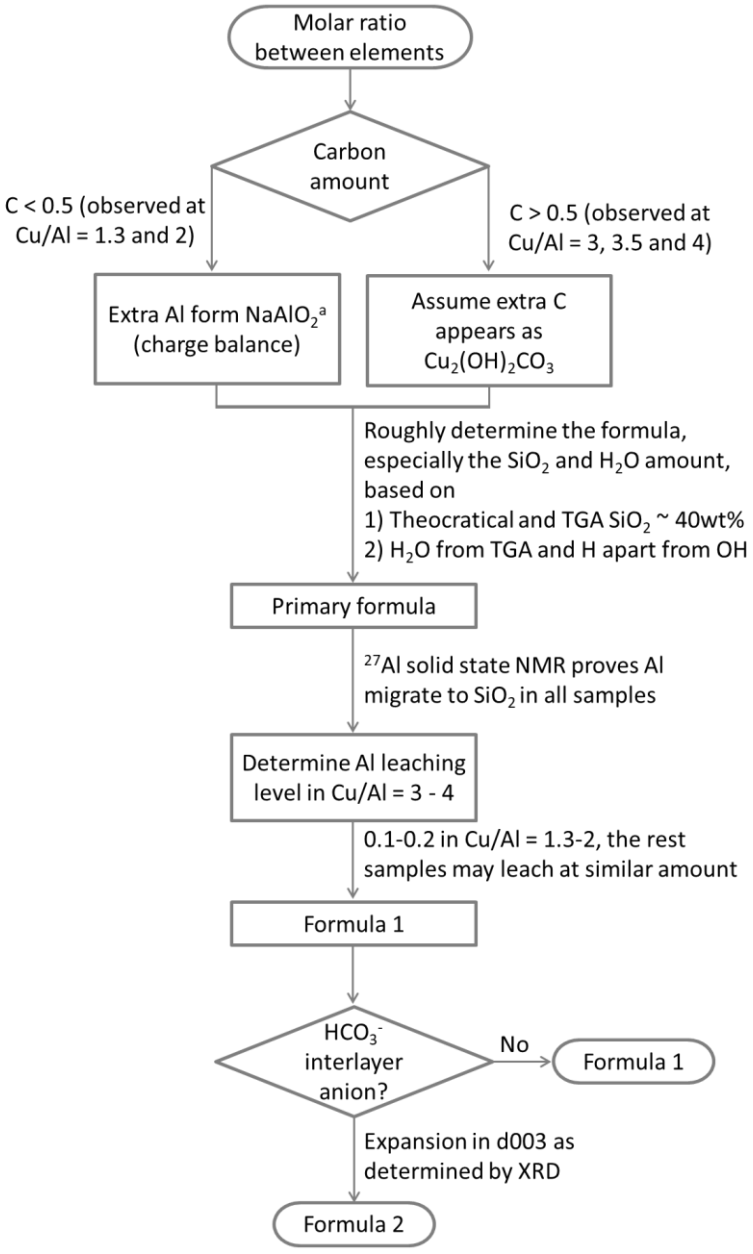


Table B5 The expected (theoretical value from chemical formula), real elemental composition of Cu_xZnAl-LDHs and deviations between them

Samples		$Cu_{1.3}ZnAl$-LDH	Cu_2ZnAl-LDH	Cu_3ZnAl-LDH	$Cu_{3.5}ZnAl$-LDH	Cu_4ZnAl-LDH
Cu	Exp	21.59	27.21	36.87	37.22	41.4
	Real	21.46	27.31	37.88	38.25	41.5
	Δ	-0.13	0.1	1.01	1.03	0.1
Zn	Exp	15.76	13.39	11.67	10.39	9.64
	Real	15.67	13.44	11.99	10.68	9.66
	Δ	-0.09	0.05	0.32	0.29	0.02
Al	Exp	6.98	5.96	5.34	4.55	4.33
	Real	6.94	5.98	5.49	4.68	4.34
	Δ	-0.04	0.02	0.15	0.13	0.01
C	Exp	1.88	2.18	2.08	1.81	2.14
	Real	1.96	2.19	2.24	1.91	2.21
	Δ	0.07	0.01	0.16	0.09	0.07
H	Exp	2.75	2.56	2.41	2.25	2.31
	Real	2.71	2.5	2.4	2.24	2.22
	Δ	-0.04	-0.06	-0.01	-0.01	-0.09

For core-shells

In ICP-OES, solid samples will firstly be fully digested using acid. The obtained solution was then diluted and analysed by optical spectrometer to get the weight of element in the solution which was then normalised by the weight of original solid sample to provide the concentration of each element. SiO_2 cannot be fully digested with acid, so the detected Si wt % would be much lower than the real value.



At Cu/Al = 1.3 and 2, The amount of C is lower than 0.5. It is expected that some Al migrate to silica rather than to the framework of LDH. Presence of tetrahedral Al resonance in the ^{27}Al solid state NMR proved this assumption. To balance the charge, counter ion is required. Consider the co-precipitation was carried out at pH 9, Na^+ should be the most likely charge balance cation ($NaAlO_2$ species formed).

At Cu/Al ≥ 3, the amount of C is larger than 0.5. At the beginning, the excess C is regarded to come from $Cu(OH)_2CO_3$ impurity.

At this stage, a charge balance and a balance in the element amount is achieved in all samples. The stoichiometry of SiO_2 and H_2O are then adjusted based on the information that 1) from TGA and expectation, the SiO_2 wt% is about 40wt %; 2) Maximum H_2O amount is estimated from TGA, the possible value is given by the residual H (besides those in OH group).

^{27}Al solid state NMR suggests that Al leaching happens in samples with Cu/Al ≥ 3 as well. It is assumed that the amount of Al migrate to SiO_2 is around 0.1–0.2 based on the finding in samples with low Cu/Al ratio. Modification of formula was carried out taking the Al leaching into account and the result is called formula 1.

An expansion in the interlayer spacing of MCM-48@$Cu_{3.5}$ and Cu_4ZnAl-LDH has been determined by XRD. It is possible some interlayer CO_3^{2-} are replace by double amount of HCO_3^-. Distribution of carbon are carried out to elevate the amount of HCO_3^-. The obtained formula is termed formula 2.

Table B6 The expected (theoretical value from chemical formula), real elemental composition of MCM-48@Cu_xZnAl-LDHs and deviations between them.

Cu/Al ratio		1.3	2	3	3.5	4	3.5[a]	4[a]
SiO_2	TGA[b]	37.7	38.1	41.8	27.3	21.0	27.3	21.0
	Real	40.7	40.9	39.1	39.6	38.4	39.3	39.6
Cu	Exp	15.90	19.73	22.89	23.57	25.25	23.43	24.99
	Real	14.94	18.85	23.43	24.67	25.31	24.67	25.31
	Δ	-0.96	-0.88	0.54	1.10	0.06	1.24	0.32
Zn	Exp	11.41	9.17	7.15	6.88	6.32	6.84	6.26
	Real	10.72	8.76	7.32	7.09	6.34	7.09	6.34
	Δ	-0.69	-0.41	0.17	0.21	0.02	0.25	0.08
Al	Exp	4.93	3.67	3.19	2.96	2.65	2.94	2.63
	Real	4.63	3.93	3.27	3.10	2.66	3.10	2.66
	Δ	-0.30	0.26	0.08	0.14	0.01	0.16	0.03
C	Exp	0.85	0.82	0.73	0.73	1.05	0.72	1.04
	Real	0.80	0.78	0.75	0.76	1.06	0.76	1.06
	Δ	-0.05	-0.04	0.02	0.03	0.00	0.04	0.01
H	Exp	1.69	1.49	1.59	1.50	1.41	1.56	1.51
	Real	1.47	1.39	1.39	1.35	1.38	1.35	1.38
	Δ	-0.23	-0.10	-0.21	-0.15	-0.03	-0.21	-0.13
Si	Exp	17.95	18.62	18.29	18.50	17.95	18.39	17.77
	Real	9.74	9.65	9.65	7.09	5.89	7.09	5.89
	Δ	-8.21	-8.97	-8.64	-11.41	-12.06	-11.30	-11.88
Na	Exp	0.96	0.38	0.27	0.51	0.45	0.51	0.45
	Real	0.00	0.00	0	0.00	0.00	0.00	0.00
	Δ	-0.96	-0.38	-0.27	-0.51	-0.45	-0.51	-0.45

a: The case where some HCO3-, b: SiO_2 composition estimated from TGA.

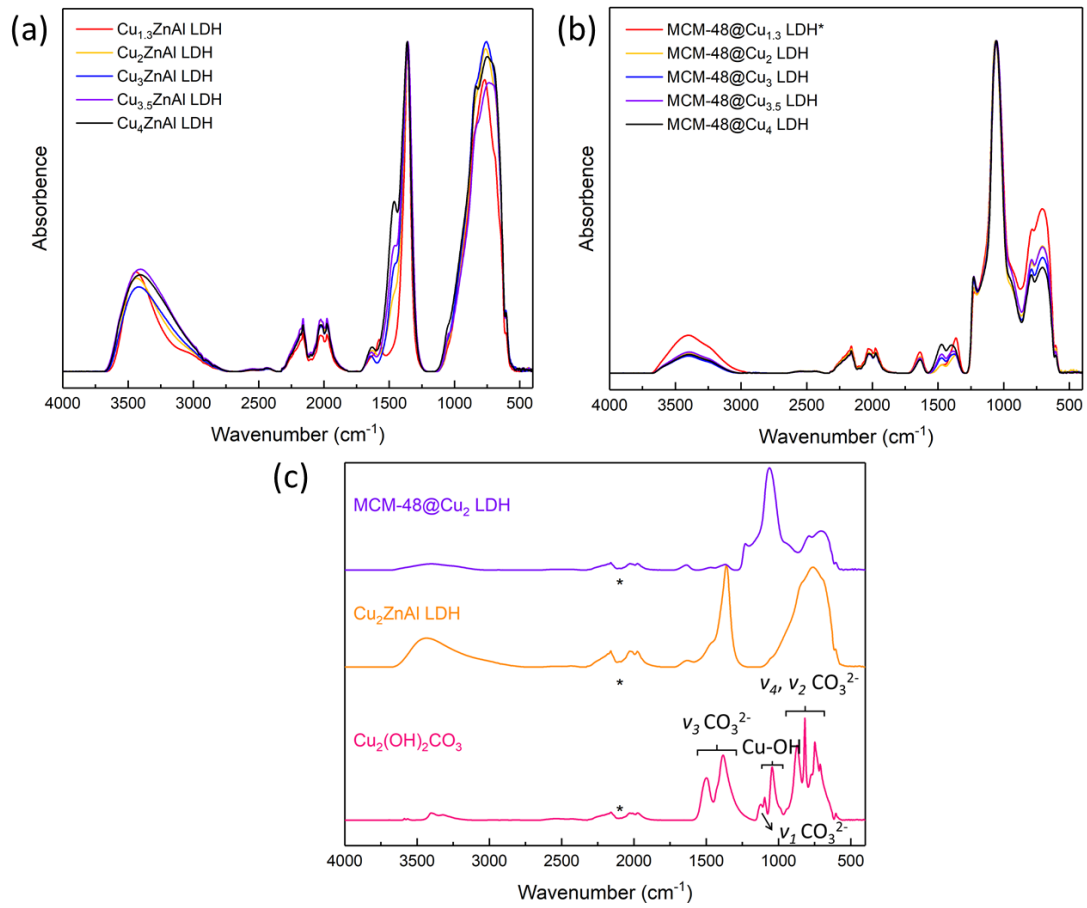


Figure B10 FTIR spectra of (a) Cu_xZnAl-LDH, (b) MCM-48@Cu_xZnAl-LDH and (c) $Cu_2(OH)_2CO_3$. Peak marked with start are due to diamond stage.

Table B7 The details of deconvoluted carbonate band and H_2O bending peak for Cu_xZnAl-LDH, MCM-48@Cu_xZnAl-LDH and $Cu_2(OH)_2CO_3$.

Cu_xZnAl-LDH (x =)	Carbonate band						H_2O bending
	Peak 1	Integ.	Peak 2	Integ.	Peak 3	Integ.	
1.3	1356.09	38.57	1383.05	61.43	1577.00		
2	1357.41	44.72	1394.95	19.92	1468.97	35.36	1634.22
3	1358.07	46.15	1397.56	19.62	1466.51	34.23	1646.66
3.5	1353.43	41.61	1398.94	20.00	1469.39	38.39	1644.23
4	1358.51	41.33	1399.12	6.56	1465.33	52.11	1642.34
MCM-48@Cu_xZnAl-LDH (x =)	Carbonate band						H_2O bending
	Peak 1	Integ.	Peak 2	Integ.	Peak 3	Integ.	
1.3	1360.39	43.74	1399.45	15.59	1464.52	40.67	1640.78
2	1363.18	38.25	1402.86	12.13	1466.50	49.62	1640.76
3	1365.56	29.72	1404.47	12.93	1471.49	57.35	1639.82
3.5	1374.48	34.90	1415.08	3.73	1472.80	61.36	1640.14
4	1359.07	16.57	1398.80	18.69	1473.83	64.74	1639.84
$Cu_2(OH)_2CO_3$	1366	52	1384	21	1504	27	

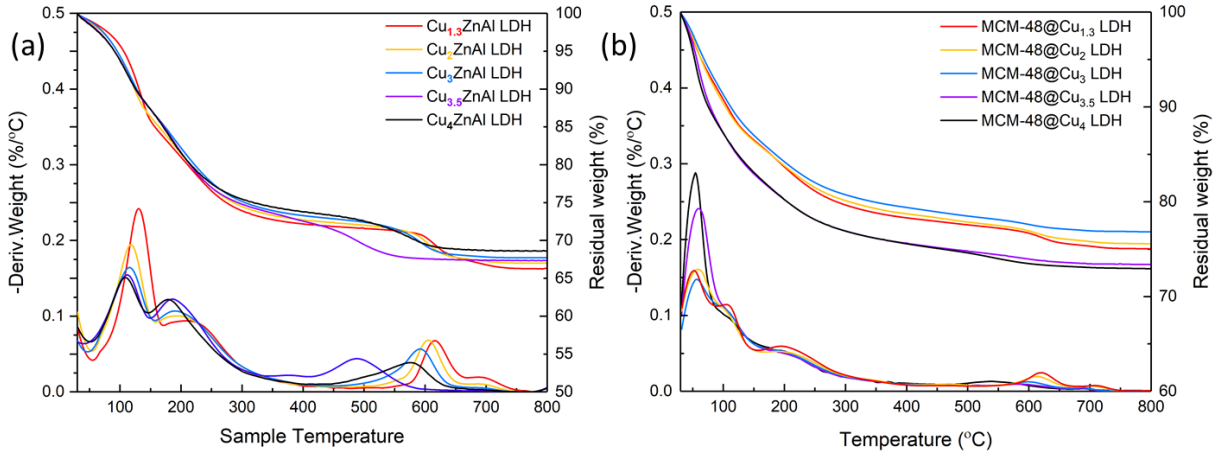


Figure B11 TGA and -Derivative TGA (dTG) plots of (a) Cu_xZnAl-LDH and (b)MCM-48@Cu_xZnAl-LDH.

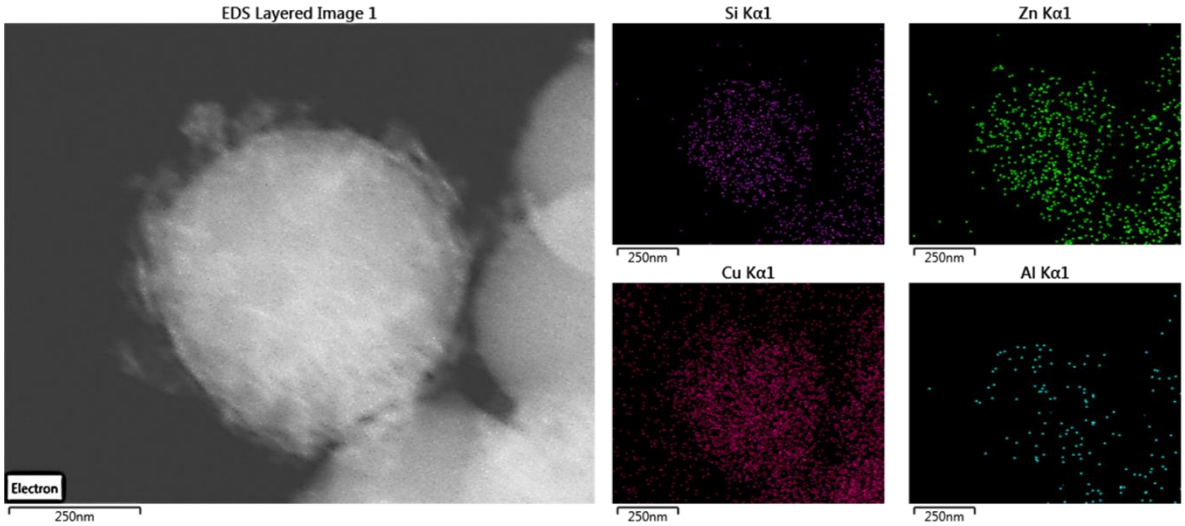


Figure B12 Electron image and TEM-EDX elemental mapping of MCM-48@Cu_4ZnAl-LDH. Sample was prepare using Cu grid which leads to the appearance of Cu at the background.

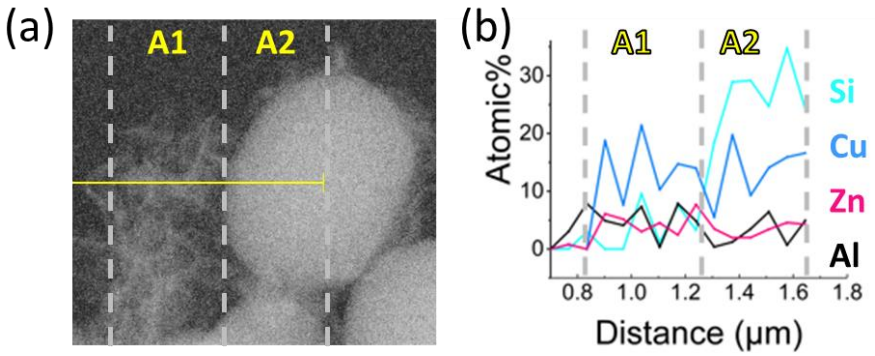


Figure B13 (a) Electron image of MCM-48@$Cu_{3.5}ZnAl$-LDH and (b) line scanning result.

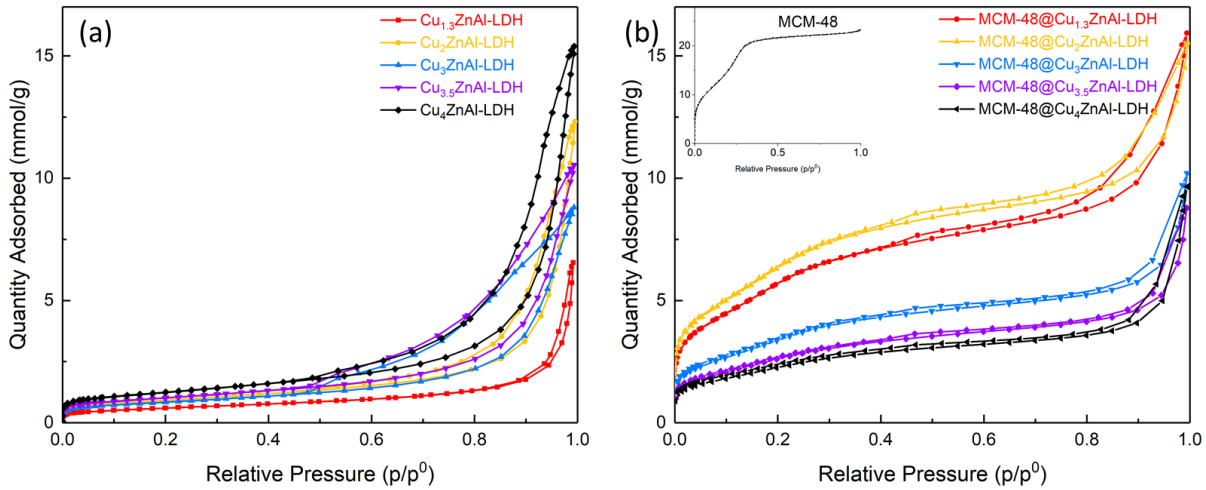


Figure B14 The N_2 adsorption and desorption isotherm at 77 K of (a) Cu_xZnAl-LDH, and (b) MCM-48@Cu_xZnAl-LDH.

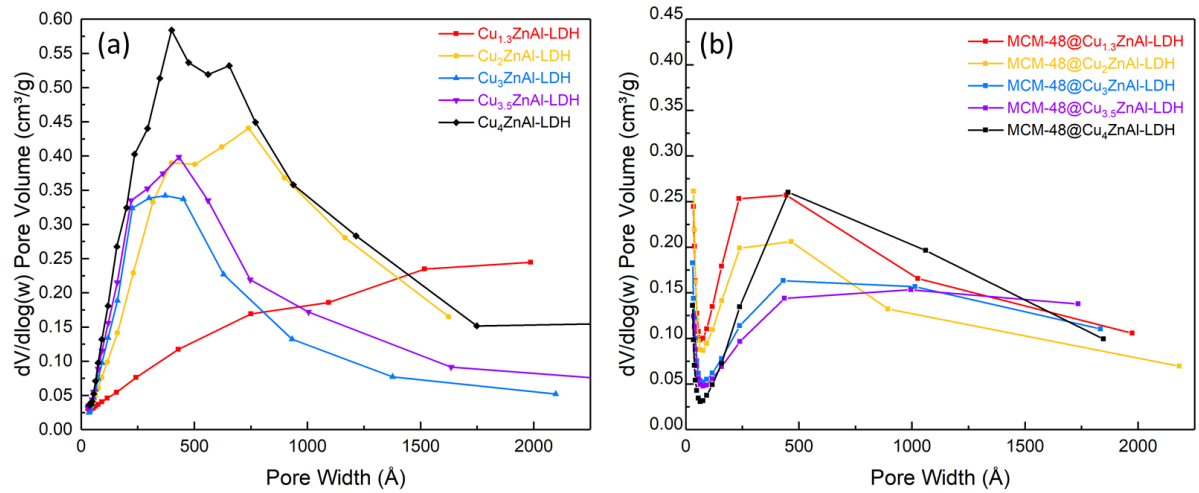


Figure B15 BJH pore size distribution of (a) Cu_xZnAl-LDH, and (b) MCM-48@Cu_xZnAl-LDH.

B.2. Synthesis and characterisation of ES757@Cu_xZnAl-CO_3-LDH

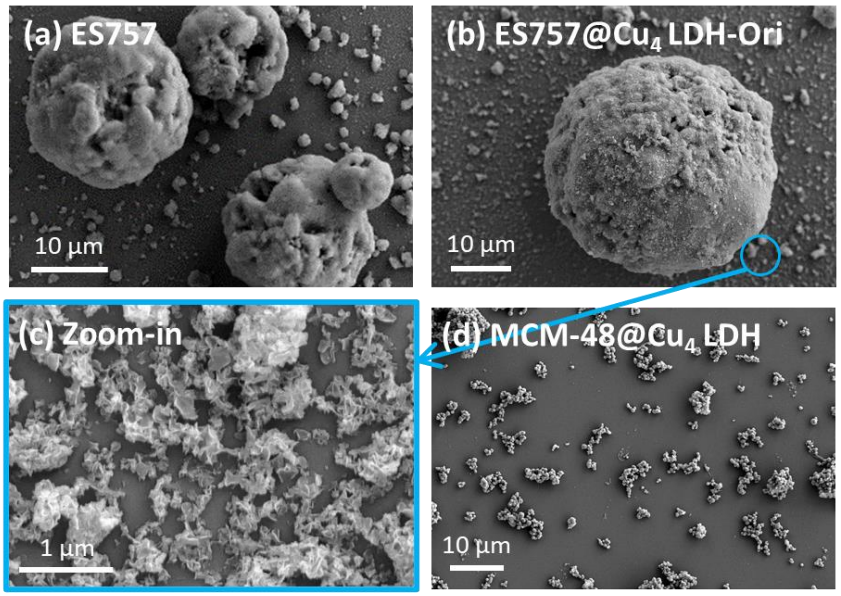


Figure B16 The SEM image of (a) fresh ES757, (b) ES757@Cu_4ZnAl-LDH-Ori, (c) The zoom-in of blue-circle region, and (d) MCM-48@Cu_4ZnAl-LDH.

Table B8 Details of Pawley Refinement and structural parameters for ES757@Cu_4ZnAl-LDH under different synthetic condition.

Sample	ES757@Cu_4ZnAl-LDH			
Condition	Original	Al impregnated	Al imp + concentrated	Concentrated
Phase component	LDH			
Space group	R-3m			
R_{wp}/%	1.60047718	1.73675024	1.94075528	1.82695534
GOF (goodness of fit)	1.20000323	1.29456449	1.45601276	1.38061274
a (=b) /Å	3.061(8)	3.058(5)	3.051(3)	3.052(4)
c /Å	23.220(60)	23.125(36)	22.737(26)	22.915(29)
d_{003}/Å	7.739934	7.708442	7.579108	7.638315
D_{00l}/nm	2.35	2.68	3.08	2.83
D_{110}/nm	2.84	3.19	3.03	2.95

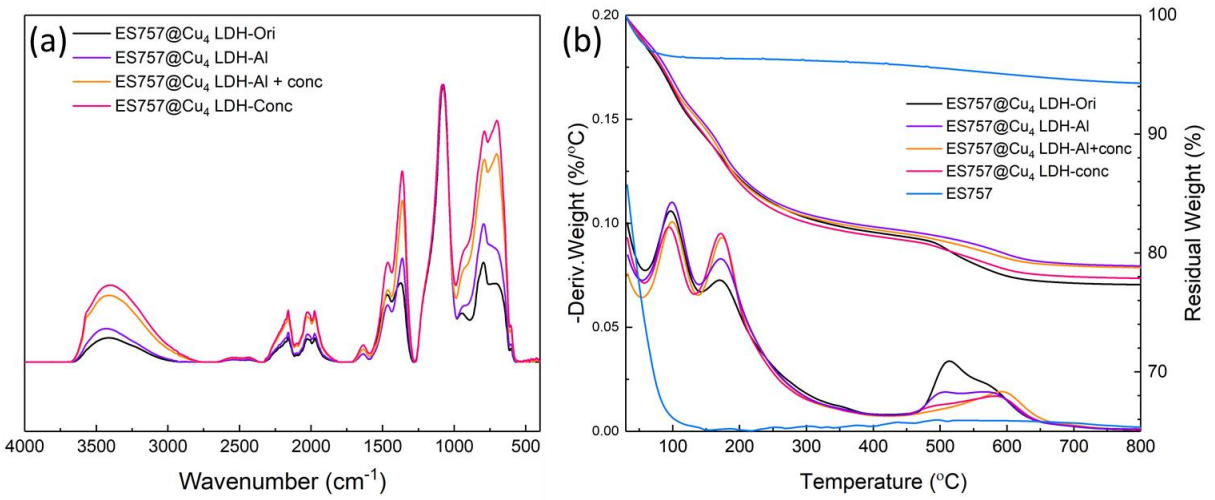


Figure B17 (a) FTIR spectra and (b) TGA and - dTG plots of ES757@Cu_4ZnAl-LDH-ori, -Al, -Al + conc and -conc.

Table B9 Details of Pawley Refinement and structural parameters for ES757@Cu_4ZnAl-LDH.

Sample	ES757@Cu_xZnAl-LDH				
Cu/Al ratio	0.8	1.3	2	3	4
Phase component	LDH				
Space group	R-3m				
R_{wp}/%	4.44115684	3.7830518	3.24767229	2.62963015	1.97047484
GOF (goodness of fit)	2.92176737	2.62589972	2.35088479	1.92901142	1.48226257
a (=b) /Å	3.070(3)	3.079(4)	3.086(6)	3.077(2)	3.051(3)
c /Å	22.646(4)	22.727(6)	22.717(8)	22.723(17)	22.730(29)
d_{003}/Å	7.548533	7.575607	7.572311	7.574211	7.576778
d_{110}/ Å	1.5349885	1.5396705	1.542807	1.5383045	1.5254745
D_{001}/nm	13.06	9.07	6.68	4.03	2.47
D_{110}/nm	11.20	8.08	5.97	4.06	2.86

Table B10 The expected (theoretical value from chemical formula), real elemental composition of ES757@Cu$_x$ZnAl-LDHs and deviations between them.

Cu/Al ratio		0.8	1.3	2	3	4
SiO_2	TGA[a]	39.1	40.9	39.5	44.3	40.6
	Real[b]	39.93	39.71	38.91	37.65	37.32
Cu	Exp	10.62	14.61	18.79	23.45	25.15
	Real	11.19	15.33	19.55	27.01	26.24
	Δ	0.57	0.72	0.76	3.56[c]	1.09
Zn	Exp	13.61	11.53	9.58	7.30	6.43
	Real	14.34	12.10	9.97	8.41	6.71
	Δ	0.73	0.57	0.39	1.11	0.28
Al	Exp	5.35	4.63	3.88	3.07	2.58
	Real	5.64	4.86	4.04	3.54	2.69
	Δ	0.29	0.23	0.16	0.47	0.11
C	Exp	1.19	1.08	1.03	1.09	1.34
	Real	1.26	1.14	1.07	1.26	1.40
	Δ	0.07	0.05	0.04	0.17	0.06
H	Exp	1.70	1.67	1.63	1.58	1.50
	Real	1.81	1.75	1.67	1.74	1.43
	Δ	0.11	0.07	0.04	0.16	-0.07
Si	Exp	18.67	18.56	18.19	17.60	17.44
	Real	0.04	0.06	0.09	0.00	0.00
	Δ	-18.63	-18.50	-18.10	-17.60	-17.44

a: SiO_2 composition estimated from TGA, b: SiO_2 composition based on the given chemical formula. c: This large difference is expected to come from the error in the ICP-OES result.

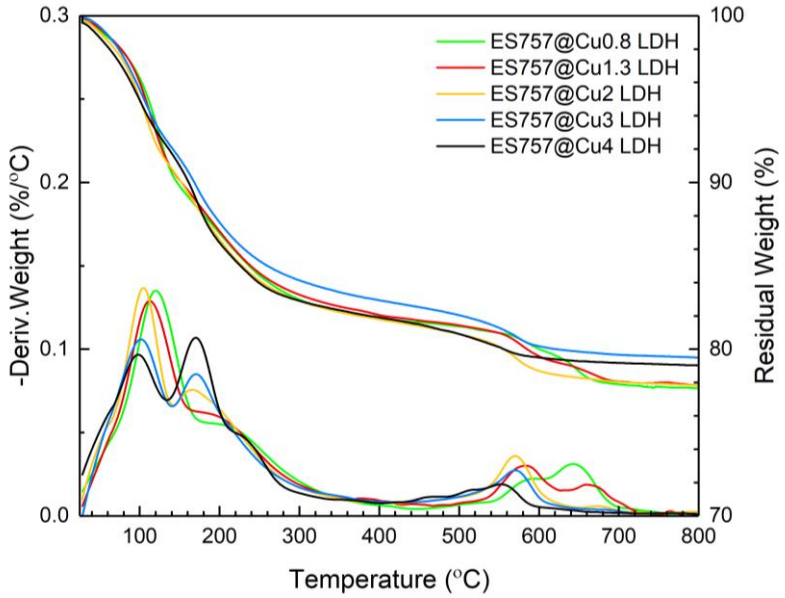


Figure B18 TGA and -dTG plots for ES757@Cu$_x$ZnAl-LDH.

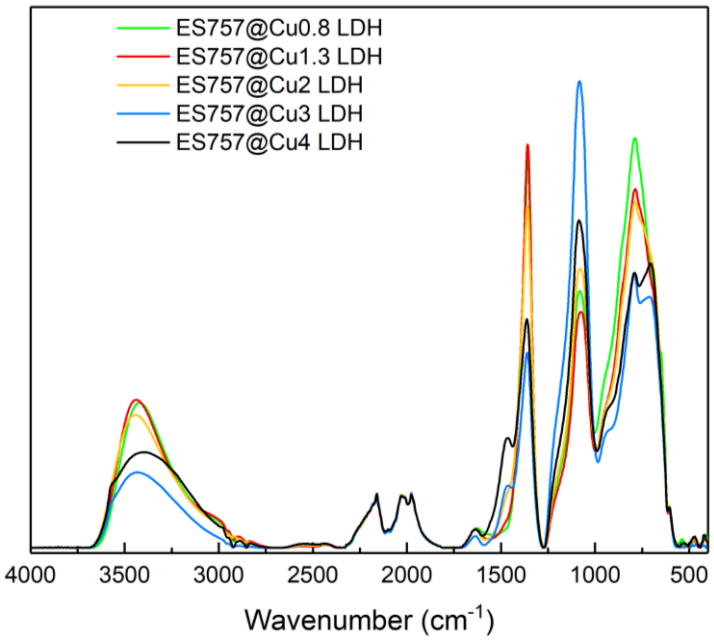


Figure B19 FTIR spectra of ES757@Cu_xZnAl-LDH.

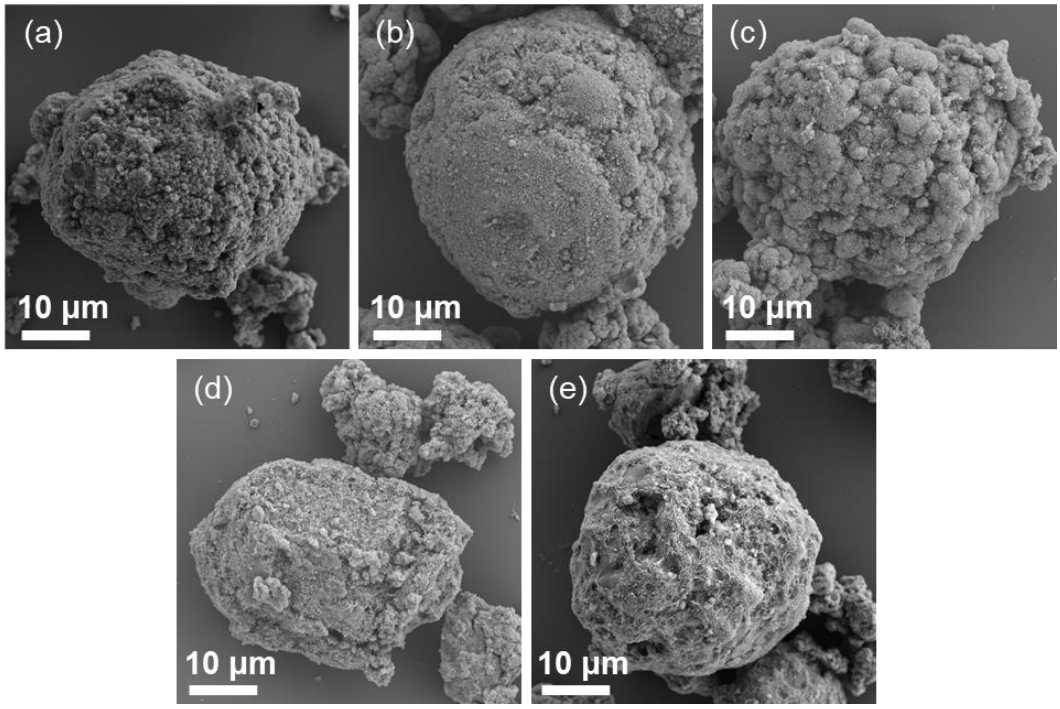


Figure B20 HR-SEM images of (a) ES757@$Cu_{0.8}$ZnAl-LDH, (b) ES757@$Cu_{1.3}$ZnAl-LDH, (c) ES757@Cu_2ZnAl-LDH, (d) ES757@Cu_3ZnAl-LDH and (e) ES757@Cu_4ZnAl-LDH.

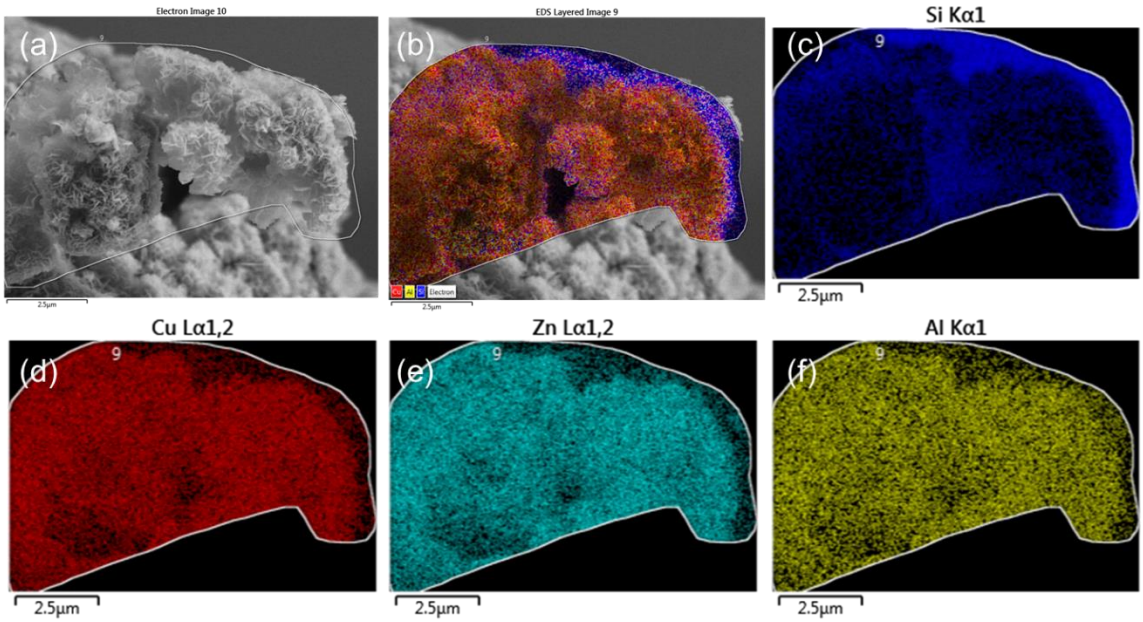


Figure B21 (a) Electron image, (b) elemental mapping layered image, (c)–(f) Si, Cu, Zn and Al mapping of ES757@$Cu_{0.8}$ZnAl-LDH.

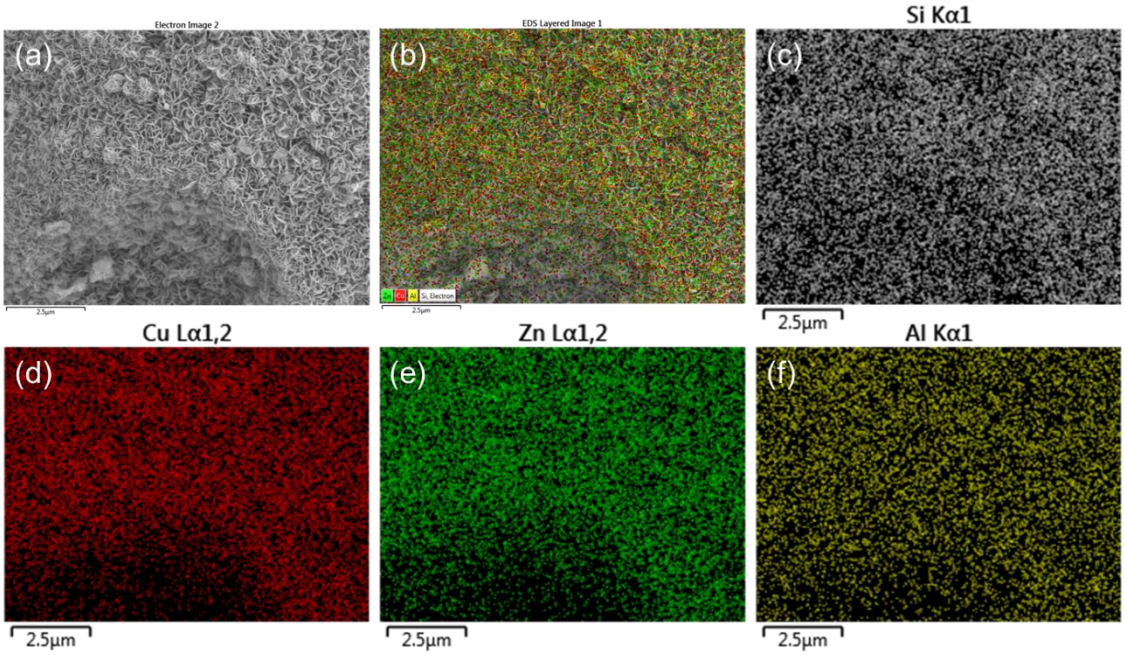


Figure B22 (a) Electron image, (b) elemental mapping layered image, (c)–(f) Si, Cu, Zn and Al mapping of ES757@$Cu_{1.3}$ZnAl-LDH.

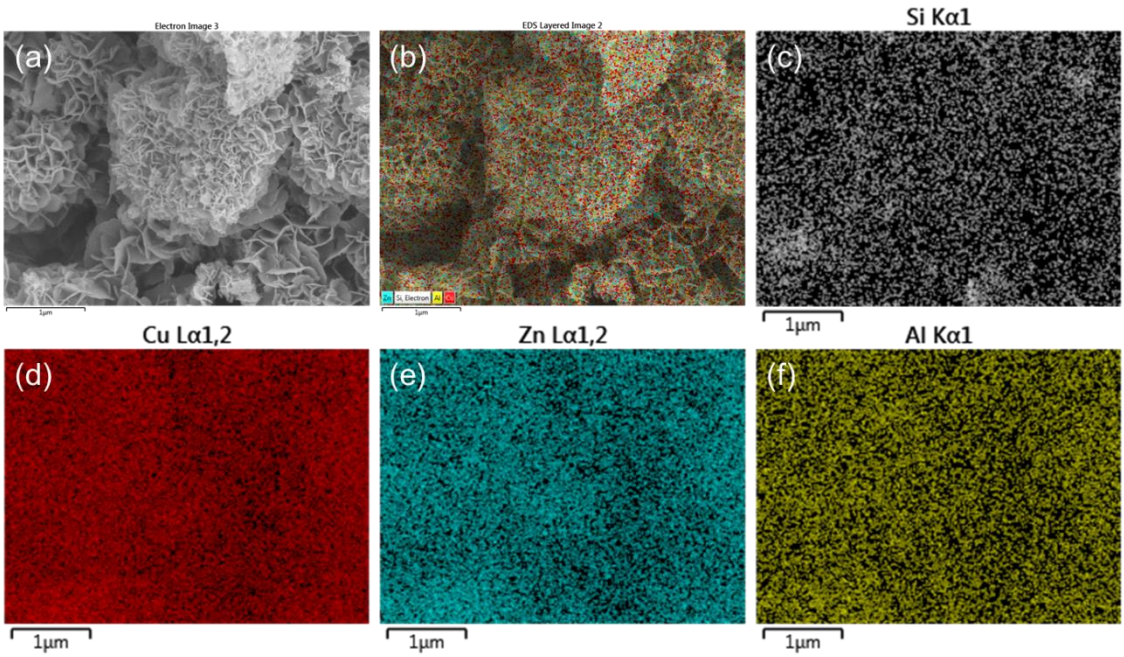


Figure B23 (a) Electron image, (b) elemental mapping layered image, (c)–(f) Si, Cu, Zn and Al mapping of ES757@Cu_2ZnAl-LDH.

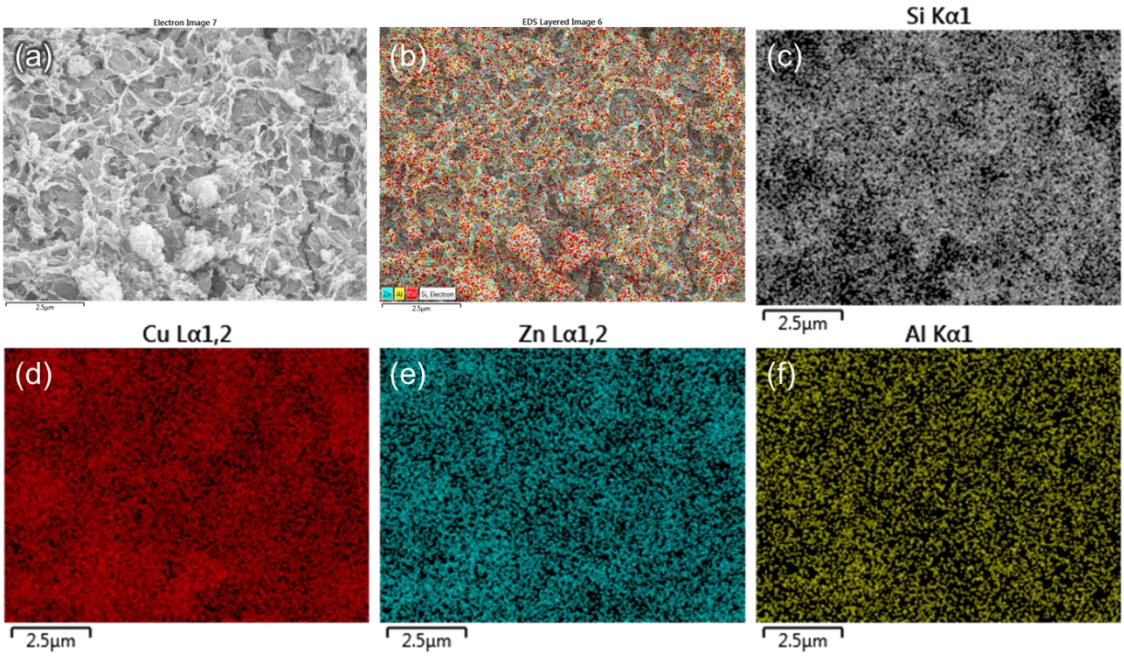


Figure B24 (a) Electron image, (b) elemental mapping layered image, (c)–(f) Si, Cu, Zn and Al mapping of ES757@Cu_4ZnAl-LDH.

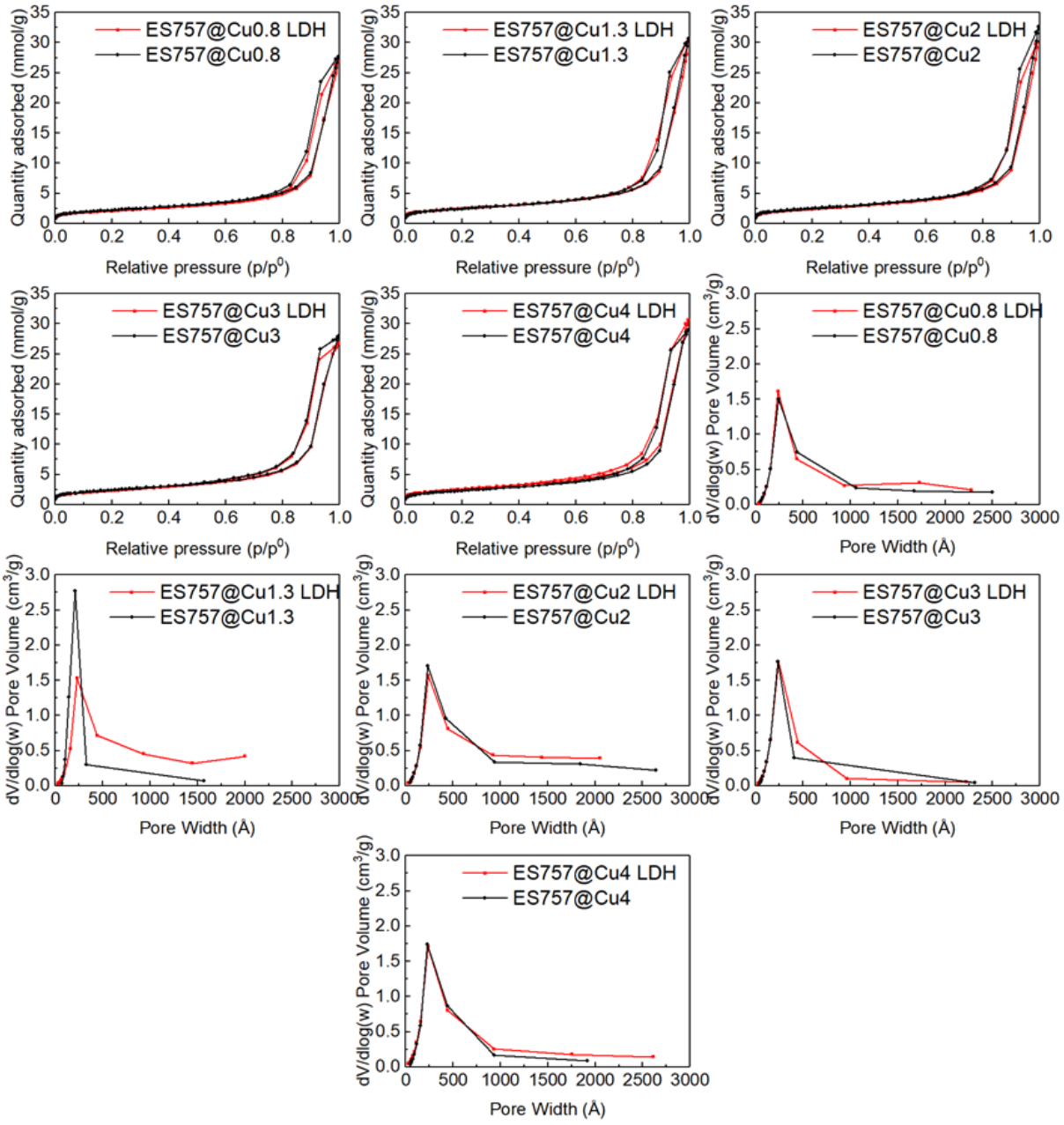


Figure B25 N_2 adsorption and desorption isotherm and BJH pore size distribution of ES757@Cu_xZnAl-LDH and derived ES757@Cu_xZnAl catalysts.

B.3. Synthesis and characterisation of mesoporous $mSiO_2$@Cu_2ZnAl-CO_3-LDH

Table B11 Details of Rietveld Refinement and structural parameters for $mSiO_2$@Cu_2ZnAl-LDH

Sample	$mSiO_2$@Cu_2ZnAl-LDH			
Core	SBA-15	SBA-16	MCM-41	MCM-48
Phase component	LDH			
Space group	R-3m			
R_{wp} /%	4.25917045	5.46769182	4.16066821	4.38050052
GOF (goodness of fit)	3.04987212	3.9627185	3.01306688	3.15042006
a (=b) /Å	3.073(2)	3.108(7)	3.133(5)	3.057(7)
c /Å	22.565(24)	23.450(121)	23.484(90)	22.123(94)
d_{003}/Å	7.521721	7.81664	7.827898	7.374398
d_{110}/ Å	1.536344	1.554136	1.566454	1.528659
Phase	Montmorillonite			
Space group	C12/m1			
a /Å	N/A	6.997(207)	6.869(66)	7.054(164)
b /Å	N/A	9.987(404)	9.147(103)	10.195(245)
C /Å	N/A	9.530(136)	10.747(73)	9.232(101)
α	N/A	90		
β	N/A	99.69		
γ	N/A	90		

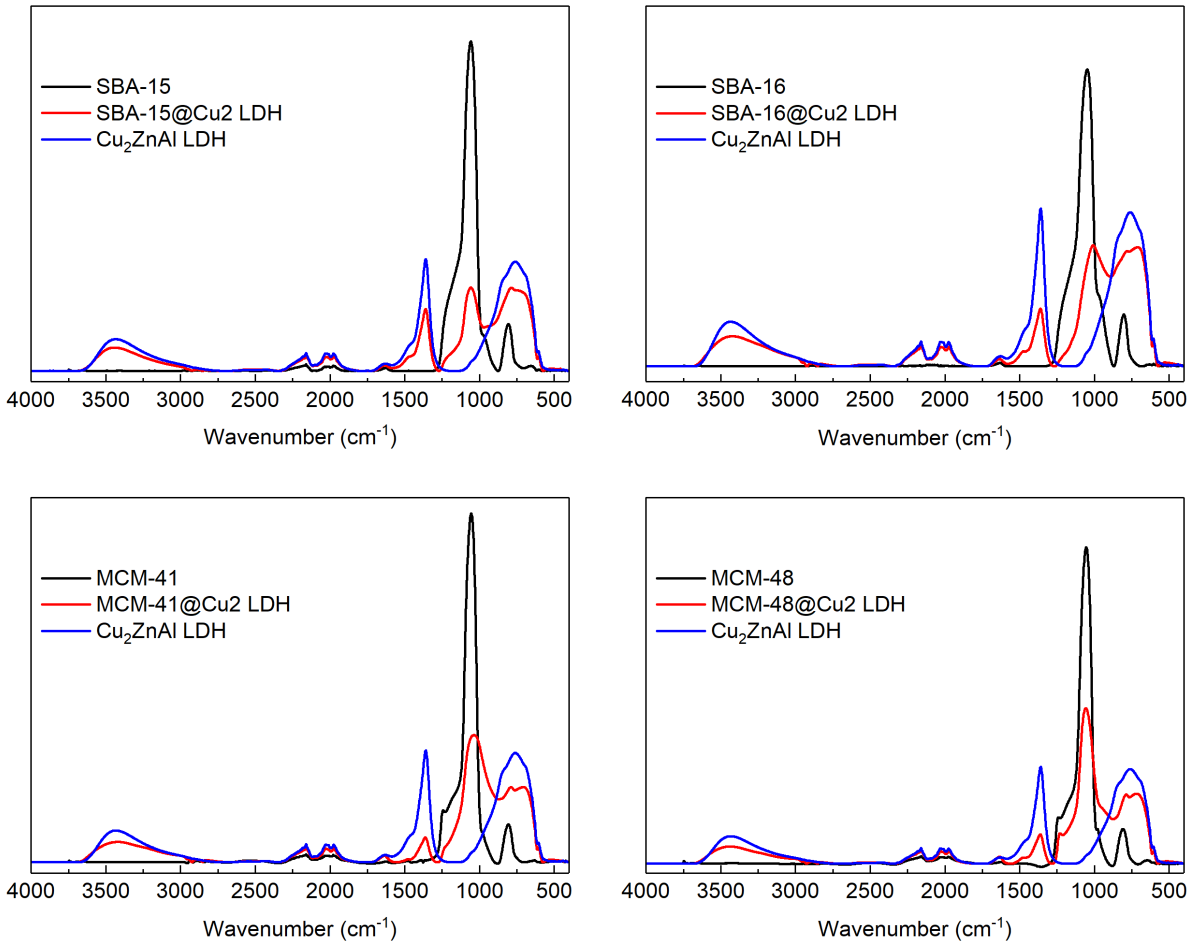


Figure B26 FTIR spectra of SBA-15, SBA-16, MCM-41, MCM-48, their corresponding $mSiO_2$@Cu_2ZnAl-LDH composites and Cu_2ZnAl-LDH.

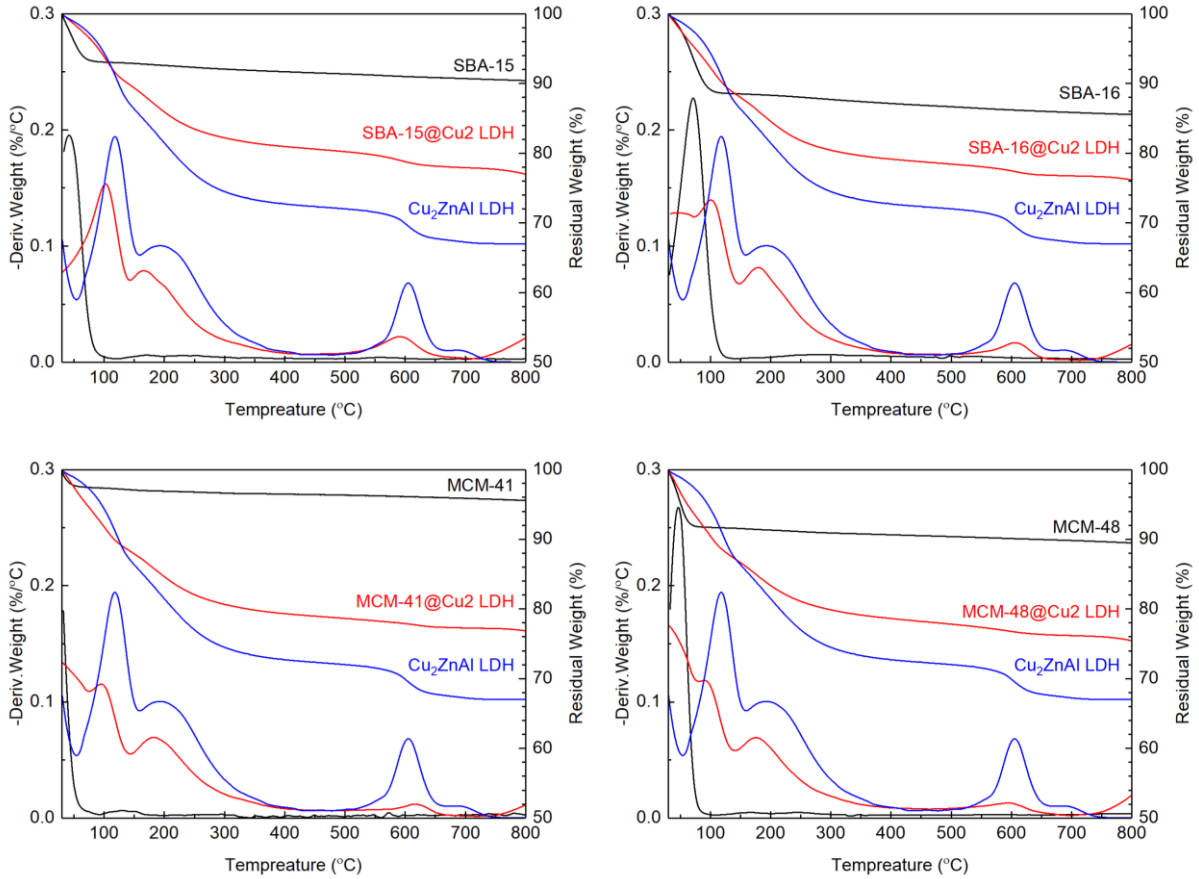


Figure B27 TGA and -dTG of SBA-15, SBA-16, MCM-41, MCM-48, their corresponding SiO_2@Cu_2ZnAl-LDH core-shells and Cu_2ZnAl-LDH.

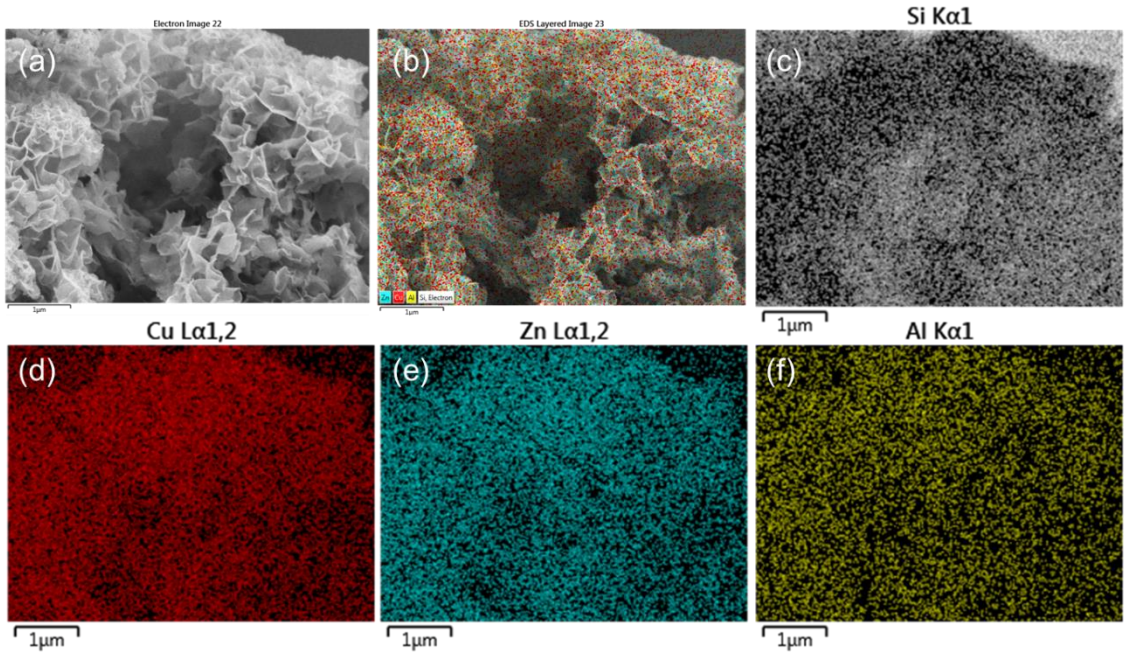


Figure B.28 (a) Electron image, (b) elemental mapping layered image, (c)–(f) Si, Cu, Zn and Al mapping of SBA-15@Cu_2ZnAl-LDH

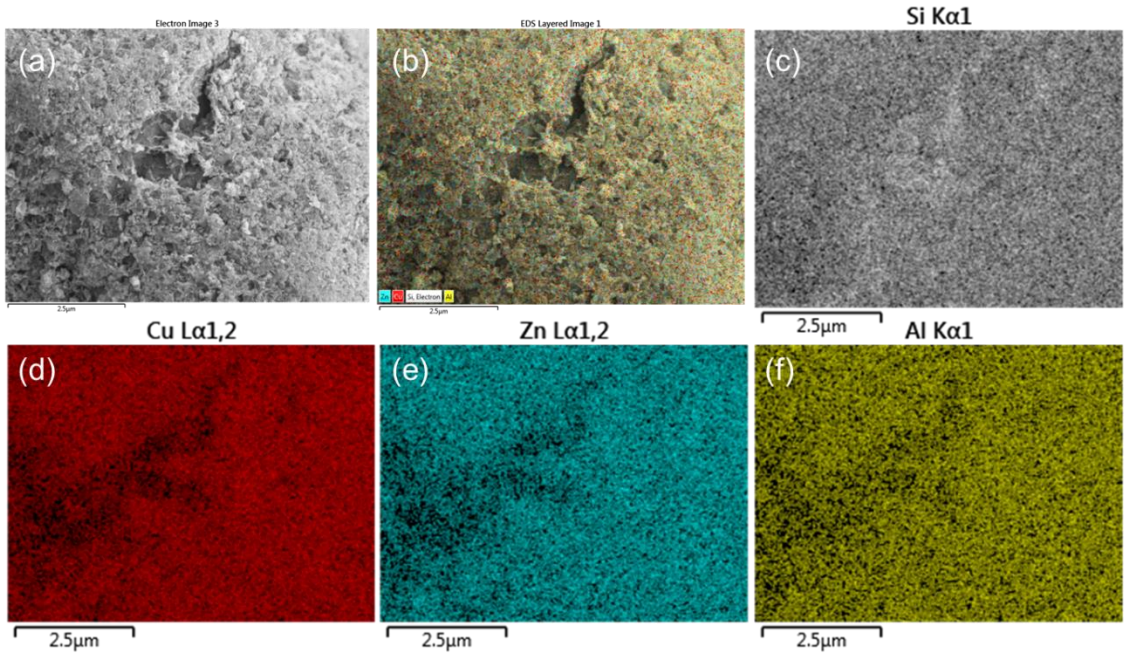


Figure B29 (a) Electron image, (b) elemental mapping layered image, (c)–(f) Si, Cu, Zn and Al mapping of SBA-16@Cu_2ZnAl-LDH.

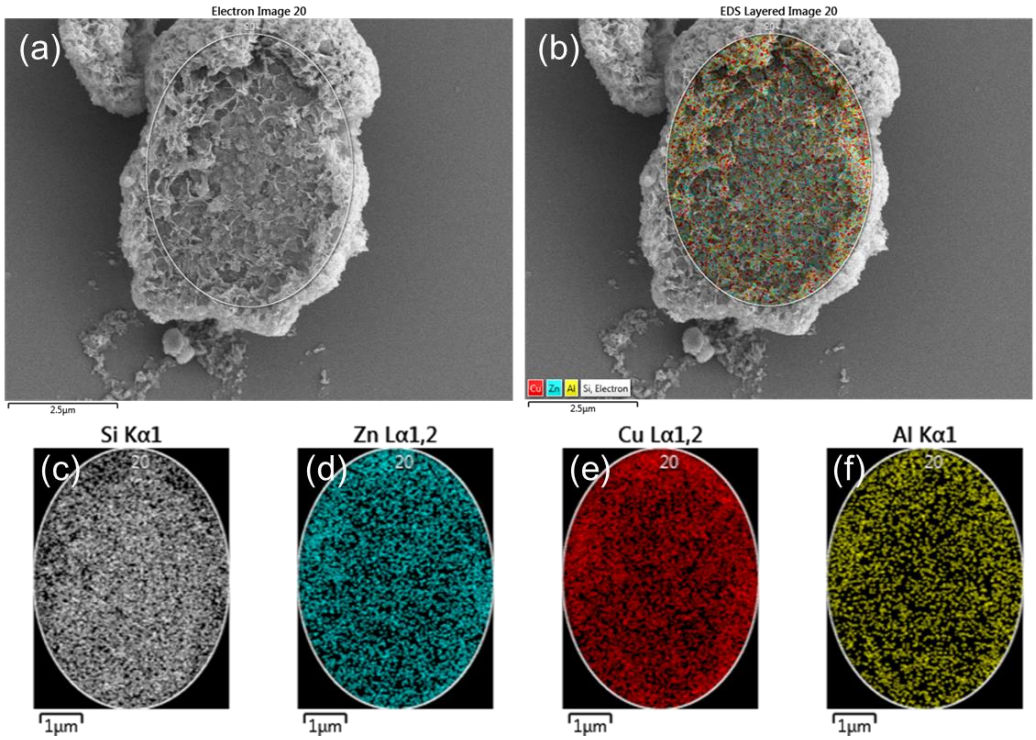


Figure B30 (a) Electron image, (b) elemental mapping layered image, (c)–(f) Si, Cu, Zn and Al mapping of MCM-41@Cu_2ZnAl-LDH.

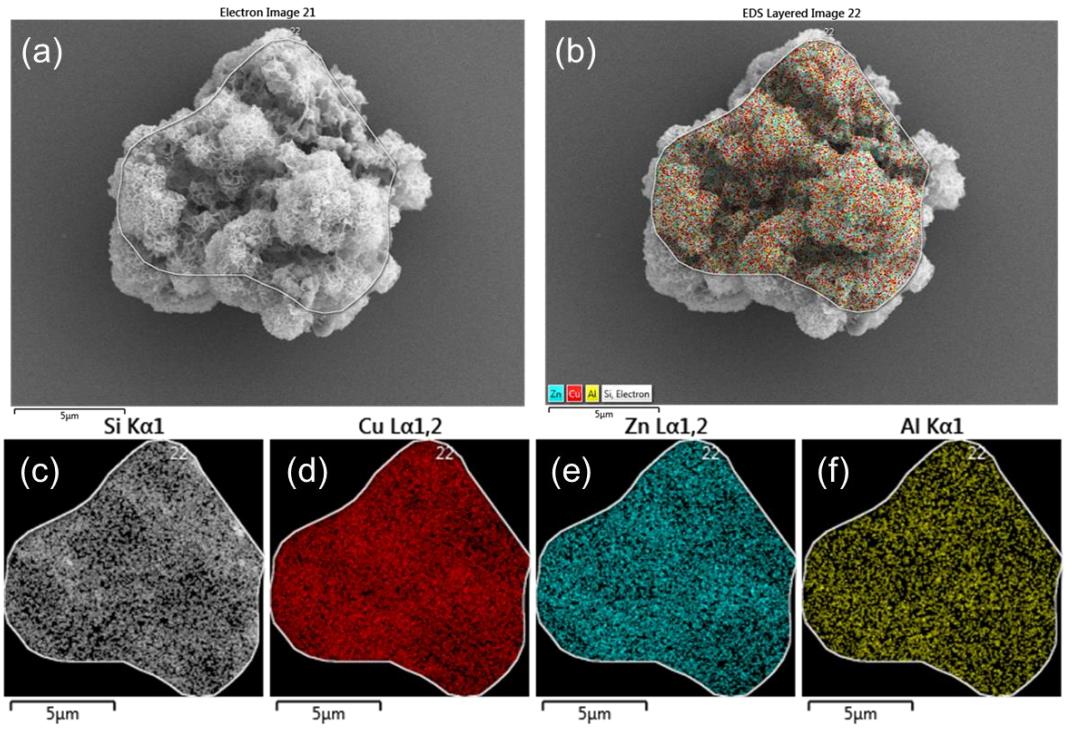


Figure B31 (a) Electron image, (b) elemental mapping layered image, (c)–(f) Si, Cu, Zn and Al mapping of MCM-48@Cu_2ZnAl-LDH.

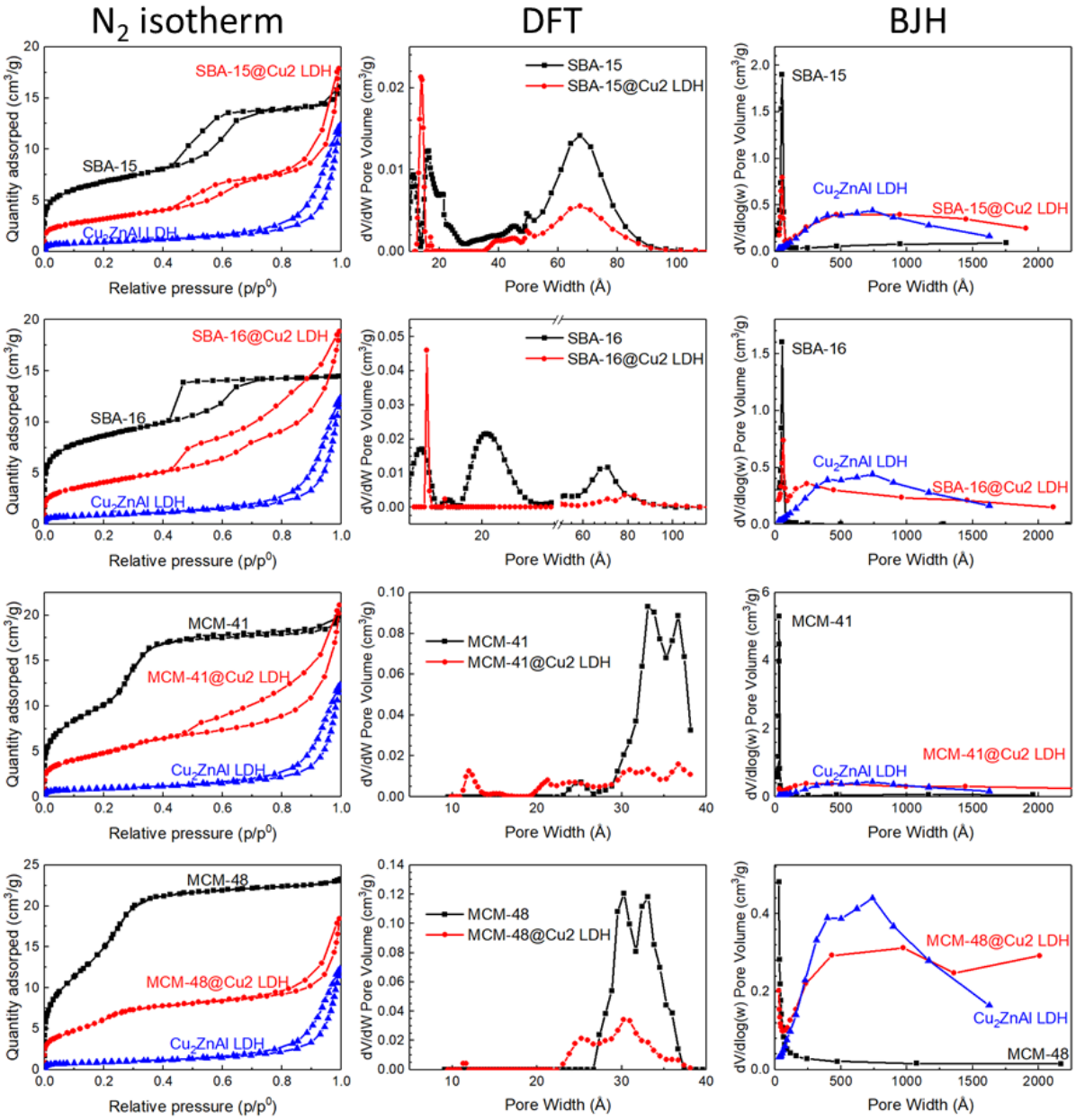


Figure B32 The N_2 adsorption and desorption isotherm, DFT pore size distribution based on the kernel of metal oxide with cylinder pore and BJH pore size distribution for $mSiO_2$@Cu_2ZnAl-LDH.

B.4. Reference

1 F. Cavani, F. Trifirò and A. Vaccari, *Catal. Today*, 1991, **11**, 173–301.

2 D. G. Evans and R. C. T. Slade, in *Layered Double Hydroxides (Structure and bonding)*, eds. D. G. Evans and X. Duan, Springer-Verlag, Berlin/Heidelberg, 1st edn., 2006, vol. 119, pp. 1–87.

Appendix C. Appendix for Chapter 4

C.1.Characterisation of ES757@Cu$_x$ZnAl-LDO

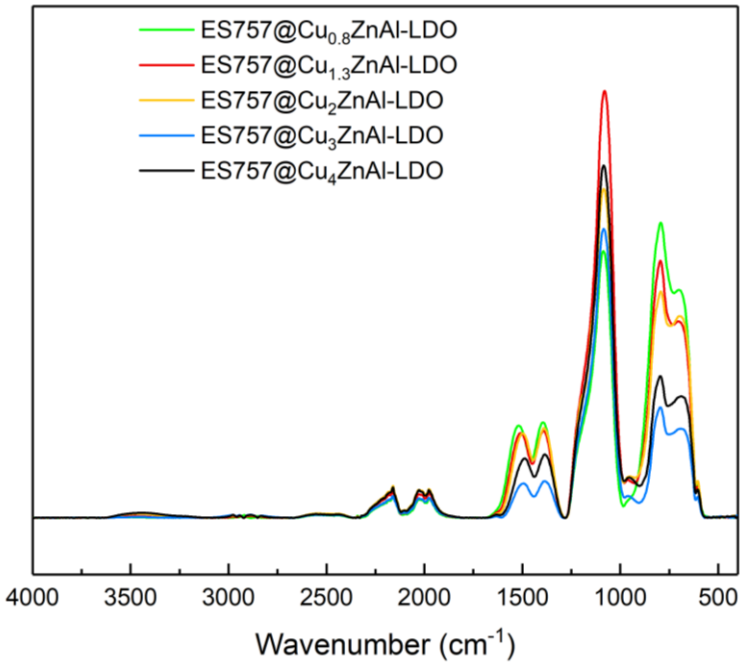


Figure C.1 FTIR spectra of ES757@Cu$_x$ZnAl-LDO.

C.2.Characterisation of ES757@Cu$_x$ZnAl catalysts

Table C.1 Details of Rietveld Refinement and structural parameters for ES757@Cu$_x$ZnAl.

Sample	ES757@Cu$_x$ZnAl				
Cu/Al ratio	0.8	1.3	2	3	4
Phase component	Cu				
Space group	Fm3m				
R_{wp}/%	2.99407622	3.02101171	3.11623335	2.29196874	2.5296537
GOF (goodness of fit)	1.05699513	1.10550662	1.09643339	1.06184398	1.09483174
a (=*b*=*c*) /Å	3.615(1)				
D/nm	1.2435	1.8283	2.2431	5.7982	5.7334

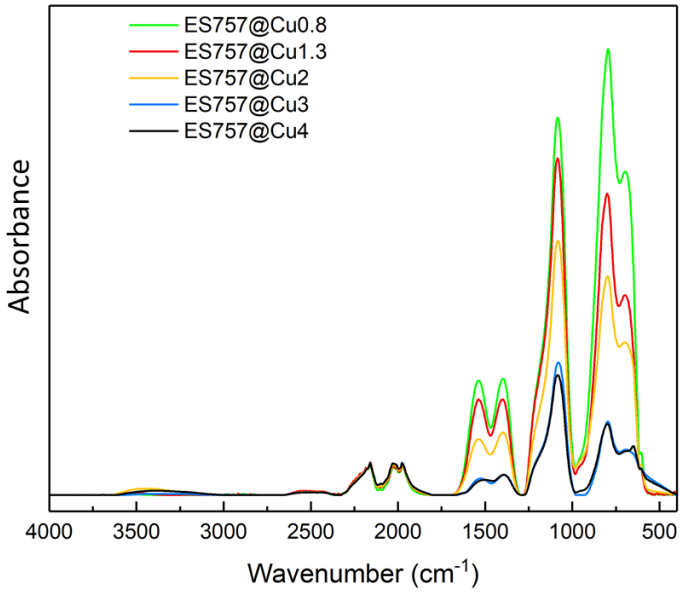


Figure C.2 FTIR spectra of ES757@Cu$_x$ZnAl.

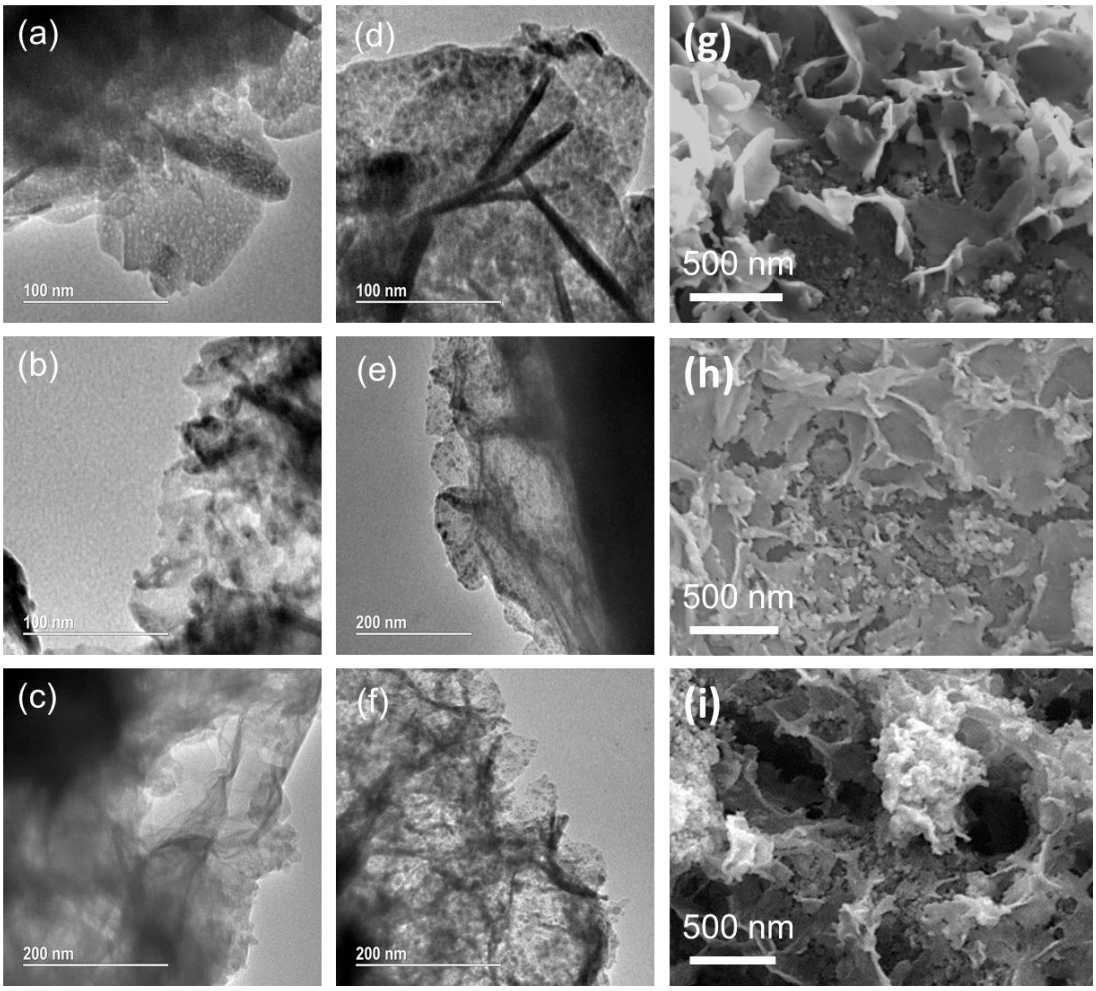


Figure C.3 TEM images of (a) ES757@Cu$_{0.8}$ZnAl-LDO, (b) ES757@Cu$_3$ZnAl-LDO, (c) ES757@Cu$_4$ZnAl-LDO, (d) ES757@Cu$_{0.8}$ZnAl, (e) ES757@Cu$_3$ZnAl and (f) ES757@Cu$_4$ZnAl. HR-SEM images showing the shell of (g) ES757@Cu$_{0.8}$ZnAl, (h) ES757@Cu$_3$ZnAl and (i) ES757@Cu$_4$ZnAl.

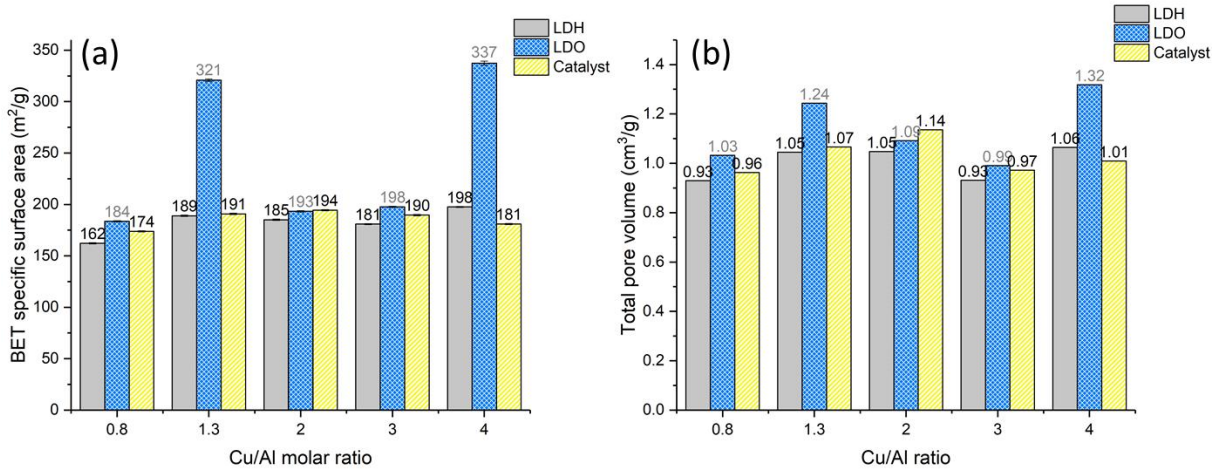


Figure C.4 (a) The BET specific surface area and (b) the total pore volume of ES757@Cu$_x$ZnAl-LDH, ES757@Cu$_x$ZnAl-LDO and ES757@Cu$_x$ZnAl catalyst, where x = Cu/Al ratio. The extreme high BET specific surface area and total pore volume that are observed in ES757@Cu$_{1.3}$ZnAl-LDO and ES757@Cu$_4$ZnAl-LDO should be due to instrument error.

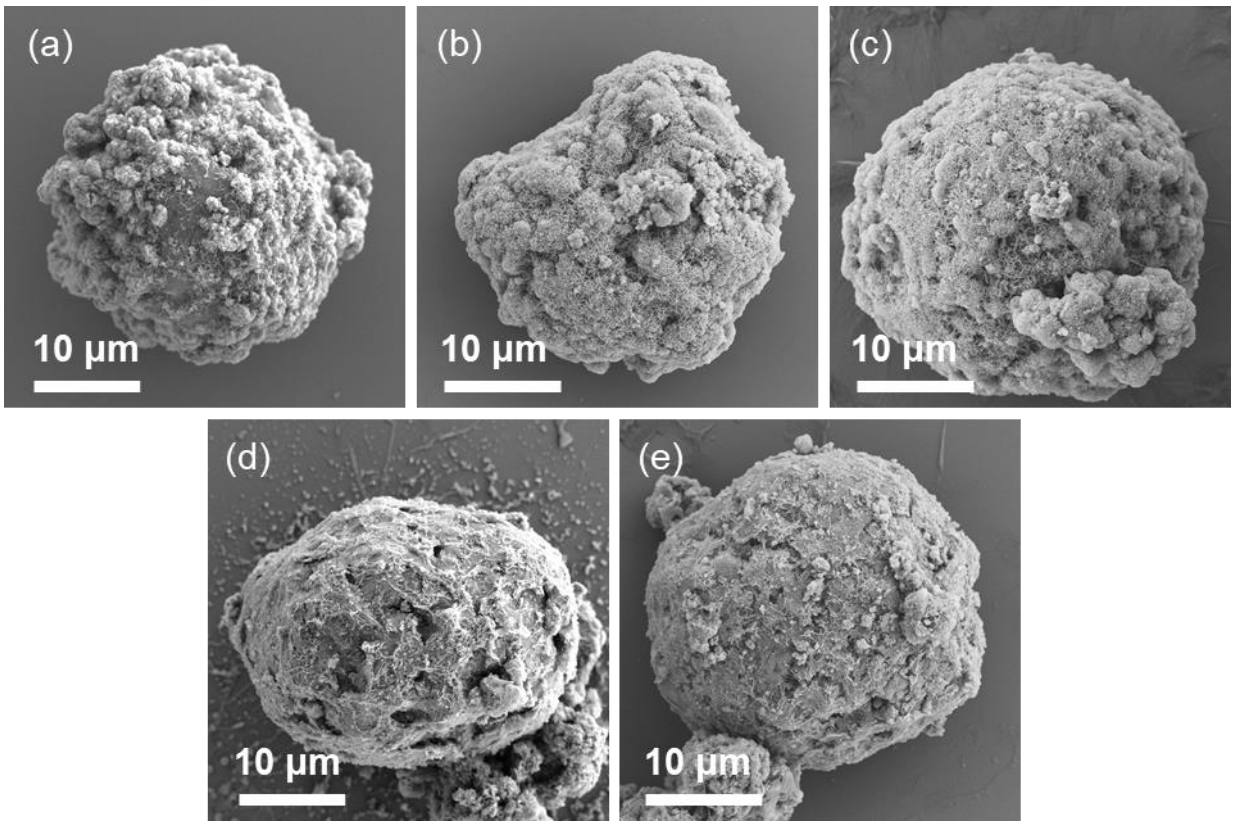


Figure C.5 HR-SEM images of (a) ES757@Cu$_{0.8}$ZnAl, (b) ES757@Cu$_{1.3}$ZnAl, (c) ES757@Cu$_2$ZnAl, (d) ES757@Cu$_3$ZnAl and (e) ES757@Cu$_4$ZnAl.

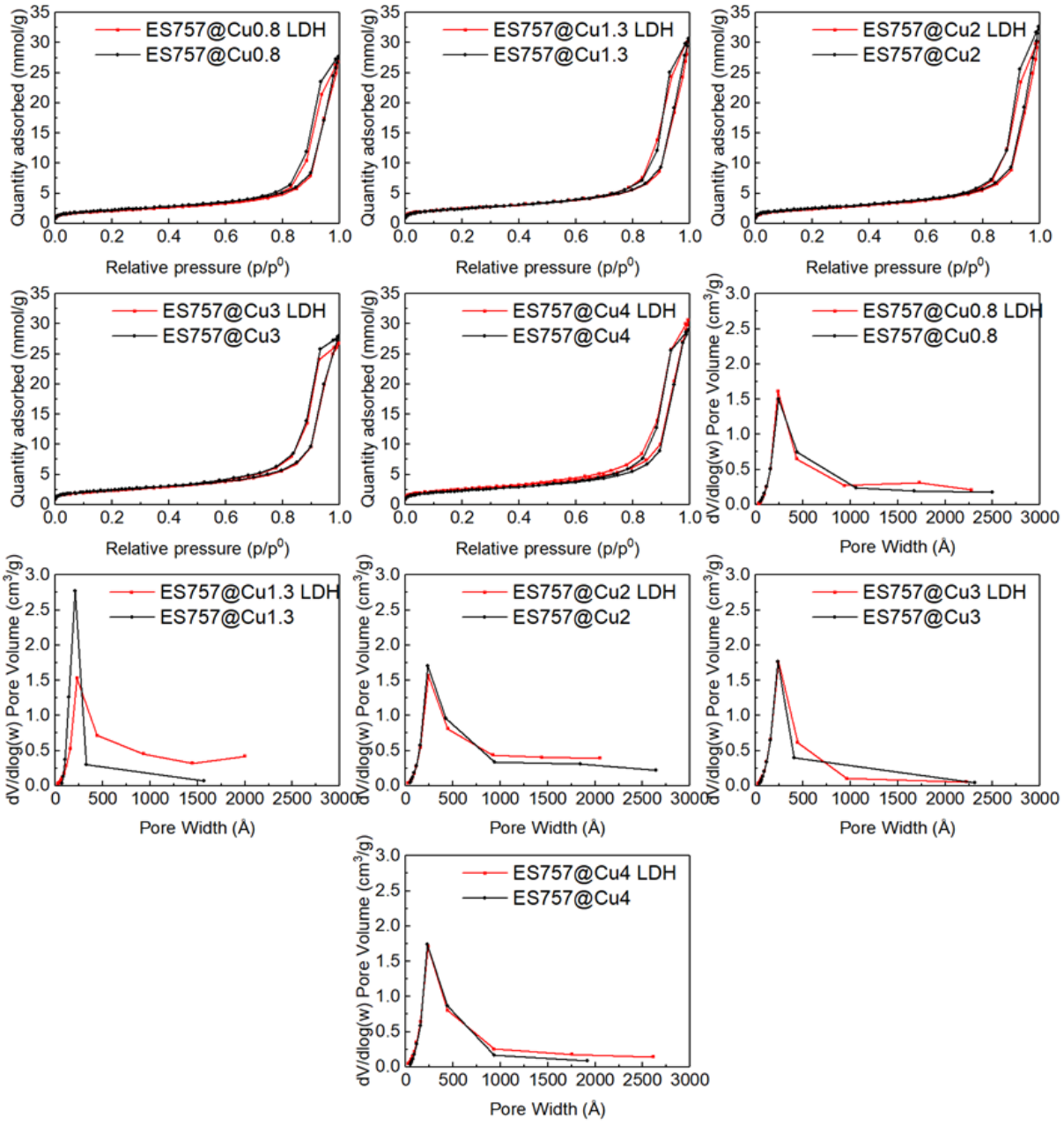


Figure C.6 N_2 adsorption and desorption isotherm and BJH pore size distribution of ES757@Cu_xZnAl-LDH and derived ES757@Cu_xZnAl catalysts.

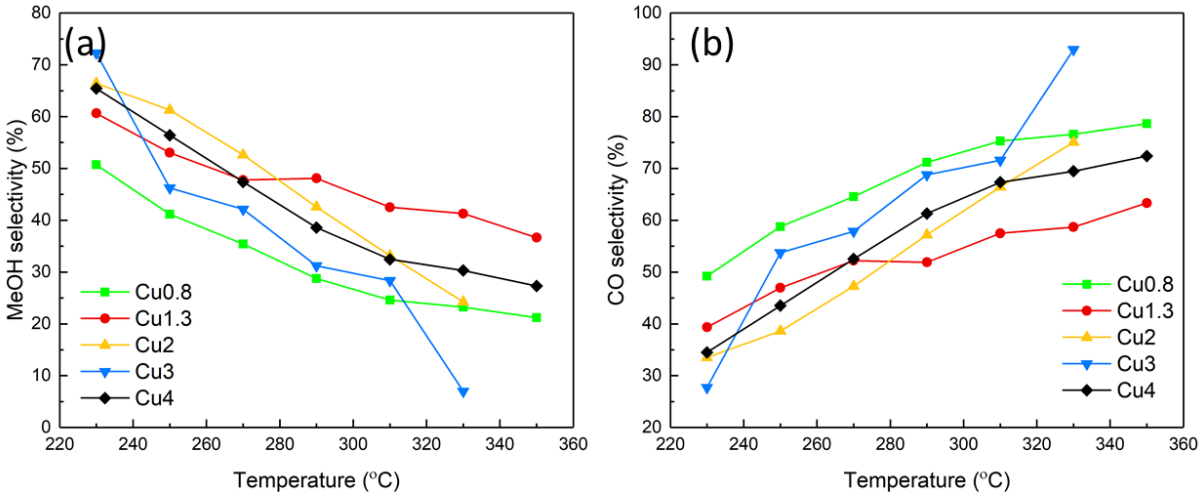


Figure C.7 (a) the MeOH selectivity and (b) the CO selectivity of ES757@Cu$_x$ZnAl in CO_2 hydrogenation to methanol.

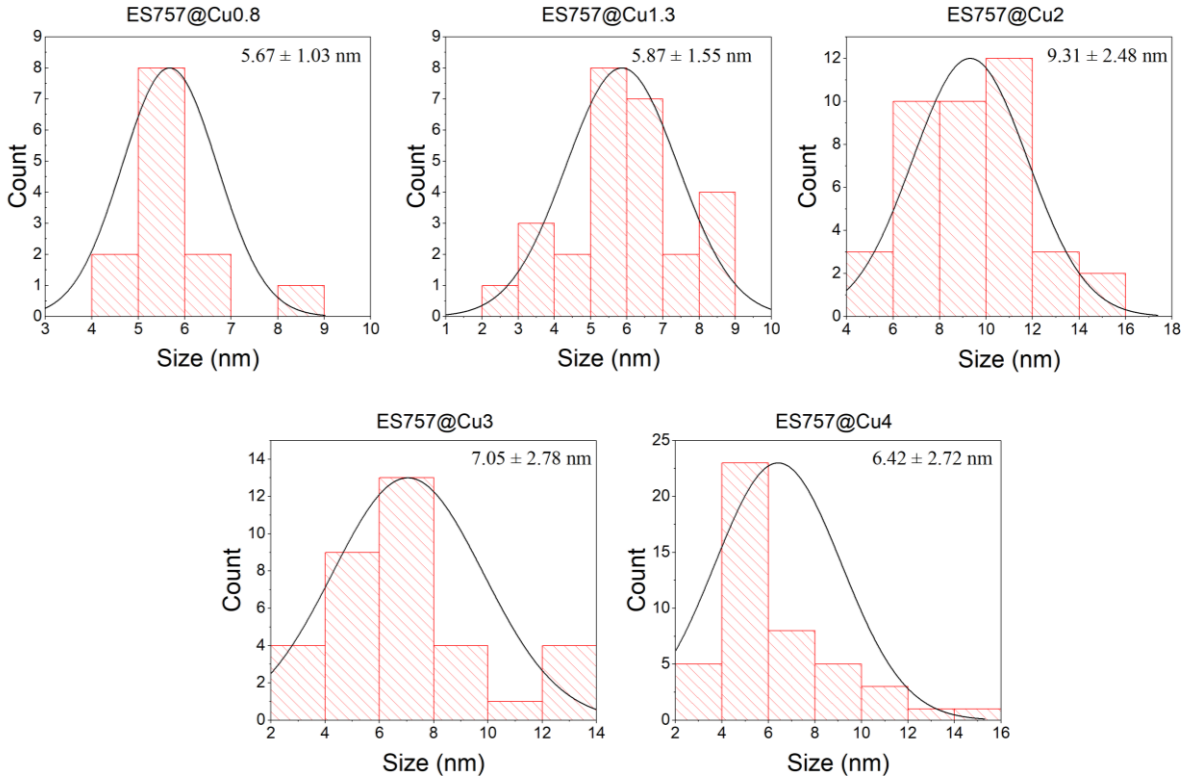


Figure C.8 The particle size distribution of spherical species in ES757@Cu$_x$ZnAl catalyst obtained from TEM images.

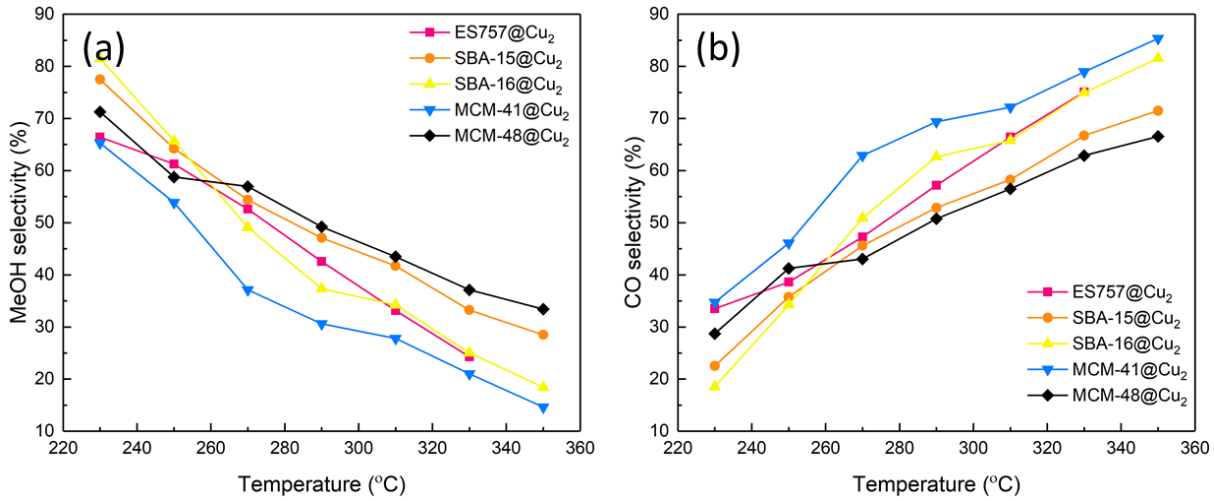


Figure C.9 (a) the MeOH selectivity and (b) the CO selectivity of $mSiO_2@Cu_2ZnAl$ in CO_2 hydrogenation to methanol.

C.3.Reference

1 G. V. Sagar, P. V. R. Rao, C. S. Srikanth and K. V. R. Chary, *J. Phys. Chem. B*, 2006, **110**, 13881–13888.

2 D. S. Brands, E. K. Poels, T. A. Krieger, O. V. Makarova, C. Weber, S. Veer and A. Bliek, *Catal. Letters*, 1996, **36**, 175–181.

3 W. R. A. M. Robinson and J. C. Mol, *Appl. Catal.*, 1990, **63**, 165–179.

Appendix D. Appendix for Chapter 5

D.1. Synthesis and characterisation of ZSM-5@$Cu_{1.3}$ZnAl LDH

Table D.1 Details of Pawley refinement for $Cu_{1.3}$ZnAl-LDH, ZSM@$Cu_{1.3}$ZnAl-LDH and H-ZSM-5.

Sample name	$Cu_{1.3}$ZnAl LDH	ZSM@$Cu_{1.3}$ZnAl-LDH	H-ZSM-5
R_{wp} /%	3.14594308	4.50873362	5.88927091
GOF (goodness of fit)	2.48615704	3.23044229	3.13841476
Phase component	LDH	LDH	
Space group	R-3m	R-3m	
a (=*b*) /Å	3.079(0)	3.077(0)	
c /Å	22.780(3)	22.725(2)	
Phase component		Zeolite	Zeolite
Space group		Pnma	Pnma
a/Å		20.172(2)	20.107(2)
b/Å		19.965(2)	19.879(1)
c/Å		13.454(2)	13.369(1)
$\alpha = \beta = \gamma$		90	90

Table D.2 The expected (value calculated from chemical formula), detected elemental composition of H-ZSM-5, ZSM@$Cu_{1.3}$ZnAl-LDH, $Cu_{1.3}$ZnAl-LDH and ZSM@$Cu_{1.3}$ZnAl-LDH-10mM and deviations between them.

Samples		H-ZSM-5	ZSM@$Cu_{1.3}$ZnAl-LDH	ZSM@$Cu_{1.3}$ZnAl-LDH-10mM	$Cu_{1.3}$ZnAl-LDH
Cu	Exp	N/A	13.14	13.16	23.50
	Real	N/A	12.58	12.59	22.63
	Δ	N/A	-0.56	-0.56	-0.86
Zn	Exp	N/A	9.97	9.99	17.83
	Real	N/A	9.56	9.26	17.18
	Δ	N/A	-0.42	-0.72	-0.66
Al	Exp	1.76	4.50	4.50	6.66
	Real	0.62	3.98	3.92	6.41
	Δ	-1.15	-0.51	-0.59	-0.24
C	Exp	0.00	1.15	1.15	2.05
	Real	0.47	1.22	1.18	1.98
	Δ	0.47	0.07	0.03	-0.08

H	Exp	0.79	1.99	2.10	3.14
	Real	1.25	2.03	2.10	3.05
	Δ	0.46	0.04	0.02	-0.09
N	Exp	0.91	0.00	0.40	N/A
	Real	1.62	0.06	0.16	N/A
	Δ	0.70	0.06	-0.24	N/A
Na	Exp	0	0.66	0.00	N/A
	Real	0.47	4.11	0.82	N/A
	Δ	0.47	3.45	0.82	N/A
Si	Exp	42.19	18.54	18.56	N/A
	Real	0.41	0.00	0.00	N/A
	Δ	-41.79	-18.54	-18.56	N/A

Table D.3 Silicon environment in H-ZSM-5 and ZSM@$Cu_{1.3}$ZnAl-LDH from ^{29}Si solid-state NMR spectroscopy.

Assignment	H-ZSM-5		ZSM@$Cu_{1.3}$ZnAl-LDH	
	δ (ppm)	I (%)	δ (ppm)	I (%)
$Si(OSi)_3(OAl)_1$ and $Si(OSi)_3(OH)_1$	-104.71	25.41	-105.30	38.77
$Si(OSi)_4$	-111.33	74.59	-111.42	61.24

Equation D.1 Loewenstein's rule equation.[1–4]

$$\frac{Si}{Al} = \frac{\sum_{x=0}^{4} I_{Si(OAl)_x}}{0.25 \sum_{x=0}^{4} x I_{Si(OAl)_x}}$$

Table D.4 Aluminium environment in H-ZSM-5, ZSM@$Cu_{1.3}$ZnAl-LDH and $Cu_{1.3}$ZnAl-LDH from ^{27}Al solid-state NMR spectroscopy.

Assignment	Pristine ZSM-5		ZSM@$Cu_{1.3}$ZnAl-LDH		$Cu_{1.3}$ZnAl-LDH	
	δ_{iso} (ppm)	I (%)	δ_{iso} (ppm)	I (%)	δ_{iso} (ppm)	I (%)
Al_1	56.35	100	55.96			
Al_2			13.66	16.47	9.66	7.66
Al_3			−86.65	45.05	−88.79	35.47
Al_4			−195.78	38.48	−199.89	56.87

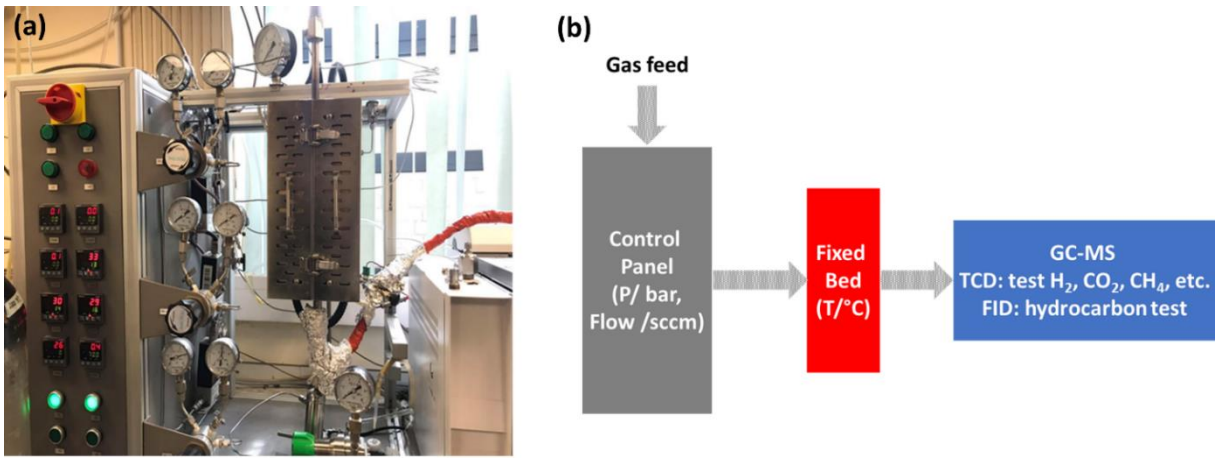


Figure D.1 (a) The picture of the gas input control panel ad tubular fixed bed and (b) The illustration of the experimental setup.

D.2. Post-treatment with ammonium salts

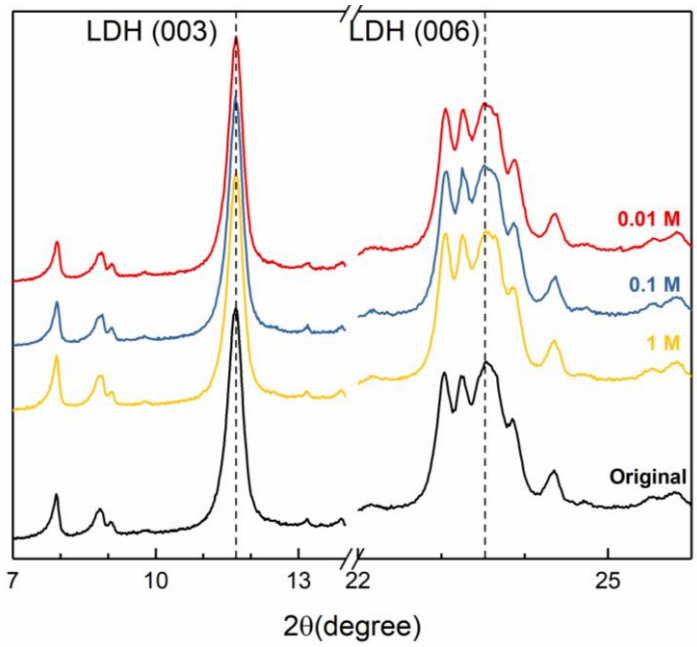


Figure D.2 Section of XRD of original, 1M, 100 mM and 10 mM NH_4HCO_3 treated ZSM@$Cu_{1.3}$ZnAl-LDH.

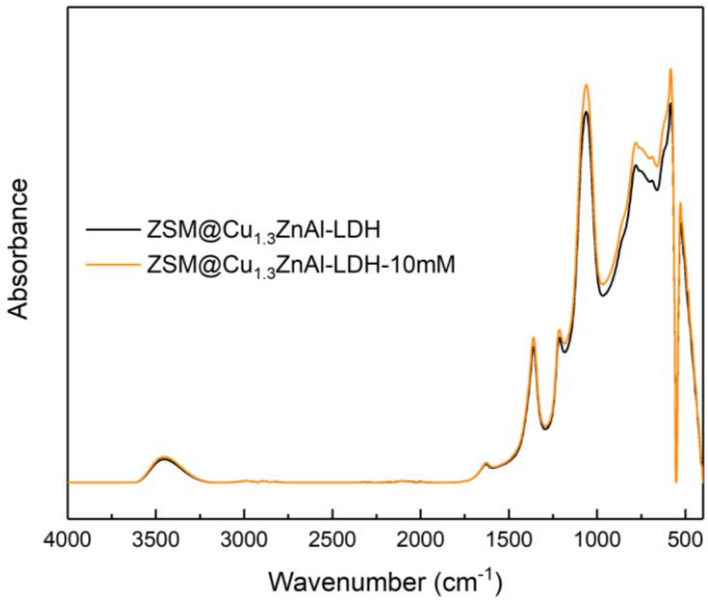


Figure D.3 FTIR spectra of ZSM@$Cu_{1.3}$ZnAl-LDH and ZSM@$Cu_{1.3}$ZnAl-LDH-10mM.

D.3. Homogeneous precipitation

Table D.5 An overview of CuZnAl LDH and MgAl LDH synthesis via homogeneous precipitation.

Entry	Cu/Zn/Al ratio	Urea/Al	Temperature	Time	Ref
1	1/1/1	6	100	3 days	[5]
2	Unknown	10	100	24 h	[6]
3	0.52/1.3/1	10	90	24 h	[7]
4	3 (Mg)/1*	20	105	18 h	[8]

*: MgAl LDH

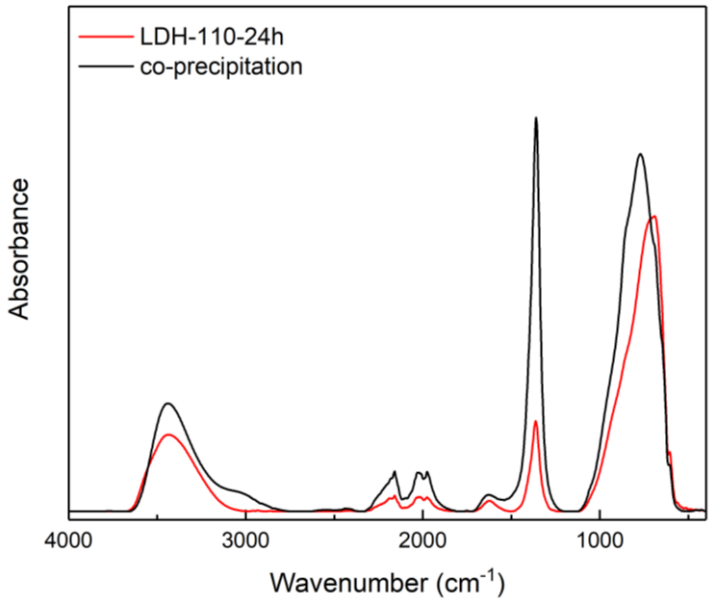


Figure D.4 FTIR spectra of $Cu_{1.3}$ZnAl-LDH prepared from homogeneous precipitation (at 110 °C for 24 h with urea/Al = 10) and from co-precipitation method.

D.4. Co-precipitation with organic base

Table D.6 Details of Pawley refinement for $Cu_{1.3}$ZnAl-LDH-TPA and ZSM@$Cu_{1.3}$ZnAl-LDH-TPA.

Sample name	$Cu_{1.3}$ZnAl-LDH-TPA	ZSM@ $Cu_{1.3}$ZnAl-LDH-TPA
R_{wp} /%	7.53887237	7.96290067
GOF (goodness of fit)	5.81382894	5.2889654
Phase component	LDH	LDH
Space group	R-3m	R-3m
a (=*b*) /Å	3.074(1)	3.071(1)
c /Å	22.739(25)	22.742(4)
Phase component		Zeolite
Space group		Pnma
a/Å		20.167(4)
b/Å		19.968(3)
c/Å		13.450(3)
$\alpha = \beta = \gamma$		90

Table D.7 The d-spacing and crystallite size of $Cu_{1.3}$ZnAl LDH, ZSM@$Cu_{1.3}$ZnAl-LDH, H-ZSM-5 and MCM-48@$Cu_{1.3}$ZnAl-LDH-pH10 obtained from the single-phase Pawley refinement.

Entry	Sample	d_{003} (Å)	d_{110} (Å)	D_{00l} (nm)[a]	D_{110} (nm)[a]	$D_{zeolite}$ (nm)[b]
1	$Cu_{1.3}$ZnAl-LDH	7.59	1.54	12.48	9.86	–
2	$Cu_{1.3}$ZnAl-LDH-TPA	7.58	1.54	5.35	6.63	–
3	ZSM@$Cu_{1.3}$ZnAl-LDH	7.57	1.54	14.71	12.33	48.0
4	ZSM@$Cu_{1.3}$ZnAl-LDH-TPA	7.58	1.54	15.55	9.25	70.12

a: the crystallite size of LDH along the (00*l*) or (110) direction calculated from Rietveld refinement. b: the crystallite size of zeolite worked out from Pawley refinement.

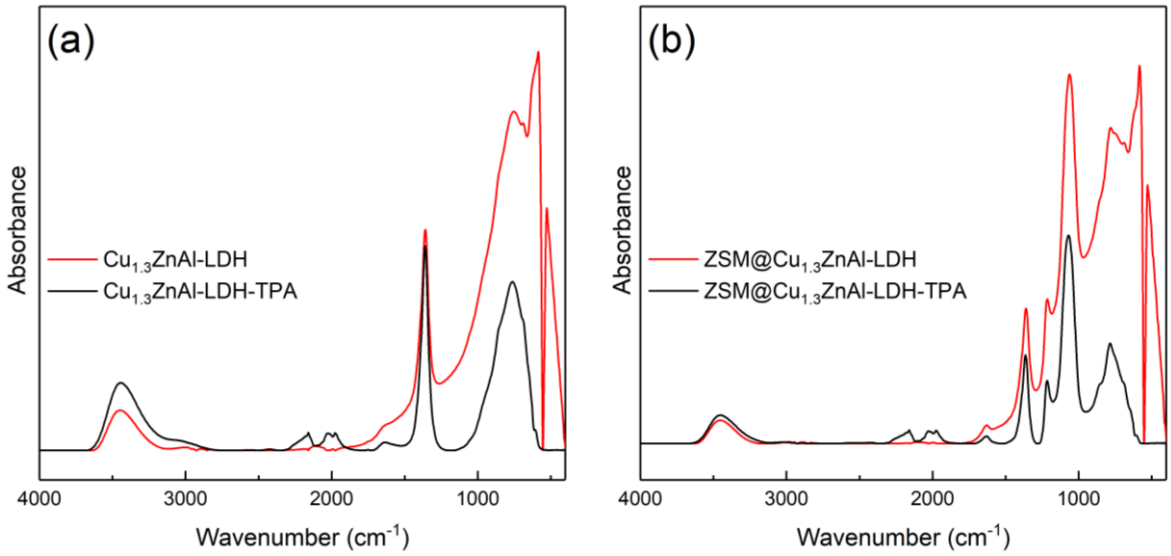


Figure D.5 FTIR spectra of (a) $Cu_{1.3}$ZnAl-LDH and $Cu_{1.3}$ZnAl-LDH-TPA and (b) ZSM@$Cu_{1.3}$ZnAl-LDH and ZSM@$Cu_{1.3}$ZnAl-LDH-TPA.

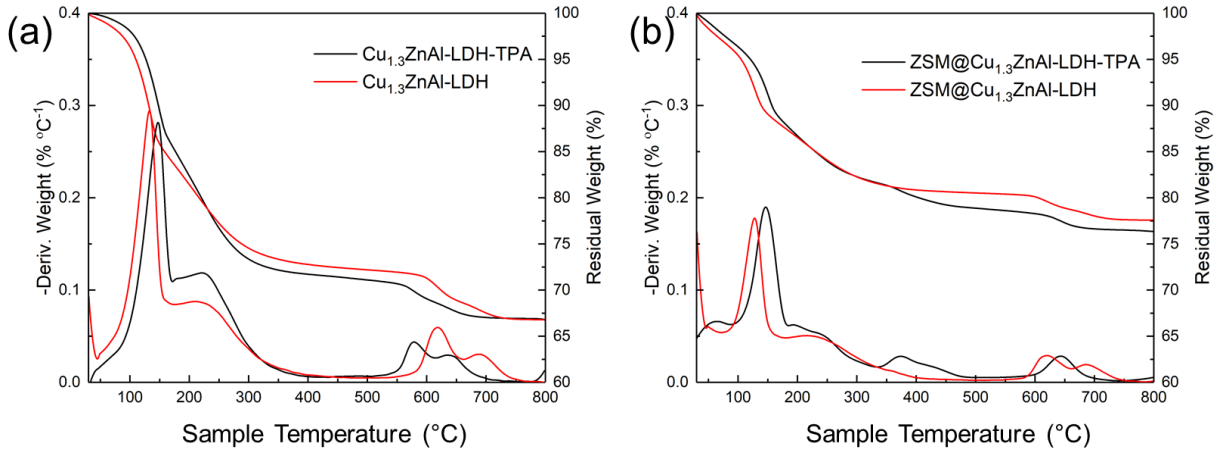


Figure D.6 TGA and derivative TG (dTG) profiles of (a) $Cu_{1.3}$ZnAl-LDH and $Cu_{1.3}$ZnAl-LDH-TPA and (b) ZSM@$Cu_{1.3}$ZnAl-LDH and ZSM@$Cu_{1.3}$ZnAl-LDH-TPA.

D.5. Reference

1 T. Liang, J. Chen, Z. Qin, J. Li, P. Wang, S. Wang, G. Wang, M. Dong, W. Fan and J. Wang, *ACS Catal.*, 2016, **6**, 7311–7325.

2 F. Dogan, K. D. Hammond, G. A. Tompsett, H. Huo, W. C. Conner, S. M. Auerbach and C. P. Grey, *J. Am. Chem. Soc.*, 2009, **131**, 11062–11079.

3 W. Loewenstein and M. Lowensterin, *Am. Mineral.*, 1954, **39**, 92–96.

4 C. A. Fyfe, Y. Feng, H. Grondey, G. T. Kokotailo and H. Gies, *Chem. Rev.*, 1991, **91**, 1525–1543.

5 M. Turco, G. Bagnasco, U. Costantino, F. Marmottini, T. Montanari, G. Ramis and G. Busca, *J. Catal.*, 2004, **228**, 43–55.

6 F. Jing, Y. Zhang, S. Luo, W. Chu and W. Qian, *Appl. Clay Sci.*, 2010, **48**, 203–207.

7 S. Murcia-Mascarós, R. M. Navarro, L. Gómez-Sainero, U. Costantino, M. Nocchetti and J. L. G. Fierro, *J. Catal.*, 2001, **198**, 338–347.

8 K. Cermelj, K. Ruengkajorn, J. C. Buffet and D. O'Hare, *J. Energy Chem.*, 2019, **35**, 88–94.